Автономная некоммерческая образовательная организация высшего образования
«Сколковский институт науки и технологий»

На правах рукописи

Ибаниес Федерико Мартин

МОДЕЛИРОВАНИЕ, УПРАВЛЕНИЕ И РЕАЛИЗАЦИЯ МНОГОПОРТОВЫХ ПРЕОБРАЗОВАТЕЛЕЙ И ИНВЕРТОРОВ ДЛЯ ИНТЕГРАЦИИ ЭЛЕКТРОМОБИЛЕЙ В ЭНЕРГОСЕТЬ

Специальность: 1.2.2. Математическое моделирование, численные методы и комплексы программ

ДИССЕРТАЦИЯ
на соискание ученой степени
доктора технических наук

Москва – 2025

Autonomous Non-Profit Organization for Higher Education
"Skolkovo Institute of Science and Technology"

As a manuscript

IBANEZ FEDERICO MARTIN

MODELING, SIMULATION AND IMPLEMENTATION OF MULTI-PORT CONVERTERS AND INVERTERS FOR INTEGRATING ELECTRIC VEHICLES IN THE UTILITY GRID

Specialty: 1.2.2. Mathematical Modeling, Numerical Methods and Software

DISSERTATION
for the Academic Degree
of Doctor of Science in Engineering

Moscow – 2025

Аннотация

Диссертационное исследование посвящено решению актуальной проблемы интеграции быстрорастущего парка электромобилей в существующую энергосистему. Основной вызов заключается в необходимости существенной модернизации сетевой инфраструктуры для удовлетворения резко возрастающего спроса на электроэнергию со стороны зарядных станций. В этом контексте зарядное устройство электромобиля рассматривается как критически важный новый элемент энергосистемы, выполняющий сложную функцию силового электронного интерфейса между аккумуляторной батареей транспортного средства и электрической сетью.

Особое внимание уделяется проблеме высокомощных быстрых зарядных устройств, которые создают экстремальные нагрузки на сеть в пиковые периоды. В качестве инновационного решения предлагается концепция "энергетического узла", предполагающая интеграцию в зарядную станцию дополнительных компонентов - систем накопления энергии и локальных генераторов. Для реализации этой концепции разрабатывается многопортовый силовой электронный интерфейс, включающий специализированные порты для подключения аккумулятора электромобиля, электрической сети, локальной батареи-накопителя и местного генератора энергии.

В работе подробно исследуются три ключевых направления. Первое направление посвящено многопортовым преобразователям энергии, где особое внимание уделяется топологии многоактивного моста. Предлагается инновационный подход к моделированию таких систем с использованием вращающейся системы координат, синхронизированной с частотой переключения преобразователя, что значительно упрощает системы управления. Теоретические выкладки подтверждаются результатами численного моделирования и экспериментальными данными, полученными на лабораторном прототипе мощностью 1 кВт.

Второе направление охватывает вопросы управления сетевыми инверторами, включая их работу в режиме двунаправленной передачи энергии. Особый акцент делается на особенностях работы в слабых сетях, где инверторы могут выполнять важные функции по стабилизации напряжения и частоты. Также рассматриваются методы защиты оборудования от переходных процессов.

Третье направление посвящено альтернативным архитектурам для частично изолированных многопортовых систем, включая резонансные преобразователи. Предлагаются новые конкретные технические решения, анализируются их преимущества и ограничения.

Результаты исследования имеют значительный практический потенциал для создания нового поколения зарядной инфраструктуры, способной минимизировать воздействие на энергосистему. Разработанные подходы также могут найти применение в системах управления энергопотреблением «умных» зданий и промышленных источниках бесперебойного питания.

ABSTRACT

This doctoral thesis addresses the critical challenge of integrating the rapidly growing electric vehicle (EV) fleet into existing power grids. The core issue lies in the substantial infrastructure upgrades required to meet the sharply increasing electricity demand from charging stations. In this context, the EV charger emerges as a pivotal new grid component, serving as a sophisticated power electronic interface between vehicle batteries and the electrical network.

The research focuses particularly on high-power fast-charging systems that create extreme grid loads during peak periods. As an innovative solution, the study proposes an "energy hub" concept that incorporates additional energy storage systems and local generators into charging stations. This approach requires developing a multi-port power electronic interface with dedicated connections for EV batteries, grid supply, local storage batteries, and distributed generation units.

The work comprehensively examines three key research areas. The first investigates multi-port power converters, with special emphasis on the Multiple Active Bridge (MAB) topology. The study introduces a novel modeling approach using a rotational reference frame synchronized with the converter's switching frequency, which significantly simplifies control systems. Theoretical findings are validated through simulation results and experimental data from a 1 kW MAB converter prototype tested in the laboratory.

The second research area covers grid-tied inverter control systems, including vehicle-to-grid bidirectional power transfer capabilities for both weak and strong grids. Particular attention is given to weak grids where the inverters can provide crucial voltage and frequency control. Weak grids are those where the inverter power capability is in the same order of magnitude than the main generators.The study also examines protection methods during the connection transient of inverters.

The third area is dedicated to alternative architectures for partially isolated multi-port systems, including resonant-link converters. The research proposes new specific technical solutions while analyzing their advantages and limitations.

The results of the research have significant practical potential for developing next-generation charging infrastructure capable of minimizing grid impact. The developed methodologies could also find applications in smart building energy management systems and industrial uninterruptible power supplies.

CONTENTS

INTRODUCTION **11**
CHAPTER 1. UNDERSTANDING THE NEED FOR FAST CHARGERS AND THE IMPACT ON THE GRID **25**
1.1. IMPACT OF EV CHARGERS ON THE GRID **25**
1.1.1. PENETRATION OF RENEWABLE ENERGY SOURCE (RES) IN THE GRID 25
1.1.2. GRID STABILITY 26
1.1.3. POWER BALANCE IN THE GRID 26
1.1.4. GRID LOSSES AND LIFETIME ON COMPONENTS 26
1.1.5. GRID VOLTAGE AND CURRENT HARMONICS 27
1.1.6. ADVANCED EV CHARGERS 28
1.2. TYPES OF EV CHARGERS **28**
1.2.1. CHARGING LEVELS ACCORDING TO IEC 29
1.2.2. AC CHARGERS VS DC CHARGERS 29
1.2.3. MULTI-SOURCE EV CHARGERS 30
1.3. OTHER APPLICATIONS USING MULTI-SOURCE SYSTEMS **31**
CHAPTER 2. THE MULTIPLE ACTIVE BRIDGE AS A SOLUTION FOR A MULTI-PORT SYSTEM **34**
2.1. EXISTING SOLUTIONS FOR A MULTIPLE PORT SYSTEM **34**
2.2. DQ-FRAME MODELING METHOD AND CONTROL ALGORITHMS FOR LARGE NUMBER OF PORTS IN MULTIPLE ACTIVE BRIDGE CONVERTERS **37**
2.2.1. MATHEMATICAL MODELING OF A MAB CONVERTER USING DQ-FRAME REPRESENTATION 37
2.2.2. CONTROL ALGORITHMS FOR MAB CONVERTERS USING DQ-FRAME REPRESENTATION 44
2.2.3. COMPUTER SIMULATIONS: THE QUADRUPLE ACTIVE BRIDGE (QAB): 50
2.2.4. EXPERIMENTAL RESULTS: THE TRIPLE ACTIVE BRIDGE (TAB): 55
2.2.5. COMPARISON WITH OTHER METHODS FOR MULTIPLE ACTIVE BRIDGE 58
2.2.6. SUMMARY 59
2.3. EFFECTS OF MEASUREMENT UNITS IN DECOUPLING BLOCKS **60**
2.3.1. FILTERS IN THE CURRENT-CONTROL AND POWER-CONTROL LOOPS 60
2.3.2. EFFECTS OF THE FEEDBACK DELAYS 64
2.3.3. SIMULATION EXAMPLE 65
2.3.4. PROPOSED COMPENSATION 67
2.3.5. SIMULATION RESULTS 71
2.3.6. SUMMARY 73
2.4. IMPROVEMENTS IN EFFICIENCY IN MAB CONVERTERS: THE "DUAL-DUTY" MODULATION **73**
2.4.1. EXISTING SOLUTIONS FOR IMPROVING MAB EFFICIENCY 74
2.4.2. NEW MODULATION TECHNIQUE – DUAL-DUTY 76
2.4.3. LOSS MODEL 82
2.4.4. SIMULATIONS 84

2.4.5. EXPERIMENTAL RESULTS 90
2.4.6. SUMMARY 95
CHAPTER 3. GRID-CONNECTED INVERTER AS THE INTEGRATION BLOCK TO THE GRID AND THE MAB CONVERTER 97
3.1. GRID-CONNECTED INVERTER – DESCRIPTION OF MAIN OPERATIONAL MODES 97
3.2. GRID-CONNECTED INVERTER – SPACE-PHASOR MODELING 98
3.2.1. INVERTER AVERAGED MODELING 98
3.2.2. SPACE-PHASOR REPRESENTATION 101
3.2.3. MODELING THE INVERTER USING THE SPACE-PHASOR REPRESENTATION 102
3.2.4. MODELING USING ALPHA-BETA FRAME REPRESENTATION 104
3.2.5. MODELING USING DQ-FRAME REPRESENTATION 105
3.2.6. MODELING THE INVERTER USING THE DQ-FRAME REPRESENTATION 106
3.2.7. SUMMARY 107
3.3. CONTROL ALGORITHM FOR GRID-CONNECTED INVERTERS USING ALPHA-BETA FRAME INCLUDING HARMONIC COMPENSATION 108
3.3.1. DESCRIPTION OF THE CONTROL ALGORITHM AND DESIGN PROCEDURE 108
3.3.2. MULTI-RESONANT CONTROL ALGORITHM 112
3.3.3. SIMULATION EXAMPLE – DESCRIPTION OF THE CONTROLLER DESIGN 113
3.3.4. SIMULATION EXAMPLE – DESIGN OF COMPONENTS (OUTPUT FILTER) 118
3.3.5. SIMULATION EXAMPLE – DESIGN OF COMPONENTS (PR CONTROLLER) 119
3.3.6. SIMULATION EXAMPLE –RESULTS 121
3.3.7. SUMMARY 126
3.4. ADAPTIVE GAINS IN CONTROL ALGORITHM FOR GRID-CONNECTED USING ALPHA-BETA FRAME AND HARMONIC COMPENSATORS 126
3.4.1. DESCRIPTION OF THE PROBLEM – VARIABLE GRID IMPEDANCE 126
3.4.2. PROPOSED SOLUTION – AUTOMATIC GAIN SELECTION 129
3.4.3. SIMULATION EXAMPLE – AUTOMATIC GAIN SELECTION 130
3.4.4. EXPERIMENTAL VALIDATION – AUTOMATIC GAIN SELECTION 135
3.4.5. SUMMARY 137
3.5. CONTROL ALGORITHM FOR GRID-CONNECTED INVERTER USING DQ-FRAME 138
3.5.1. MAIN DIFFERENCES BETWEEN αβ-FRAME AND DQ-FRAME CONTROL METHODS 138
3.5.2. SYNCHRONIZATION METHODS 138
3.5.3. MODELING OF A PHASE-LOCKED LOOP (PLL) 141
3.5.4. MODELING OF A PLL: IMPACT OF THE LINE IMPEDANCE 145
3.5.5. MODELING OF NEGATIVE FEEDBACK PHASE-LOCKED LOOP (NFPLL) 150
3.5.6. MODELING OF THE CURRENT CONTROL LOOP IN DQ-FRAME 152
3.5.7. EFFECT OF PLL PHASE MISALIGNMENT IN THE CURRENT CONTROL LOOP IN DQ-FRAME 155
3.5.8. SUMMARY 156
3.6. VOLTAGE CONTROL LOOP AND POWER SHARING METHODS 156
3.6.1. VOLTAGE CONTROL LOOPS 156
3.6.2. POWER CONTROL METHODS: TRADITIONAL DROOP CONTROL 161
3.6.3. INTRODUCTION OF VIRTUAL IMPEDANCE 164
3.6.4. SIMULATION OF AN INVERTER USING A POWER SHARING TECHNIQUE WITH VIRTUAL IMPEDANCE 164

3.6.5. EXPERIMENTAL VALIDATION – POWER SHARING 168
3.6.6. SUMMARY 170
3.7. NEW ADVANCED POWER SHARING METHODS 171
3.7.1. THE REASON FOR A PHASE LIMITER IN DROOP MODE POWER SHARING METHODS 171
3.7.2. MATHEMATICAL MODEL FOR ANALYSIS OF INVERTER CONNECTION PROCESS ... 174
3.7.3. INTRODUCTION OF PHASE LIMITER 192
3.7.4. SIMULATIONS A GRID OF TWO INVERTERS WITH PHASE LIMITERS 195
3.7.5. EXPERIMENTAL VALIDATION 198
3.7.6. SUMMARY 205
3.8. LOW-BANDWIDTH COMMUNICATION BETWEEN INVERTERS 206
3.8.1. MOTIVATION ON COMMUNICATION THROUGH POWER LINES TO ENHANCE THE POWER SHARING METHODS 206
3.8.2. DROOP CONTROL METHOD IN NON-INDUCTIVE POWER LINES 210
3.8.3. VIRTUAL IMPEDANCE AS AN ADAPTIVE CONTROLLER 212
3.8.4. VIRTUAL IMPEDANCE AS AN ADAPTIVE CONTROLLER 215
3.8.5. ANALYSIS OF THE STABILITY OF THE PROPOSED CONTROL TECHNIQUE 219
3.8.6. EXPERIMENTAL VALIDATION 225
3.8.7. SUMMARY 233
CHAPTER 4. PARTIAL ISOLATION: ALTERNATIVE TOPOLOGIES FOR MULTI-PORT SYSTEM 234
4.1. NON-ISOLATED MULTI-PORT CONVERTERS 234
4.1.1. EXISTING SOLUTIONS 235
4.1.2. MULTI-PORT HIGH-GAIN CONVERTER: STEADY-STATE ANALYSIS 237
4.1.3. MULTI-PORT HIGH-GAIN CONVERTER: SMALL-SIGNAL ANALYSIS AND ITS CONTROLLER 244
4.1.4. COMPARISON ANALYSIS 249
4.1.5. SIMULATIONS AND EXPERIMENTAL RESULTS 251
4.1.6. SUMMARY 257
4.2. ISOLATED SERIES RESONANT DC/DC CONVERTERS – DISCONTINUOUS MODE .. 257
4.2.1. SERIES RESONANT CONVERTER FOR BIDIRECTIONAL APPLICATIONS 258
4.2.2. DISCONTINUOUS MODE – DISCRETE STATES 261
4.2.3. STEP-DOWN MODE 265
4.2.4. STEP-UP MODE 268
4.2.5. DESIGN GUIDELINES 271
4.2.6. SIMULATIONS AND EXPERIMENTAL VALIDATION 272
4.2.7. COMPARISON OF THE STEP-UP BIDIRECTIONAL SRC WITH OTHER TOPOLOGIES . 277
4.2.8. EXTENSION OF USE OF DISCONTINUOUS MODE STEP-UP BIDIRECTIONAL SRC WITH OTHER SEQUENCES OF STATES. 278
4.2.9. ANOMALOUS BEHAVIOR AT LIGHT LOADS 281
4.2.10. SUMMARY 282
4.3. ISOLATED SERIES RESONANT DC/DC CONVERTERS – CONTINUOUS MODE 284
4.3.1. STEADY-STATE MODELING 284
4.3.2. SMALL-SIGNAL MODELING 291
4.3.3. SIMULATIONS AND EXPERIMENTAL RESULTS 294
4.3.4. SUMMARY 301

4.4. ISOLATED RESONANT MULTI-PORT INVERTER 302
4.4.1. RESONANT SOLUTION FOR OBTAINING A MULTIPLE PORT CONVERTER WITH AC AND DC PORTS 303
4.4.2. MULTIPLE PORT CONVERTER WITH AC AND DC PORTS – BASIC ANALYSIS 304
4.4.3. CONTROL DIAGRAM 319
4.4.4. VOLTAGE CONVERSION RATIO 320
4.4.5. SOFT-SWITCHING PROCESS 321
4.4.6. NUMERICAL SIMULATIONS 323
4.4.7. EXPERIMENTAL RESULTS 328
4.4.8. SUMMARY 333
CONCLUSIONS 335
PUBLICATIONS OF THE AUTHOR ON THE SUBJECT OF THE DISSERTATION 338
BIBLIOGRAPHY 342
LIST OF FIGURES 369
LIST OF ACRONYMS AND ABREVIATIONS 379
ACKNOWLEDGEMENTS 384

INTRODUCTION

The relevance of the research topic is due to the increased demand on the electric grid associated with the increased number of electric vehicles in Russia and, in general, in the world. A fraction of fuel-based vehicles will be replaced by electric vehicles (EVs), which will draw power from the electric grid. This will have an impact on the electric grid consumption and it will require new infrastructure investments. In order to smooth this transition, electric vehicles can be partially charged by local generation and storage. Thus, the grid does not need to supply all the power directly from main power plants.

To implement this idea, local photovoltaic panels and batteries can be installed at the point of charging and use that energy to charge the vehicle when it is needed. Thus, multiple sources can simultaneously charge the EV through a power converter or a set of power converters. These converters must manage power flow from different sources, including the grid, batteries, and photovoltaic panels.

In case of using a set of two-port converters, the converters will have a common DC link in one of their ports and the other port will be connected to the sources or loads. Thus, one converter will be connected to the grid, one converter will be connected to the internal batteries, one converter will be connected to the photovoltaic panels (PVs) and another one to the vehicle to be charged. Internally, all of them must be interconnected via a common DC link as shown in Figure 1(a). In this way, the system will need as many converters as the number of connected sources or loads. This solution is valid but it requires the coordination of multiple devices and an excess of components. A multi-port converter can perform the same functions but in a single circuit which is easier to manage. Figure 1(b) clarifies the idea of the multi-port converter and compares it with the alternative solution which consists of a set of two-port converters. Multi-port converters are a relatively new concept in which energy is delivered to multiple points at different voltage and current levels.

In addition, multi-port converters can also find other relevant applications such as uninterruptible power supplies (UPS), power electronic transformers (to connect different

grids electronically with galvanic isolation), multiple output power supplies, (for example in aircrafts where many voltages are needed), and hybrid energy storage systems.

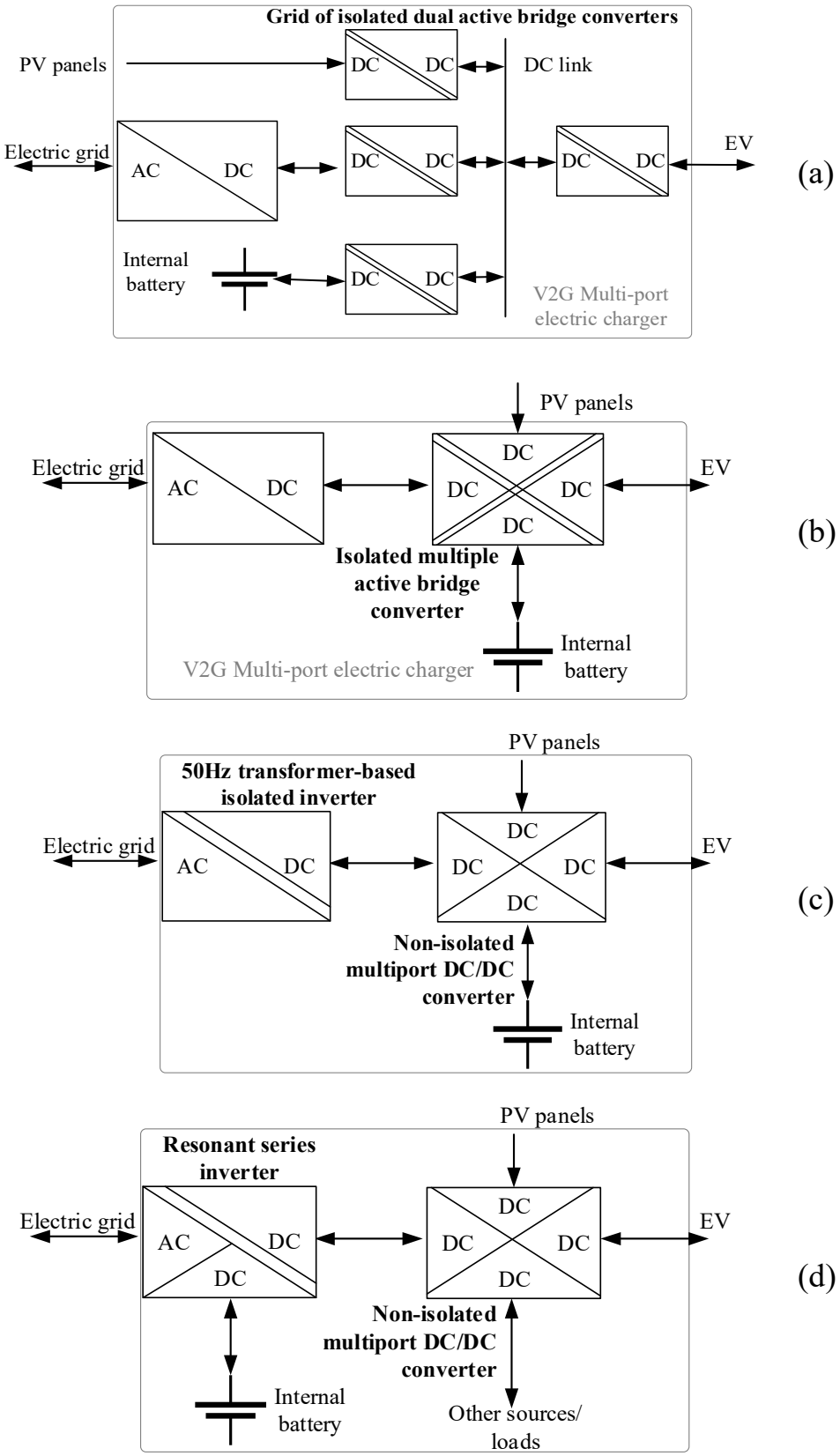

Figure 1–Electric charger: (a) using 2-port converters and (b) using a MAB converter (c) partial isolation solution based on non-isolated converter (d) partial isolated resonant DC/AC.

The degree of scientific development of the problem. Researchers worldwide have been actively studying multi-port converters. These converters are becoming relevant due to their ability of multidirectional power flow and galvanic isolation [1]. In general, multi-port converters include converters based on transformers and other impedance networks, such as resonant converters [2], multi-transformer converters [3], complex impedance networks [4-6] and single multi-winding transformer-based converters [7, 8]. Converters based on transformer are attractive because of the implicit galvanic isolation between ports. High-frequency (kHz range) transformers allow galvanic isolation between ports, however, they should be carefully designed in order to keep parameters such as its magnetizing inductance and leakage inductances under design requirements [9].

Among multi-port converters, multiple active bridge converters or MAB converters are particularly of interest due to the fact that they require the minimum number of passive elements and a moderate number of active elements such as electronic switches (bipolar junction transistors, MOSFETs, IGBTs or others). A general MAB converter is shown in Figure 2, where each DC port is connected through a DC/AC bridge, which, in general, can be a half-bridge, a full-bridge, Neutral Point Clamped (NPC) DC/AC, T-type DC/AC and even three-phase configurations. Each solution for the bridge allows different number of output levels. A half-bridge allows 2 levels, a full-bridge allows 3 levels and the others more but require more components. Each type of bridge has its benefits and drawbacks. This research work is focused on MAB converters based on a single multi-port transformer connected to several full-bridge DC/AC stages. However, the same proposal can be applied to any other type of MAB converters. In Figure 2, the version of four ports is presented, however, the number of ports is arbitrary and depends on the application.

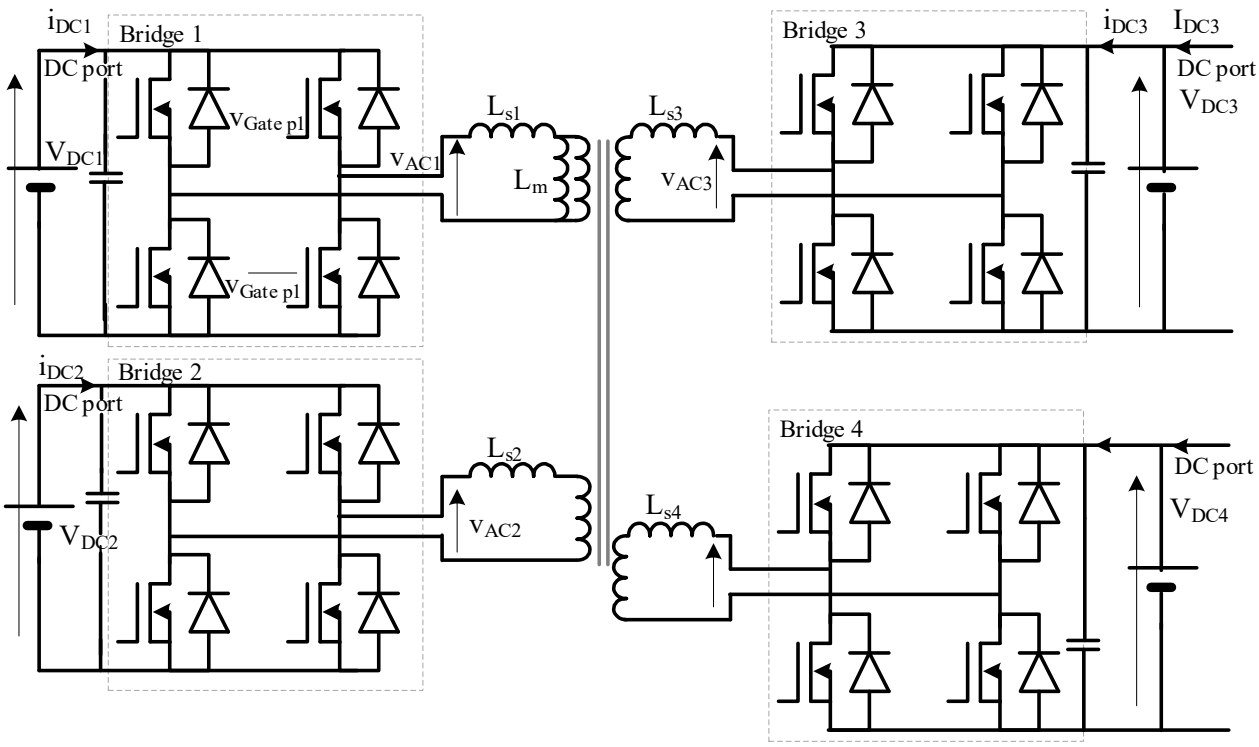

Figure 2–Example of a MAB converter: QAB (quad-active bridge) power stage diagram, which can be easily extended to a larger number of ports.

MAB converters can be seen as an extension of dual active bridge (DAB) converters [10] in terms of DC/AC bridges, the transformer as the element to transfer the energy and the modulation techniques. DAB converters are extremely useful in systems which need to be isolated from the grid, so the isolation can be performed using small-size high-frequency transformers. The main method to transfer the energy from one port to the other one is based on a phase shift modulation between the two ports, also known as single-phase-shift (SPS) [10]. The technique is commonly used for transferring power in electric grids, where the phase difference between ports is a function of the amount of transferred power. This modulation works well if the voltages at each port are similar, however, if the voltage at the ports are able to vary, the efficiency droops drastically due to the excessive reactive power involved. This happens typically for battery or supercapacitor charging/discharging processes, where the voltage is a function of the state of charge [11, 12].

The first MAB converter was the triple active bridge (TAB) converter [13-15] introduced by Zhao, Kolar *et al* in 2004. It provides good efficiency, bidirectional power

flow and galvanic isolation. The TAB suffers from coupling effects between ports, meaning that delivering power from port 1 to port 2 might have some power delivery to port 3. This coupling effect should be minimized by advanced control methods in which the phase modulation should be accurately selected in order to keep the power flow in the desired direction cancelling any non-desired direction.

For that reason, Zhao, Kolar *et al* have proposed a decoupling method for TAB which allows to control the power in each port independently based on phase shift modulation [12]. The method is attractive but it has some limitations: it is difficult to extend it to a larger number of ports and it does not include the transformer dynamics [14]. The phase shift modulation to control power transfer [15-16] is simple, but it has some drawbacks, such as recirculating currents which increase the losses particularly when DC voltages at the ports should vary. This structure and control method have been used in certain applications such as solid-state transformers [14, 17], multi-port DC/DC converters for medium voltage DC grids [18], aircrafts [19] and electric vehicle chargers [20].

Recently, modern techniques were proposed to extend TAB converter's control to a larger number of ports and to minimize the DC current recirculation. The phase shift methods produce an excess of reactive power in the transformer which results in extra losses at low power transfer, thus a phase shift with duty cycle modulation were proposed in [7, 21]. There, the duty cycle is selected for increasing the efficiency [7]. However, this problem is non-linear and it is difficult for real-time calculations. Therefore, tables for selecting the proper duty cycles were obtained based on desired DC currents. However, as the number of ports increases, the table sizes increase dramatically, so this method is hard to scale for a larger number of ports. Furthermore, this method neither includes the voltage dependence on DC ports nor the transformer dynamics.

Using Fourier decomposition allows to compute active and reactive power inside the converter (in the transformer ports) [22, 23] and this can be used to select the proper duty cycles. Resonant techniques were also explored in [2], however these techniques are too complex to extend them to a large number of ports.

Related to transients and dynamic performance of the MAB converter, authors from [7] claim that the transformer dynamics are always at a frequency close to the switching frequency, so they can be neglected. However, to have good efficiency and control of the power flow using phase shift, the reactance-resistance ratio (X/R) in each port should be large. As the ratio increases, the winding time-constant increases as well. Thus, the transformer dynamics can affect the plant and must be taken into account, otherwise the control bandwidth should be limited. This aspect was not explored yet, and it is one of the novelties of the presented work. The research work will allow the multiple active bridge converter to work with variable DC sources. This includes bidirectional flow in every port and an improvement in efficiency.

As the MAB is a DC/DC converter so all of its ports are DC ports. Therefore, for connecting it to the electric AC grid an inverter must be added, the complete EV charger is shown in Figure 1(b). There are many inverter topologies that can do that connection successfully, such as voltage source inverters (VSI) [24], current sources [25] inverters, multi-level inverters and others [26]. For low voltage AC grids (three-phase 230V-50Hz), VSI are preferred due to the minimal number of components. It consists of a three-leg bridge of switches and a passive filter with no isolation.

As the EV charger proposed in Figure 1(b) has an isolated multiple port converter, the inverter does not require additional galvanic isolation, which makes the VSI a good choice due to its compactness. The control technique of VSI is an actual topic because it allows to perform many services to the grid. VSIs can work in any mode by absorbing or delivering active or reactive power. So, they can be used for controlling the voltage of the grid at a certain grid node by injecting reactive power, or for example, they can assist the frequency regulation by transferring active power [27]. They can also emulate variable passive elements such as capacitors or inductors to improve the grid quality and they can work as an active filter for reducing the harmonic components in the grid [28]. For the case of the EV charger, due to the extensive possibilities of the inverter control methods and the bidirectional power flow feature of the MAB converter, the charger can deliver or absorb energy to/from the grid, performing grid-to-vehicle (G2V) and vehicle-to-grid (V2G) modes. In the absorbing mode, it is clear that it will charge the EV battery and it

will work as a rectifier to provide a DC voltage to the MAB converter. However, in V2G mode, the inverter can work as a slave by delivering power according to a reference or can work as a grid-forming inverter.

Grid-forming inverters are one of the current topics in inverter control. Inverters can control the grid by regulating the voltage delivering the necessary power to the loads. However, if the consumption is higher than the inverter power capacity, more than one inverter should be connected and they need to share the load. For this purpose, several modern techniques have been developed, particularly the droop control method, a decentralized approach that enables load sharing among inverters. While droop control facilitates power sharing, transient conditions can lead to power oscillations and voltage and current spikes [29].

For mitigating such oscillations, this research work includes the modeling of the paralleling inverter problem and from that guidelines for a proper control were extracted. In addition, to limit high currents during transients, new protections have been proposed which includes virtual impedance, phase limiters and power filters.

The solution of a MAB converter with an inverter is not the only alternative to Figure 1(a). This depends on the characteristics of each DC ports in terms of isolation. Partial isolated systems can be an alternative to Figure 1(a) and (b). This research work also suggests new topologies of EV chargers: in Figure 1(c), a combination of a non-isolated multiple port converter and inverter with an isolation transformer, and, in Figure 1(d), a resonant DC/AC converter which has one isolated DC port. Resonant converters have been studied for several years. They are attractive due to their high efficiency but their control becomes complicated for variable loads. Most common resonant converters are series, parallel and series-parallel or LLC converters [30]. Usually these converters work in only one power flow direction but they can be extended to bidirectional applications with some modifications. The author has introduced novel techniques for obtaining a bidirectional series resonant converter for energy storage applications in [31-37]. Based on that, in this research work a series resonant inverter with one isolated and one non-isolated DC ports is proposed as a compact solution for EV charger.

The **goal** of the study is to model, simulate and implement a system based on power electronic converters capable of sharing energy between its multiple ports with high efficiency and ease of implementation. Most ports are “DC type” such as DC sources (batteries, supercapacitors, fuel cells, photovoltaic panels) or loads and at least one port is an “AC type” due to the grid connection possibility. The system or **object** should be able to manage a large number of ports with bidirectional power flow; thus, a control algorithm must be designed.

For achieving this goal, it requires to **address the following research problems**:

- To identify the main issues by studying the existing control methods.
- To make a mathematical model of a multiple active bridge converter.
- To propose a control method that can consider variable voltage DC sources in the converter’s DC ports.
- To implement the control method for conducting experiments.
- To evaluate the method by means of computer simulation of mathematical models and real experiments.
- To compare the different proposed techniques and highlight their benefits and drawbacks.
- To make a mathematical model of a grid-connected inverter.
- To propose a new control method for parallel inverters in the grid for sharing power with smooth transients.
- To suggest an alternative to the MAB converter with the inverter considering partial isolation using non-isolated converters
- To suggest an alternative to the MAB converter with the inverter considering partial isolation using resonant techniques for having at least one isolated AC port.

The scientific novelties which are also **the main results submitted for the defense** are:

1. A new mathematical model for describing the multiple active bridge converter based on a rotational frame synchronized with the main operational frequency.
2. A decoupling control method that allows the use of any number of ports in a multiple active bridge converter and allows to transfer energy from any port to any other

port without sending power to any third port. The proposed decoupling method allows to control the active power between ports and also the amount of reactive power in each transformer's winding.

3. Efficiency improvements for multiple active bridge converters. The control method considers the effect of the voltage change in the DC ports which are compensated internally by the modulation technique. Thus, efficiency is higher in comparison with other control methods (single phase shift method) in the condition of non-equal voltage at the DC ports. Also, a new specific modulation called "dual duty" was proposed and implemented in order to reduce even more the conduction losses and increase efficiency for delivering power among ports.

4. As a grid-connected inverter is also required to integrate the proposed DC/DC converter to grid applications, modeling of grid inverters in weak and strong grids was developed. Based on this modeling, improvements in connection transients of grid-forming inverters by means of introduction of phase limiters, controllable virtual impedance and power filters were achieved.

5. The controller of the inverter should tolerate changes in the grid, thus, an adaptive controller was proposed which controls the output current of the inverter and compensated the possible harmonics.

6. As an alternative to the MAB converter with inverter, when complete isolation is not needed (only one of the ports needs to be isolated), the design, modeling, simulation and testing of two new more compact solutions were performed: a non-isolated high-gain DC/DC/DC converter with reduced number of components, and a multiple port power converter with one isolated DC port and other AC and DC ports (DC//DC/AC) avoiding the inverter.

The theoretical and practical significance of the research. The main conclusions of the dissertation research can be used for developing real fast electric vehicle chargers with the possibility to reduce the peak power consumption of the grid. The results of the research work include new models and control algorithms for multi-port systems which allow the connection of multiple AC or DC sources in a system where the power flow can be totally controlled. Many applications can benefit from these new methods. The

research work proposes a circuit that improves fast EV chargers with local generation and storage for reducing the grid peak power demand. This has a direct practical application and can be implemented massively in the electric grid. For that reason, a patent was published in 2024.

Furthermore, the same system can also be used for other multiple port systems such as uninterruptible power supplies (UPS), electronic transformers, hybrid energy storage systems, interconnection with multiple voltage grids such as in aircrafts and other vehicles, smart houses and others.

The **methodology** is based on analyzing multi-port systems, particularly multiple active bridge (MAB) DC/DC converters. The research is based on other traditional converter analysis such as dual active bridge (DAB) converter and triple active bridge (TAB) converters proposed by Prof. Kolar and Prof. Zhao The research involved modeling, control techniques, electronic circuit design, and coding. The research was validated through numerical simulations and laboratory experiments, including prototype development and testing with using high-quality measurement instruments and bidirectional power sources to emulate the different elements of the system and its applications.

The **validity and reliability of the results and conclusions** were confirmed by numerical simulation and experimental validation with accurate electronic instruments such as digital oscilloscopes, current and differential voltage probes, laboratory power supplies, impedance analyzers, and prototypes developed in the laboratories of Skolkovo Institute of Science and Technology. The reproducibility of the results was confirmed by repeating experiments three times and comparing them with numerical simulations. The statements and conclusions formulated in the dissertation have been approved by the committees of experts in international scientific conferences. The credibility is also confirmed by the publications of research results in peer-reviewed scientific journals.

The **personal contribution of the author** includes three main parts: inverters, multi-port DC/DC converters, and resonant converters. In terms of inverters, the proposition of new control techniques for inverters related to power sharing, protection and transients, particularly advanced droop control methods, virtual impedance, phase

limiter and low-bandwidth communication for achieving power sharing and soft transients. For that, the modeling of inverters and implementation of the techniques in simulations and real inverters were performed. In multi-port DC/DC converters, the author has proposed a new modeling of the converter based on a rotational frame synchronized with the main operational frequency, usually called dq-frame or dq-reference frame and due to that a novel control algorithm. The author modeled, simulated, and experimentally validated the system. Finally, in resonant converters, the author also proposed new ideas to reduce the size of converters in terms of number of switches. For that, intensive modeling and simulation was performed and finally validated through experiments.

Approbation of the work. 27 papers reflecting the main provisions of the study were published on the research topic, including 13 proceedings in international conferences with a total volume of 5 printers sheet, 14 publications in journals and collections of scientific papers with a total volume of 11 printers sheet. In addition, 1 patent in the Russian Federation was granted due to the invention in 2024. The list of papers is in the Section “Publications of the Author” at the end of the dissertation.

The research results were presented at international conferences in: IEEE PowerTech (Belgrade, Serbia, 2023), IEEE Applied Power Electronics Conference (APEC, Orlando, USA, 2023), IEEE Annual Conference of Industrial Electronics Society (IECON , Brussels, Belgium, 2022), IEEE International Conference on Renewable Energy Research and Applications (ICRERA , Istanbul, Turkey, 2022), IEEE Industry Applications Society Annual Meeting (Vancouver, Canada, 2021), IEEE PES General Meeting Washington, DC, USA), IEEE PowerTech (Milan, Italy, 2019), IEEE International Symposium on Power Electronics for Distributed Generation Systems (PEDG, Xi'an, China, 2019). The main results of the dissertation research are also presented in the Electromobility course in the energy system master program of Skolkovo Institute of Science and Technology.

The structure and content of the work are determined by the conceptual idea, which reflects the goal and objectives of the research. The dissertation consists of an

introduction, 4 chapters, conclusion, and a list of 233 references. The main text spans 384 pages, including 23 tables, 171 figures.

Chapter 1 "Understanding the need for fast chargers and the impact on the grid". This chapter introduces the problem of fast chargers and the impact of them in the electric grid. This chapter clearly indicates the reason of new solutions for fast chargers and in general multi-port systems. In addition, it shows other applications where multi-port converters can be used.

Chapter 2 "The multiple active bridge as a solution for a multi-port system". This chapter is divided in four sections. The first one, Section 2.1, reviews and studies the existing mathematical control methods to create a multi-port system for exchanging energy. It starts with simple integration of two-port systems to obtain a multi-port system and after that, it introduces the multiple active bridge as a promising solution, mentioning the main benefits and challenges. Based on that the research gaps are identified and the solutions are proposed.

Section 2.2 is focused on the multiple active bridge, its modeling and its control algorithms. It explains in details the novelty of the proposed control method. It describes the development of new methods and algorithms for interpreting the behavior of a multiple active bridge converter based on its mathematical model. It explains the algorithms for inner and outer control loops and their main benefits regarding new degrees of freedom in control references. The section also includes the development of computer simulation of the multiple active bridge mathematical model including the dq-frame control algorithms. In addition, the algorithms were implemented in the form of c-language program inside a microcontroller which was tested in a real experiment in 1kW prototype.

Section 2.3 is focused on the impact of signal and measurement delays. The control loops are affected to that and this section models this effect and proposes a solution to mitigate that.

Section 2.4 is a comprehensive analysis of the power losses. It is presented based on mathematical models and computational simulations. Due to that, the section adds a novel modulation technique, the “dual-duty” modulation, that can reduce the conduction

losses of the converter and increase efficiency by minimizing the root-mean-square currents through the winding. The implementation of this special modulation techniques in the form of pseudo-code for conducting computer simulations and real experiments are detailed in this section. The section concludes with the benefits and challenges of the dual-duty modulation.

Chapter 3. "Grid-connected inverter as the integration block to the grid and AC loads". This chapter is focused on grid connected inverters. Inverters are the interface between multiple DC port converters and the AC grid. Therefore, if any of these multiple DC port converters must be connected to the grid, an inverter is required. The chapter is divided in 7 sections. Section 3.1 describes the main operation modes. Section 3.2 reviews the modeling of the inverter, which is the basis for advanced control methods. Based on that, Section 3.3 proposed a methodology for designing the control block in a proportional multi-resonant scheme where the harmonics of the grid can be compensated. Section 3.4, as a contribution, modifies that control method and makes it adaptive to grid changes. Section 3.5 is focused on another control method, the dq-frame-based control. It models the inverter in dq-frame and, particularly, it is focused on the synchronization method and how the line impedance affects that method. Section 3.6 considers that the inner (main) control loop is performed and uses the outer control loops to make a voltage control loop, or in other words, a grid-forming inverter. It describes the model of the whole inverter including the high-level control blocks: virtual impedance, droop control and power filter. It provides simulation of a whole system with two connected inverters based on the introduced model.

Section 3.7 explains the limitations of the power sharing introduced in the previous section. The section analyses the effect of the elements introduced in Section 3.6 and gives a guideline in the selection of the parameters. In addition, the section introduces a new method for limiting the inverter's power, particularly in transients, where, traditionally, the power sharing is not well controlled.

Section 3.8 is focused on the reactive power sharing and proposed a communication between inverters based on the power lines to adjust such power.

Chapter 4. "Partial isolation: Alternative topologies for multi-port system". This chapter suggests new topologies for multiple port converters in the case that not all of the ports require galvanic isolation. It includes two main parts: a hard-switching compact non-isolated topology and a resonant technique to allow AC and DC sources to share power.

Section 4.1 proposes a non-isolated converter to be connected to an isolated inverter which suits for low voltage, from low to middle power devices to be connected to the grid at a ~700V port. It suggests a cheap solution for domestic applications.

Sections 4.2 and 4.3 introduces a new series-resonant converter especially designed for energy storage applications where the port voltages change and the bidirectional power is required. Both sections analyze two-port converters clarifying in detail the operation of them by extensive modeling, numerical simulations and experiments.

Section 4.4 proposes a combination of inverter techniques with the resonant DC/DC converter techniques introduced in Section 4.2 and 4.3, that can reduce the number of components of the whole system. This converter is the most attractive in terms of reducing number of components.

Finally, the Conclusions section summarizes the contribution and the impact of the proposed techniques.

Chapter 1. UNDERSTANDING THE NEED FOR FAST CHARGERS AND THE IMPACT ON THE GRID

1.1. Impact of EV chargers on the grid

Many nations, including the Russian Federation, have implemented policies to promote electric vehicle (EV) adoption through production incentives and usage support programs. This rapid EV market expansion will drive substantial growth in charging infrastructure, significantly increasing electricity demand on utility grids. Consequently, developing technologies to mitigate these grid impacts has become crucial. This section examines the effects of EV chargers as emerging grid loads.

1.1.1. Penetration of Renewable Energy Source (RES) in the grid

Modern power systems face increasing difficulties in managing the variable nature of renewable energy sources. The additional load variability introduced by EV chargers further complicates grid operations. Researchers have explored various approaches to address these challenges. Some studies focus on adapting wind power to grid demands [38], while other works have focused on maintaining stable power at connection points serving both EV chargers and renewable sources [39]. The potential of islanded microgrid configurations has been demonstrated through case studies [40], and successful integration of photovoltaic generation with EV charging has been documented [41, 42]. Collectively, these studies indicate that proper coordination between renewable sources and EV charging can enhance overall grid capacity and renewable energy utilization [43].

1.1.2. Grid stability

The operational characteristics of EV chargers as either constant-current or constant-power loads present unique challenges for grid stability. When grids operate near their stability limits, the introduction of EV charging loads may push systems toward instability, necessitating thorough pre-installation assessments. Using IEEE 3-bus test systems, researchers quantified how EV charger loads reduce stability margins [44]. Subsequent studies confirm these findings through constant-power load modeling [45, 46]. However, alternative operational modes such as vehicle-to-grid (V2G) show promise for enhancing stability margins, particularly when chargers are configured to function as grid-forming inverters [47, 48, 49].

1.1.3. Power balance in the grid

International research efforts have revealed the potential consequences of uncoordinated EV charging on grid operations. Studies conducted in Australia and the United Kingdom have shown that uncontrolled charging can disrupt the critical balance between supply and demand, potentially leading to blackout conditions [50, 51]. In response to these findings, researchers have proposed coordinated charging strategies [52, 53] and investigated the benefits of co-locating renewable energy sources with charging infrastructure to help mitigate demand impacts [54, 55, 56].

1.1.4. Grid losses and lifetime on components

The continuous growth of fast EV chargers introduces significant new demands on grid infrastructure. The resulting increases in current flow lead to greater energy losses

through Joule heating effects [51, 52, 53], which in turn elevates operating temperatures across system components. This thermal stress particularly affects critical infrastructure elements including transformers, transmission lines, and protective devices [57, 58], with sustained high temperatures accelerating component aging and reducing operational lifespan [59, 60, 61]. These effects may ultimately require substantial infrastructure upgrades to maintain reliable operation [62]. Strategic placement of charging stations must therefore consider both user demand patterns and available grid capacity to optimize system performance [63].

To conclude, the unregulated expansion of EV charging infrastructure poses significant risks to grid reliability and component longevity. Implementing smart charging protocols that incorporate vehicle-to-grid capabilities offers a promising solution to maintain system stability while operating within safe operational parameters [64, 65, 66].

1.1.5. Grid voltage and current harmonics

The rising power demand from electric vehicles significantly affects power quality, particularly impacting grid voltage characteristics including amplitude and phase balance [67, 68]. To maintain proper voltage conditions and grid stability, coordinated smart charging strategies must actively manage both active and reactive power flows.

EV chargers employ switching-mode power electronics that inherently generate current harmonics. The total harmonic distortion (THD), a key metric for quantifying harmonic content, varies according to the specific employed power electronic topology [69]. International standards establish the maximum permissible THD levels based on power consumption, with lower-power loads typically permitted higher distortion levels than high-power installations. For kW-range loads, the generally accepted maximum THD threshold stands at 5%, necessitating the integration of additional filtering components at AC input ports [70]. Contemporary mitigation approaches encompass both passive and active power conditioning solutions. All modern EV chargers now

incorporate power factor correction and low-THD generation capabilities as standard features [71, 72], effectively eliminating harmonic distortion as a significant concern for grid-connected charging systems.

1.1.6. Advanced EV chargers

The development of next-generation smart chargers represents a crucial solution for mitigating EV charging impacts on electrical networks. These advanced systems must incorporate grid-forming inverter functionality to provide voltage support and optimize power flow management. Bidirectional power conversion capability forms an essential requirement for such systems. Furthermore, the integration of local generation and storage components with charging infrastructure can substantially reduce grid demand, thereby minimizing transmission losses and extending asset lifespans. This dissertation provides a detailed examination of the fundamental technologies enabling these advanced EV charging solutions.

1.2. Types of EV chargers

EV chargers are the devices that connect the EVs to the grid and together they act as a new type of load. The EV chargers are mainly divided in two big groups: domestic chargers and public chargers. The first one is exclusively for the use of the vehicle owner and is often used at night from low to moderate power consumption. Public chargers on the contrary are installed in shopping malls and different parking places for charging EVs in a short amount of time at high power.

1.2.1. Charging levels according to IEC

The international standards (International Electrotechnical Commission, IEC) defines power levels for slow and fast chargers. Mode 1 chargers are for domestic use, delivering up to 4 kW in AC single-phase connection and up to 11 kW in AC three-phase connection. Mode 2 chargers are more powerful, they can still be domestic with extra infrastructure and they can reach up to 22 kW in its three-phase AC connection. Mode 3 is oriented to public places and it can charge up to 43 kW in its three-phase AC connection. Finally, mode 4 is a DC mode fast charging that can charge up to 80 kW also for public places.

As an example, a Tesla Model S requires around 5 hours to charge the vehicle for 100 km autonomy in a Mode 1 (AC single-phase 4 kW) charger, while it takes 22 minutes if a 50 kW Mode 4 DC charger is used. Thus, those fast chargers are attractive from the point of view of the end-user (driver) but they can increase dramatically the grid consumption. Therefore, solutions that still allows the end-user high available power while demanding lower power from the grid are of great relevance. Otherwise, the grid infrastructure should tolerate those high-power peaks while EVs are being charged.

1.2.2. AC chargers vs DC chargers

Regarding the technology, two types of chargers are mentioned: AC and DC chargers. An AC charger delivers AC (single- or three-phase connection) to the vehicle and there is an “on-board” charger which transforms the energy from the grid to the suitable values for the batteries in terms of voltage, current and waveform. In other words, there is an AC/DC circuit which controls the charging current inside the vehicle. Thus, those AC chargers are mainly a protection system with measuring features in order to understand the amount of energy delivered to the vehicle.

DC chargers are much more complex. DC chargers are directly connected to the EV battery. They do not use any “on-board” charger, the electronic circuits are inside the DC charger and this is why, it is possible to increase the transferred power. The size of the DC chargers at high powers is too big to be installed on board and it should be located at the charging point. The standards suggest up to 80 kW, but companies have reached up to 300 kW using different improvements such as water-cooled cables and other thermal technologies.

DC chargers require converting three-phase AC power to the battery DC levels with galvanic isolation, so the vehicle is not in contact with the grid. For that, different types of electronic circuits have been proposed (see chapter II). The main issue is that in any case the energy should be extracted from the grid and delivered to the EV and this produces high demand in short time intervals which can overload the grid infrastructure. A possible solution is to have in the charging point and additional energy source which can contribute to the charging process. This can be an in-site extra battery, photovoltaic panels or any other source of energy. This new architecture mitigates the high consumption in the grid, however, it requires a multiple port system which should be able to share the EV load among different sources. The following chapter will introduce the mentioned multiple port systems in their current state [43].

1.2.3. Multi-source EV chargers

DC chargers with inner storage system form a multi-source charger. This type of chargers can reduce the peak power demand in the grid by using internal energy at the charging point. In [73], an application of this charger is suggested in a parking lot for shopping malls. The authors suggested how to size the battery for different objectives. A prototype of an EV charger with storage was installed in Italy [74] for evaluating its benefits. It shows good performance in the implementation of peak shaving function, in respect to the main distribution grid. It makes the prototype like a network component with nearly zero-impact on the system.

A high level of energy management is needed to minimize the impact in the grid using EV chargers with renewables and local storage, in [75], the authors suggest several control strategies for that. Researchers in [76] have optimized the energy management to minimize the cost of the charging process.

1.3. Other applications using multi-source systems

Multi-port converters can also find other relevant applications such as uninterruptible power supplies (UPS), power electronic transformers (to connect different grids electronically and with galvanic isolation), multiple output power supplies, (for example in aircrafts where many voltages are needed), and hybrid energy storage systems.

Multiple port converters in UPS applications have been discussed in [77] [78] for isolated topologies, see Figure 1.3.1. They demonstrate that multiple port converters have improvements in the overall efficiency and size of the UPS. In addition, in [79], the authors present a cost-effective solution based on three port, five level, single-phase inverters for non-isolated on-line UPS. The converter has good load protection and high efficiency.

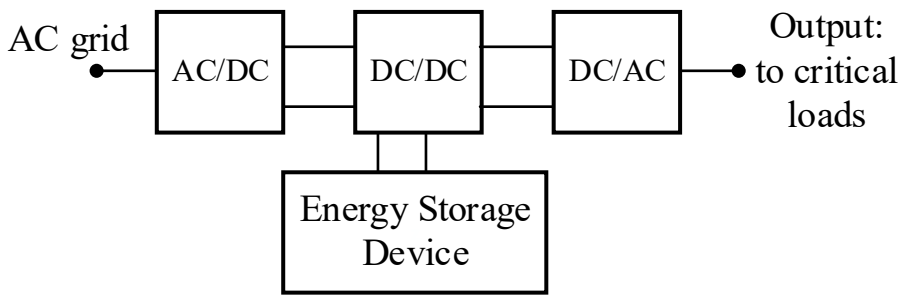

Figure 1.3.1–UPS using a tri-port converter [77]

Power electronic transformers are another application of multiple port converters. Due to the high penetration of various distributed energy resources and DC loads in modern power system, AC/DC hybrid distributed grid attracts attention due to its compatibility with those new loads. Aiming for interface of the AC/DC hybrid distributed grid, a multiple port power electronic transformer (PET) is attractive due to its properties

to have DC and AC voltages available with isolation. In [80], an example for medium voltages is presented. Figure 1.3.2 shows the general scheme of a power electronic transformer. A full review of PET (Power Electronic Transformer) technologies can be found in [81][82].

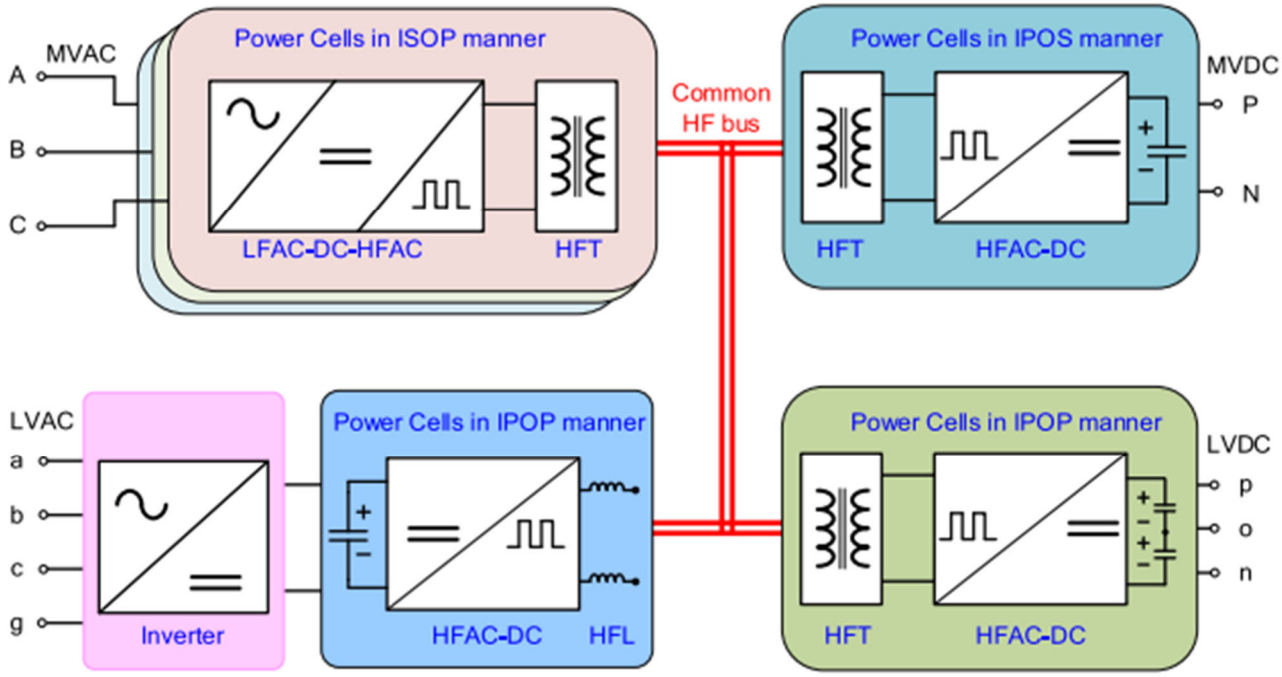

Figure 1.3.2–Power Electronic Transformer using multiple port converters [80]

Regarding applications with renewable energy sources, multiple port converters can be used for increasing their penetration to the grid [83]. In [84], authors show several non-isolated topologies for integrating DC renewable sources. In [85], an isolated multiple port alternative is proposed for applications with renewables.

Aircraft, vehicles, and ships typically feature complex electrical systems including several DC and AC voltages to power different loads. Figure 1.3.3 shows where a multiple port converter can be used in an electric grid of a plane [86] [87].

Furthermore, hybrid energy storage system which combines batteries, supercapacitors and loads are applications of multiple port converters. The author has research on hybrid system for electric motorcycle using non-isolated multiple port converters in [88][89] but also isolated are found in the literature [90].

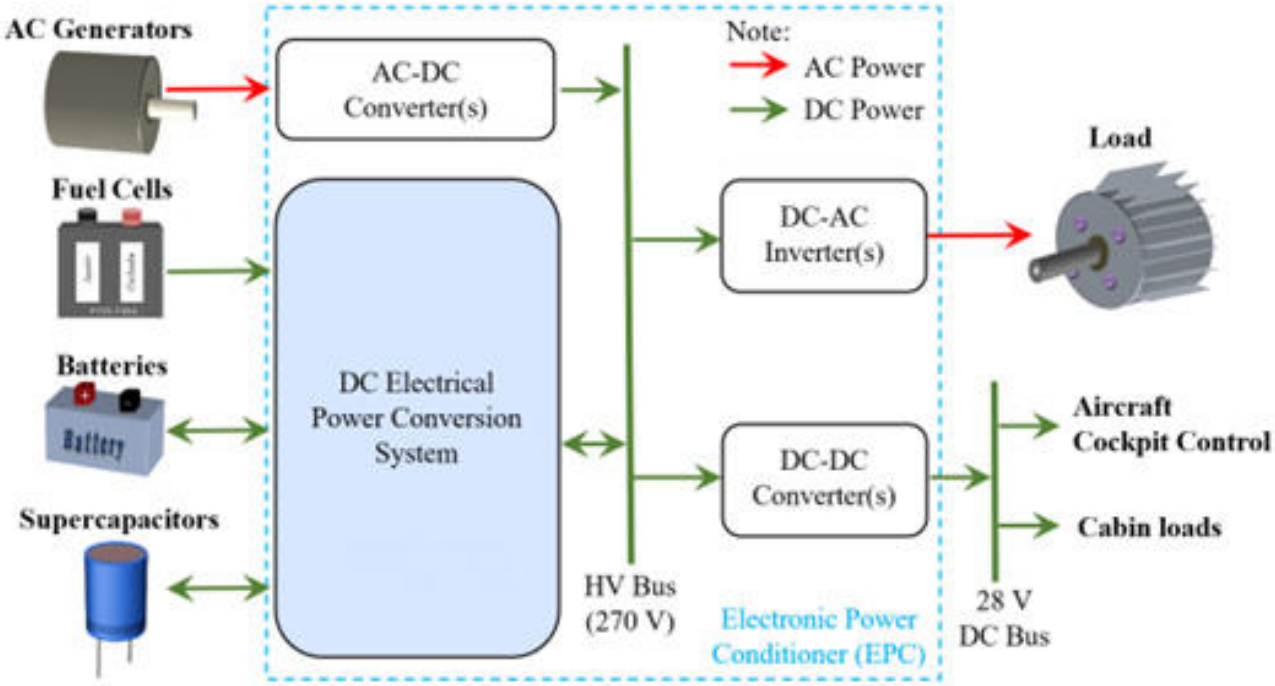

Figure 1.3.3–Multiple port converter applied to electric grids in planes [86]

Chapter 2. THE MULTIPLE ACTIVE BRIDGE AS A SOLUTION FOR A MULTI-PORT SYSTEM

2.1. Existing solutions for a multiple port system

This section examines the modeling and control of the multiple active bridge (MAB) converter. As was mentioned, a first solution for a multiple port system is a combination of two-port DC/DC converters with one common DC link. Then, the ports which need single-phase or three-phase AC connection must be connected through an additional bidirectional DC/AC converter in order to have the required power signal.

A more compact solution is based on a multiple port converter in which several DC ports are interconnected [1-8]. A good candidate from these family of converters is the multiple active bridge (MAB) converter, which provides controllable bidirectional power flow, electrical isolation and compactness.

MAB converters are becoming important due to their ability to enable multidirectional power flow and galvanic isolation. In general, MAB converters are part of a family of converters based on transformers [1] and other impedance networks, such as resonant converters [2], multi-transformer converters [3], complex impedance networks [4-6] and single multi-winding transformer based converters [7-8]. One of the key elements of the MAB converter is the high-frequency (kHz range) transformer, which allows the isolation between ports, however, it must be carefully designed to maintain parameters like magnetizing and leakage inductances within specifications [9]. A basic diagram of a MAB converter is shown in Figure 2.2.1, where each DC port is connected through a full-bridge (but it can be any other topology).

MAB converters can be seen as an extension of dual active bridge (DAB) converters in terms of ports. The transformer, its leakage inductances and the modulation techniques are the key elements to transfer power between the ports. DAB converters are extremely useful in systems which need to be isolated from the grid, so the isolation can be performed using small-size high-frequency transformers. The main method to transfer the energy from one port to the other one is based on a phase-shift modulation between

the two ports, also known as single-phase-shift (SPS) [10]. This technique is commonly used to transfer power in electric grids, where the phase difference between ports is a function of the amount of transferred power. SPS modulation works well if the voltages of each port are similar, however, if the ports' voltages vary, the efficiency drops drastically due to the excessive reactive power involved in the conversion process. This happens typically for battery or supercapacitor charging/discharging processes, where the voltage is a function of the state of charge [11, 12].

For that reason, some advanced modulation techniques have appeared for DAB converters, such as the extended-phase-shift (EPS), double-phase-shift (DPS) and triple-phase-shift (TPS) modulations, in which the voltages at the transformer's windings are controlled through pulse width modulation to build three-level AC signals. In this way, the converter has more degrees of freedom to guarantee the power transfer with high efficiency, extending the zero-voltage-switching (ZVS) operation range of the converter, minimizing the reactive power and, thus, the current stress of the semiconductor devices. In addition, some authors have implemented a variable frequency modulation scheme to extend the ZVS operation range of the DAB converter over a wide voltage operation range.

In the case of MAB converters, the development was similar. In 2004, Prof. Zhao *et al.* introduced the first MAB in which the main control consisted of a phase-shift modulation with some initial ideas of duty modulation [13-15]. In 2007, J. Duarte *et al.*, proposed a phase-shift modulation for controlling hybrid fuel cells [16]. In 2008, Tao *et al.* incorporated duty modulation in order to reduce the switching losses.

Unfortunately, the control algorithm is complex because there is a coupling behavior between ports. This means that delivering power from one port to another one might affect a third port if the control is not aware of that. For that reason, in 2008, a decoupling method was developed by Prof. Kolar team [7]. Using this technique, the pulse width modulation signals for each port were selected in order to minimize the power losses and to allow power decoupling. Unfortunately, it was difficult to extend this method to more than three ports due to the increase in the computational burden. In

addition, the method does not consider that the optimal efficiency point also depends on the input voltage ratio of the ports.

In 2017, a different approach was introduced by Vermulst, Duarte *et al.* [23]. The method, based on Fourier series, is extremely complex because it extracts the Fourier components of the currents and controls them. In addition, the acquisition of the Fourier components can be noisy and can drag significant error [22, 23].

In 2022, a recent approach based on "perturb-and-observe" technique was introduced by O. M. Hebala *et al.* to search for the minimum RMS currents that guarantee the desired power flow [22]. The method is computational effective but it is slow due to the perturb and observe strategy. S. Bandyopadhyay *et al* have been used a linear active disturbance rejection controller to decouple the ports as well [91]. In 2024, another solution by Y. Cai *et al.* was to create virtual DABs inside the MAB and control them individually, the method uses Newton iterative algorithm in each control update [92]. It works for three ports but it becomes too complex for larger amount of ports.

As mentioned, a Fourier decomposition method was used to evaluate and minimize the losses by Vermulst, Duarte *et al.* [23]. The approach is interesting, however, obtaining high-frequency harmonics in a noisy environment is difficult. Due to that, in this research work, it is proposed to obtain the fundamental harmonic by hardware, and to use a real-imaginary decomposition to control the active and reactive power of each port independently. In this approach, both types of power are well controlled, so a desired amount of reactive power can be added to the active power to increase the phase-shift between current and voltage and to achieve soft switching (ZVS) in the full-bridges.

The dq-control method proposed in this research work presents great efficiency for variable voltages at the DC ports and ease of control due to its fast response and decoupling capabilities. However, it still requires high-bandwidth current measurements for controlling its inner current loops. Thus, in order to tackle this and still use the proposed control, a digital observer is part of the future work to eliminate the need for those wide-band current sensors and many analog-to-digital conversions. This reduces the cost of the converter and simplifies the hardware.

2.2. DQ-frame modeling method and control algorithms for large number of ports in multiple active bridge converters

This section details the modeling and control method that can be used in MAB converters with a large number of ports. It starts with the development of a mathematical model of a MAB converter in a dq-frame representation. After that, the section proposed a control algorithm, which is implemented in the form of block diagram. Using the model, numerical simulations were performed to evaluate the control algorithm. This evaluation includes the comprehensive study of harmonic problems and decoupling effects. The simulations were compared with real experiments where the control algorithms were implemented in c-code in a microcontroller. The main content of this section is published by the author in [93].

2.2.1. Mathematical modeling of a MAB converter using dq-frame representation

The MAB converter basic circuit, shown in Figure 2.2.1, consists of an AC circuit and multiple AC/DC or full-bridges making all output ports DC. The AC/DC bridges have two ports, the DC port (or external ports) and the AC port or internal ports. The AC circuit can be considered as a $\mathbb{C}^{NxN}$ impedance matrix as shown in Figure 2.2.2 (a), where N is the total number of ports. The next subsections detail the different sub-blocks of the whole converter [93].

AC/DC converter (full-bridge). Each DC port has an interface, an AC/DC bridge, which transforms the DC power into the AC signals according to pulse width modulation (PWM). Particularly, the full-bridge topology can set three voltage levels in the AC port: $+V_{DC}$, $-V_{DC}$ and 0V, as Figure 2.2.1 shows. Other AC/DC circuits can have a different number of levels. Using these levels different AC signals can be obtained. The proposed modulation technique considers that the control will be performed on the fundamental harmonic ($\omega_0 = \omega_s = 1/T_s$, the switching frequency) of each AC port. The voltage

signal in n-th AC port is:

$$v_n(t) = \underbrace{Im\left(\bar{V}_n . e^{j\omega_0 t}\right)}_{fully\ controllable} + \underbrace{Im\left(\sum_{p=2}^{\infty} \bar{V}_{np} . e^{jp\omega_0 t}\right)}_{non-controllable\ perturbation} \tag{2.2.1}$$

It is a combination of a sine wave controllable in phase and amplitude and its non-controllable harmonics. Figure 2.2.3(a) shows an example of the modulation and its 1st harmonic component.

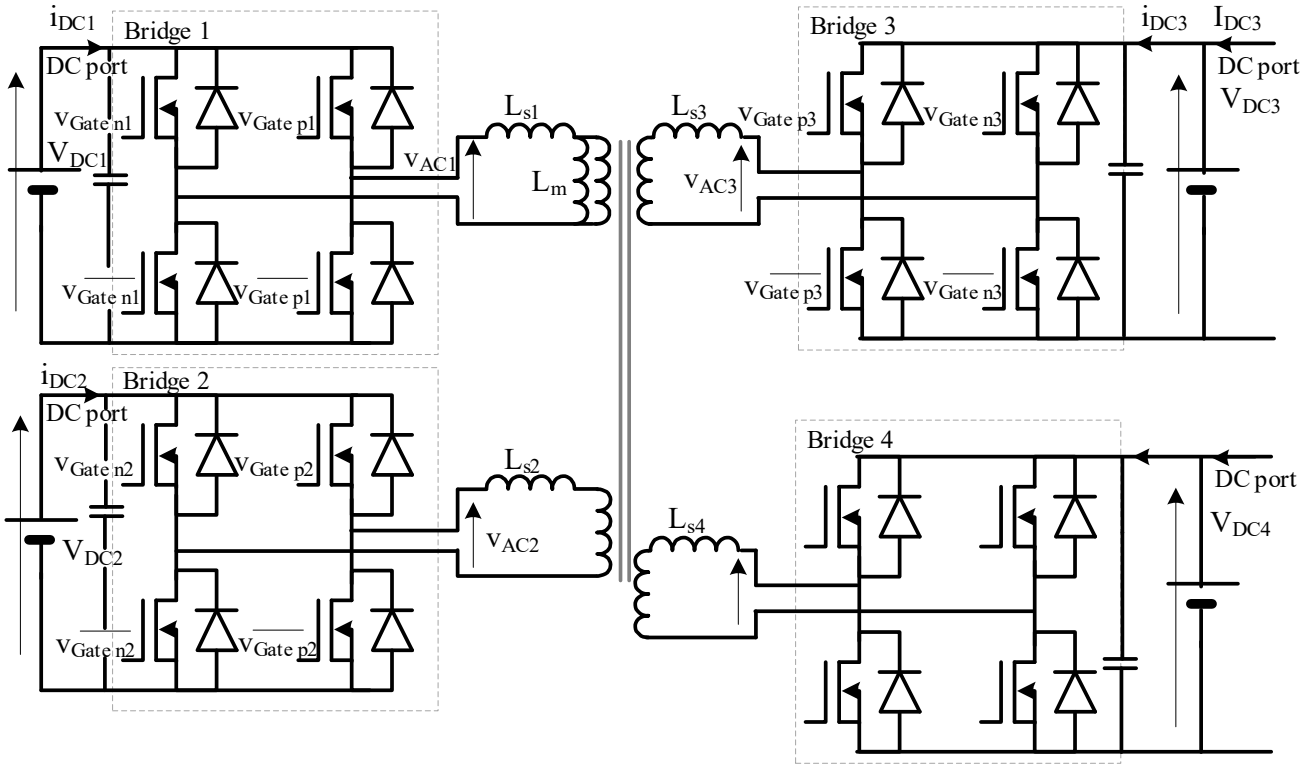

Figure 2.2.1–Example of a MAB converter: QAB (quad-active bridge) power stage

It is assumed that the power of the harmonics is smaller than the fundamental. Thus, harmonics will produce a power flow that can be considered as a perturbation at the AC power and it will be compensated using a DC power control loop as it is explained below in this section. In other words, the first harmonic approximation (FHA) is considered for the analysis and used in an inner (fastest) current control loop.

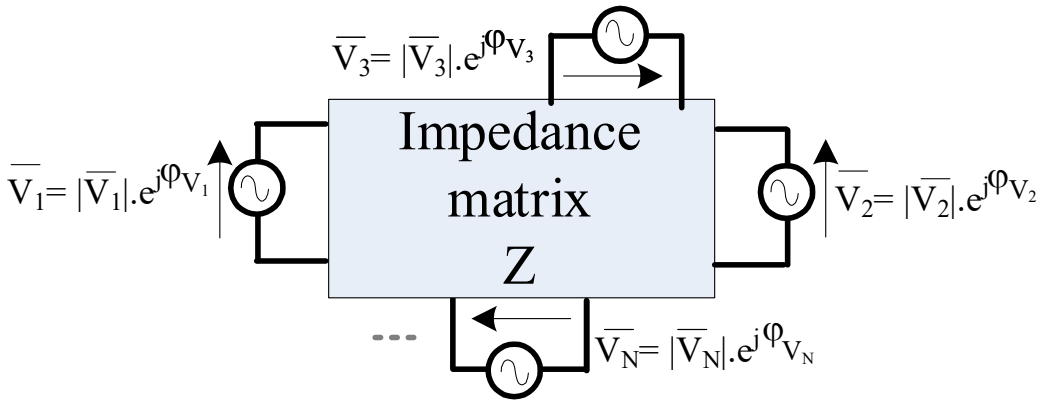

(a)

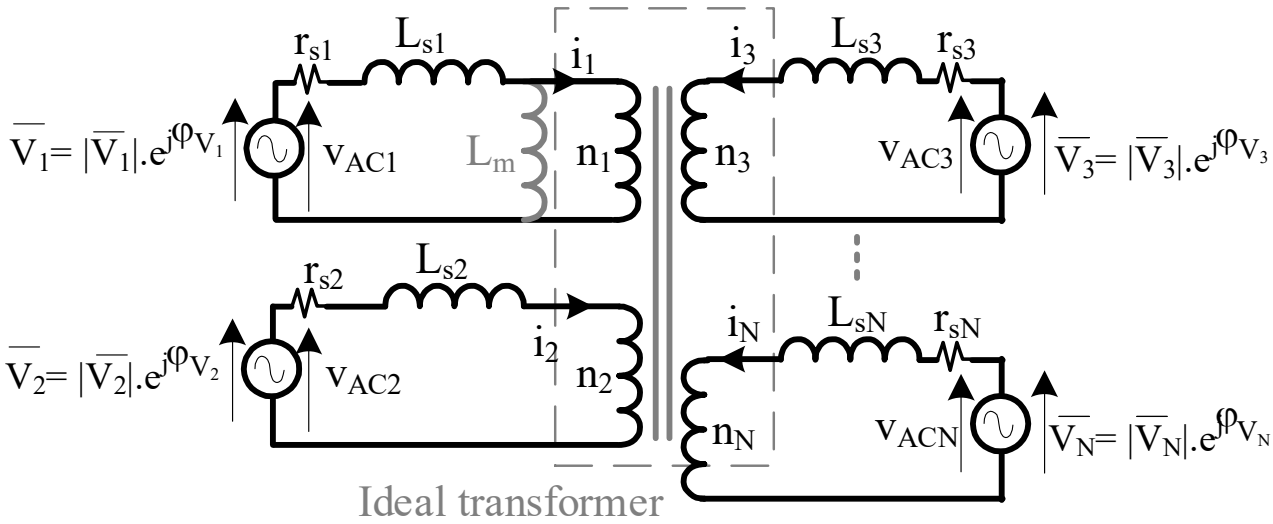

(b)

Figure 2.2.2–Example of MAB: (a) AC simplified diagram and (b) transformer model

The amplitude and phase of the n-th port 1st harmonic signal is a function of the duty cycle of the PWM signals:

$$|\bar{V}_n| = \frac{4}{\pi} V_{DCn}.\sin(D_n\pi)\ and\ \angle\bar{V}_n = \varphi_n, \tag{2.2.2.a}$$

and for its k-th harmonics:

$$|\overline{V}_{nk}| = \frac{4}{\pi k} V_{DCn}.sin(k\pi D_n) \tag{2.2.2.b}$$

where D_n is the equivalent duty cycle from 0 to 0.5. $\bar{V}_n$ is a complex number, and $\angle\bar{V}_n$ is its phase considering the origin of the phases (zero phase shift) at the origin of the switching period T_s. Thus, (2.2.2.a) gives the relationship between the equivalent duty cycle and the amplitude of the 1st harmonic. The phase can be easily obtained by

considering the time delay via:

$$\varphi_n = -\frac{t_{Dn}}{T_S} \cdot 360° = -\frac{\omega_0\, t_{D\,n}}{2\pi} \cdot 360°, \tag{2.2.3}$$

where t_{Dn} is the time delay of the n-th bridge and φ_n is in degrees. The last bridge can be arbitrarily selected as the reference with zero phase shift. Figure 2.2.3(b) shows the logic block diagram inside the controller that converts the desired amplitude and phase into duty cycle and time delay. By modulating the duty cycle, the AC/DC bridge produces the desired AC output. Notice that the inputs of the block are $v_d(t)$ and $v_q(t)$, which are the real and imaginary (or in-phase and quadrature) components of the fundamental signal and not the amplitude and phase because this simplifies the control technique.

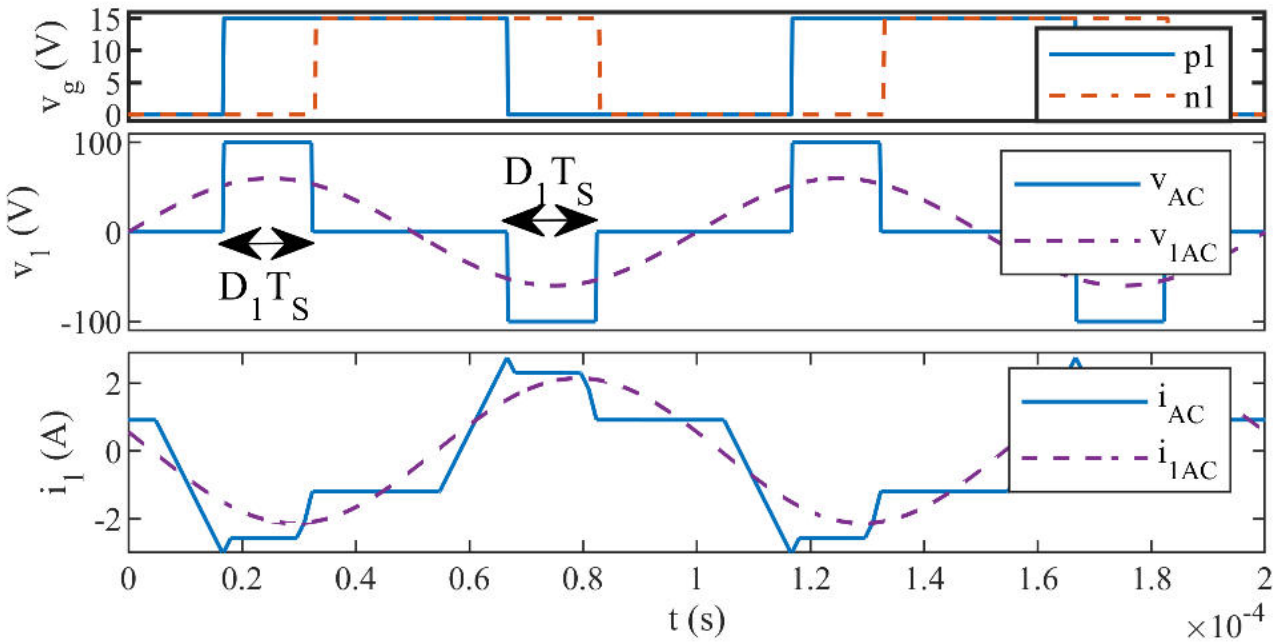

(a)

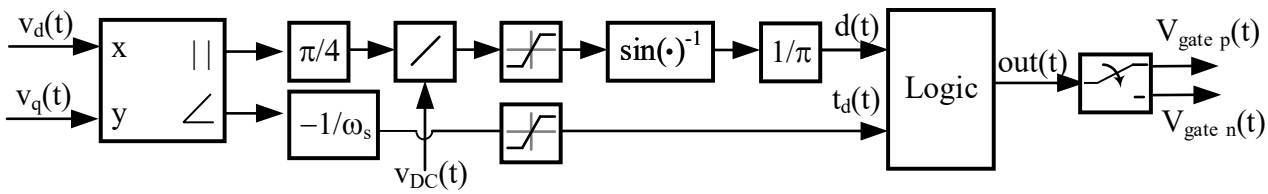

(b)

Figure 2.2.3–Single bridge diagram: (a) waveforms, (b) control logic diagram

AC circuit. In Figure 2.2.1, the transformer is connected to all of the AC ports of the DC/AC bridges, which are considered as voltage sources as Figure 2.2.2 (a) shows. In this figure, only one harmonic is represented. The following analysis is performed based on the fundamental harmonic, but it can be easily extended to any other harmonic.

According to Figure 2.2.2(b), the impedance matrix is obtained. Using the impedance matrix, $\bar{\bar{Z}}$, the voltage at each AC port can be calculated based on the current in each AC port:

$$\vec{V}.e^{j\omega_0 t} = \bar{\bar{Z}} \cdot \vec{I}.e^{j\omega_0 t} \tag{2.2.4}$$

where

$$\bar{\bar{Z}} = \begin{pmatrix} j\omega_0(L_{s1}+L_m)+r_{s1} & j\omega_0 L_m & \dots & j\omega_0 L_m \\ j\omega_0 L_m & j\omega_0(L_{s2}+L_m)+r_{s2} & j\omega_0 L_m & \vdots \\ \vdots & j\omega_0 L_m & \ddots & j\omega_0 L_m \\ j\omega_0 L_m & \dots & j\omega_0 L_m & j\omega_0(L_{sN}+L_m)+r_{sN} \end{pmatrix} \in \mathbb{C}^{NxN}$$

$$\vec{V} = \begin{pmatrix} \overline{V}_1 & \overline{V}_2 \dots \overline{V}_N \end{pmatrix}^T \in \mathbb{C}^{Nx1}$$

$$\vec{I} = \begin{pmatrix} \overline{I}_1 & \overline{I}_2 \dots \overline{I}_N \end{pmatrix}^T \in \mathbb{C}^{Nx1}$$

where ω_0 is the fundamental frequency, in our case is also the switching frequency of the converter, $\omega_0 = \omega_s$. The AC voltages and currents are grouped into the complex vectors $\vec{V}$ and $\vec{I}$. A single line above a symbol denotes a scalar complex variable, while an arrow denotes a vector and a double line a matrix. The impedance matrix can be decomposed as:

$$\bar{\bar{Z}} = j\omega_0.\bar{\bar{L}} + \bar{\bar{r}} \tag{2.2.5}$$

where $\bar{\bar{L}}$ is inductance matrix (a symmetric matrix) and $\bar{\bar{r}}$ is the resistive matrix (a diagonal matrix). In addition, if we neglect the losses ($\bar{\bar{r}} = 0$):

$$\vec{I} \approx \bar{\bar{Z}}^{-1}.\vec{V} = \bar{\bar{Y}}.\vec{V} = \frac{\bar{\bar{L}}^{-1}}{j\omega_0}.\vec{V}. \tag{2.2.6}$$

The lossless admittance matrix is $\bar{\bar{Y}} = \frac{\bar{\bar{L}}^{-1}}{j\omega_o}$ for steady-state sinusoidal waveforms. The vector of complex powers is:

$$\vec{S} = \frac{\vec{V}.\vec{I^*}}{2} = \frac{j.\vec{V}.\bar{\bar{L}}^{-1}.\vec{V^*}}{2\omega_0} = [S_1 \quad \dots \quad S_N]^T. \tag{2.2.7}$$

where each component is the complex power of each port. Thus, by controlling the amplitude and phase (or real and imaginary parts) of the voltage at each AC port, it is possible to control the power flow. One of the aims of the converter is to transfer power between different ports efficiently, this includes reducing the reactive power, and this is why it is important to measure both active and reactive power.

To conclude, the power through the converter can be controllable based on the AC port voltages according to (2.2.7), and these voltages are controllable based on (2.2.2) and (2.2.3).

Dynamic linear analysis. This analysis considers that the signals vary in order to obtain a dynamic model. The analysis is used to propose a decoupling block and a control loop. The system plant consists of a transformer in its linear range and DC/AC bridges in which the DC voltages vary smoothly, so they are assumed constant. Thus, the plant is linear and the analysis can be extended to large signals. In order to include the dynamics, (2.2.4) needs to be re-written:

$$\bar{\bar{L}}.\frac{d\left(\vec{I}.e^{j\omega_0 t}\right)}{dt} + \bar{\bar{r}}.\vec{I}.e^{j\omega_0 t} = \vec{V}.e^{j\omega_0 t}, \tag{2.2.8.a}$$

which is the equation of each port of the transformer in the stationary reference frame. In Laplace domain, considering that the signals vary, they are expressed as $\vec{v} = \vec{V}(s)$ and $\vec{\imath} = \vec{I}(s)$, where s is the Laplace variable. Using rotational reference frame (dq-frame), complex exponentials appear in all of the terms and can be removed:

$$\left(s\bar{\bar{L}} + \bar{\bar{r}} + j\omega_0.\bar{\bar{L}}\right).\vec{\imath} = \vec{v}. \tag{2.2.8.b}$$

However, a new term, $s\bar{\bar{L}}$, has appeared in comparison with (2.2.5). Also notice that the equation has real and imaginary parts. Small letters express variables in Laplace domain. In this section, the contribution of the magnetizing inductance of the transformer (L_m) is omitted because $L_m >> L_{sn}$ and it can be considered as a second order effect. Thus, the sum of the ampere-turns, including all of the windings in the ideal inner transformer, is zero:

$$\sum_{n=1}^{N} n_n \cdot \bar{\iota}_n \approx 0. \tag{2.2.9}$$

Therefore, using (2.2.9) and considering the N-th port as the fixed reference, the matrices $\bar{\bar{L}}$ and $\bar{\bar{r}}$ can be reduced. The expansion of (2.2.8.b), which includes (2.2.9), shows that:

$$\left(s\bar{\bar{L}} + \bar{\bar{r}} + j\omega_0.\bar{\bar{L}}\right).\begin{pmatrix} \bar{\iota}_1 \\ \bar{\iota}_2 \\ \vdots \\ \dfrac{-\sum_{n=1}^{N-1} n_n \cdot \bar{\iota}_n}{n_N} \end{pmatrix} = \begin{pmatrix} \bar{v}_1 \\ \bar{v}_2 \\ \vdots \\ \bar{v}_N \end{pmatrix}. \tag{2.2.10}$$

In addition, if $\bar{v}_N$=V_N is the fixed real reference, the last row can be subtracted from the other rows:

$$\left[(s + j\omega_0).\underbrace{\begin{pmatrix} L_{11}^R & \cdots & L_{1(N-1)}^R \\ \vdots & \ddots & \vdots \\ L_{(N-1)1}^R & \cdots & L_{(N-1)(N-1)}^R \end{pmatrix}}_{\bar{\bar{L}}^R} + \bar{\bar{r}}^R\right].\underbrace{\begin{pmatrix} \bar{\iota}_1 \\ \vdots \\ \bar{\iota}_{N-1} \end{pmatrix}}_{\vec{\iota^R}} = \underbrace{\begin{pmatrix} \overline{v_1} - \overline{V_N} \\ \vdots \\ \bar{v}_{N-1} - \overline{V_N} \end{pmatrix}}_{\vec{v^R}}, \tag{2.2.11.a}$$

$$\left[(s + j\omega_0).\bar{\bar{L}}^R + \bar{\bar{r}}^R\right].\vec{\iota^R} = \vec{v^R} \in \mathbb{C}^{(N-1)x1} \tag{2.2.11.b}$$

where the upper index 'R' means reduced matrices $\in \mathbb{C}^{(N-1)x(N-1)}$ or vectors $\in \mathbb{C}^{(N-1)x1}$. As an example, in a three-port converter with a unitary transformer turns-ratio (n_1=n_2=n_3), leakage inductances L_{s1}, L_{s2} and L_{s3}, and magnetizing inductance L_m, the matrix $\bar{\bar{L}}$ is:

$$\bar{\bar{L}} = \begin{pmatrix} L_{s1} + L_m & L_m & L_m \\ L_m & L_{s2} + L_m & L_m \\ L_m & L_m & L_{s3} + L_m \end{pmatrix} \tag{2.2.12}$$

and the reduced matrices are:

$$\bar{\bar{L}}^R = \begin{pmatrix} L_{s1} + L_{s3} & L_{s3} \\ L_{s3} & L_{s2} + L_{s3} \end{pmatrix} \text{ and} \tag{2.2.13.a}$$

$$\bar{\bar{r}}^R = \begin{pmatrix} r_{s1} + r_{s3} & r_{s3} \\ r_{s3} & r_{s2} + r_{s3} \end{pmatrix}. \tag{2.2.13.b}$$

By using the reduced equations, the current $\vec{\iota^R}$can be controlled, which means that currents can be controlled in all ports but one. However, due to $\bar{\bar{L}}^R$ and $\bar{\bar{r}}^R$, the voltage at

each port influences the others. Therefore, a decoupling block is needed to provide independence to each port. By achieving that, the control loops will only be a combination of single-input-single-output control loops at each port. In addition, as the signals are complex variables there is also a coupling between real and imaginary parts due to the "$j\omega_0$" term. Figure 2.2.4(a) shows the block diagram of the power stage, where the inputs are the AC voltages of each bridge and the outputs are the AC currents in each bridge, based on (2.2.11.b). Real and imaginary (dq) components of $\vec{v} = \overrightarrow{v_d} + j\overrightarrow{v_q}$ and $\vec{\imath} = \overrightarrow{\imath_d} + j\overrightarrow{\imath_q}$ are used. For that (2.2.11.b) is decomposed in its dq-frame representation, and this is the plant model:

$$\overrightarrow{\imath_d^R} = \left(s.\bar{\bar{L}}^R + \bar{\bar{r}}^R\right)^{-1}\overrightarrow{v_d^R} + \omega_0.\bar{\bar{L}}^R.\overrightarrow{\imath_q^R} \tag{2.2.14.a}$$

$$\overrightarrow{\imath_q^R} = \left(s.\bar{\bar{L}}^R + \bar{\bar{r}}^R\right)^{-1}\overrightarrow{v_q^R} - \omega_0.\bar{\bar{L}}^R.\overrightarrow{\imath_d^R}. \tag{2.2.14.b}$$

2.2.2. Control algorithms for MAB converters using dq-frame representation

Decoupling blocks. In order to control $\overrightarrow{\imath_d}$ and $\overrightarrow{\imath_q}$ independently in each AC port, the controller must have a decoupling block. The idea is to create an auxiliary complex vector, $\vec{u} = \overrightarrow{u_d} + j\overrightarrow{u_q}$ in which each component affects only to an exact AC (real or imaginary) current at a certain port. For that, based on (2.2.14), the non-coupled current terms are grouped in one side of the equations while the other side can be replaced by the auxiliary control vector:

$$\left(s\bar{\bar{r}}^{R^{-1}}.\bar{\bar{L}}^R + \bar{\bar{I}}\right)\overrightarrow{\imath^R}(s) = \left[-j\omega_0\bar{\bar{r}}^{R^{-1}}.\bar{\bar{L}}^R.\overrightarrow{\imath^R}(s) + \bar{\bar{r}}^{R^{-1}}.\overrightarrow{v^R}(s)\right] = \vec{u} \tag{2.2.15.a}$$

where $\bar{\bar{I}}$ is the identity matrix. Thus, $\vec{u}$ is defined and has ampere units, and so, $\overrightarrow{v^R}$ can be defined in terms of $\vec{u}$ as:

$$\overrightarrow{v^R} = \left[j\omega_0.\bar{\bar{L}}^R\overrightarrow{\imath^R}(s) + \bar{\bar{r}}^R\vec{u}\right]. \tag{2.2.15.b}$$

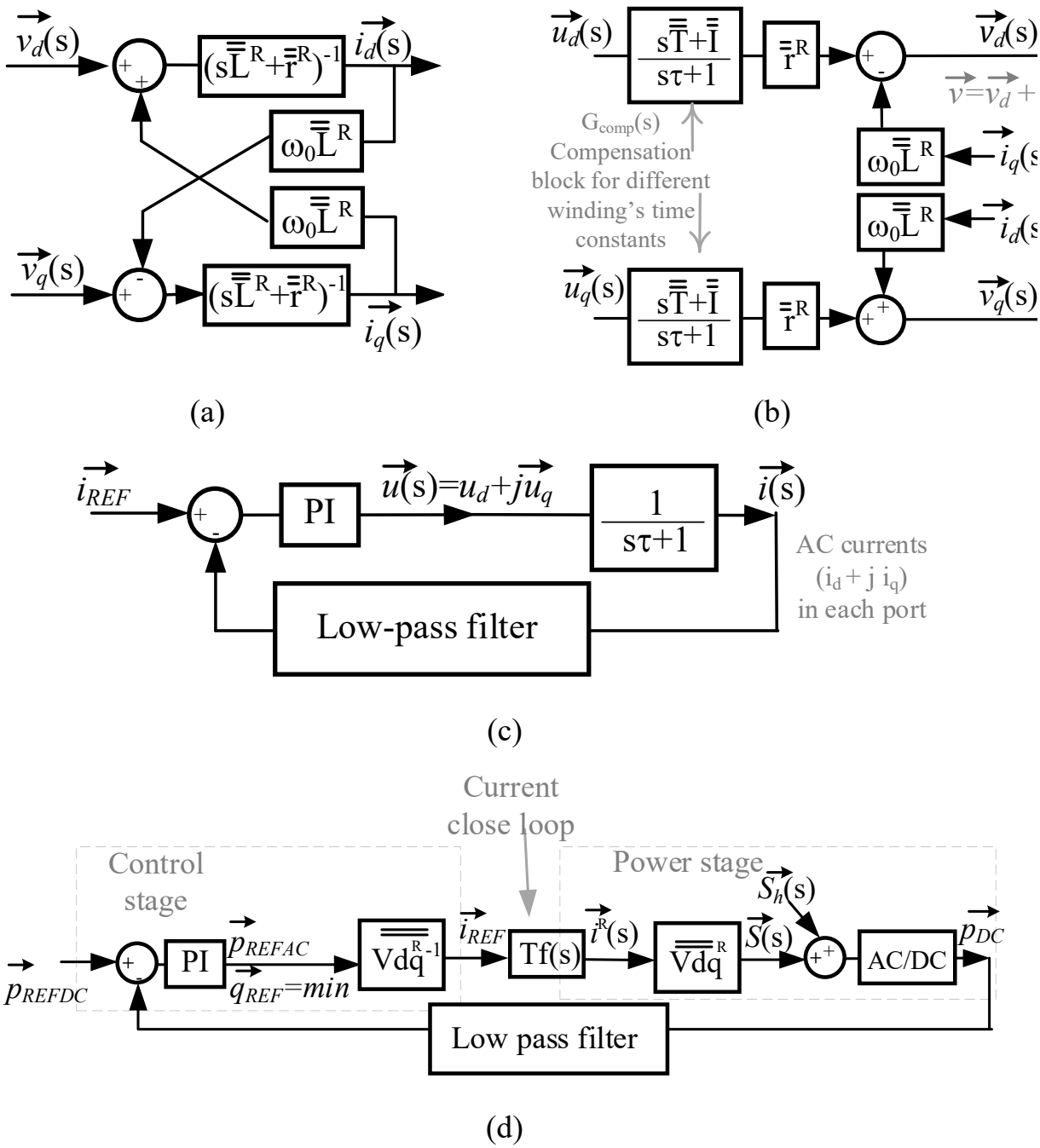

Figure 2.2.4-Control diagram: (a) (coupling) power stage, (b) decoupling control stage, (c) equivalent current loop diagram and (d) DC power control loop

Finally, using $\vec{u}$, the transfer function matrix that relates $\vec{\imath^R}$ and $\vec{u}$, "$\frac{\vec{\imath^R}}{\vec{u}(s)}$", from (2.2.15.a) is:

$$\vec{\imath^R}(s) = \left(s\bar{\bar{r}}^{R^{-1}}\bar{\bar{L}}^R + \bar{\bar{I}}\right)^{-1}\vec{u}(s) = \left(s\bar{\bar{T}} + \bar{\bar{I}}\right)^{-1}\vec{u}(s). \tag{2.2.16}$$

If the matrix in (2.2.16) is diagonal, then each u-component controls independently each i^R-component in both real and imaginary parts. Therefore, it is important to have a

diagonal matrix in (2.2.16). For that, $\bar{\bar{T}} = \bar{\bar{r}}^{R^{-1}} . \bar{\bar{L}}^{R}$ should be diagonal. To obtain a diagonal matrix, the ratio between leakage inductance, L_{sn}, and series resistance, r_{sn}, of each winding—or, in other words, the time constants of the windings—must be the same. Two possible controls can be applied: 1) when the windings' time constants are equal or 2) when they are unequal.

Equal time constants: $\bar{\bar{T}} = \tau\bar{\bar{I}}$*:* according to (2.2.16), defining $\tau = \frac{L_{sn}}{r_{sn}}$ (the winding time constant), and to keep the plant as a single-pole transfer function, the current is controlled by $\vec{u}$ as:

$$\overrightarrow{\imath^{R}}(s) = \left(s\bar{\bar{T}} + \bar{\bar{I}}\right)^{-1}\vec{u} = \left(s\tau\bar{\bar{I}} + \bar{\bar{I}}\right)^{-1}\vec{u} = \frac{\vec{u}}{s\tau + 1}. \tag{2.2.17}$$

Therefore, from the point of view of $\vec{u}$, this implies an independent first order plant per component. For achieving that, the decoupling equation (2.2.15.b) is used. A block diagram that clarifies the decoupling block is presented in Figure 2.2.4(b). Notice that by combining both the decoupling block and the power stage from (2.2.14) also depicted in Figure 2.2.4(a), the coupling effects are cancelled and the i^R-components follow the u-components through the first order system. For the diagram, the dq-components were extracted from (2.2.15.b), in a similar manner that (2.2.14) from (2.2.11.b). As the decoupling is not always equal than the coupling the perfect match is not achieved. Details are included in [96] and will be discussed in detail in Section 2.3.

Non-equal time constants: If the time constants are not the same, (2.2.16) has coupling effects between the ports based on the matrix transfer function "$\frac{\overrightarrow{\imath^{R}}}{\vec{u}(s)}$" = $\left(s\bar{\bar{T}} + \bar{\bar{I}}\right)^{-1}$. The solution for that is to add a compensation block before $\vec{u}(s)$:

$$G_{comp}(s) \approx \frac{\left(s\bar{\bar{T}} + \bar{\bar{I}}\right)}{s\tau + 1}. \tag{2.2.18.a}$$

Then $\vec{u}$ is replaced by $\vec{u}'$

$$\vec{u}'^{(s)} = G_{comp}(s)\vec{u}(s). \tag{2.2.18.b}$$

Thus, (2.2.16) becomes:

$$\overrightarrow{\imath^{R}}(s) = \left(s\bar{\bar{T}} + \bar{\bar{I}}\right)^{-1}\vec{u}' \approx \left(s\bar{\bar{T}} + \bar{\bar{I}}\right)^{-1}\frac{\left(s\bar{\bar{T}} + \bar{\bar{I}}\right)}{s\tau + 1}\vec{u} \approx \frac{\vec{u}}{s\tau + 1}. \tag{2.2.19}$$

The equation is approximated because the matching between poles and zeros is not perfect due to measurement errors. Figure 2.2.4(b) shows the compensation blocks in the control chain. However, if the mismatch is not large, the equal-time constant strategy can still be applied. Note that (2.2.19) shows that the $\overrightarrow{\imath^R}(s)$ and $\vec{u}$ are linked with a simple transfer function which is single-input-single-output (SISO). There is a SISO transfer function for each current at each port. Thus, to control them, a simple controller can be implemented plus some algebraic equations which allows decoupling of the d and q components at each port. These equations (controller and decoupling block) are simple and can be easily implemented discretely in a microprocessor. Therefore, this new technique allows extending the converter to work with any number of ports because the processing time of a digital proportional-integral (PI) controller with the decoupling block is only several microseconds in a microprocessor.

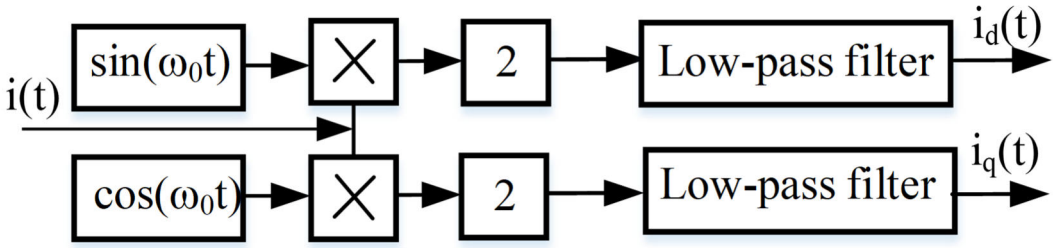

Figure 2.2.5–dq-transformation for AC currents

Current control loop. Having modeled the power stage (coupling block) and proposing the decoupling block, the next step is to close the loop and control $\overrightarrow{\imath^R}$. For that, by joining Figure 2.2.4(a) and Figure 2.2.4(b), a simple control block diagram is obtained in Figure 2.2.4(c). There, the plant is the combination of the power stage and the decoupling stage and it is governed by $\vec{u}$. In addition, in the feedback loop, the currents are measured using the transformation block from

Figure 2.2.5. Notice that this block is working with analog multipliers and analog filters [93][94]. The low-pass filter (LPF) can be first or second order because it needs to filter frequencies higher than twice the switching frequency while keeping the DC

components (i_d and i_q) unchanged.

The design of the control loop involves the selection of the controller. In this case, a simple PI controller is suggested. The open-loop transfer function for current control, OL_{Tf_C}, is:

$$OL_{Tf_C}(s) = k_{P_c}\frac{sT_{i_c}+1}{sT_{i_c}}\frac{1}{s\tau+1}LPF(s), \tag{2.2.20}$$

where T_{iC} is the integration time constant and k_{Pc} is the proportional constant of the PI controller. The low-pass filter (LPF) can be written as:

$$LPF(s) = \frac{1}{\left(\frac{s}{\omega_{c_c}}\right)+1}, \tag{2.2.21}$$

where ω_{c_c} is the cut-off frequency of the filter. This is a first order filer but also a second order filter can be used. The plant is represented according to (2.2.17-2.2.19). A simple approach indicates that if T_{iC} cancels the plant time constant, $\tau=L_{sn}/r_n$, the order of the system is reduced. Then, to select k_{Pc} a conservative approach is to set the frequency corresponding to the 0dB open-loop, ω_{0dB}, far from the filter cut-off frequency, ω_{c_c}, so by using (2.2.20) and neglecting the low pass filter:

$$\omega_{0dB} \approx \frac{k_{P_c}}{T_{i_c}}. \tag{2.2.22}$$

Thus, the approximate closed-loop transfer function for the current control, CL_{Tf_C}, in the control region will be (for a 1st order measurement filter):

$$CL_{Tf_C}(s) = \frac{1}{s\frac{T_{i_c}}{k_{P_c}}+\frac{1}{1+\frac{s}{\omega_{c_c}}}}, \tag{2.2.23}$$

and, if the plant pole is dominant, $\omega_{0dB} << \omega_{c_c}$, it can be approximated to:

$$CL_{Tf_C}(s) = Tf(s) \approx \frac{1}{1+s\underbrace{\left(\frac{T_{i_c}}{k_{P_c}}\right)}_{\omega_{0dB}}}. \tag{2.2.24}$$

Because within the bandwidth the filter $LPF(s) \approx 1$. Based on this control loop in each AC port and for real and imaginary parts, an AC power control loop can be

implemented straight forward. By using the dominant pole approximation in (2.2.24), the closed-loop transfer function $\frac{i^R}{I^R_{REF}}(s)$ for any d and q components and at any port can be considered as a first order system. This will be used in the secondary control loop.

AC power calculation. Being able to control the currents, since the voltages are well-known, active and reactive powers can also be controlled. The AC power at the n-th port is:

$$\bar{S}_n = \overline{v_n}.\overline{i_n}^*/2 = (v_{nd} + jv_{nq}).(i_{nd} - ji_{nq})/2 \tag{2.2.25}$$

$$\begin{pmatrix} P_n \\ Q_n \end{pmatrix} = \underbrace{\begin{pmatrix} v_{nd}/2 & v_{nq}/2 \\ v_{nq}/2 & -v_{nd}/2 \end{pmatrix}}_{\overline{\overline{V_{dq_i}}}} . \begin{pmatrix} i_{nd} \\ i_{nq} \end{pmatrix}. \tag{2.2.26}$$

Therefore, the AC power calculation block must extract the current references as:

$$\begin{pmatrix} i_{nd_{ref}} \\ i_{nq_{ref}} \end{pmatrix} = \frac{2\begin{pmatrix} v_{nd} & v_{nq} \\ v_{nq} & -v_{nd} \end{pmatrix}}{({v_{nd}}^2 + {v_{nq}}^2)} . \begin{pmatrix} P_{n_{ref}} \\ Q_{n_{ref}} \end{pmatrix}, \tag{2.2.27}$$

where v_{nd} and v_{nq} represent the voltage in the d- and q-axis of the n-th bridge respectively. This block is included in the final control loop as "V_{dq}^{-1}", see Figure 2.2.4(d). Note that, both active and reactive power can be controlled. Active power is useful for transferring power between DC ports and reactive power for achieving zero-voltage switching (ZVS). The reactive power lags the current phase so the switches can turn-on while the current is still negative and the ZVS is achieved using the anti-parallel diodes. The amount of reactive power depends on the needed phase shift.

DC Power controller – the secondary controller. A DC power controller is implemented for improving the accuracy of the DC power transfer due to the effect of the power in the harmonic signals which are not under control and can be considered as an external perturbation. The DC power is controlled at each DC port using measurement units (sensors) and DC power references that provide the proper AC references for the inner loops. Figure 2.2.4(d) shows the block diagram of the outer control loop. The design of the control loop is similar to the current control loop. Voltage blocks do not add any dynamics, the transfer function $T_f(s)$ from the current loop and some extra delays due to

the DC power measurements must be considered.

2.2.3. Computer simulations: The quadruple active bridge (QAB):

Design of control loops for the simulation. As an example, to test the proposed method, let us consider a 4-port active bridge (QAB), it might be the case illustrated in Figure 2.2.1 in which all of the ports have bidirectional power flow. It is convenient that all the QAB transformer's windings have the same time constant $\tau=L_n/r_n$ as was explained in Section 2.2.2. Thus, the poles of each winding are located in the same place which simplifies the controller. This can be achieved with a special design of the magnetic components, designing a single transformer or a set of inductors and a transformer [9].

In order to design the control loops: (inner) dq-frame current-control loop and DC power control loop, the diagrams in Figure 2.2.4(c) and Figure 2.2.4(d) were used. Eq. (2.2.20) is used considering that the decoupling network in Figure 2.2.4(b) matches the coupling network in Figure 2.2.4(a). For this example, the values are shown in Table 2.2.1 and ω_{0dB} was set at $0.1\omega_{Cc}$, thus (2.2.24) is valid and the design procedure follows Section 2.2.2.

Figure 2.2.6(a) shows the open-loop frequency response for one port: $i_{d1}^R/(I_{dREF1}^R-i_{d1}^R)$. All other ports have the same transfer function because they have the same time constants. The simulations include a time delay ($1.5/f_S$) due to the discretization and PWM techniques and this is why the phase is continuously decreasing. Two curves are shown: a) the dashed curve represents the ideal model where the decoupling block perfectly matches the power plant, and b) the continuous adds the low pass filter.

The inner control loop design follows Section 2.2.2 and the values of the PI controller are shown in Table 2.2.1. Once the current loop is designed, the next step is the DC power controller design. For that the closed-loop current control transfer function "$T_f(s)$" is needed (shown in

Figure 2.2.6(b)). A simplified model follows (2.2.24) and the same transfer

function can be obtained for all other currents of the QAB ($I_{d3}^R, I_{q3}^R I_{d2}^R, I_{q2}^R, I_{q1}^R$).

Table 2.2.1 QAB converter parameters for simulations

Symbol	Quantity	Value
f_S	Switching frequency	40kHz
$V_{DC1,2,3}$	DC Input voltages	650-800 V
$L_{s1,2,3}$	Leakage inductances	20uH
n_1,n_2,n_3	Windings' turns-ratio	1
$r_{s1,2,3}$	Windings' resistances	0.3Ω
$\omega_{C\,c}$	Cut-off freq. for low-pass filter in dq-transformation (Figure 2.2.5)	$2\pi f_s/5$= 50krad/s
ω_{0dB}	Frequency at 0dB open current loop gain	5 krad/s
L_m	Magnetizing inductance	1mH
$T_{i\,c}$	Current controller integration time	0.07ms
$k_{P\,c}$	Current controller proportional gain	0.33
$T_{i\,p}$	Power controller integration time	0.2ms
$k_{P\,p}$	Power controller proportional gain	0.5
$\omega_{C\,p}$	Cut-off freq. for low-pass filter in power calculation	$2\pi f_s/5$

For obtaining the AC power, the V_{dq} block was added in Figure 2.2.4(d) to get the power corresponding to the 1st harmonic approximation. However, as some vestigial power is on the harmonics, the control loop is on the DC power as shown in Figure 2.2.4(d). Due to the measurements and the DC capacitors a delay exists for measuring DC power, thus another filter is considered, $LPF_P(s)$. The open-loop transfer function of the complete DC power control scheme is:

$$OL\,Tf_P(s) = k_{P_P}\frac{sT_{i_P}+1}{sT_{i_P}}\frac{1}{\frac{s}{\omega_{0dB}}+1}LPF_P(s), \tag{2.2.31}$$

where the sub-index P means DC power control loop. In this case, the filter transfer function can be considered out of the bandwidth, the pole at ω_{0dB} can be cancelled with

the PI pole ($\omega_{0dB} = 1/T_{ip}$), and finally the k_{Pp} is adjusted to the desired bandwidth. In order to validate this control system, several simulations based on the proposed model were performed.

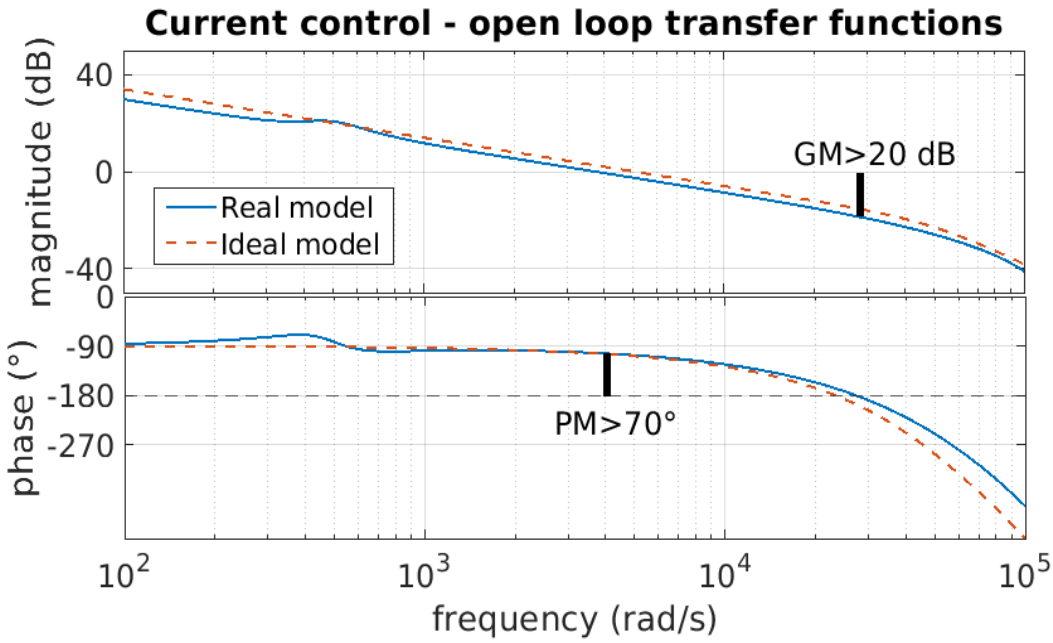

(a)

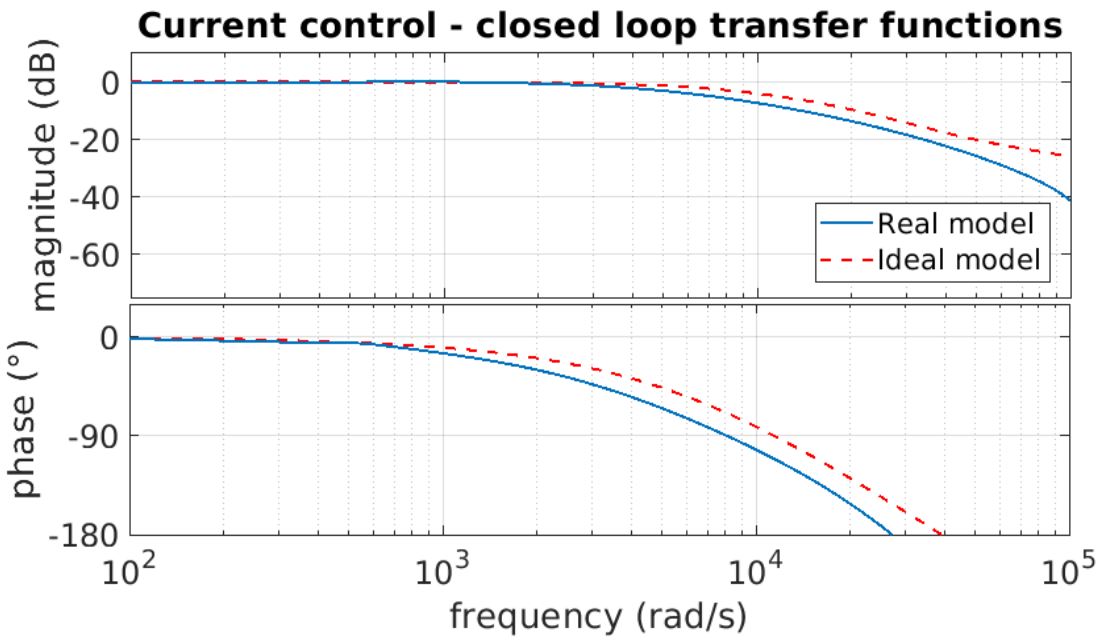

(b)

Figure 2.2.6–Frequency response plot of (a) the open-loop current loop, $i_{d1}^R/(I_{dREF1}^R - i_{d1}^R)$ and (b) closed-loop transfer function, i_{d1}^R/I_{dREF1}^R. The ideal model is the model which was considered in the design guide with exact decoupling

Dynamic behavior. In order to test the converter a power step was performed. The initial power per port was: P_{DC1}=10kW, P_{DC2}=5kW, P_{DC3}=0kW and P_{DC4} balances the power. After 5ms, the power changes to P_{DC1}=2.5kW, P_{DC2}= P_{DC3}=-5kW. Figure 2.2.7(a) shows the results, the time response is about 2ms and the power control is accurate. In addition, Figure 2.2.7(b) shows a similar case but when the transformer windings' time constants are different because of different leakage inductances: L_{s1}=10uH, L_{s2}=20uH, L_{s3}=30uH and L_{s4}=20uH. The results show that the time response is about 5ms, slightly slower than the case of equal inductances but the system is still working properly.

Waveforms. Figure 2.2.8 shows the simulation waveforms for the proposed approach at two different power operational points, at the end of each interval shown in Figure 2.2.7: interval 1) P_{DC1}=10kW, P_{DC2}=5kW, P_{DC3}=0kW and interval 2) P_{DC1}=2.5kW, P_{DC2}= P_{DC3}=-5kW. Notice that port one, three and four are at V_{DC1}=V_{DC3}=V_{DC4}=650V while V_{DC2}=800V, in order to show that the converter can work at different voltages as well with different duty cycles. Figure 2.2.8(a) shows the voltages in each AC port, Figure 2.2.8(b) shows the AC current waveforms and Figure 2.2.8(c) shows the DC currents in each DC port.

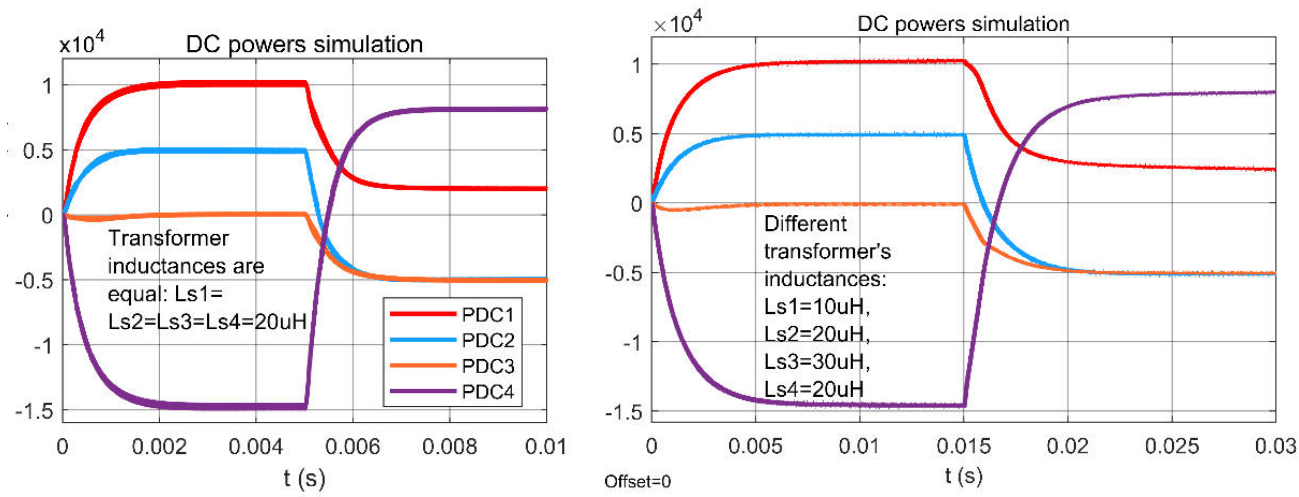

(a) (b)

Figure 2.2.7–Simulations using DC power control diagram (a) power response after a step in the references and (b) dq-frame currents

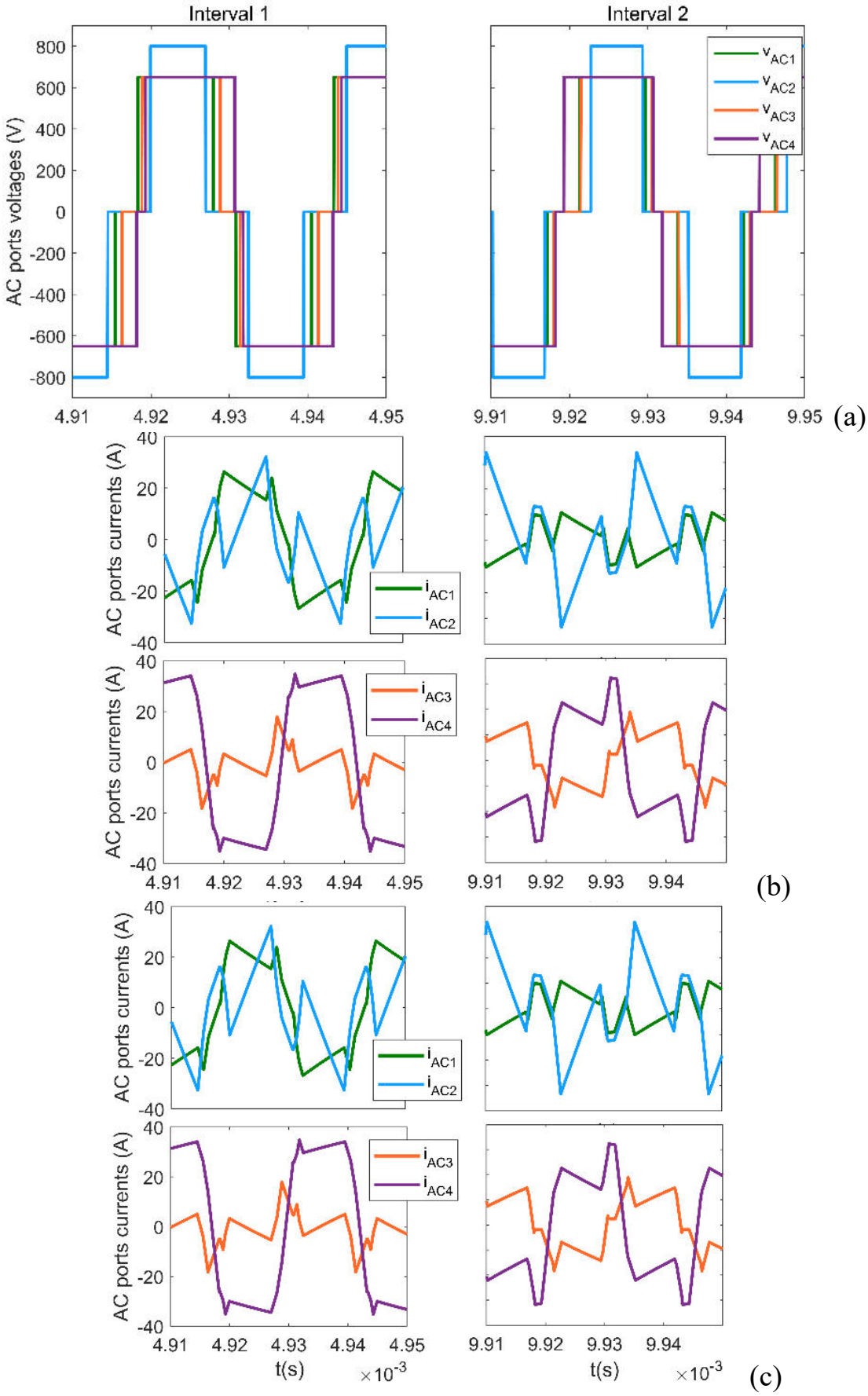

Figure 2.2.8–Simulation waveforms at different power and voltages: (a) AC voltages, (b) AC currents and (c) DC currents

2.2.4. Experimental results: the triple active bridge (TAB):

In order to validate the proposed control, a 400W-triple active bridge (TAB) converter was built and tested, see Figure 2.2.9. The main circuit consists of three bridges connected to a transformer and controlled with a driver stage. A controller (microprocessor) sends the gate signals to the drivers and receives all the information using current sensors. Table 2.2.2 lists the details of the converter. The dq-decomposition is done using an analogue multiplier and a set of filters as shown in

Figure 2.2.5. Finally, all of the measurements go to the analogue-to-digital conversion (ADC) in to the microprocessor.

Table 2.2.2 Triple Active Bridge, Prototype parameters

Symbol	Quantity	Value
f_s	Switching frequency	40kHz
$V_{DC1,2,3}$	DC Input voltages	150-220 V
$L_{s1,2,3}$	Leakage and external inductances	28uH, 26uH, 28uH
n_1,n_2,n_3	Windings' turns-ratio	1
$r_{s1,2,3}$	Windings' resistances	0.2Ω
ω_{C_c}	Cut-off freq. for low-pass filter in dq-transformation (Fig. 5.d)	$2\pi f_s/5$
	Switches, MOSFETs	IPW60R060
L_m	Magnetizing inductance	1mH
dq-frame current measurement based on analogue multiplier AD633		
digital signal processor: TMS320F28379D		

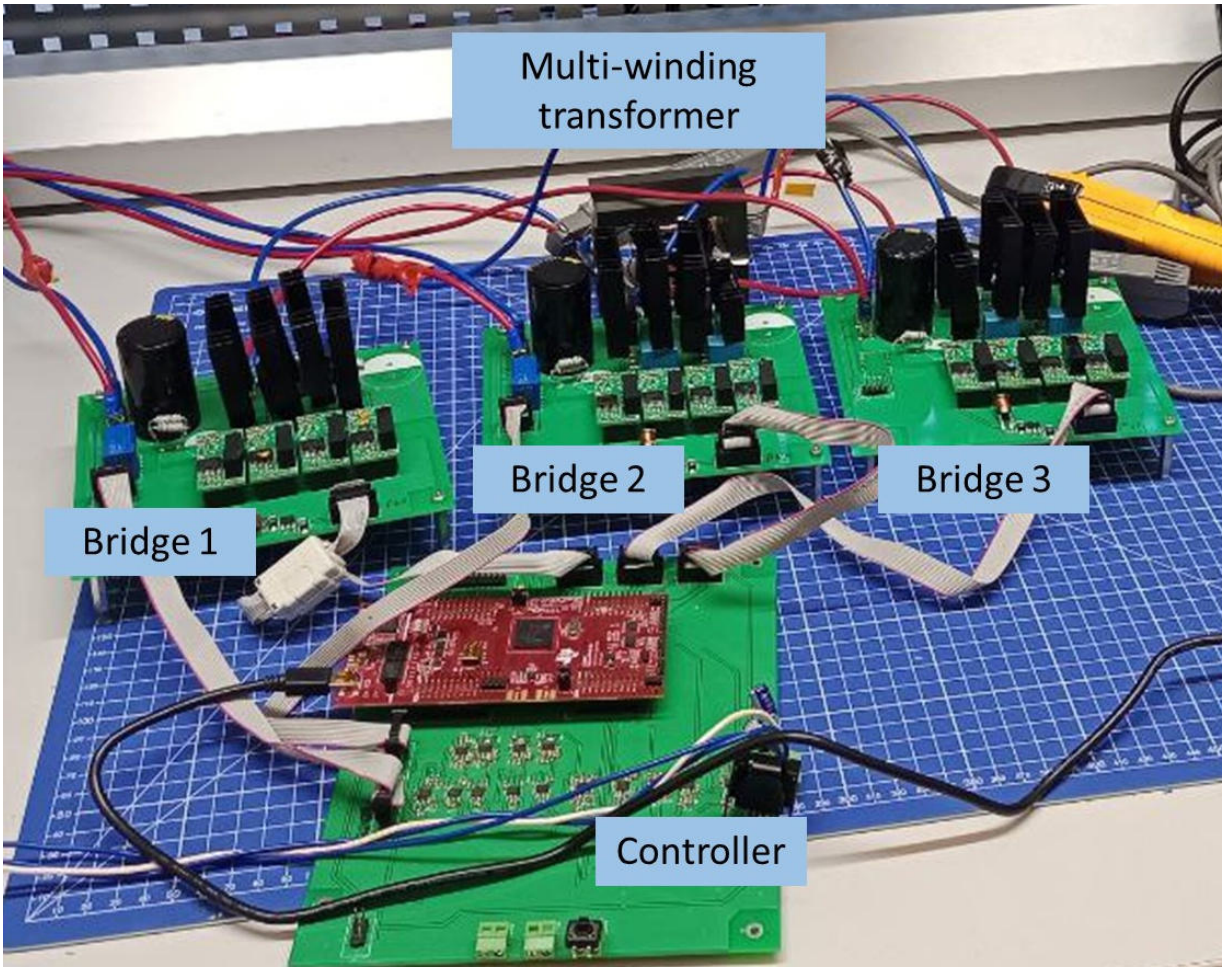

Figure 2.2.9–Prototype

Figure 2.2.10(a) demonstrates bidirectional operation and transient response during a power step test. In the 1st interval port 1 absorbs 400W and port 2 zero, P_{DC1}=-400W, P_{DC2}=0W. In the 2nd interval both ports deliver the same power P_{DC1}=P_{DC2}=200W, in the 3rd interval P_{DC1} is set to zero while P_{DC2}=400W and finally in the last interval P_{DC2} is set to zero while P_{DC1}=400W. These test covers all of the power flows conditions including positive, zero and negative power flows. The time response is about 8ms for the power loop and the inductances are not equal.

Figure 2.2.10(b) shows the real waveforms of AC voltage, AC currents and DC currents in three time-intervals. The V_{DC} at port 2 is 180V while V_{DC1}=V_{DC3} are 150V. This shows that the converter can work within a voltage range. In addition to the waveforms, an AC power analysis was done to evaluate the active and reactive power in each harmonic. Results show that mostly all of the power flows at the 1st harmonic and the reactive power is minimal.

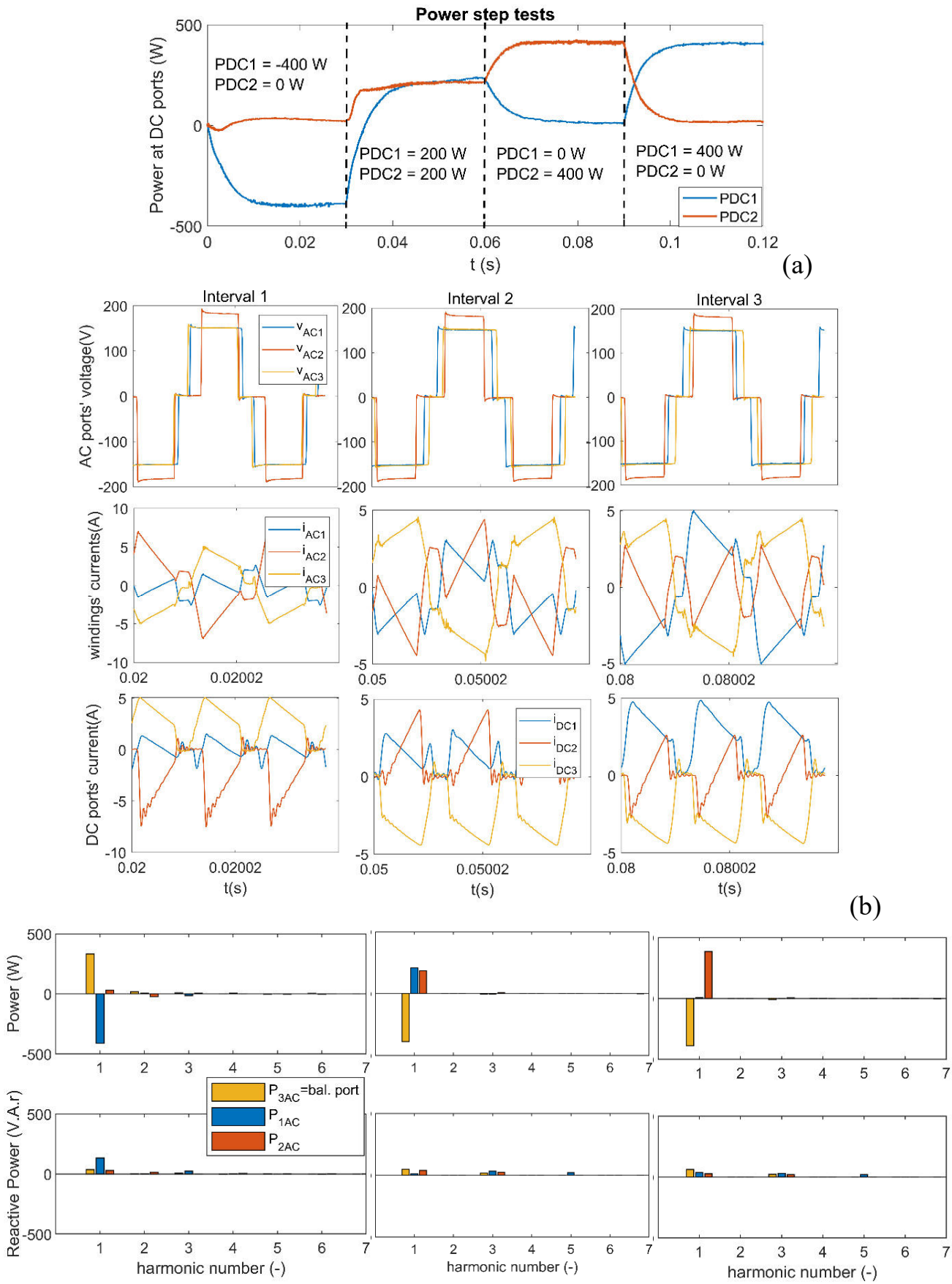

Figure 2.2.10–Power step test: (a) Power at three DC powers when the reference changes to several points: P_{DC1},P_{DC2}=[-400W,0W], [200W,200W], [0W,400W], (b) waveforms within the intervals, (c) AC harmonic active and reactive power distribution

Table 2.2.3 Comparison with MAB different control methods

Method	Zhao, Round and Kolar [7]	Vemulst, Duarte *et al* [23]	Dq-frame control (the proposal in this dissertation)
Type of control	Closed-loop, accurate	Open-loop very fast, inaccurate	Closed-loop, accurate
Time response	Fast	Very fast (open-loop)	Fast (8 ms)
Complexity	Very complex, Extendable for more than three ports at the cost of very large *lookup* tables	Extendable to large number of ports but very complex math.	Without lookup tables, using simple SISO transfer functions Extendable to any number of ports
Soft-switching (SS) capability	only the 1st harmonic current considered in the optimization model for minimizing losses.	only the 1st harmonic current considered in the optimization model for minimizing losses	Allow by controlling the reactive power reference, simpler
DC voltage range	Limited	Large	Large, by adjusting D to have similar 1st harmonic voltages in all of the ports

2.2.5. Comparison with other methods for Multiple Active Bridge

The proposed method is compared with other existing methods for controlling multiple active port converters. Table 2.2.3 shows the main advantages of the method.

The proposed method has a fast time response, allows the use of asymmetrical transformers, it does not require any lookup table to work with multiple active ports and by controlling the reactive power it is possible to achieve soft-switching. In addition, it supports a wide range of DC voltages. Therefore, using the proposed method, the number of ports can be easily increased. In this section, converters with three and four ports were simulated and tested.

2.2.6. Summary

This section introduces a new model of multiple active bridge (MAB) converter based on a rotating frame (dq-frame) synchronized with its switching frequency. Based on this model, a control method was proposed to allow the connection of any number of ports in the MAB converter. Due to that, all the ports can be controlled independently with a fast time-response. For achieving that, AC current signals were decomposed in their dq-components and the first harmonic was controlled. It was shown that, by controlling the first harmonic, it is possible to control most of the power flow. Moreover, by adding a secondary DC power control loop, any perturbation from the harmonics can be minimized and the DC power flow is accurate. In order to avoid the excess of current flowing through the converter, the fundamental reactive power is also controlled. Finally, it was proved that the DC ports can have a variable voltage range modulating their duty cycles. The model and the control technique were validated in simulations and real experiments in a 1kW prototype.

Further work is required for low duty cycles. The first harmonic approximation works well for high duty cycles (D>0.3, wide pulses), however, as the duty cycles decrease, more power flows at the harmonics and the approximation is less accurate. As the fixed real reference for one of the ports (V_N) is a degree of freedom, it can be set high enough to keep harmonics low, however, this limits the converter's operational voltage range . The main content of this section is reflected in [93].

2.3. Effects of measurement units in decoupling blocks

This section continues analyzing the control loops of the multiple active bridge converter, using the first harmonic approximation and the dq-decomposition at switching frequency. This allows using decoupling blocks which aid for controlling the power flows independently. However, as the measurements provided to the decoupling blocks are delayed by the filters in the acquisition system, this can decrease or even violate the stability margins. This section is focused in the analysis and design of such control loops in order to mitigate the effect of the measurement filters on the decoupling blocks. For that, based on the model from Section 2.2, a feed-forward technique with compensators that improve the stability of the converter without sacrificing the time response is proposed. The method is validated through extensive simulations.

As the power signals work at switching frequencies, the section proposes a method for minimizing the delay in measurements which impacts the performance of the decoupling stage. Several variations of the proposed technique are presented, supported with Bode plots and stability margin analysis. For the best one, the time-domain simulation results are provided. The main content of this section was published by the author in [94].

2.3.1. Filters in the current-control and power-control loops

Figure 2.3.1 shows the whole block diagram of a TAB converter. The control scheme is detailed in Figure 2.3.2. The power stage is represented by the following coupled equations:

$$\overrightarrow{\imath_d^R} = \left(s.\bar{\bar{L}}^R + \bar{\bar{r}}^R\right)^{-1}\overrightarrow{v_d^R} + \omega_0.\bar{\bar{L}}^R.\overrightarrow{\imath_q^R} \tag{2.3.1.a}$$

$$\overrightarrow{\imath_q^R} = \left(s.\bar{\bar{L}}^R + \bar{\bar{r}}^R\right)^{-1}\overrightarrow{v_q^R} - \omega_0.\bar{\bar{L}}^R.\overrightarrow{\imath_d^R}. \tag{2.3.1.b}$$

As in Section 2.2, the N-th port is set as reference, or power balancing port, $\bar{\bar{I}}$ is the

identity matrix, ω_0 is the PWM switching frequency, s is the Laplace variable. $\bar{\bar{L}}^R$ and $\bar{\bar{r}}^R$ are the reduced matrices built from the inductances and resistances of the converter's AC ports.

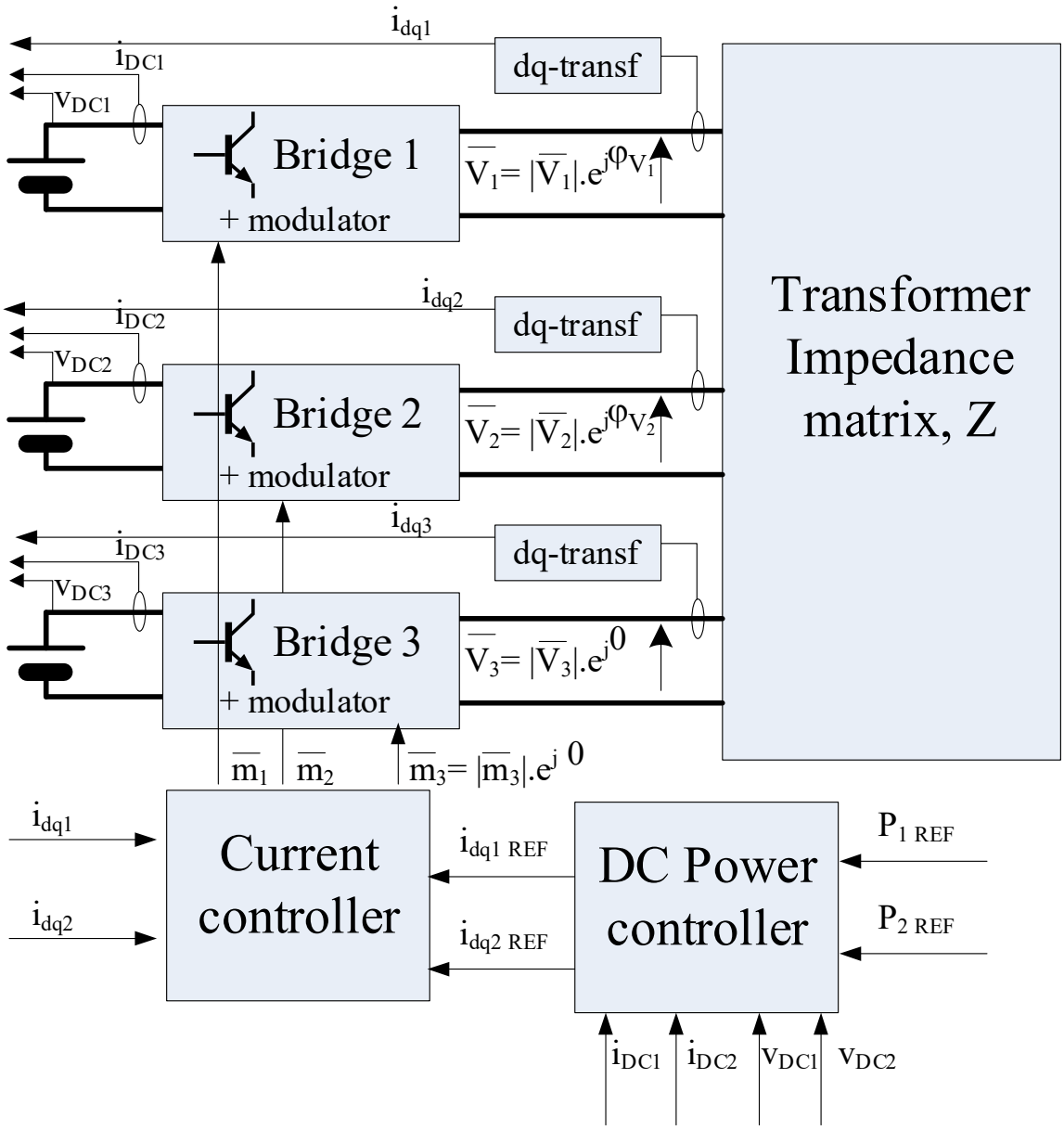

Figure 2.3.1–TAB: block diagram

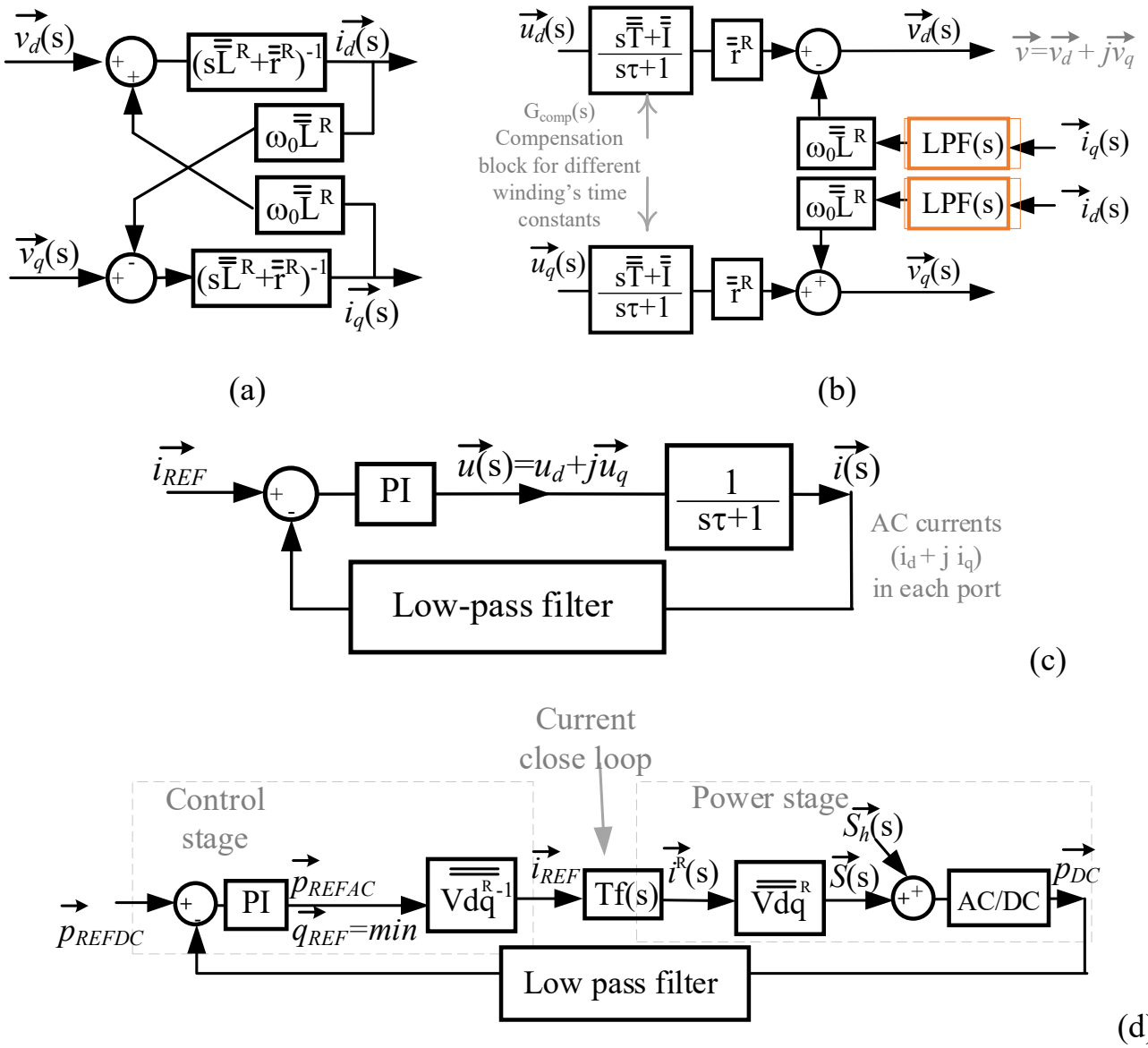

Figure 2.3.2–Control diagram: (a) (coupling) power stage, (b) decoupling control stage with delays, (c) equivalent current loop diagram and (d) DC power control loop

The decoupling block (Figure 2.3.2 (b)) provides a transformation from the control vector $\overrightarrow{u_d} + j\overrightarrow{u_q}$ (s) to AC port voltages $\overrightarrow{v_d}^R$ +j$\overrightarrow{v_q}^R$ (s) in a way to compensate coupling equations (2.3.1):

$$\overrightarrow{v_d^R}\,(s) = \frac{s\overline{\overline{L^R}} + \overline{\overline{r^R}}}{sL_N + r_N}\overrightarrow{u_d}(s) - \omega_0.\overline{\overline{L^R}}.\overrightarrow{\imath_q^R}(s) \tag{2.3.2.a}$$

$$\overrightarrow{v_q^R}\,(s) = \frac{s\overline{\overline{L^R}} + \overline{\overline{r^R}}}{sL_N + r_N}\overrightarrow{u_q}(s) + \omega_0.\overline{\overline{L^R}}.\overrightarrow{\imath_d^R}(s). \tag{2.3.2.b}$$

L_N and r_N are the parameters of the reference AC port. In the case when time

constants, τ, are equal: $\frac{L_{11}^R}{r_{11}^R} = \frac{L_{S1}+L_{SN}}{r_1+r_N} = \frac{L_{Sn}}{r_n} = \frac{L_{SN}}{r_N} = \tau$, (2.3.2) can be rewritten as:

$$\overrightarrow{v_d^R}(s) = \frac{\overline{\overline{L^R}}}{L_N}.\overrightarrow{u_d}(s) - \omega_0.\overline{\overline{L^R}}.\overrightarrow{i_q^R}(s) \tag{2.3.3.a}$$

$$\overrightarrow{v_q^R}(s) = \frac{\overline{\overline{L^R}}}{L_N}.\overrightarrow{u_q}(s) + \omega_0.\overline{\overline{L^R}}.\overrightarrow{i_d^R}(s), \tag{2.3.3.b}$$

because the pole cancels with the zero.

Ideally, the power stage block and the decoupling block connected together should behave like a single-pole plant $\frac{1}{sL_N+r_N}$ as it is shown in Figure 2.3.2 (c). To create a current control loop, a PI controller is added. A low-pass filter (LPF) appears because the AC ports of the converter operate at the switching frequency and the conversion in dq-frame uses an analog low-pass filter (Figure 2.2.5). For example, a filter can be represented by a second order Butterworth approximation. Then, the open-loop (OL) transfer function for the AC currents control can be approximated by the following equation:

$$OL\,Tf_C(s) = k_{P\,c}\frac{sT_{i\,c}+1}{sT_{i\,c}}\frac{1}{sL_N+r_N}\frac{1}{\left(\frac{s}{\omega_{c\,c}}\right)^2+\sqrt{2}\left(\frac{s}{\omega_{c\,c}}\right)+1}. \tag{2.3.4}$$

Here, $\omega_{c\,c}$ is the cut-off frequency of the low-pass filter. $k_{P\,c}$ and $T_{i\,c}$ are the parameters of the PI controller. $T_{i\,c}$ is chosen to be L_N/r_N or to cancel the single-pole plant. Then, $k_{P\,c}$ is set to have a zero dB gain at the frequency $\omega_{0dB\,c}$. This frequency is chosen to be 10 times smaller than $\omega_{c\,c}$ in order to be able to neglect the low-pass filter.

Figure 2.3.2 shows the outer DC power control loop. If we neglect the low-pass filter in (2.3.4), then the closed-loop (CL) transfer function for the current control will be:

$$CL\,Tf_C(s) = \frac{1}{\frac{s}{\omega_{0dB\,c}}+1}, \tag{2.3.5}$$

and the open-loop transfer function for the DC power control loop becomes:

$$OL\,Tf_P(s) = k_{P_P}\frac{sT_{i\,P}+1}{sT_{i\,P}}\frac{1}{\frac{s}{\omega_{0dB\,c}}+1}\frac{1}{\left(\frac{s}{\omega_{c\,p}}\right)^2+\sqrt{2}\left(\frac{s}{\omega_{c\,p}}\right)+1}, \tag{2.3.6}$$

where the sub-index P means DC power control loop. Similar to the current control, the

integration time constant $T_{i\,P}$ can be chosen to cancel the pole at $-\omega_{0dB\,c}$. The proportional gain k_{P_P} is set to have zero dB gain at the frequency $\omega_{0dB\,P} = \omega_{c\,c}/10$.

2.3.2. Effects of the feedback delays

To analyze the real behavior of the conventional dq-frame decoupling, it is necessary to consider $\overrightarrow{i_m{}^R}$, where the sub-index m means measurement (after the filters in Figure 2.3.2.b) are not the real values ($\vec{i}(s)$) but measured ($\overrightarrow{i_m{}^R}(s)$) with the transfer function of the low-pass filter. Thus, the coupling and decoupling blocks are not exactly transformed to the single-pole plant $\frac{1}{sL_N+r_N}$.

Ideally, after substituting the decoupling equation (2.3.3.a) for $\overrightarrow{v_d^R}\,(s)$ into the power stage equation (2.3.1.a) for $\overrightarrow{\imath_d^R}$ (s), the $\overrightarrow{\imath_q^R}$ (s) terms should be cancelled. The same is applied in (2.3.1.b), (2.3.3.b), for the q components. Therefore, we have:

$$\overrightarrow{\imath_d^R} = \frac{\tau}{L_N}\frac{1}{s\tau+1.}\overrightarrow{u_d} + \frac{\tau\omega_0}{s\tau+1.}.\left(\overrightarrow{\imath_{m\,q}^R} - \overrightarrow{\imath_q^R}\right) \tag{2.3.7.a}$$

$$\overrightarrow{\imath_q^R} = \frac{\tau}{L_N}\frac{1}{s\tau+1.}\overrightarrow{u_q} - \frac{\tau\omega_0}{s\tau+1.}.\left(\overrightarrow{\imath_{m\,d}^R} - \overrightarrow{\imath_d^R}\right). \tag{2.3.7.b}$$

Then, to obtain the open loop behavior, the control vector $\vec{u}$=$\overrightarrow{u_d} + j\overrightarrow{u_q}$ (s) is replaced by the PI controller, and the left sides of the equations are replaced by the measured current values:

$$\overrightarrow{\imath_{m\,d}^R} = \frac{\omega_{0dB\,c}}{s}LPF(s)\overrightarrow{e_d} + \frac{\tau\omega_0}{s\tau+1.}LPF(s)[1-LPF(s)]\overrightarrow{\imath_q^R} \tag{2.3.8.a}$$

$$\overrightarrow{\imath_{m\,q}^R} = \frac{\omega_{0dB\,c}}{s}LPF(s)\overrightarrow{e_q} - \frac{\tau\omega_0}{s\tau+1.}LPF(s)[1-LPF(s)]\overrightarrow{\imath_d^R}, \tag{2.3.8.b}$$

where

$$\overrightarrow{e_d} = \overrightarrow{\imath_{ref\,d}^R} - \overrightarrow{\imath_{m\,d}^R}\ and \overrightarrow{e_q} = \overrightarrow{\imath_{ref\,q}^R} - \overrightarrow{\imath_{m\,q}^R}$$

and

$$LPF(s) = \frac{1}{\left(\frac{s}{\omega_{c\,c}}\right)^2 + \sqrt{2}\left(\frac{s}{\omega_{c\,c}}\right) + 1}.$$

The first term in (2.3.8.a) and in (2.3.8.b) is the ideal open loop behavior, while the second term is the added part because of non-exact decoupling. After substituting the coupling equation for $\overrightarrow{\iota_q^R}$ (s) to (2.3.8.a) the system's order will grow to fourth order. The increased order of the system can cause significant phase deviations from the ideal model described by (2.3.4). As a result, it can lead to decrease of phase margins and produce instability.

2.3.3. Simulation example

To demonstrate the effects of the described problem, the model of TAB converter shown in Figure 2.3.1 with the parameters shown in Table 2.3.1 is used. All ports are identical and have the windings' turn ratio equal to 1 which simplifies the decoupling equations (2.3.3). However, the same analysis can be done for non-equal time constants. Since this study is focused on the current control loop, only values for the current controllers are presented. Further, the power controller will be added. The values $T_{i\,c}$, $k_{P\,c}$ were chosen based on the guidelines presented in Section 2.2 which is a simple approach to select a controller values without a detailed analysis. To analyze the current controller, a linear model was created in MATLAB/Simulink as it is shown in Figure 2.3.2. The power stage is represented by (2.3.1). From this model, the Bode plots were obtained. The open loop transfer function of the dq-frame control with measurement delays for the given case study is shown in Figure 2.3.3(a) (initial model) and is compared to the ideal model. The significant phase deviations caused by the low-pass filter in the decoupling block lead to the negative phase margin, i.e. the system is unstable. To achieve a stable system, the zero dB gain should be significantly lowered, which increases the time response of the system. With the frequency $\omega_{0dB\,c}$ = 25rad/sec, the system is stable according to the open loop transfer function. The transfer function of the slow model is

also presented in Figure 2.3.3(a). In addition, the $\overrightarrow{i^R_{m\,d}}/\overrightarrow{i^R_{Ref\,q}}$ transfer function should be analyzed. Ideally, the magnitude of this transfer function should be small at the whole frequency range, otherwise it can cause oscillations of the system. Figure 2.3.3(b) shows the transfer function of the initial and slow models. The peak responses are -3dB and -18 dB respectively.

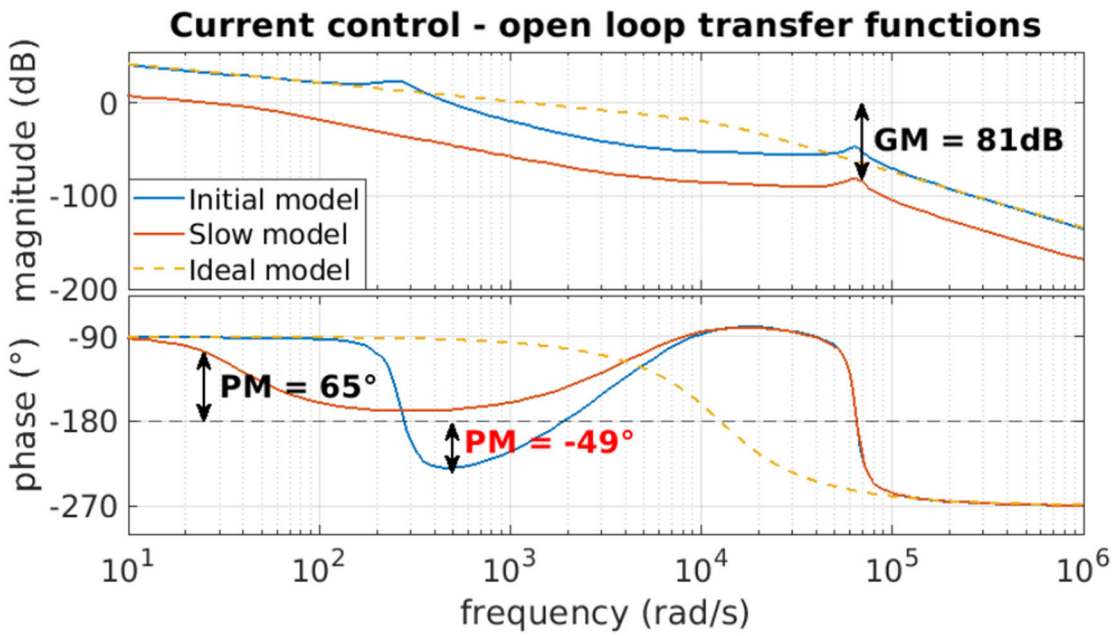

(a)

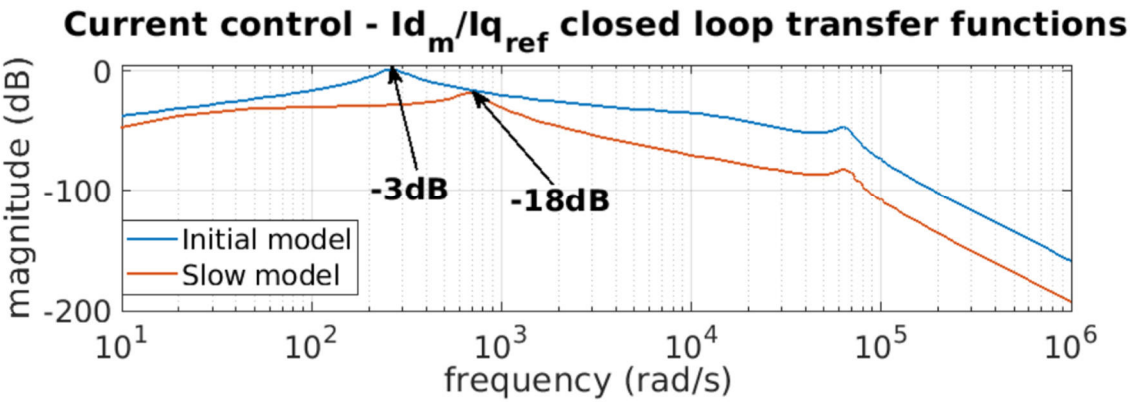

(b)

Figure 2.3.3–Control Transfer functions for the conventional dq-frame control with measurement delays: (a) open loop transfer functions, (b) $I_{d\,m}/I_{q\,ref}$ closed loop transfer functions

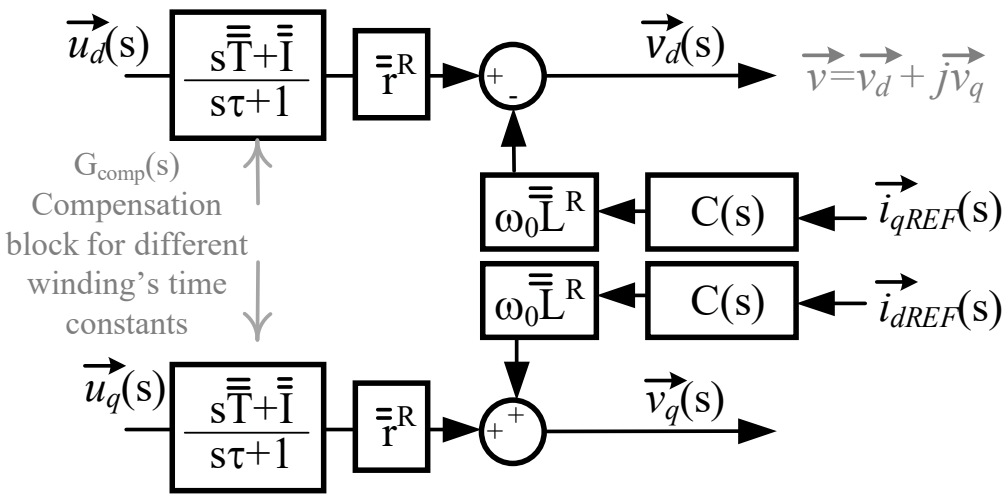

Figure 2.3.4–Decoupling block with compensated reference current

2.3.4. Proposed compensation

Decoupling with compensated reference currents. To reduce the effect of the measurement filter on decoupling, reference current values can be used to form the predicted currents. In order to cancel the additional term in (2.3.8.a), (2.3.8.b), a compensator $C(s)$ should be added to the decoupling block as it is shown in Figure 2.3.4. The compensator is the desired closed loop behavior of the system. It can follow the simplified current control loop:

$$C(s) = \frac{1}{\frac{s}{\omega_{0dB\,c}} + 1}. \tag{2.3.9}$$

Note that the open loop transfer function analysis cannot be applied in the same way as for the conventional feedback systems. The reason is that the reference values $\overrightarrow{\iota^R_{Ref}}$ do not only form the error signals, but they are also included in the control loop diagram. This means that the perturbation at the $\overrightarrow{\iota^R_{Ref}}$ propagates both to the error signal and to the plant. So, for further analysis, the most informative will be the closed loop transfer functions $\overrightarrow{\iota^R_{m\,d}}/\overrightarrow{\iota^R_{Ref\,d}}$ and $\overrightarrow{\iota^R_{m\,d}}/\overrightarrow{\iota^R_{Ref\,q}}$.

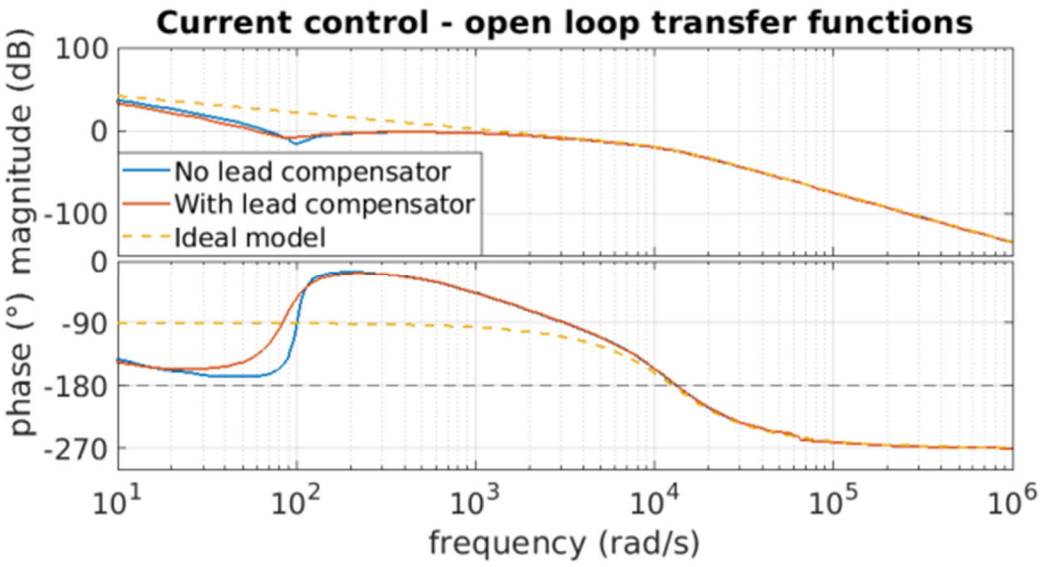

(a)

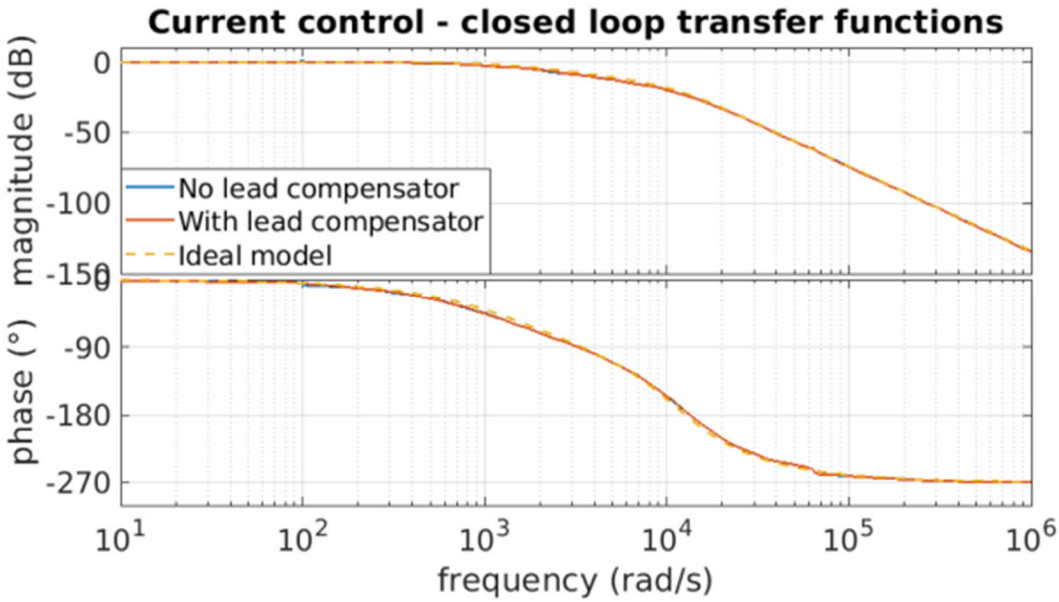

(b)

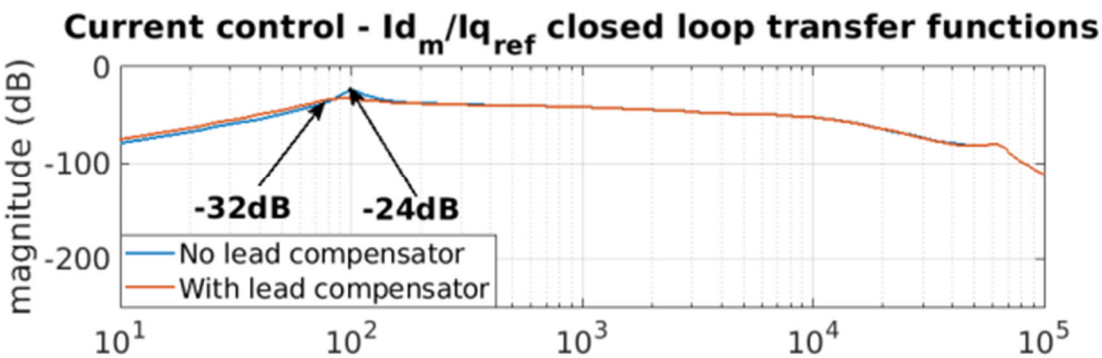

(c)

Figure 2.3.5–Transfer functions for the dq-frame control, decoupled with the compensated reference currents: (a) Open loop transfer function (b) Closed loop transfer function, (c) $I_{d\,m}/I_{q\,ref}$ closed loop transfer function

Figure 2.3.5 shows the transfer functions in case of decoupling with the compensated reference currents. The closed loop transfer function $\overrightarrow{\iota_{m\,d}^{R}}/\overrightarrow{\iota_{Ref\,d}^{R}}$ is very close to the ideal one and the peak in $\overrightarrow{\iota_{m\,d}^{R}}/\overrightarrow{\iota_{Ref\,q}^{R}}$ response is -24dB at the frequency 95 rad/s. The phase margin point of the open loop transfer function is at the same frequency. It means that adding a phase lead compensator to the control loop at ω_k= 95 rad/s after the PI controller can improve the $\overrightarrow{\iota_{m\,d}^{R}}/\overrightarrow{\iota_{Ref\,q}^{R}}$ response:

$$Lead(s) = \frac{1 + aTs}{1 + Ts}, a > 1, \omega_k = \frac{1}{\sqrt{a}T}. \tag{2.3.10}$$

The Bode plots after adding a phase lead compensator are also presented in Figure 2.3.5. The peak in $\overrightarrow{\iota_{m\,d}^{R}}/\overrightarrow{\iota_{Ref\,q}^{R}}$ response was decreased to -32 dB. However, because the open loop transfer function was changed, the predictive compensator $C(s)$ has a bigger error. So, the phase lead compensator can be considered as a cheap option to increase stability, but it requires separate analysis for each system or its parameters. Figure 2.3.6(a) shows the simulation results for the currents control after adding the phase-lead compensator. Small 15Hz oscillations can still be observed.

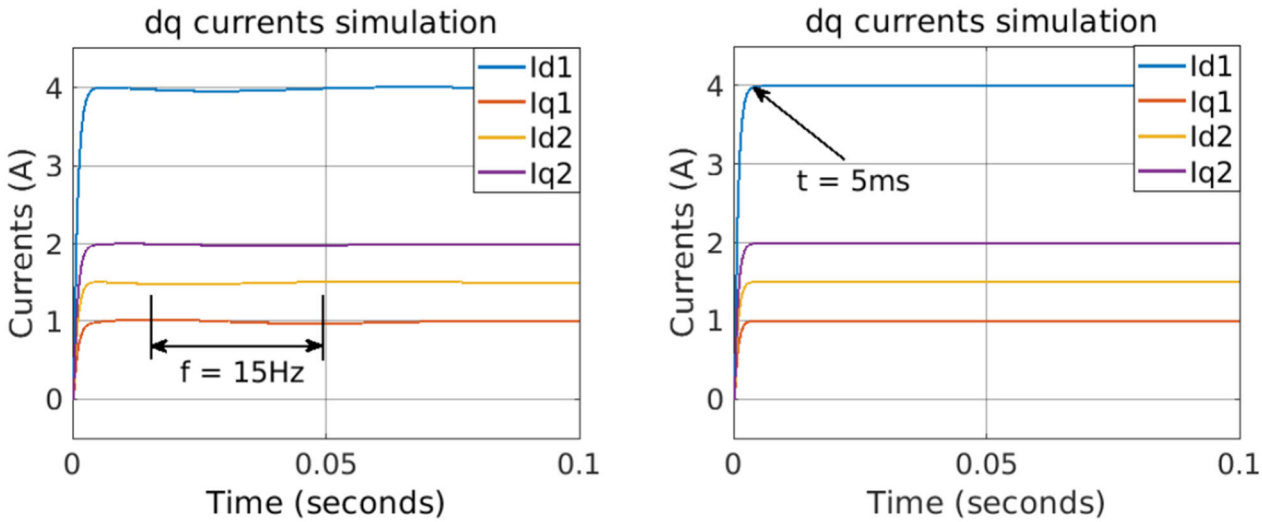

(a) (b)

Figure 2.3.6–dq-frame currents simulation results for decoupling with the compensated reference currents: (a) using simple compensator with phase lead compensator, (b) using advanced compensator

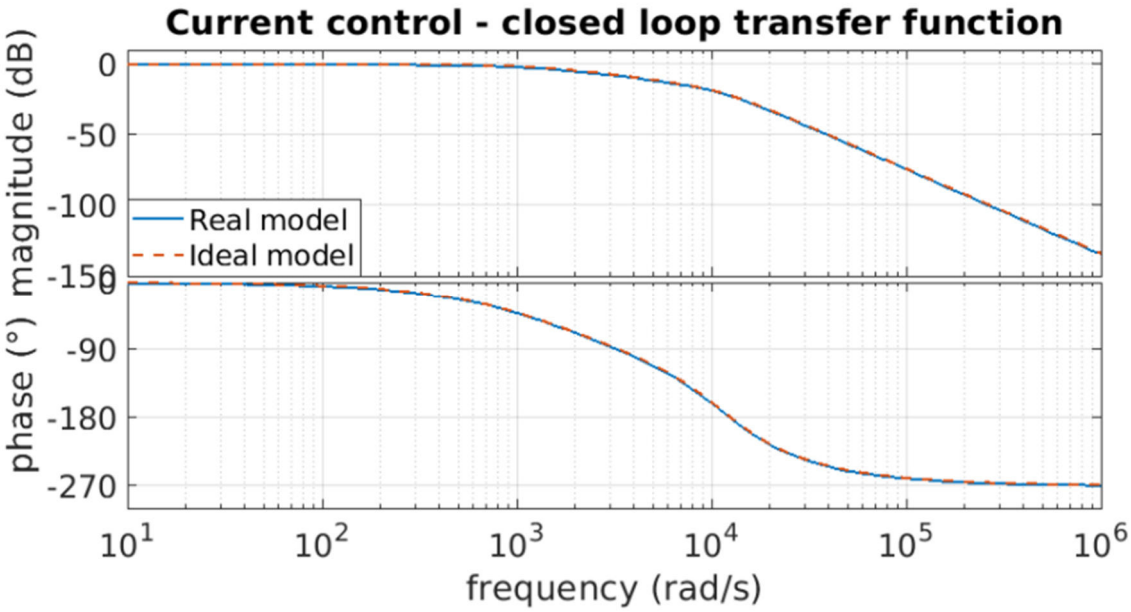

(a)

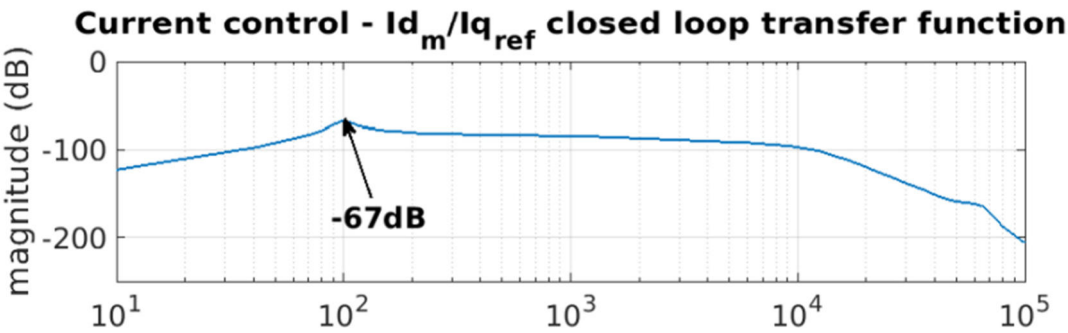

(b)

Figure 2.3.7- Transfer functions for the dq-frame control, decoupled with the advanced compensated reference currents: (a) Closed-loop transfer function, (b) $I_{d\,m}/I_{q\,ref}$ closed loop transfer function

Advanced compensator for reference currents. In order to avoid analyzing each system separately, a more advanced compensator $C'(s)$ which includes effects of the filter should be obtained:

$$C'^{(s)} = \frac{i^R_{1\,d}}{i^R_{1\,Ref\,d}} = \frac{\frac{\omega_{0dB\,c}}{s}}{1 + \frac{\omega_{0dB\,c}}{s} LPF(s)}. \tag{2.3.11.a}$$

$$C'^{(s)} = \frac{\left(\frac{s}{\omega_{c\,c}}\right)^2 + \sqrt{2}\left(\frac{s}{\omega_{c\,c}}\right) + 1}{\frac{s}{\omega_{0dB\,c}}\left(\frac{s}{\omega_{c\,c}}\right)^2 + \sqrt{2}\left(\frac{s}{\omega_{c\,c}}\right)\frac{s}{\omega_{0dB\,c}} + \frac{s}{\omega_{0dB\,c}} + 1}. \tag{2.3.11.b}$$

The compensator $C'(s)$ can be considered as an ideal form of compensator for the reference currents in decoupling block. Figure 2.3.7 shows the Bode plots with the advanced decoupling compensator. The $\overrightarrow{\iota^R_{m\,d}}/\overrightarrow{\iota^R_{Ref\,q}}$ transfer function exactly matches the ideal closed loop transfer function. The peak $\overrightarrow{\iota^R_{m\,d}}/\overrightarrow{\iota^R_{Ref\,q}}$response is very small (-67dB).

Figure 2.2.6(b) shows the simulation results for the currents. No oscillations are observed, and the time response is 5 ms.

2.3.5. Simulation results

In the previous subsections, the analysis and the simulation results were based on the linear model which may not account for some effects of the PWM switching processes. Also, only current control was simulated. In this subsection, the simulation results of control over a PLECS TAB circuit are presented, details are given in Table 2.3.1. The external loop for DC powers control was added. The zero-dB gain frequency $\omega_{0dB\,P}$ was selected to be $\omega_{c\,c}/10$ = 1250rad/sec. Figure 2.3.8(a) presents the simulation results for the DC powers control. Initially, the DC powers are set to be +500W for the first port and +1000W for the second port. Then, at t = 25ms, the power reference is changed to -500W for the first port and +250W for the second port. The time response of the system is 5 ms. Figure 2.3.8(b) and (c) show the simulation results for the instantaneous three-port transformer voltages and currents in steady-state. The results show that using the advanced compensator in the ideal case the effect of measurement delays in the decoupling block can be fully eliminated. In a real implementation, it can be affected by the tolerances of inductances and resistances. The other method presented in subsection 2.3.4 can also be used with simpler calculations for improving the stability margins and time response of the original converter.

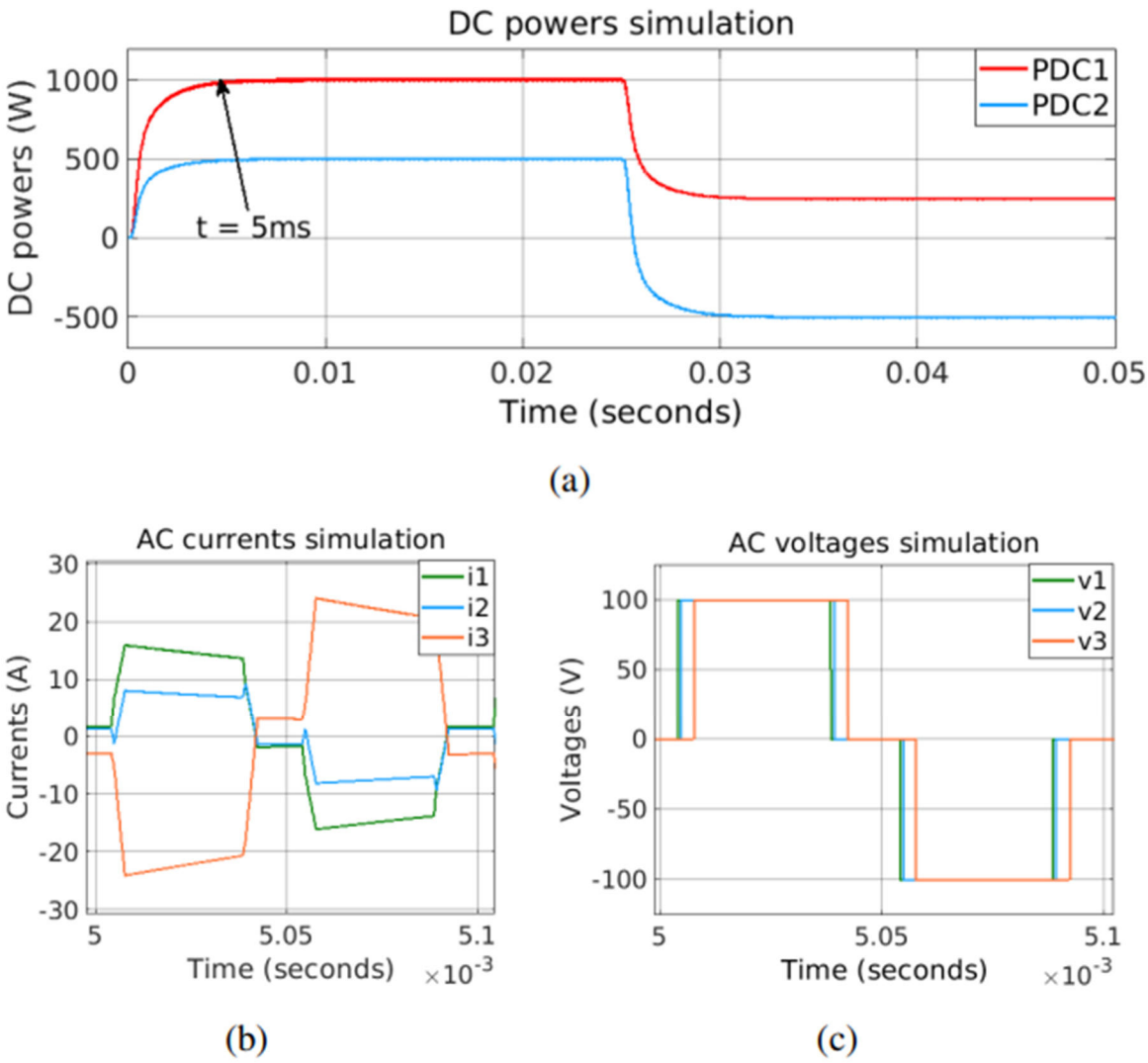

Figure 2.3.8–Simulation results: (a) DC powers for port 1-2, (b) transformer currents, (c) transformer voltages

Table 2.3.1 MAB parameters

Symbol	Quantity	Value
f_s	Switching frequency	10kHz
V_{DC}	Input DC voltages	100V
L_s	AC port leakage inductances	10uH
r_s	AC port windings' resistances	0.05Ω
$\omega_{c\,c}$	Cut-off frequency in the measurements	2πfs/5
$\omega_{0db\,c}$	Frequency at zero dB open current loop gain	1250 rad/s
$T_{i\,c}$	Current controller integration time	0.2ms
$k_{P\,c}$	Current controller proportional gain	0.0125

2.3.6. Summary

This section presents a clear analysis of a powerful technique for controlling independently the power flow at the different ports with a fast time response. The section analyzes the converter in a comprehensive manner and clearly explains the limits of the feed-forward decoupling techniques. Based on that, a compensator block is proposed to improve the stability of the control loop which allows to minimize the time-response. The proposal was validated in simulations using PLECS software, with a notable improvement in the time-response from 200ms to 5-10ms. The details of this section were published in [94].

2.4. Improvements in efficiency in MAB converters: the “dual-duty” modulation

This section introduces an advanced dual-duty modulation technique for MAB converters designed to significantly reduce conduction losses over a wide range of input voltages by minimizing the harmonics’ reactive power on the AC stage (the transformer). Consequently, it can improve the converter's efficiency when dealing with non-constant voltage sources such as batteries and supercapacitors. The overall control technique is based on the dq-frame control described in Section 2.2. The proposed method is modeled, verified through simulations and implemented in a 1000W triple-port prototype. In the simulation, conductive and switching losses are modelled, and the trade-off between these loss types is discussed. The experimental results affirm an overall improvement in efficiency for certain scenarios involving non-unit voltage conversion ratios. Details of this section are in [96].

2.4.1. Existing solutions for improving MAB efficiency

The traditional approach for controlling the power transfer of a MAB is to produce a phase shift between bridges [13, 15, 16]. The method is simple, but it has some drawbacks, such as recirculating currents at DC ports and significant efficiency reduction when the DC voltages at the ports are not equal. In addition, it is difficult to extend it to a larger number of ports. More advanced techniques were proposed to improve efficiency, to simplify the control technique in order to extend the TAB to a larger number of ports, and to minimize the recirculating DC currents.

A method based only on phase shift control introduces an excess of reactive power in the transformer, which results in extra losses, especially when the input voltages change. Therefore, simultaneous duty cycle and phase shift control techniques were proposed in [7, 21, 93]. Using these, the best duty cycles were selected to minimize the losses in [7]. As the minimization problem is non-linear, pre-calculated optimal values were recorded in lookup tables using DC currents as indexes. This method is hard to scale for a larger number of ports as the table size increases considerably. In addition, the method does not consider that the optimal point also depends on the input voltage ratio of the ports. Another approach presented in [22] has introduced a “perturb & observe” algorithm to find the minimum RMS current point in real time without the need of pre-calculated values. The optimization becomes slower but reaches the minimal losses for the conventional modulation strategy. In [23, 97, 98], a Fourier decomposition is used to evaluate and minimize the losses.

Certain optimization strategies are based on minimizing reactive powers [99]. The DC components at the DC ports can be determined by summing all the harmonics of the active powers flowing through the transformer, while reactive powers create additional recirculating currents at DC ports. In addition, such sources as batteries and supercapacitors operate under a wide DC voltage range. Therefore, the normalized DC voltages, equal to $\frac{V_{DCn}}{n_n}$, where n_n is the transformer’s turn ratio for the n-th port, become unequal between ports. This is referred as non-unit voltage conversion ratios. In this case,

the reactive power transferred by harmonics increases. In [100], this issue is addressed using a Machine Learning approach for a three-port converter.

Given the typically high switching frequency of MAB converters, recent research papers also take into account switching losses. For instance, in [101], an optimization problem is formulated, focusing on minimizing RMS currents under zero-voltage switching constraints (ZVS). This problem is solved using the particle swarm optimization (PSO) algorithm to achieve a global optimal solution. In [101], a multivariable optimization approach is employed, allowing the model to minimize either the total switching losses or conductive losses. Both of the aforementioned algorithms take into consideration the optimal operating point's dependency on the DC voltages.

Since many papers treat conduction losses as the dominant source of losses when employing MOSFET power switches [18, 22, 102], it is worth noting that optimizing switching losses can come at the expense of conduction losses. Consequently, the global optimal point represents a trade-off between minimizing conduction and switching losses.

In Section 2.2 [93], the author introduced a dq-control (or real-imaginary decomposition) technique under the first harmonic approach (FHA). The dq-decomposition of AC currents and voltages is performed at the switching frequency using analog methods. Subsequently, the currents are chosen for the control loops based on the desired power levels at the DC ports. In addition, using the dq-frame currents, it is possible to control reactive powers through the AC ports. This section further develops this control method by introducing an advanced modulation technique. The proposed algorithm can be applied for any number of ports.

The contributions of this Section are:

- Introducing an advanced dual-duty modulation technique designed to reduce harmonics in the transformer currents and consequently decrease conductive power losses at high frequencies for MAB converters.
- Outlining how the presented modulation technique can be combined with the dq-frame power flow control method presented in Section 2.2 [93] to ensure accurate power tracking while maintaining low conductive losses.

- Evaluation of conductive and switching losses through extensive simulations, focused on the impact of the dual-duty modulation technique on these types of losses. The proposed technique is compared to some recently proposed methods.
- Validating the proposed method with experimental tests conducted on a 3-port 1 kW prototype, including efficiency measurement and step response tests.

2.4.2. New modulation technique – Dual-duty

This subsection explains how to reduce RMS currents using a special modulation technique [96]. For that, the model and the control method introduced in Section 2.2 is used. Without loss of generality, for further analysis we consider that the transformer has equal number of turns for each AC bridge. The same analysis can be applied for any transformer's turn ratio by replacing V_{DCn} with $\frac{V_{DC\,n}}{n_n}$ and $\overline{V}_n$ with $\frac{\overline{V}_n}{n_n}$, where n_n is the transformer's turn ratio for the n-th port.

Since the active power is controlled and AC bridges are connected with mostly inductive lines (see Section 2.2), the AC ports' voltages have nearly equal first harmonic magnitudes (considering a turns-ratio equals to one). However, the DC port voltages can vary significantly for sources such as battery and supercapacitors. This results in different input voltages $V_{DC\,n}$ among the different bridges. In this case, to get equal magnitudes $|\overline{V}_n|$ in the AC ports, different duty cycles must be applied.

According to (2.2.2.b):

$$|\overline{V}_{nk}| = \frac{4}{\pi k} V_{DCn}.\, sin(k\pi D_n), \tag{2.4.1}$$

different duty cycles lead to different harmonic voltage magnitudes. The difference in magnitudes in turn produces high reactive power from harmonics, which is hard to control. To eliminate this effect, a new modulation technique is introduced, called "dual-duty" modulation, shown in Figure 2.4.1(a), with two duty cycles, D_A and D_B [96]. With D_B = 0, PWM signal becomes the same as for the previous (Section 2.2) modulation.

Thus, D_A is the main duty cycle, and D_B is the secondary one. The secondary duty cycle is then used as an additional degree of freedom. The main objective is to have almost the same harmonic amplitude to minimize the currents at high order harmonics, by means of selecting the appropriate values of D_A and D_B. Therefore, for the inductive impedance matrix, the reactive power from harmonics will decrease.

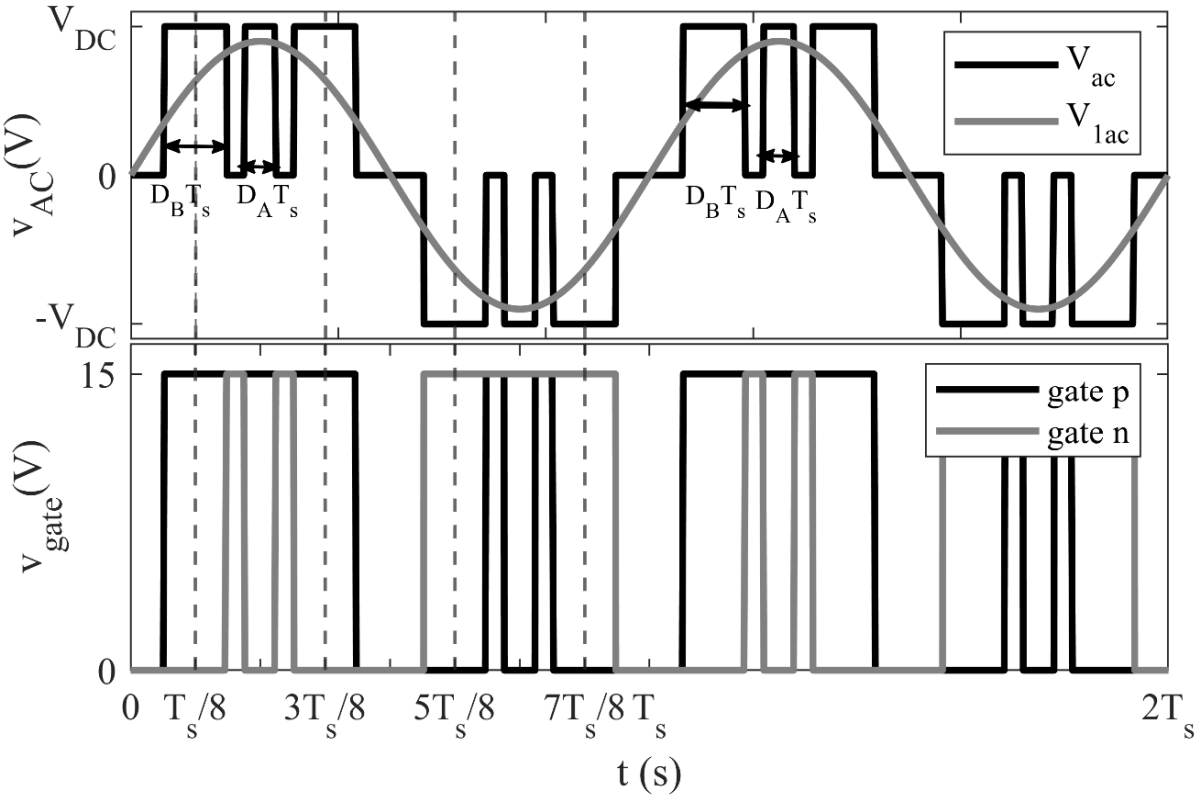

(a)

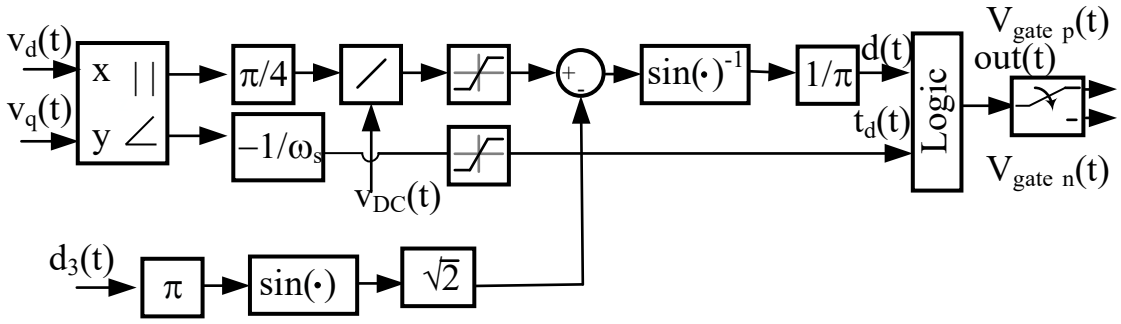

(b)

Figure 2.4.1–(a) proposed dual-duty modulation, (b) control logic diagram for dual-duty modulation including lookup tables

The AC output voltages are generated from a combination of two symmetric duty cycle signals in $v_{Gate\ p}$ and $v_{Gate\ n}$ (voltage in the gates of the switches) and their

complementary signals (see Figure 2.4.1(a)). Three levels of AC output voltage are produced: a positive level, where $v_{Gate\ p}$ is on and $v_{Gate\ n}$ is off; a zero level, where both are on or both are off; and a negative level, where $v_{Gate\ p}$ is off and $v_{Gate\ n}$ is on.

Figure 2.4.1 (a) shows the gate-pulse waveforms for a single bridge. If $D_B \neq 0$, $v_{Gate\ p}$ is on during time periods $\left[\frac{T_S}{8} - \frac{D_B T_S}{2}, \frac{3T_S}{8} + \frac{D_B T_S}{2}\right]$, $\left[\frac{5T_S}{8} + \frac{D_B T_S}{2}, \frac{3T_S}{4} - \frac{D_A T_S}{2}\right]$, $\left[\frac{3T_S}{4} + \frac{D_A T_S}{2}, \frac{7T_S}{8} - \frac{D_B T_S}{2}\right]$. Otherwise, for $D_B = 0$ (same as in Figure 2.2.3), $v_{Gate\ p}$ is on during time period $\left[\frac{T_S}{4} - \frac{D_A T_S}{2}; \frac{T_S}{4} + \frac{D_A T_S}{2}\right]$. The $v_{Gate\ n}$ signal behaves symmetrically relative to the half of the switching period. The same procedure applies to obtain the gate signals of the other bridges.

Figure 2.4.1(b) details the transformation block used for obtaining the gate pulses from the signals in the dq-frame. The logic block first selects the secondary duty cycle D_B to minimize the higher harmonics' contribution, as described further in this section. Then it calculates the main duty cycle (D_A) and phase shift for the first harmonic from the dq-frame voltages (v_d and v_q). Then, the duty cycles, D_A and D_B, and phase shift are translated into $v_{Gate\ p}$ and $v_{Gate\ n}$. The result is shown in Figure 2.4.1(a), where the gate signals ($v_{Gate\ p}$, $v_{Gate\ n}$) and the AC output voltage (v_{ac}) are presented, in addition to the 1st harmonic (v_{1ac}). The equations for the fundamental harmonic and any odd k-th harmonic can be written as:

$$\left|\overline{V}_n\right| = \left|\overline{V}_{n1}\right| = \frac{4}{\pi} V_{DCn}\left(sin(\pi D_{An}) + \sqrt{2} sin(\pi D_{Bn})\right), \tag{2.4.2.a}$$

$$\left|\overline{V}_{nk}\right| = \frac{4}{\pi k} V_{DCn}\left(sin(k\pi D_{An}) + 2cos\left(\frac{\pi k}{4}\right) sin(k\pi D_{Bn})\right), \tag{2.4.2.b}$$

where (2.4.2.c)

$$D_{Bn} + D_{An} < 0.25, \text{ if } D_{Bi} > 0$$

From (2.4.2.a), various combinations of the main and secondary duty cycles can be used to generate the same first harmonic voltage. The first harmonic voltage is obtained from the control loop, described in Section 2.2. Thus, we use the secondary duty cycle D_B as an additional degree of freedom for each bridge.

As described earlier, the impedance connecting the bridges is mostly inductive. Thus, the minimal first harmonic reactive power will be achieved with nearly the same voltage magnitudes in each port (so the minimal current). Therefore, we can minimize the harmonic voltage magnitude differences to decrease the reactive power from harmonics.

First, we explain how the harmonic reactive power is minimized between two bridges. After that, we provide the algorithm for any number of bridges. For any given two bridges *n* (reference bridge) and *p* this can be formulated as an optimization problem:

$$\frac{1}{3}\left(|\overline{V}_{n3}| - |\overline{V}_{p3}|\right)^2 + \frac{1}{5}\left(|\overline{V}_{n5}| - |\overline{V}_{p5}|\right)^2 + \frac{1}{7}\left(|\overline{V}_{n7}| - |\overline{V}_{p7}|\right)^2 \rightarrow min, \tag{2.4.3.a}$$

under constraints:

$$\frac{4}{\pi}V_{DCn}\left(sin(\pi D_{An}) + \sqrt{2}sin(\pi D_{Bn})\right) \equiv |\overline{V}_{n1}| \tag{2.4.3.b}$$

$$\frac{4}{\pi}V_{DCp}\left(sin(\pi D_{Ap}) + \sqrt{2}sin(\pi D_{Bp})\right) \equiv |\overline{V}_{p1}| \tag{2.4.3.c}$$

that are derived from (2.4.2.a) and (2.4.2.b).

In (2.4.3.a), harmonics 3, 5, 7 are considered. $D_{B\,n,p}$ are the optimization variables. $D_{A\,n,p}$ are then uniquely determined by (2.4.3). $\overline{V}_{n1}$, $\overline{V}_{p1}$ are the values calculated by the control loop (see Section 2.2). Other harmonic voltages used in (2.4.3.a) are calculated from (2.4.2.b).

Because the inductive reactance increases with frequency, weighting coefficients $\frac{1}{3}$, $\frac{1}{5}$, $\frac{1}{7}$ are used, higher harmonics contribute less to reactive power. In other words, for the kth harmonic, the impedance matrix:

$$\overline{\overline{Z}}_k = jk\omega_S\overline{\overline{L}} = jk\omega_S\begin{pmatrix} (L_{s1}+L_m) & L_m & \cdots & L_m \\ L_m & (L_{s2}+L_m) & L_m & \vdots \\ \vdots & L_m & \ddots & L_m \\ L_m & \cdots & L_m & (L_{sN}+L_m) \end{pmatrix} \tag{2.4.4}$$

in Section 2.2.1 is multiplied by *k*.

Expanding (2.4.3.a) according to (2.4.2.b), we can rewrite it as:

$$\sum_{k=3,5,7} \frac{1}{k}\left(\frac{V_{DCn}}{V_{DCp}} y_k(D_{An}, D_{Bp}) - y_k(D_{An}, D_{Bp})\right)^2 \rightarrow min, \tag{2.4.5.a}$$

where:

$$y_k(D_A, D_B) \equiv \frac{1}{k}\left(sin(k\pi D_A) + 2cos\left(\frac{\pi k}{4}\right) sin(k\pi D_B)\right) . \tag{2.4.5.b}$$

From the equations (2.4.3.b-c), (2.4.5) and assuming that $|\overline{V}_{n1}| \approx |\overline{V}_{p1}| \approx |\overline{V}_{AC}|$, the optimal secondary duty cycles $D_{B\,n,p}$ depend on $\frac{V_{DCn}}{|\overline{V}_{AC}|}$, $\frac{V_{DCn}}{V_{DCp}}$ ratios. Thus, the optimal values can be pre-calculated and stored in lookup tables. For the proposed control, two lookup tables are defined. Table *lookup1* is two-dimensional with the aforementioned parameters (ratios) as inputs. It is used when both D_{Bn} and D_{Bp} are unknown. For the cases when D_{Bn} is known, we create another table *lookup2* with D_{Bn} as 3rd dimension.

The overall algorithm for calculating the main (D_{An}) and secondary (D_{Bn}) duty cycles is the following:

(a) Find bridges with maximum and minimum input voltages, V_{DCmax} and V_{DCmin} respectively. Determine $D_{B\,vmax}$ and $D_{B\,vmin}$ using table *lookup1* for these two ports.

(b) For any other bridge "*t*", to apply the same technique as with two bridges, first determine the reference bridge (*n*). If $(V_{DCmax} - V_{DC"t"}) > (V_{DC"t"} - V_{DCmin})$, then the reference bridge (*n*) is the one with V_{DCmax}, otherwise, select the bridge with V_{DCmin} as the reference bridge (*n*).

(c) For the bridge "*t*", find D_{Bt} using table *lookup2* with $\frac{V_{DCn}}{|\overline{V}_{AC}|}, \frac{V_{DCn}}{V_{DCt}}$ and D_{Bn} as input parameters.

(d) Using (2.4.2.a), calculate main duty cycles D_{At} to get the exact desired fundamental harmonic voltages $|\overline{V}_{t1}|$ for the "*t*" bridge. These come from the control loop, as described in Section 2.2.2.

(e) If for bridge "*t*" (2.4.2.c) is not satisfied, then bridge "*t*" works in the single-duty mode with duty cycle calculated from (2) and D_{Bt}=0.

The common structure of the dual-duty optimization is shown in Figure 2.4.1(b). One of the benefits of the proposed algorithm is that it is easy to scale. The size and the values of the lookup tables depend only on the normalized AC and DC voltage ranges, and do not depend on the number of ports. First, the harmonic power is optimized between the bridges with minimum and maximum input voltages (n and p). After that, the other bridges are optimized relative to the bridge with the largest V_{DCn-p} difference. It is important to note that this algorithm is heuristic and may not always provide a globally optimal solution. However, it is designed to ensure scalability. To solve the full optimization problem, all DC voltages would need to be indexed in a lookup table. In addition, since (2.4.3.a) does not exactly represent the minimum reactive power, the solution for two bridges is also sub-optimal, as it might be affected by the phase shift between ports. However, as it will be shown in the next subsections, this solution still results in a significant reduction of conductive losses in the whole power range.

While it may initially appear that storing a two-dimensional and a three-dimensional table could consume a significant amount of memory, this concern is mitigated by the relatively small ranges of the indexes. For instance, with the $\frac{V_{DCn}}{V_{DCp}}$ ratio limited from 1 to 1.5, and step size of 0.05 for all the parameters, the size of tables *lookup1* and *lookup2* would be 14x11x2 (for both $D_{B\ vmax}$ and $D_{B\ vmin}$) and 6x14x17, respectively. These dimensions are suitable for storage in a moderate-sized digital signal processor (DSP), and these sizes will not change with the increased number of bridges.

The components of the converter with the proposed control technique are illustrated in Figure 2.4.2. The overall proposed method includes the advanced modulation technique ("duty factory" block) that improves the harmonic impact of the currents, the dynamic control technique (power and current controllers) that forms the dq-frame voltages for the duty factory and the acquisition unit (analog dq-decomposition + low-pass filter, detailed in Section 2.2). The converter's dynamic that includes the rest of the blocks was presented in Section 2.2 and 2.3.

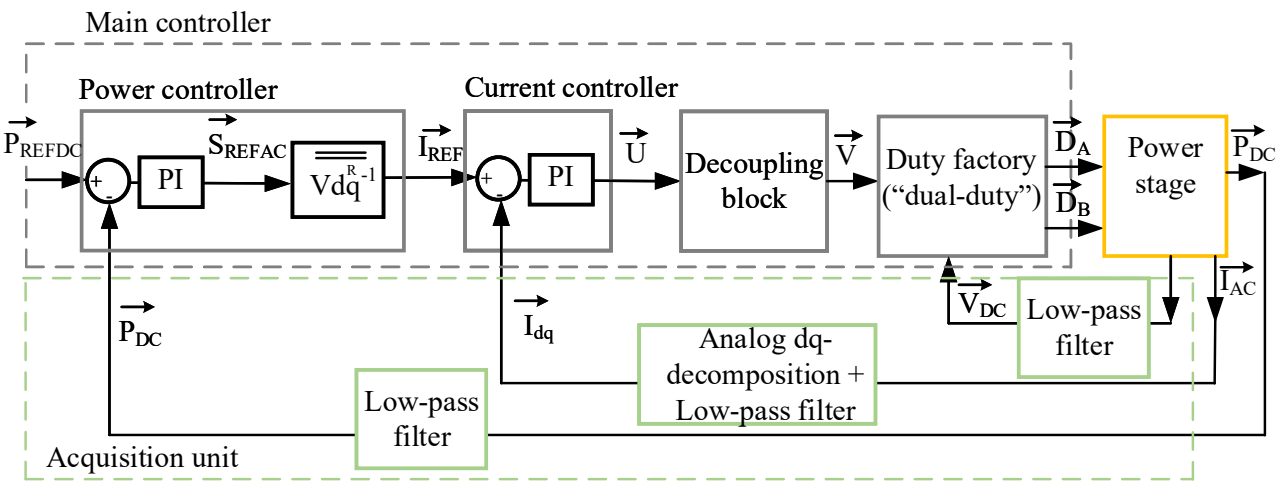

Figure 2.4.2–Complete block diagram of the proposed solution.

2.4.3. Loss model

To evaluate how different parameters can affect the converter's losses, a mathematical power loss model is introduced in this section. The conductive losses in a bridge are dependent on the RMS currents at each port. They can be expressed as:

$$P_{cond} = \sum_{n=m}^{N} (I_{RMS\,m}^{2} r_{s\,m}). \tag{2.4.6}$$

Here, $I_{RMS\,m}$ represents the RMS current of port n, which depends on all harmonic currents at this port. $r_{s\,n}$ is the equivalent series resistance, which includes the transformer winding's resistance and on-state switches resistance.

For the switching losses, the energy dissipated on a switch (transistor) during its commutations needs to be calculated. Since currents and voltages are half-wave symmetrical, only the first half period is analyzed. In the conventional modulation technique, each switch commutes once in a half period. Therefore, the switching losses can be estimated as:

$$P_{sw} = \frac{2}{T}\sum_{m=1}^{N}\left[E_{sw\,m}\left(i\left(\frac{T_S}{4}-\frac{DT_s}{2}\right),V_{DC\,m}\right)\right.$$
$$\left.+E_{sw\,m}\left(-i\left(\frac{T_S}{4}+\frac{DT_s}{2}\right),V_{DC\,m}\right)\right] \tag{2.4.7.a}$$

where

$$E_{sw\,m}(i,V) = E_{on\,m}(i,V) + E_{off\,m}(-i,V) \tag{2.4.7.b}$$

and $E_{on\,m}(i,V), E_{off\,m}(i,V)$ are single turn-on and turn-off energies, given that the current i(t) is flowing through the transistor after (for the turn-on) or before the switching (for the turn-off), and the blocking voltage is V. Therefore, $E_{sw\,m}(i,V)$ denotes the total energy loss of a single leg. The current can be determined as an AC current at the corresponding port, with the sign depending on the transistor position. The energy values can vary depending on the transistor model. Hence, the index m is used to identify that the transistors might be different depending on the bridge rated parameters. It can be roughly said that the values are proportional to the instantaneous parameters:

$$E_{on\,m}(i,V), E_{off\,m}(i,V) \propto i \cdot V \tag{2.4.8.a}$$

and the soft-switching conditions should be taken into account:

$$E_{on\,m}(i,V), E_{off\,m}(i,V) = 0, \qquad if\ \ i < 0. \tag{2.4.8.b}$$

The latter equation states that if the current during the switching process is flowing through the diode (in negative direction), then the soft-switching condition is fulfilled, and the dissipated energy is ideally zero. From (2.4.7.b), it can be seen that one of the two complementary transistors at a given switching instance will be in a soft-switching mode. In [25, 26], more accurate conditions are derived, that require a negative current threshold. That threshold depends on the transistor's output capacitance, inductance values, and instantaneous AC voltages, so the model is complex. However, this threshold is typically small.

For the proposed approach, (2.4.7) can be used for the ports that operate in a single-duty mode. For the dual-duty mode, it should be modified to take into account additional switching instances:

$$P_{sw\,dd} = P_{sw} + \frac{2}{T}\sum_{m=1}^{N}\left[E_{sw\,m}\left(i\left(\frac{T_S}{8} - \frac{D_B T_s}{2}\right), V_{DC\,m}\right)\right.$$
$$+E_{sw\,m}\left(-i\left(\frac{T_S}{8} + \frac{D_B T_s}{2}\right), V_{DC\,m}\right)$$
$$+E_{sw\,m}\left(i\left(\frac{3T_S}{8} - \frac{D_B T_s}{2}\right), V_{DC\,m}\right)$$
$$\left.+E_{sw\,m}\left(-i\left(\frac{3T_S}{8} + \frac{D_B T_s}{2}\right), V_{DC\,m}\right)\right]. \tag{2.4.9}$$

From (2.4.9), it can be noticed that the switching losses are expected to be higher for the ports operating in dual-duty mode. However, this can be mitigated by lower instantaneous currents, as it will be shown in the next subsection. The conducting losses are expected to be lower due to lower RMS currents as well.

2.4.4. Simulations

In order to validate this control system, several numerical simulations were performed in MATLAB/Simulink including both static and dynamic tests. For the static tests, which are intended to evaluate the losses, a 3-port converter (TAB) is considered with the parameters specified in Table 2.4.1. As future work, the plan is to conduct analysis for a larger number of ports. The dynamic tests are aimed to verify that the decoupling capabilities are preserved in fast control loops. For that, we consider a 4-port active bridge (QAB).

Static validation. The evaluation of the benefits of the proposed dual-duty modulation technique involves the estimation of various types of losses, depending on the specific characteristics of the system. Two primary types of losses are taken into account: conducting losses and switching losses. Conducting losses can be estimated based on the squared RMS AC currents. Switching losses, on the other hand, depend on the switching frequency and the instantaneous currents and voltages during the switching events.

Table 2.4.1 MAB converter parameters for simulations

Symbol	Quantity	Value
f_s	Switching frequency	40kHz
V_{DC}	Input DC voltages	650-900V
L_s	AC port leakage inductances	50uH
n_1,n_2,n_3	Windings' turns-ratio	1
$P_{DC\ nom}$	Rated DC power	5 kW
$r_{s1,2,3,4}$	Windings' resistances	0.5Ω
$\omega_{C\ c}$	Cut-off freq. for low-pass filter in dq-transformation	$2\pi f_s/5 \approx 50$krad/s
ω_{0dB}	Frequency at 0dB open-loop current gain	5026 rad/s
L_m	Magnetizing inductance	1mH
$T_{i\ c}$	Current controller integration time	0.1ms
$k_{P\ c}$	Current controller proportional gain	0.25
$T_{i\ p}$	Power controller integration time	0.2ms
$k_{P\ p}$	Power controller proportional gain	0.5
$\omega_{C\ p}$	Cut-off freq. for low-pass filter in power measurement	$2\pi f_s/5$
SWs	MOSFET SCT3080KL,E_{on} = 132 uJ, E_{off} = 18 uJ @650V, 10 A	

The proposed modulation can significantly reduce the conducting losses, which are often considered as the main source of losses. However, it also leads to an increase in switching losses.

As a demonstration, a case study involving a three-port converter was examined. To quantify the conducting losses, the calculation method involves summing up the squares of the RMS AC currents multiplied by the equivalent series resistances r_{sm}, as stated in (2.4.6). This accounts for both transistors and transformer-related conducting losses. For this model, the total equivalent series resistance r_{sm} is set at 0.5 Ohms for each port. The actual value of r_{sm} depends on the characteristics of the transformer and transistors. Notably, higher resistance values tend to yield greater benefits from the proposed approach, while lower resistance values result in comparatively lesser benefits.

To estimate the switching losses, a model of SiC MOSFET power switches (SCT3080) appropriate for the provided case study was chosen. The manufacturer's supplied Spice model of the transistor was integrated into the overall model.

Subsequently, the energy dissipated in the transistors during the switching instances was calculated as:

$$P_{sw\,model} = \frac{1}{T}\sum_{m=1}^{N}\sum_{i=1}^{4}\sum_{t\in\{t_{sw\,m,i}\}}\left(\int_{t}^{t+\Delta t} P_{SW_i}(\tau)d\tau\right). \tag{2.4.10}$$

Here, P_{SW_i} is the power dissipated on switch i ($i = 1...4$) in the bridge m. $\{t_{sw\,m,i}\}$is the set of switching instances for the given switch. Δt was selected to ensure that all switching processes are finished within the integration interval.

For the purpose of comparison, two recent developed algorithms were chosen. In [22], the optimization is focused solely on conducting losses. This optimal point, named as the minimum current point (MCP), is achieved through a "perturb and observe" approach which seeks to minimize total RMS current by adjusting the fundamental harmonic voltage. The second algorithm described in [101] involves pre-computed optimal duty cycles using the particle swarm optimization (PSO) algorithm. This approach optimizes the voltages across all bridges, with the addition of Zero Voltage Switching (ZVS) constraints, which can slightly sacrifice the conducting losses. It should be noted that this algorithm can also result in some switching losses as turn-off losses are not considered in the optimization model.

The result of these evaluations is presented in Figure 2.4.3. Two groups of tests were conducted to determine the conditions under which the proposed approach yields benefits. In the first group of tests, the percentage of conductive losses versus the total delivered DC power was plotted under fixed DC voltages with the maximum voltage difference (V_{DC1} = 900 V, V_{DC2} = V_{DC3} = 650 V). For this voltage configuration, only the port with the higher voltage operates with dual-duty modulation (see AC voltage waveforms in Figure 2.4.4).

Initially, the power at port 1 was set to zero, while the power at port 2 was varied from 500 W to 5 kW. Port 3 balances the power, so that $P_{DC1} + P_{DC2} + P_{DC3} \approx 0$. Then, the DC powers on both port 1 and port 2 were varied from 500 W to 2.5 kW. Figure 2.4.3.a depicts the results for the first group of tests in terms of conducting and switching losses. When the power at the first port is zero or small, the switching losses do not

increase significantly, as the switching currents at port 1 are small due to the proposed modulation (see AC currents in Figure 2.4.4). Simultaneously, the conductive losses are significantly reduced with the proposed approach as the harmonic contribution is optimized.

When both ports deliver DC power, the switching losses increase. However, the proposed algorithm has still benefits over most of the power range. The most notable improvement is observed when the ports deliver 1.5 kW each. The conducting losses are reduced by 0.5%, while the switching losses increase by 0.16%. As the power demand reaches its maximum, the benefits due to the reduced conducting losses become closer to the increased switching losses.

In the second group of tests, the DC powers were kept constants, while V_{DC1} was varied from 650 V to 900 V (see Figure 2.4.3.b). In the first test, $P_{DC1} = 0$, $P_{DC2} = 3$ kW. As before, in this case the increase in switching losses is negligible. In the second test, $P_{DC1} = P_{DC2} = 1.5$ kW. Here, the benefits are observed starting from $V_{DC1} = 800$ V, which corresponds to a voltage conversion ratio of 1.23.

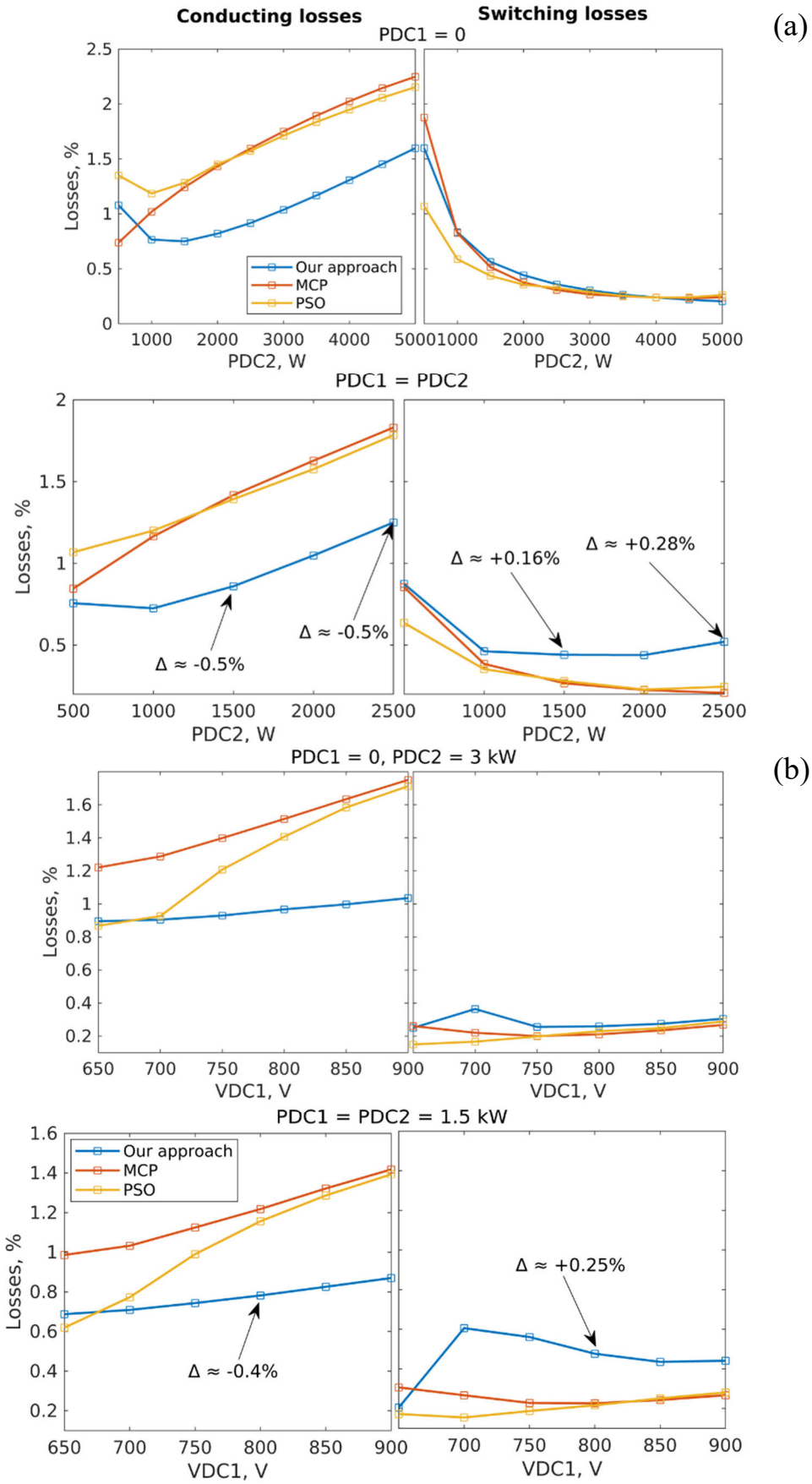

Figure 2.4.3–Conducting and switching losses estimation compared to MCP [22] and PSO [101] (a) at fixed DC voltages ($V_{DC1,2,3}$={900V, 650V 650V} and varying DC powers and (b) at fixed DC powers and varying DC voltage at port 1, while others are at 650V

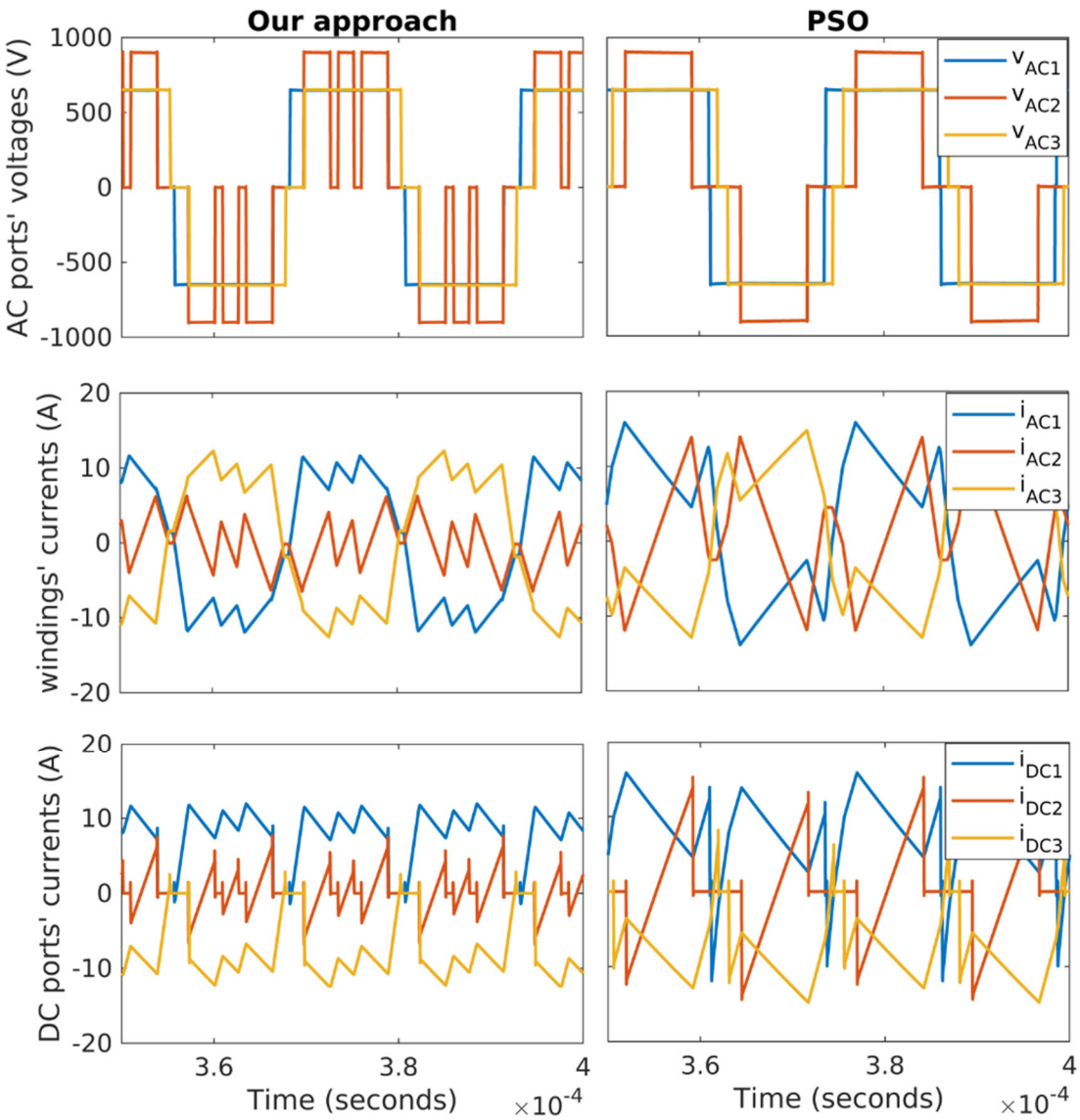

Figure 2.4.4–Simulation waveforms for our approach and PSO [101] for V_{DC1} = 900 V, P_{DC1} = 0 W, P_{DC2} = 5 kW

Figure 2.4.4 shows the simulation waveforms for our approach and PSO, with the large voltage difference (V_{DC2} = 900 V, V_{DC1} = V_{DC3} = 650 V), P_{DC1} = 0 W, P_{DC2} = 5 kW. It can be observed that the peak currents are smaller for our approach. The maximum current reaches 15 A. Therefore, the selected 31 A 650 V switch is a proper choice for the current and voltage levels in the provided setup and the comparison of switching and conductive losses is valid.

Dynamic validation. To validate that the dynamic behavior of the system is preserved, we performed step tests for the DC power control loop. In this test, we consider

a four-port converter (QAB). It demonstrates that, in general, the approach can be applied to a larger number of ports. To increase the possible harmonic impact on the control loop, the input voltage of the second bridge V_{DC2} was set to 900 V, while the other ports of the QAB were kept at 650 V.

Figure 2.4.5 shows the simulation results. First, the 1st bridge is delivering 5 kW at DC, the 2nd is delivering 2.5 kW, the 3rd bridge is set to 0W, and the 4th bridge is balancing the power. Then, after 5 ms, the power references are changed to 1 kW, -2.5 kW, and -2.5 kW while the 4th bridge still balances the power. It can be seen that the control tracks the DC powers fast and accurately.

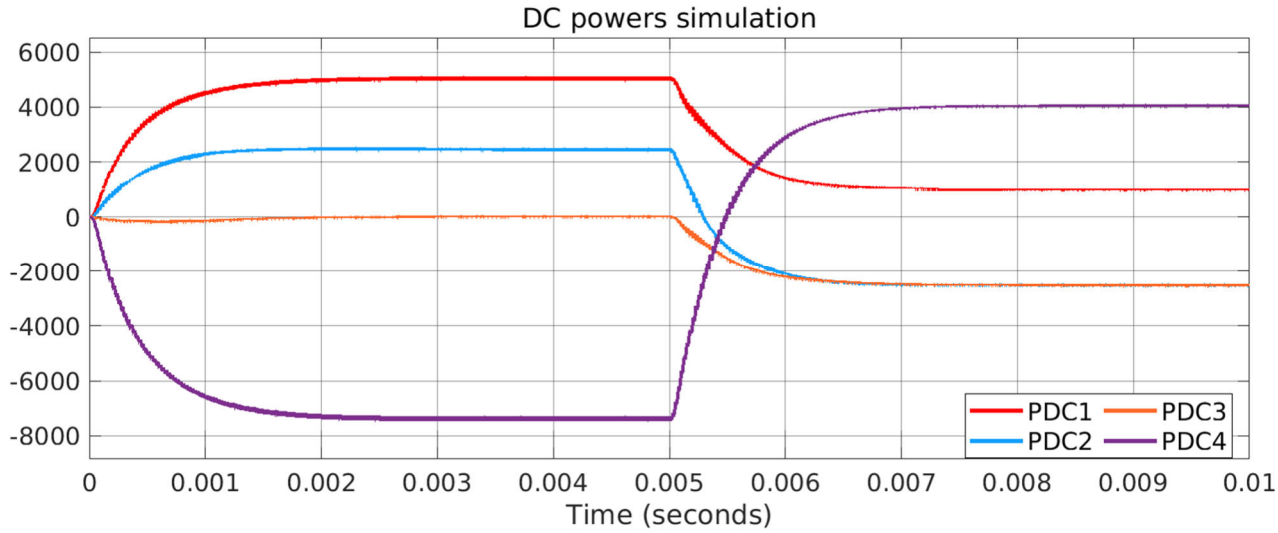

Figure 2.4.5–Simulations using DC power control diagram. Power response after a step in the references

2.4.5. Experimental results

To verify the effectiveness of the proposed control approach, a low-power TAB was built and tested. Table 2.4.2 lists the details of the converter.

The tables *lookup1* and *lookup2* have sizes of 14x11x2 (for D_{Bi} and D_{Bj}) and 6x14x17 values respectively, which is acceptable for storage in the microcontroller. Static and dynamic tests were performed to validate the proposal. During the static tests, the converter efficiency was measured and compared to other methods: the minimum

current point (MCP) and particle swarm optimization (PSO) approaches, as in the previous section. The tests were conducted at three different voltage conversion ratios under $P_{DC1} = P_{DC2}$. The DC voltages at ports 2 and 3 were set to 150 V, while the DC voltage at port 1 was successively set to 180 V, 200 V, and 220 V.

The results are shown in Figure 2.4.6. At the lowest DC voltage conversion ratio considered (V_{DC1} = 180 V), the proposed approach is less efficient. However, at higher values of V_{DC1}, the efficiency is improved, especially in the mid-power range. At V_{DC1} = 200 V, the peak efficiency of the proposed approach reaches 96.9 %, which is slightly higher compared to the other methods (96.3 % - 96.4 %). At V_{DC1} = 220 V, the peak efficiency is 96.7 %, which is 1 % more that the state of the art. This behavior is similar to what can be observed in Figure 2.4.3.b for $P_{DC1} = P_{DC2}$ = 1.5 kW. When V_{DC1} is high enough, the reduction in conductive losses begins to outweigh the increase in switching losses. The voltage conversion ratio can be treated as a border condition to decide whether the dual-duty modulation should be selected in a particular port. As a future work, it is planned to estimate these conditions more accurately depending on the DC powers and voltages of the different ports.

Figure 2.4.7 shows the waveforms comparison for $P_{DC1} = P_{DC2}$ = 300 W. The currents and voltage stresses for the transistors in this specific scenario can be identified. The voltage stresses are equal to the corresponding DC voltages for each modulation technique. The current stresses for the transistors in one particular bridge are equal to the peak AC current at the corresponding port. For instance, for port 3, the peak current is 5.9 A for the proposed approach and 11.9 A for the PSO approach. The lower current stress mitigates the increased number of commutations for the proposed approach. In addition, it can be derived from Figure 2.4.7 that the ZVS conditions are satisfied for the proposed approach, as all transitions from 0 to $+V_{DC}$ occur under negative AC currents, and transitions from $+V_{DC}$ to 0 occur under positive AC currents. Therefore, the main source of switching losses in this case are turn-off losses.

It can be noted that the proposed approach holds high duty cycles, corresponding to high first harmonic voltages. This can be treated as a degree of freedom for future optimizations.

To test the dynamic performance, several DC power references were commanded to the control loop to see how the converter delivers power in different directions. Figure 2.4.8 shows the delivered power measured by the microcontroller. Negative power means that the power is being absorbed. During the first interval port 1 absorbs 1000W, then during interval 2, port 1 and port 2 deliver 500W each, during interval 3, port 1 is at zero power and port 2 delivers 1000W. Thus, this test shows all the possibilities of the multi-port converter.

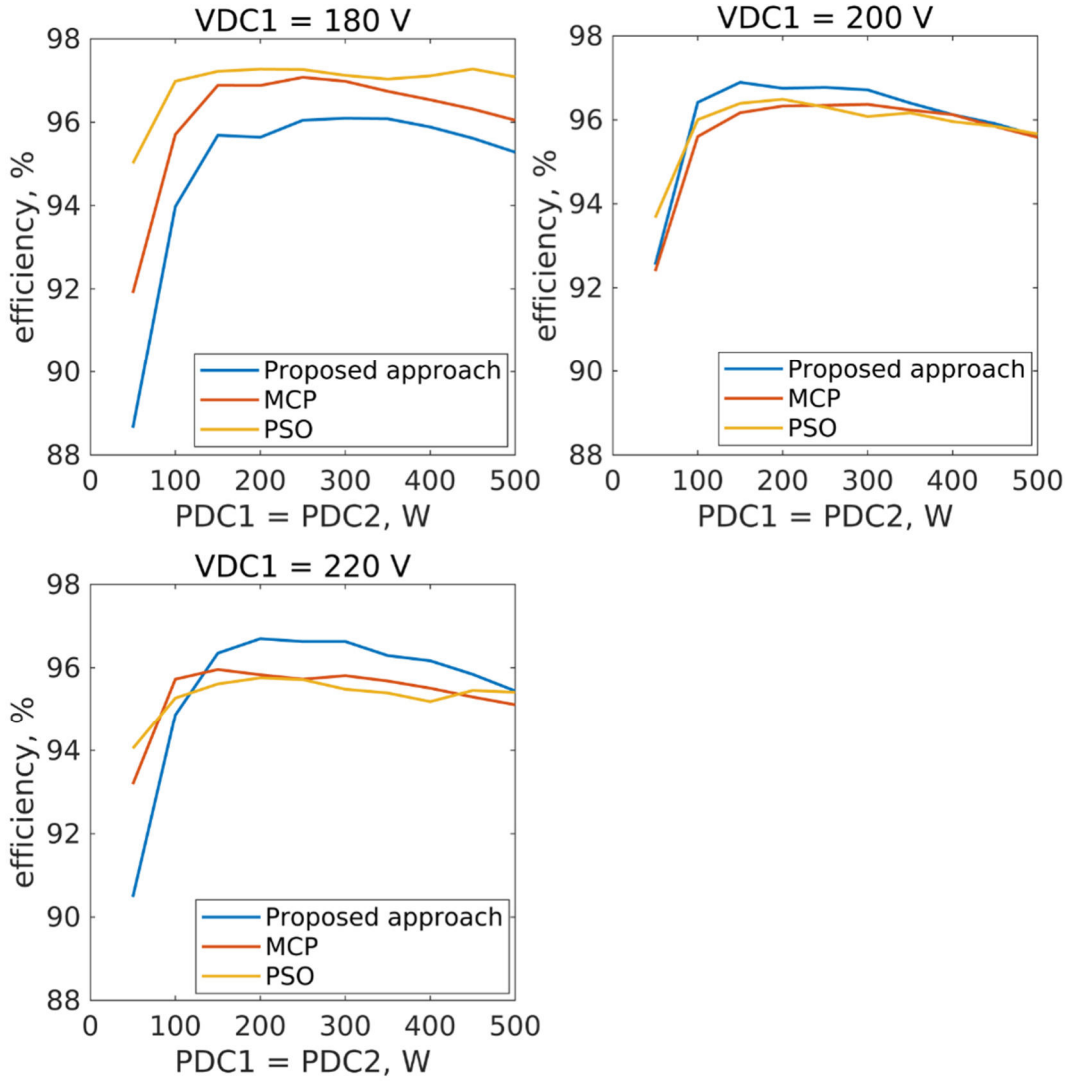

Figure 2.4.6–Efficiency for tests under different DC voltages, compared to MCP and PSO approaches

Table 2.4.2 Prototype parameters

Symbol	Quantity	Value
f_s	Switching frequency	20kHz
$V_{DC1,2,3}$	DC Input voltages	150-220 V
$L_{s1,2,3}$	Leakage and external inductances	26, 28, 32uH
n_1,n_2,n_3	Windings' turns-ratio	1
ω_{C_c}	Cut-off freq. for low-pass filter in dq-transformation	$2\pi f_s/5$
L_m	Magnetizing inductance	1mH
SWs	MOSFET IPW60R090CFD7XKSA1	
dq-frame current measurement based on analog multiplier AD633		
digital signal processor (DSP): TMS320F28379D		

Table 2.4.3 MAB Comparison of the proposed "dual duty" approach with the state of the art

Criteria	MCP [22]	PSO [101]	Proposed
Efficiency at V_{DC1}=180 V*	97%	97.3%	96.1%
Efficiency at V_{DC1}=220 V*	95.9%	95.4%	96.7%
Response time	25 ms	200 ms	10 ms
Model dependency	Low	High	Low
Scalability	High	Low	Medium
*where other ports are at 150V, so ratio 1.2 and 1.46 respectively			

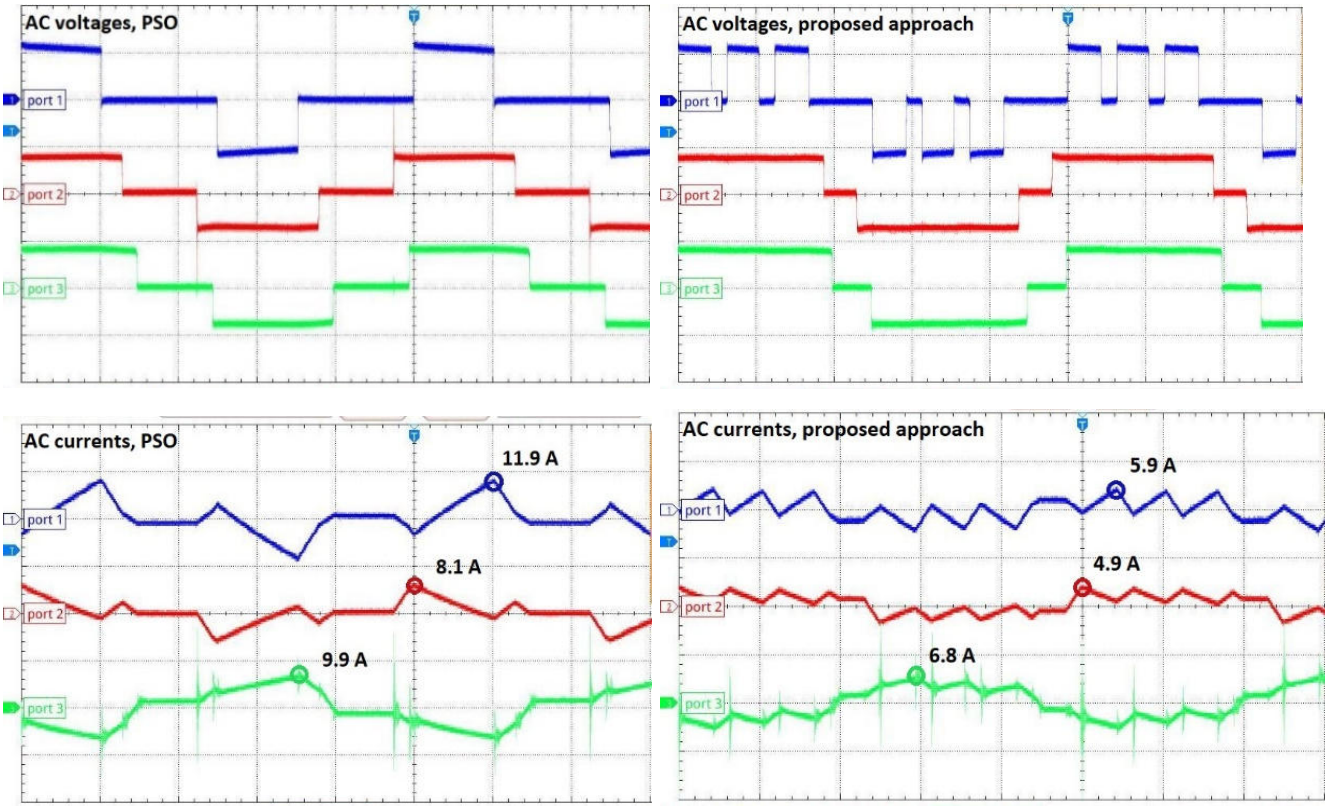

Figure 2.4.7–Prototype waveforms for our approach and PSO [101] for V_{DC1} = 220 V, V_{DC1} = V_{DC2} = 150 V, P_{DC1} = P_{DC2} = 300 W, Time base: 10us/div, Port 1 in blue, Port 2 in red, Port 3 in green

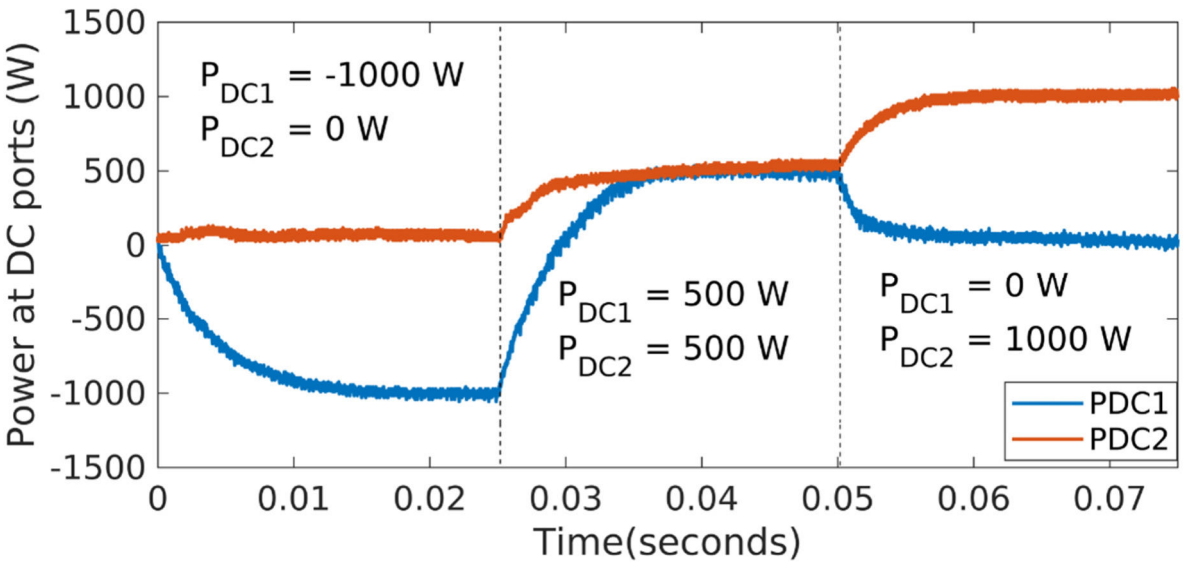

Figure 2.4.8–Power steps in different directions

2.4.6. Summary

The section presents an advanced modulation method for Multiple Active Bridge (MAB) converters that reduces the conduction power losses under non-unitary DC voltage conversion ratios. This method can be particularly useful for connecting batteries and supercapacitors to multi-port systems, because these types of sources operate under wide voltage ranges.

The proposed dual-duty modulation optimizes the reactive power from higher harmonics flowing through the transformer. Therefore, the high-frequency recirculating currents at DC ports are reduced. This, in turn, leads to a significant reduction of conducting losses, up to 40% in certain cases, compared to MCP (minimum current point) and/or PSO (particle swarm optimization) algorithms which are one of the most efficient methods.

The dual-duty modulation is incorporated into the already mentioned dq-frame control method under first harmonic approximation at the switching frequency. In general, it can be incorporated into other power control techniques, given that all the first harmonic assumptions are satisfied.

The proposal is validated in simulations and with experimental results in a three-port MAB (TAB) prototype. The method is general and can be applied to any number of ports. However, in this section, the static analysis is focused on a three-port system. The comparison of the proposed approach to the existing methods is presented in Table 2.4.3. As mentioned earlier, the proposed approach results in higher efficiency at large voltage conversion ratios. This is beneficial for the systems involving non-constant DC sources.

The response time of the proposed method is fast, 5-10 ms and it depends on the time constants of the transformer. In comparison to others, 25 ms in MPC [22] and 200 ms and in PSO [101], the proposed method has fast response time.

The MCP method is fully model-independent, while the PSO approach requires all model parameters to solve the optimization problem. In the proposed “dual-duty” switching technique, no specific model parameters are needed. In addition, the PSO

method is difficult to scale, as it uses lookup tables, and its dimensions will increase. The proposed method employs a sub-optimal solution which does not require additional dimensions in the lookup tables when increasing the number of ports. The proposed method shows a clear benefit at high DC voltage conversion ratios. The exact voltage and power conditions for selecting dual-duty in a particular port is a part of the future work.

Overall, the results show that despite the increased switching losses, the proposed dual-duty modulation can achieve a reduction in the total power losses under certain conditions of DC powers or voltage conversion ratios, because of a noticeable reduction in the conduction losses. In the future work, the exact criteria for using the dual-duty modulation should be established based on various system's parameters. The details of this section were published in [96].

Chapter 3. GRID-CONNECTED INVERTER AS THE INTEGRATION BLOCK TO THE GRID AND THE MAB CONVERTER

3.1. Grid-connected inverter – description of main operational modes

This chapter is focused on the connection between the multiple active bridge and AC systems such as the electric grid or an EV with an on-board charger through an inverter. This inverter must be flexible, because if it is delivering energy to the MAB converter, it mainly works as a rectifier, but when it provides energy to the grid, it will work as an inverter with limited current for protecting the EV battery.

In addition, these inverters connected to the grid should be able to provide grid services. For example, in case of grid failure, inverters from the EV chargers can take energy from the EV and give it to the grid to keep the grid stable for a short amount of time. For that, inverters should be able to work in different modes:

- Current-mode or slave mode: For absorbing or delivering a controlled amount of current (or power) from/to the grid according to some reference
- Voltage-mode or master mode: For delivering or absorbing as much power that the grid needs to keep the voltage stable.
- Multi-master mode or droop-mode: Similar to the previous one but the inverters can work in parallel with the grid without any communication link. This is extremely useful in case of faults so inverters can share the power of a microgrid.
- DC voltage control mode: In this mode the inverter works as a rectifier following a DC voltage reference. This is the mode for the EV charging.

3.2. Grid-connected inverter – space-phasor modeling

3.2.1. Inverter averaged modeling

In order to control an inverter, hardware modeling is required. There are several topologies in the literature that can allow the DC to AC transformation and vice versa [103]. The most common for low-voltage grid applications 3x400VAC and moderate power (kW range) is the voltage-source inverter (VSI) comprising six fully controllable switches (see Figure 3.2.1)

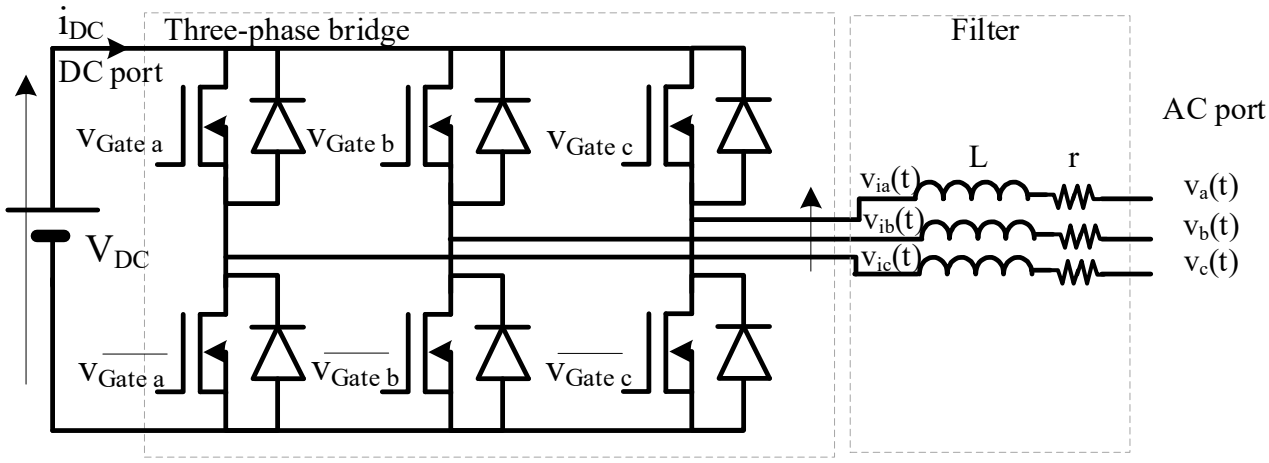

Figure 3.2.1–Complete block diagram of the proposed solution

Figure 3.2.1 shows a typical circuit using MOSFET switches (Metal Oxide Semiconductor Field Effect Transistor) but these switches can be replaced with any other technology. The inverter has two parts, the three-phase bridge and the filter. The three-phase bridge is controllable with three signals: v_{Gatea}, v_{Gateb} and v_{Gatec} which control the state (on or off) of the top switches. The bottom switches operate complementarily, thus, if the top switch is on, the bottom switch is off and vice versa.

The bridge is controlled by three pulse-width-modulated (PWM) signals (one per gate). Those signals are generated by a PWM modulator which converts a voltage signal, the modulating signal, into a signal with two-level signal, as Figure 3.2.2 shows. When the signal is at the high state, the switch associated to it is on, and when it is at low state,

the swich is off. The switches change periodically with the period, T_s, the switching period (f_S=1/T_S) as Figure 3.2.2 shows). Therefore, the bridge's AC output voltages: v_{ia}, v_{ib} and v_{ic} have two levels $V_{DC}/2$ and $-V_{DC}/2$ and the average voltage per period varies according to the on-state time to T_s ratio or duty cycle, D. The duty cycle is proportional to the modulating signal. The output voltage of the inverter in phase a is (others are similar):

$$v_{ia}(t) = \int_0^{Ts} V_{DC} \frac{2s_a(t) - 1}{2} dt + \sum_{n=2}^{\infty} A_n \sin(n.\omega_s.t + \varphi_n)\,, \tag{3.2.1.a}$$

where $\omega_s = 2\pi f_s$ and s_a is the switching signal in the bridge's a branch. The average signal is:

$$\langle v_{ia}(t) \rangle = \int_0^{Ts} V_{DC1} \frac{2s_a(t) - 1}{2} dt = \frac{V_{DC}}{2}(2d - 1). \tag{3.2.1.b}$$

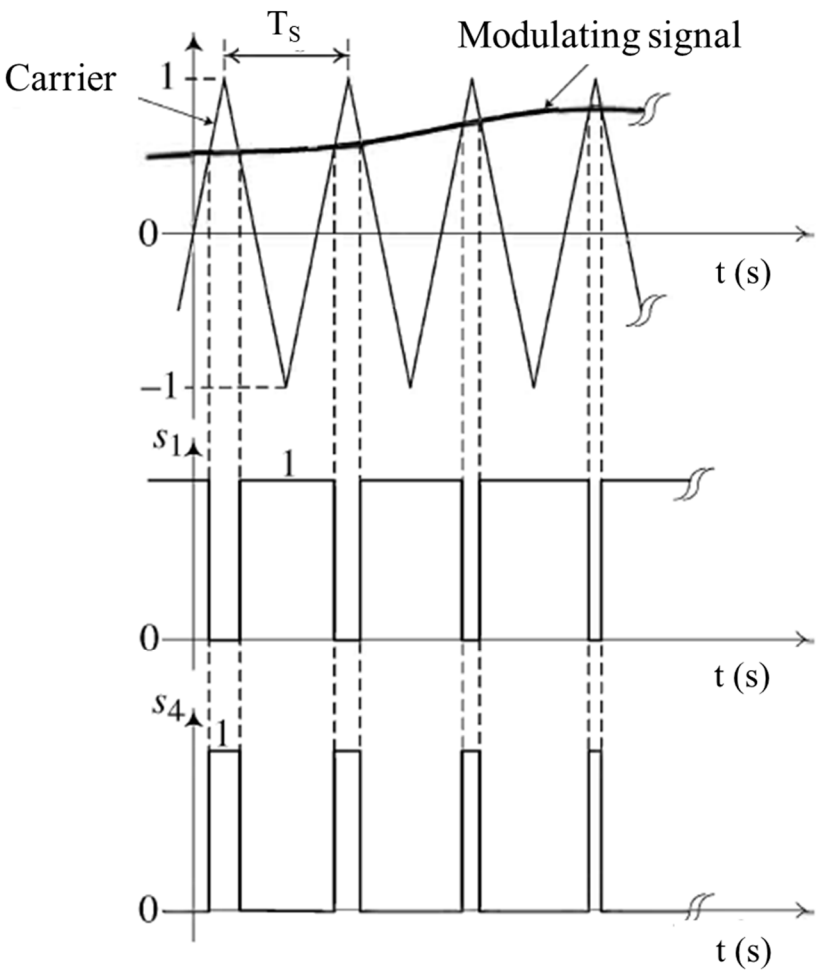

Figure 3.2.2–Modulation signal and PWM [24]

The filter in Figure 3.2.1 can be as simple as an inductor or more complex, but in any case, the idea is to remove high frequencies and keep only the low frequency (50 Hz), thus considering only an L-r current filter, the current is:

$$L\frac{di_a(t)}{dt} + ri_a(t) = \int_0^{Ts} V_{DC}\frac{2s_a(t)-1}{2}dt - v_a(t) + \sum_{n=2}^{\infty} B_n \sin(n.\omega_s.t + \varphi_n). \quad (3.2.2)$$

The solution has two main parts: the fundamental current and the high frequency components at f_s and its harmonics: $i_a(t) = \langle i_a(t)\rangle + i_{ah}(t)$. Considering that $i_{ah}(t)$ is highly attenuated due to the inverter output filter, $i_a(t) \approx \langle i_a(t)\rangle$. This is called averaged model, and it is valid for current variation with frequencies much lower than the switching frequency. In practice, the switching frequency is at least an order of magnitude bigger than the modulating frequency and usually more than two orders. Thus (3.2.2) becomes:

$$L\frac{d\langle i_a(t)\rangle}{dt} + r\langle i_a(t)\rangle = V_{DC}\frac{2d_a-1}{2} - v_a(t). \quad (3.2.3)$$

In addition, the modulation index is defined as: (3.2.4)

$$m_a = 2d_a - 1,$$

where d_a is the duty cycle which varies from 0 (totally off) to 1 (totally on), and m_a can vary from -1 to 1. This averaged model for the three-phase bridge can be described as:

$$\langle v_{ia}(t)\rangle = \frac{V_{DC}}{2}m_a(t) \quad (3.2.5.a)$$

$$\langle v_{ib}(t)\rangle = \frac{V_{DC}}{2}m_b(t) \quad (3.2.5.b)$$

$$\langle v_{ic}(t)\rangle = \frac{V_{DC}}{2}m_c(t). \quad (3.2.5.c)$$

And the output currents for the three–phases follow:

$$L\frac{d\langle i_a(t)\rangle}{dt} + r\langle i_a(t)\rangle = \frac{V_{DC}}{2}m_a(t) - v_a(t) \tag{3.2.6.a}$$

$$L\frac{d\langle i_b(t)\rangle}{dt} + r\langle i_b(t)\rangle = \frac{V_{DC}}{2}m_b(t) - v_b(t) \tag{3.2.6.b}$$

$$L\frac{d\langle i_c(t)\rangle}{dt} + r\langle i_c(t)\rangle = \frac{V_{DC}}{2}m_c(t) - v_c(t). \tag{3.2.6.c}$$

3.2.2. Space-Phasor Representation

The three modulation indexes can be selected arbitrary and the controller is in charge of that. For a three-phase system, those signals can be:

$$m_a(t) = \hat{m}.\cos(\omega t + \theta_0), \tag{3.2.7.a}$$

$$m_b(t) = \hat{m}.\cos\left(\omega t + \theta_0 - \frac{2\pi}{3}\right), \tag{3.2.7.b}$$

$$m_c(t) = \hat{m}.\cos\left(\omega t + \theta_0 + \frac{2\pi}{3}\right). \tag{3.2.7.c}$$

The space phasor is defined as (with the under bar):

$$\underline{m}(t) = \frac{2}{3}\left[m_a(t)e^{j0} + m_b(t)e^{+j2\pi/3} + m_c(t)e^{-j2\pi/3}\right] \tag{3.2.8.a}$$

which is:

$$\underline{m}(t) = \left(\hat{m}e^{j\theta_0}\right)e^{j\omega t} = \overline{m}e^{j\omega t} \tag{3.2.8.b}$$

where $\overline{m}$ is the complex modulation index which affects $m_a(t), m_b(t), m_c(t)$. Note that (3.2.8.b) is only valid because the three signals' amplitudes are equal, in other words, the system is balanced.

Using this representation, it is possible to use a single complex variable to represent a three-phase system. Figure 3.2.3 shows the representation of $\underline{m}(t)$ in the complex plane. From that, it can be understood that the signal in each phase (a,b,c) can be obtained using the projection of the space phasor $\underline{m}(t)$ in the axis of the phases (at 0, 4π/3 and -4π/3):

$$m_a(t) = \hat{m}.\cos(\omega t + \theta_0) = Re\{\underline{m}(t)e^{-j0}\}, \tag{3.2.9.a}$$

$$m_b(t) = \hat{m}.\cos\left(\omega t - \frac{2\pi}{3}\right) = Re\left\{\underline{m}(t)e^{-\frac{j2\pi}{3}}\right\}, \tag{3.2.9.b}$$

$$m_c(t) = \hat{m}.\cos\left(\omega t + \frac{2\pi}{3}\right) = Re\left\{\underline{m}(t)e^{+\frac{j2\pi}{3}}\right\}. \tag{3.2.9.c}$$

In case of harmonics and non-balance systems, the space phasor representation must be modified by adding more terms including negative sequence and harmonics.

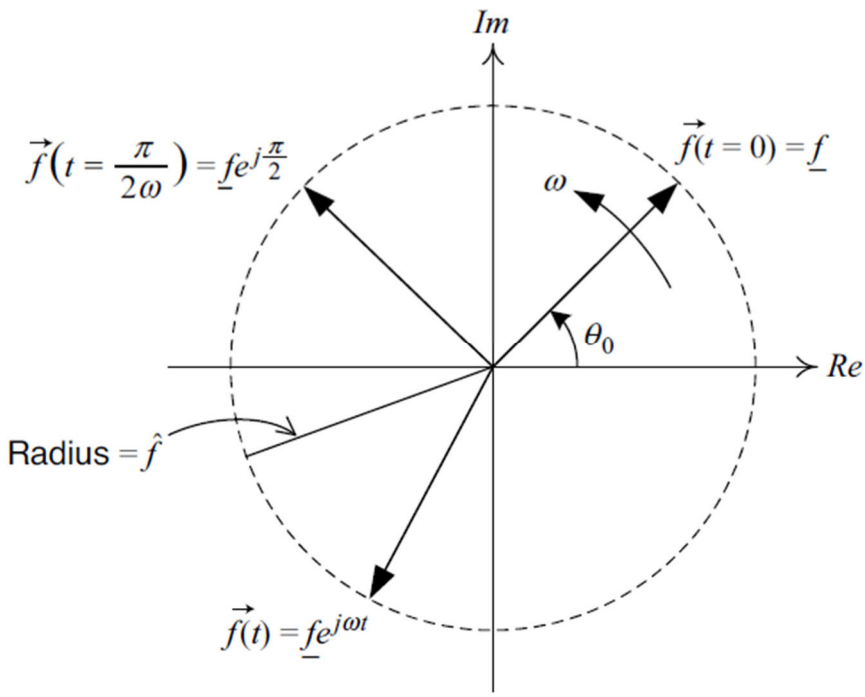

Figure 3.2.3–Phasor representation in the complex plane [24]

3.2.3. Modeling the inverter using the space-phasor representation

Assuming constant DC input voltage, the output voltage of the three-phase bridge is proportional to the modulation index and it can also be represented as a space-phasor:

$$\langle \underline{v_i}(t) \rangle = \frac{V_{DC}}{2}\underline{m}(t). \tag{3.2.10}$$

The output currents $\langle i_a(t)\rangle, \langle i_b(t)\rangle$ and $\langle i_c(t)\rangle$ that where obtained using (3.2.6), can now be expressed in a single complex equation:

$$L\frac{d\underline{i}}{dt} + r\underline{i} = \frac{V_{DC}}{2}\underline{m}(t) - \underline{v}(t), \tag{3.2.11}$$

where $\underline{v}$ is the space-phasor of the output voltage. In Laplace transform, this becomes:

$$(sL + r)\underline{i}(s) = \frac{V_{DC}}{2}\underline{m}(s) - \underline{v}(s), \tag{3.2.12.a}$$

or for any other type of output filter:

$$LPF(s)\underline{i}(s) = \frac{V_{DC}}{2}\underline{m}(s) - \underline{v}(s). \tag{3.2.12.b}$$

where s is the Laplace variable. Using space-phasor representation the three-phase power can also be calculated. The three-phase power is defined as:

$$P(t) = v_a(t).i_a(t) + v_b(t).i_b(t) + v_c(t).i_c(t). \tag{3.2.13}$$

Using (3.2.9), the $P(t)$ can be written as:

$$P(t) = Re\left\{\frac{3}{2}\underline{v}(t).\underline{i}^*(t)\right\}, \tag{3.2.14}$$

the reactive power as:

$$Q(t) = Im\left\{\frac{3}{2}\underline{v}(t).\underline{i}^*(t)\right\}, \tag{3.2.15}$$

and the complex power as:

$$\bar{S}(t) = P(t) + jQ(t) = \frac{3}{2}\underline{v}(t).\underline{i}^*(t). \tag{3.2.16}$$

This model cannot be applied when the phases are not balanced (or asymmetrical systems with phases with different magnitudes), and it is limited in case of coupling transfer functions between phases.

3.2.4. Modeling using alpha-beta frame representation

Considering that a space-phasor is a complex magnitude, it can be represented in its real and imaginary parts, termed alpha and beta:

$$\underline{m}(t) = \left(\hat{m}e^{j\theta_0}\right)e^{j\omega t} = \bar{m}e^{j\omega t} = m_\alpha + jm_\beta. \tag{3.2.17}$$

By combining (3.2.9) and (3.2.17) the abc-frame to $\alpha\beta$-frame transformation can be obtained:

$$\begin{pmatrix} m_\alpha(t) \\ m_\beta(t) \end{pmatrix} = \frac{2}{3}\underbrace{\begin{pmatrix} 1 & -1/2 & -1/2 \\ 0 & \sqrt{3}/2 & -\sqrt{3}/2 \end{pmatrix}}_{\bar{\bar{C}}}\begin{pmatrix} m_a(t) \\ m_b(t) \\ m_c(t) \end{pmatrix} \tag{3.2.18}$$

and vice versa

$$\begin{pmatrix} m_a(t) \\ m_b(t) \\ m_c(t) \end{pmatrix} = \bar{\bar{C}}^T\begin{pmatrix} m_\alpha(t) \\ m_\beta(t) \end{pmatrix} = \frac{2}{3}\begin{pmatrix} 1 & 0 \\ -1/2 & \sqrt{3}/2 \\ -1/2 & -\sqrt{3}/2 \end{pmatrix}\begin{pmatrix} m_\alpha(t) \\ m_\beta(t) \end{pmatrix}. \tag{3.2.19}$$

The power in αβ-frame, according to (3.2.14), (3.2.15) and (3.2.16), is:

$$P(t) = \frac{3}{2}\left[v_\alpha(t)i_\alpha(t) + v_\beta(t)i_\beta(t)\right], \tag{3.2.20}$$

and the reactive power as:

$$Q(t) = \frac{3}{2}\left[-v_\alpha(t)i_\beta(t) + v_\beta(t)i_\alpha(t)\right]. \tag{3.2.21}$$

The modeling in $\alpha\beta$-frame follows the same procedure as space-phasor representation. It works well for symmetric systems, for asymmetric systems or phase coupled systems cannot be directly applied. However, this representation is useful in practical implementation because all α and β components are real which helps to the development of algorithms and control loops. Based on this model representation, a special control for harmonic compensation was introduced by the author. Details are covered in Section 3.3, 3.4 [104, 105].

3.2.5. Modeling using dq-frame representation

Using $\alpha\beta$-frame representation, currents and voltages in the inverter are sinusoidal at grid frequency (50Hz). In order to control those signals, high order controllers are needed [104][105], which complicates the design, particularly if the frequency is not fixed. The dq-frame allows to have a DC waveform under steady-state operation. Then, to control a DC magnitude, simpler controllers can be used, such as proportional-integral controllers. The dq-frame representation of a space-phasor is:

$$\underline{m}(t) = \left(\hat{m}e^{j\theta_0}\right)e^{j\omega t} = \bar{m}e^{j\omega t} = \left(m_d + jm_q\right)e^{j\varepsilon(t)} \tag{3.2.22.a}$$

or:

$$m_d + jm_q = \underline{m}(t)e^{-j\varepsilon(t)} \tag{3.2.22.b}$$

where

$$\varepsilon(t) = \varepsilon_0 + \int \omega(\tau)d\tau. \tag{3.2.22.c}$$

The key point is that $\frac{d\theta}{dt} = \frac{d\varepsilon}{dt}$, thus d and q components of the signal are constant. The choice of $\varepsilon_0$determines which is the component in phase with frame or d (direct) component and which is the q component (quadrature). To change from $\alpha\beta$-frame to dq-frame the Park transformation is used:

$$m_d + jm_q = \left(m_\alpha + jm_\beta\right)e^{-j\varepsilon(t)} \tag{3.2.23.a}$$

or:

$$\begin{pmatrix} m_d \\ m_q \end{pmatrix} = \begin{pmatrix} \cos\varepsilon(t) & \sin\varepsilon(t) \\ -\sin\varepsilon(t) & \cos\varepsilon(t) \end{pmatrix}\begin{pmatrix} m_\alpha \\ m_\beta \end{pmatrix}. \tag{3.2.23.b}$$

Figure 3.2.4 shows the dq-frame.

The power calculation becomes

$$P(t) = \frac{3}{2}\left[v_d(t)i_d(t) + v_q(t)i_q(t)\right], \tag{3.2.24}$$

and the reactive power as:

$$Q(t) = \frac{3}{2}\left[-v_d(t)i_q(t) + v_q(t)i_d(t)\right]. \tag{3.2.25}$$

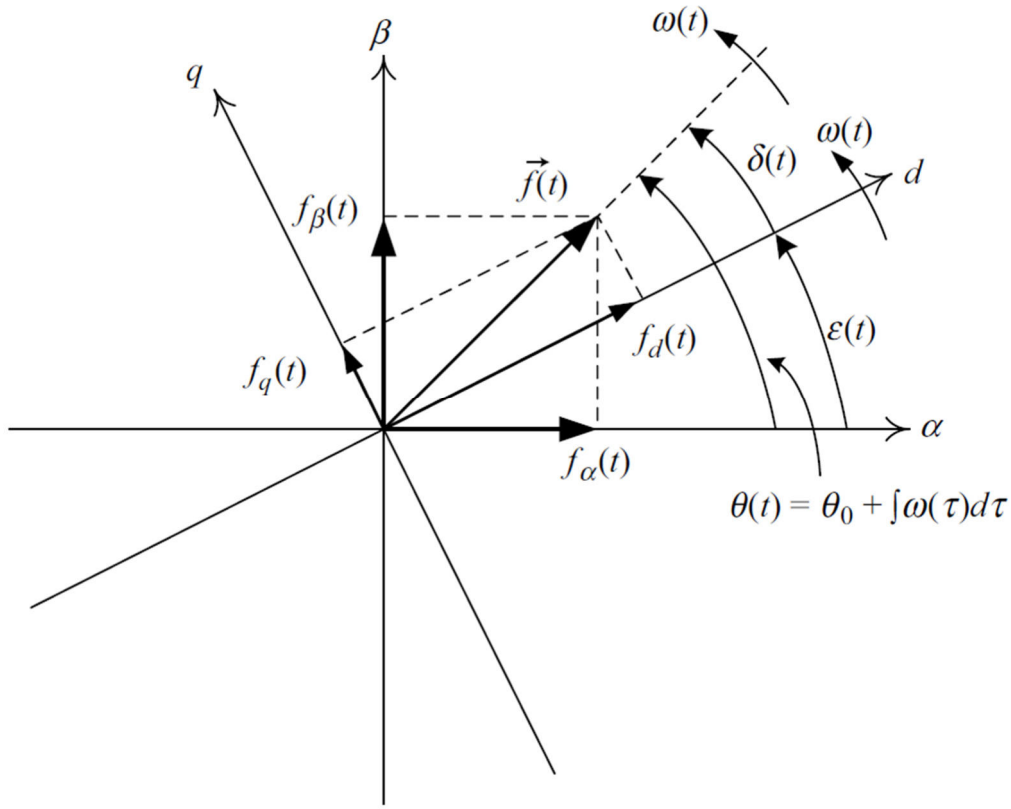

Figure 3.2.4–$\alpha\beta$-frame and dq-frame coordinate systems [24]

3.2.6. Modeling the inverter using the dq-frame representation

As in the Section 3.2.3, the dq-representation can be used for solving differential equations in the inverter model. Let's consider the same example of output current in the inverter in (3.2.11), but using dq-frame representation:

$$\underline{i} = \left(i_d + ji_q\right)e^{j\varepsilon(t)} = \overline{\imath_{dq}}e^{j\omega t} \text{ and the same for } \underline{v} \text{ and } \underline{m} \tag{3.2.26}$$

considering $\varepsilon(t) = \omega t$ and $\overline{\imath_{dq}} = i_d + ji_q$.

Thus,

$$L\frac{d\left(\overline{\imath_{dq}}e^{j\omega t}\right)}{dt} + r\overline{\imath_{dq}}e^{j\omega t} = \frac{V_{DC}}{2}\left(\overline{m_{dq}}e^{j\omega t}\right) - \overline{v_{dq}}e^{j\omega t} \tag{3.2.27.a}$$

applying the derivatives:

$$L\frac{d\overline{\imath_{dq}}e^{j\omega t}}{dt}+j\omega L\overline{\imath_{dq}}e^{j\omega t}+r\overline{\imath_{dq}}e^{j\omega t}=\frac{V_{DC}}{2}\left(\overline{m_{dq}}e^{j\omega t}\right)-\overline{v_{dq}}e^{j\omega t} \tag{3.2.27.b}$$

and as this is valid for any t, $e^{j\omega t}$can be removed from the equation:

$$L\frac{d\overline{\imath_{dq}}}{dt}+j\omega L\overline{\imath_{dq}}+r\overline{\imath_{dq}}=\frac{V_{DC}}{2}\overline{m_{dq}}-\overline{v_{dq}}. \tag{3.2.28}$$

This represents two differential equations, the real and the imaginary part:

$$L\frac{di_d}{dt}-\omega Li_q+ri_d=\frac{V_{DC}}{2}m_d-v_d \tag{3.2.29.a}$$

$$L\frac{di_q}{dt}+\omega Li_d+ri_q=\frac{V_{DC}}{2}m_q-v_q, \tag{3.2.29.b}$$

which reflects the effect of coupling between d component and q component. This effect appears naturally in any derivative in the dq frame. Due to that, decoupling algorithms have been reported in the literature [106, 107], but the key advantages to have DC signals which are simpler for control.

3.2.7. Summary

This section reviews the modeling techniques in inverters based on the averaged signals in one switching period. The section defines the space-phasor representation which is useful for reducing the number of differential equations from three to one, in balanced three-phase systems. In addition, as the space-phasor is a complex magnitude, real and imaginary parts are analyzed. From there, the alpha-beta frame or static frame is introduced, where the alpha component is the real part of the space-phasor and beta is the imaginary part. Finally, if the frame rotates synchronously with the space-phasor, the signals in the frame are static. Then, the rotating frame is defined as the dq-frame, where the signals are “DC types”, the d-component is the real part in the frame and the q-component is the imaginary part. Frames and space-phasors are essential for designing the control loops in the next sections.

3.3. Control algorithm for grid-connected inverters using alpha-beta frame including harmonic compensation

This section presents the modeling in $\alpha\beta$-frame for designing a multi resonant controller which can reduce harmonics in the current injection to the grid. The section suggests a new methodology for choosing the parameters considering the influence of the LCL filter. The proposed model was implemented in the real-time simulator with the real connected loads to verify the simulation results. The details of this section were published in [105].

3.3.1. Description of the control algorithm and design procedure

Having defined the $\alpha\beta$-frame representation, the model for the inverter connected to the grid, according to Figure 3.3.1, can be described as:

$$(sL + r)\left[i_\alpha(s) + ji_\beta(s)\right] = \frac{V_{DC}}{2}\left[m_\alpha(s) + jm_\beta(s)\right] - v_\alpha(s) - jv_\beta(s) \tag{3.3.1}$$

for each component, and, in general, for any output filter the currents are:

$$i_\alpha(s) = LPF(s)\left[\frac{V_{DC}}{2}m_\alpha(s) - v_\alpha(s)\right] \tag{3.3.2.a}$$

$$i_\beta(s) = LPF(s)\left[\frac{V_{DC}}{2}m_\beta(s) - v_\beta(s)\right], \tag{3.3.2.b}$$

where LPF(s) means low-pass filter. Thus, the current of the inverter is a function of the grid voltage $v_\alpha(s) + jv_\beta(s)$ and the modulation index $m_\alpha + jm_\beta$. They are totally independent (no coupled elements between α and β components). In order to control the inverter output, the block diagram of Figure 3.3.2 is suggested where the controller generates $m_\alpha + jm_\beta$ based on feedback and feedforward signals:

$$m_\alpha(s) = \frac{\tilde{v}_\alpha(s) + u_\alpha(s)}{V_{DC}/2} \tag{3.3.3.a}$$

$$m_\beta(s) = \frac{\tilde{v}_\beta(s) + u_\beta(s)}{V_{DC}/2}, \tag{3.3.3.b}$$

where $\overline{u_{\alpha\beta}} = u_\alpha + ju_\beta$ is the output signal of the controller which is a function of the error between the reference and measured currents and $\tilde{v}_\alpha(s)$ and $\tilde{v}_\beta(s)$ are the measurement signals of the grid voltage.

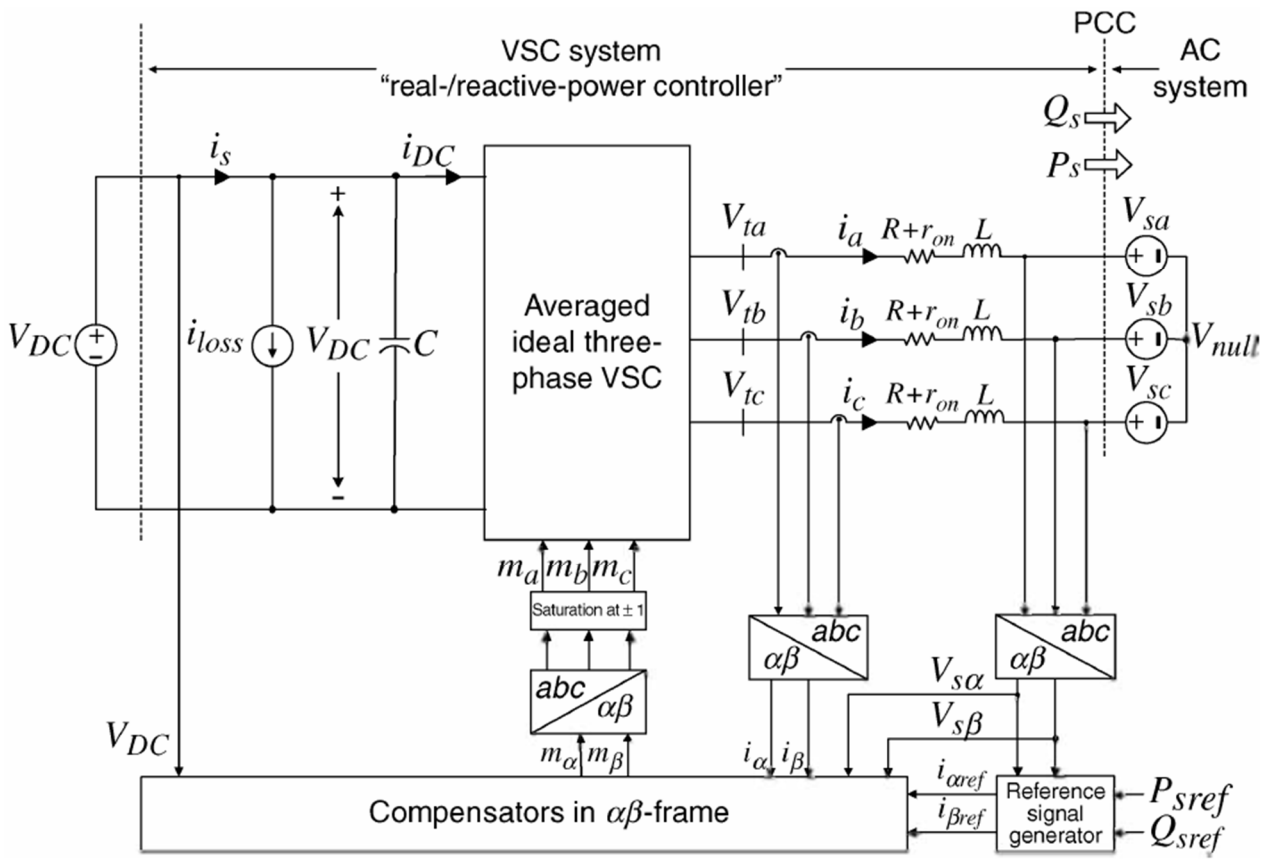

Figure 3.3.1–Model of inverter connected to the grid in the $\alpha\beta$-frame coordinate systems [24]

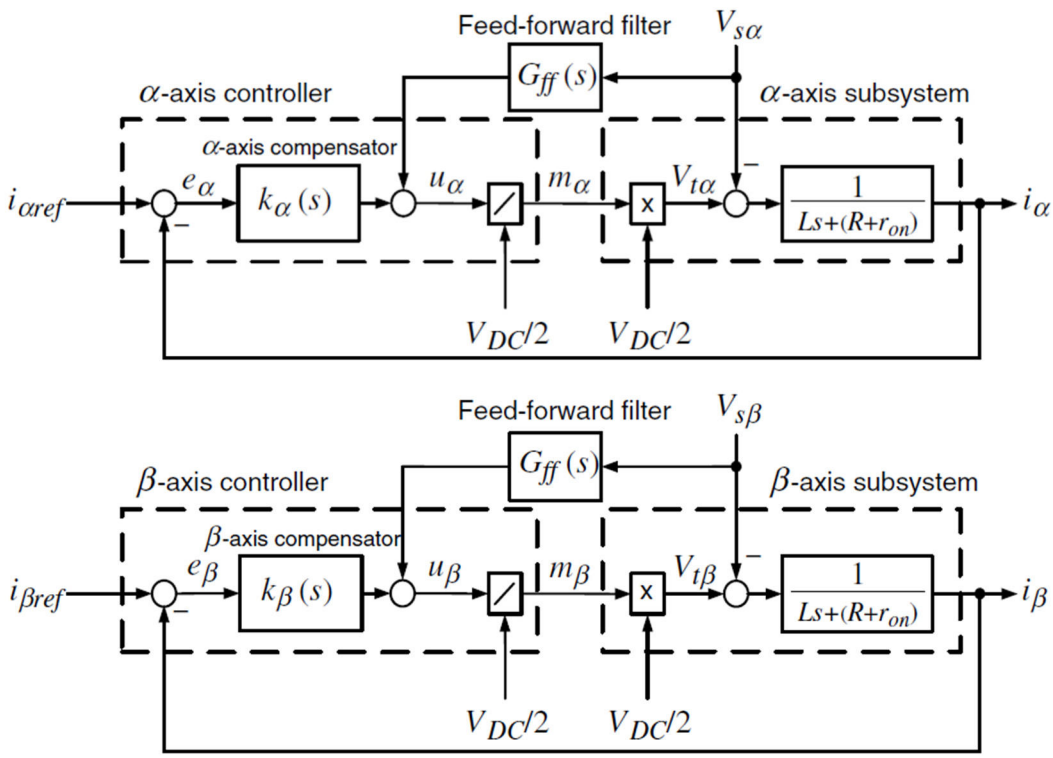

Figure 3.3.2–Current-control loop in $\alpha\beta$-frame coordinate systems of a grid-connected inverter [24]

According to Figure 3.3.2, the control signals $u_\alpha(s)$ and $u_\beta(s)$are:

$$u_\alpha(s) = k_\alpha(s)\left[i_{ref\,\alpha}(s) - i_\alpha(s)\right] = k_\alpha(s)e_\alpha(s) \tag{3.3.4.a}$$

$$u_\beta(s) = k_\beta(s)\left[i_{ref\,\beta}(s) - i_\beta(s)\right] = k_\beta(s)e_\beta(s), \tag{3.3.4.b}$$

where $e_\alpha(s)$ is the error between the reference and the measurements. In order to design the controller's transfer function, it is important to recall that the reference currents are sinusoidals at the grid frequency. Thus, it is expected that the control loop has a high gain at those frequencies. The preferable controllers are proportional resonant controllers [108-109], with a transfer function similar to:

$$k_\alpha(s) = k_\beta(s) = k_P + \frac{2k_I}{s^2 + {\omega_G}^2}, \tag{3.3.5}$$

where k_P is a proportional constant and k_I emulates the integral part but at the resonant frequency ω_G which should be equal to the grid frequency ($\omega_G = \omega_g$). Unfortunately, this function might produce instabilities in the current-control loop due to the -180° phase shift

for frequencies above ω_G and the infinite gain at ω_G. Thus, an alternative function is the damped one:

$$k_\alpha(s) = k_\beta(s) = k_P + \frac{2k_I\omega_c s}{s^2 + 2s\omega_c + {\omega_G}^2}, \tag{3.3.6}$$

where ω_c represents the bandwidth of the converter at high gain.

Eventually, if the control-loop is still unstable, compensators might be added. The complete transfer function for the current control in open loop is:

$$G_{OL}(s) = \frac{i_\alpha(s)}{e_\alpha(s)} = \left(k_P + \frac{2k_I\omega_c s}{s^2 + 2s\omega_c + {\omega_G}^2}\right) e^{jsT_d}\, LPF(s), \tag{3.3.7}$$

considering that the feed-forward signal perfectly cancels the grid voltage: $\tilde{v}_\alpha(s) = v_\alpha(s)$. For the simple case of L+r output filter:

$$G_{OL}(s) = \frac{i_\alpha(s)}{e_\alpha(s)} = \left(k_P + \frac{2k_I\omega_c s}{s^2 + 2s\omega_c + {\omega_G}^2}\right) e^{jsT_d}\, \frac{1}{sL + r}, \tag{3.3.8}$$

where T_d is the delay in the transfer function due to the discretization of the signals using a microprocessor and the acquisition time. The selection guideline of the controller parameters, k_P and k_I, is in [105]:

1) Approximate the delay transfer function by its first order approximation:

$$e^{jsT_d} \approx \frac{1}{sT_d + 1}, \tag{3.3.9}$$

where $T_d = 1.5T_S$ where T_S is the switching period.

2) Reduce the order to 3rd by considering that s is analysed for frequencies higher than the resonance:

$$G_{OL}(s)|_{s \gg \omega_c} \approx \frac{i_\alpha(s)}{e_\alpha(s)} = \frac{1}{r} \frac{k_P s + 2k_I\omega_c + 2\omega_c}{(s + 2\omega_c)\left(s\frac{L}{r} + 1\right)(sT_d + 1)}. \tag{3.3.10}$$

3) Calculate the closed loop transfer function and compare the transfer function with the model:

$$G_{CL}(s) = \frac{i_\alpha(s)}{i_{ref\,\alpha}(s)} = \frac{b_1 s + b_0}{a_3 s^3 + a_2 s^2 + a_1 s + a_0}, \tag{3.3.11}$$

$$a_3 = T_r T_d\,(T_r T_d + 2T_r T_d \omega_c)$$

$$a_2 = T_r + T_d + 2\omega_c T_r T_d$$
$$a_1 = 1 + 2\omega_c(T_r + T_d) + k_P/r$$
$$a_0 = 2\omega_c(1 + (1 + k_P/r) + 2k_I/r$$
$$b_1 = k_P/r$$
$$b_0 = 2k_I/r + 2\omega_c k_P/r.$$

4) Select β according to the phase margin

$$Phase\ Margin\ (PM) = tg^{-1}\left(\frac{\beta - 1}{2\sqrt{\beta}}\right). \tag{3.3.12}$$

5) Apply the Extended Symmetrical Optimum method [109]

$$\sqrt{\beta} a_1 a_3 = {a_2}^2 \tag{3.3.13}$$
$$\sqrt{\beta} a_0 a_2 = {a_1}^2.$$

Thus k_P and $k_I$can be obtained. Aproximately, they are:

$$k_P \approx r\frac{T_r}{\sqrt{\beta} T_d} \quad k_I \approx r\frac{T_r}{2\beta\sqrt{\beta}{T_d}^2}.$$

This design procedure was detailed by the authors in [105].

3.3.2. Multi-resonant control algorithm

The previous section details the control in $\alpha\beta$-frame using a proportional gain and a resonant controller. The resonant controller is tuned at the grid frequency $\omega_G = \omega_g$. This technique can also be implemented for controlling different harmonics, having one controller per harmonic. This is called multi-resonant control algorithm and the transfer function of the controller can be defined as:

$$k_\alpha(s) = \frac{u_\alpha(s)}{e_\alpha(s)} = k_P + \frac{2k_I\omega_c s}{s^2 + 2s\omega_c + {\omega_G}^2} + \sum_{h=2}^{H} \frac{2k_{Ih}\omega_c s}{s^2 + 2s\omega_c + (h\omega_G)^2}. \tag{3.3.14}$$

The last sum can be added to control several harmonics. The number of harmonics is limited due to the switching operation process, and the discretization in the

microcontroller. The procedure for selecting the gains can follow the same procedure as in the previous section.

3.3.3. Simulation example – description of the controller design

In order to validate the proposed controller, a numerical simulation of a single-phase inverter is used. Figure 3.3.3 shows the main diagram of the inverter, notice the similarities with the proposed control loop of Figure 3.3.1, the simulations have been performed in MATLAB/Simulink. It is a single-phase grid-connected bidirectional VSI with an LCL filter (instead of L-r filter) and proportional-resonant (PR) current controller. This circuit is designed with two purposes: keep the DC side constant to apply the voltage to a DC/DC controller to charge an EV battery and to provide a service to the grid by controlling the reactive power injected.

The implemented filter is not just a simple *L-r* filter, but a more practical one *LCL*, which reduces the harmonics at the grid connection or point of common coupling (PCC). The inverter is supposed to be attached to a DC/DC converter in an EV charger [110][111]. Thus, for this application, inverter is controlling the voltage at the DC side (v_{dc}), by adjusting the current in the grid side, i_g.

The grid voltage and current are expressed as:

$$v_g(t) = \hat{V}_g \, cos\omega_g(t) \tag{3.3.15.a}$$

$$i_g(t) = \hat{I}_g \, cos(\omega_g t + \varphi) = \hat{I}_P \cos(\omega_g \, t) - \hat{I}_Q \sin(\omega_g \, t), \tag{3.3.15.b}$$

where $\hat{I}_P = \hat{I}_g \, cos \, \varphi \, \hat{\mathrm{I}}_\mathrm{P} = \hat{\mathrm{I}}_\mathrm{s} \cos \emptyset$ is the peak value of the active current (in- phase with the grid voltage) and $\hat{I}_Q = \hat{I}_s \, sin \, \varphi$ is the peak value of reactive current (in quadrature with the grid voltage). To simplify the analysis, the variables are transformed in the $\alpha\beta$-frame $\boldsymbol{x}(t) = x_\alpha(t) + jx_\beta(t)$ where the real and imaginary parts are the components of the Clarke transformation.

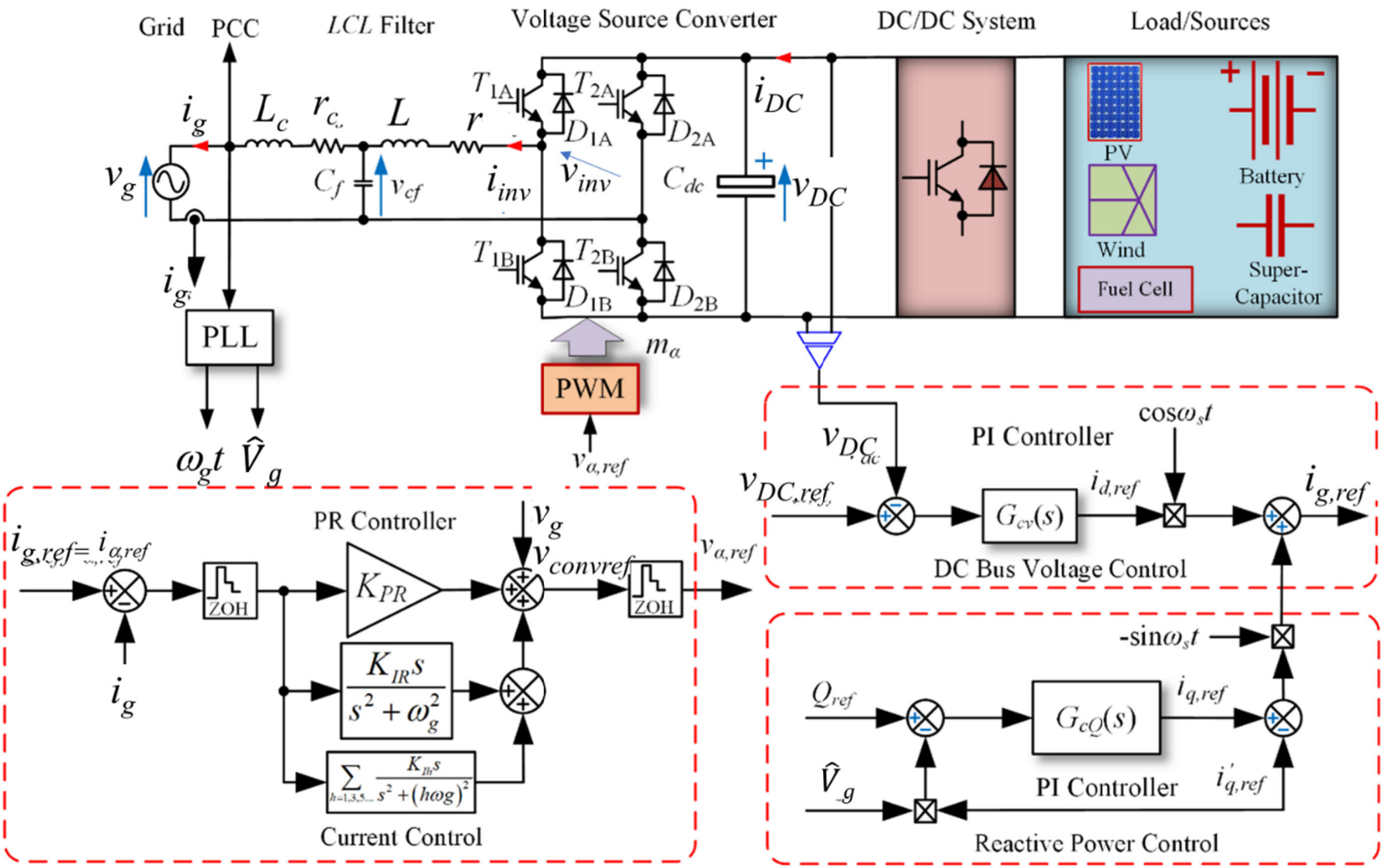

Figure 3.3.3–The overall diagram of a single-phase grid-connected bidirectional VSI with an LCL filter employing PR controller

By applying circuits laws to the output filter, the derived state equations of the converter are

$$L_c \frac{d\underline{i_g}(t)}{dt} + R_c \underline{i_g}(t) = \underline{v_g}(t) - \underline{v_{cf}}(t) \tag{3.3.16.a}$$

$$C_f \frac{d\underline{v_{cf}}(t)}{dt} = \underline{i_g}(t) - \underline{i_{inv}}(t) \tag{3.3.16.b}$$

$$L \frac{d\underline{i_{inv}}(t)}{dt} + R\underline{i_{inv}}(t) = \underline{v_{cf}}(t) - \underline{m}(t)v_{dc}(t) \tag{3.3.16.c}$$

where the under bar variables are space phasors. L and L_c are the inverter side and grid side inductances with the winding resistances R and R_c respectively. C_f is the filter capacitance. The $\underline{m}$ is the modulating signal given to the PWM switches. The grid current (i_g) is controlled by the PR current controller, which is already in $\alpha\beta$-frame and is compared with the reference current ($i_{g,ref}(t)$). The error goes through a zero-order hold (ZOH) to the PR controller. The ZOH is added because of the computational and processing delay caused by the digital pulse-width modulator (PWM).

The transfer function of the ideal PR controller with harmonic compensator (HC) was introduced in (3.3.5) and it is explicitly shown in Figure 3.3.3 as α and β have the same transfer functions and the converter has no coupling effects between α and β components, a single PR controller can be used instead of $k_\alpha(s)$ and $k_\beta(s)$. However, the converter has two references, in α for controlling the DC voltage and in β for adjusting the reactive power injection. The resonant terms have a damping but in the Figure 3.3.3 was omitted to simplified the diagram. The controller frequency is the same as the grid frequency $\omega_G = \omega_g$ and $\omega_c \langle\langle \omega_G$ in (3.3.6).

From Figure 3.3.3, the output of the PR controller ($v_{conv,ref}$) is passed through the ZOH and to feed the PWM generator, which creates the gate signals and finally the converter's output voltage (v_c). The desired reactive power is injected/delivered to the grid to support the voltage profile at the PCC employing the proper design of the reactive power loop in a secondary controller, a PI controller.

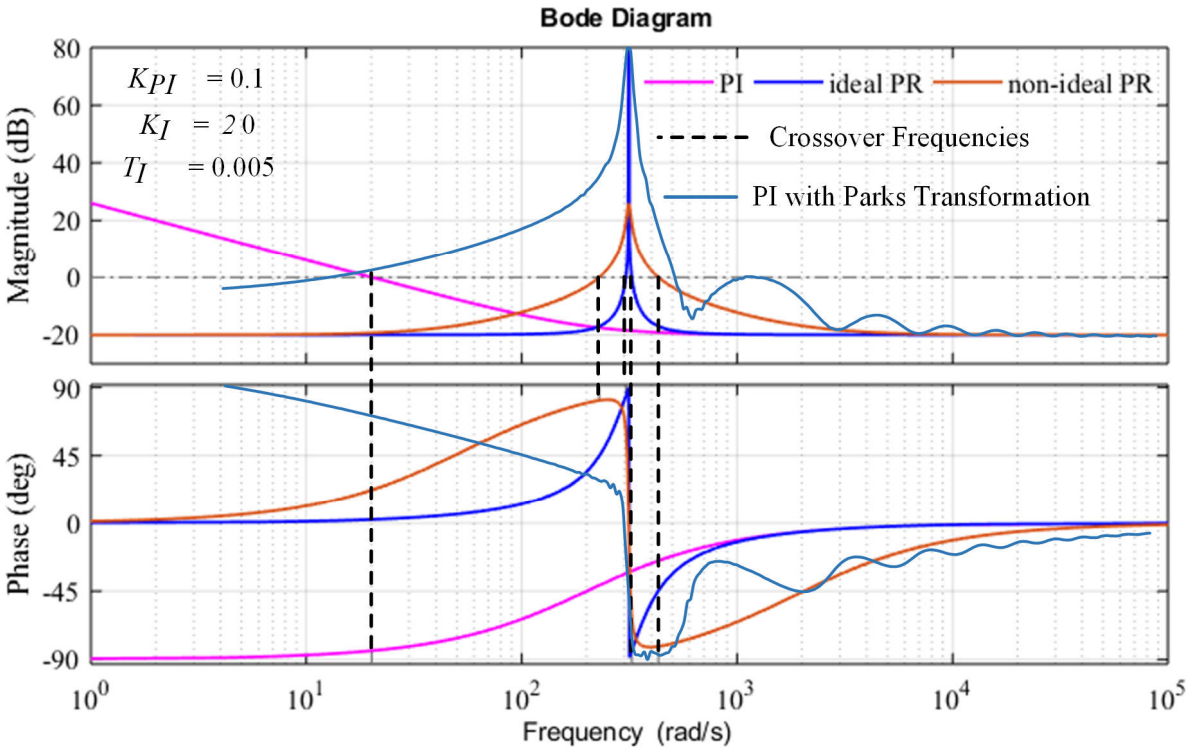

(a)

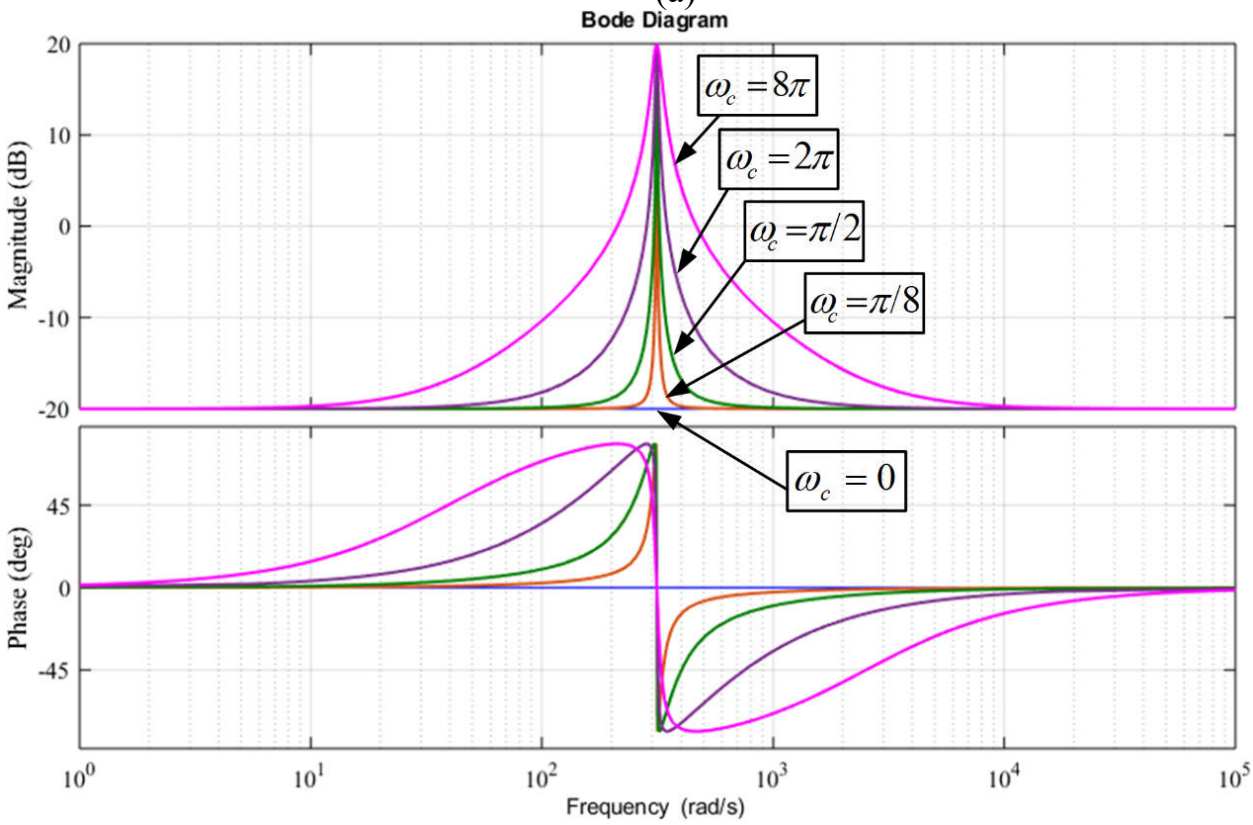

(b)

Figure 3.3.4–Frequency response of (a) different controllers, (b) the practical PR controller with a varying ω_c parameter

Figure 3.3.4(a) shows the open loop Bode plot of: a conventional PI transfer function, a PI controller with the Park and inverse Park transformation (see dq-frame controllers in Section 3.5), which moves the transfer function to the grid frequency, and the ideal and practical (non-ideal) PR controllers extracted from (3.3.5) and (3.3.6) respectively. Note that the PR controller behaves similar to the PI controller with the dq-frame transformations but having a better attenuation in the harmonics [108]. Moreover, the crossover frequencies of the controller can be seen in the figure with their respective phase margin (dashed lines).

The ideal and practical PR controllers have two crossover frequencies, where the phase margin of the practical PR can be widened by adjusting the ω_c. For the PR controller (Figure 3.3.3), the transient response is governed by the proportional gain (k_P) as in the traditional PI controllers. The transient system response would be faster with larger (k_P). Figure 3.3.4(b) depicts the effect of the ω_c for the practical PR given in (3.3.6). It is recommended to use the practical PR controller by adjusting the ω_c to achieve the desired bandwidth and the phase margin with finite gain to avoid system instability. k_I = 20, ω_g =314 rad/s and ω_c=10 rad/s were chosen in the Bode plot of Figure 3.3.4 (a), and (b). Figure 3.3.5 shows the ideal and non-ideal PR controller including the harmonic compensators at several frequencies according to (3.3.14). The ideal PR with a higher peak (blue) and the damped one are shown. There are different design methodologies for selecting the controller's coefficients. In [112], it is suggested to choose the proper k_P to stable the controller with the good transient response, and then, choose the k_I to provide steady state-phase and amplitude error without making the phase margin too small. However, in this work a design methodology is also proposed based on the Extended Symmetrical Optimization method [105, 109, 113].

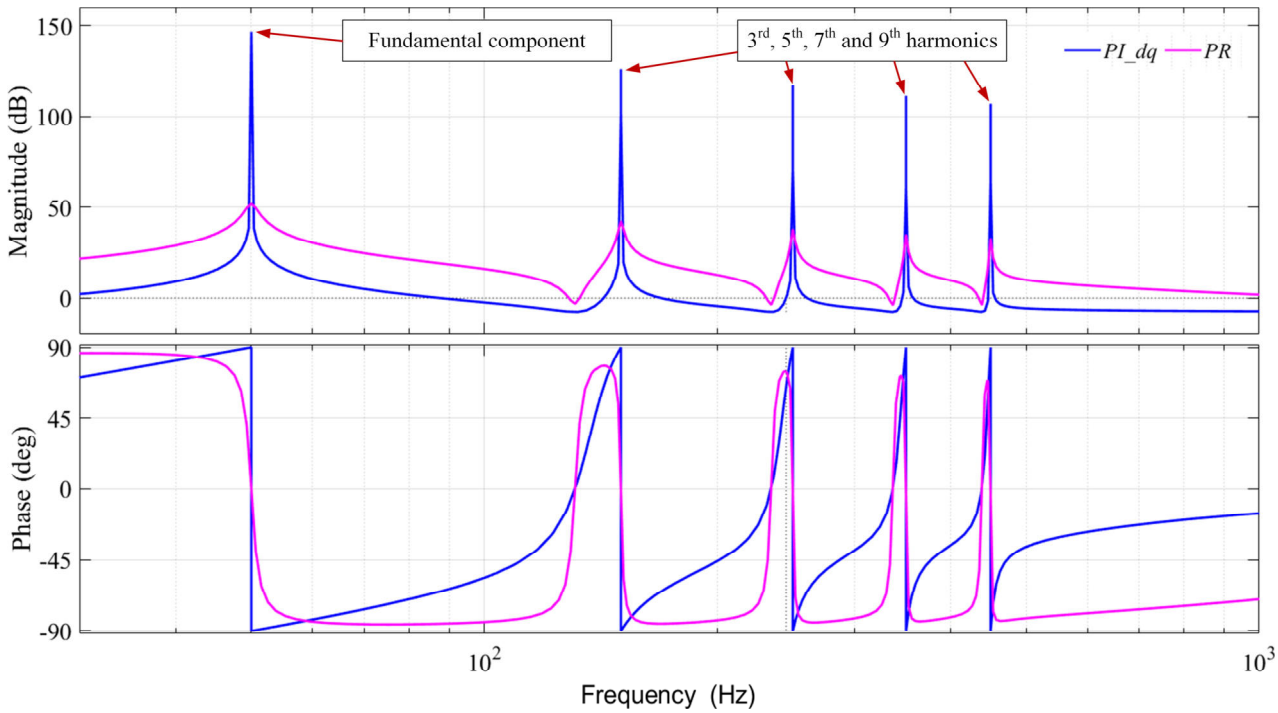

Figure 3.3.5–Comparison between ideal and practical PR controller with harmonic compensations

3.3.4. Simulation example – design of components (output filter)

The total harmonic distortion (THD_i) of the injected grid current can be notably reduced by the proper design of the *LCL* filter. However, the resonance of the *LCL* filter might cause the system to be unstable. This must be avoided by the careful filter design. The *LCL* filter parameters are designed based on the system rated voltage V_g =230 V, apparent power S_N=1.5 kVA, DC link voltage V_{DC} =400 V and the nominal grid frequency ω_g= 2π.50 rad/s and the switching frequency f_s =10 kHz [114]. First, calculate the base impedance and base capacitance as:

$$Z_b = \frac{V_g^2}{S_N} \text{ and } C_b = \frac{1}{\omega_g . Z_b} \tag{3.3.17}$$

Second, the allowable current ripples $\Delta i_{L\,max}$ on the inverter side is taken as

$$\Delta i_{Lmax} = ripple\%.\frac{S_N\sqrt{2}}{V_g} \tag{3.3.18}$$

Third, the inverter side inductance L is calculated based on the unipolar sinusoidal PWM switching technique as

$$L = \frac{V_{DC}}{8\Delta i_{Lfmax} f_s} \tag{3.3.19}$$

The filter capacitor is calculated as $C_f = x \cdot C_b$ where "x" decides the percentage of the reactive power required by the filter capacitor C_f. A practical recommendation is to put the resonant frequency of the filter, f_r:

$$\frac{f_s}{2} > f_r > \frac{f_s}{4} \text{ or} \tag{3.3.20}$$

$$10 f_g \leq f_r \leq f_s/2$$

Thus, the grid inductance can be obtained as [115]:

$$L_c = \frac{L}{\left(\omega_r^2 L \;\; C_f\right) - 1} \tag{3.3.21}$$

The resonant frequency range suggested in (3.3.20) reduces instability issues. However, if higher control bandwidth is used, instability may arise [112]. Design results are given in Table 3.3.1.

3.3.5. Simulation example – design of components (PR controller)

The design procedure of the PR controller is based on the methodology suggested in Section 3.3.1. C_f is neglected to simplify the design of the PR controller. Thus, the total inductance is $L_T = L_c + L$. The first order time delay (T_d) is approximated to the one and a half of the switching periods ($1.5T_s$). The open loop transfer function is the product of the PR controller, time delay and the plant transfer functions including inverter and output filter, and it is shown in equations (3.3.7)-(3.3.10). By applying the methodology suggested in Section 3.3.1 proportional and integral gains of the PR controller are obtained.

Table 3.3.1 System and LCL Filter Parameters

Parameters	Values
Line (RMS) voltage, V_g	230 V
Nominal grid frequency, ω_g	2π.50 rad/s
DC output voltage, V_{DC}	400 V
Apparent power, S_N	1.5 kVA
Base Impedance Z_b and base capacitance C_b	35 Ω, 90 μF
Converter side inductor with 16% of permissible ripples with respect to the rated current gives L	3.4 mH
Grid side inductor, coupling inductor, L_c	0.35 mH
Filter Capacitor, C_f with x =2.5% (x < 5%)	2.25 μF
Resonance frequency, f_r	6 kHz
Switching frequency, f_s	10 kHz

Figure 3.3.6 shows a simulation of the open loop Bode diagram with the gain and phase crossover frequencies of the system including PR controller and *LCL* plant with β = 10. Three crossover frequencies (point at 0dB) are observed: ω_{g1}, ω_{g2} and ω_{g3} with the respective phase margins (PMs) θ_{g1}, θ_{g2} and θ_{g3} respectively [116]. By adjusting the β of the controller, the k_P and k_I of the PR controller can be adjusted to achieve the optimum range of the phase margin (θ_m=θ_{g1}) as suggested in Section 3.3.1. Moreover, there are two more phase margins (PMs), θ_{g2} and θ_{g3}, related to the crossover frequencies at the filter resonance which need to be high enough to have the system stable. The range of the PM can be made larger by adjusting the β from 4 to 16 or adapting the damping of the resonant controller.

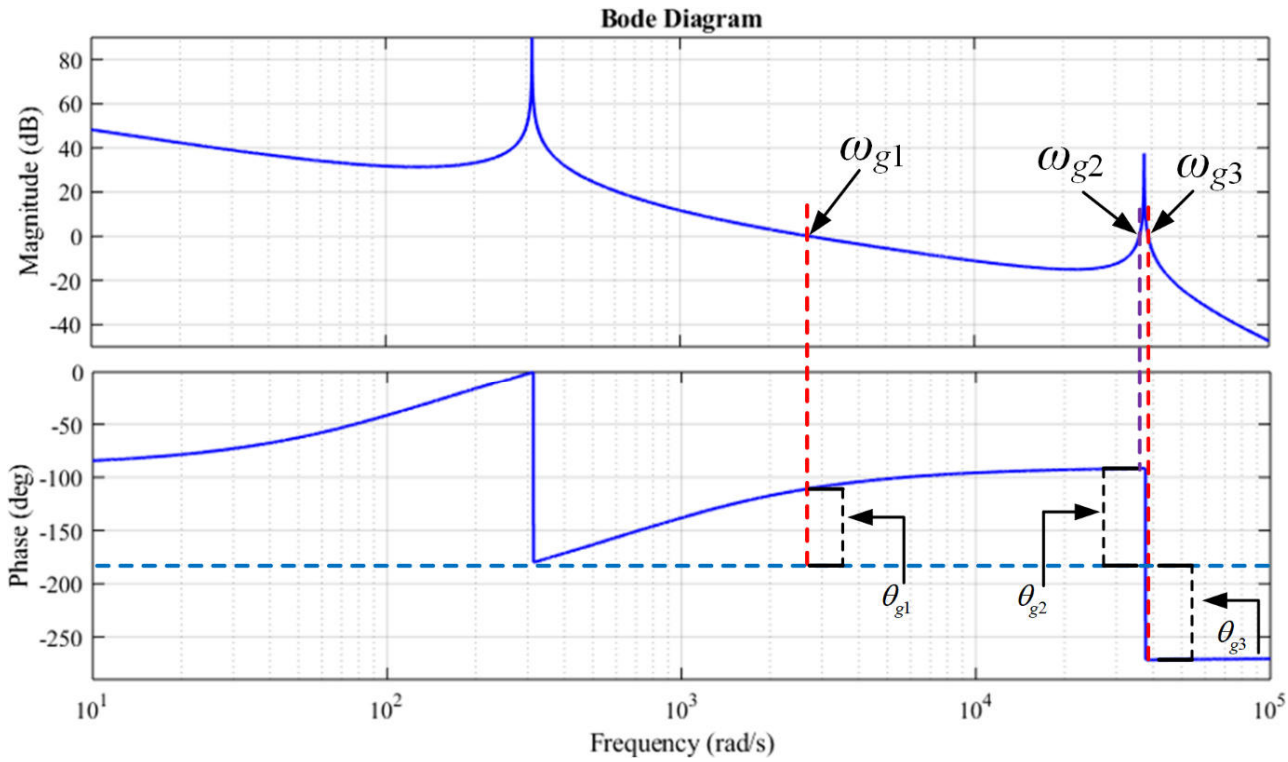

Figure 3.3.6 The frequency response of the system with β=10

3.3.6. Simulation example –results

The simulation of a VSI with a PR controller was performed in MATLAB/Simulink according to Figure 3.3.3. The PR controller parameters are k_P is 0.128 and k_{IR} 127.9 with a chosen β = 10 extracted from Section 3.3.1. Using αβ-frame, a single PR controller is used for controlling active and reactive power in the grid (at PCC). Figure 3.3.7 shows the simulated transient response of the rectifier operation of the single-phase VSI and an output *LCL* filter. At t = 0.02s a step change in the $i_{d,ref}$ is applied at a resistive load of 1 kW and a step change at t = 0.06s is applied in the $i_{q,ref}$ with 750 VAr of the reactive power.

It can be seen that the grid current (i_g) is fully following the reference current ($i_{g,ref}$) with almost zero steady-state error with the step change in active and reactive currents. Moreover, at t = 0.1s, it shows the simulated transient response of the inverter operation of the single-phase VSI where the power flows from DC to AC. At t = 0.14s a step change

is applied in the $i_{q,ref}$ with 1500 VAr of the reactive power and the reference current ($i_{g,ref}$) is following the grid current with almost zero steady-state error. The reference active and reactive currents ($i_{d,ref}$, $i_{q,ref}$) can also be seen with a step change in the error between the reference and measured currents, e=($i_{g,ref}$ - i_g).

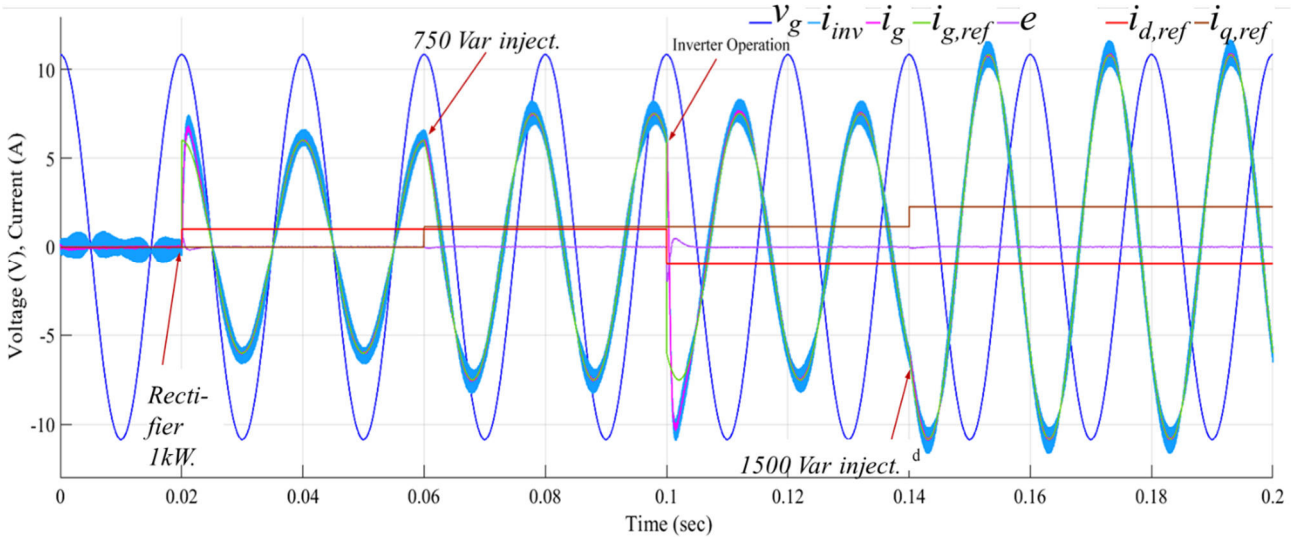

Figure 3.3.7–The simulated transient response of the VSI (Rectifier/Inverter operation) with a step change in ($i_{d,ref}$) and ($i_{q,ref}$) with line current i_g (t) error

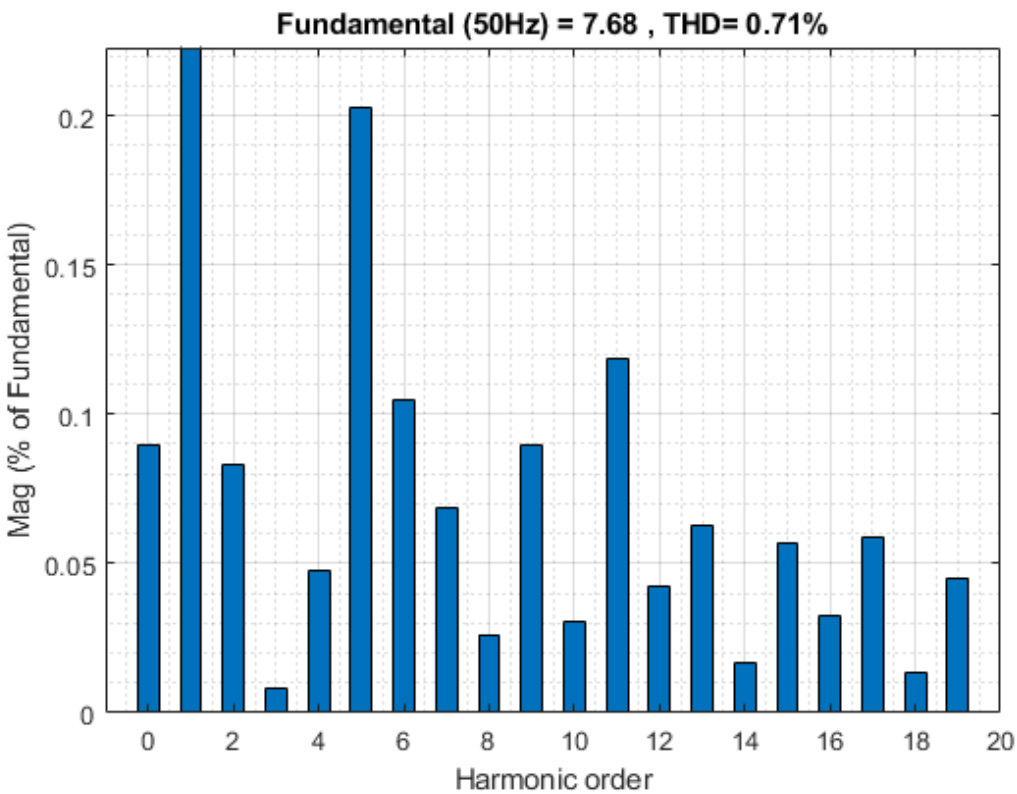

Figure 3.3.8–Harmonic order of the grid side current i_g (t)

The VSI operates in the bidirectional mode where power flows to and/or from the grid to regulate the grid voltage at the PCC. Figure 3.3.8 exhibits the THD_{ig} of the grid current (i_g) around 0.71% employing PR controller with HC and an allowable current ripple of 16% in the design of the inverter side inductance of the filter, L. The injected ripples in the grid current are less than the 5% following the IEEE-1547 (inverter operation) and IEEE-519 (rectifier operation) standards.

Furthermore, the inverter with a PR controller and LCL filter was implemented in a real-time simulator, which was connected to the real loads at a reduced voltage. Figure 3.3.9 shows the grid voltage (v_g), grid current (i_g), the current reference ($i_{g,ref}$) and the error between the $i_{g,ref}$ and i_g, which is taken from the real-time simulator.

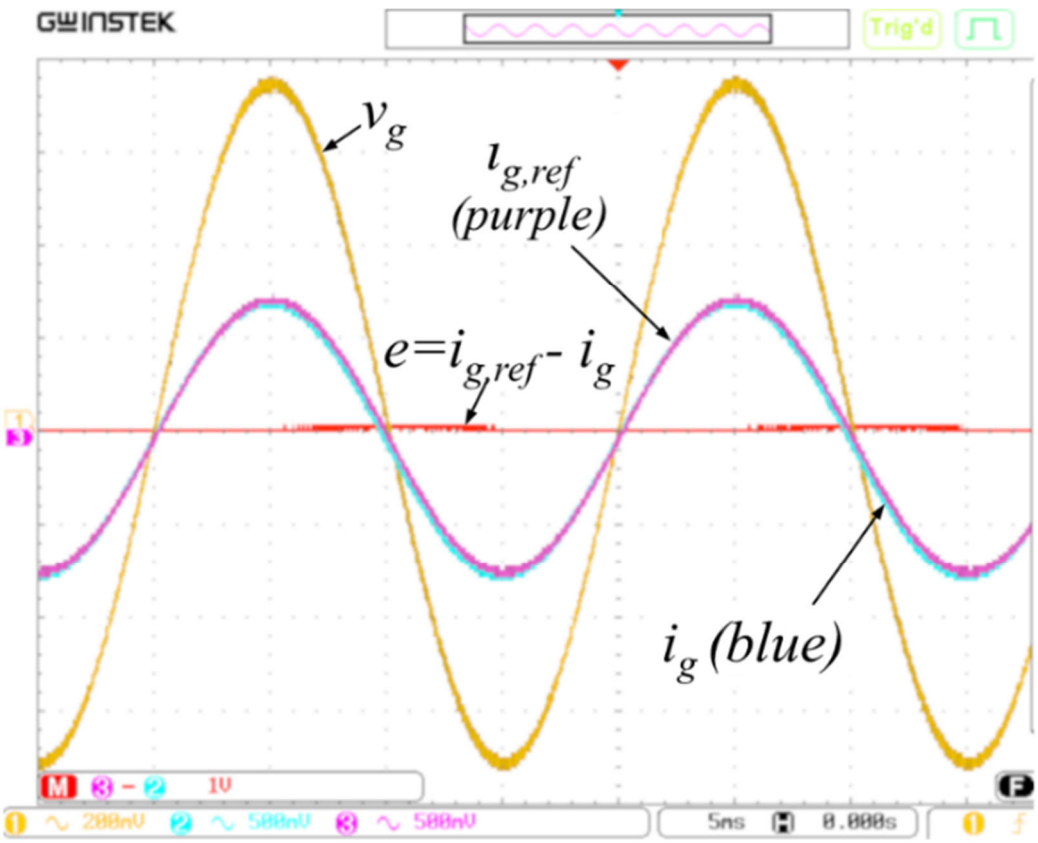

Figure 3.3.9–Single-phase grid-tied inverter with PR controller in real time simulator

In order to obtain the grid sinusoidal signal, a phase-locked loop (see Section 3.5) was implemented in the real-time simulator to extract the frequency, $\omega_g(t)$, phase angle,

$\theta_g(t)$, and the peak value of the grid voltage $\hat{V}_g$. In Figure 3.3.10 depicts the step change in the grid current (i_g) where the i_g becomes stable after three cycles. Note that as the inverter injects real power, i_g is in phase with the grid voltage (v_g). Figure 3.3.11 shows the Bode plot of the closed-loop system. The measurements were taken using a real-time simulator with a time step of 50 µs. It was connected to a signal generator in parallel with a small resistor emulating the grid. A small-variation was introduced in the current reference and the current output was measured. The gain and phase were obtained using the gain-phase meter HP 3575. Notice the *LCL* filter resonance frequency is at 6 kHz and the linear model coincides with the measurements with β=10. Figure 3.3.12 shows the experimental test bench with a real-time simulator.

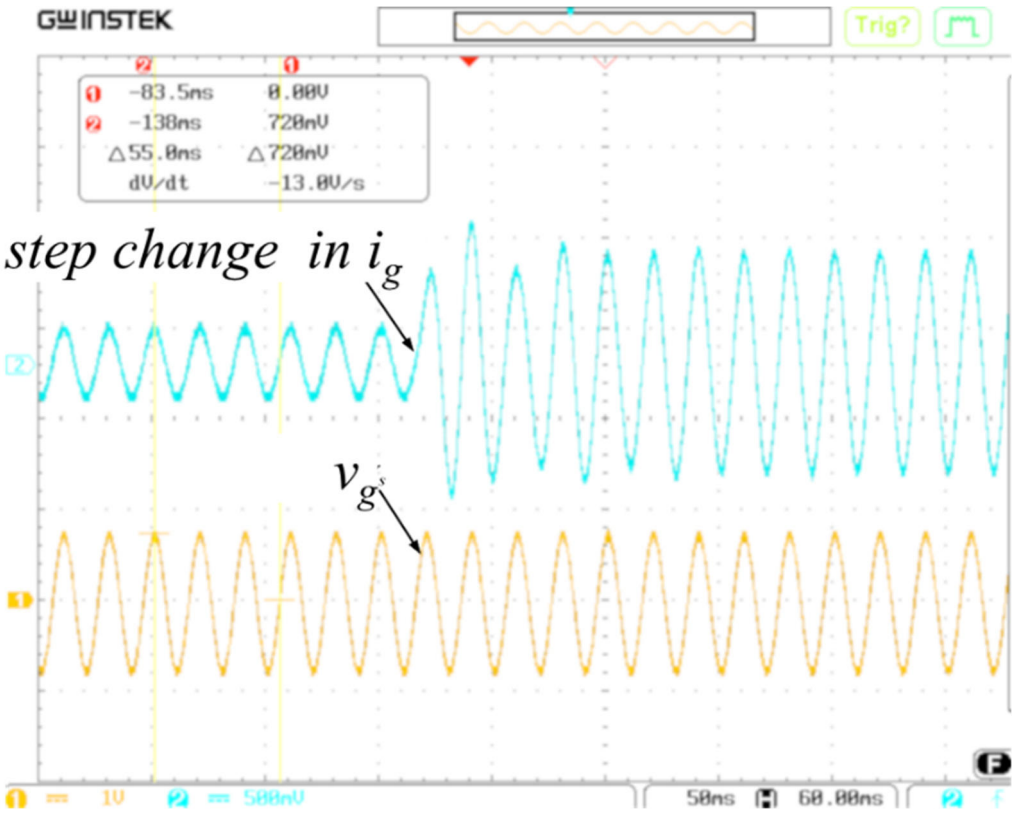

Figure 3.3.10–Transient response of the VSI in the PR controller with a step change in line current in real time simulator

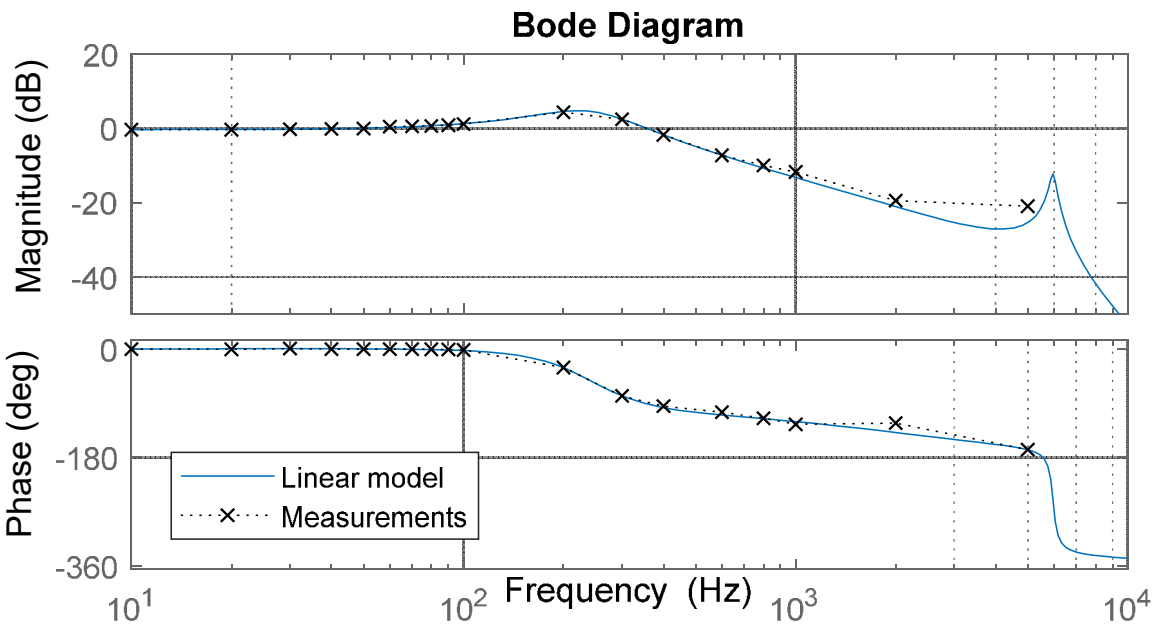

Figure 3.3.11–Closed loop plot of the system with the grid current feedback in the PR controller ($\beta=10$) in the real-time simulator

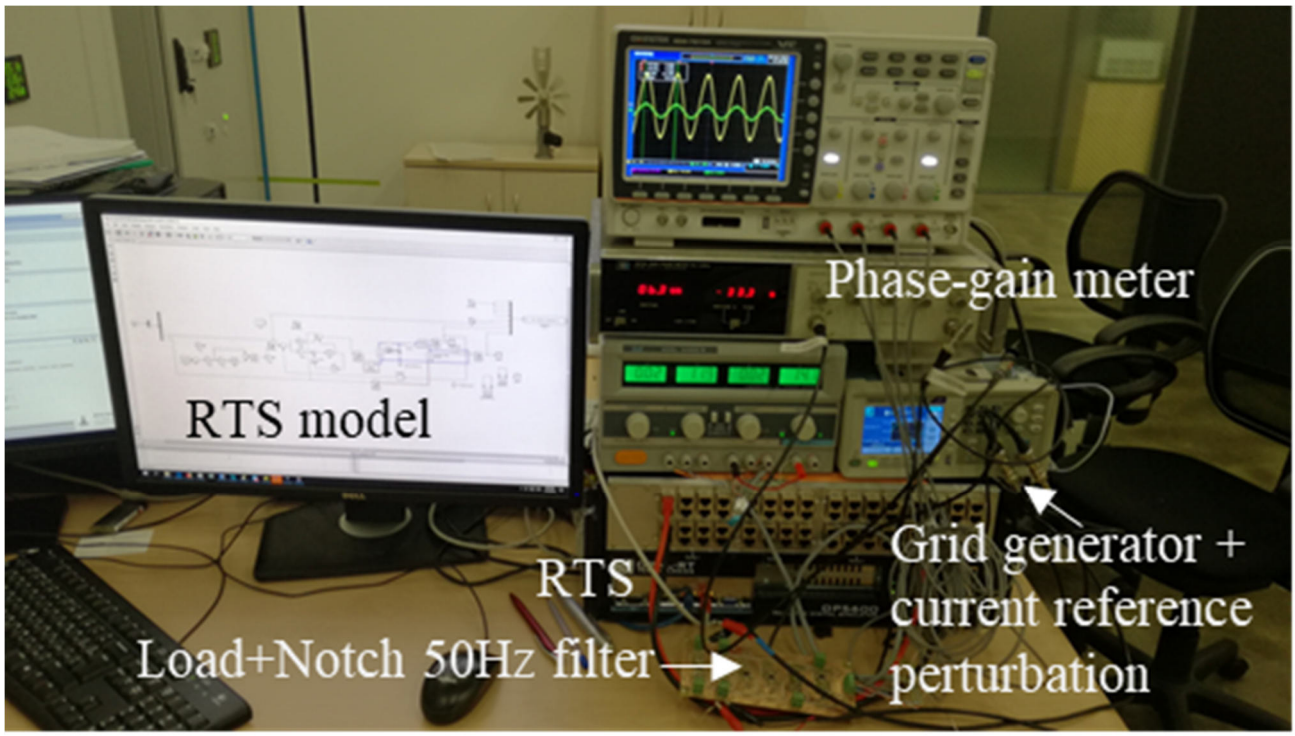

Figure 3.3.12–The experimental prototype of the system with real loads in the real-time simulator

3.3.7. Summary

In this section, the modeling in $\alpha\beta$-frame was used to design multi resonant controllers for grid connected inverters. These controllers can regulate the fundamental (grid) frequency and can also minimize the harmonic contents of the inverter's output current. A design procedure and control of the proportional-resonant (PR) controller with harmonic compensators, also called multi-resonant controller, in a single-phase bidirectional inverter with an output *LCL* filter was proposed. The *LCL* filter parameters were obtained by considering the stability margins of the resonance frequency to dampen the resonance of the filter and to mitigate the injected switching harmonic ripples to the grid. The PR controller parameters were tuned with the methodology suggested in Section 3.3.1. The control system is able to track a sinusoidal current with the desired phase margin.

Distortion analysis was performed and shown that the PR controller has low harmonic distortion due to its harmonic reduction method. Finally, the proposed model was implemented in the real-time simulator with the real connected loads to verify the proposal. The details of this section were published in [105].

3.4. Adaptive gains in control algorithm for grid-connected using alpha-beta frame and harmonic compensators

3.4.1. Description of the problem – Variable grid impedance

Section 3.3 explains the control of an inverter, in three-phase or single-phase using the αβ–frame. The model of the inverter was presented, a design methodology was developed and simulations in a computer and in a real-time simulator validated the propositions.

The design considered that the grid was an ideal voltage source. This works well in "strong grids" in which the inverter under analysis is small, in terms of power, in comparison to the grid nominal power, or the power of the main generators. However, in "weak" grids, the power of the inverter is relevant and the impedance of the grid is not so small to be neglected. In addition, the impedance of the grid changes according to the connected loads and generators. Thus, the grid impedance is variable. The design of the inverter relies on the inverter's filter impedance: $j\omega L_T = j\omega L_c + j\omega L$ and in general, $Z_{inv,filter}(\omega)$. However, if the grid impedance is relevant, the design must consider: $Z_{inv,filter}(\omega) + Z_{grid}(\omega)$, which changes in time and the controller design needs to be adapted to the current impedances. In [104], the author proposed a gain automatic control for keeping the inverter stable while the grid impedance changes.

Figure 3.4.1 shows an inverter controller using proportional multi-resonant controller, G_{PMR}. The G_{PMR} is the proportional multi-resonant controller (also called proportional resonant controller with harmonic compensation). The expression of the controller was shown in (3.3.14) in Section 3.3 and it is repeated here:

$$G_{PMR}(s) = \frac{v_i^*(s)}{e_\alpha(s)} = k_P + \frac{2k_I\omega_c s}{s^2 + 2s\omega_c + \omega_G{}^2} + \sum_{h=2}^{H} \frac{2k_{Ih}\omega_c s}{s^2 + 2s\omega_c + (h\omega_G)^2} \tag{3.4.1}$$

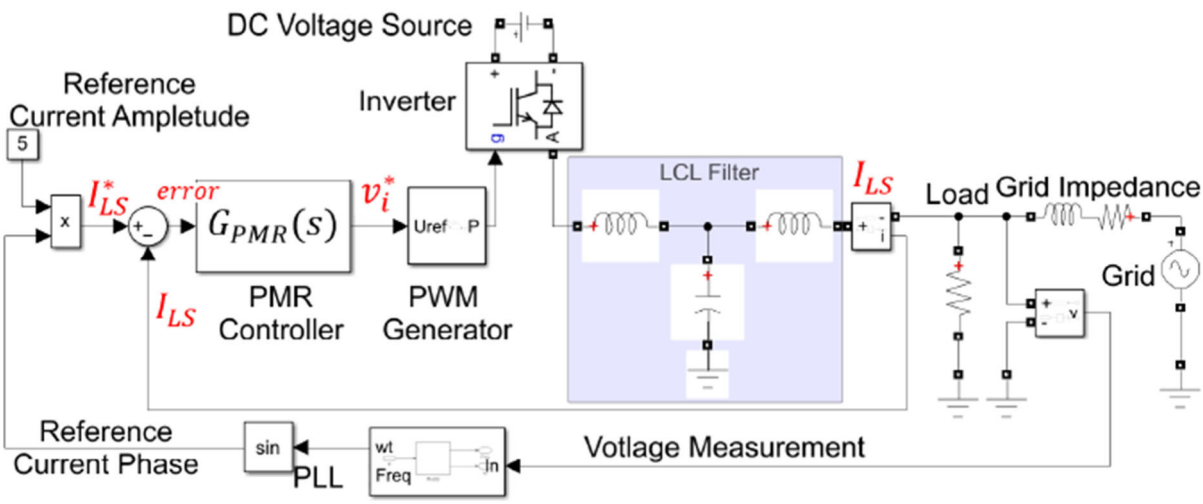

Figure 3.4.1–Basic diagram of the three-phase inverter with proportional resonant converter

Notice that the connection of the grid includes loads and line series impedances. The current equivalent grid impedance has to take into account all of the loads connected to the grid and this is why it is fluctuating.

After following the proposed procedure to select the gains of the controller in Section 3.3, a Bode plot was obtained using simulation with MATLAB/Simulink Linearization Tool. The results are shown in Figure 3.4.2(a). The phase margin decreases dramatically after a change in the grid impedance. Thus, all resonant gains have to decrease significantly for a worst-case scenario, achieving a phase margin increase from 5 to 24 degrees, and the system is stable again in Figure 3.4.2 (b).

This problem could be solved by using smaller resonant gain values from the very beginning for all cases. This example highlights the problem mentioned in [116], where the authors have used a design method based on the Naslin Polynomials and they prove that it does not guarantee the best solution for resonant harmonic gains of a PMR controller. This is a common design method for pre-calculating the resonant gains values and after that a manual tuning is performed. For the proposed automatic gain, the same approach has been used (precalculating the values using the Naslin polynomial method) and let the algorithm to select the proper values automatically in real time.

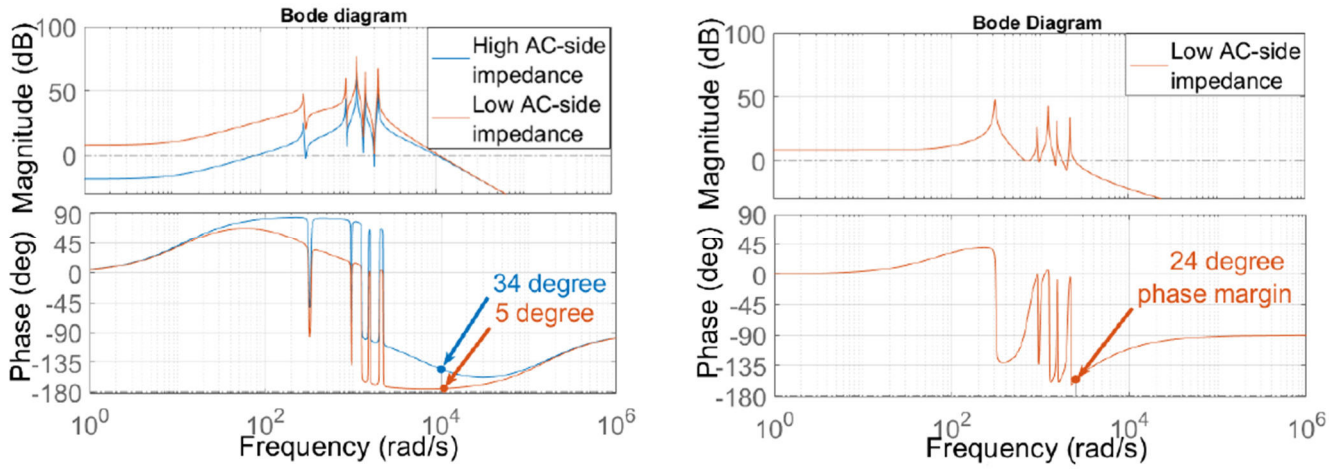

(a) (b)

Figure 3.4.2–Frequency response of PMR current-controlled converter (I_{LS}/error in Figure 4.1) with the impact of the grid impedance for high (6 Ω) and low (0.3 Ω) impedance: (a) using high resonant gains, (b) using reduced gains for a worse case

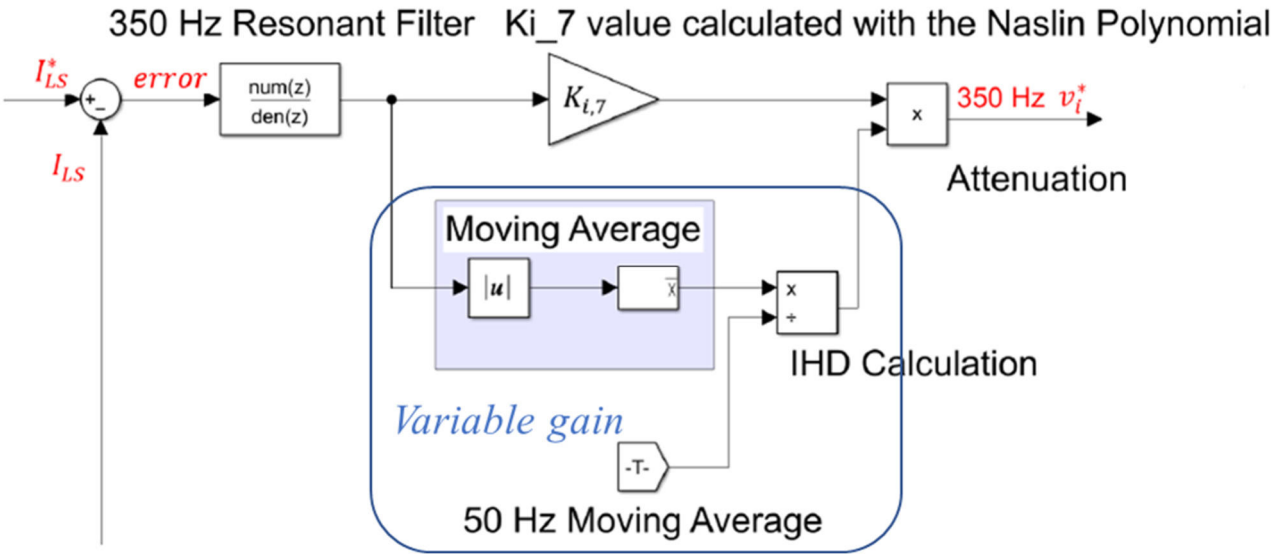

Figure 3.4.3–Proposed real-time attenuation algorithm

3.4.2. Proposed solution – Automatic gain selection

Instabilities caused by harmonic compensators are usually because the resonant gain values (k_I) that are too high for the current inverter-grid system [116, 117]. The proposed idea is to supplement the controller's resonant paths with an attenuation mechanism to prevent "overcompensation" on certain frequencies. This attenuation is possible with an additional variable gain ∈ [N_{min};1] where 0<N_{min}<1, placed after each k_{Ih} coefficient, as it is shown in Figure 3.4.3. These gains are being recalculated continuously by the microcontroller and they are proportional to the weights of the corresponding harmonics.

To calculate the weight of an individual harmonic, the absolute value of the resonant filter's output signal is averaged over a certain period, then normalized by the obtained value from the fundamental 50 Hz resonant path, and after that, this ratio is placed after the corresponding k_{Ih} coefficient. Thus, the compensator's k_{Ih} values decrease or increase following the decrease or increase of a corresponding harmonic's weight. Note that the new k_{Ih} value cannot be higher than the initial one, as a weight of a harmonic cannot be higher than 100%.

3.4.3. Simulation example – Automatic gain selection

The auto-adjusted system was simulated numerically in MATLAB/Simulink. The results are shown in Figure 3.4.4. At t=1s the compensator turns on, decreasing the corresponding harmonic and its own k_I value simultaneously, (i.e. it decreases its own impact on the system). k_I decreases until it reaches the value, when further decrease will increase the harmonic's weight (in Figure 3.4.4 it happens at t=1.25s), at this moment, the minimum value of k_I is reached, and this value is constant until the system (mainly the grid impedance) will be changed again. The averaging function is implemented on a microcontroller, which allows to keep a certain amount of data points for averaging (windows size).

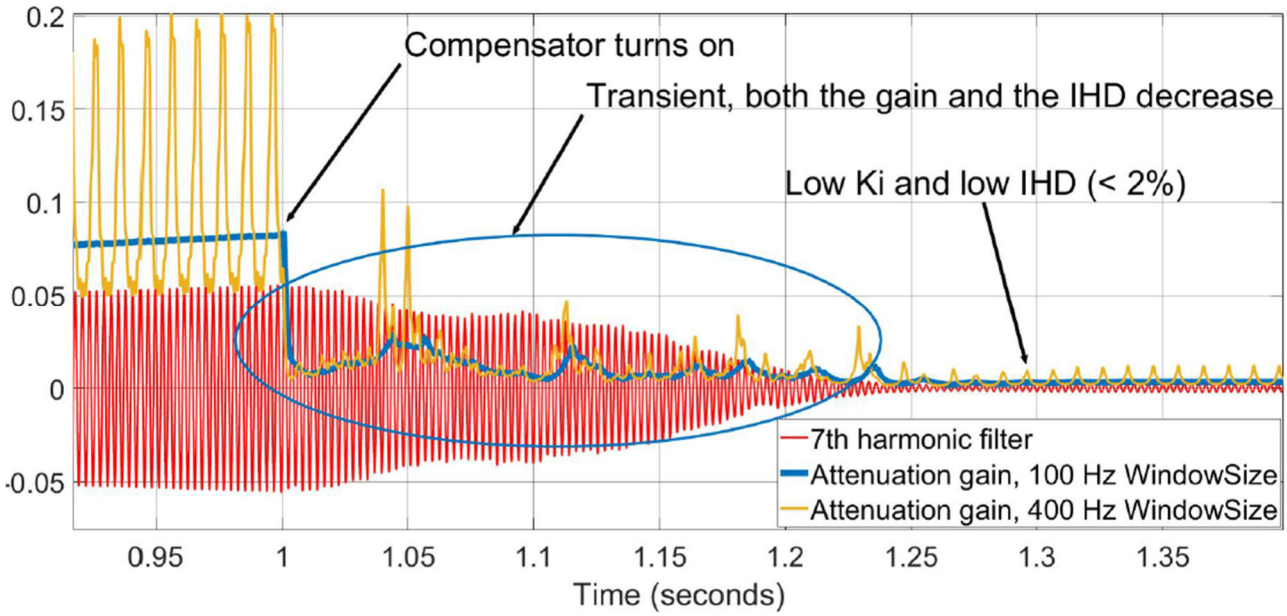

Figure 3.4.4–Evolution in time of a single harmonic gains (k_{Ih}) for h=7 following the proposed algorithm [104]. In red, G_{PMR} output of the 7th harmonic, in blue, filtered signal with 100Hz bandwidth and in yellow for 400Hz bandwidth

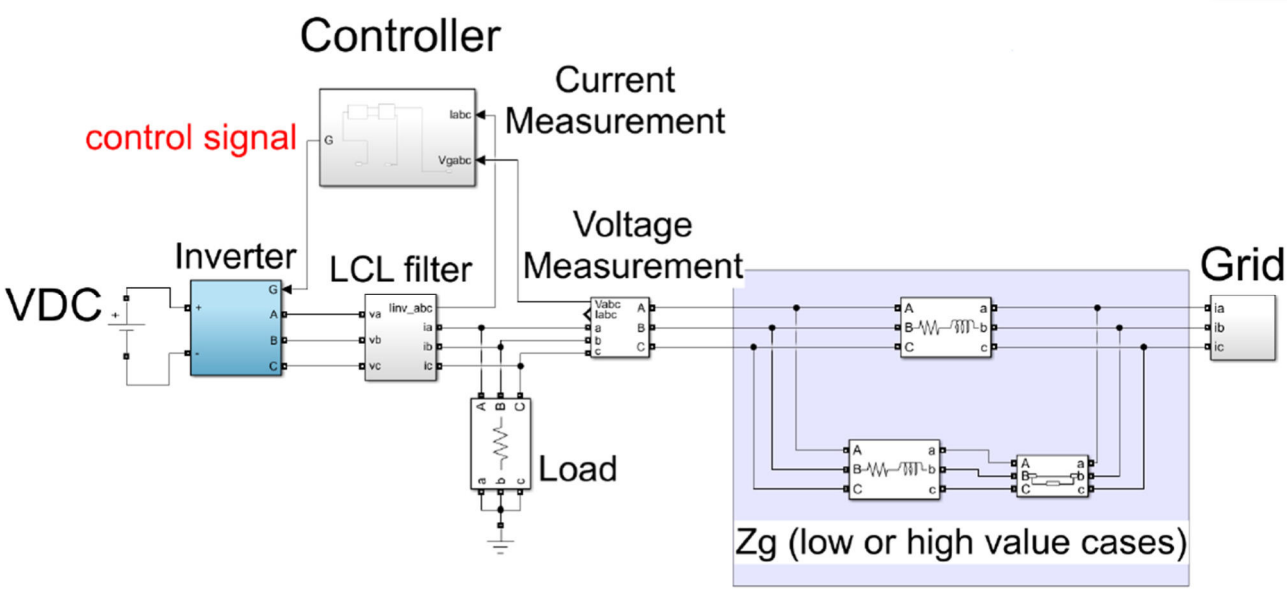

Figure 3.4.5–Simulation of a three-phase grid-connected inverted with the adaptive gain controller

The effect of different moving averaged filter bandwidth is presented in Figure 3.4.4. Low averaging leads to the appearance of spikes in the attenuation value that can cause additional harmonics. The selected filter has an average of 200 points, providing fast response. In the case of a 20 kHz digital system, a 200 points window corresponds to a bandwidth of about 100 Hz, which is the period of an absolute 50 Hz sine wave signal.

For the simulation test, the model in Figure 3.4.5 was created. It represents a system with grid-connected inverter, where energy from a DC voltage source is converted to a 50 Hz AC, synchronous to the grid voltage, with a three-phase grid-connected inverter. The inverter is controlled with a PMR controller. The AC-side impedance (Z_g) in this experiment changes instantly and big enough to highlight the advantages of the proposed auto-adjusted PMR controller over a static one. This change in Z_g can be understood as a generator disconnected near the inverter under test. The model corresponds to the experimental standards in terms of DC source voltage value, LCL filter parameters, grid voltage and frequency, and load values for the low-voltage grid. Model parameters are listed in Table 3.4.1.

Table 3.4.1 System and LCL Filter Parameters

Parameters	Values
Line-neutral (RMS) voltage, V_g	230 V
Inverter Side Inductance, L	1 mH
Inverter Side Resistance, R	100 mΩ
LCL Filter Capacity, C_f 2.25e-6 F	2.25 uF
Load Side Inductance, L_c	1 mH
Load Side Resistance, R_c	100 mΩ
High AC-side Impedance	6 Ω
Low AC-side Impedance	0.3 Ω
Load	400 Ω
VDC	680 V

The initial tuning was performed based on Naslin Polynomial Method. According to that, k_P and k_I values for the fundamental PR controller are calculated based on converter-side sum of the inductance ($L + L_c$), the converter side parasitic resistance (R), damping factor, signal frequency, and V_{DC}:

$$\alpha = \left(\frac{1}{{T_d}^2 {\omega_G}^2}\right)^{\frac{1}{5}} \quad \omega_0 = \frac{\omega_G}{\alpha^{\frac{1}{2}}}$$
$$\frac{k_P}{R} = \frac{T_r {\omega_0}^3 \alpha^{\frac{1}{2}}}{{\omega_G}^2} \quad and \quad \frac{k_I}{R} = \frac{k_P {\omega_G}^2}{2\omega_c} \tag{3.4.2}$$

For this example, using Naslin polynomial method:

$$k_P/R = 46dB$$
$$k_I R = 110dB$$

with a PM=56°. And using the methodology from subsection 3.3:

$$k_P/R = 55dB$$
$$k_I/R = 123dB$$

Using the Naslin Polynomial Method for tuning fundamental PR controller operating on 50 Hz is a mainstream approach, however, notice that the method is more

conservative in its gains that the proposal in Section 3.3 [105] and the stability in terms of the PM does not increase considerably.

In order to simulate a disturbed network, a 7th harmonic was added artificially on the grid side to the model; the inverter current harmonics of a such system are shown in Figure 3.4.6(a), when only the fundamental 50 Hz PR controller is used and, when an additional compensator is used for the 7th harmonic in Figure 3.4.6(b). Although successfully compensating the corresponding harmonic, additional high-gain resonant path diminishes the system's phase margin and robustness, as was shown in Figure 3.4.2. As a result, Figure 3.4.7(a) shows that the control algorithm is not capable for tracking the reference for a system with constant parameters at t=0.1s when the AC-side impedance (Z_g) changes from low to high value, and the system produces oscillations with the current constant k_{I7} gain value.

On the contrary, Figure 3.4.7(b) shows the superiority of the proposed auto adjusted control technique. After adding the proposed gains attenuation technique to the PMR controller's structure, the system adapts its control loops against changes in the AC-side impedance, although still capable of compensating the harmonics, as can be seen in Figure 3.4.7(b). The stability region of the system is extended and now the same change in the AC side that happened in Figure 3.4.7(a) does not cause oscillations.

The main advantage is that the resonant gains were not just reduced using the trial and error method, which is very common solution for PMR controllers tuning, but were adjusted automatically in real-time according to grid conditions.

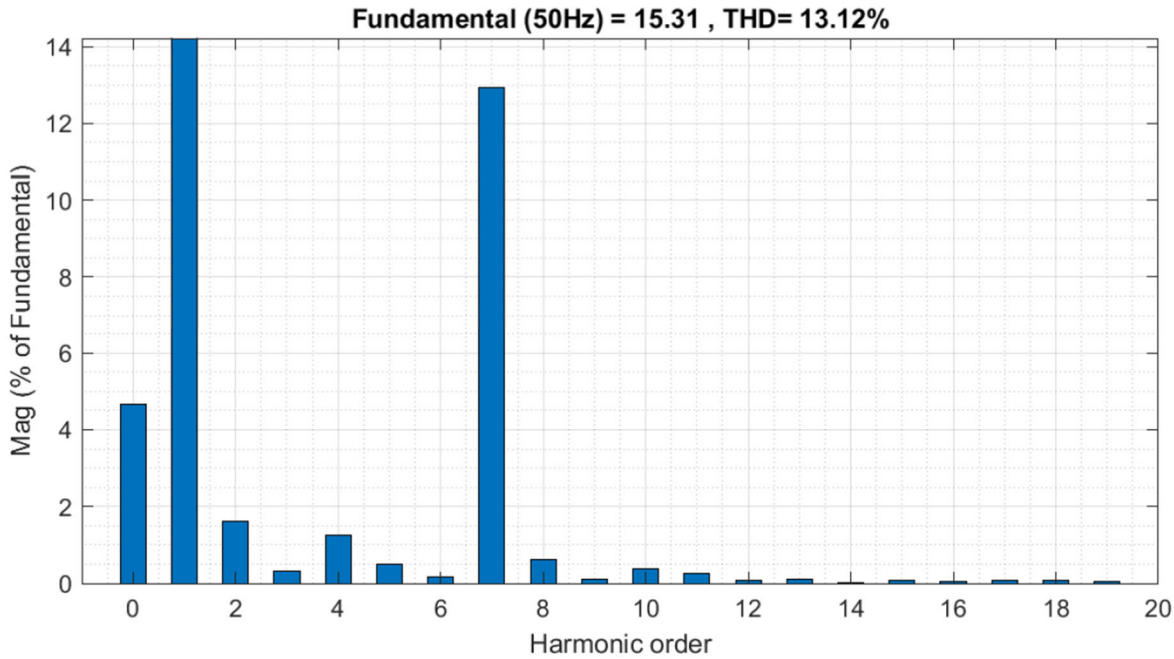

(a)

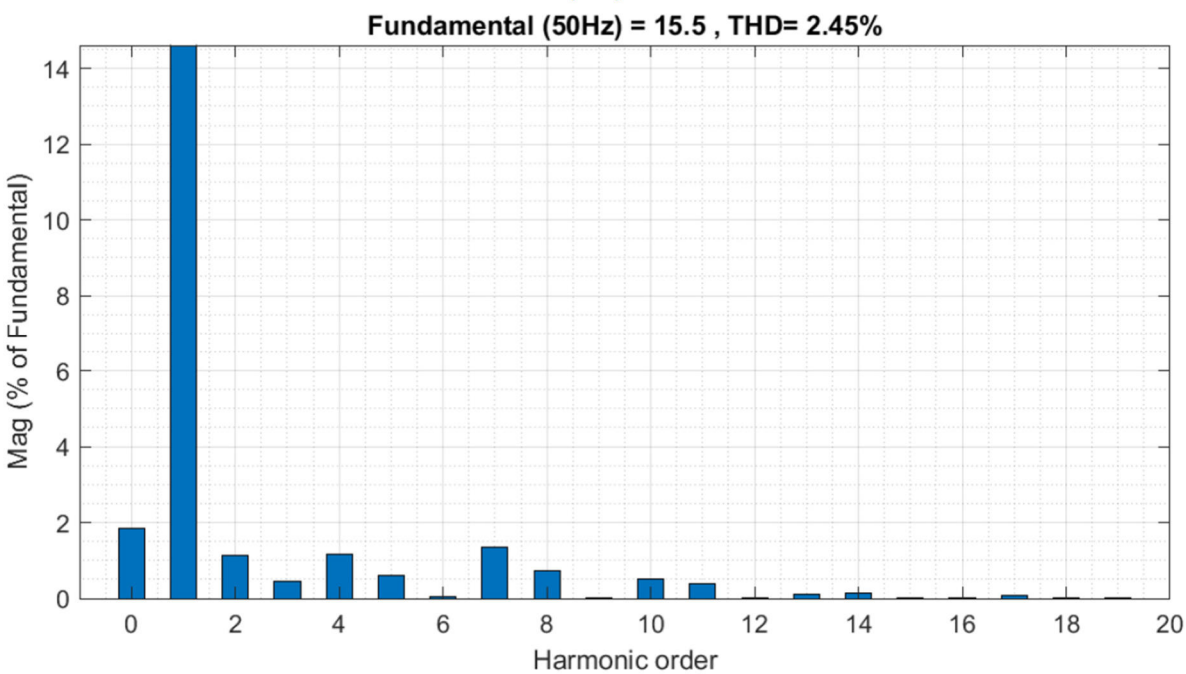

(b)

Figure 3.4.6–Harmonics of the injected current: (a) using only fundamental PR controller, (b) adding harmonic compensator

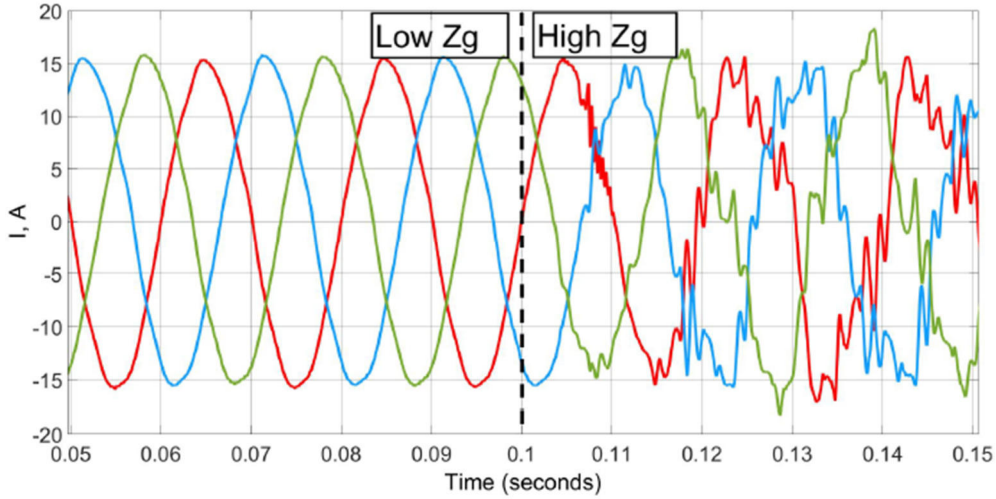

(a)

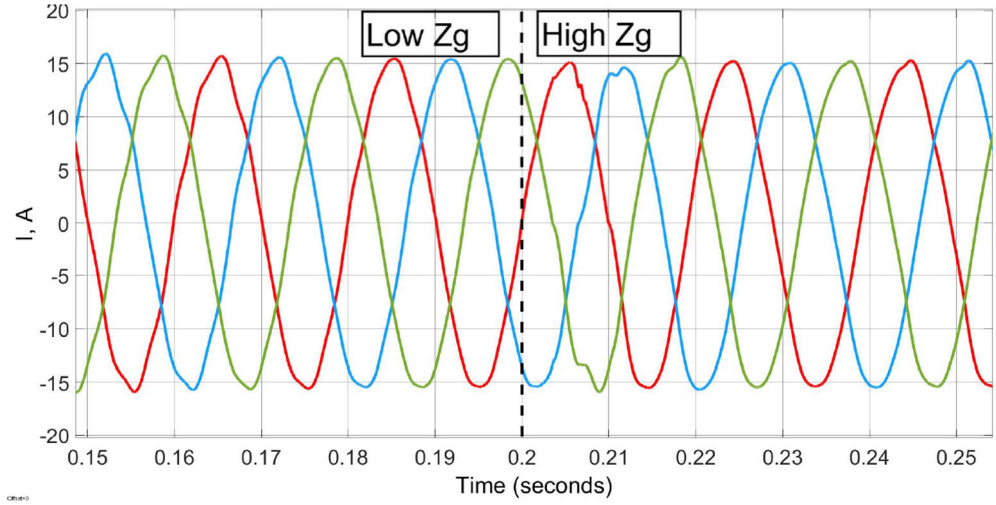

(b)

Figure 3.4.7–Simulation with (a) static-gains control, (b) the proposed auto-adjusted technique

3.4.4. Experimental validation – Automatic gain selection

The proposed control strategy was tested on a laboratory 5kW three-phase inverter, see Figure 3.4.8. The system corresponds to the simulation model described in Figure 3.4.5 and Table 3.4.1. The control strategy has been implemented on a TMS320F28379D microcontroller platform in c-code. Figure 3.4.9 shows the inverter current in one of the phases, for two conditions: high and low AC-side impedance, with the static and real-time adjusted gains. A non-linear load was used to supplement the system with harmonics

in order to see how the compensation method works using the traditional approach with static gains and with the proposed one with auto-adjustable gains.

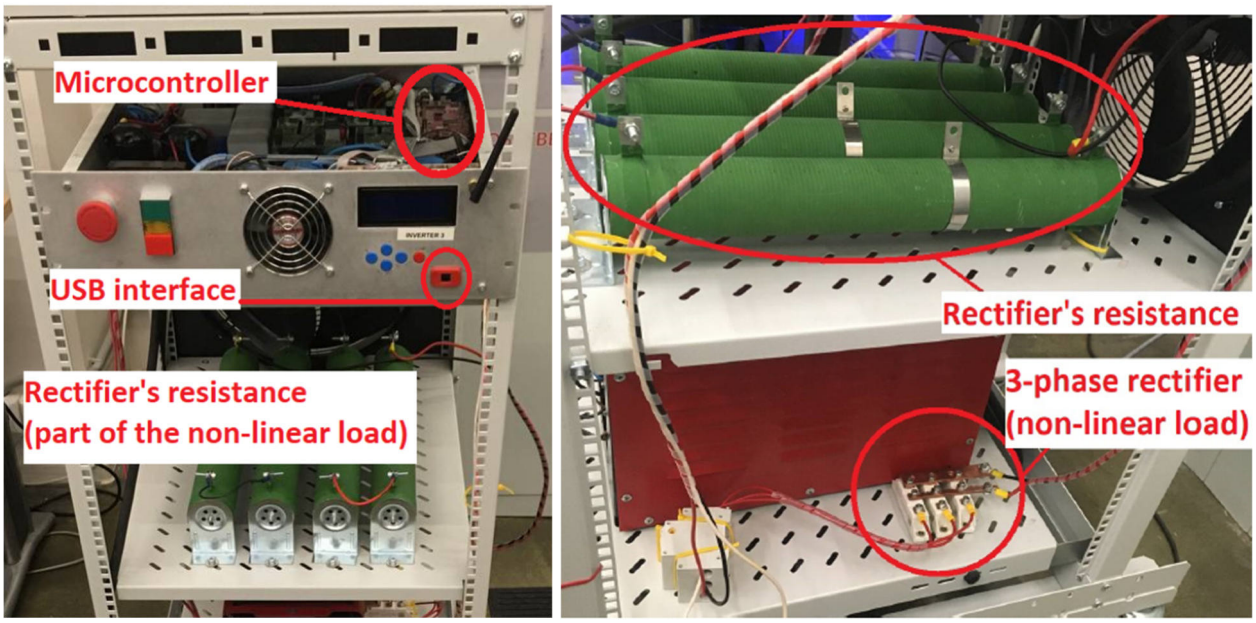

(a) (b)

Figure 3.4.8–Experimental setup: (a) front view, three-phase inverter, (b) side view. Rectifier as a non-linear load

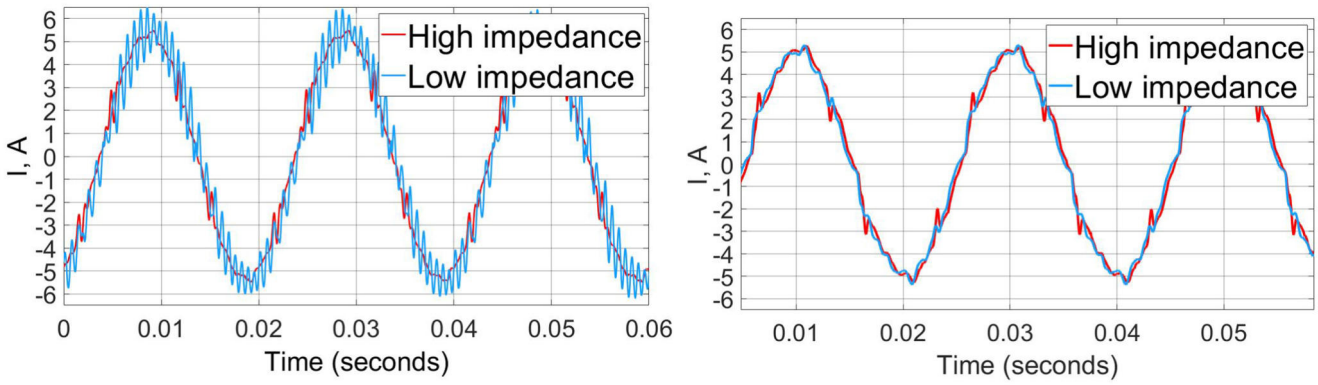

(a) (b)

Figure 3.4.9–Injected current, phase A, using: (a) static-gains control, (b) auto-adjusted control

A comparison of these two approaches is presented in Figure 3.4.9, where the AC-side impedance was changed between the tests. Note that although it is possible to retune the static-gains system to operate properly with the new AC-side impedance, in this test, it is compared the ability of the two methods to operate within different environments

without additional external retuning. It is seen from Figure 3.4.9 that the static-gains approach does not provide the system the robustness to AC-side impedance variations, operating much worse in an environment it was not tuned to operate in. On the contrary, the proposed technique is capable of operating in a variable environment.

3.4.5. Summary

In this section, a new control strategy based on proportional a multi resonant controller has been modelled, simulated numerically and implemented in c-code in a microcontroller which controls a 5kW three-phase bidirectional voltage source inverter.

The proposed technique simultaneously simplifies the common tuning procedure of a multi resonant controller and improves inverter robustness. Unlike most of the previous works, where analytically obtained multi resonant gain values are used just starting points for further manual tuning, this work avoids manual tuning at any stage. The proposed auto-adjustment of gains of the multi resonant controller allows a grid-connected inverter to be connected with different grid impedances. Compared to other tuning methods including particle swarm optimization or MATLAB SISO tool, the proposed technique does not require many computational resources and can be implemented on a microcontroller for real-time system adjustment in each iteration, making the system auto-adjustable for fast changing grid conditions.

The proposed technique does not guarantee finding the global harmonic minimum and can be improved. In this section, the case of controlling the output current of the inverter was examined. However, the proposed technique is not limited to this, and other applications such as load current control or voltage control are also possible and will be analyzed in the future. The details of this section were published in [104].

3.5. Control algorithm for grid-connected inverter using dq-frame

3.5.1. Main differences between αβ-frame and dq-frame control methods

In Section 3.3 and 3.4, algorithms for controlling inverters were discussed. Particularly, for controlling the currents in the AC port. In those sections, the control methods were developed in $\alpha\beta$ frame, thus, in order to have a minimal error between the reference and the output currents, proportional-resonant controllers were discussed. In this section, dq-frame will be discussed. Dq-frame methods shift the frequencies to be controlled to DC so resonant controllers become proportional-integral (PI) controllers which can perfectly track DC signals, so the error is zero. However, for that, the dq-frame must be perfectly synchronized with the grid. Therefore, on one hand the current control loops are simplify by using PI controllers but on the other hand, it requires a synchronization unit and, as it was discussed in Section 3.2, new coupling elements appear between d and q components (see 3.2.29).

This section reviews the techniques of synchronization, and the current control method in dq-frame. It put emphasis in the modeling of the phase-locked loop (PLL) as a synchronization unit. It shows the effects of a mismatch between the grid phase and the PLL particularly due to the influence of the line impedance. In addition, the section suggests the negative feedback PLL (NFPLL) as an alternative to the traditional one [28]. The modeling of a non-perfect PLL behavior is the main contribution of this section and it is reflected in [118].

3.5.2. Synchronization methods

There are many methods for synchronizing the dq-frame with the grid signal such as zero crossing detection (ZCD) [119], Kalman Filter [120], discrete Fourier transform

(DFT) [121], nonlinear least square (NLS) [122], adaptive notch filtering (ANF) [123], artificial intelligence (AI) [124], delayed signal cancellation (DSC) [125], phase locked loop (PLL) [126], and frequency locked loop (FLL) [127]. These methods can be classified in different categories: open-loop, closed-loop, frequency domain or time-domain, for single-phase or multi-phase systems. Figure 3.5.1 shows the main classification [128].

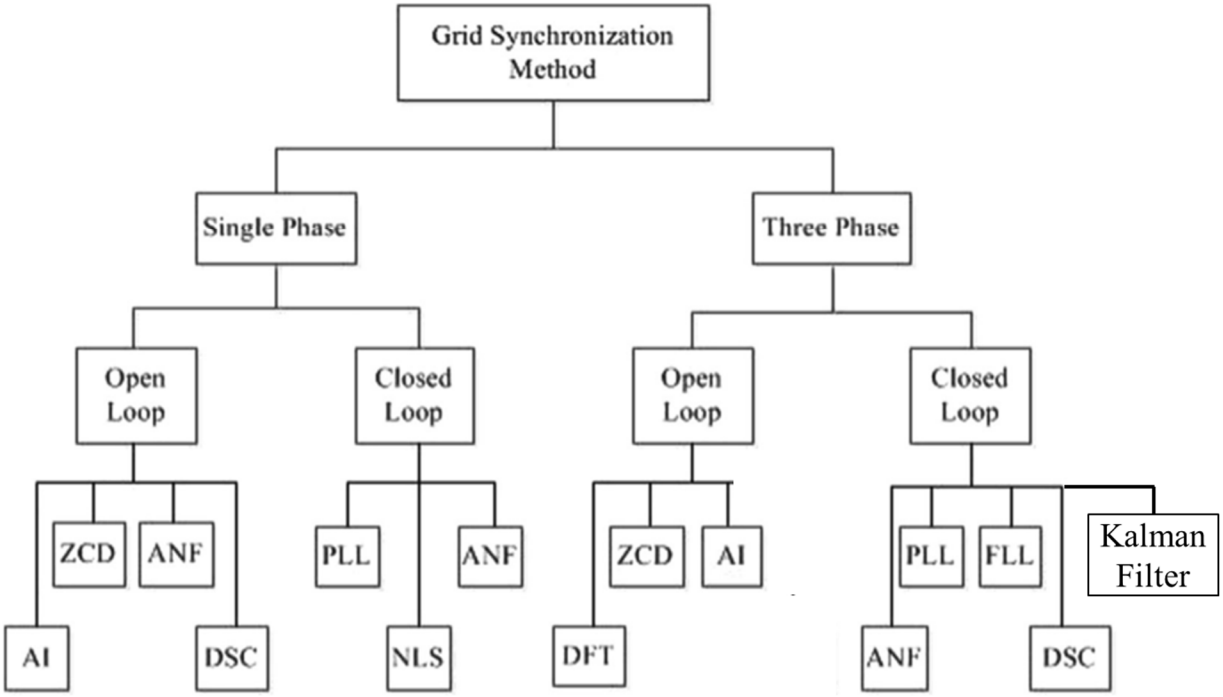

Figure 3.5.1– Overview of grid synchronization methods [128]

A comparison of the different synchronization methods was given in [128], Table 3.5.1 is a summary table.

Table 3.5.1 Comparison with different synchronization methods [117]

Method	Advantages	Disadvantages
Zero crossing detection	Simplest implementation Robust under frequency variations	Poor performance under grid voltage variation such as harmonics or notches Sensitive to transient and noise
Kalman filter	Accurate under frequency variations	Difficulty in covariance selection Computational burden

Continuation of the Table 3.5.1

Discrete Fourier transform	Stable and accurate even in the presence of noise Noise immunity Suitable for very distorted environments that require good filtering characteristics	Not able to cope with unbalanced conditions Produce phase shift when the DFT sampling is asynchronous with power grid
Nonlinear least-square	Easy to implement Low computational burden	Long transient time intervals in detecting frequency changes
Adaptive notch filter	Simple implementation Transient response is faster than PLL-based Can also detect symmetrical components, harmonics, active power and reactive power	The adaptation process is inevitably slow
Artificial intelligence	High computational speed	Neural network complexity is proportional with harmonic component
Delayed signal cancellation	High convergence rate Stable	Insensitive to small frequency variations
Phase-locked loop	Simple implementation Accurate synchronization	Might have negative impact on the performance of VSC-HVDC in weak ac system During asymmetrical voltage faults, 2nd harmonic produced by negative sequence will propagate through PLL system and will be reflected in the θ'
Frequency-locked Loop	Better rejection of grid harmonics & notches Most sophisticated and reliable under frequency variations, voltage unbalance and harmonics	Introduce double frequency oscillation to the phase error signal High computational burden

Among the methods presented here, the most popular is the phase-locked loop (PLL) due to its simplicity, effectiveness and robustness in various grid conditions. The author has explored modifications of the synchronous PLL, using a negative-feedback loop which increases the bandwidth of the standard PLL [28] which was used in shunt active power filters to minimize the total harmonic distortion of the grid currents. The following section will explain details on the PLL modeling.

3.5.3. Modeling of a phase-locked loop (PLL)

Figure 3.5.2 shows a synchronous PLL structure which comprises three main blocks: a phase detector, a controller and an integrator. The phase detector is performed by using an abc-to-dq transformation, the controller is a combination of a Notch filter, lead compensators and an integrator to produce the obtain the grid frequency. Finally, the last integrator produces the PLL angle which is compared with the grid angle closing the loop. In order to have a zero error in the control loop, two poles at the origin are needed, or in other words, a double integrator.

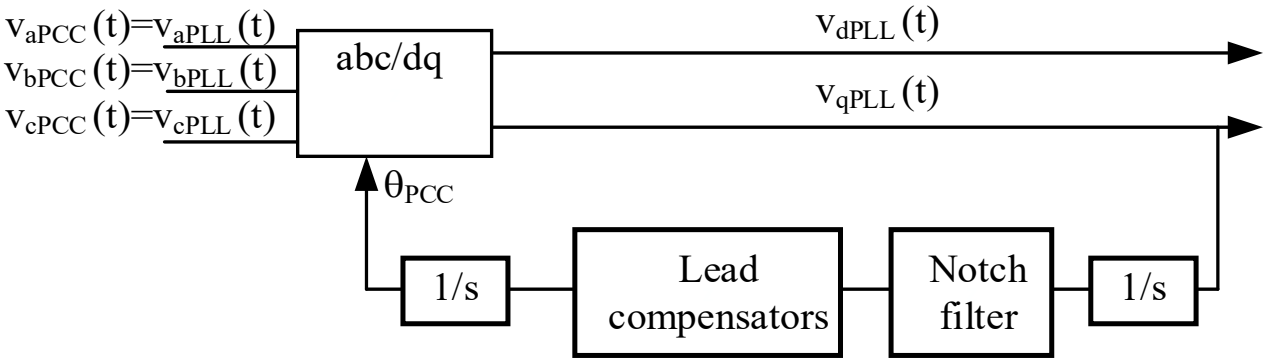

Figure 3.5.2–Diagram of a synchronous reference phase-locked loop [118]

In the normal operation, the abc-to-dq transformation block, which is the combination of (3.2.18) and (3.2.23) transforms the three-phase grid voltages to dq-components in the reference plane given by $\theta_{PLL}(t)$.

The grid voltages are: $v_{PCC\,a}(t), v_{PCC\,b}(t), v_{PCC\,c}(t)$. In general, they can be not equal so the space phasor can be represented as:

$$\underline{v_{PCC}}(t) = \overline{v_{PCC}}e^{j\omega_g t} + \overline{v_{PCC\,n}}e^{-j\omega_g t} + \sum \overline{v_{PCC\,h}}e^{jh\omega_g t} \tag{3.5.1}$$

where the phasor includes: the main positive sequence, a negative sequence component due to unbalanced grid and harmonics. Applying this phasor to the dq-transformation, we have:

$$\underline{v_{PCC}}(t) = \overline{v_{PCC}}e^{j\omega_g t}e^{-j\theta_{PLL}(t)} + \overline{v_{PCC\,n}}e^{-j\omega_g t}e^{-j\theta_{PLL}(t)} + \sum \overline{v_{PCC\,h}}e^{jh\omega_g t}e^{-j\theta_{PLL}(t)} \tag{3.5.2}$$

Thus, it can be seen that, in the case when the PLL is tracking the grid phase, the first term will be constant but the second will be a complex exponential of twice the grid frequency, and the harmonics will go down by one. Considering that the harmonics can be filtered by a low-pass filter at high frequencies, still the double grid frequency signal will perturb the behavior of the PLL. Thus, a common practice is to use a notch filter which cancels at the double of the grid frequency (100Hz).

The dq-values of the space phasor are:

$$\begin{aligned} v_{PCC\,d}(t) = {} & |v_{PCC}|cos[\omega_g t - \theta_{PLL}(t)] \\ & + |v_{PCC\,n}|cos[\omega_g t + \theta_{PLL}(t) + \theta_n] \\ & + \sum |v_{PCC\,h}|cos[h\omega_g t + \theta_h - \theta_{PLL}(t)] \end{aligned} \tag{3.5.3.a}$$

$$\begin{aligned} v_{PCC\,q}(t) = {} & |v_{PCC}|sin[\omega_g t - \theta_{PLL}(t)] \\ & + |v_{PCC\,n}|sin[\omega_g t - \theta_{PLL}(t) + \theta_n] \\ & + \sum |v_{PCC\,h}|sin[h\omega_g t - \theta_{PLL}(t) + \theta_h] \end{aligned} \tag{3.5.3.b}$$

Notice that the $v_{PCC\,q}(t)$ component has the $sin[\omega t - \theta_{PLL}(t)]$ which, when the argument is small: $\sin(x) \approx x$. Thus, this is a good angle comparator. The $v_{PCC\,q}(t)$ can be used as the error signal between the grid angle and $\theta_{PLL}(t)$. Then, a controller which

keeps the loop stable and has a second order integrator can be implemented using control methods in frequency response. Usually, a lead compensator is used to increase the phase margin of the loop in addition to the Notch filter and the integrator [24]. The open-loop transfer function is:

$$G_{OL} = k_{OL} \frac{s^2 + (2\omega_g)^2}{s^2(s + 2\omega_g)^2} \left(\frac{\frac{s}{\omega_C} + 1}{\frac{s}{\omega_C \alpha} + 1} \right)^2 \tag{3.5.4}$$

This transfer function can satisfy the phase margin for the stability design and can ensure the tracking of the phase as the theorem of the final value suggests. The error between the grid phase and θ_{PLL} is:

$$\theta_g - \theta_{PLL}(s) = \frac{1}{1 + G_{OL}} \theta_g(s) = \frac{1}{1 + G_{OL}} \frac{\Delta\theta}{s^2} \tag{3.5.5}$$

The theorem of the final value indicates that the error in steady-state is:

$$\lim_{t \to \infty} \theta_g(t) - \theta_{PLL}(t) = \lim_{s \to 0} \left[\theta_g(s) - \theta_{PLL}(s) \right] s = \lim_{s \to 0} \frac{s}{1 + G_{OL}} \frac{\Delta\theta}{s^2} = 0 \tag{3.5.6}$$

Thus, the PLL tracks the grid. As an example, Figure 3.5.3 shows the frequency response (Bode plot) of the open-loop gain in a PLL. Notice the Notch filter at 2π100Hz and the slope of -40dB/dec of the 2nd order integrator. In Figure 3.5.4, the closed-loop is shown,

Finally, in Figure 3.5.5, a time-domain simulation, considered a distorted grid with 5% of negative sequence and 3% of the 5th harmonics is presented. The frequency is tracked at 50Hz and the phase has low distortion despite the harmonics.

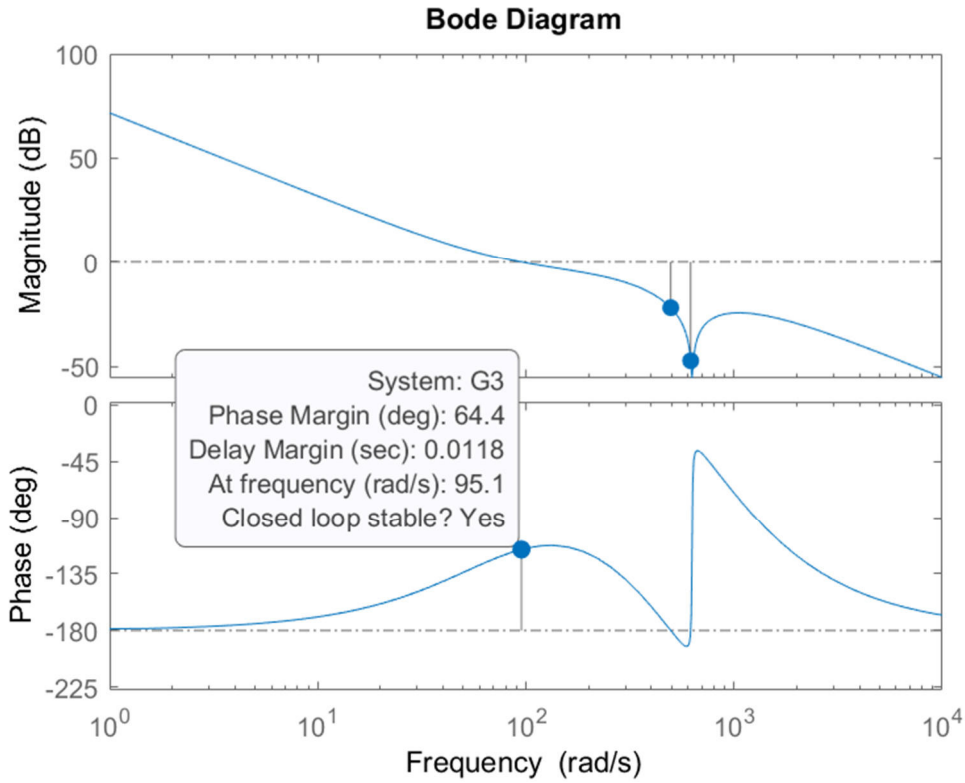

Figure 3.5.3–Example of a PLL open-loop gain

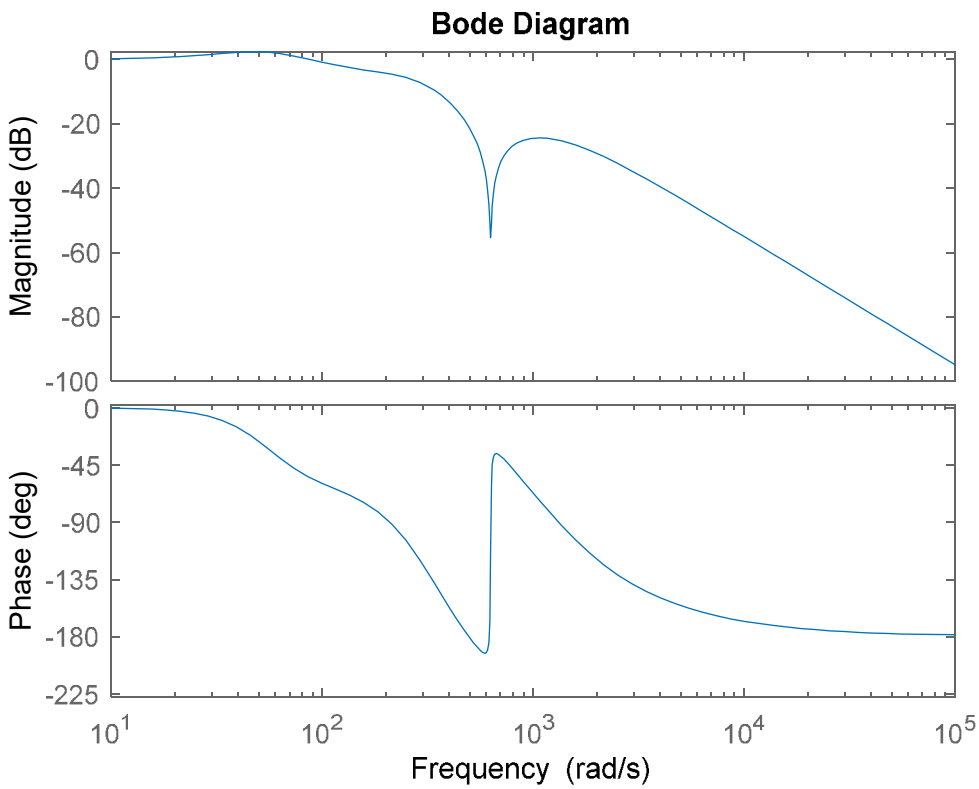

Figure 3.5.4–Example of a PLL closed-loop gain

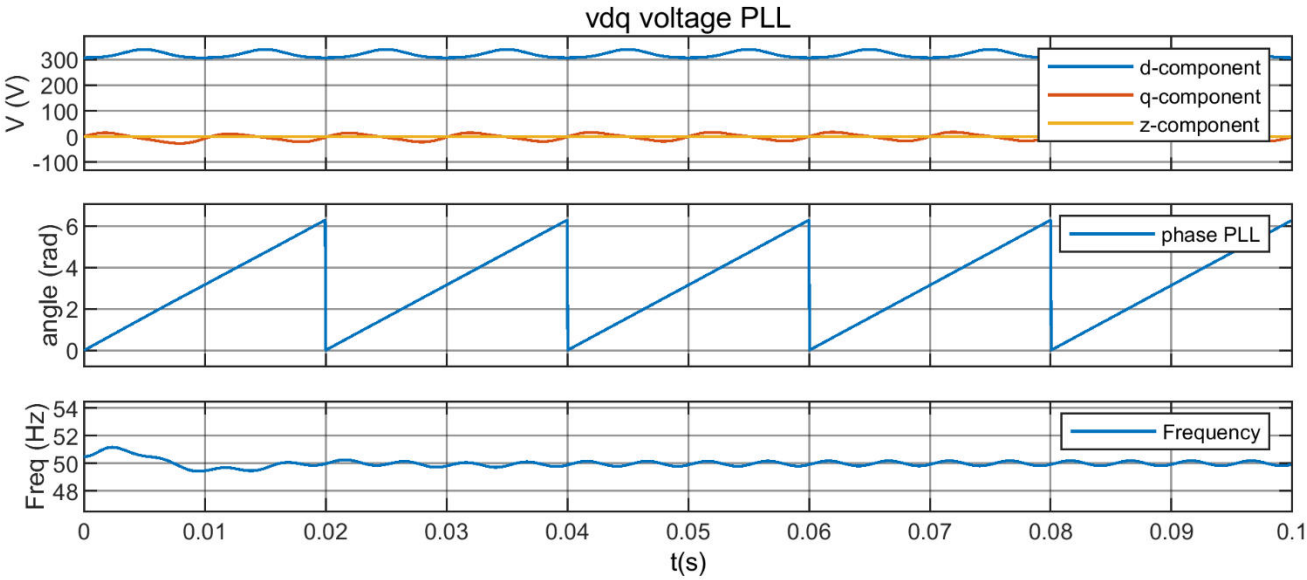

Figure 3.5.5–Example of a PLL. Time-domain response under a distorted grid. The PLL is able to keep the tracking

3.5.4. Modeling of a PLL: impact of the line impedance

The PLL transfer function can be altered due to the impact of the line impedance. Considering Figure 3.5.6, the PLL measures the grid voltage through the line impedance. Therefore, the PLL input voltage rotating phasor voltage in a balance system is:

$$\underline{v_{PCC}}(t)e^{j\theta_g(t)} = \overline{v_g}(t)e^{j\theta_g(t)} + r.\overline{i_g}(t)e^{j\theta_g(t)} + j\omega_g L.\overline{i_g}(t)e^{j\theta_g(t)} + \frac{d\overline{i_g}(t)}{dt}e^{j\theta_g(t)}, \quad (3.5.7.a)$$

$$\underline{v_{PCC}}(t)e^{j\theta_g(t)} = \overline{v_g}(t)e^{j\theta_g(t)} + r.\overline{i_{inv}}(t)e^{j\theta_g(t)} + j\omega_g L.\overline{i_{inv}}(t)e^{j\theta_g(t)} + \frac{d\overline{i_{inv}}(t)}{dt}e^{j\theta_g(t)}, \quad (3.5.7.b)$$

$$\overline{i_{inv}}(t) = I_{inv\,d} + jI_{inv\,q}. \quad (3.5.7.c)$$

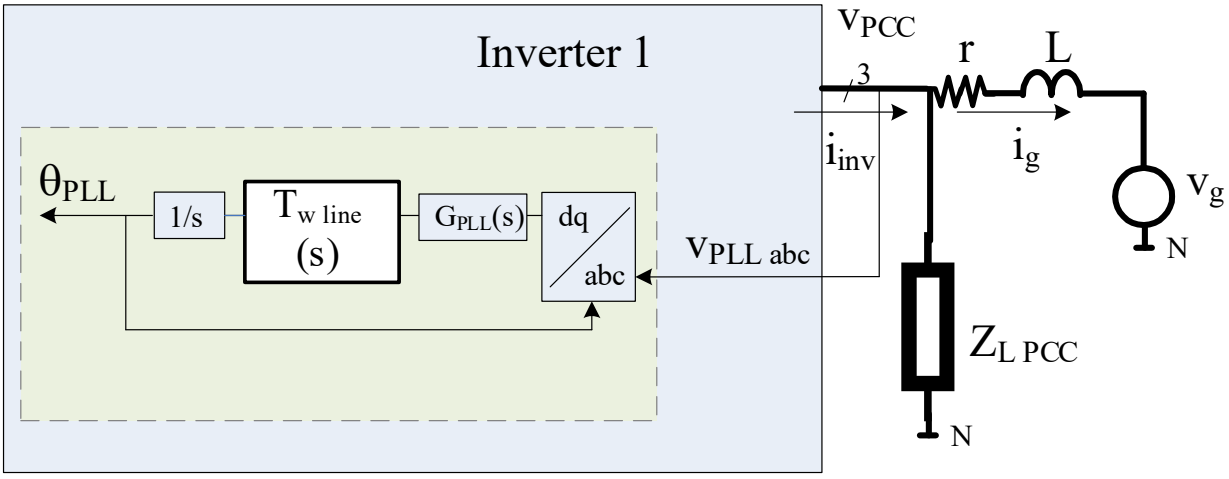

Figure 3.5.6. Diagram of a synchronous reference phase-locked loop [118]

Considering that the phasor grid amplitude $v_g(t) = V_g$ and the output phasor amplitude current can be expressed as a constant current plus a small-signal perturbation: $\bar{\imath_g}(t) = I_{g\,d} + jI_{g\,q} + \tilde{\imath}_{g\,d} + j\tilde{\imath}_{g\,q}$, the PLL, input voltage phasor, in Figure 3.5.2, is:

$$v_{PCCd} + jv_{PCCq} = \left[V_g + r.\bar{\imath_g} + j\omega_g L.\bar{\imath_g}(t) + \frac{d\bar{\imath_g}(t)}{dt}\right] e^{j[\theta_g(t) - \theta_{PLL}(t)]}. \tag{3.5.8}$$

For small angle difference $\theta_g(t) - \theta_{inv}(t)$, the imaginary part (q) tends to zero, so it is a good error detector:

$$\begin{aligned} v_{PLLd} + jv_{PLLq} &\approx \left(V_g + r\bar{\imath_g}(t) + j\omega_g L.\bar{\imath_g}(t) + \frac{d\bar{\imath_g}(t)}{dt}\right)(1 \\ &+ j[\theta_g - \theta_{inv}]), \end{aligned} \tag{3.5.9}$$

so

$$\begin{aligned} \tilde{v}_{PLL\,q} \approx [\theta_g - \theta_{PLL}]\left(V_g + r.I_{g\,d} - \omega_g L.I_{g\,q} + L\frac{d\tilde{\imath}_{g\,d}}{dt}\right) \\ + \left(r.\tilde{\imath}_{g\,q} + \omega_g L.\tilde{\imath}_{g\,d} + L\frac{d\tilde{\imath}_{g\,q}}{dt}\right). \end{aligned} \tag{3.5.10}$$

Thus, the impacts in the phase detector due to the current in the transmission lines are: gain modulation and adding phase. When this current is not present, the gain in the phase detector is V_g and when the current is present: $\left(V_g + r.I_{g\,d} - \omega_g L.I_{g\,q} + L\frac{d.\tilde{\imath}_{g\,d}}{dt}\right)$.

In addition, a new term appears which adds some phase due to the current flowing: $\left(r.\tilde{\imath}_{g\,q} + \omega_g L.\tilde{\imath}_{g\,d} + L\frac{d\tilde{\imath}_{g\,q}}{dt}\right)$.

If we now considered that $\overline{\imath_{inv}}(t) = \overline{\imath_g}(t)$, or in other words, if the only current to the grid is the inverter current. An impact in the PLL will occur due to the inverter current and Z_g. The variation of the current in the dq frame as a function of the phase error can be considered as, based on the control loop of Figure 3.5.6:

$$\tilde{\imath}_{inv\,d} = \frac{I_{inv\,q}[\theta_g - \theta_{PLL}]}{s\tau_C + 1} \text{ and } \tilde{\imath}_{inv\,q} = -\frac{I_{inv\,d}[\theta_g - \theta_{PLL}]}{s\tau_C + 1}, \tag{3.5.11}$$

where τ_C is the time-constant of the dq-frame current control loop. Details of that will be described in the subsection 3.5.7. By combining (3.5.10) and (3.5.11), the output voltage of the q-axis in the abc/dq frame transformation is:

$$\tilde{v}_{PLLq} \approx V_g[\theta_g - \theta_{inv}]\left[1 + \frac{rI_{inv\,d} - \omega_g L.I_{inv\,q}}{V_g} + \frac{-rI_{inv\,d} + \omega_g L I_{inv\,q} - sLI_{inv\,q}}{V_g(s\tau_C + 1)}\right], \tag{3.5.12.a}$$

$$\tilde{v}_{PLLq} \approx V_g[\theta_g - \theta_{inv}]\frac{s\left[\tau_C\left(1 + r\frac{I_{inv\,d} - \omega_g L.I_{inv\,q}}{V_g}\right) - \frac{LI_{inv\,q}}{V_g}\right] + 1}{s\tau_C + 1}. \tag{3.5.12.b}$$

Thus, if the line impedance is small, the second term in the brackets is neglected, but, if the line impedance is relevant, a zero appears which depends on $I_{inv\,q}$. This can produce a zero in the right-hand-plane (RHP) of the s-domain and with it, instabilities. Following the diagram from Figure 3.5.6:

$$\tilde{v}_{PLLq} \approx T_{w_{line}}(s).[\theta_g - \theta_{inv}]. \tag{3.5.13}$$

After that, an integral controller, a notch-filter and a compensator are added and finally and integrator. The complete transfer function is complex, but can be plotted using frequency response diagrams. Notice that if the current is zero, or if the line time constant is small the PLL works ideally. If not, a zero-pole additional transfer appear which is particularly problematic for negative I_{invq} where the zeros can appear in the RHP.

As an example, the PLL without any effect in the line impedance is shown with one with a line impedance of $r=0.5\Omega + X_L=10\ \Omega$ for $I_{inv\ d}=0A$ and $I_{inv\ q}=30\ A$ and for $I_{inv\ d}=30A$ and $I_{inv\ q}=0A$, $\tau_C = 0.5$ ms. In the reactive current case, the system is critically stable as Figure 3.5.7 and Figure 3.5.8 show. However, when $I_{inv\ d}= 30A$ and $I_{inv\ q}=0$ the system remains stable as Figure 3.5.9 confirms.

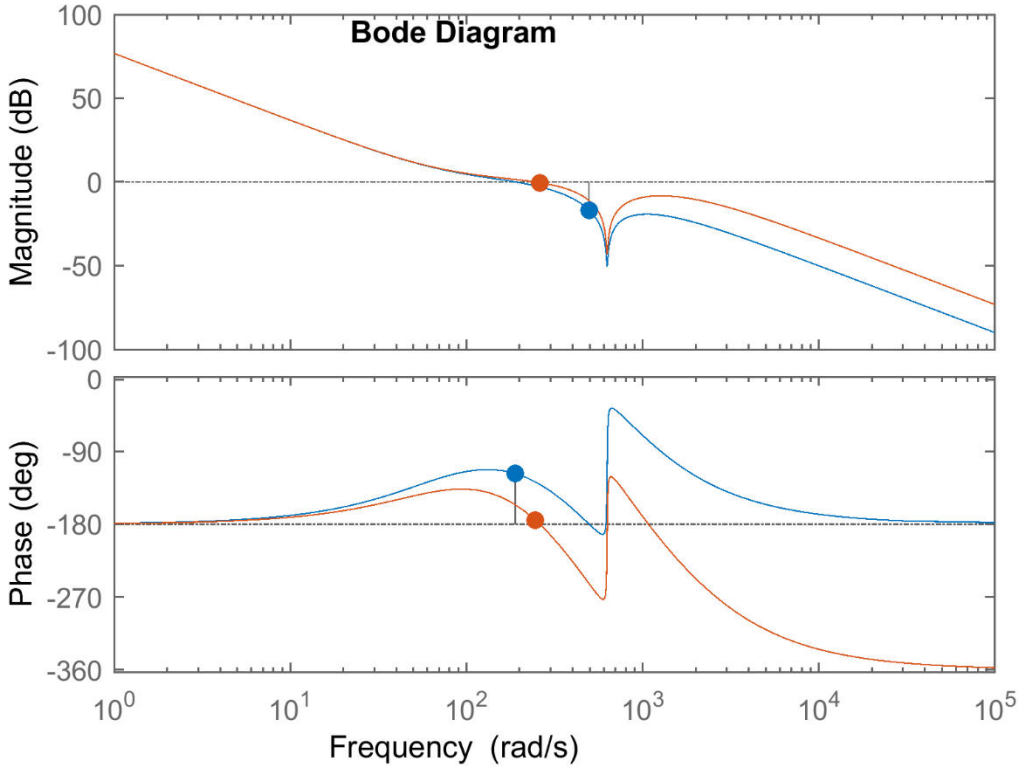

Figure 3.5.7–PLL with line impedance effect, the blue line is the PLL without considering the line effect, the red one, considers the line effects, a RHP pole appear, and the system is almost unstable (phase margin almost zero)

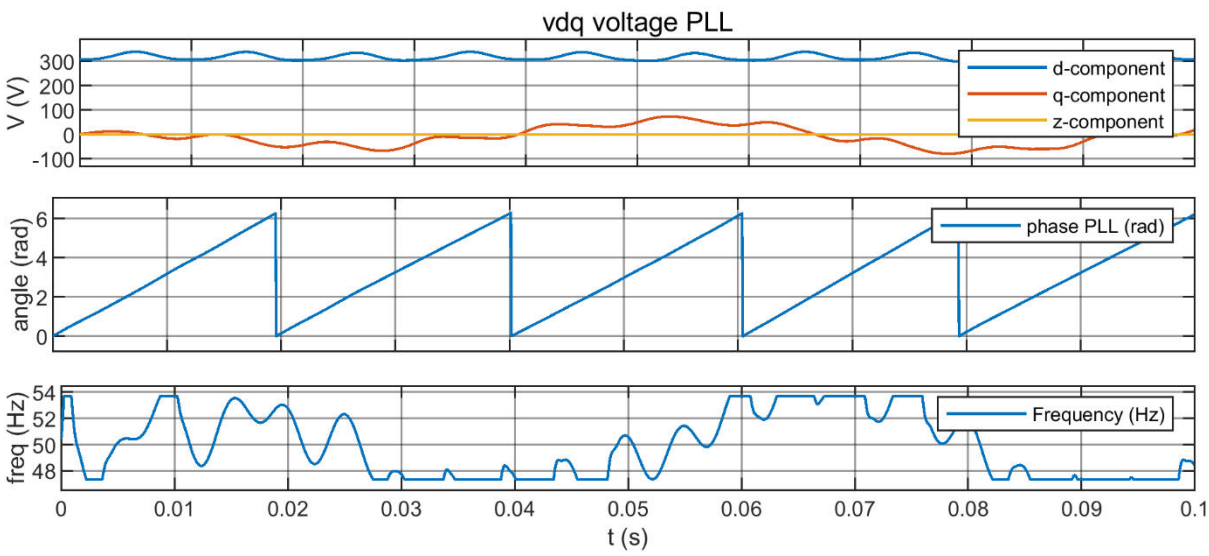

Figure 3.5.8–Time-domain simulation of the PLL tracking with the line impedance effect injecting reactive power

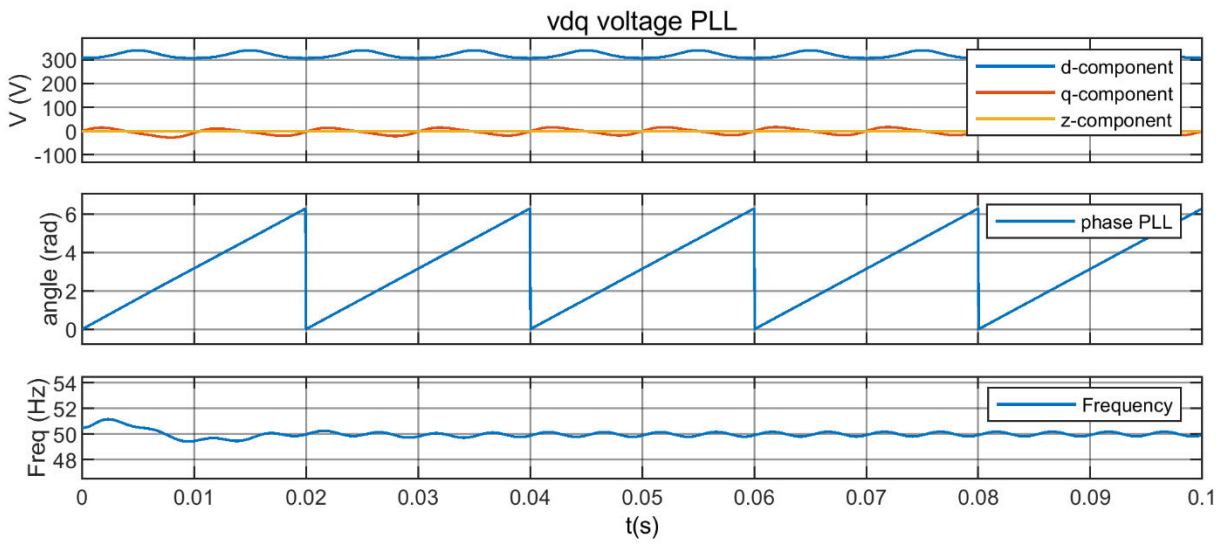

Figure 3.5.9–Time-domain simulation of the PLL tracking with the line impedance effect injecting active power

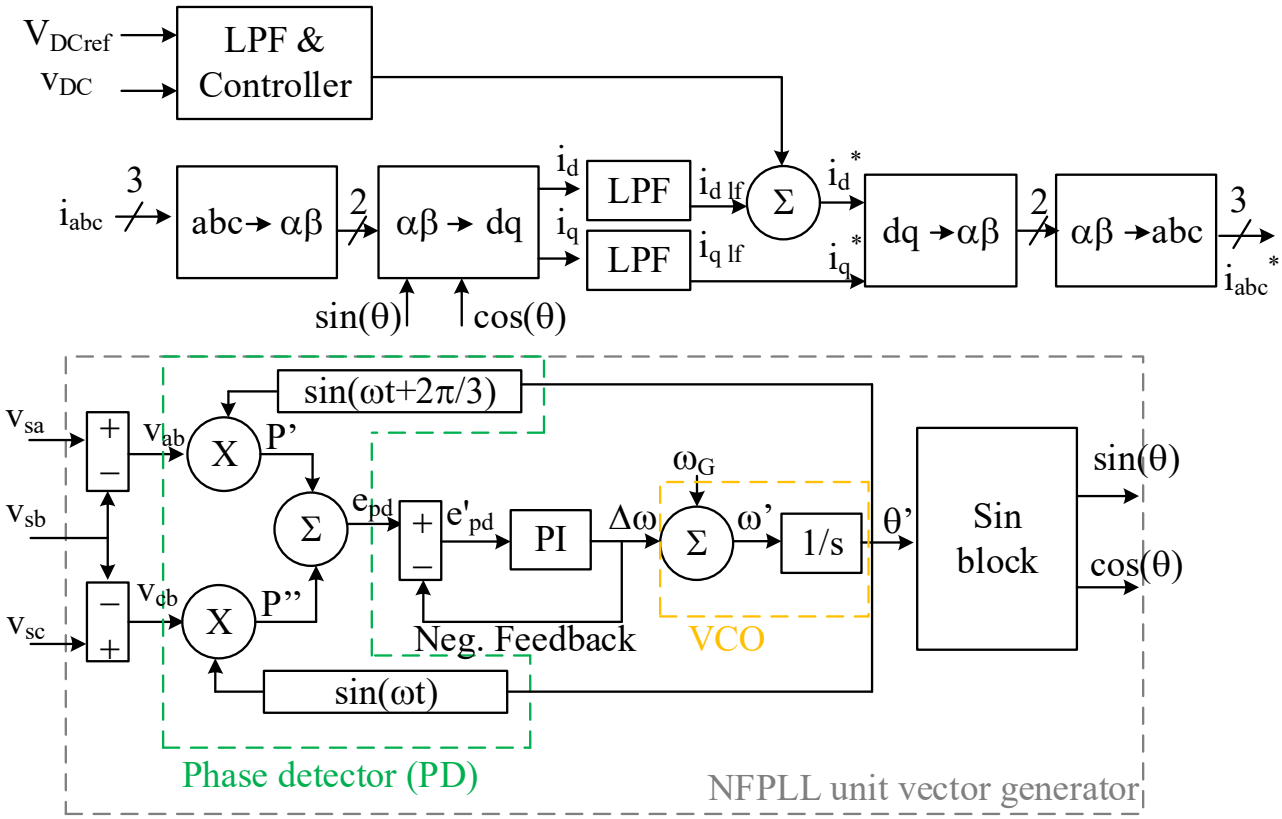

Figure 3.5.10–Schematic diagram of a proposed negative feedback PLL, NFPLL [28]

3.5.5. Modeling of negative feedback phase-locked loop (NFPLL)

Another grid synchronization block was proposed by the authors: the negative feedback phase-locked loop (NFPLL) also based on dq-frame representation, shown in Figure 3.5.12. In this, the unitary signals: sine and cosine signals are obtained based on the proposed NFPLL and using that, the control of the inverter can be achieved. This solution can replace the synchronous reference frame or dq-PLL from Section 3.5.3. The architecture of the proposed NFPLL block consists of a negative feedback signal given to a proportional-integral controller, a nonlinear adaptive filter-based PD circuit and a VCO block, which help to extract positive sequence signals from the supply. Negative feedback improves the bandwidth of the loop. Thus, a negative feedback signal helps in mitigating the impacts of noise and disturbances on the system's performance. In addition, the nonlinear adaptive filter-based PD approach can track changes in the input signal's amplitude, phase angle, and frequency while effectively calculating the fundamental component. The LPF block is made up of PI control blocks with a negative feedback loop. The VCO block consists of an adder, an integrator, and a sine block. The adder in the VCO block adds the fundamental angular frequency signal (ω_G) to the frequency deviation components ($\Delta\omega$). The VCO block takes input from the LPF block and produce its output (θ'). This θ' is given as input of a sine block for producing the sin(θ) and cos(θ) signals.

The operation of the proposed controller is the following. Initially, the V_{sabc} is applied at the input of NFPLL. Then, the in-phase, $V_{ab} = V_m\sin(\omega t + \phi)$, and in-quadrature phase, $V_{bc} = V_m\cos(\omega t + \phi)$, voltages are obtained by subtracting the phase-b voltage (V_{sb}) from the phase-a (V_{sa}), and phase-c voltages (V_{sc}) from phase-b voltage (V_{sb}) respectively.

The θ' is used to generate the signals P' and P'' as it is shown in Figure 3.5.10:

$$P' = V_{ab}.\sin\left(\omega t + \frac{2\pi}{3}\right) \text{ and } P'' = V_{bc}.\sin(\omega t). \tag{3.5.14}$$

Thereafter, these P' and P'' are added to obtain the phase error signal (e_{pd}), which is further subtracted from the negative feedback signal ($\Delta\omega$) before being given as an input

to PI controller (e'_{pd}). The ω' signal is obtained by adding ω_G with $\Delta\omega$ as presented in (24). The e'_{pd} is processed in the PI controller to generate $\Delta\omega$. The value of K_p and K_i can be calculated using open loop frequency response and select the proper gains to obtain the desired gain margin [24].

The tracking results using the same experiment as in the previous PLL, the synchronous frame PLL are shown in Figure 3.5.11. The grid is at 50Hz with a fraction of negative sequence and the 5th harmonic. The initial condition of the PLL is at 50.5Hz so the transients can be observed until the PLL is locked. The NFPLL has a higher rejection to harmonics, however, there is a constant phase error which should be compensated in the current control loop. A small phase difference can be observed in the angle plots.

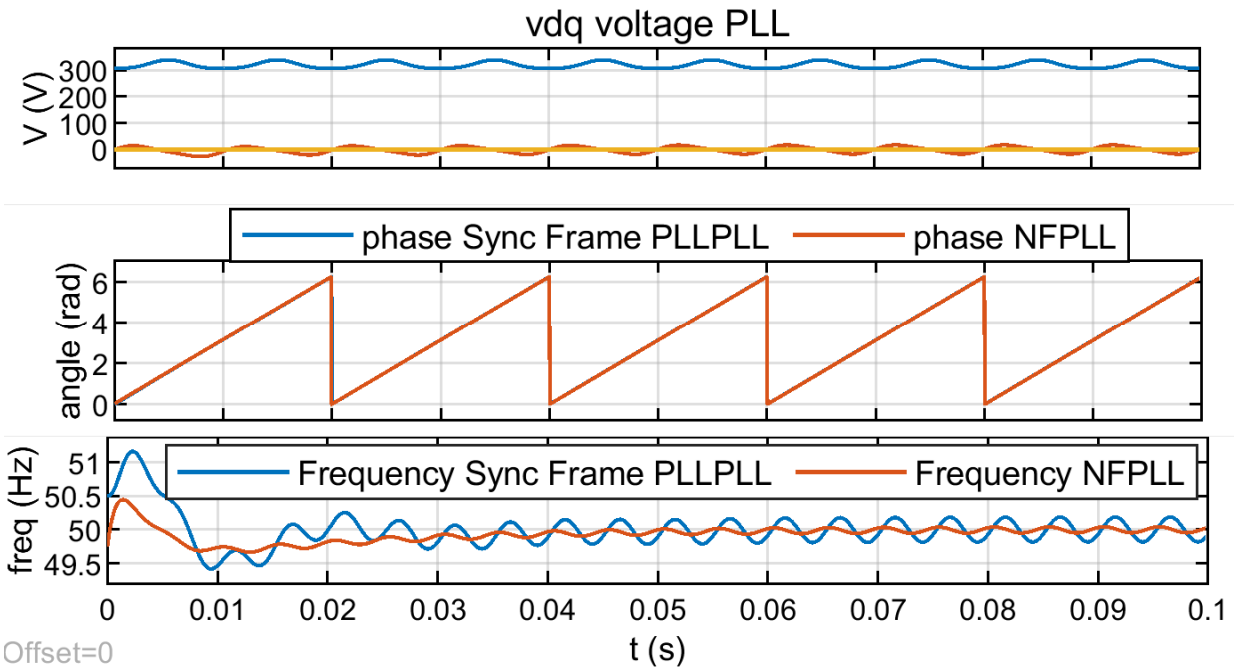

Figure 3.5.11–Time-domain simulation of the NFPLL tracking compared with the previous one, the synchronous frame PLL in the same conditions

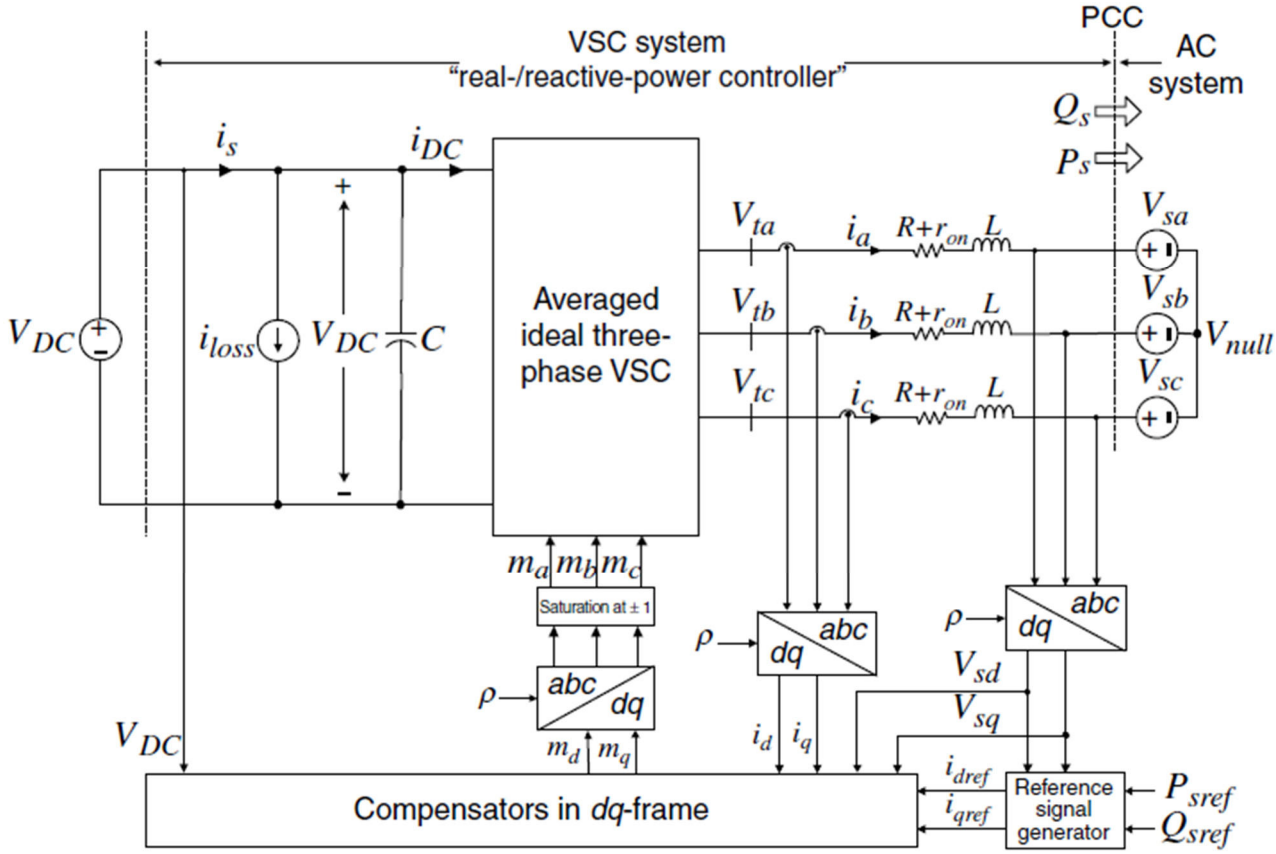

Figure 3.5.12–Schematic diagram of an inverter with a current controller in dq-frame [24]

3.5.6. Modeling of the current control loop in dq-frame

Using any of the introduced PLLs and based on the inverter diagram controlled in dq-frame shown in

Figure 3.5.12, the output equation of the inverter can be written in dq frame using (3.2.29):

$$L\frac{di_d}{dt} - \omega L i_q + r i_d = \frac{V_{DC}}{2} m_d - v_d \tag{3.5.14.a}$$

$$L\frac{di_q}{dt} + \omega L i_d + r i_q = \frac{V_{DC}}{2} m_q - v_q, \tag{3.5.14.b}$$

where the coupling effect between d and q components can be observed $\omega L i_q$ in the d-equation and $\omega L i_d$ in the q equation. In order to decoupled these equations and have a pair of single-input-single-output (SISO) systems, a decoupled block can be introduced by defining an auxiliary variable u:

$$u_d = -\omega L i_{inv\,q} + \frac{V_{DC}}{2} m_d - v_{g\,d} \tag{3.5.15.a}$$

$$u_q = +\omega L i_{inv\,d} + \frac{V_{DC}}{2} m_q - v_{g\,q}. \tag{3.5.15.b}$$

Thus, the equations can be simplified as:

$$(sL + r) i_{inv\,d} = u_d \tag{3.5.16.a}$$

$$(sL + r) i_{inv\,q} = u_q, \tag{3.5.16.b}$$

which represent two SISO systems and can be controlled by proportional-integral (PI) controllers as Figure 3.5.13 shows. The selection of the gains of the controllers is simple, the PI time constant should match the L/r time constant of the inverter, and then the proportional gain is used to adjust the bandwidth of the control loop. Usually, this bandwidth is around the switching frequency over 10, $f_s/10$, which gives great bandwidth to the control system. The closed-loop transfer functions are:

$$i_{inv\,d} = \frac{1}{s\tau_C + 1} i_{Ref\,d} \tag{3.5.17.a}$$

$$i_{inv\,q} = \frac{1}{s\tau_C + 1} i_{Ref\,q} \tag{3.5.17.b}$$

As it can be seen from Figure 3.5.13, the PI controllers control the variables u_d and u_q, but the inverter control requires the modulation indexes: m_d and m_q. This transformation is done in the decoupling block based on (3.5.15):

$$m_d = \frac{2}{V_{DC}} \left(u_d + \omega L i_{inv\,q} + v_d \right) \tag{3.5.18.a}$$

$$m_q = \frac{2}{V_{DC}} \left(u_q - \omega L i_{inv\,d} + v_{g\,q} \right) \tag{3.5.18.b}$$

The full coupling and decoupling blocks are represented in Figure 3.5.14.

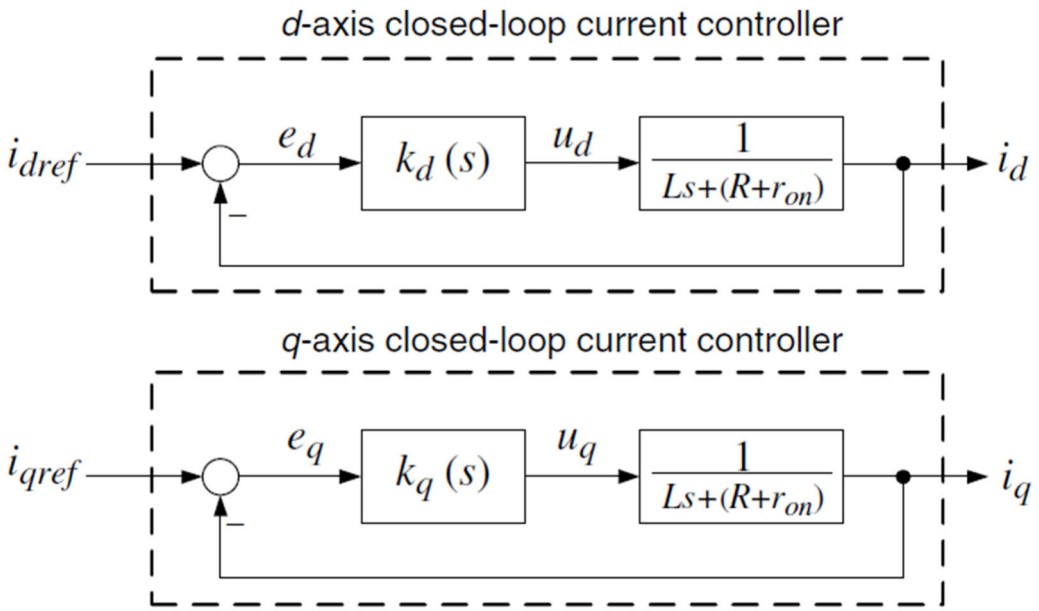

Figure 3.5.13–Simplified current control loops [24] ($i_{inv\,d} = i_d$ and $i_{inv\,q} = i_q$)

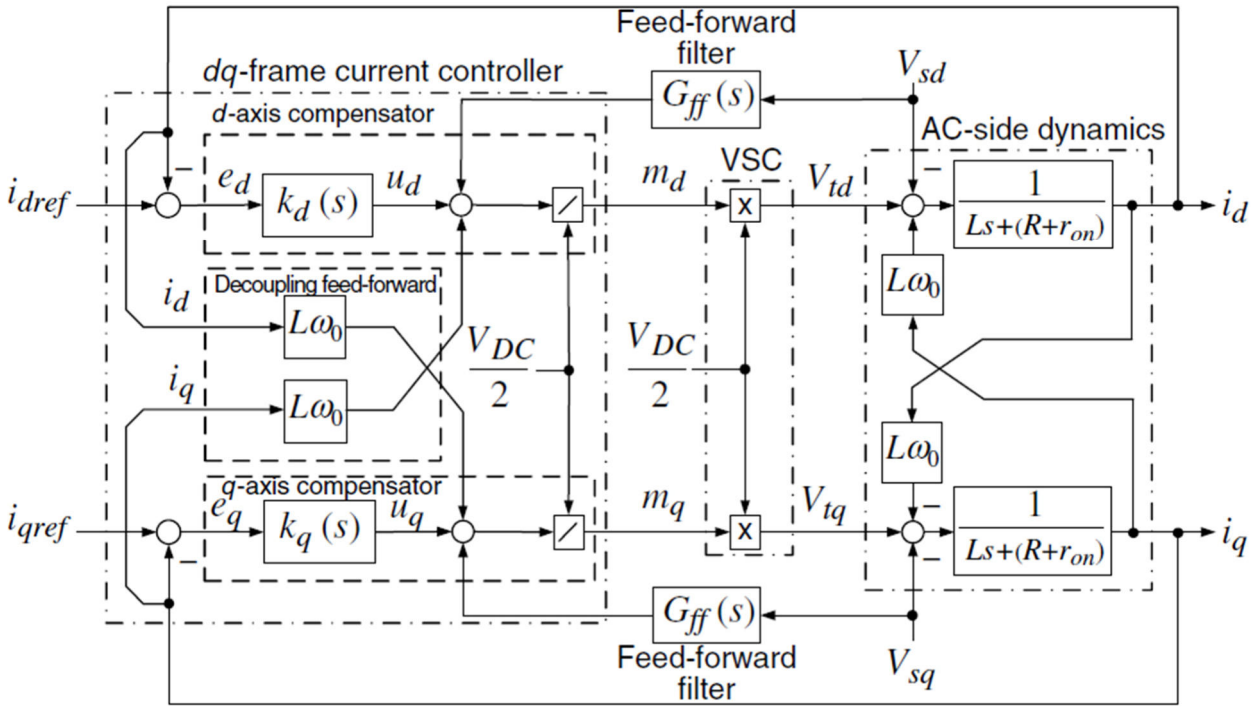

Figure 3.5.14–Complete current control loops [24] ($i_{inv\,d} = i_d$ and $i_{inv\,q} = i_q$, $v_{g\,d} = v_{s\,d}$ and $v_{g\,q} = v_{s\,q}$)

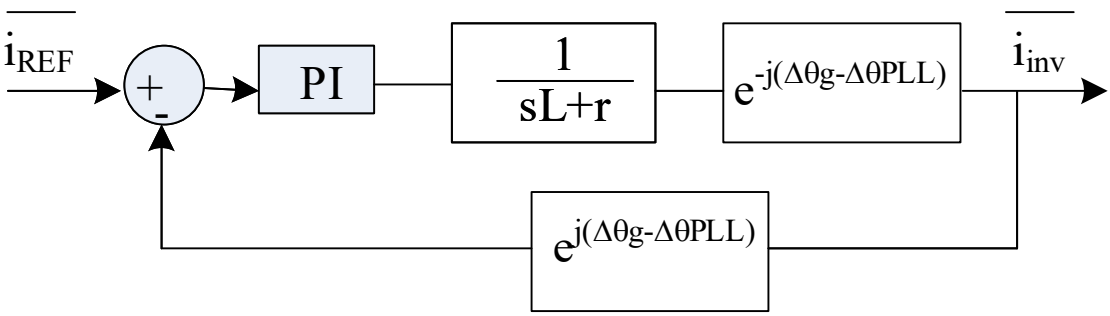

Figure 3.5.15–Simplified current control loop including phase errors from PLL

3.5.7. Effect of PLL phase misalignment in the current control loop in dq-frame

The control loop described in subsection 3.5.5 might be altered if the PLL cannot match the grid due to the effect of the power lines introduced in subsection 3.5.4. Considering a phase error different from zero, the simplified control diagram is modified as Figure 3.5.15 shows. If the phase error is small, the complex exponential can be reduced to: $e^{j[\theta_g(t)-\theta_{PLL}(t)]} \approx 1 + j[\theta_g(t) - \theta_{PLL}(t)]$ and the transfer functions of (3.5.17) take the form of:

$$i_{inv\,d} = \frac{1}{s\tau_C + 1} i_{Ref\,d} - \frac{i_{Ref\,q}[\theta_g(t) - \theta_{PLL}(t)]}{s\tau_C + 1} \tag{3.5.19.a}$$

$$i_{inv\,q} = \frac{1}{s\tau_C + 1} i_{Ref\,q} + \frac{i_{Ref\,d}[\theta_g(t) - \theta_{PLL}(t)]}{s\tau_C + 1}. \tag{3.5.19.b}$$

Thus, the impact of the errors in the phase angle are clearly shown in the control loop and they were used it in the line impedance analysis in the PLL in subsection 3.5.4. These results were presented in [118].

3.5.8. Summary

This section reviews the control of inverters in dq-frame, putting particular emphasis in the modeling of the phased-locked loops and the current-control loop. The models were simulated in order to check the stability of the system and the models were used for evaluating the effect of the line impedances in the synchronization processes. Due to the proposed model, the effect is well quantified. The model of the PLL and the control loops under grid line perturbations are the main contribution of this section and they are discussed in [37, 118].

3.6. Voltage control loop and power sharing methods

3.6.1. Voltage control loops

Having analyzed the inner loops of inverters, an outer control loop can use the inner loop to control other variables such as the output voltage [105, 129]. Thus, from the point of view of the outer control loop, the converter is a controllable current source, which can be used to control an AC or DC voltage or even power. In this subsection, the voltage control loops of the inverter will be reviewed.

The voltage control loop considers the current control loop as a single transfer function. The exact transfer function of the closed-loop current control: $G_{CL\ CC}(s)=i_{L\alpha\beta}/i_{L\alpha\beta Ref}$ is shown in Figure 3.6.2, where Figure 3.6.1 indicates which are those currents. Notice that due to the high gain in the designed open loop transfer functions, the closed loop transfer function has a wide bandwidth. The voltage control loop consider this loop as a first order system with a certain bandwidth ω_{CI}. The controller is designed

under a no-load condition where the stability margin is low [108]. The open-loop transfer function of $G_{OL\ CV}(s) = v_{C\alpha\beta}/v_{C\alpha\beta\ Ref}$ is given as:

$$G_{OL\ CV}(s) = \frac{v_{C\alpha\beta}}{v_{C\alpha\beta\ Ref} - v_{C\alpha\beta}} = \left(k_{PV} + \frac{2k_{IV}\omega_c s}{s^2 + 2s\omega_c + {\omega_G}^2}\right)\frac{1}{\frac{s}{\omega_{CI}} + 1}\frac{1}{C_f s}. \tag{3.6.1}$$

The selection of k_{PV} and k_{IV} follows the same procedure as in Section 3.3. The closed-loop transfer function is compared with a normalized polynomial and the values are designed according to the desired phase margin (PM). With the PM, the coefficient β is selected and used for the selection of the parameters (see equations from (3.3.10) to (3.3.13).

For this particular transfer function, the results are:

$$\omega_{CV} = \frac{\omega_{CI}}{\sqrt{\beta}}$$
$$k_{PV} = \frac{\omega_{CI}C_f}{\sqrt{\beta}} \text{ and } k_{IV} = \frac{\omega_{CI}K_{PV}}{2\beta} \tag{3.6.2}$$

The voltage and current controllers are implemented in a real microcontroller which must update the PWM signals of the switches once per switching period. Thus, the controller should be discretized and implemented in c-code. First, the controller must be discretized with the switching period $T_S=1/f_s$, for that Tustin approximation was used:

$$s = \frac{\omega_c}{\tan(\omega_c T_S/2)}\frac{1 - z^{-1}}{1 + z^{-1}} = k_W\frac{1 - z^{-1}}{1 + z^{-1}} \tag{3.6.3}$$

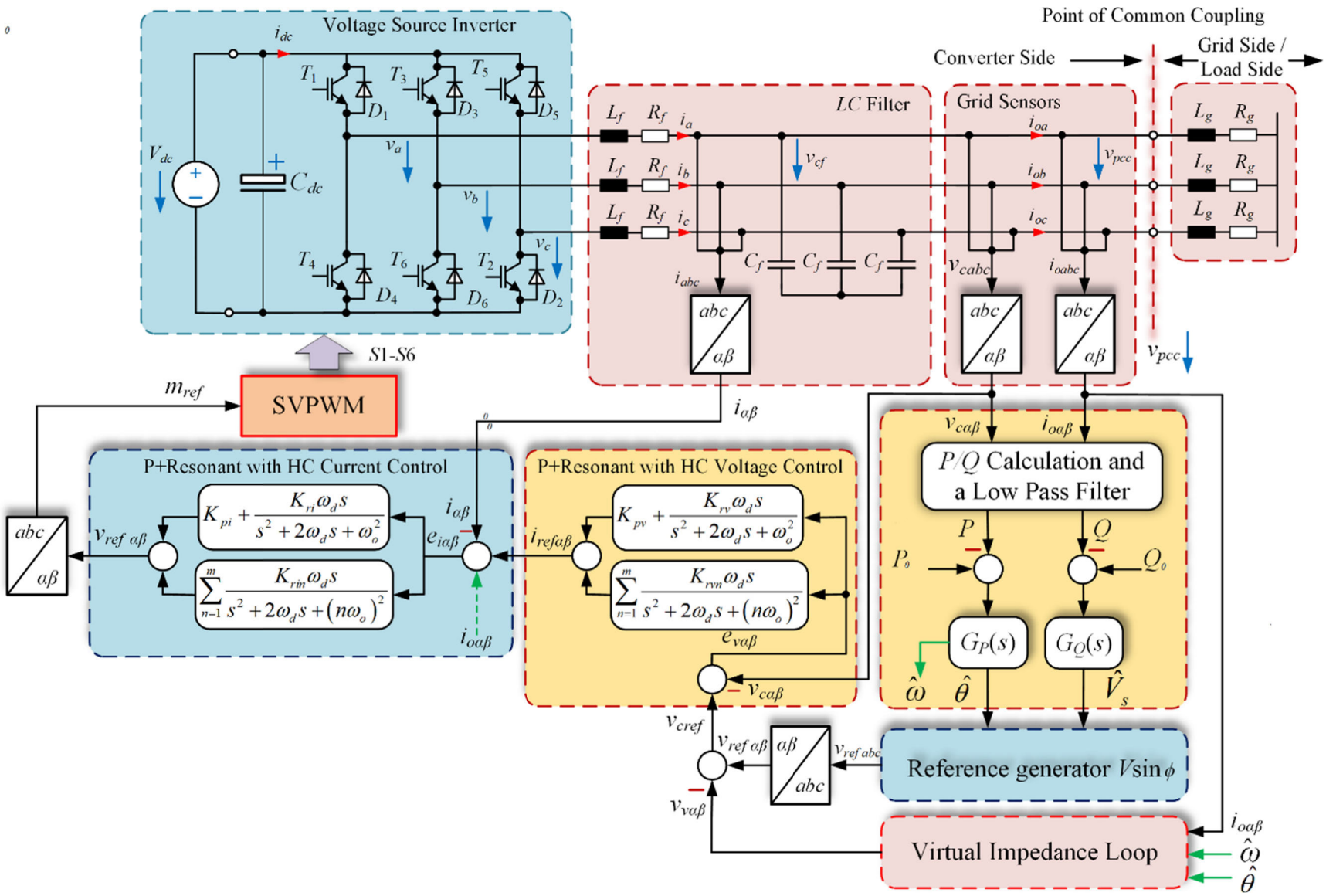

Figure 3.6.1–Full diagram of a three-phase grid-connected inverter with current and voltage control loops and droop control power sharing method

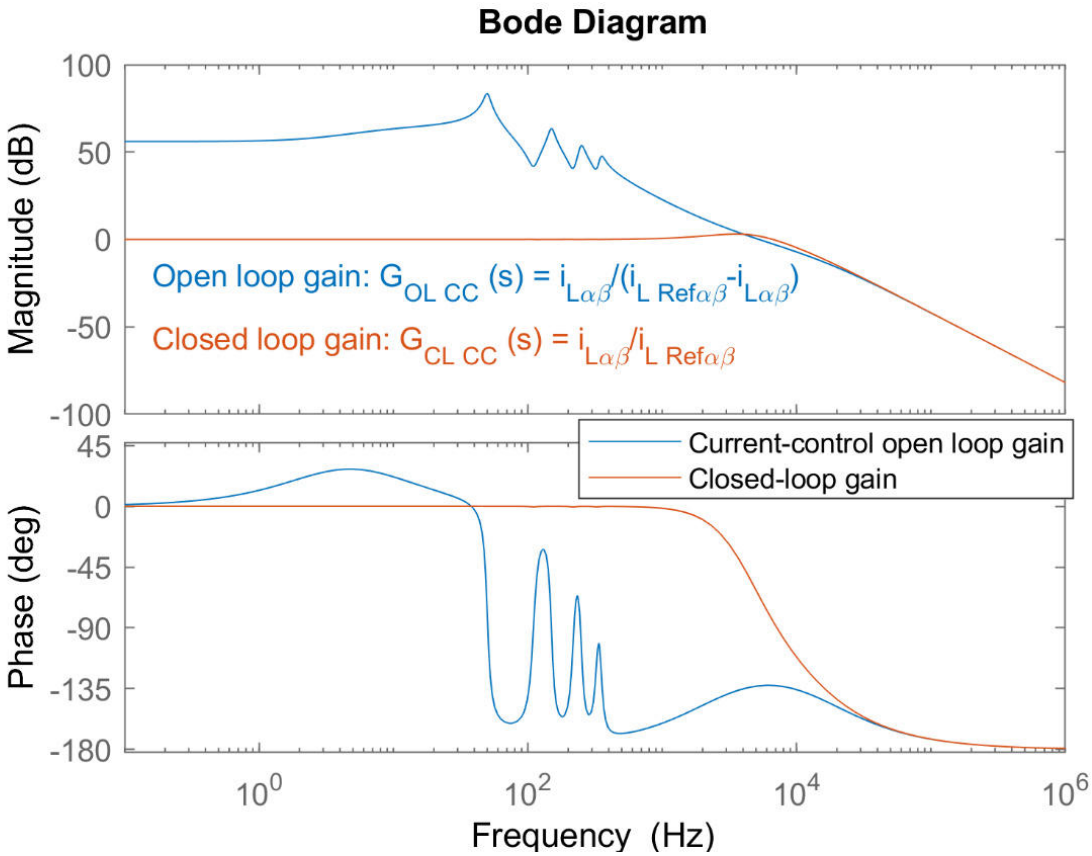

Figure 3.6.2–Open- and closed-loop transfer functions for the inner current control obtained from Section 3.3 and 3.4

The controller transfer function is (for a single resonance):

$$G_{PR}(s) = k_{PV} + \frac{2k_{IV}\omega_c s}{s^2 + 2s\omega_c + {\omega_G}^2}. \tag{3.6.4.a}$$

Thus,

$$G_{PR}(z) = k_{PV} + \frac{2k_{IV}\omega_c k_W \frac{1-z^{-1}}{1+z^{-1}}}{\left(k_W \frac{1-z^{-1}}{1+z^{-1}}\right)^2 + 2\omega_c\left(k_W \frac{1-z^{-1}}{1+z^{-1}}\right) + {\omega_c}^2}, \tag{3.6.4.b}$$

which can be represented as:

$$G_{PR}(z) = k_{PV} + \frac{b_0 + b_1 z^{-1} + b_2 z^{-2}}{1 + a_1 z^{-1} + a_2 z^{-2}}, \tag{3.6.4.c}$$

where: (3.6.4.d)

$$b_0 = \frac{2k_{IV}\omega_c k_W}{{k_W}^2 + 2\omega_c k_W + h^2{\omega_G}^2} \quad (3.6.4.e)$$

$$b_1 = 0 \quad (3.6.4.f)$$

$$b_2 = -b_0 \quad (3.6.4.g)$$

$$a_1 = \frac{2h^2{\omega_G}^2 - 2{k_W}^2}{{k_W}^2 + 2\omega_c k_W + h^2{\omega_G}^2} \quad (3.6.4.h)$$

$$a_2 = \frac{{k_W}^2 - 2\omega_c k_W + h^2{\omega_G}^2}{{k_W}^2 + 2\omega_c k_W + h^2{\omega_G}^2},$$

where $z = e^{sT_S}$. The representation of the discrete transfer function is shown in Figure 3.6.3. All of the previous discussed controllers were also discretized using Tustin algorithms to implemented in a microcontroller. Any harmonic compensation at different frequencies works in parallel with this diagram. Thus, it is equal with different coefficient values. The *h* indicates the harmonic number so the values can be calculated directly. The proportional term also acts in parallel with the structure of Figure 3.6.3.

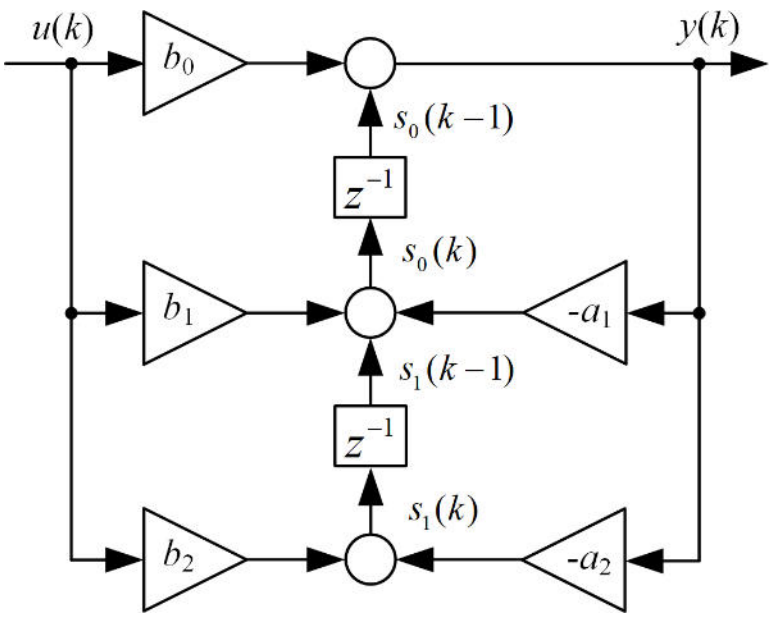

Figure 3.6.3–Direct form II transpose (DFIIt) structure for digital implementation of a PR controller

3.6.2. Power control methods: traditional droop control

In order to control power in the AC side (grid side), the inverter should control active and reactive power. This can be as simple as controlling the current as a function of the grid voltage. Thus, by selecting the current amplitude and phase and considering that the grid voltage does not change and it is a perfect sinusoidal waveform, the active and reactive power is controlled. The apparent power that the inverter delivers to the grid using only a current control loop is:

$$\bar{S}_{INV} = \bar{S}_{PCC} = \frac{\bar{V}_{g\alpha\beta}\bar{I}_{INV\alpha\beta}{}^{*}}{2} = \frac{\bar{V}_{PCC\alpha\beta}\bar{I}_{O\alpha\beta}{}^{*}}{2} = \frac{\bar{V}_{C\alpha\beta}\bar{I}_{O\alpha\beta}{}^{*}}{2} \tag{3.6.2}$$

Thus, by selecting the current reference in phase with the voltage only active power is delivered and the power is controlled by the current amplitude. The same is applied for reactive power but with a phase shift of 90 degrees. In that case, the power is exactly controlled by the inverter. This diagram is usually implemented in grid-following inverters, where the reference can be the current or the power.

However, when the inverter is controlling the voltage, it is in the master mode, or grid-forming mode. It delivers as much power as the load needs to have the desired output voltage at the PCC.

If the power that the load demands is greater that the maximum available power in the inverter, it will not be able to keep the voltage at the desired level. Therefore, an algorithm is needed to allow the inverter to share the power among other generators. For that, a distributed control algorithm is commonly used: the droop control.

To decouple active and reactive powers and share powers properly, first, a power calculation block is needed in the inverter controller (see Figure 3.6.1). The inverter's output voltages ($v_{o\alpha\beta} = v_{C\,\alpha\beta}$) and output currents ($i_{o\alpha\beta}$) are given to the power controller block to calculate the instantaneous active and reactive powers, $p_{PCC}(t) + jq_{PCC}(t)$.

$$\bar{s}_{PCC}(t) = p_{PCC}(t) + jq_{PCC}(t) = \frac{v_{C\alpha}i_{\alpha} + v_{C\beta}i_{\beta}}{2} + j\frac{-v_{C\alpha}i_{\beta} + v_{C\beta}i_{\alpha}}{2} \tag{3.6.3}$$

These powers are passed through a low-pass filter (LPF) to eliminate ripples and high frequencies. This results in:

$$P_{PCC}(s) + jQ_{PCC}(s) = \frac{1}{\frac{s}{\omega_{CP}} + 1}(p_{PCC}(s) + jq_{PCC}(s)) \tag{3.6.4}$$

where ω_{CP} is the cut-off frequency of the LPF, which should be lower than the nominal grid frequency (ω_g). This affects the system response as it is detailed in the following subsections [130].

The traditional P/ω and Q/V droop controls have inherent trade-off between P/Q-sharing accuracy and frequency/amplitude output voltage regulation [131][132]. The regulation of active and reactive powers depends on the angle and the inverter voltage. Figure 3.6.4 clarifies that [132].

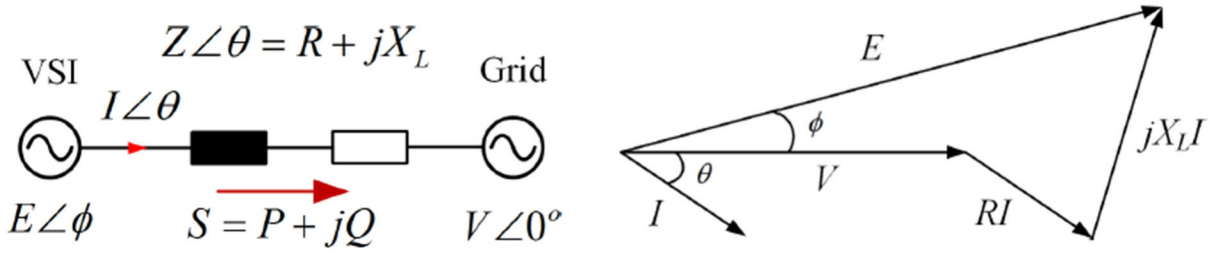

(a) (b)

Figure 3.6.4–Voltage-source inverter connected to the grid through a line impedance in a grid-forming mode: (a) Power flow through the line impedance, (b) vector diagram of the power flow

It indicates that the complex power is:

$$P + jQ = \frac{EV}{2X}\sin(\phi) + j\frac{EVcos(\phi) - V^2}{2X} \tag{3.6.5}$$

If $X \gg R$

Applying to the inverter in Figure 3.6.1, the equation is:

$$P_{PCC}(t) + jQ_{PCC}(t) = \frac{|v_C||v_s|\sin(\phi_{c-s})}{2\omega_g L_S} + j\frac{|v_C||v_s|\cos(\phi_{c-s}) - |v_s|^2}{2\omega_g L_S} + coupling\ term\ due\ to\ Rs \tag{3.6.6}$$

Considering that $\sin(\phi_{c-s}) \approx \phi_{c-s}$ and $\cos(\phi_{c-s}) \approx 1$ and neglecting R_s:

$$P_{PCC}(t) + jQ_{PCC}(t) \approx \frac{|v_C||v_s|}{2\omega_g L_S}\phi_{c-s} + j\frac{|v_s|}{2\omega_g L_S}(|v_C| - |v_s|) \tag{3.6.7}$$

It can be seen that the active power is mostly dependent on the phase difference between the inverter and the grid and the reactive power is mostly dependent on the voltage difference between the inverter and the grid.

Thus, proper P − V and Q − ω droop functions are needed to achieve proper active and reactive power-sharing. The traditional droop control functions can be defined as [133][134]:

$$\phi_{c-s} = \phi_{(c-s)0} - G_P(s)(P - P_0) \tag{3.6.8}$$
$$|v_C| = |v_C|_0 - G_Q(s)(Q - Q_0)$$

where ϕ_{c-s} is the phase of the v_{Ref}(see Figure 3.6.1) which is the reference of the voltage control loop and $\phi_{(c-s)0} = \omega_g t$. $G_P(s)$ and $G_Q(s)$ are the transfer functions that adjust the desired voltage amplitude and phase as a function of the delivered output active and reactive power. The droop control is responsible for generating the reference of the voltage control loop v_{Ref} with its respective phase angle ϕ_{c-s} according to the active (P) and reactive (Q) powers [132]. Traditionally, the transfer functions are defined as:

$$G_P(s) = k_{Pdroop} + \frac{k_{Idroop}}{s} \tag{3.6.9}$$
$$G_P(s) = k_{Qdroop}$$

where k_{Idroop} and k_{Qdroop} are the static droop coefficients and k_{Pdroop} is known as the transient droop term. The static droop coefficient $k_{Idroop} = \Delta\omega/\Delta P$ can be selected based on the maximum frequency deviation over nominal active power and $k_{Qdroop} = \Delta V/\Delta P$ can be selected based on maximum amplitude deviation over nominal reactive power. The $G_P(s)$ and $G_Q(s)$ should set the steady-state control objective, ensure stability and achieve good transient response [134].

3.6.3. Introduction of virtual impedance

The virtual impedance loop can be added to the voltage reference to add a voltage drop as a function of the current. This creates a virtual output impedance in the inverter in terms of magnitude and phase. The output impedance affects the power-sharing accuracy of the droop controllers [135]. The output of the droop controller is given to the virtual impedance block as shown in Figure 3.6.1. To implement the desired output impedance, the output voltage reference is reduced proportionally to the output current as:

$$\bar{v}_{C\alpha\beta\ Ref} = \bar{v}_{\alpha\beta\ Ref} - \bar{Z}_{v\alpha\beta} \,.\, \bar{\imath}_{o\alpha\beta} = \bar{v}_{\alpha\beta\ Ref} - \bar{v}_{v\alpha\beta} \tag{3.6.9}$$

where:

$$\bar{v}_{v\alpha\beta} = v_{v\alpha} + j v_{v\beta}$$

$$v_{v\alpha} = R_v \,.\, i_{o\alpha} - \omega_G L_v \,.\, i_{o\beta}$$

$$v_{v\beta} = R_v \,.\, i_{o\beta} + \omega_G L_v \,.\, i_{o\alpha}$$

where $\bar{Z}_{v\alpha\beta}$ is the virtual output impedance and the voltage reference $\bar{v}_{\alpha\beta\ Ref}$ is the output of a signal generator based on the droop controller (see Figure 3.6.1). Then $\bar{v}_{C\alpha\beta\ Ref}$ is the reference given to the voltage controller as shown in Figure 3.6.1. R_v and L_v are the virtual resistance and inductance, $\bar{v}_{v\alpha\beta}$ is the voltage drop due to the virtual impedance and $\bar{\imath}_{o\alpha\beta}$ is the output current. The parameters of the virtual impedance can be chosen arbitrarily and they can improve the transient response and the power sharing as it will be discussed further in this section [37, 136, 137].

3.6.4. Simulation of an inverter using a power sharing technique with virtual impedance

Three inverters in parallel with line impedances connected to a three-phase linear load and a non-linear load have been simulated in MATLAB/Simulink as Figure 3.6.5

shows. The inverters include proportional and resonant controllers with several harmonic compensators which are discretized using DFIIt structure as shown in Figure 3.6.3. The primary control contains the droop controller, the inner voltage and current control loops and the virtual impedance as it is shown in Figure 3.6.1.

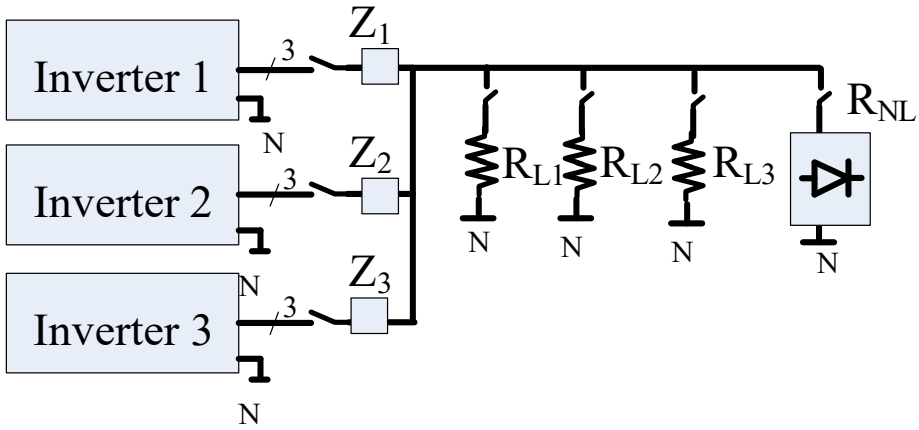

Figure 3.6.5–Diagram of the simulations of the inverter grid

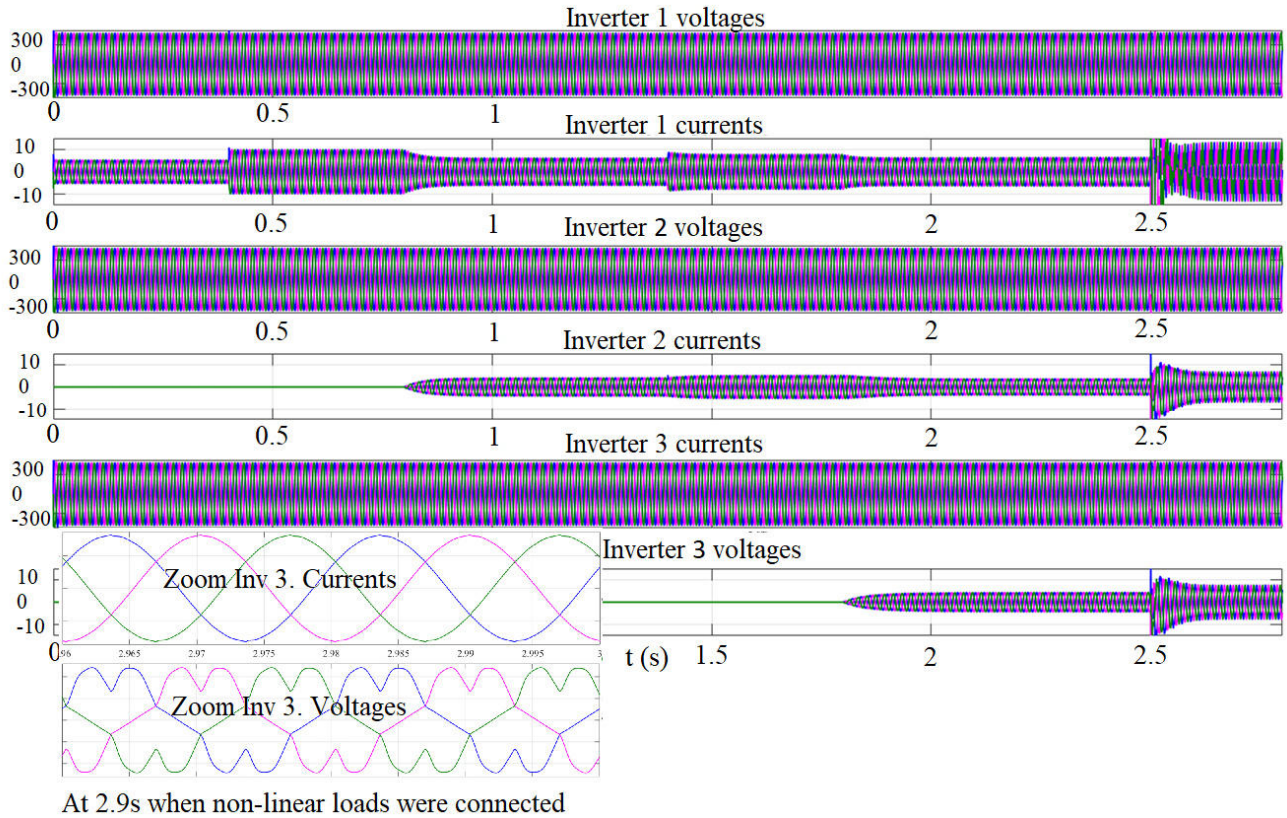

Figure 3.6.6. Simulation tests of three inverters delivering power the different loads and being connected and disconnected to the system to observe the power sharing, and the harmonic compensation in non-linear loads

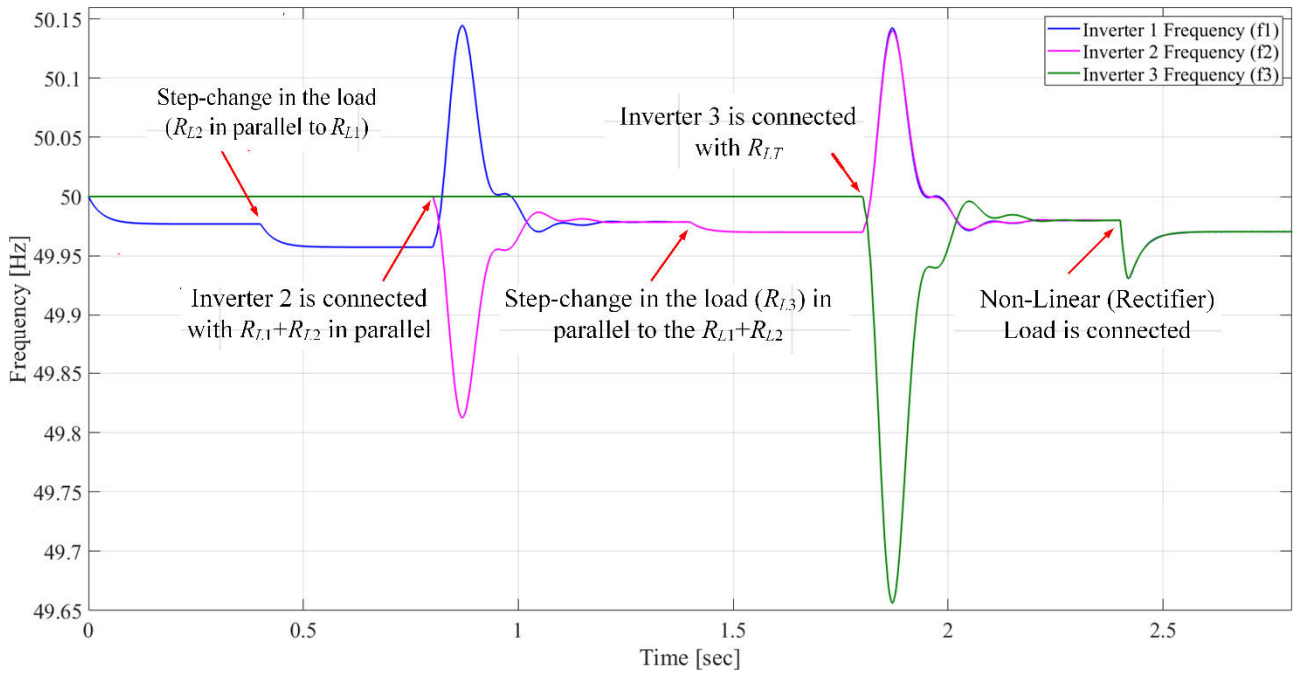

Figure 3.6.7–Frequency in each inverter

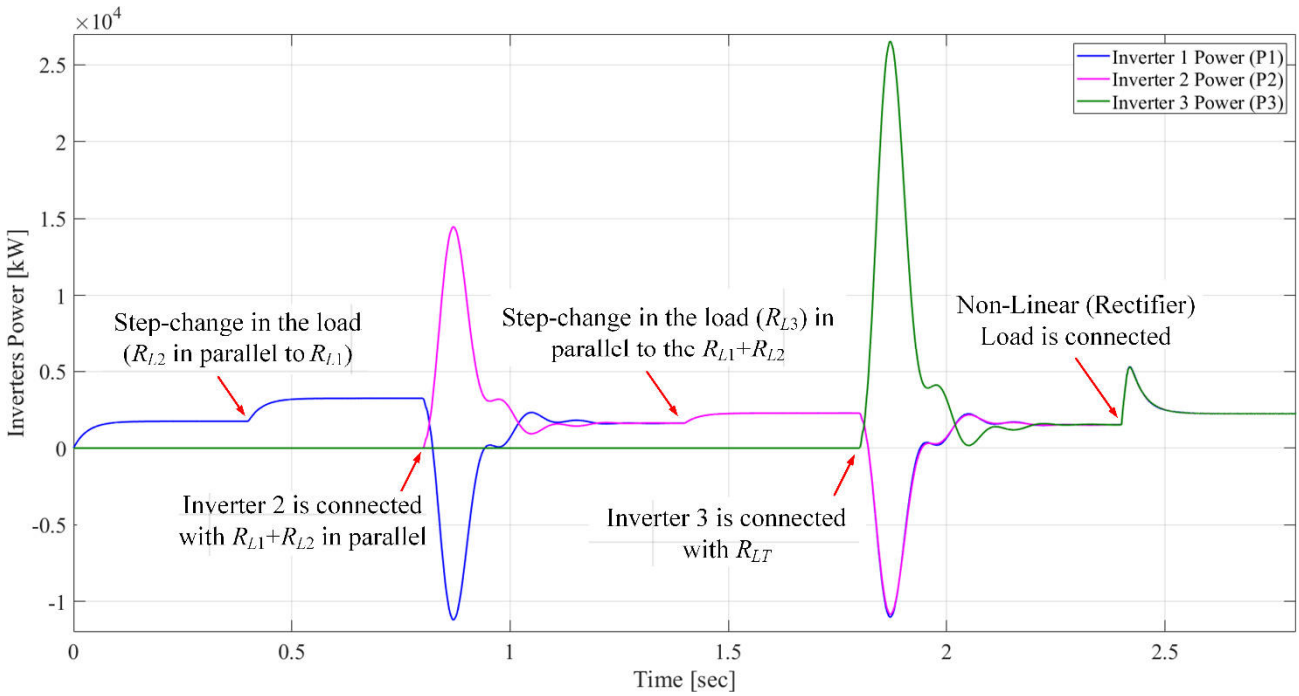

Figure 3.6.8–Power sharing

Table 3.6.1 shows the simulated parameters. The loads R_L are (60/70/120 Ω) connected in parallel to the inverters. Figure 3.6.6 shows the transient response of the three inverters with step changes in the load and connection/disconnection processes. It starts with a single inverter connected to R_{L1}=60 Ω at t= 0s. At t=0.4s, a step-change in the load is applied from R_{L1} =60 Ω to $R_{L1}//R_{L2}$=60//70 Ω = 32 Ω, and at t=0.8s, a second inverter is connected in parallel to the first one. At t=1.4s, a second step change is applied

from 32 Ω to $R_{L1}//R_{L2//}R_{L3}$=29 Ω. The third inverter is connected at t=1.8s. A nonlinear load is connected to the system at t=2.5s. The dynamic performance of the PR+HC control in voltage and current loops can be seen in the zoomed version of the voltages and currents where the load current harmonics are well-damped.

Figure 3.6.7 and Figure 3.6.8 show how the frequency is altered in order to allow the power sharing in inverters. Notice the huge power during the transient and the big frequency change, in the next sections, new methods for improving the transients during connections and disconnections will be developed.

Table 3.6.1 System and LCL Filter Parameters – for simulations

Parameters	Values
Power Stage	
Line-neutral (RMS) voltage, V_g	230 V
Nominal grid frequency f_0	50 Hz
Switching frequency, f_s	10 kHz
Time delay, T_d	150 us
Nominal Active Power	15 kW
Nominal Reactive Power	12 kVAr
Inverter Side Inductance, L	1.5 mH
Inverter Side Resistance, R	100 mΩ
LCL Filter Capacity, C_f	2.2 uF
Load Side Inductance, L_c	0.2 mH
Load Side Resistance, R_c	100 mΩ
INV 1 line impedance Z_1	0.2 + j0.002 Ω
INV 2 line impedance Z_2	0.4+j0.004 Ω
INV 3 line impedance Z_3	0.6+j0.006 Ω
Primary Control	
Droop controller, power measurement cut-off frequency, ω_{CP}	10 Hz
Voltage loop Propoportional Resonant gain, k_{PV}	0.085
Voltage control Integral gain k_{IV}	41.1
Current loop PR gains k_P/R_c	291
Current loop PR gains k_I/R_c	6.10^4
Proportional frequency droop k_{Pdroop}	0.0003 rad/W
Integral frequency droop k_{Idroop}	0.000042 rad/(W.s)
Proportional amplitude droop k_{Qdroop}	0.0006 V/Var
Virtual inductance, L_v	2 mH
Virtual resistance, R_v	0.8 Ω

3.6.5. Experimental validation – Power sharing

An experimental validation was performed using a real-time simulator connected with two inverters and a load. Figure 3.6.9 shows the test bench and Table 3.6.2 summarizes the main parameters of the test. The DC power source feeds the inverters at their DC input port. The real-time simulator delivers the three-phase signals that are injected to the PWM units in each inverter and trigger the inverters' MOSFETs. The three-phase inverters are connected to an LC filter. The grid is formed by two inverters and a load with a switch that can change the load from full load to half and vice versa. The connected loads are inductive-resistive loads. Both inverters can be connected and disconnected to and from the grid in real-time with a switch in series. Figure 3.6.10 shows the detail of the experiments, where four intervals occur. Figure 3.6.10(a) shows the load voltages and currents of the inverter 1 and (b) shows the load voltages and currents of the inverter 2 respectively.

Table 3.6.2 System and LCL Filter Parameters – real-time simulations with hardware in the loop

Parameters	Values
Power Stage	
Peak grid voltage, V_s	50 V
Nominal grid frequency f_0	50 Hz
DC link voltage V_{DC}	100 V
Switching frequency, f_s	20 kHz
Virtual impedance Zv	0.8 + j2 Ω
Filter capacitance, C_f	10 uF
Load R_L	12.5 / 50 Ω

In steady-state operation, the inverter 1 is connected to the grid with half load as shown in Figure 3.6.10. At t=1.5s, the second inverter is connected in parallel to the first

one. At t=2.04s, a step change appears in the load from half load to full load. At t=2.55s, a second step change is done from full load to half load and at t=3.1s, the inverter 1 is disconnected and the inverter 2 is operating alone as shown in Figure 3.6.10. The oscilloscope shows a load step while in the real-time simulator the frequency of each inverter is shown too. Figure 3.6.11 shows the frequency reference from each droop controller in each inverter. Note, the Figure 3.6.10 were extracted from the oscilloscope while Figure 3.6.11 was extracted from the controller (real time simulator).

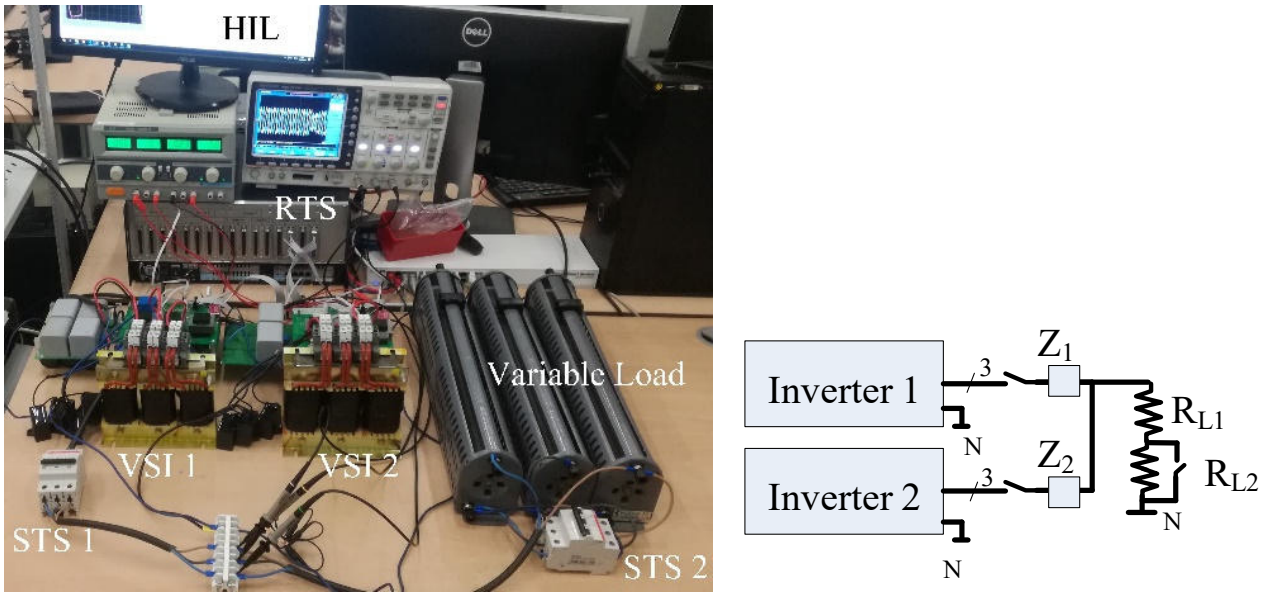

Figure 3.6.9–Experiment of two inverters connected in parallel for power sharing

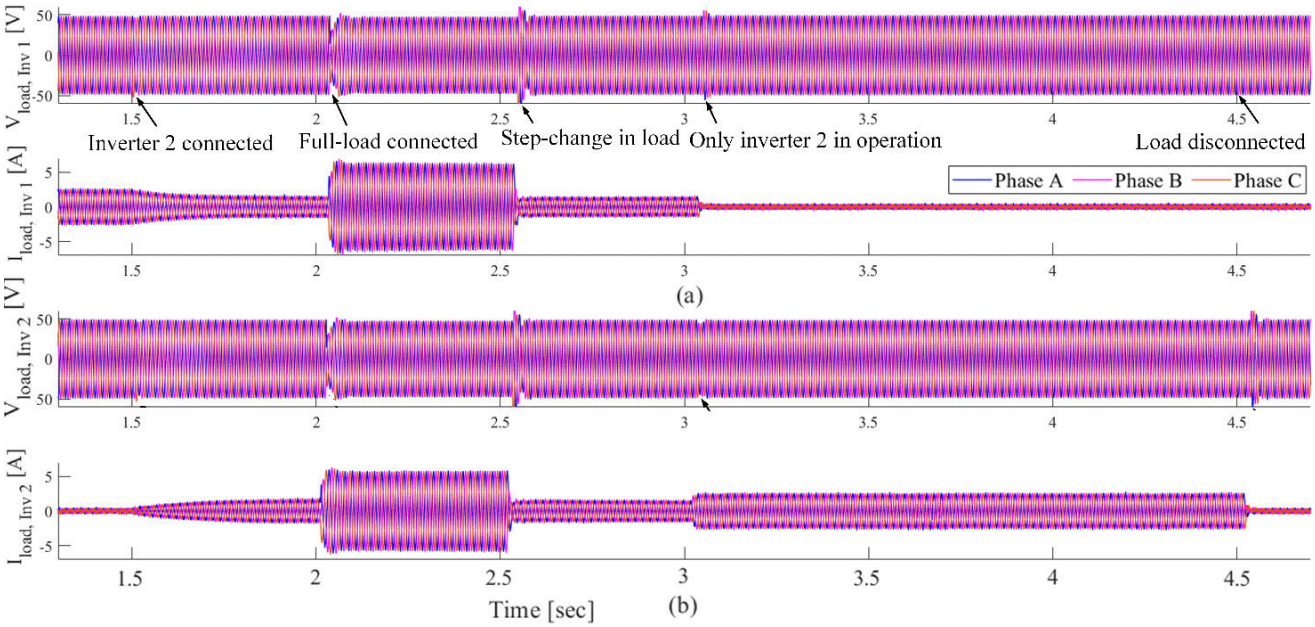

Figure 3.6.10–Current and voltage waveforms from real inverters controlled under real-time simulators

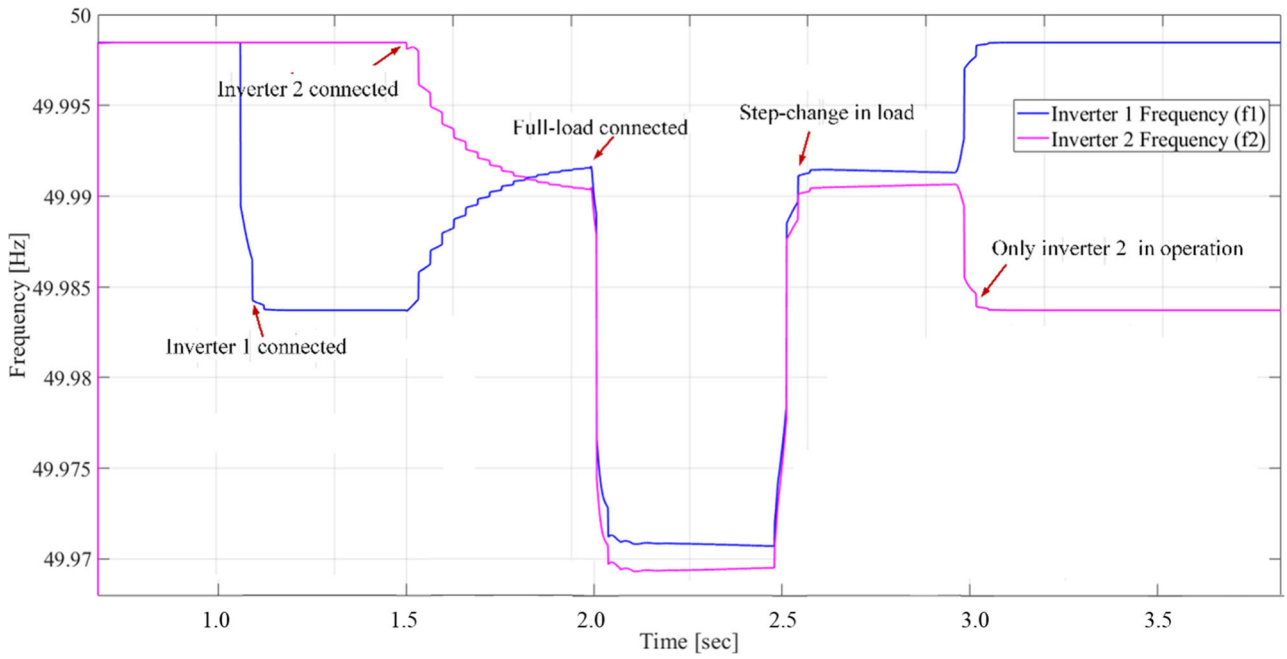

Figure 3.6.11–Frequency response of each inverter from real-time simulator

3.6.6. Summary

In this section, a three-phase inverter with current and voltage control loops was fully modelled. In addition, the droop controller was added for power sharing. The voltage and current controller of the system were designed and modeled using PR controllers with harmonic compensators to achieve almost zero-steady state error and reduced harmonics. A droop control method was used to share the power among the inverters. A virtual impedance has also been implemented in the primary controller to decouple active and reactive powers and to help with the robustness of large variations in the line impedance. Details of virtual impedance will be analyzed in the following sections as well.

Several simulations were performed to test the proposed control loops. For that, different connections and disconnections of inverters in a grid of three inverters and loads were realized to observe how the inverters' controllers react to power changes. Finally, a control-in-the-loop experiments has been performed to validate the design methodology by connecting two real inverters in parallel to the grid and the load. The control was run

in a real-time simulator which has given the commands to the real inverters. The results show that the modeling, the control design and simulations are consistent with the experiments. The details of this section were published in [105, 129].

3.7. New advanced power sharing methods

3.7.1. The reason for a phase limiter in droop mode power sharing methods

As was mentioned before, a grid-forming inverter is a device which behaves as a voltage generator. For sharing the power in the grid, voltage and frequency droop controllers of inverters were proposed to ensure proper power sharing, by imitating the control of synchronous machines in the conventional power systems as was detailed in the previous section [138, 139]. The procedure for power sharing is simple when the inverters are already connected to the grid. However, after the inverter connects to the grid, a transient occurs starting from the point of zero power injection to the steady state with the desired power, frequency and angle. Thus, high currents might be expected due to the frequency changes and angle differences during the connection transient process. This can be seen in Figure 3.6.7 and Figure 3.6.8 from Section 3.6.

Connection and disconnection transients are of great interest in power electronic industry because they can activate the protections or even damage the inverters. Therefore, these transients must be controlled in a way that enables the inverter to increase its power smoothly avoiding any type of high currents and voltages. Several authors have been working on droop control techniques but a formal mathematical analysis on the details of connection of the inverters have not been reported in the literature [140-141].

Researchers have provided solutions for improving the connection transients, including current limiters, virtual-impedance, phase locked loop (PLL) and modified droop-control techniques. Denis *et al.* [142] presented a current limiter during transients for smoothing the connection process, keeping the inverter in grid-forming mode. In

addition, in [143], authors proposed a technique which directly considers the current rise inside the droop controller, limiting the transient currents and smoothing the transients. In [144], a method using a virtual impedance is proposed for smoothing and limiting the current during transients, however the duration of the transients becomes too long. Another improvement in transients was achieved by limiting the current using an adaptive virtual impedance [145, 146]. In [131] a method for limiting the inrush current was also proposed. The method relies on using a high virtual resistance at the instance of connection which is reduced to its nominal value gradually. However, as it will be presented later in this section, the use of the phase limiter further enhances this method allowing for a faster and smoother connection.

Rodriguez *et al.* [147] presented an advanced PLL technique in which the converter changes from grid-forming to grid-following in order to avoid high current transients during the connection to and disconnection from the main grid. A similar approach is presented by Azevedo *et al.* [148] for reconnecting to grid using a DSOGI-FLL (dual second order generalized integrator - frequency locked loop) to match the angle between the main and the inverter frequency but using the DSOGI-FLL the synchronization is quite slow (~800ms).

Canizares *et al.* in [149] have modified the conventional droop control to allow for a better transient response using adaptive techniques. A similar approach is presented in [150] which includes adding a differential term with a damping part to the controller which can enable proper damping of oscillations during step changes in generation or load.

Based on the mentioned literature review, the transients can be improved using current limiters, PLLs, adaptive virtual impedance or advanced droop controllers. As shown before, if carefully designed, the transients can be smoothed to certain extend. However, these approaches do not exploit the fact that the angle difference between the grid and the inverter is a variable that directly defines the amplitude of transients. Therefore, the angle difference seems to be a good variable that can be controlled to limit transient current amplitude. To study this mechanism a suitable model for analysis of the connection process is required, which is currently missing in the existing literature.

Finally, the literature does not provide experimental evidence of the performance of the proposed control schemes.

In this section, an angle difference limiter to better control the output power during transients, keeping it within predefined limits is proposed. An angle difference limiter is defined as a control algorithm which is measuring continuously the phase of the grid at the point of common coupling (PCC) and limits the angle difference between the inverter and the grid. Thus, as the impedance between the grid and the inverter is known, the power is controlled. The grid phase angle measurement can be done by an internal phase locked loop (PLL) or by a phase measurement unit (PMU).

To develop this angle difference limiter, a formal mathematical model suitable for analyses of the grid-forming inverter connection process in weak grids, which consist of other grid-forming inverters with similar characteristics have to be developed. The mathematical model assumes that the inverter is initially synchronized with the grid at the moment of connection, so there is no angle difference between the inverter and the grid. Since the inverter works in grid-forming mode, the inverter goes through the transient period until it reaches its steady state of frequency and angle.

In addition, the formulated mathematical model is used to derive a guidance for the design of the measured power filter in the droop controller. The measured power filter has a relation with the “virtual inertia” in the sense of time-response for changing the inverter’s frequency [141, 151]. Finally, the section validates the proposed diagram using simulations and experiments in real hardware.

To summarize, this section offers the following contributions:

1) It develops a mathematical model for analysis of the inverter connection process and a guideline of the droop control dynamics including filters for measuring power (power filters).

2) It introduces the concept of angle difference limiter. The angle difference is the variable that predominantly defines the transient current amplitude. A PLL or a PMU tracks the angle difference between the inverter and the grid, which is then limited to avoid high power peaks and high current transients improving overall transient performances. The details of this section were published in [37, 118, 136].

This section is organized as follows. Section 3.7.2 reviews the droop control of the converter, analyses the behavior of the inverter in the connection process and proposes a method for selecting the filter in the droop controller. Section 3.7.3 proposes an angle difference limiter in order to protect the inverter to be out of phase and to reduce the current in the transients. This allows reducing time-response in the connection process. Section 3.7.4 and 3.7.5 validate the proposal in a micro grid based on two three-phase inverters. Finally, Section 3.7.6 summarizes the conclusions.

3.7.2. Mathematical model for analysis of inverter connection process

A mathematical model is developed assuming a typical voltage source converter topology. Grid-forming inverters' internal loops, such as current and voltage control loops are omitted and considered ideal in order to focus on the power control loop. Details about internal loops can be found in the previous sections (from 3.2 to 3.6) of this chapter. Figure 3.7.1(a) shows the main blocks of a typical grid-forming inverter: the power stage (voltage source inverter, VSI), voltage and current controllers, droop controller with virtual impedance controllers and power calculators with its own dynamics (power filters). Figure 3.7.1(b) shows the simplified circuit model which will be used in this section.

The droop control works on top of the voltage control loop and also modifies the operational angle of the inverter's controller (θ_{inv}) as it shifts the rotational frame, "dq-frame", according to the delivered power.

The main idea of the droop control is to reduce the frequency of the inverter (ω_{inv}) with the increase of the delivered active power and to reduce the output voltage with the increase of the delivered reactive power. Thus, the well-known droop control main equations can be written as:

$$\omega_{inv} = \omega_0 - G_P(s)P_{inv}, \tag{3.7.1}$$

$$V_{cref} = V_{c\,ref0} - G_Q(s)Q_{inv},$$

where $G_P(s)$ and G_Q are transfer functions that describe the dynamic behavior of measured active and reactive powers or, in other words, the measured power filter transfer function and the controller. In comparison with Section 3.6, it is considered that this transfer function includes the filter and the controller. The controllers are proportional, notice that the equation (3.7.1) is in frequency and not in phase, so the proportional controller here is the integral in Section 3.6, (3.6.9), k_{Idroop}.

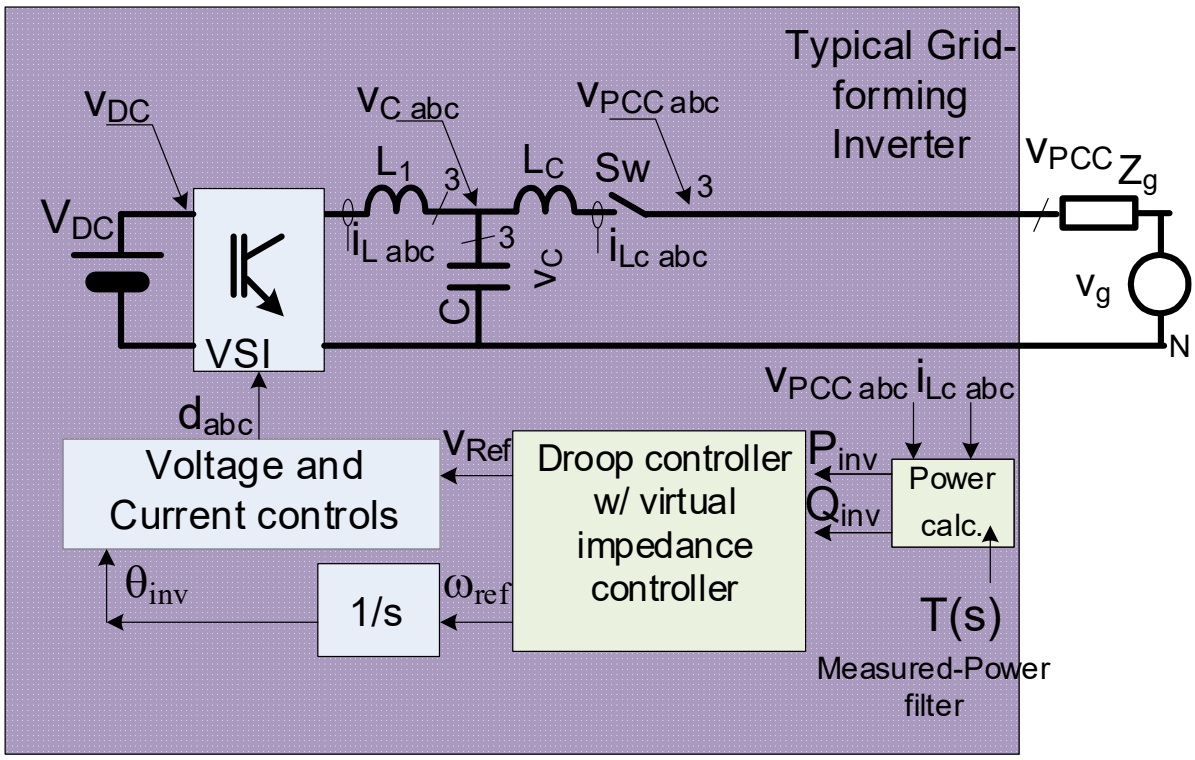

(a)

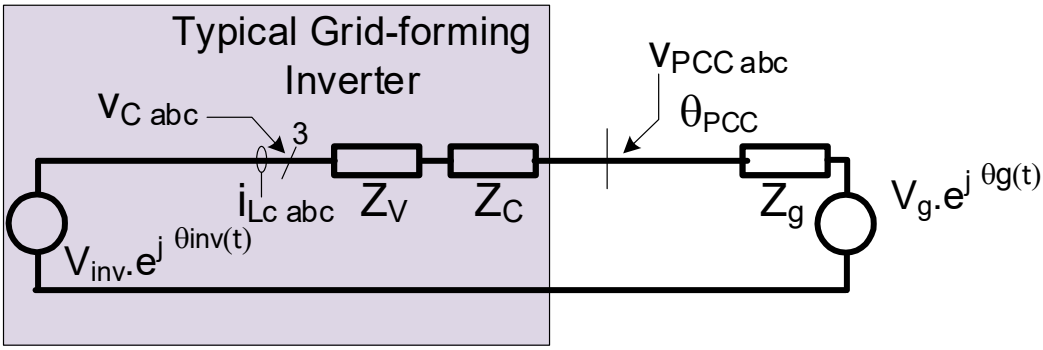

(b)

Figure 3.7.1–(a) Typical grid-forming inverter, (b) simplified output circuit

These transfer functions can be assumed to have a structure of a single-order low-pass filter:

$$G_P(s) = \frac{k_{Idroop}}{\frac{s}{\omega_C} + 1}, \tag{3.7.2.a}$$

$$G_P(s) = \frac{k_{Qdroop}}{\frac{s}{\omega_C} + 1}, \tag{3.7.2.b}$$

where ω_C is the cut-off frequency of the filter and creates a delay between input and output. It acts as virtual inertia [152], expressing the rate of change of the frequency as the inverter's power increases but not as an energy storage device.

Notice that the inverter internal frequency (ω_{inv}) is now a function of the output power and it does not directly depend on the grid frequency (ω_g). Hence, the inverter angle (θ_{inv}) is not equal to the angle at the point of common coupling (θ_{PCC}) and care must be taken to have this angle difference limited to avoid potentially dangerous transients and inverter current peaks.

Inverter's output power model. The inverter's output power is given by the output circuit, the voltages and angles values of the inverter and the PCC. According to the simplified model from Figure 3.7.1(b) the output power equation is:

$$\overline{S_{inv}} = P_{inv} + jQ_{inv} = \frac{\overline{V_{inv}} - \overline{V_{PCC}}}{\overline{Z_c} + \overline{Z_v}} \cdot \frac{\overline{V_{PCC}}^*}{2} = -\overline{S_g}, \tag{3.7.3.a}$$

$$\overline{S_g} = P_g + jQ_g = \frac{\overline{V_g} - \overline{V_{PCC}}}{\overline{Z_g}} \cdot \frac{\overline{V_{PCC}}^*}{2}, \tag{3.7.3.b}$$

where $\overline{Z_c} = r_{Lc} + j\omega_g L_c$ is the coupling impedance composed by a coupling inductance and its internal resistance, $\overline{Z_v}$ is the virtual impedance, which can be defined as a virtual resistor, virtual reactance or a combination of both and $\overline{Z_g}$ is the grid impedance. The upper line indicates complex number and the * is the conjugate of the variable. $\overline{V_{inv}}$, $\overline{V_{PCC}}$, and $\overline{V_g}$ are the complex voltages of the inverter, PCC and grid. The power equation is divided by two (because the voltages are amplitudes and not RMS).

Design criteria for droop coefficients, virtual impedance and filter cut-off frequency. Once the inverter is already designed, only droop coefficients k_{Idroop} and

k_{Qdroop}, virtual impedance Z_v and ω_C are the variables to tune. In this subsection, a brief overview of the inverter parameters will be detailed which can serve as a guideline of the inverter's design.

Eq. (3.7.3.a) can be developed further to see the impact of the angle difference between the inverter and the PCC:

$$P_{inv} + jQ_{inv} = \frac{V_{inv}V_{PCC}\cos(\theta_{inv} - \theta_{PCC}) - V_{PCC}^2}{\overline{Z_c} + \overline{Z_v}} + j\frac{V_{inv}V_{PCC}\sin(\theta_{inv} - \theta_{PCC})}{\overline{Z_c} + \overline{Z_v}}. \tag{3.7.4}$$

This well-known equation indicates that the increase of virtual impedance, Z_v, decreases the output power (active or reactive depending if Z_v is imaginary or real). Moreover, in order to have a decoupled control of active and reactive power using angle difference, $\phi(t) = \theta_{inv} - \theta_{PCC}$, and voltage, it is important to have the sum of the impedance $\overline{Z_c} + \overline{Z_v}$ mostly imaginary. Meaning that $\overline{Z_v}$ could have a negative resistance to increase the X/R ratio of the total impedance.

Figure 3.7.2(a) shows the impact in output power by changing $\overline{Z_c} + \overline{Z_v} \approx jX_v$ and Figure 3.7.2(b) shows the angle difference $\phi(t) = \theta_{inv} - \theta_{PCC}$ as a function of X_v normalized with $Z_{sh} = \frac{V_g^2}{2S_{max}}$. The output power is treated as a parameter. Z_{sh} is considered the short circuit impedance and relates the nominal voltage with the inverter's maximum apparent power. It is used for normalization.

Notice that for the X_v higher than ~$0.3Z_{sh}$, the output power is limited by the overall impedance (Figure 3.7.2(a)). If the virtual impedance is lower than ~$0.3Z_{sh}$, the inverter can reach the maximum power with an angle difference (inverter-grid) lower than 10°.

If during the connection transient, the phase reaches the maximum angle, the inverter will deliver a power higher than the maximum and will trip off. Therefore, an angle difference limiter is proposed in this section, which is constantly measuring the grid angle and limits the inverter's angle. Figure 3.7.3 shows the proposed inverter controller with the angle limiter. It adds an angle difference limiter as a variable saturation block and a phase locked loop (PLL) which is constantly measuring the grid. The PLL can be

replaced by a PMU for higher accuracy. The analysis of the limiter is described in subsection 3.7.3.

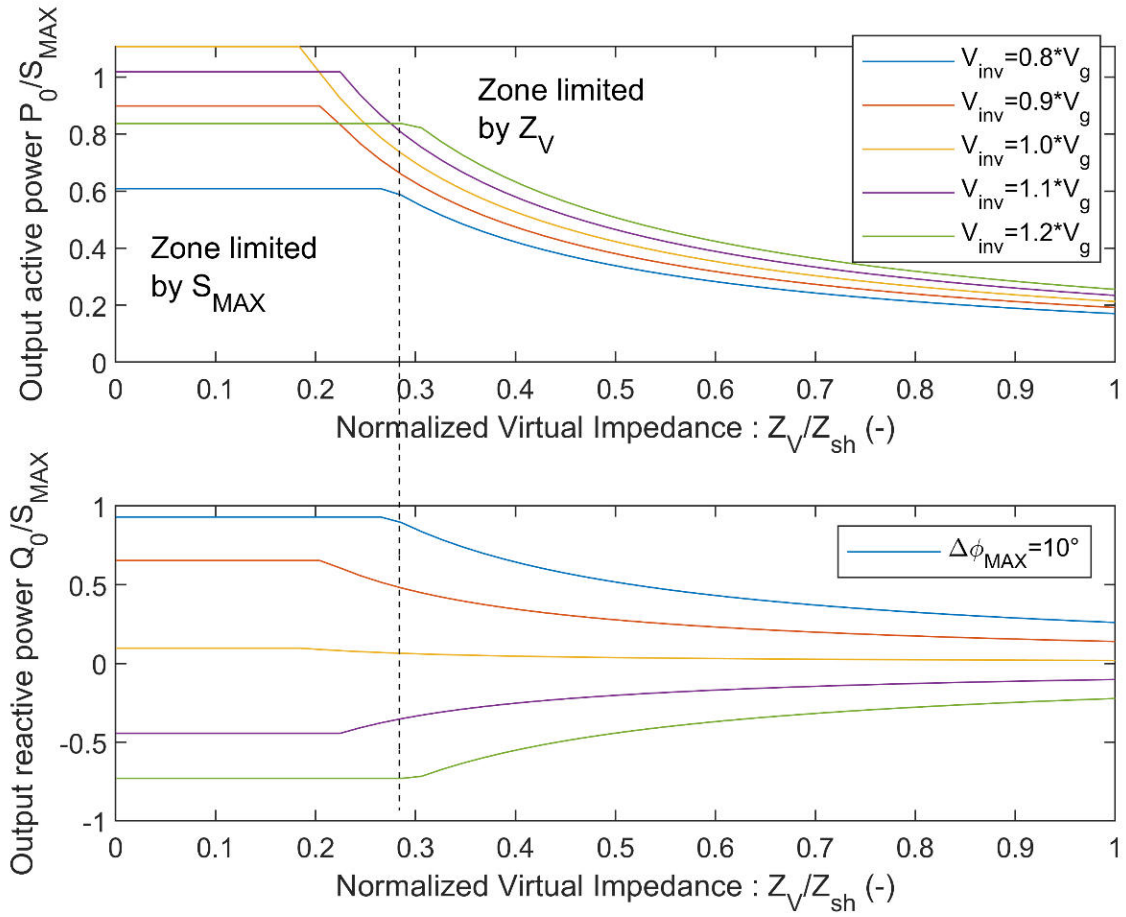

(a)

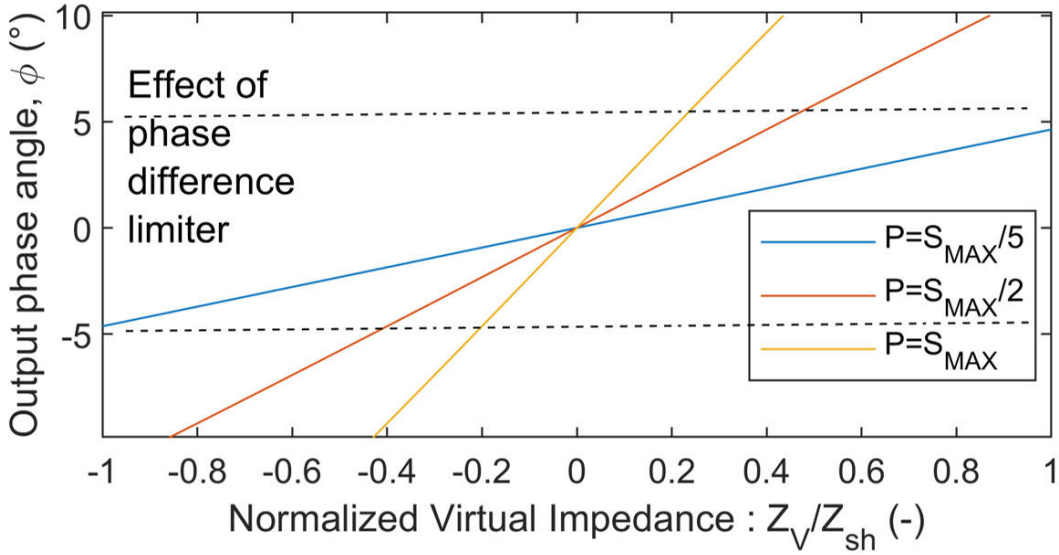

(b)

Figure 3.7.2–(a) Inverter's output power as a function of Z_v and (b) $\theta(t)$- $\varphi(t)$ as a function of Z_v at different output powers

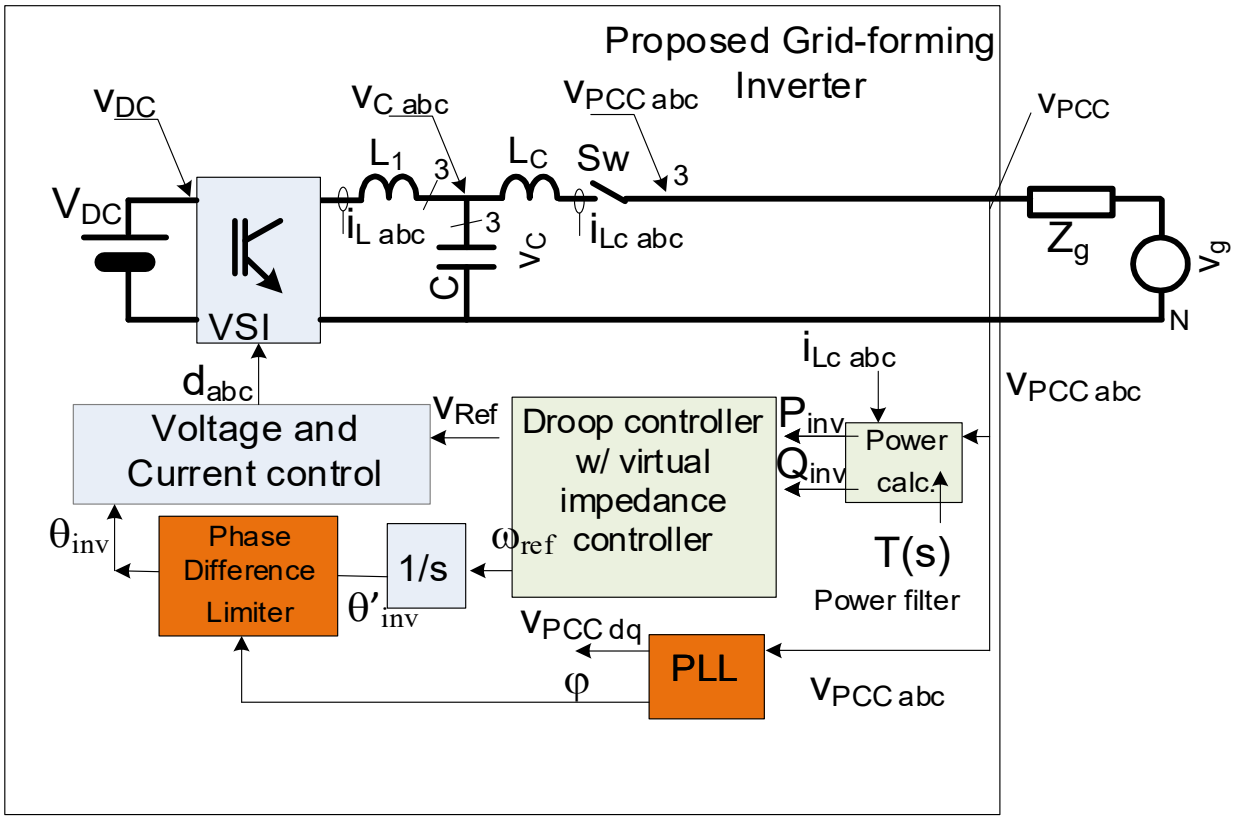

Figure 3.7.3–Modified droop control method

Regarding the power filter design, if the power filter is slow, the inverter's reference frequency will change slowly, so the transient will be slow. Slow changes in frequency are related to big virtual inertia. To analyze the system behavior during transients, a small-signal analysis will be presented to show the impact of the filter and coupling inductance (L_c), where $\overline{Z_c} = r_{Lc} + j\omega L_c$.

Regarding the droop control coefficients, very small k_{Idroop} produces small frequency variations which can be considered as noise in the PLL unit. In other words, the power sharing might be lost. On the contrary, too large k_{Idroop} might cause too large frequency fluctuations. The same occurs with k_{Qdroop}, where large k_{Qdroop} magnifies the impact of the reactive power in the voltage allowing big voltage fluctuations.

In general, k_{Idroop} and k_{Qdroop} can be designed by considering the system in steady-state. By limiting the extreme frequency and voltage variations at nominal active and reactive power, the values are:

$$k_{Idroop} = \frac{\Delta\omega_{MAX}}{P_{MAX}} \tag{3.7.5.a}$$

$$k_{Qdroop} = \frac{\Delta V_{MAX}}{Q_{MAX}}. \tag{3.7.5.b}$$

The virtual impedance, Z_v, and the power filter cut-off frequency must be designed to follow a certain transient but without losing output power range, so Z_v<0.3 Zsh.

The connection process (Small-signal analysis). A critical moment in the inverter operation is the connection transient. In order to perform a smooth connection, inverters first smoothly increase their voltages to reach the grid voltage value by using an internal PLL, which tracks the PCC voltage angle (θ_{PCC}) and amplitude (V_{PCC}). Thus, the inverter, before the connection, has the same voltage and angle of the PCC, so at the moment of connection, the inverter power is equal to zero. In other words, it is working as a grid-following inverter with zero power injection.

Once the inverter is connected and injecting zero power, the mode of the inverter operation is changed to the grid-forming mode. Initially, the inverter's dq-frame is aligned with the PCC dq-frame due to the synchronization: θ_{inv} (t=0) = θ_{PCC} (t=0).

Later, due to grid-forming mode, the inverter dq-frame rotates slightly faster than the grid frame, increasing the phase difference and inverter's output power. This process can be summarized in four steps:

i) Starting point, no power is delivered to grid (grid-following mode).

ii) The phase in the inverter will increase because of the higher inverter frequency according to (3.7.1): $\theta_{inv}(t > 0) > \theta_{PCC}(t > 0)$ for t<T_1.

iii) The power will increase and the frequency will reduce due to the droop control.

iv) Finally, the equilibrium and the power sharing will be achieved, keeping the phase difference ($\theta_{inv}(t \to \infty) - \theta_{PCC}(t \to \infty)$) constant.

How the grid will arrive to that equilibrium is the one of the motivations of this section.

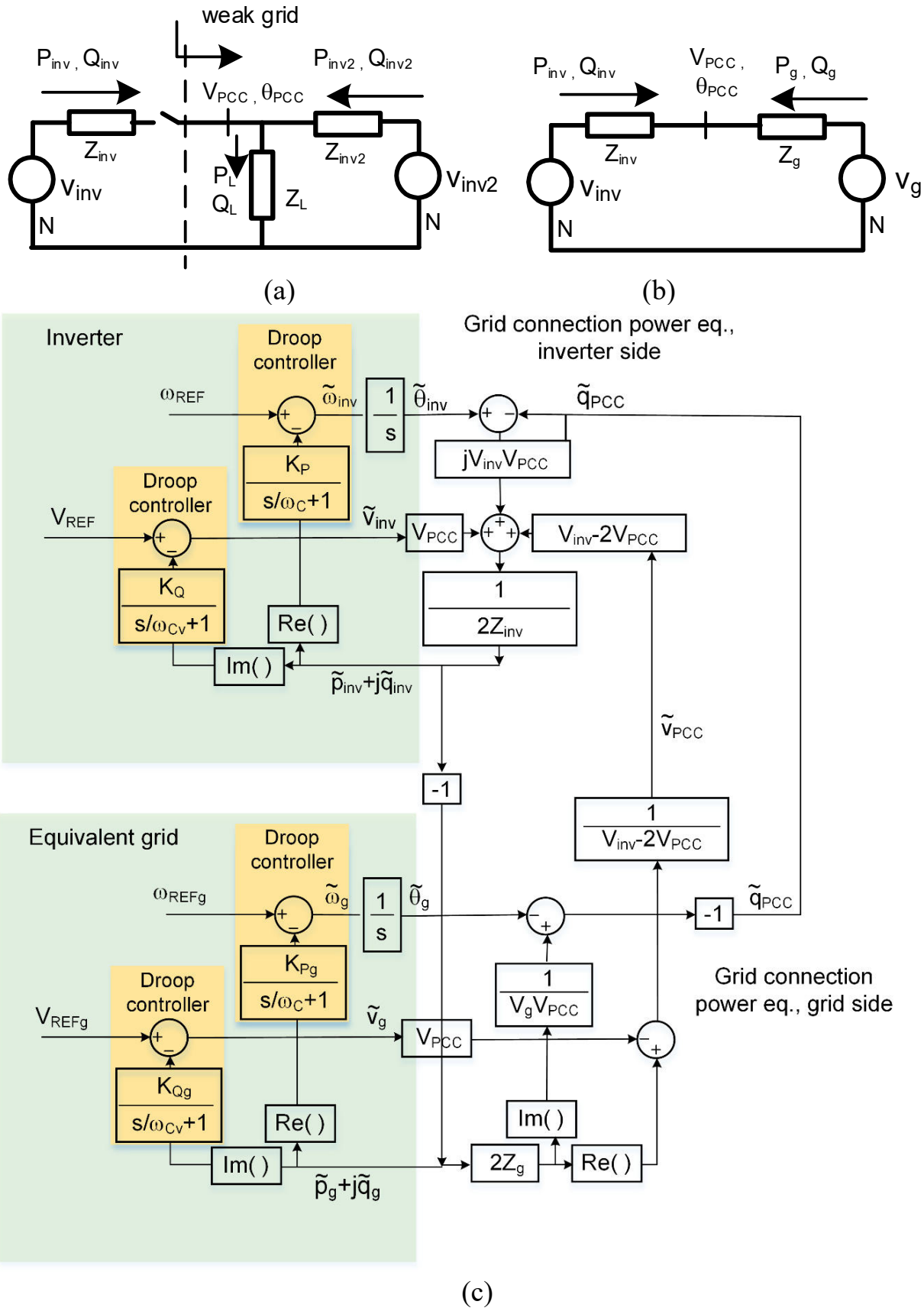

(c)

Figure 3.7.4–Simplified grid for inverter connection: (a) grid with a generator and a load, (b) equivalent circuit of the grid, (c) small-signal model of an inverter in droop control connected to the grid

In order to understand the transient process, a small-signal model was developed by linearizing (3.7.4) around the operating points. Two operating modes are of interest: first, when the phase limiter is not active and second, when the phase-limiter is active. For linearizing (3.7.4), small perturbations were considered around a steady-state point so:

$$p_{inv}(t) = \langle P_{inv} \rangle + \tilde{p}_{inv}(t) \tag{3.7.6.a}$$

$$q_{inv}(t) = \langle Q_{inv} \rangle + \tilde{q}_{inv}(t) \tag{3.7.6.b}$$

$$\omega_{inv}(t) = \langle \omega_{inv} \rangle + \tilde{\omega}_{inv}(t) \tag{3.7.6.c}$$

$$V_{inv}(t) = V_{inv} + \tilde{v}_{inv}(t) \tag{3.7.6.d}$$

where in the initial transient process, t=0, we consider $\langle P_{inv} \rangle = 0,\ \langle Q_{inv} \rangle = 0, \langle \omega_{inv} \rangle = \omega_0$ and $V_{inv} = V_g$. In addition, it is considered two cases: a simple grid with two inverter connections in droop control mode (weak grid) and an equivalent grid of several inverters in droop control mode (strong grid).

For analyzing weak grids, we will consider the connection with two inverters that feed a load. In other words, the "weak" grid is another inverter and a load as Figure 3.7.4.

Weak-grid – Active power analysis. Figure 3.7.4 (a) shows the equivalent circuit of a weak grid. It consists of an inverter (inverter 2) and a load. The inverter under test will be connected to this weak grid. This circuit can be simplified to have only two sources as shown in Figure 3.7.4 (b). The parameters from the simplified grid side are due to the combinations of the load and the inverter 2 and they are:

$$\bar{v}_g = \frac{\bar{Z}_L}{\bar{Z}_L + \bar{Z}_{inv2}} \bar{v}_{inv2} \tag{3.7.7.a}$$

$$\omega_g = \underbrace{\omega_0 - \frac{k_{Idroop\ g}}{\frac{s}{\omega_C} + 1} P_L}_{\omega_g = \omega_{0\ g} - G_{P\ g}(s) p_g} - \frac{k_{Idroop\ g}}{\frac{s}{\omega_C} + 1} p_g = \tag{3.7.7.b}$$

$$v_{gref} = \underbrace{V_{c\ ref} - G_{Q\ g}(s) Q_L}_{v_{gref} = V_{g\ ref} - G_{Q\ g}(s) q_g} - k_{Qdroop\ g} G_Q(s) q_g = \tag{3.7.7.c}$$

$$\bar{Z}_g = \frac{\bar{Z}_L \bar{Z}_{inv2}}{\bar{Z}_L + \bar{Z}_{inv2}}. \tag{3.7.7.d}$$

A weak grid has not only a grid impedance comparable with the inverter output impedance but also has a droop coefficient comparable with the inverter's droop coefficient. For a strong grid, grid droop coefficient and impedance are much smaller than the inverter under test.

It is considered that, in general, the parameters of the grid and the inverter are different, such as droop coefficients, virtual and coupling impedances. Thus, $\overline{Z_g} \neq \overline{Z_c} + \overline{Z_v} = \overline{Z_{inv}}$. However, to simplify the math analysis, the power filters are equal in both the inverter and the grid, following (3.7.2). A more advanced analysis can include different transfer functions. By linearizing (3.7.3) and using Laplace transform, it brings:

$$\begin{aligned}\tilde{p}_{inv}(s) + j\tilde{q}_{inv}(s) \\ &= \frac{V_{PCC}.\tilde{v}_{inv}(s)}{2\overline{Z_{inv1}}} + \frac{(V_{inv} - 2V_{PCC}).\tilde{v}_{PCC}(s)}{2\overline{Z_{inv1}}} \\ &+ j\frac{V_{PCC}.V_{inv1}.\left(\widetilde{\theta_{inv}}(s) - \widetilde{\theta_{PCC}}(s)\right)}{2\overline{Z_{inv}}}.\end{aligned} \tag{3.7.8}$$

Notice that, instead of simplifying the circuit by adding the grid and the inverter impedances in Figure 3.7.4 (b), it was preferred to have them independent because V_{PCC} and θ_{PCC} can always be measured but the voltage and the angle of the grid cannot because it is an artificial model.

The main block diagram for this analysis is presented in Figure 3.7.4 (c), which shows all of the relations between the inverter and the grid. The angle is the integral of the frequency, so:

$$\theta_{inv}(s) = \frac{\omega_{inv}(s)}{s}, \text{ and } \theta_g(s) = \frac{\omega_g(s)}{s}. \tag{3.7.9}$$

The droop control method in (3.7.1) adds the relation between the inverter's output power, output voltage and frequency. The power in the grid side will be the opposite to the power of the inverter side, following Figure 3.7.4 (b):

$$p_g = -p_{inv} \; and \; \tilde{p}_g = -\tilde{p}_{inv}. \tag{3.7.10}$$

Considering (3.7.1), (3.7.2) and (3.7.9), the inverter's angle can be obtained using Figure 3.7.4 (c) as:

$$\theta_{inv}(s) = \frac{\omega_0 - k_{Idroop}\tilde{p}_{inv}(s)}{\left(\frac{s}{\omega_C} + 1\right)s}, \tag{3.7.11}$$

and the grid angle (considering that it is another inverter):

$$\theta_g(s) = \frac{\omega_{0g} - k_{Idroop\,g}\,\tilde{p}_g(s)}{\left(\frac{s}{\omega_C} + 1\right)s}, \tag{3.7.12}$$

where $p_{inv} = 0 + \tilde{p}_{inv}(s)$. The angle difference can be extracted from (3.3.11) and (3.7.12) as:

$$\Delta\theta(s) = \theta_{inv} - \theta_g = \frac{-\left(k_{Idroop} + k_{Idroop\,g}\right)\tilde{p}_{inv} + \omega_0 - \omega_{0g}}{\left(\frac{s}{\omega_C} + 1\right)s}. \tag{3.7.13}$$

In addition, the inverter's output power is a function of the angle difference according to (3.7.8), neglecting, in this first model, the effect of the voltage, the transfer function of the angle difference at the connection moment can be obtained. The inverter's output power becomes:

$$\tilde{p}_{inv} = \frac{V_{inv1}V_{PCC}}{2X_{inv}}\phi(s) = S_{sh}\phi(s), \tag{3.7.14}$$

where S_{sh} is defined as the power in the output reactance in a short circuit condition, $\phi(s) = \theta_{inv} - \theta_{PCC}$ and the power from the grid is:

$$\tilde{p}_g = -\tilde{p}_{inv} = \frac{V_g V_{PCC}}{2X_g}\left(\theta_g - \theta_{PCC}\right) \tag{3.7.15}$$

and also:

$$\tilde{p}_{inv} = \frac{V_{inv1}V_g}{2(X_{inv} + X_g)}\Delta\theta(s) = S_{shT}\Delta\theta(s). \tag{3.7.16}$$

Thus:

$$\Delta\theta(s)\left[\left(\frac{s}{\omega_C} + 1\right)s + \left(k_{Idroop} + k_{Idroop\,g}\right)S_{shT}\right] = \omega_0 - \omega_{0g}. \tag{3.7.17}$$

In which the solution is:

$$\Delta\theta(s) = \frac{\omega_C.\left(\omega_0 - \omega_{0g}\right)_{step}}{(s+p_1)(s+p_2)} \tag{3.7.18.a}$$

where

$$p_{1,2} = -\frac{\omega_C}{2} \pm \frac{\omega_C}{2}\sqrt{1 - \frac{\left(k_{Idroop} + k_{Idroop\,g}\right)S_{shT}}{\omega_C}}. \tag{3.7.18.b}$$

If $\omega_C > \left(k_{Idroop} + k_{Idroop\,g}\right)S_{shT}$, two poles are in the real negative axis, therefore an oscillating behavior in $\Delta\theta$(t) and in the power transfer between the grid and the inverter will not be expected.

On the one hand, increasing the filter frequency, ω_C, will detect high frequency harmonics, reduce the equivalent virtual inertia and perturb the grid frequency faster. On the other hand, a low ω_C will cause the poles to become complex conjugate with an oscillating time-response. Therefore, it is important to have ω_C higher than $\left(k_{Idroop} + k_{Idroop\,g}\right)S_{sh}/2$ but not very high.

Unfortunately, $\Delta\theta$ is unknown, but what we can obtain ϕ based on PCC and inverter angles and we know that:

$$S_{sh}\phi(s) = S_{shT}\Delta\theta(s), \tag{3.7.19}$$

Thus,

$$\phi(s) = k\Delta\theta(s) = \frac{S_{shT}}{S_{sh}}\Delta\theta(s) \approx \frac{X_{inv}}{X_{inv} + X_g}\Delta\theta(s) = k\Delta\theta(s). \tag{3.7.20}$$

Notice that when X_g is small, $\phi \approx \Delta\theta$, which is the case of a strong grid. On the contrary, if X_g is comparable with the inverter impedance, the effect of the grid is notable (weak grid).

In time domain, the angle difference is:

$$\phi(t) = \frac{\tilde{p}_{inv}}{S_{sh}} = \frac{k\Delta\omega(0)}{\left(k_{Idroop} + k_{Idroop\,g}\right)S_{sh}}\left[1 - e^{-\alpha t}\cos(\beta t)\right] + \frac{k\Delta\omega(0)\left[1 - \frac{2\omega_C}{\left(k_{Idroop} + k_{Idroop\,g}\right)S_{sh}}\right]}{\beta}e^{-\alpha t}\sin(\beta t), \tag{3.7.21}$$

where $\alpha = \frac{\omega_C}{2}$, $\beta = \frac{\omega_C}{2}\sqrt{1 - \frac{(K_P+K_{Pg})S_{sh}}{\omega_C}}$ and $\Delta\omega(0) = (\omega_0 - \omega_{0g})$ is the initial frequency difference between the inverter and the grid. From (3.7.21), the transient behavior can be obtained, particularly the maximum angle difference is of interest because it is proportional to the output power. Thus, it should be kept below the maximum power output. Figure 3.7.5 shows the behavior of a complex-conjugate solution. The maximum angle difference is presented as a red line according to (3.7.2), considering that the maximum power is due to the ϕ variation. Thus, the output power is proportional to ϕ (valid for small ϕ). Notice that even if the output power in steady state is much lower than the maximum, in the transients due to ϕ variation, the maximum power can be reached. For limiting this, an angle difference limiter is proposed, which always tracks the θ_{PCC} using a phase locked loop, and using that, the inverter angle, θ_{inv} is limited to the $|\theta_{inv} - \theta_{PCC}| < \phi_{MAX}$. Details will be explained in subsection 3.7.3.

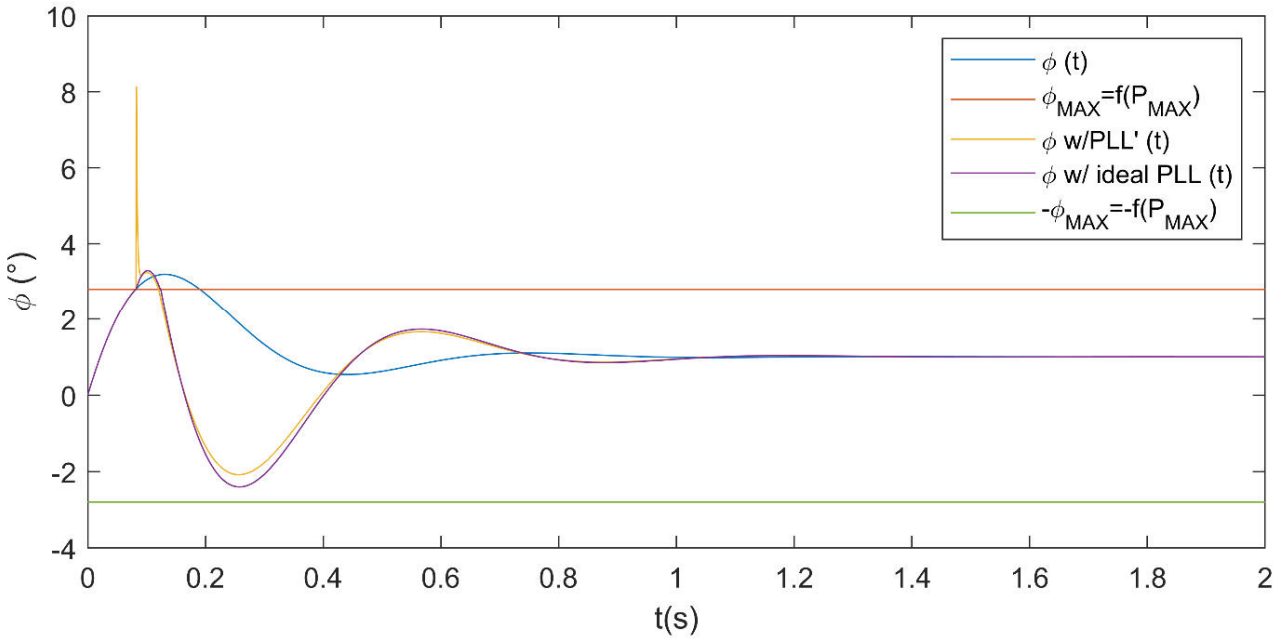

Figure 3.7.5–Phase difference transient in the moment of connection

In this analysis, (3.7.17) and (3.7.21) consider the simplest case where the total impedance is completely inductive: $\overline{Z_g} + \overline{Z_c} + \overline{Z_v} \approx jX_T$ and the real inductance (Z_c) is neglected masked by the virtual reactance. A more complex model that assumes $\overline{Z_g} +$

$\overline{Z_v} + \overline{Z_C} = (R_T + sL_C) + jX_T$ adds higher order poles. Thus, the more advanced transfer function is:

$$\phi(s) \approx \frac{k\left(\omega_0 - \omega_{0g}\right)_{step}}{\left[1 + \left(\frac{sL_C}{2X_T} + \frac{R_C}{2X_T}\right)^2\right]\left(\frac{s}{\omega_C} + 1\right)s + \left(k_{Idroop} + k_{Idroop\,g}\right)S_{shT}}. \tag{3.7.22}$$

In this case, two more poles appear, but they do not change much their position with ω_C, as Figure 3.7.6(a) shows. They are almost constant at:

$$p_{3,4} \cong -\frac{R_C}{L} \pm j\frac{2X_T}{L}. \tag{3.7.23}$$

In order to avoid the effect of these poles, real and imaginary parts must be large. Furthermore, it is clear that that virtual impedance diminishes the importance of these poles. As Figure 3.7.6 shows, the effect of the inductance generates a pole close to the jω-axis, which can be damped using a virtual impedance with a real part. Thus, on one hand, it is good to have a virtual reactance to reinforce the decoupling between P-ω and Q-V loops, however, in order to damp the oscillations a resistive impedance is also desirable. A reasonable trade-off is to have a reactive part at least 5 times bigger than the real part, so $Z_T \approx jX_T$.

To analyze the coupling effect between active and reactive power, an even more accurate model is required. This model is too complicated to express in a single transfer function, but the root locus was computed and shown in Figure 3.7.6(b). This model includes the interaction (coupling) between active and reactive powers. Due to that also a fifth pole appears in the negative real axis. The conclusion from this root locus analysis is that the fundamental poles (p_1 and p_2) are affected by ω_C. The impedance poles (p_3 and p_4) do not change much with ω_C, as shown in Figure 3.7.6(a) and Figure 3.7.6(b). However, they will change as R_C, L and X_T change as in (3.7.22). Finally, the coupling effect can be understood as a side effect.

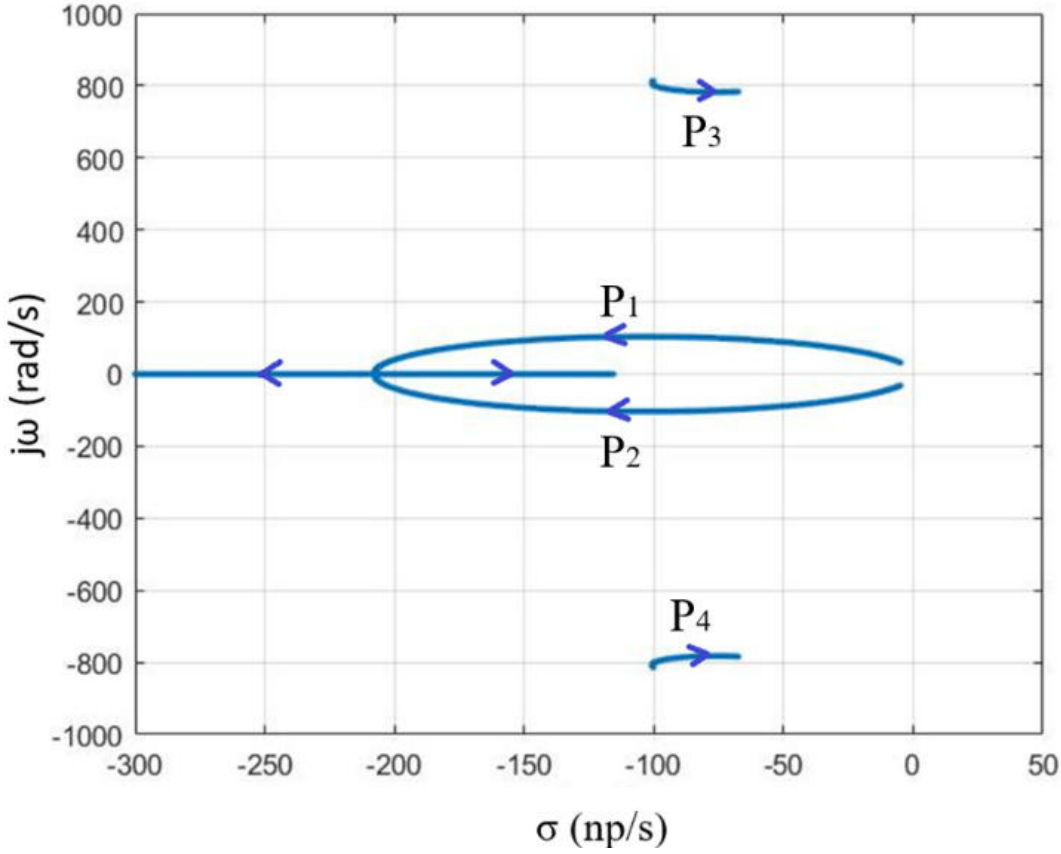

(a)

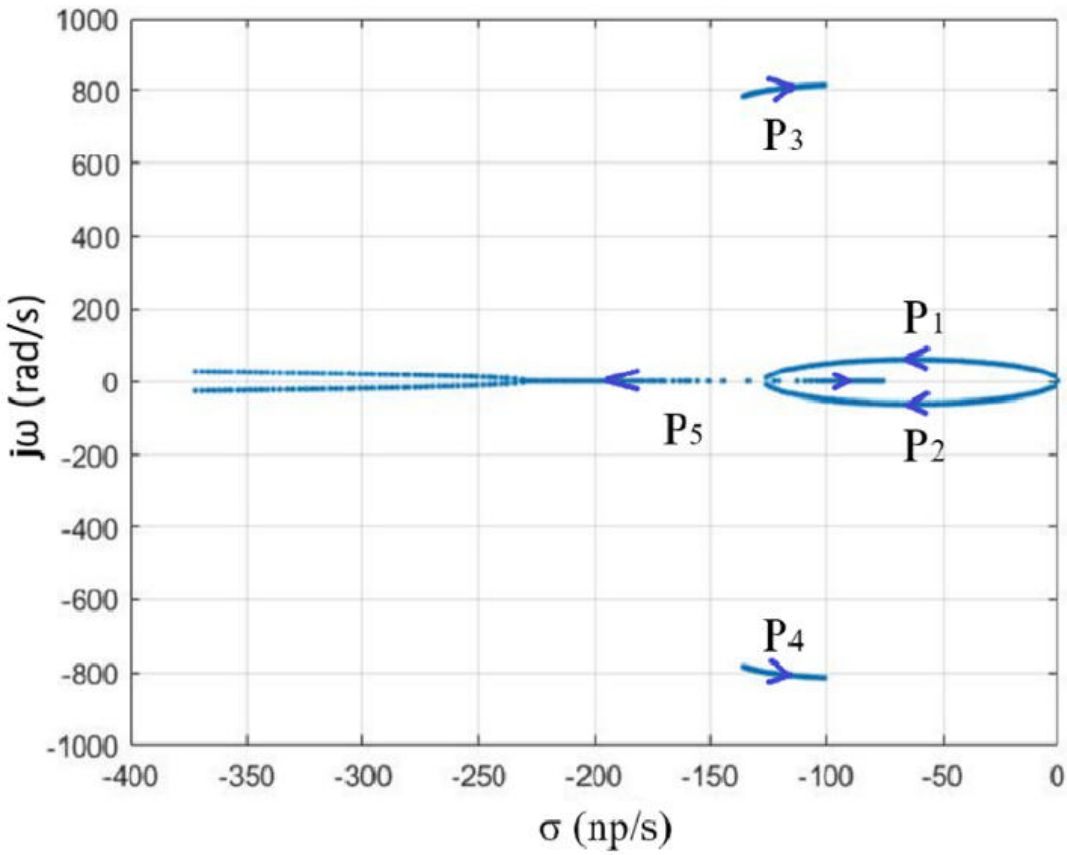

(b)

Figure 3.7.6–Root-locus as a function of (a) filter cut-off frequency (ω_C) (simplified model) eq. (22), (b) filter cut-off frequency (ω_C) (advanced model)

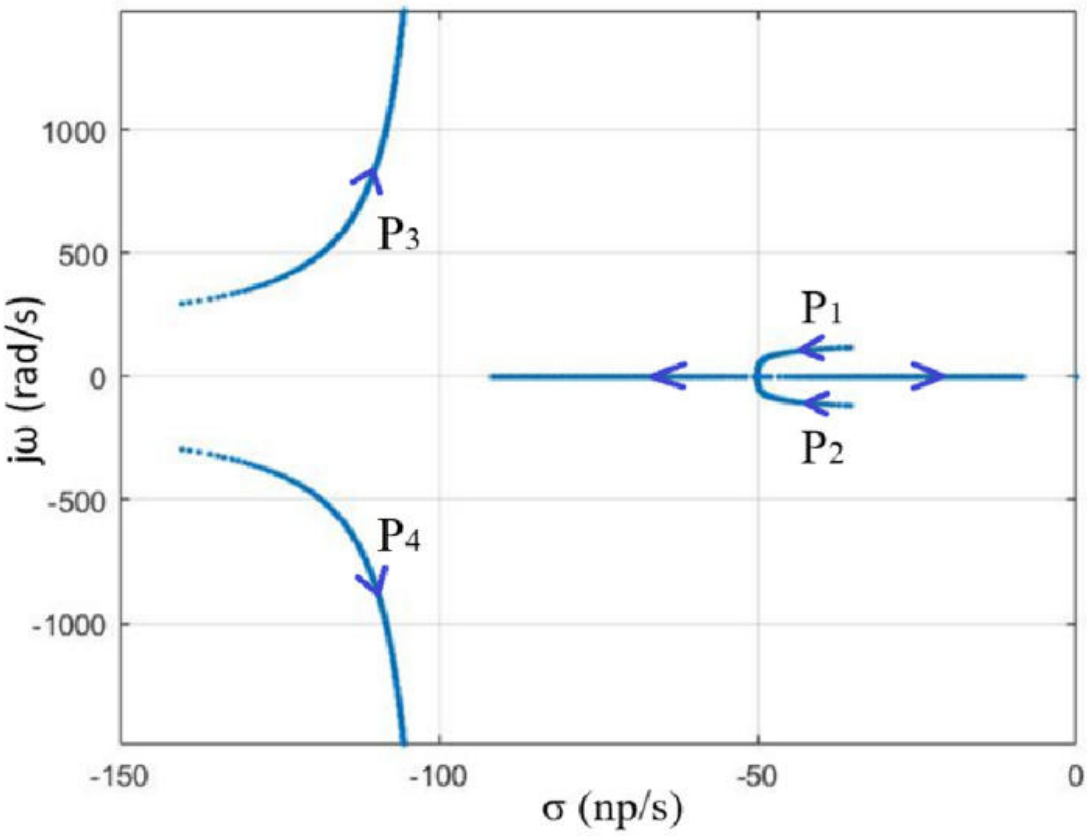

(a)

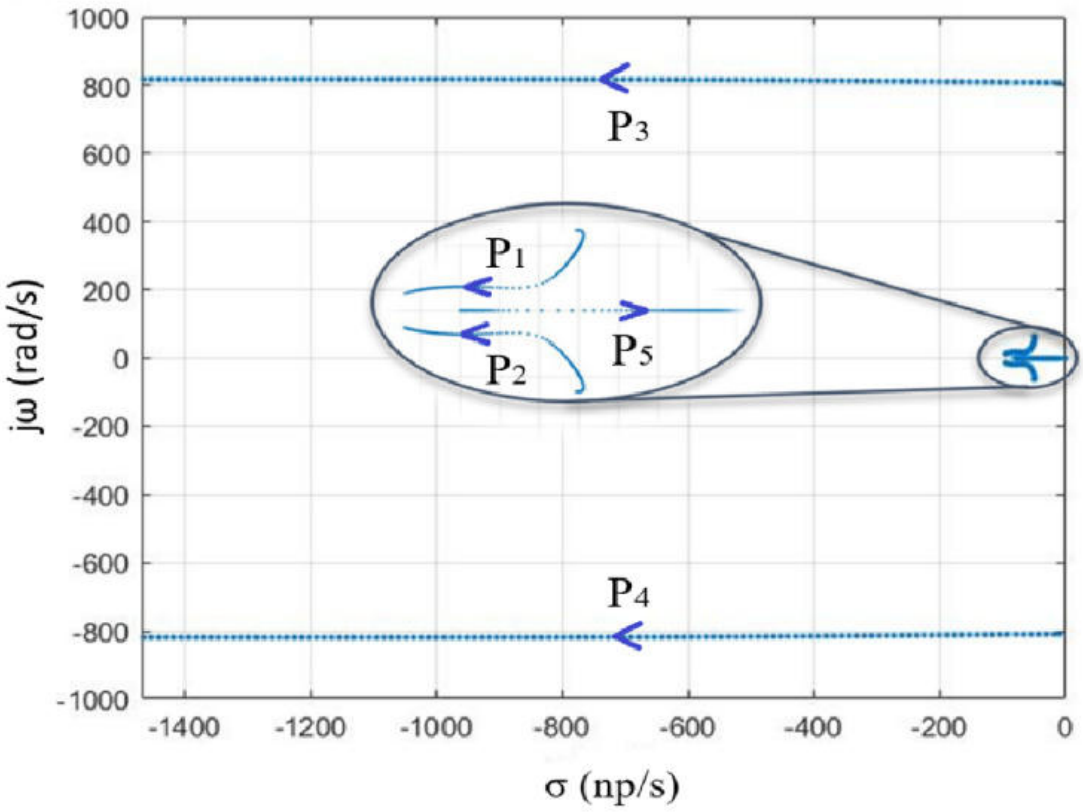

(b)

Figure 3.7.7–Root-locus as a function of (a) total (including virtual) reactance (X_T) at fixed resistance of 0.02, (b) virtual resistance (R_C)

In Figure 3.7.7(a) a large range of virtual reactance change is shown [0.314 – 15.7] Ω while virtual resistance is fixed at 0.02 Ω and the cut-off frequency of the power filter is ω_C =100 rad/sec. In Figure 3.7.7 (b), a large range of virtual resistance change is shown [0.02 – 10] Ω with a fixed virtual reactance of 1 Ω and a power filter cut-off frequency of ω_C =100 rad/sec. As shown in Figure 3.7.7 (a), the change of the poles with regards to the change in the virtual inductance will have a main effect in the imaginary axis. However, with the increase of virtual resistance, the poles will have a more negative real component as shown in Figure 3.7.7 (b). Thus, the system becomes more stable. This is also validated in the subsection 3.7.4 where the effect of virtual resistance with regards to stability is highlighted.

Weak grid – reactive power sharing. Following the same analysis, the reactive power transfer function is obtained based on Figure 3.7.4(c):

$$q_{inv}(s) \approx \frac{\frac{V_{PP}}{2X_{inv}}\left(V_{REF} - V_{REFg}\right)_{step}}{1 + \frac{\left(k_{Qdroop} + k_{Qdroop\,g}\right)}{\left(\frac{s}{\omega_{Cv}} + 1\right)} \frac{V_{PCC}}{2\left(X_{inv} + X_g\right)}}. \tag{3.7.24}$$

In this simplified transfer function, the response time is controlled by ω_{Cv}, which is the cut-off frequency of the reactive power filter in the droop controller. This model, (3.7.24), is simplified because it neglects the coupling between active and reactive power and the real-part of the impedance. Similar study as in case of active power can be performed, following the same procedure. Notice that at the initial state, t=0 ($s \to \infty$), the inverter's reactive power is $\left(V_{REF} - V_{REFg}\right)\frac{V_{PP}}{2X_{inv}}$ and after the transient the power sharing is achieved ($s \to 0$) based on $k_{Qdroop} + k_{Qdroop\,g}$.

Strong grid – active power analysis. If the grid is more complex, with several inverters and loads distributed around the grid, an equivalent circuit can always be obtained with one generator, one complex impedance, a droop control with a reference and a droop coefficient with a certain dynamic behavior.

The equivalent impedance will be the output impedance of the grid that the inverter "sees" from the PCC. The voltage generator values will follow the Thevenin theorem. In addition to that, the reference frequency and droop coefficients will be considered as:

$$\omega_{0\,g} = \omega_0 - G_{Pg}(s)P_{LTotal} \tag{3.7.25.a}$$

and

$$\left[G_{Pg}(s)\right]^{-1} = \sum_{i=1}^{N}\left[G_{P(i)}(s)\right]^{-1}, \tag{3.7.25.b}$$

where $G_{P(i)}$ represents the dynamics of the i-th generator and its droop coefficient. If the equivalent parameters (impedances and droop coefficients) are much smaller than those of the inverter under test, the grid is strong, otherwise is weak.

The power sharing equation follows (3.7.20) and (3.7.21) in the strong-grid case, with k equals to one. The dynamics are mainly determined by the inverter impedance and not by the grid contribution. However, the power sharing accuracy might be affected if k_{Idroop} (of the inverter) is much bigger than the equivalent grid droop coefficient $k_{Idroop\,g}$.

Again, this is a simplified model, the full model must include grid impedance effects in the output power equation (see Figure 3.7.3 and Figure 3.7.4(c)). If the grid impedance has high order terms, they will appear in the output power equation and will modify the transient processes. However, in strong grids, the grid impedance is considerably smaller than the inverter impedance. Thus, the inverter impedance is dominant, and this effect can be neglected.

If the grid is weak, the equivalent grid impedance and the inverter's impedance can be joined, and they will produce high order effects, thus:

$$\phi(s) \approx \frac{k\left(\omega_0 - \omega_{0g}\right)}{\left[1 + \left(\frac{Z_g(s) + Z_C(s) + R_v}{X_v}\right)^2\right]\left(\frac{s}{\omega_C} + 1\right)s + \left(k_{Idroop} + k_{Idroop\,g}\right)S_{shT}}. \tag{3.7.26}$$

This equation is the same as (3.7.17) but considering that the grid impedance cannot be considered as "$r + \mathrm{j}\omega\mathrm{L}$" and added to the coupling impedance Z_C.

The effects of the higher order poles can be mitigated using the virtual resistance and virtual reactance as (3.7.22) shows, if X_v and/or R_v are much bigger than $Z_g(s)$. Thus, a value that is small enough to not limit the output power but as big as possible to minimize the effects of the higher order poles of a grid impedance is desired. The same procedure can be done for the reactive power analysis. Notice that the virtual resistance plays an important role for damping high frequency oscillations produced by the grid (or line) impedance.

3.7.3. Introduction of phase limiter

After having modelled precisely the transient process, the effect of each element was described in detail and the impact of different virtual impedances and power filter values. In addition, it was noticed that the phase change behavior during the transients directly affects to the delivered power. This can produce high power peaks and destroy the inverters.

For mitigating this, a phase limiter is introduced. It is a control block which is based on the internal PLL but it can also use a PMU instead. Using the PLL, the phase at the point of common coupling (PCC) is measured, and can be used to limit the dq-frame angle reference of the inverter with respect to PCC dq-frame, which is not linked anymore with the grid frequency and is following its own frequency because it is working in grid-forming mode. The phase limiter and a PLL for measuring the θ_{PCC} are shown in Figure 3.7.3. Then, the phase limiter limits the difference:

$$|\theta_{inv} - f_{PLL}(\theta_{PCC})| = |\hat{\phi}| < \phi_{LIM} \tag{3.7.27}$$

and gives the new value to the inverter phase. The phase difference $\hat{\phi}$ is not exact, ϕ, because of the PLL dynamics represented as $f_{PLL}(\theta_{PCC})$. A PLL in Laplace domain can be roughly represented as:

$$F_{PLL}(s) \approx \frac{\frac{s}{\omega_z}+1}{\left(\frac{s}{\omega_{PLL}}\right)^2+\frac{s}{\omega_{PLL}}+1}. \tag{3.7.27}$$

This model does not contain the effect of the coupling line impedance that can destabilize the transfer function due to a zero in the right half-plane of the s-domain (see Section 3.5 – control in dq-frame).

The limiter controls the difference between the measured grid angle and the inverter angle. If that angle becomes too big, the inverter frequency will follow the grid frequency. This will directly impact on the phase dynamics during the transients if the angle will be higher than the limits. So, when the phase difference reaches the limits the power output will be:

$$\bar{S}_{LIM} = \frac{V_{inv}(t)e^{j\phi_{LIM}} - V_{PCC}}{\overline{Z_c}+\overline{Z_v}} \cdot \frac{V_{PCC}^*}{2}. \tag{3.7.28}$$

Thus, the active power will be at the maximum possible, only limited by inverter and PCC voltages. Considering that those voltages do not change (during the short transients) with power variations as the simple model suggests, the active power is clamped to:

$$P_{LIM} = \frac{V_{inv}V_{PCC}}{2X_{inv}}\phi_{LIM} = S_{sh}\phi_{LIM} = S_{sh\,g}(\theta_g - \theta_{PCC}), \tag{3.7.29}$$

where $S_{sh\,g}=\frac{V_g V_{PCC}}{2X_g}$. It is important to notice that if this behavior is temporal, in other words, if the inverter should return to the non-limited angle difference mode. In order to verify that the angle difference will return to the linear (non-limited) range, let us consider that the angle change in the connection process as in (3.7.17):

$$\phi(s) \approx \frac{k}{\left(\frac{s}{\omega_C}+1\right)s + \left(k_{Idroop} + k_{Idroop\,g}\right)S_{shT}}\left(\omega_0 - \omega_{0g}\right)_{step} \tag{3.7.30}$$

for unlimited angle difference.

The numerator indicates the reference frequency difference between the inverter and the equivalent grid model at the moment of connection. The denominator models the dynamics of the angle difference and when t is large, shows the final value after the transients:

$$\phi(t \to \infty) \approx \frac{k(\omega_0 - \omega_{0g})}{(k_{Idroop} + k_{Idroop\ g})S_{shT}}. \tag{3.7.31}$$

Meaning that the angle difference is constant, and the frequencies of the grid and inverter are the same.

The inverter is still computing the angle ($\theta_{inv}{}'$) and the PLL angle difference $\hat{\phi}'$. The $'$ is used to indicate that this is not the real value. From Figure 3.7.4(c), the grid angle, which is not affected by the limiter, is:

$$\theta_g = \frac{\omega_{0g}}{s} + \frac{k_{Idroop\ g}P_{LIM}}{s\left(\frac{s}{\omega_C} + 1\right)}. \tag{3.7.32}$$

So, the PCC angle is

$$\theta_{PCC} = \theta_g + \frac{P_{LIM}}{S_{sh\ g}}, \tag{3.7.33}$$

and the angle difference using the internal algorithm is:

$$\hat{\phi}'(s) = \frac{[1 - F_{PLL}(s)].\omega_{0_{step}}}{s\left(\frac{s}{\omega_C} + 1\right)} - \frac{(k_{Idroop} + k_{Idroop\ g}).F_{PLL}(s).P_{LIM}}{s} - \frac{F_{PLL}(s).P_{LIM}}{S_{sh\ g}} \tag{3.7.34}$$

which in time-domain is (if we neglect the PLL behavior):

$$\phi'(t) = \left[(\omega_0 - k_{Idroop}P_{LIM}) - (\omega_{0g} + k_{Idroop\ g}P_{LIM})\right]t + \frac{(k_{Idroop} + k_{Idroop\ g})P_{LIM}}{\omega_C}(1 - e^{-\omega_C t}) + \phi_{LIM}. \tag{3.7.35}$$

This equation shows that if the slope: $\left[(\omega_0 - k_{Idroop}P_{LIM}) - (\omega_{0g} + k_{Idroop\ g}P_{LIM})\right]$ is negative, ϕ' will be lower than ϕ_{LIM} and after the transients, it will go back the linear model (3.7.30). This will happen only if

$$(\omega_0 - k_{Idroop}P_{LIM}) < (\omega_{0g} + k_{Idroop\ g}P_{LIM}). \tag{3.7.36}$$

In other words:

$$\omega_{inv} < \omega_g \text{ , at maximum power.} \tag{3.7.37}$$

If the inverter frequency is lower than the grid at its maximum power, then it is expected that the angle limit lasts only the transients. Figure 3.7.5 shows ϕ' considering the angle limiter. The solution considering the PLL dynamics is more complex but the transients are quite similar as Figure 3.7.5 shows. The only difference is the moment when the PLL suddenly changes the frequency, when the limiter starts working but at that moment the angle is already limited, so there is no impact in the behavior.

3.7.4. Simulations a grid of two inverters with phase limiters

A simulation test-bench which includes two inverters and a connection to the main grid through an inductor was developed in MATLAB/Simulink, the diagram is the same as in the experimental section and it is shown in Figure 3.7.8. Figure 3.7.9 shows the main results, which includes all of the critical points.

The simulation starts when the first inverter is connected to a micro-grid and no other inverter is present. As the loads were already connected, it starts delivering power from the beginning. At the very beginning, t<0.1s the inverter's PLL tries to synchronize with the grid but fails and reaches the lower limit. After that it changes to droop mode and the internal frequency and the grid frequencies match.

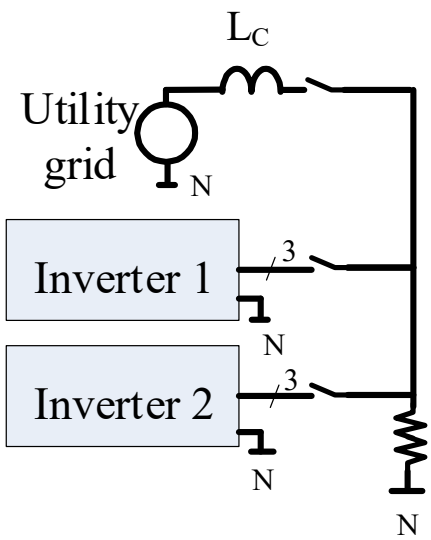

Figure 3.7.8–Simulation diagram for testing

At 0.3s, a 2nd inverter is connected which quickly adapts its own frequency and shares the load with the 1st inverter. Finally, at 0.7s, the utility grid is connected, so the grid has no notable droop coefficient compared with the inverters and almost all of the power is delivered by the grid due to the inverters' droop coefficients being much bigger than the grid's frequency variations, in other words, the grid behaves as a huge generator. In order to change this behavior and allow the inverters to supply power, a secondary control must be added.

In addition, no rush currents or voltage spikes are present during the transients. This is because of the angle limitation in the droop control and the special switch which allows the connection the grid with zero angle difference. Parameters of the simulation test are the same is in the experimental section and are shown in Table 3.7.1.

Table 3.7.1 Main components of the micro grid test bench

Devices	Values
Loads	3 phase 3kW, 3 x RL R=50 Ohm, L=50uH
Inverters	• 4kW 4-quadrant in-house inverters • Type of control: dq-frame current control, voltage control and droop control. • Main controller: TI 28379D working at 20kHz switching frequency
Inverter's contactors	Electromechanical contactors
Grid's contactor	Solid-state contactor (fast) with a special angle detector, in order to close the switch only if the voltages match.

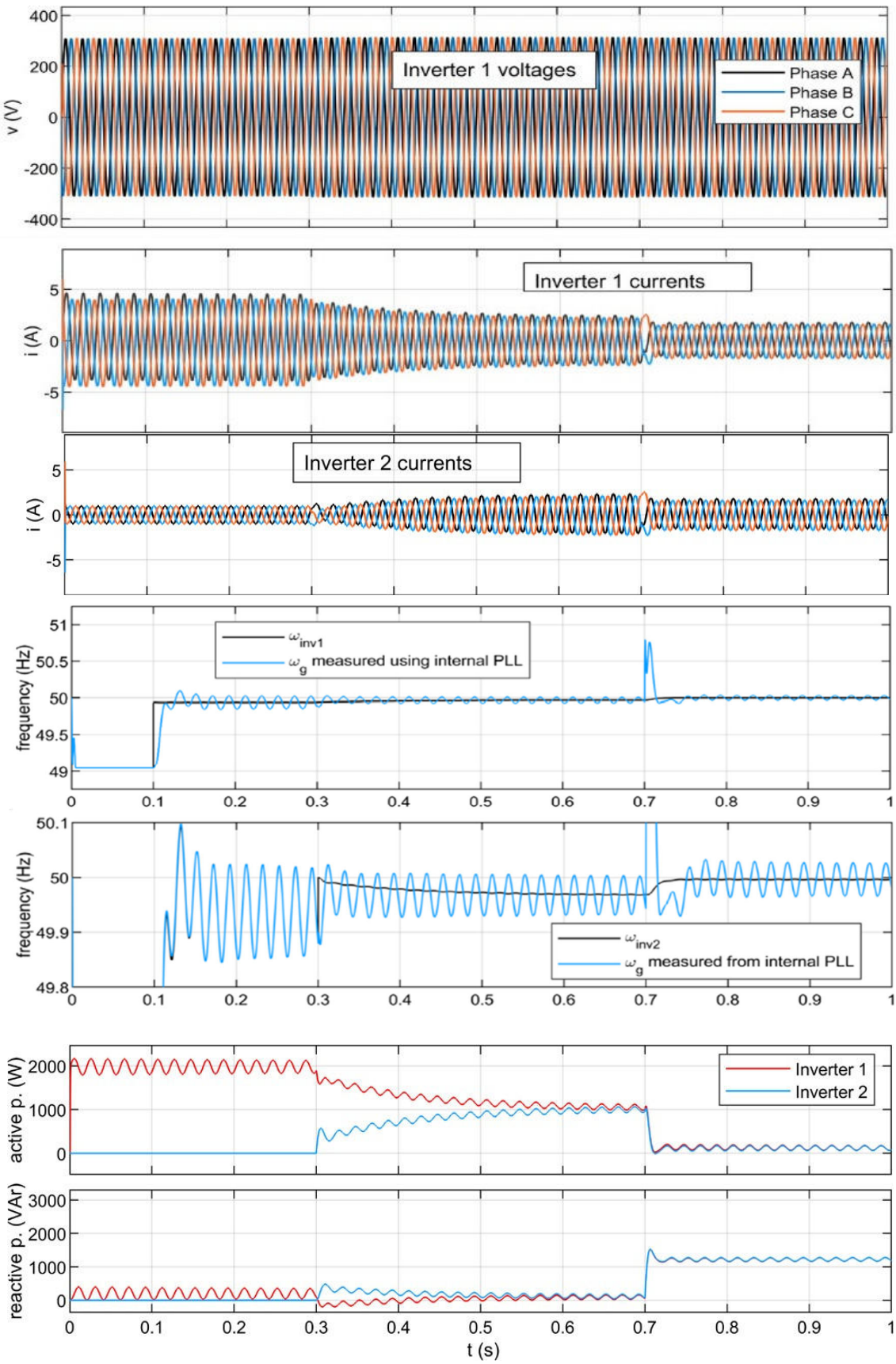

Figure 3.7.9–Simulations: inverter 1 connected at 0s change from fixed frequency to droop mode in 0.1s, inverter 2 connected at 0.3s, utility grid connected at 0.7s

3.7.5. Experimental validation

In order to validate the proposed mathematical model and analysis, different transient experiments were done. The first experiment shows how the power filter works, the second experiment introduces the phase limiter, the third experiment analyzes the virtual impedance effect on the inverter performance and the last one, the connection to a strong grid. The test bench for the experiments is shown in Figure 3.7.10(a) with its main diagram in Figure 3.7.10(b). The details of the hardware are in Table 3.7.1

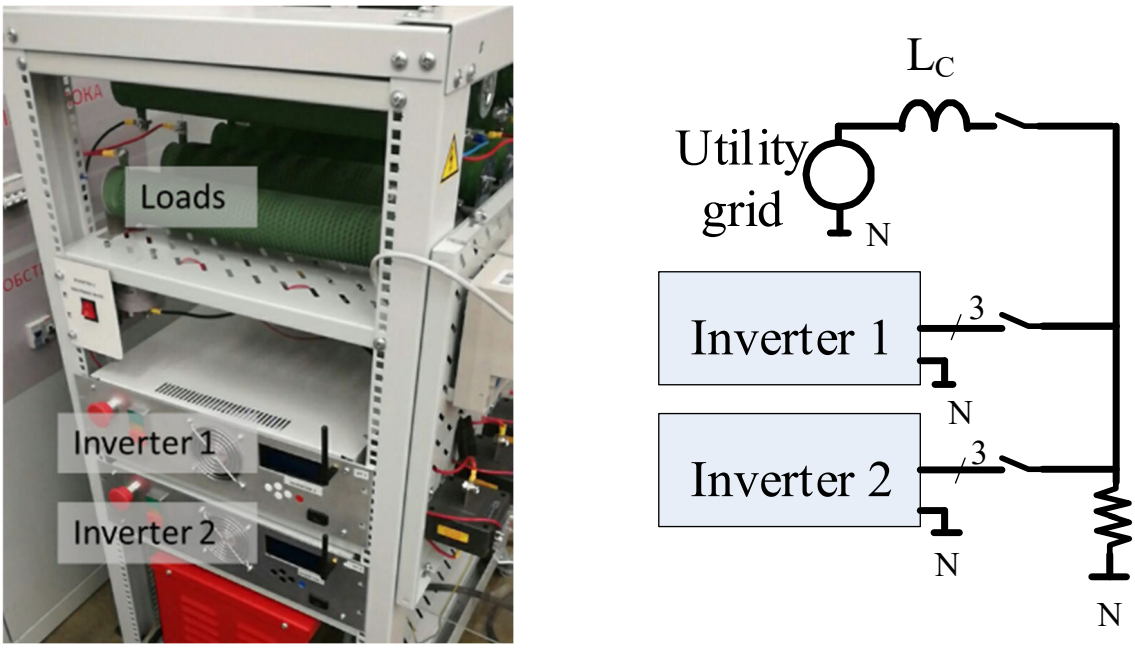

(a) (b)

Figure 3.7.10–Experimental Setup for validation (a) set-up (b) main diagram

Impact of the power filter with regards to transients. Figure 3.7.11 shows the first experiment where the micro grid is represented by a grid-forming inverter and a load. First, the micro grid consists of one inverter connected to a load. Then, a second inverter is connected. The figure shows the transient when the power cut-off filter is 5 rad/s (a), 10 rad/s (b) and 100 rad/s (c). In the experiment shown in Figure 3.7.11 (a) and (b), two complex poles are present, notice the oscillations in the current signals. For Figure 3.7.11(b), the oscillation period is about 330ms, which is approximately the imaginary poles from (3.7.18.b), with $(\omega_C, k_{Idroop} + k_{Idroop\ g}, S_{shT})$ = (10rad/s, 0.002 rad/s/W, 35000 W).

As shown in the figures, with increasing the filter's cut-off frequency, the settling time decreases and the damping of the oscillation increased. The decrease of the settling time as a function of the power filter cut-off frequency is shown in Figure 3.7.12.

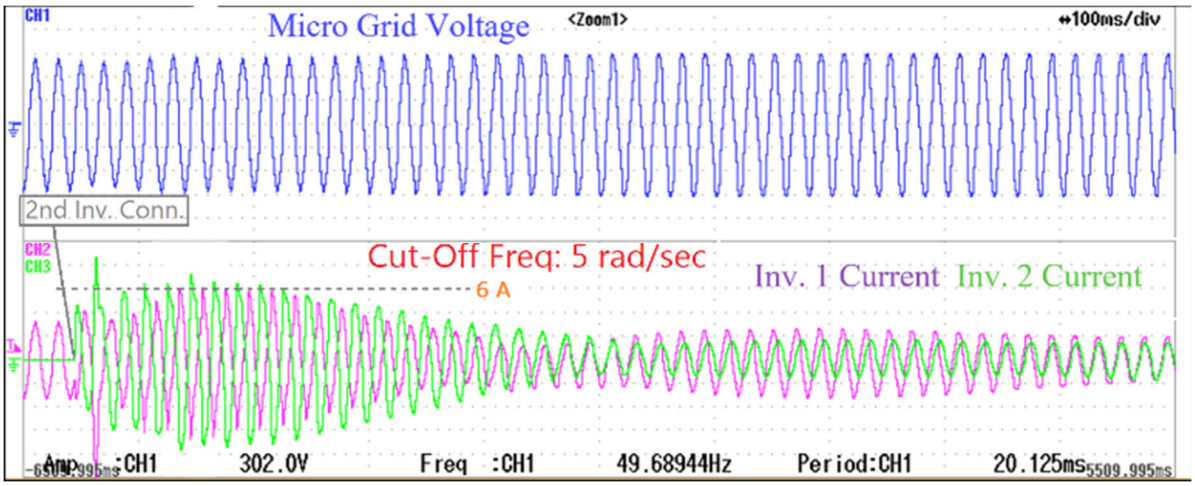

(a)

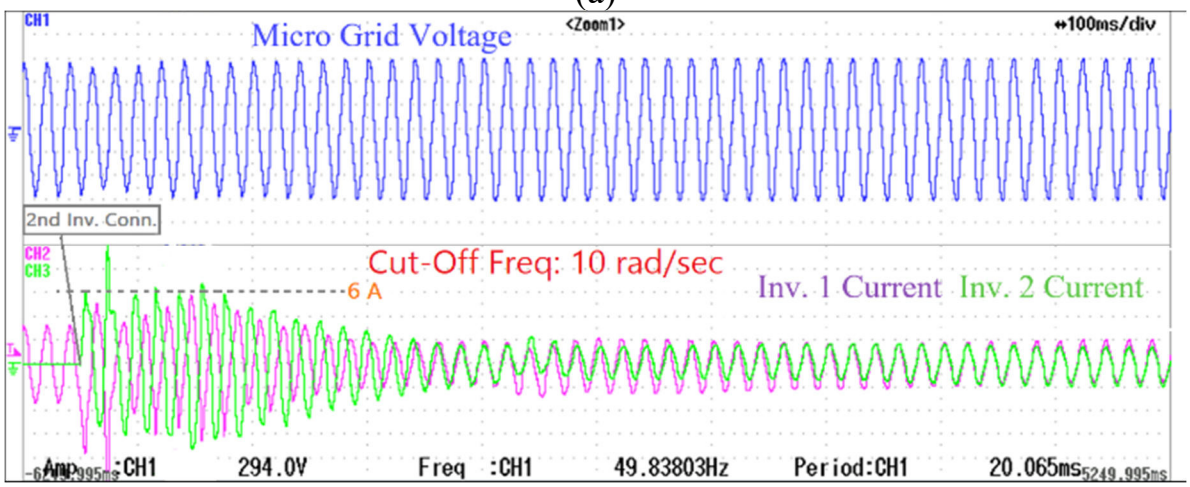

(b)

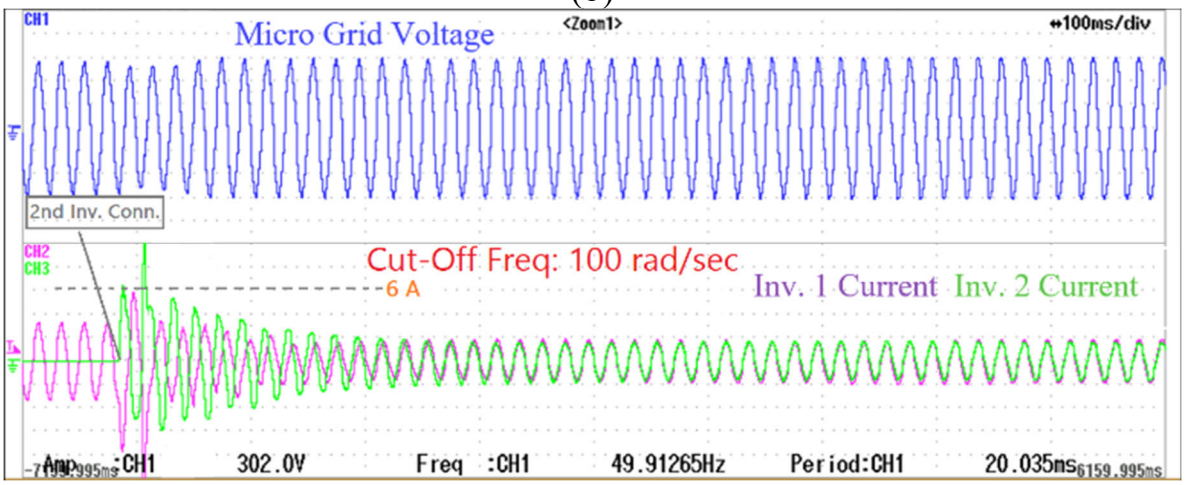

(c)

Figure 3.7.11–Inverters connection with (a) filter cut-off frequency of 5 rad/s, (b) filter cut-off frequency of 10 rad/s and (c) filter cut-off frequency of 100 rad/s

Impact in the transient of the phase limiter. The impact of the phase limiter is shown in Figure 3.7.13, notice that even if there are power fluctuations, they are never above a certain limit, which make the system more robust. In Figure 3.7.13(a) no angle limitation was used and as a result, the connection of the second inverter failed due to tripping of the protection relays. Comparing Figure 3.7.13(b) and (c), it is clear that with decreasing the angle limitation, a smoother connection is achieved with much less settling time. The proposed limiter uses the PCC angle which at the end limits the inverter's output power. In addition, an ultimate current limiter is always included in the (fast) inner current loop of the inverters, to limit the power as well.

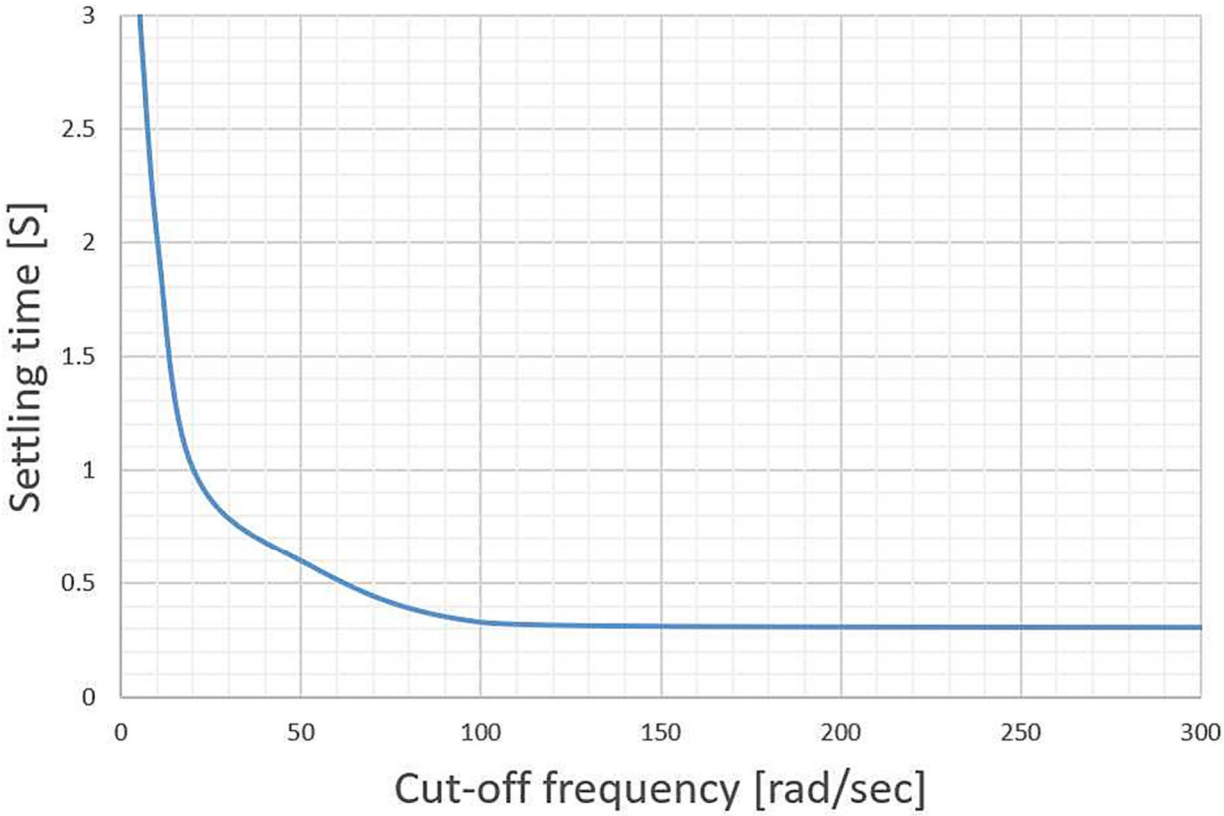

Figure 3.7.12. Settling time with respect to power filter cut-off frequency

Impact in the transient of the virtual impedance. The third experiment is focused on the impact of the virtual impedances and it is presented in Figure 3.7.14 and Figure 3.7.15. The simplest model only predicts the effect of the power filter and the droop coefficients and suggests that the best virtual impedance is a reactance. However, going into the details of the advanced model, it can be noticed that the real part of the virtual impedance helps to move the high frequency poles far from the imaginary axis avoiding

oscillations that can be critical in the transients (Note Figure 3.7.15(a) vs (b)). For such reason, a high value of virtual resistance can enhance the transients providing soft start as shown in Figure 3.7.14.

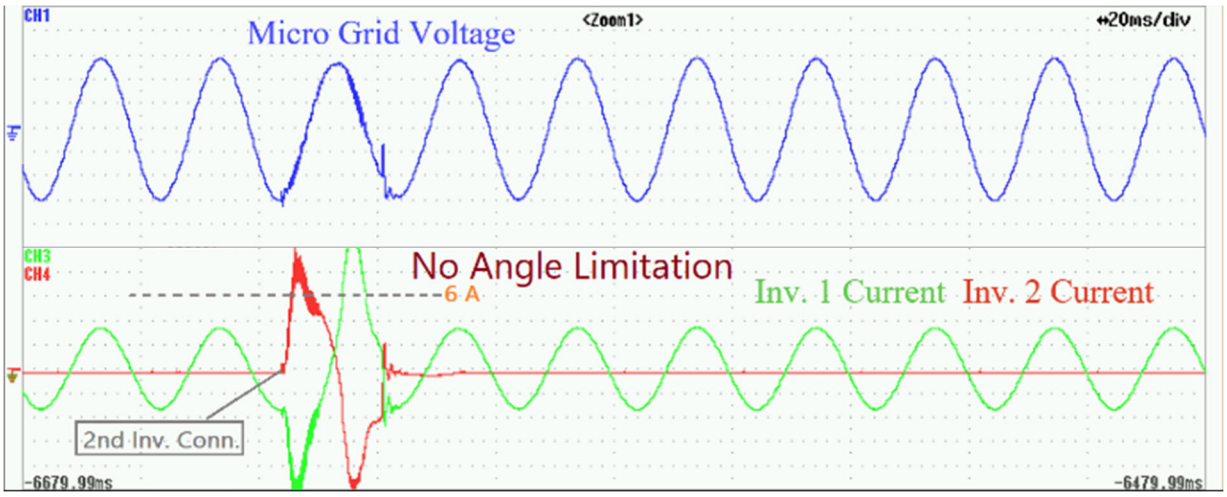

(a)

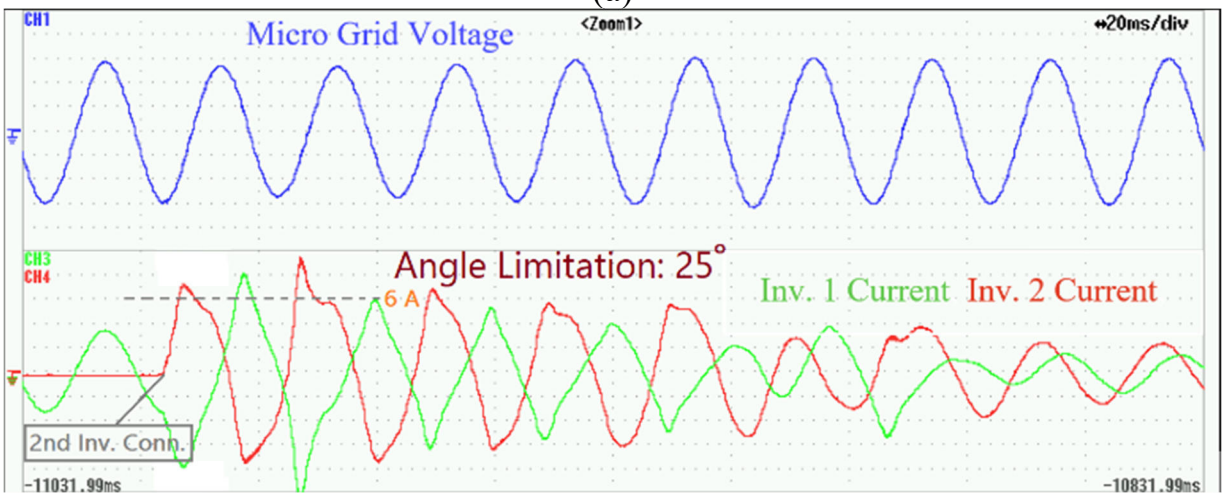

(b)

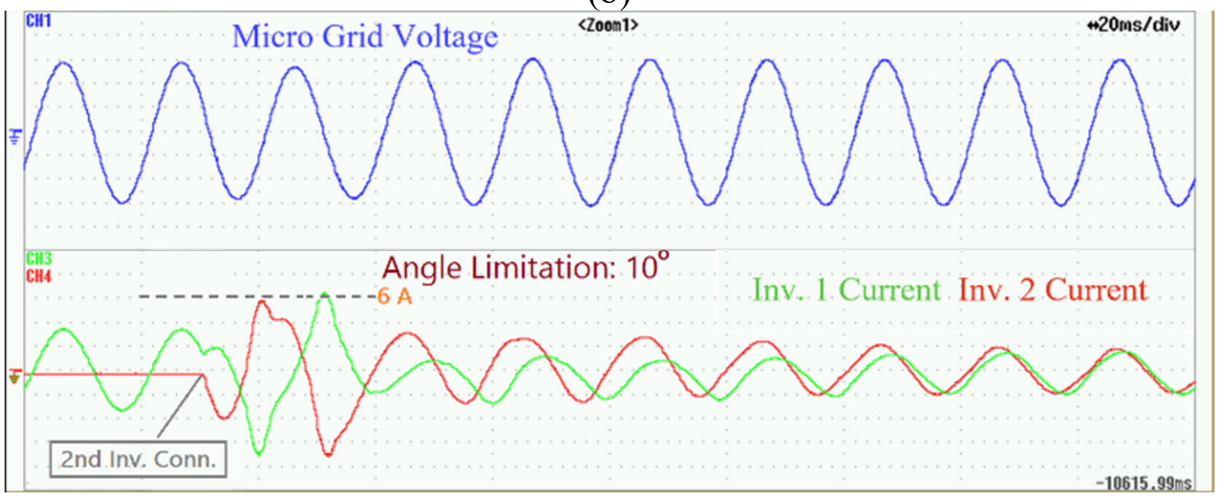

(c)

Figure 3.7.13–Inverters connection with (a) no angle limitation (b) angle limitation of 25 °, (c) angle limitation of 10°

Table 3.7.2 shows a list of experiments with different virtual impedances and different angle limitations. On the one hand, as shown in the table, decreasing the angle limitation allows for the use of a smaller value of virtual resistance during the connection which is quickly reduced to the nominal value afterwards providing a faster and smoother connection. Notice that the virtual resistance values in the table are the values at the instance of connection (see Figure 3.7.14). As highlighted in the figure, if the rate of change of the virtual impedance is fixed, then using a smaller initial value of virtual impedance (R_v0 1 compared with R_v0 2) allows for reaching the steady state nominal value of virtual impedance faster (t soft-start 1 compared with t soft-start 2). This is an advantage as a smaller virtual impedance causes less voltage drop and requires less secondary controller action to restore the voltage to its nominal value. On the other hand, using a very small angle limit causes oscillations during transients, because the controller is always above the phase limits.

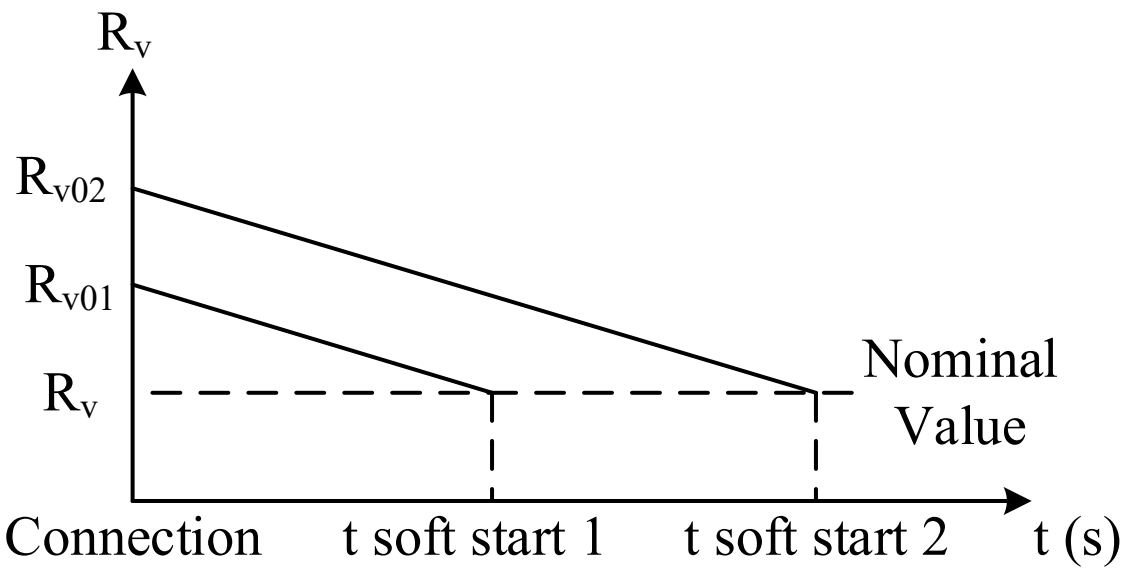

Figure 3.7.14–Virtual resistance adjustment during inverter connection providing soft start operation

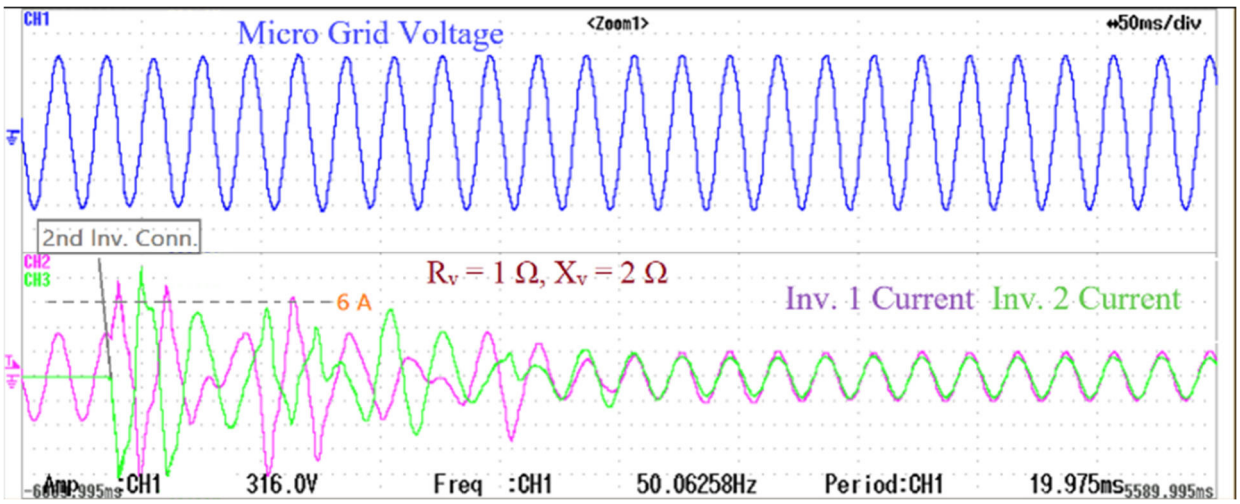

(a)

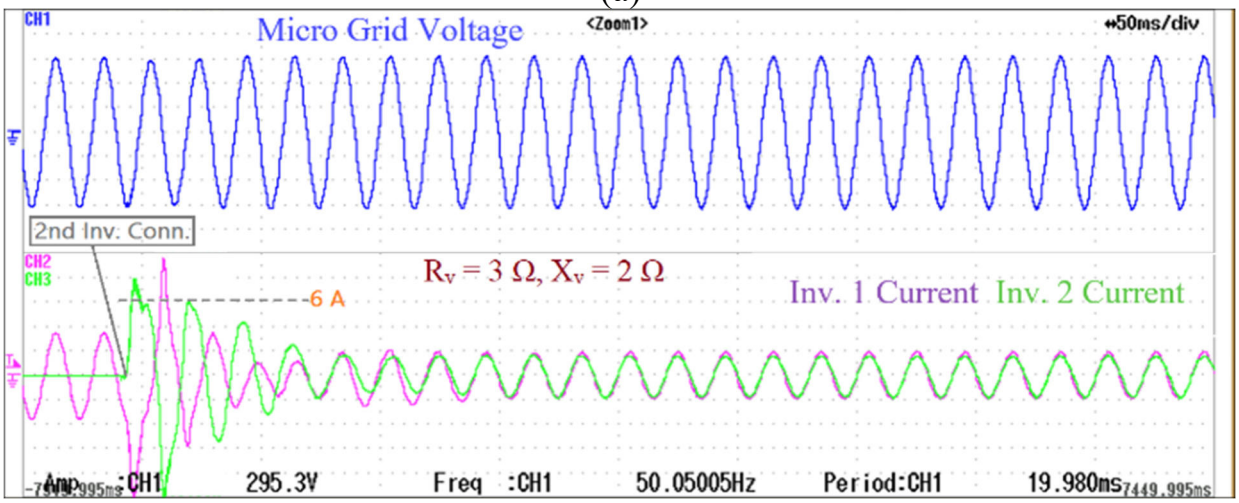

(b)

Figure 3.7.15–Inverters connection with (a) R_V = 0.1 Ω, X_V = 2 Ω, (b) R_V = 0.3 Ω, X_V = 2 Ω. at angle limitation of 10°

In addition, there is a clear relationship between the power filter's cut-off frequency and the settling time; using smaller cut-off frequency increases the settling time significantly. On the contrary, using an excessively large cut-off frequency with small virtual impedance may result in fast frequency variations, which can produce instabilities (similar to systems with very low inertia). According to experiments, the most suitable cut-off frequency is 100 rad/sec. The relation between the settling time and the power filter was shown in Table 3.7.2. The smoothest connection according to experiments is highlighted in the table and also shown in Figure 3.7.15(b). In this condition, $(\omega_C, k_{Idroop} + k_{Idroop\,g}, S_{shT})$ = (100rad/s, 0.002 rad/s/W, 20000 W, thus based on

(3.7.18), the poles are real and negative and close to each other (almost equal), so critically damped.

Table 3.7.2 Experiments with different virtual impedances and different angle limitations, Load = 1.8 kW

Cut-Off Frequency [rad/s]	Initial R_v0 [Ω]	Steady State R_v [Ω]	X_v [Ω]	Angle limit [°]	Settling Time [S]	Stability	Transients Oscillations
10	10	0.3	5	25	~2	Stable	Present
10	3	0.3	5	10	~1	Stable	Present
100	10	0.3	5	25	~0.3	Stable	Absent
100	3	0.3	5	10	~0.25	Stable	Present
100	3	0.3	2	10	~0.1	Stable	Absent
100	3	0.3	0.5	10	~0.18	Stable	Absent
100	3	0.3	1	10	~0.15	Stable	Present
100	1	0.3	2	10	~0.2	Stable	Present
100	1	0.3	3	5	~0.25	Stable	Present
1000	10	0.3	5	25	~0.3	Stable	Absent
1000	3	0.3	5	10	-	Unstable	-
1000	1	0.3	5	10	-	Unstable	-
1000	1	0.3	10	10	-	Unstable	

Connection to a strong grid. The last experiment is to connect the weak micro grid (the two inverters) with a strong utility grid and to see that the power sharing among inverters is still valid but with a reduced contribution. Figure 3.7.16 shows a two-inverter based micro grid connected to the main grid. Before the connection, main grid and micro grid are not synchronized, and both inverters are delivering equal current. After that, they become synchronized to the main grid and the circuit breaker is closed. As the inverters' droop coefficients are big in comparison with the strong grid, the inverters do not play a

significant role. Hence, if the inverters need to deliver power in the strong grids, a grid-following strategy must be used.

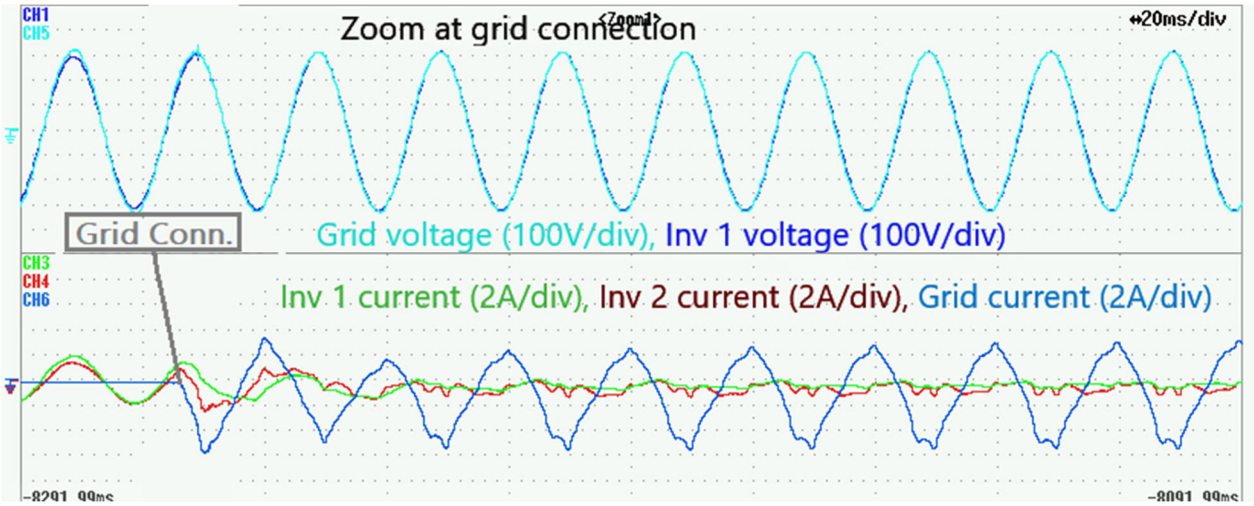

Figure 3.7.16–Two-inverter based microgrid connected to the main grid

3.7.6. Summary

The main goal of this section is to detail the connection transient of an inverter in a weak grid, which is formed by other similar grid-forming inverters. The section analyzes in detail the effect of the droop coefficients, measuring power filters, which are also related with virtual inertia, and virtual impedance coefficients. For that analysis, the section introduces a model which assists for selecting the proper range of parameters. The model is useful for understanding the dynamics of virtual inertia and impedance. In addition, a phase limiter is proposed and analyzed. The limiter allows inverters to have fast transients without over sizing the virtual impedance. Finally, all of the proposals were validated in a grid based on 5kW three-phase inverters. The details of this section were published in [37, 136].

3.8. Low-bandwidth communication between inverters

3.8.1. Motivation on communication through power lines to enhance the power sharing methods

As mentioned in the previous sections, active and reactive powers should be properly shared among sources to allow delivering the power to loads when a single inverter is not enough. Thus, EV chargers can work together to support the grid when it is needed. This avoids instability problems and improves reliability in inverter-based microgrids and power grids in general. For this task, there are several control techniques including hierarchical, centralized and decentralized control. Decentralized control techniques offer extra reliability to the system in addition to the plug and play functionality of distributed generators and this is why it is the main technique discussed in the dissertation. The decentralized control method is conventionally done using a droop controller.

However, droop control has certain limitations, particularly regarding reactive power sharing. Improper reactive power sharing can lead to serious problems when reactive power surges occur, such as severe circulating reactive powers, instability issues and even a complete shutdown of inverters. This section presents a new method for proper sharing of reactive power by utilizing a low-bandwidth communication through power lines. Using these communication signals, the virtual impedances of the inverters are automatically adjusted to achieve accurate reactive power sharing.

The method is described and analyzed in detail, including stability analysis related to communication loss and delay effects. For this analysis, we propose an inverter model incorporating communication links. The same power line communication can share additional grid information for secondary control tasks. The proposed method is verified by simulations and using a hardware prototype. Results show that the proposed algorithm is able to accurately achieve reactive power sharing while maintaining the expected power quality at load buses.

In decentralized control schemes, distributed generators (DGs), storage and EV chargers, commonly based on inverters, are controlled by using only local measurements. Hence no critical communication is needed between DGs [153]. When this restriction is taken into consideration, the droop control method is commonly used to achieve active (P) and reactive (Q) power sharing between DGs [130, 154, 155, 156 ,157]. However, communication links between inverters and, in general, converters are important to support the grid and to act as cluster of devices working together.

Although the droop control method allows for proper power sharing between DGs and is also considered as very efficient and reliable, it has some drawbacks. For example, the accurate reactive power sharing based on the inverter's power rating regardless of connected line impedance is not guaranteed, in the case of unequal feeder line impedance. Furthermore, to share active and reactive powers properly, line impedance should be dominantly inductive [153, 158]. Unfortunately, in low voltage (LV) distribution grids, lines have significant resistive impedances. Hence, a proper conventional droop control performance is not guaranteed [156]. Moreover, harmonic currents sharing is not possible with conventional droop control methods in case of non-linear load sharing [154, 159].

To address the aforementioned problems of the conventional droop control method (the inaccurate active and reactive power sharing between different inverters) and also enhance the system dynamics, many methods have been proposed to improve droop control in the literature. For instance, a control scheme based on an adaptive Q/V droop coefficient was proposed in [160, 161] in which, the droop gain is adaptively adjusted to improve the accuracy of reactive power sharing. Similarly, in [162] a method for adjusting the voltage droop coefficient is proposed, where reactive power signals are exchanged between inverters through low-bandwidth communication. According to the received reactive powers signals, the voltage droop coefficients can be adjusted to allow accurate reactive power sharing. In addition, a similar approach can be applied using adaptive virtual impedance [163].

The enhanced droop control approach [160, 161] typically has some drawbacks, such as increasing output voltage variation and reducing the system stability margin, even if it can directly improve reactive power sharing. The virtual impedance control method,

introduced in Section 3.6 can be used to match line impedances. When the load is nonlinear and unbalanced, the virtual impedance control technique can perform better in addition to enhancing reactive power sharing [164].

As was previously discussed, the virtual impedance technique relies on adding a control unit, which adjusts the reference in the voltage controller within the voltage source inverter (VSI) based on the measured inverter current [154]. The added virtual impedance can be a combination of resistance, capacitance and inductance. This technique can be used to improve active and reactive powers sharing accuracy in the case of unequal feeder line impedances. It can decrease the mismatch between line impedances and increase the inductive behavior of the line seen by each inverter [155]. Thus, in LV networks, the virtual impedance can improve the frequency and voltage decoupling of droop controllers [154, 165].

Several methods for choosing the proper virtual impedance values have been proposed in the past. One simple idea is to choose a large enough inductive virtual impedance in order to achieve the decoupling needed for the proper performance of droop control loop. This method can achieve better power sharing, but choosing an excessively large impedance can affect the system dynamics and cause large frequency and voltage deviations [166].

Another method is proposed in [153] where an adaptive virtual impedance algorithm properly chooses the inductive virtual impedance of each inverter. The method is based on neighboring inverters' reactive power outputs where graph theory is used to determine the neighboring inverters. Although this method shows good performance and accurate reactive power sharing, it requires that two-way communication systems must be installed in each inverter. This increases system's complexity and decreases reliability.

A more interesting method is to choose the virtual impedance based on an optimization algorithm located in a central unit using the estimated line impedances [166]. However, in [166], line impedances are estimated through a complex procedure in which all inverters should be operated synchronously to ensure reliable estimations. In addition, grid variations will require an update of the algorithm, so the "plug & play" mechanism is not guaranteed.

A more recent study has also applied virtual impedance control with a first-order consensus process to share reactive power accurately. To reduce the communication burden and system complexity, a basic pseudo-unidirectional communication network with a restricted communication band is used for the proposed distributed control [167]. However, a communication network is still needed to be established in the grid which adds complexity and reduces scalability.

Conventionally, information is exchanged between DGs using an external communication network. However, using such network may increase the cost of the overall system especially if the distance between DGs becomes large and reduce reliability. Some authors have proposed the use of the power lines as a communication network to achieve data exchange. Most of the proposed methods are applied only to DC MGs [168, 169, 170] with few papers applying power line communication to AC grids [171, 172, 173]. In [171, 173], the authors proposed their power line communication technique as a monitoring system without emphasizing the applicability of such technique to control DGs. In [172], a power line communication technique is proposed to exchange information about output active power of the DGs. They use the main control loop of the inverter as the signal generator by introducing high order harmonics for sending data. However, researchers have only focused on the active power control with no remarks on the reactive power control. In addition, although the use of the main control loop as the signal generator is economically beneficial, it can add some limitation to the communication signal in terms of frequency range due to filtering of higher harmonics by the output LC filter and requires a very fast controller to be capable of detecting the carrier signal's frequency. Furthermore, the detection of the communication signal using the inverter's sensors may require the communication signal amplitude to be within a certain value depending on the resolution of the voltage and current measurements.

In this section, a new method for addressing the problem of inaccurate reactive power sharing using an adaptive virtual impedance controller is proposed and modelled [146, 174]. The method utilizes power lines low bandwidth communication (PL-LBC) to send reactive power data between inverters, and these data are used by the virtual impedance controller to achieve better reactive power sharing with a reduced adjustment

of the virtual impedance. In this work, adjustments are made to allow relative power sharing in case of different inverters' power ratings. The proposed method is analyzed for delays and communication loss, where the controller shows a stable behavior in both cases.

The PL-LBC does not add any new communication network, thus reducing the system complexity and costs. Moreover, if the PL-LBC is totally lost from one inverter, the system can still work but at a reduced performance, so the reliability of the system is not compromised. The proposed communication and control techniques are validated through dynamic simulations of a proposed model and by using an experimental test bench. The results have been published in [146, 174].

Subsection 3.8.2 reviews the droop control method in the case of non-dominant inductive lines. Sub section 3.8.3 presents the proposed inverter's control diagram based on adaptive virtual impedance. Subsection 3.8.4 introduces the new power line low bandwidth communication scheme. Subsection 3.8.5 presents numerical simulations for analyzing stability and sensitivity of the system based on the proposed model. Subsection 3.8.6 presents the results of experimental tests and subsection 3.8.7 concludes the section.

3.8.2. Droop control method in non-inductive power lines

The droop control mechanism guarantees desired power sharing only if the line impedance is dominantly inductive [153]. However, in the case of distribution lines, a significant resistive element is present. When the effect of the resistive component of the distribution lines is taken into consideration, the active and reactive powers are given by the following equations (see Figure 3.8.1):

$$P + jQ = \frac{jEV\sin(\phi) - EVcos(\phi) - V^2}{R + jX}. \tag{3.8.1}$$

Thus:

$$P + jQ = \frac{XEV\sin(\phi) - R[EVcos(\phi) - V^2]}{R^2 + X^2} + j\frac{X[EVcos(\phi) - V^2] + REV\sin(\phi) +}{R^2 + X^2}. \quad (3.8.2)$$

where, R and X are the resistive and reactive component of the power line, E is the voltage at the inverter output, V is the voltage at the PCC and ϕ is the voltage angle. The case of R<<X was detailed in (3.6.5) and was used extensively in Section 3.6 and 3.7. In this section, the case of resistive lines is considered.

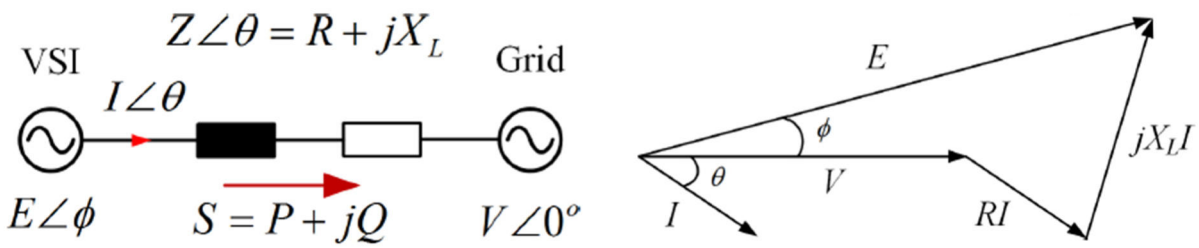

(a) (b)

Figure 3.8.1–Power through a power line: (a) circuit diagram, (b) phasor diagram

Now, the active and reactive powers are no longer primarily dependent on the power angle and the voltage magnitude respectively. In other words, active and reactive powers equations are coupled. As discussed above, this coupling can be decreased by introducing an inductive virtual impedance to reach again X>>R, and hence; (3.8.2) can be reduced to (3.6.5) and a better performance of the droop control is obtained.

Inaccurate reactive power sharing can lead to certain problems in terms of stability in grids. One of these problems is the severe circulating reactive powers among inverters under extreme conditions [175]. In addition, the inverter's reactive and active powers are related [176]. The maximum inverter´s current is limited, which imposes a relationship between the active and reactive power outputs [178]:

$$P_{inv}{}^2 + Q_{inv}{}^2 = S^2 < \left(\frac{3V_{inv}I_{invMAX}}{2}\right)^2, \quad (3.8.3)$$

where P_{inv} and Q_{inv} are the inverter active and reactive powers output, V_{inv} is the peak voltage at the inverter output and I_{invMAX} is the maximum peak current at the inverter.

According to equation (3.8.3), at the current limit, the higher the inverter's reactive power output, the lower the active power limit. This can cause a problem during reactive power surges when the reactive power output of inverters connected near loads may cause the current to reach its limit. This will produce the inability to supply the demanded active power, shutdown of the inverter or voltage instability in case of poor reactive power sharing. Thus, in order to minimize such effects, the reactive power sharing control needs to be independent of the feeder line impedance.

3.8.3. Virtual impedance as an adaptive controller

For testing the proposed low-bandwidth communication scheme, the inverter in Figure 3.8.2 is used. It is the same inverter type as in Section 3.6 and 3.7, but with an adaptive virtual impedance algorithm.

The virtual impedance controller uses the measurements from other connected inverters (sent through PL-LBC) and generates a correction factor for the virtual impedance (ΔL_v). The reactive power measurements are exchanged between inverters using the power lines as a low-bandwidth communication network. Details are given in the subsection 3.8.4.

Commonly, on top of all of the local controllers, a secondary controller (a centralized controller) measures the voltage and frequency at the load bus and sends restoration signals to all operating inverters to mitigate the effect of droop control method and restore the voltage magnitude and frequency to their nominal voltage. This occurs for both grids and micro grids. However, in this section, the focus is on the primary controller. As a future work, the secondary controller can also be implemented using PL-LBC.

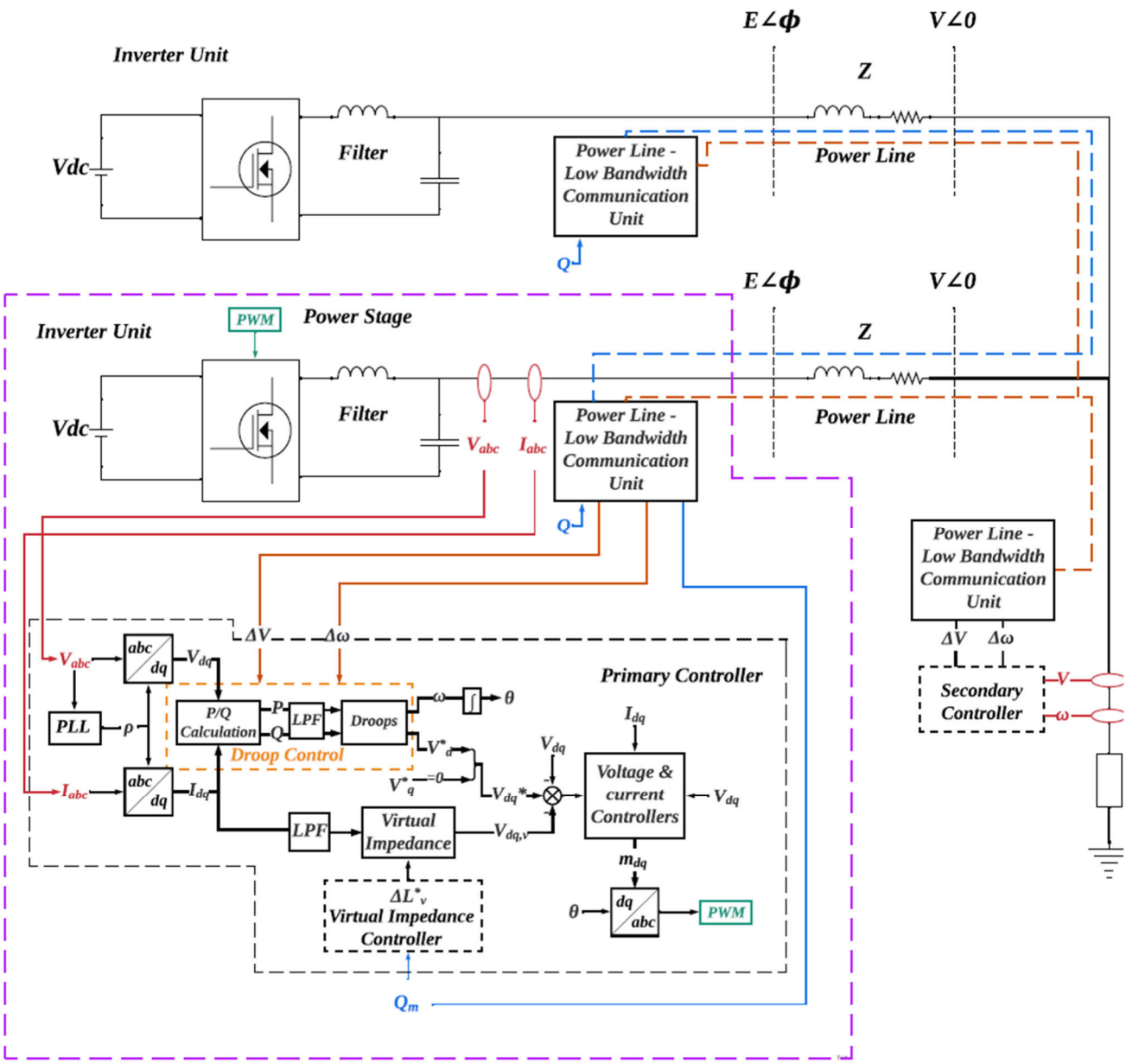

Figure 3.8.2–Inverter with an adaptive virtual impedance controller

Primary Controller. The primary controller represents the control elements which depend on the local measurements acquired by the inverter. The primary controller is the inverter's main voltage and current controllers. Other higher-level controllers adjust the primary controller to achieve accurate active and reactive power sharing as well as to restore grid voltage and frequency. Each element of the primary controller was discussed in the sections from 3.3 to 3.7, including the inner current control loops (Section 3.3, 3.4 and 3.5), voltage control loop (Section 3.6) and power sharing control loops (Section 3.6 and 3.7). The droop equations are repeated here because they will be used after in this

section. The inverter power is measured at PCC and it is filtered with a first order filter (3.6.4):

$$P_{inv} + jQ_{inv} = \frac{1}{\frac{s}{\omega_{CP}} + 1}(p_{inv} + jq_{inv}). \tag{3.8.4}$$

After that the droop controller is applied (3.7.1):

$$\omega_{inv} = \omega_0 - k_{Idroop}P_{inv}, \tag{3.8.5}$$

$$V_{cref} = V_{c\,ref0} - k_{Qdroop}Q_{inv}.$$

Virtual impedance controller. The virtual impedance concept was introduced in Section 3.6, and used in Section 3.7 to improve the transient processes when inverters are connected to the grid and when the load changes. Here it is reviewed to understand the adaptative virtual impedance controller. The virtual impedance in $\alpha\beta$-frame was introduced in subsection 3.6.3. In case of dq-frame, this can be re-written as:

$$\bar{Z}_{v\,dq} = R_v + j\omega_G L_v\,. \tag{3.8.6}$$

The virtual impedance algorithm takes as input the measured output current in dq frame (i_{dq}) which is passed through a LPF. The voltage drop $\bar{v}_{vd} + j\bar{v}_{vq}$ is calculated according to (3.8.7) and then, subtracted from the voltage reference, $\bar{v}_{Cdq\,Ref}$ or $\bar{v}_{inv\,dq\,Ref}$ and fed to the voltage control loop:

$$\bar{v}_v = \bar{Z}_{v\,dq}LPF(i_{dq}) \tag{3.8.7}$$

$$\bar{v}_{Cdq\,Ref} = \bar{v}_{inv\,dq\,Ref} = V_{cref} - \bar{v}_v\,.$$

In order to eliminate the error in reactive power sharing, the proposed controller adjusts the inverter's virtual impedance, by using a correction signal $\Delta L_v{}^*$. The controller takes as input the inverter reactive power and the received measured signals representing the reactive power of the other connected inverters. Then, the reference for the reactive power is given by

$$Q^* = \frac{Q_{inv\,MAX}}{Q_{inv\,MAX} + \sum_{n=1}^{N} Q_{M\,MAX(n)}}\left[Q_{inv} + \sum_{n=1}^{N} Q_{M\,(n)}\right], \tag{3.8.8}$$

where Q^* is the reactive power reference, Q_{inv} is the local reactive power, $Q_{M(n)}$ is the measured reactive power signal of the other inverters and n is the number of the inverter. $Q_{inv\,MAX}$ represents the reactive power rating of the local inverter and $Q_{M\,max(n)}$ represents

the reactive power rating of the inverter's measured signal at n-th inverter transmitted through PL-LBC. Thus, the reactive power reference is obtained by using a weighted sum of the rating of the local inverter and the other connected inverters in the grid. The number of received signal from the PL-LBC depends on the modulation technique and number of channels. Increasing the number of measurement channels can increase the reliability and the rate of data transfer. However, it must be limited to ensure that no significant amount of added noise is present in the power lines of the grid. If we consider two inverters of the same reactive power ratings, this equation is reduced to equal power sharing.

The virtual impedance correction factor, $\Delta L_v{}^*$, is then given by:

$$\Delta L_v{}^* = k_{P\,v}(Q^{*\prime} - Q_{inv}) + k_{I\,v}\int (Q^{*\prime} - Q_{inv})dt, \tag{3.8.9}$$

where $k_{P\,v}$ and $k_{I\,v}$ are the virtual impedance proportional-integral (PI) controller gains. This controller should be slow enough to allow the power-lines low-bandwidth communication (PL-LBC) system to measure and transmit the data.

3.8.4. Virtual impedance as an adaptive controller

In order to achieve proper reactive power sharing, signals for reactive power are transmitted between inverters through PL-LBC, as shown in Figure 3.8.3. The technique for sending the data in the power lines is as follows. First, the reactive power signal is converted into a binary signal. Then, this binary signal is transformed into a sequence of on-off transmissions of a high frequency signal (carrier) which is injected into the power line. The carrier frequency and amplitude must be designed properly in order to keep the total harmonic distortion (THD) within allowable limits while achieving a signal-to-noise ratio that is high enough to be measured accurately. For receiving the data, a coupling inductor is placed after the inverter's output LC filter as Figure 3.8.3 shows.

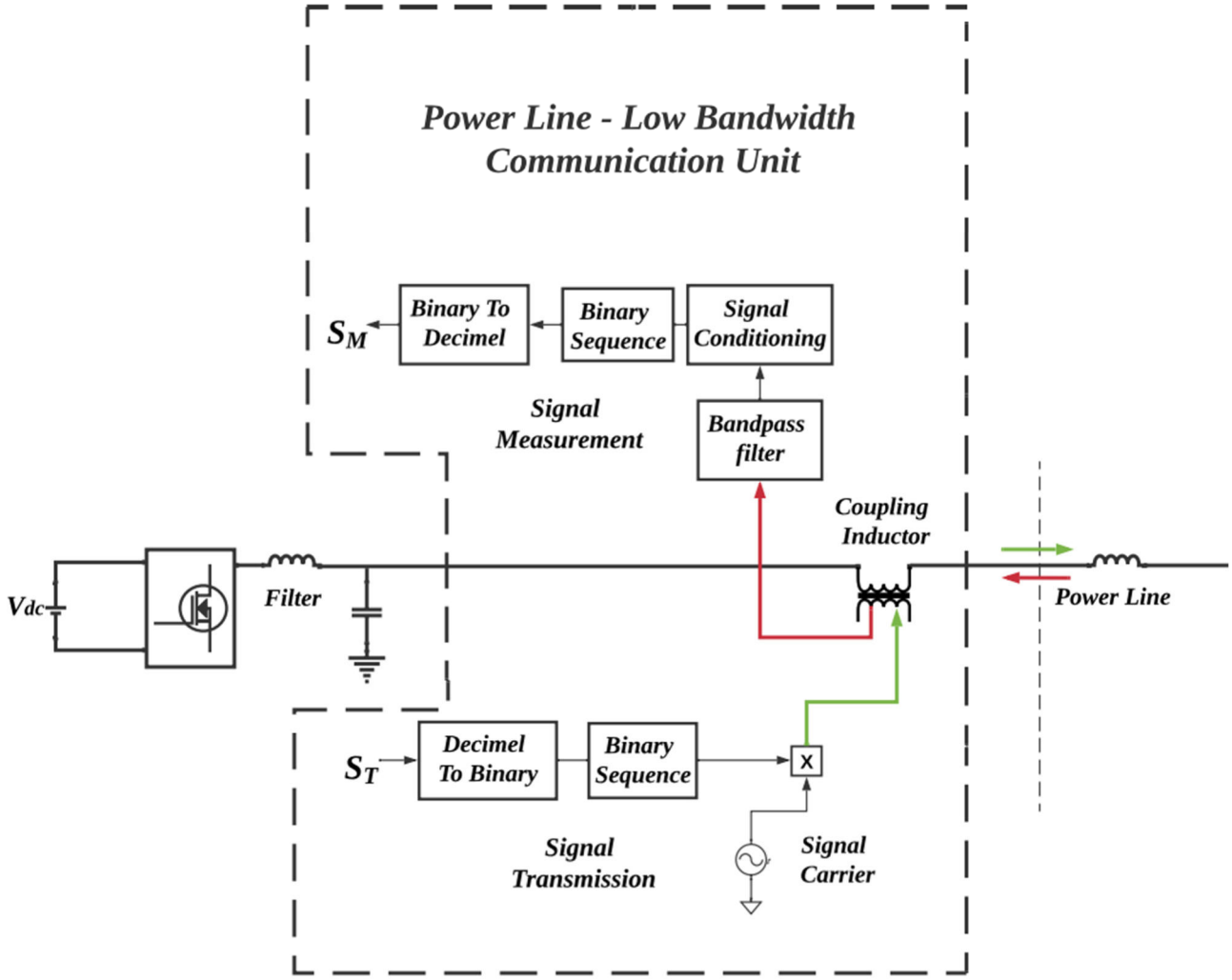

Figure 3.8.3–Power line – Low Bandwidth Communication (PL-LBC) Scheme

The voltage across this inductor is sent to a bandpass filter and the output is transformed back from a binary sequence into a decimal output representing the reactive power sent signal. Note that the inductance of the (grid-side) coupled inductor must be small enough to avoid any stability issues in the grid. In three-phase networks, it is possible to use any of the phases. In addition, it is possible to add more than one frequency carrier if the system needs to transfer more data. Other modulation techniques can also be used, such as frequency modulation (FM), frequency shift keying (FSK), phase shift keying (PSK), quadrature amplitude modulation (QAM), and others, which may allow for more reliable or faster data transfer. Note that the signal is transmitted and received after the output LC filter of the inverter. This is to avoid filtering of the signal by the inverter's output filter.

It is considered that the reactive power is measured in one of the inverters and through a certain delay (100 ms) is transferred to the other one, one data package per 180 ms. The model of the package transfer represents the discretization of the signal and can be approximated using zero order hold block. Thus, the transfer function for the delay is given by:

$$G_{delay}(s) = e^{-sTd}, \tag{3.8.10}$$

where, T_d represents the time delay of the signal which is related to the length of data package and the period of a single bit of information (for example, 100 ms). $H_{ZOH}(s)$ represents the zero-order hold transfer function and is given by:

$$H_{ZOH}(s) = \frac{1 - e^{-sT_s}}{sT_s}, \tag{3.8.11}$$

where T_s represents the sampling time of the signal (180 ms) and is related to the bandwidth of the communication. Then, the effect of the delay and discretization is given by the following transfer function,

$$G_{LCB}(s) = G_{delay}(s)H_{ZOH}(s). \tag{3.8.12}$$

In order to model that effect. $Q^{*\prime}$ in equation (3.8.9) represents the added effect of the delay where Q^* is multiplied by $G_{LCB}(s)$. Then, transforming (3.8.9) it into frequency domain, the equation becomes:

$$\Delta L_v{}^* = \left(k_{P\,v} + \frac{k_{I\,v}}{s}\right)[G_{LCB}(s)Q^* - Q_{inv}], \tag{3.8.13}$$

which can be expanded to:

$$\Delta L_v{}^* = \left(k_{I\,v}\frac{e^{-sT_d} - e^{-s(T_d+T_s)}}{T_s}\frac{1}{s^2} + k_{P\,v}\left[\frac{e^{-sT_d} - e^{-s(T_d+T_s)}}{T_s}\right]\frac{1}{s}\right)Q^* - \left(\frac{k_{I\,v}}{s} + k_{P\,v}\right)Q_{inv}. \tag{3.8.14}$$

Using this equation along with equations (3.8.2), (3.8.4), (3.8.5), (3.8.7), the gains of the PI controller can be tuned while considering the delays arising from signal transmission through the power line. In simple terms, the bandwidth of the reactive power controller needs to be lower than the bandwidth of the communication for the system to be stable.

From this, it can be noticed that the bandwidth of the communication system has a direct effect on the sampling time which must be taken into consideration when designing the gains of the PI controller. In addition, the delay due to signal transfer is related to the width of the data package as well as the bit rate of the signal and must be also taken into consideration. The effect of the delay is discussed in the next subsection. If the delay is not taken into consideration while designing the PI controller gains, the system can become unstable after a certain delay threshold.

The low-bandwidth, or low-speed, communication means that the control does not need the updated data in each inverter's switching cycle. This allows using redundancy and other techniques to ensure that the received data is correct which is critical for power line communications that are susceptible to data loss or degradation. In addition, if the communications are lost, the system can still work in a non-optimal mode. Low bandwidth means, in the proposed solution, that new data is transmitted every 180ms. Thus, the controller does not need a quick update of the measurements in order to control the reactive power. Increasing the bandwidth would mean better accuracy and faster dynamics in control of the reactive power. However, this would also increase the harmonics injected into the system from the power line communications and may cause power quality issues. The impact of the communication signals is shown in the experimental subsection. It can be seen the effect in the grid voltage and current due to the added carrier. The THD increased to 1.17% which is still below than the maximum THD required in the standards (<5%). By increasing the bandwidth, we can expect an increase in the THD as well which may not be desirable.

In addition, considering the impedance of the lines, we need to choose the signal carrier frequency carefully to maintain a high enough signal-to-noise ratio so the transferred signal can be effectively measured with minimal degradation. For instance, the power line impedance magnitude ranges from 0.1 Ω to 100 Ω in the frequency band from 0 Hz to 500 kHz [177]. A high frequency signal carrier, which can allow for higher bandwidth communication, will suffer further degradation by the power line impedance. As for the bandwidth lower limit, we can theoretically decrease the bandwidth while redesigning the gains of the reactive power controller and the system would still operate.

However, this will cause slow transient response and the system would take longer time to reach the steady state in the cases of reactive load changes. Thus, choosing a proper bandwidth is a trade-off between achieving a better transient response of the controller and maintaining good power quality.

3.8.5. Analysis of the stability of the proposed control technique

In order to check that the system is still stable although the virtual impedance is changing in real-time, a small-signal dynamic model was created based on Figure 3.8.2. The analysis considers two aspects: a) effect of communication delay which perturbs the main inverter´s loop and b) effect of communication loss.

Stability Analysis. In this model, a perturbation in the virtual inductance is made to see the impact in the output reactive power. The small signal model assumes that current and voltage inner controllers are ideal with no-delay, in addition the model is performed in the alpha-beta frame considering a balanced system. The small-signal equations which represent the system are:

Droop control equation in $\alpha\beta$-frame for voltage control:

$$v_{droop\,\alpha} = \cos(\theta)\left(v_{ref} - k_{Q\,droop}\frac{1}{\frac{s}{\omega_C}+1}q_{inv}(s)\right) \tag{3.8.15.a}$$

$$v_{droop\,\beta} = \sin(\theta)\left(v_{ref} - k_{Q\,droop}\frac{1}{\frac{s}{\omega_C}+1}q_{inv}(s)\right) \tag{3.8.15.b}$$

where (power droop controller):

$$\theta = \frac{\omega_{inv}}{s} = \frac{= \omega_0 - k_{Idroop}\frac{1}{\frac{s}{\omega_C}+1}p_{inv}}{s}. \tag{3.8.16}$$

The virtual voltage drops, according to the voltage balance is:

$$v_{v\,\alpha} = v_{droop\,\alpha} - v_{line\,\alpha} - v_{load\,\alpha} \tag{3.8.17.a}$$

$$v_{v\,\beta} = v_{droop\,\beta} - v_{line\,\beta} - v_{load\,\beta} \tag{3.8.17.b}$$

while the virtual drop voltage also is:

$$v_{v\,\alpha} = R_v \,.\, i_{o\alpha} - \omega_G L_v \,.\, i_{o\beta} \tag{3.8.18.a}$$

$$v_{v\,\beta} = R_v \,.\, i_{o\beta} + \omega_G L_v \,.\, i_{o\alpha}. \tag{3.8.18.b}$$

Thus,

$$i_{o\alpha} = \frac{v_{v\,\alpha} R_v + v_{v\,\beta}\omega_G L_v}{{R_v}^2 + (\omega_G L_v)^2} \tag{3.8.19.a}$$

$$i_{o\beta} = \frac{v_{v\,\beta} R_v - v_{v\,\alpha}\omega_G L_v}{{R_v}^2 + (\omega_G L_v)^2}. \tag{3.8.19.b}$$

The line impedance voltage drop is:

$$v_{line\,\alpha} = (R + sL) i_{o\alpha} \tag{3.8.20.a}$$

$$v_{line\,\beta} = (R + sL) i_{o\beta}. \tag{3.8.20.b}$$

And the load voltage drop is:

$$v_{line\,\alpha} = \frac{sR_{load}L_{load}}{R_{load} + sL_{load}} i_{o\alpha} \tag{3.8.21.a}$$

$$v_{line\,\beta} = \frac{sR_{load}L_{load}}{R_{load} + sL_{load}} i_{o\beta}. \tag{3.8.21.b}$$

Power calculations are:

$$p_{inv} = \frac{3}{2}\left(v_{droop\,\alpha} i_{o\alpha} + v_{droop\,\beta} i_{o\beta}\right) \tag{3.8.22.a}$$

$$q_{inv} = \frac{3}{2}\left(v_{droop\,\beta} i_{o\alpha} - v_{droop\,\alpha} i_{o\beta}\right), \tag{3.8.22.b}$$

using equations (3.8.15-3.8.22), the output current of each inverter $i_{o\alpha}$ and $i_{o\beta}$ and the load current $i_{load\,\alpha}$ and $i_{load\,\beta}$ are the summation of the inverters' currents:

$$i_{load\,\alpha} = \sum_{n=1}^{N} i_{o\alpha\,(n)}. \tag{3.8.22}$$

This subsection shows a tool to analyze the proposed virtual impedance controllers based on communication systems. As the model is too complex to express it in a single transfer function, a Simulink block diagram using (3.8.15-3.8.23) was used to extract the open-loop frequency response to analyze stability. The Simulink diagram is shown in

Figure 3.8.4, the virtual inductance is controlled using a PI controller as (3.8.9) shows. To have the reactive power from (3.8.8) in the inverter 1, the reference of the controller relies on the received signal from other inverters. Therefore, in order to include this effect in the analysis of the control loop, an artificial reference equals to zero is used while the computation of Q^* is considered as a part of the feedback loop. Thus, the possible communication delays and loss of data can be included in the open-loop transfer function for stability analysis.

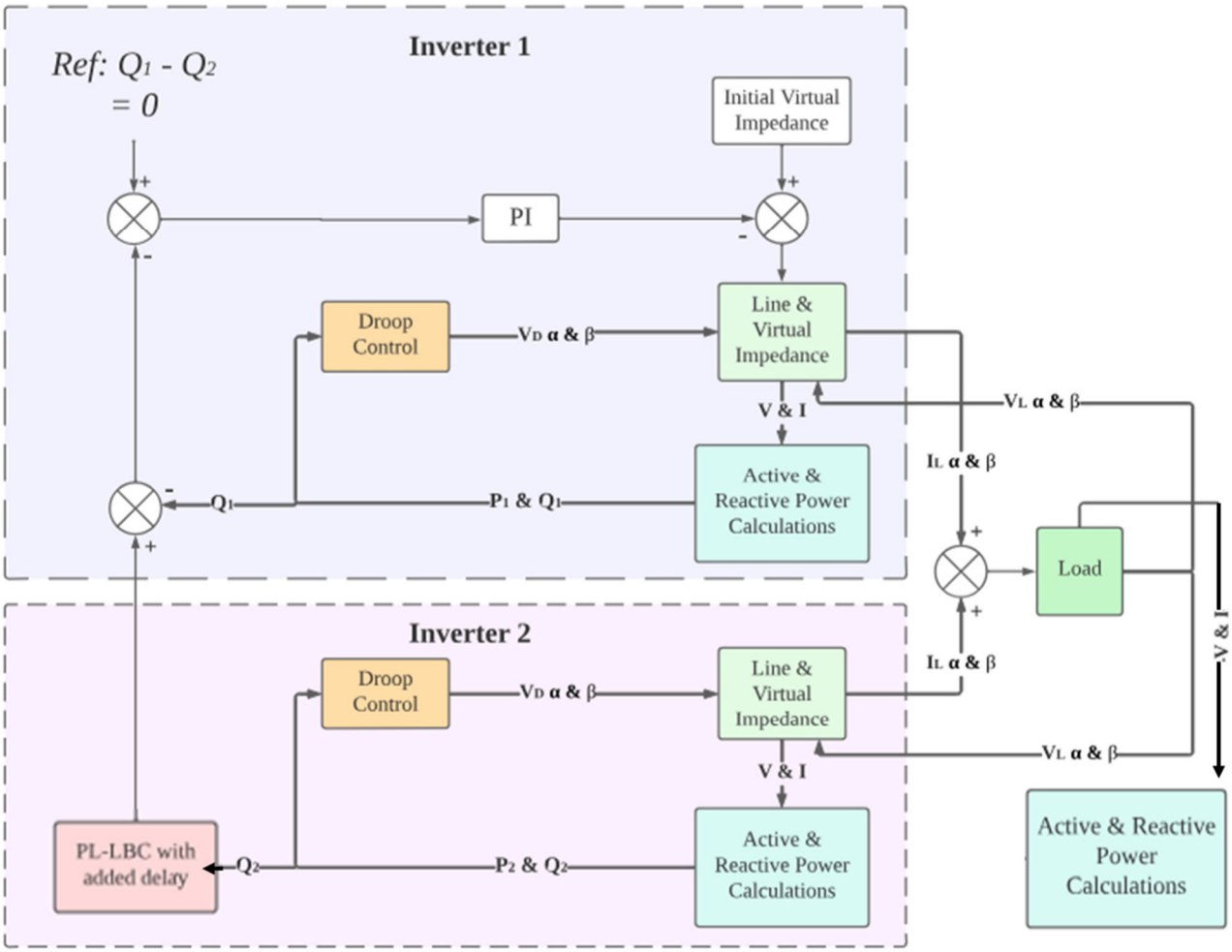

Figure 3.8.4–Simulink model

The open-loop transfer function as $(q_2 - q_1)/error(s)$ (see Figure 3.8.4) was extracted from simulations and is plotted in Figure 3.8.5. Several simulations at different delays were performed from 0.1 s to 0.4 s. The values are marked in the plot. In addition, an approximate model is shown with continuous line. As the amplitude frequency response is almost the same for the different delays only one curve is shown (grey line).

In the phase plot, three curves are shown at three different delays, markers are the exact simulation points and continuous lines are the approximate model.

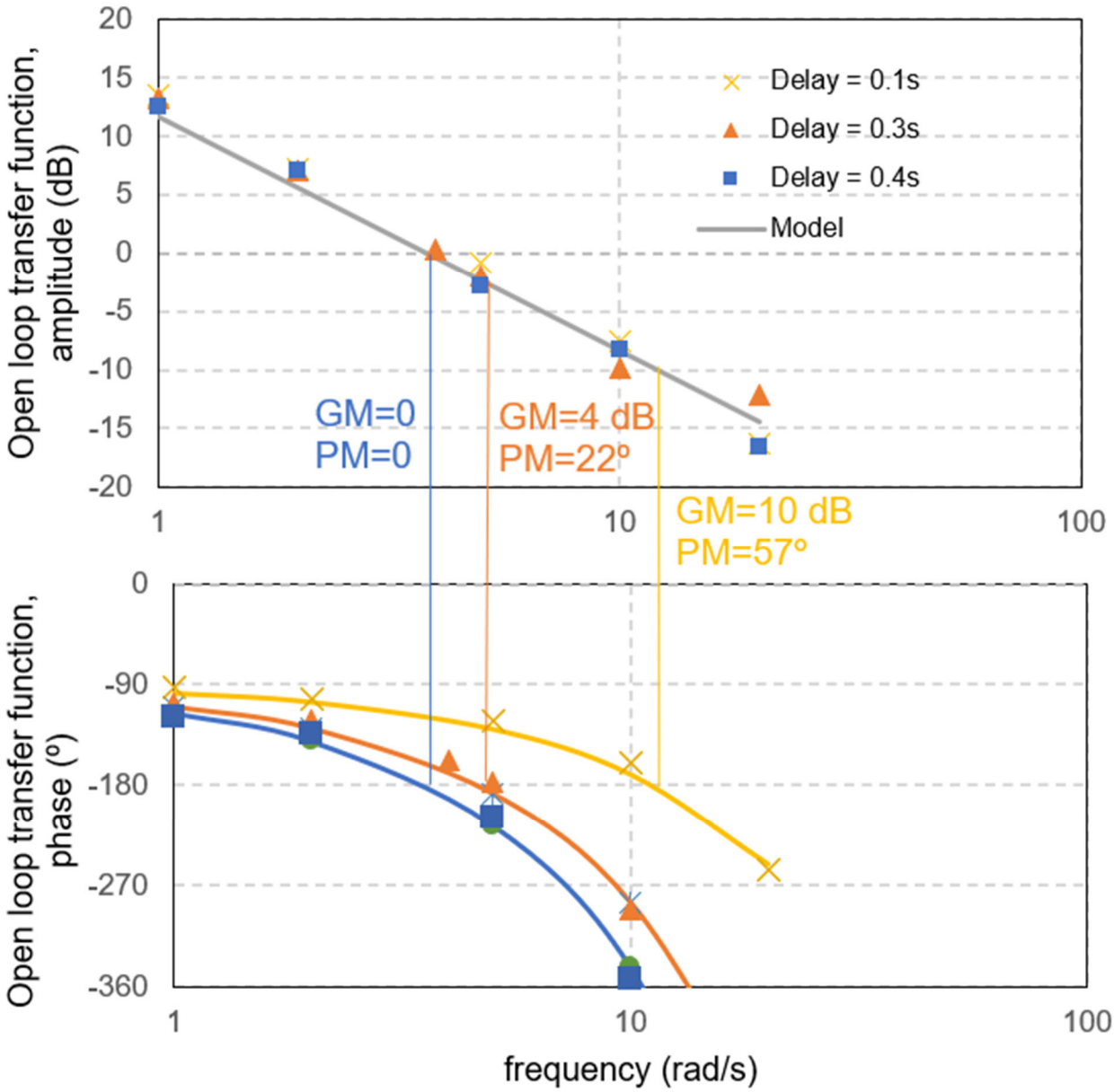

Figure 3.8.5–Open-loop transfer function $(q_2 - q_1)/error(s)$, for several communication delays. Approximate model in continuous line, markers are the simulations points in the Simulink model

From the plots, the approximate transfer function is:

$$q_2 - q_1 = \frac{k_1}{s} e^{-s(T_d + T_{d\,internal})}, \tag{3.8.23}$$

where k_1 is the integral constant, T_d is the communication delay and $T_{d\ internal}$ is the internal delay. The open-loop transfer function is analyzed for different communication time delays in a system of two inverters with a load of 26kW + 10kVAr. From Figure 3.8.5, the maximum allowable delay for a normal operation is 100ms, which achieves a phase margin of about 52º. For longer delay times, the phase shift is notably reduced and at a delay of 0.4s it becomes unstable for the current inverters and controller parameters. If a delay in the communication system is higher than 0.1 s, the virtual impedance controller must be re-adjusted. In addition to the frequency response of the open-loop system, the time-domain step test in Figure 3.8.6 also shows that the system is stable. For the test, the system of two inverters is connected to a load of 26kW + 10kVAr during 5 seconds and then the load is suddenly changed to 14kW + 3.6kVAr. In both cases the active and reactive power is perfectly shared.

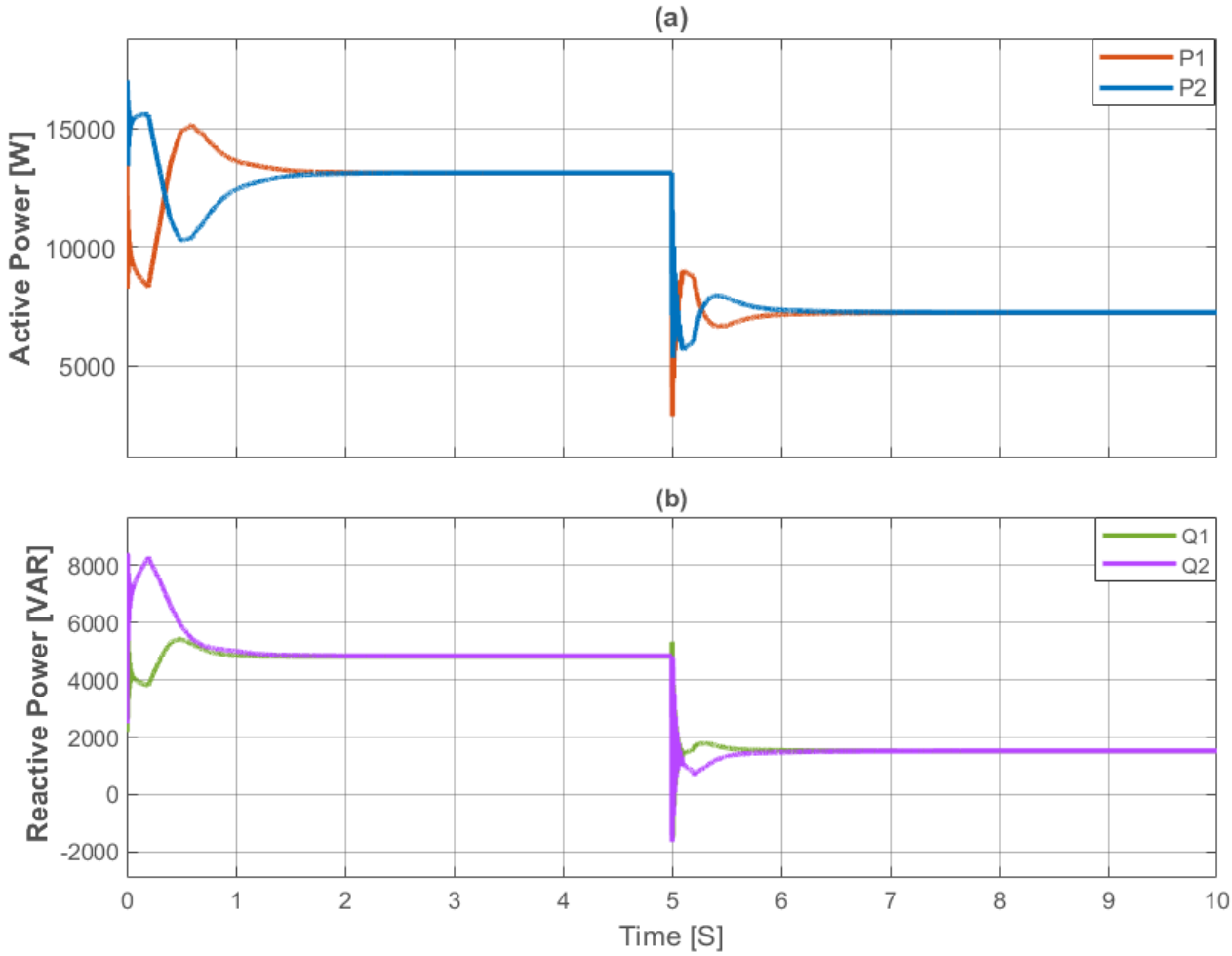

Figure 3.8.6–(a) Active and (b) Reactive powers under normal operation (No signal loss)

Sensitivity Analysis with respect to communication loss. In this subsection, the performance of the system is evaluated with respect to communication losses. The analysis is done using the same model described in the previous section with the virtual impedance control loop described in subsection 3.8.3. In order to mimic the low-bandwidth communication scheme described in subsection 3.8.4, the reactive power information is exchanged between the two inverters with a delay of 100 ms representing the delay of arrival of the 10-bit signal from one inverter to the other. Different scenarios were simulated.

No Signal losses. This scenario represents the normal expected operation of the proposed control algorithm and the communication scheme. As shown in Figure 3.8.6, the active and reactive power sharing is in line with the presented experimental validation shown in Figure 3.8.13(a) and the powers are perfectly shared among inverters.

50% Signal losses. In this test, one signal packet is lost every two packets. This represents a received signal with a 50% loss or in other words, a 50% slower communication bandwidth. As shown in Figure 3.8.7, the controller is still capable of achieving proper active and reactive power sharing. However, the behavior of the system is not as smooth as in normal operational conditions.

80% Signal losses. Now, 4 packets are dropped between each two received signals representing a communication loss of 80%. As shown in Figure 3.8.8, although the behavior of the system is much worse with fluctuations of both active and reactive powers, the controller is still able to achieve the proper sharing and reach a steady state of operation. One solution to reduce those power fluctuations is to limit the rate of change of the output power using a phase limiter (see section 3.7). Another solution is to change the virtual impedance controller's parameters considering the possibility of such a huge communication loss.

The dynamic of the droop controller when several inverters are interacting is reflected in Figure 3.8.6, Figure 3.8.7 and Figure 3.8.8. The oscillating transient can be mitigated using different modified droop control techniques, some alternatives were studied by the author in Section 3.7.

3.8.6. Experimental validation

To validate the proposed communication scheme and control method, a test bench consisting of two three-phase inverters based on the 2-level inverter topology with an LC output filter was constructed (see Figure 3.8.12). Each inverter has its own measurement system and its own controller (Texas Instruments F28379D DSP). The controller receives data from the measurement and communication circuits (discussed below) and generates the proper switching signal for the inverter and a binary sequence of the inverter's reactive power, which is sent to the communication circuit. Both inverters are connected to the same load through two power lines of different impedances. Each power line consists of a three-phase resistor and a three-phase inductor to mimic the resistance and the inductance of actual distribution power lines. The test bench is shown in Figure 3.8.9 and the details are shown in Table 3.8.1.

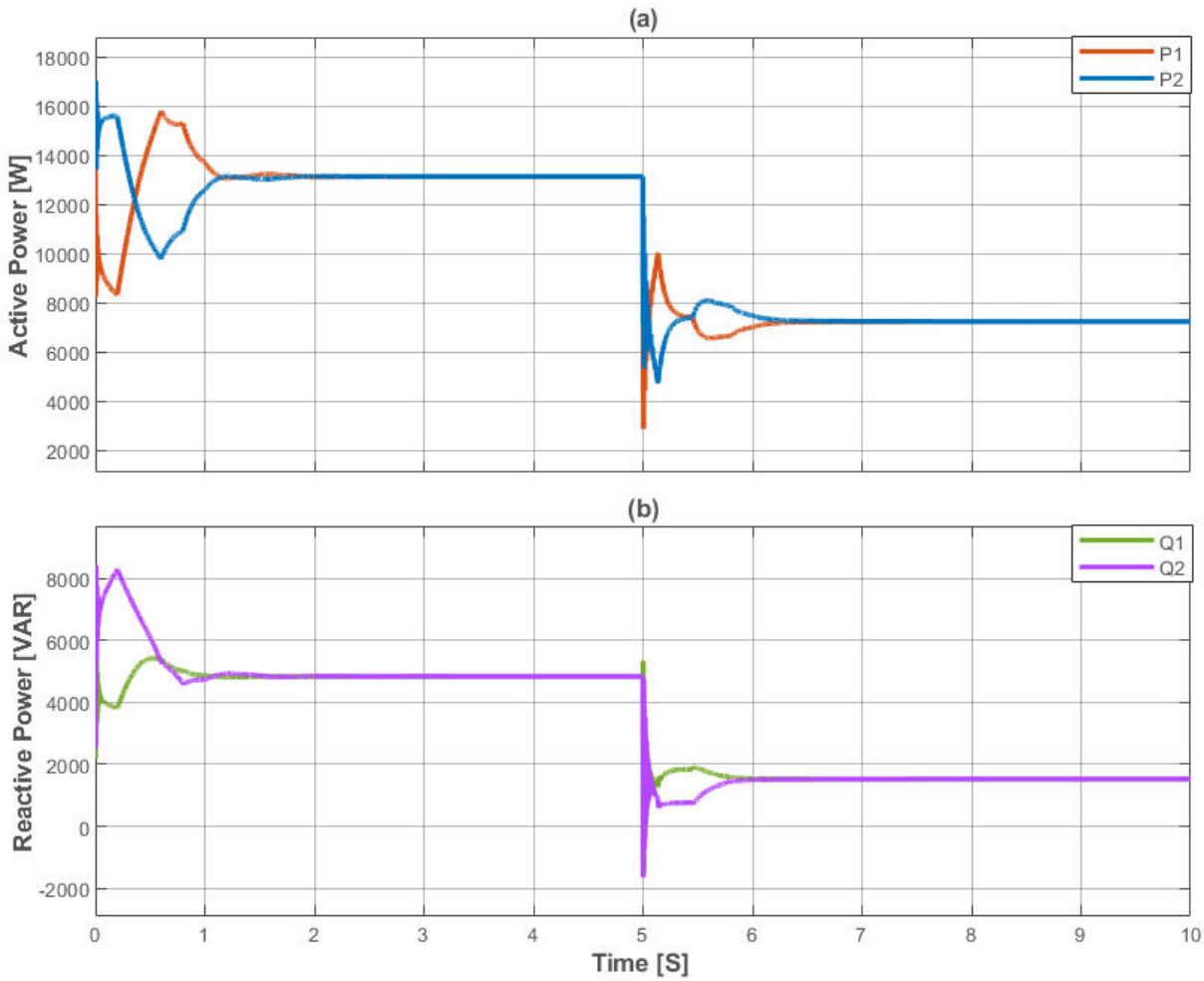

Figure 3.8.7–(a) Active and (b) Reactive powers with 50% signal loss

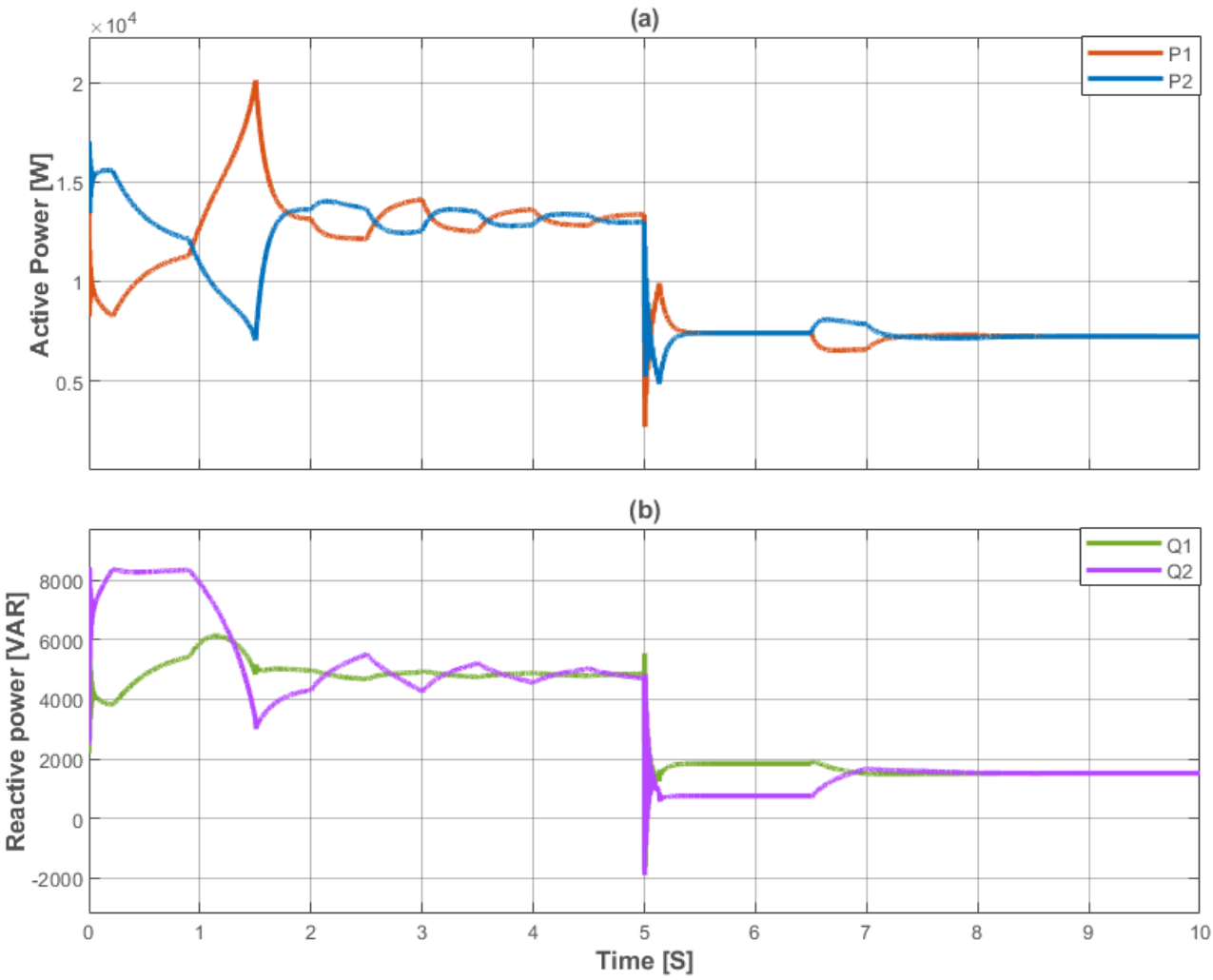

Figure 3.8.8–(a) Active and (b) Reactive powers with 80% signal loss

Table 3.8.1 Details of the experimental setup

Parameters	Values
Nominal grid frequency f_0	50 Hz
DC link voltage V_{DC}	650 V
Switching frequency, f_s	20 kHz
Filter inductance, L_f	1.1 mH
Filter capacitance, C_f	11 uF
Peak grid voltage, V_s	311 V
P_{L1}	0.1 + j0.236 Ω
P_{L2}	0.5 + 0.785 Ω

Power line communication PL-LBC. In order to share reactive power information between two inverters through a power line, a communication board was developed for each inverter. As shown in Figure 3.8.9, each board consists of two separate parts: detection and injection circuits. The detection circuit is an active band-pass filter based on the multiple feedback topology followed by a precision rectifier to transform the measured AC signal into a DC signal. After that, a comparator is used to adjusts the voltage so it matches the controller's digital voltage level. The injection circuit consists of a waveform function generator integrated circuit (AD9833) which generates a sine wave with a specific frequency (see Table 3.8.2).

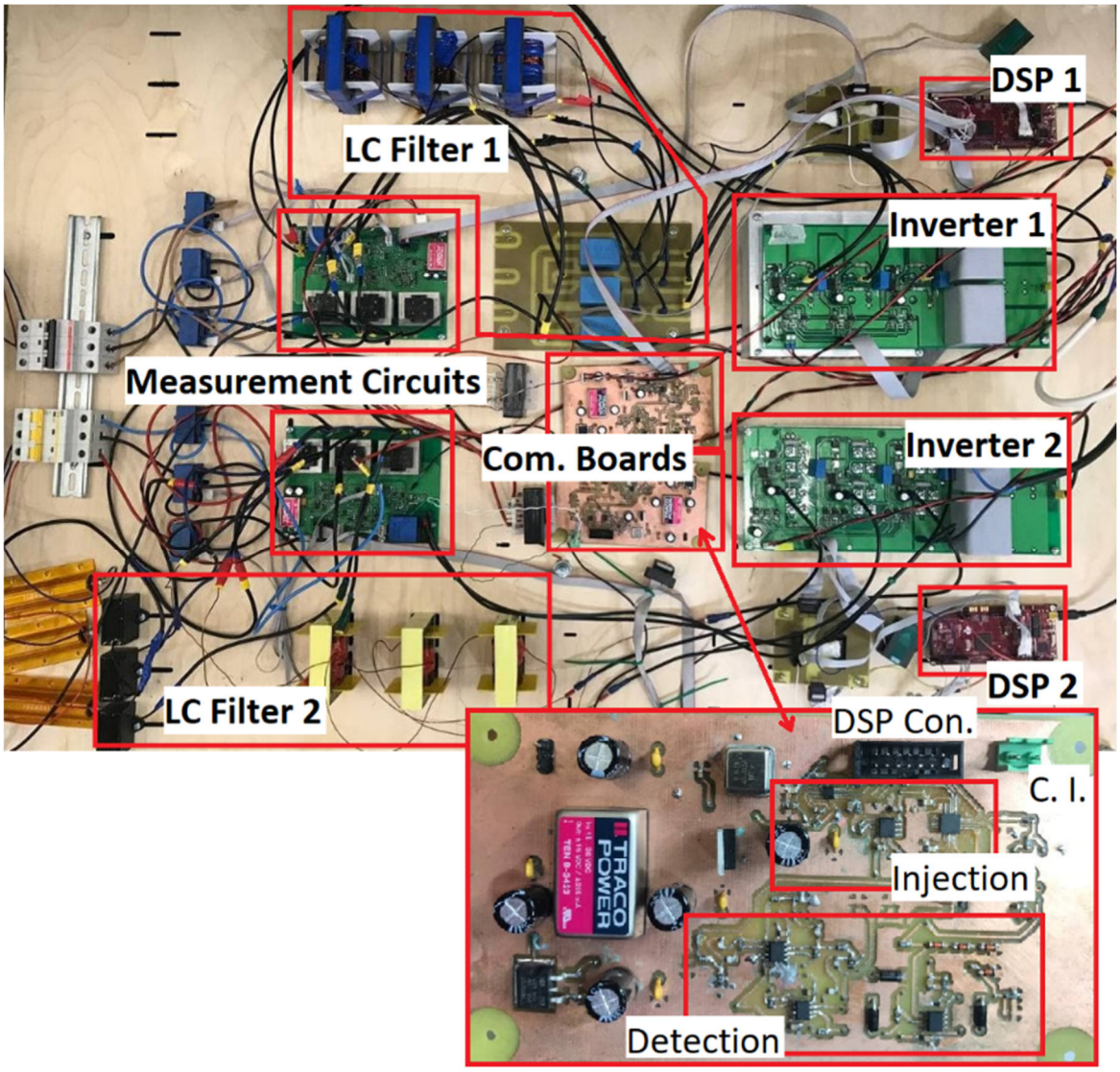

Figure 3.8.9–Experimental Test Setup

Table 3.8.2 Details of the inverter controller

Parameters	Values
Primary control	
Frequency droop coefficient k_{Idroop}	8.14e-4
Voltage droop coefficient k_{Qdroop}	0.025
Power filter cut-off frequency, ω_C	3 Hz
Initial virtual Impedance, Zv	0 + j0.9424 Ω
Virtual impedance control	
Virtual impedance control proportional term, kp v	1.07e-5
Virtual impedance control integral term, kp v	3.05e-5
Low pass filter for virtual impedance controller, ω_{Cv}	3Hz
PL_LBC power lines – low bandwidth communication	
Signal carrier frequency, $f_{inv,1}$	12kHz
Coupling transformer primary inductance, L_M	50 uH
Signal sampling time, Ts	0.18 s
Binary signal resolution	12 bit

The output sine wave of the AD9833 is amplified using a power amplifier and then injected into the power line through a coupling transformer. A multiplexer (MAX14778) is used to switch between the signal injection and detection modes. In addition, the multiplexer is used to modulate the signal based on the digital binary signal received from the controller. The protocol used in the experimental test is based on asynchronous communication, where each data frame contains 12 bits. Figure 3.8.10, shows the modulated power line communication signal (in orange) and the voltage at the inverter (in blue).

As show in the zoomed figure, the high logic is represented by the presence of the high frequency signal carrier on top of the 50 Hz voltage signal while the absence of this signal indicates a low logic. Figure 3.8.11 shows the injected (blue) signal and the detected (orange) signal. As shown in the zoomed figure, the modulated sinusoidal carrier

signal generated by the injection circuit of the communication board of the first inverter is received by the second one and transformed into a square signal using the signal detection circuit of the communication board as described above.

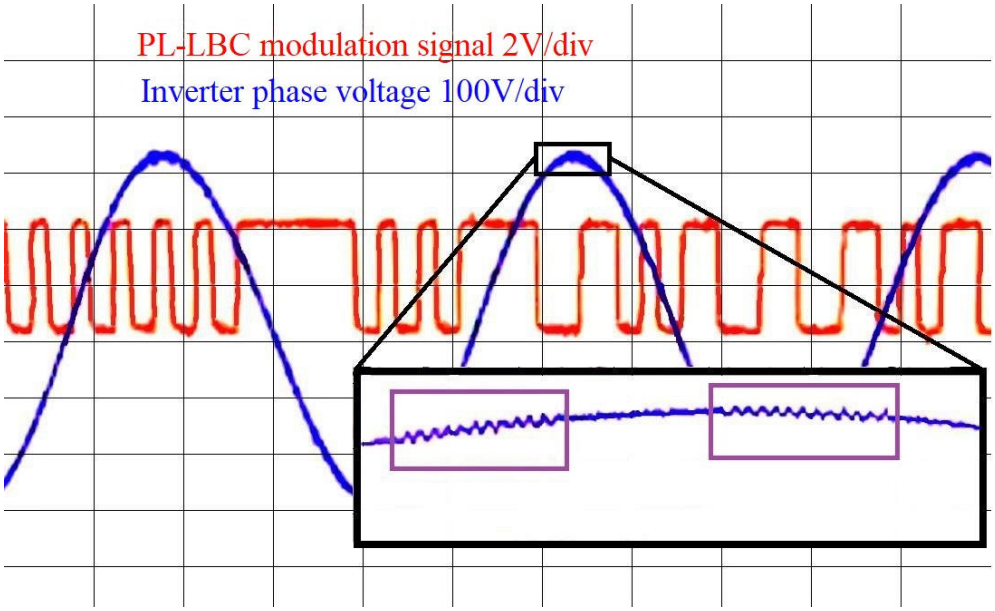

Figure 3.8.10–Experimental demonstration of proposed power line communication technique

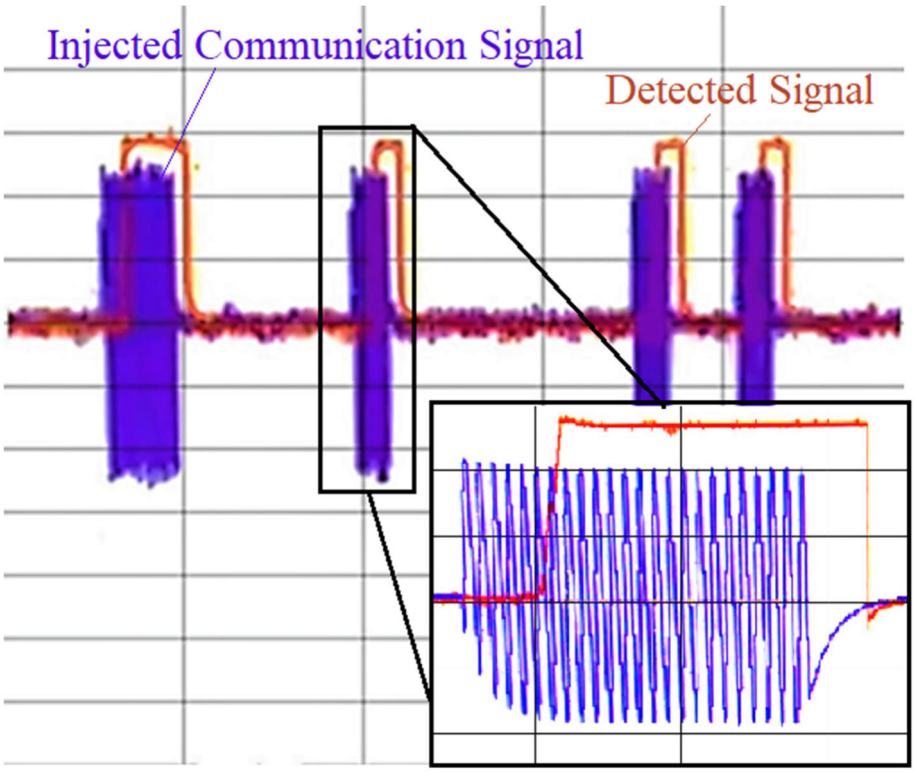

Figure 3.8.11–Experimental demonstration of proposed power line communication technique, blue: injected communication signal by inverter 1, orange: detected signal by inverter 2

In the first test, the reference test (see Figure 3.8.12), the first inverter is connected at t = 3s and the second inverter at t = 6s. After that, the power is increased at t = 15s and decreased again at t = 23.5s. The virtual impedance controller is not deployed in this test and there is no communication between the two inverters. As shown in Figure 3.8.12, the active power is shared properly. However, the reactive power is poorly shared between the two inverters. Figure 3.8.13 illustrates voltage and frequency of both inverters.

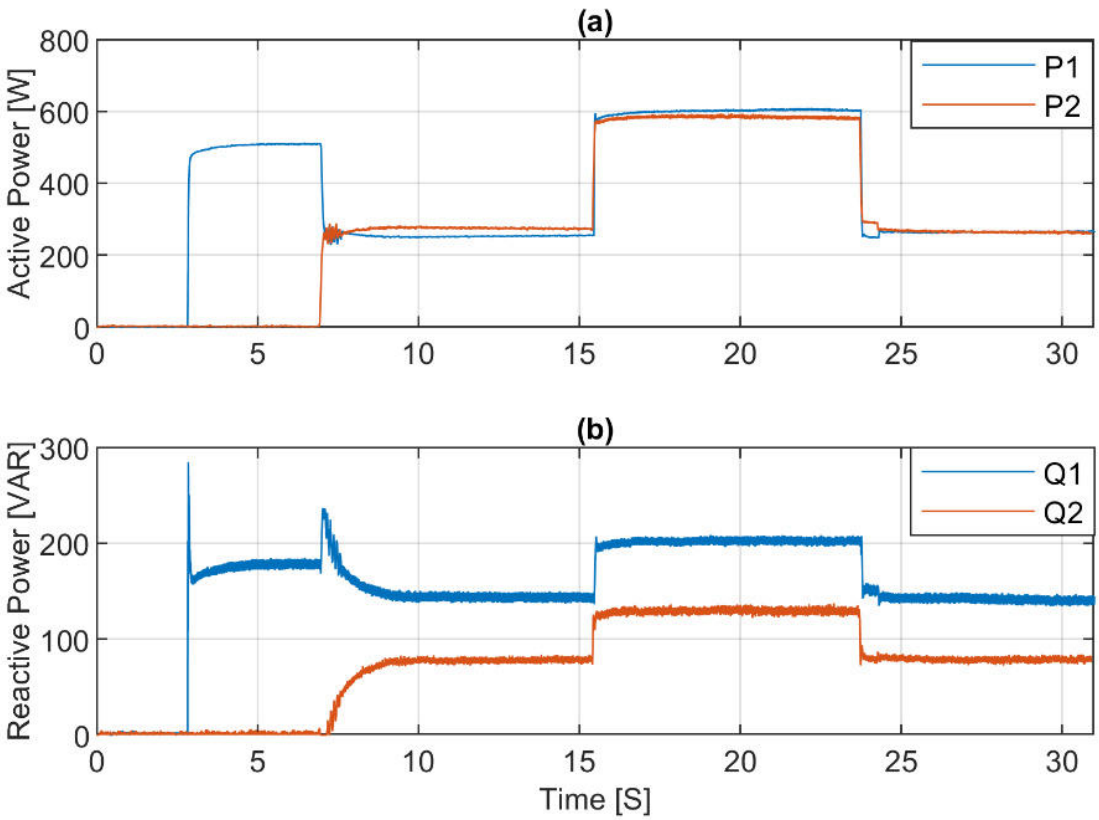

Figure 3.8.12. (a) Active power output of both inverters, (b) Reactive power of both inverters, no reactive power control.

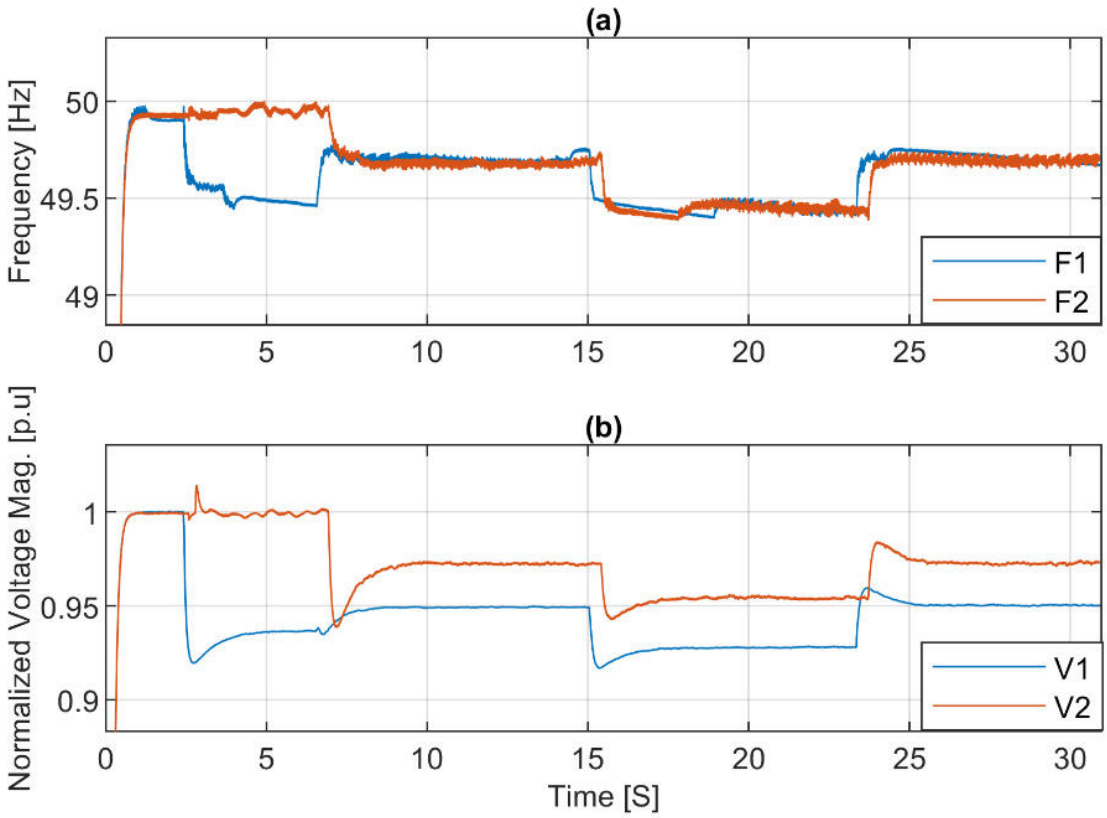

Figure 3.8.13–(a) Frequency of both inverters, (b) Voltage magnitude of both inverters, without reactive power control.

In the second test, the first inverter is connected at t = 4s, and the second inverter at t = 8s. Then, the power is increased at t = 28s and decreased again at t = 43s. The virtual impedance controller is now deployed and communication is allowed between the two inverters. Figure 3.8.14 shows that the active power is shared properly. In addition, the reactive power in now properly controlled after a settling time of about 5 seconds. Figure 3.8.15 shows the voltage and frequency of both inverters. The proposed controller is capable of properly sharing active and reactive power between the two inverters with a satisfactory response time. The settling time can be further decreased by increasing the bandwidth of the signal transmission or by using other modulation techniques that allow for higher data transfer. Furthermore, the effect of this communication technique on the load voltage is small, only a 960 mV compared to the 310 V of the fundamental component of the signal.

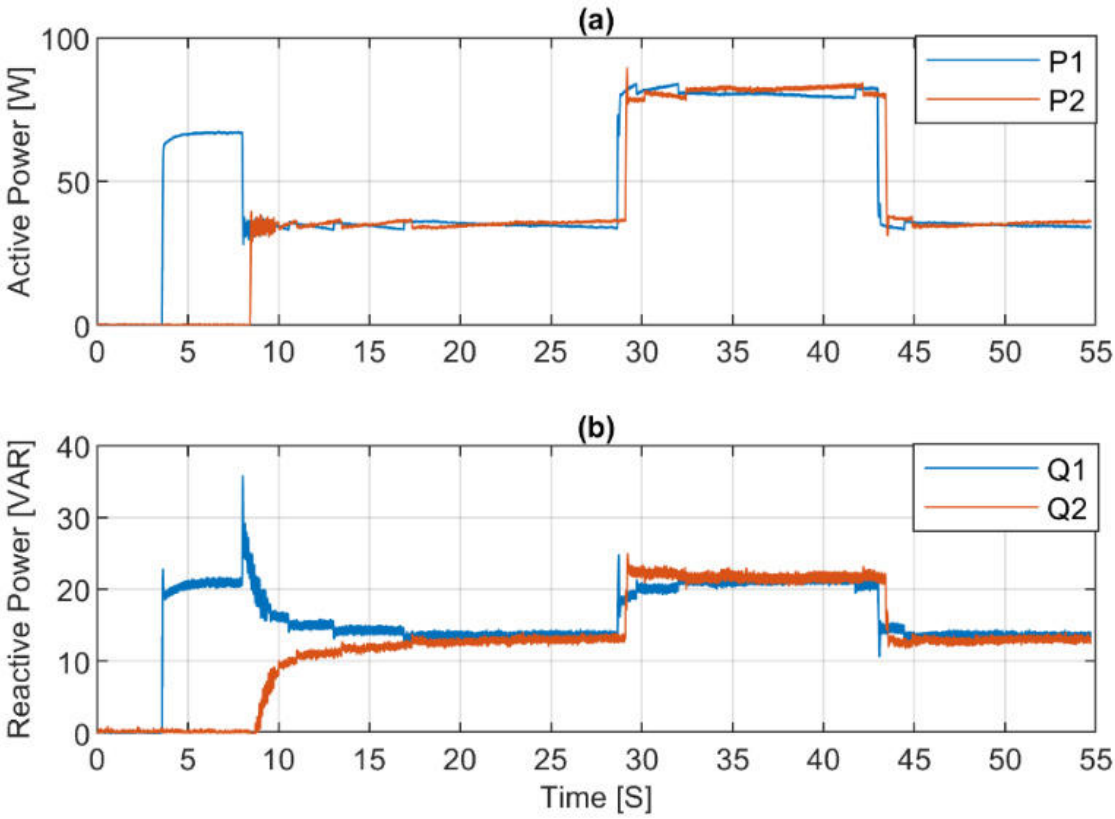

Figure 3.8.14–(a) Active power output of both inverters, (b) Reactive power of both inverters, with reactive power control

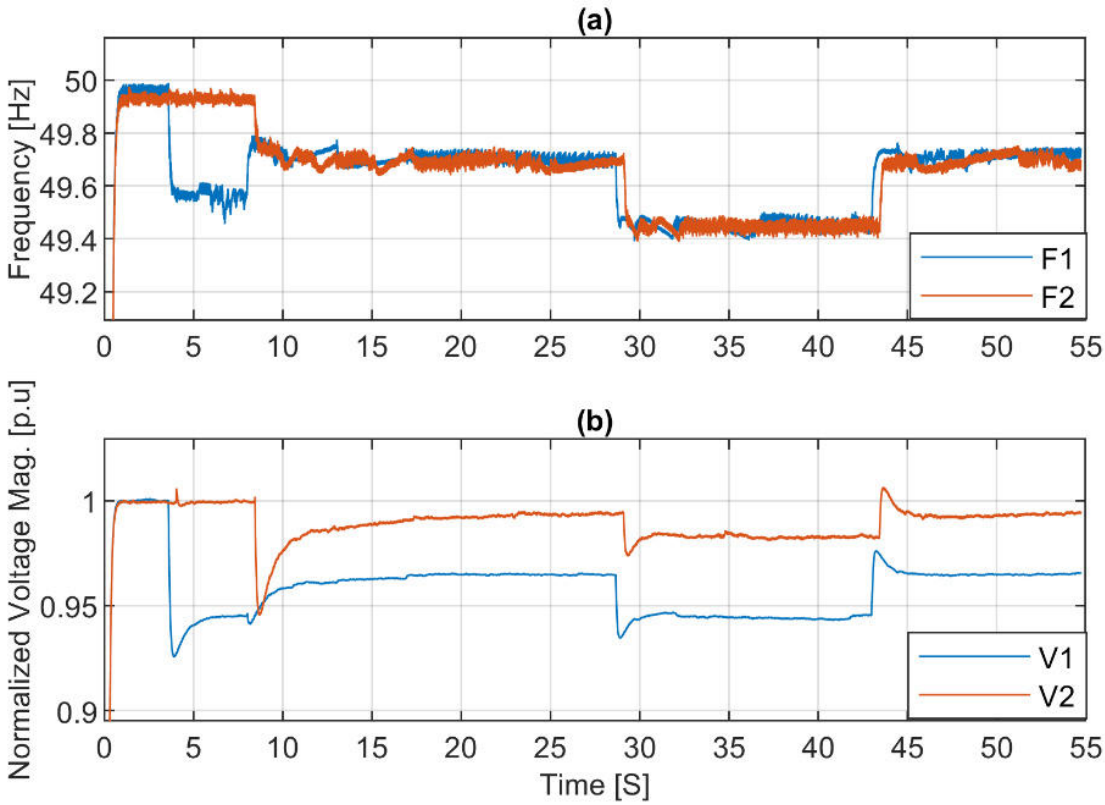

Figure 3.8.15. (a) Frequency of both inverters, (b) Voltage magnitude of both inverters, with reactive power control.

3.8.7. Summary

Inverters can deliver a fixed amount of apparent power limited by their maximum voltage and currents. Therefore, if the reactive power is poorly shared, the active power will be limited and this may lead to shut down of inverters or voltage instabilities. As a solution, a communication scheme is proposed for sending reactive power signals between inverters through power lines. By utilizing these shared signals, an adaptive virtual impedance controller was proposed to adjust the inverter's virtual impedance, resulting in accurate reactive power sharing. The reactive power sharing is significantly enhanced with the proposed communication and the new control scheme compared to the conventional droop control.

In addition, as shown in the analysis presented in subsection 3.8.4, the proposed control algorithm and communication technique is stable under normal operating conditions and under communication loss or excessive time delays. Moreover, the power line communication technique utilizes the existing microgrid infrastructure to establish communication links between inverters and the load buses without a need of any external communication hardware. This avoids additional costs and allows easier installation of inverters. As a future work, the proposed communication technique will be used for achieving the secondary voltage and frequency control. Furthermore, the extendibility of the proposed method to achieve proper reactive power sharing among several inverters in a grid will be investigated. This includes using concepts from more advanced communication protocols such as: CAN-BUS where each inverter is given a priority for sending its reactive power which is received by all other inverters, RS485 using the asynchronous start-stop method and others. The details of the proposed technique were published in [146, 174].

As the inverters are the interface in EV chargers and many other applications, they can get the advantages of this proposal in order to coordinate efforts using communication through power lines in vehicle-to-grid applications for grid support.

Chapter 4. PARTIAL ISOLATION: ALTERNATIVE TOPOLOGIES FOR MULTI-PORT SYSTEM

In case that there is no requirement of having all of the ports isolated, partial isolation allows simplifying the hardware design and the number of components. In this chapter, two types of partial isolation will be discussed. Section 4.1 proposes a non-isolated converter to be connected to an isolated inverter and Sections 4.2, 4.3, 4.4 propose a combination of inverter techniques with resonant DC/DC converters techniques that can reduce the number of components of the whole system by creating a AC and DC multi-port converter.

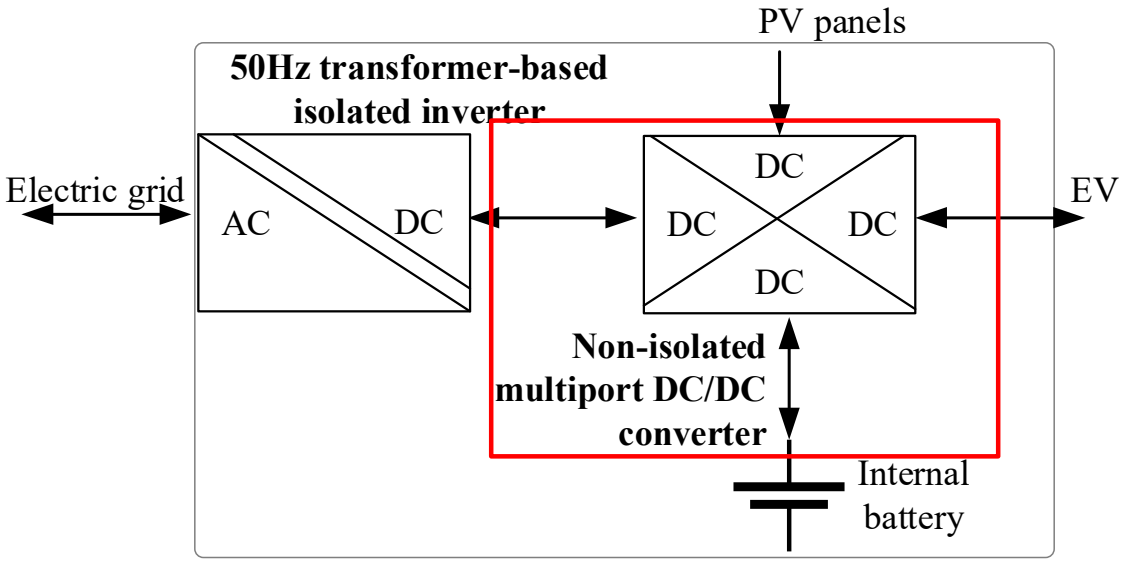

Figure 4.1–Electric charger using partial isolation solution based on non-isolated converter

4.1. Non-isolated multi-port converters

Non-isolated multi-port converters can be used in multiple port systems when the several ports can be connected without isolation. The ports that require isolation must be connected through an isolated DC/DC converter or an inverter. In Figure 4.1, the connection is shown where the only port which has isolation is the one connected to the

grid. This Section describes a novel non-isolated multi-port converter with reduced number of components and high gain which allows to connect small storage and local generation to grid inverters. This is useful in domestic applications. The details of the section were published in [189].

4.1.1. Existing solutions

Several works can be found in the literature related to non-isolated multi-port converters [179]–[188]. In [179], a bidirectional multi-input converter with a single inductor is presented to integrate multiple DC sources to a DC grid. In [180], a new converter capable of reconfigure its energy sources is shown, however, it has a high ripple current for batteries, and it also uses too many switches, therefore it is complex and not cost-effective. In [185], the proposed converter uses a coupled inductor to increase the converter´s gain. Unfortunately, it is not able to control the current from each port independently.

A converter that can independently control the current of each input port, and has a fewer number of components is presented in [188]. Unfortunately, the energy storage devices should be the same or at least in the same voltage range and power capabilities to guarantee a high conversion efficiency, and the conversion ratio is equivalent to a traditional buck or boost converter.

This section presents a non-coupled, non-isolated high-gain, highly efficient DC/DC converter which makes use of only six switches to achieve the bidirectional power flow of three ports [189]. In comparison to other similar converters, the proposed converter has the highest conversion gain in one port, and the number of components is moderate enough with no diodes or other elements that can reduce the efficiency of the system at low voltage, details can be seen in subsection 4.1.5. The converter controls the input port currents independently. Moreover, the high-gain conversion ratio allows to use a small energy storage device in one of the ports with a reduced voltage (<50V) and easily reach a DC voltage grid (500-1000V) at the output port (port 3). Therefore, it fits

applications where small electric vehicles, in which the energy storage elements are not too large and require a highly efficient converter to preserve battery's capacity.

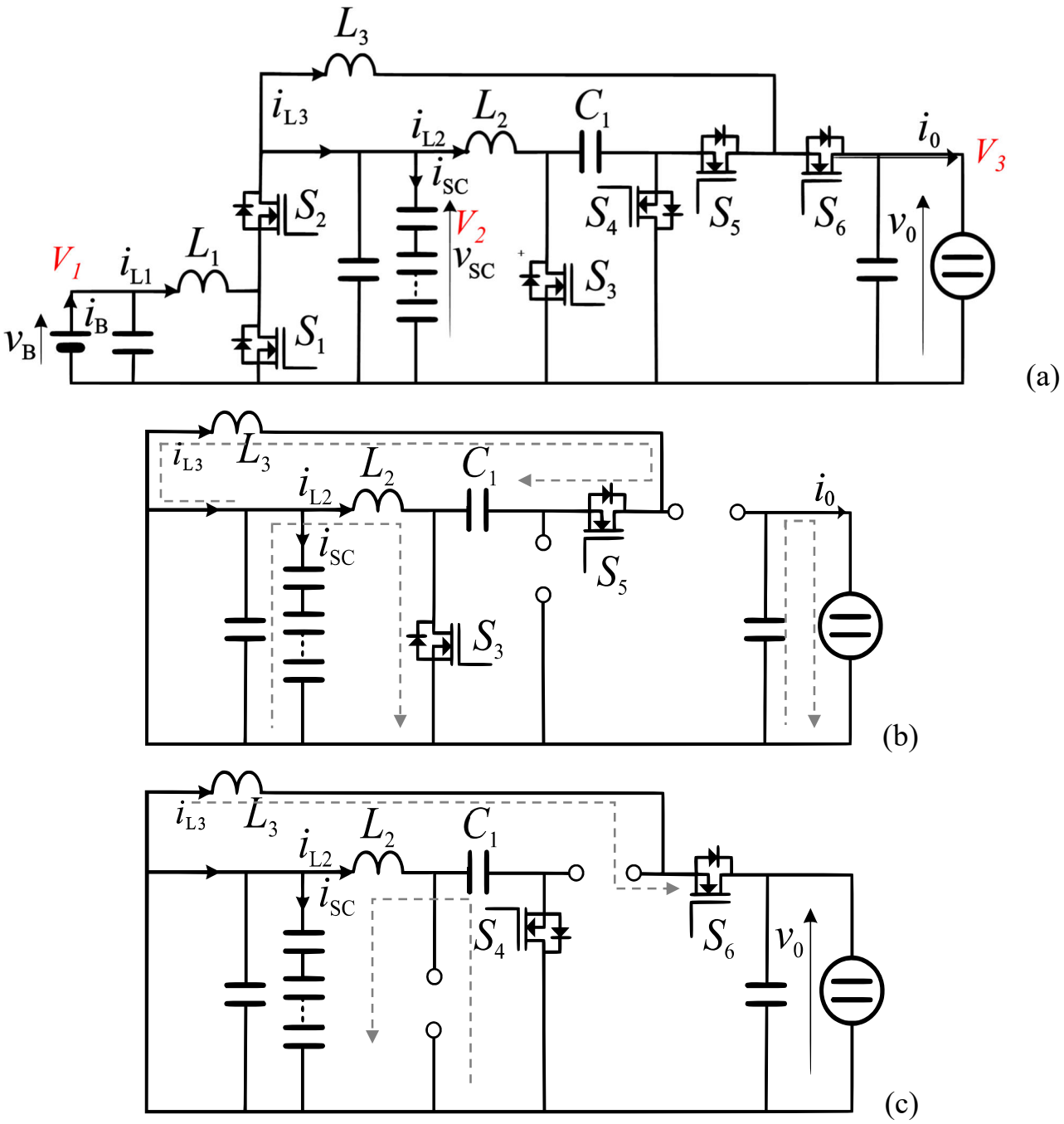

Figure 4.1.1–Proposed converter (a) topology, (b) interval D_2T and (b) interval $(1-D_2)T$

4.1.2. Multi-port high-gain converter: steady-state analysis

The proposed converter is shown in Figure 4.1.1. It consists of three inductors and six switches and four capacitors. Notice that the proposed converter can be understood as two cascade converters, in which the first one is a traditional half-bridge converter and the second one is a high-gain converter. However, in this research, the whole converter is considered as a multi-port input converter because a single controller is dealing with all the switching signals in order to control the power flow. More ports can be added if they are needed using the same principle.

The analysis of the converter will be divided in two operation modes: step-up (or boost) mode and step-down (or buck) mode. Using these modes, six transfer operations can be done:

a) port 1 delivers power to port 3 while port 2 is off,

b) port 1 delivers power to port 2 while port 3 is off,

c) port 2 delivers power to port 3 while port 1 is off,

d) port 1 absorbs power from port 3 while port 2 is off,

e) port 2 absorbs power from port 3, while port 1 is off,

f) port 2 delivers power to port 1 while port 3 is off.

It is considered that port 1 is connected to an EV battery, port 2 to a set of supercapacitors and port 3 to a DC grid.

The step-up mode. During this mode, S_2, S_4 and S_6 are always off. The active switches are S_1, S_3 and S_5. S_1 is switched on during D_1T and off during $(1-D_1)T$, where T is the switching period and D_1 is the duty cycle of the switch S_1. S_3 and S_5 are switched on during D_2T, as shown in Figure 4.1.1(b) and switched off during $(1-D_2)T$, as shown in Figure 4.1.1(c). Considering continuous current mode, the voltage in L_1 is:

$$v_{L1}(t) = L_1 \frac{di_{L1}}{dt} = V_1 \text{ during } \Delta t_{1\text{on}} = D_1 T \text{ } (S_1\text{=on}) \text{ and} \tag{4.1.1.a}$$

$$v_{L1}(t) = L_1 \frac{di_{L1}}{dt} = V_1 - V_2 \text{ during } \Delta t_{1\text{off}} = (1 - D_1)T \text{ } (S_1\text{=off}). \tag{4.1.1.b}$$

The voltage conversion ratio between V_1 and V_2 follows the boost converter's voltage conversion ratio:

$$V_2 = \frac{V_1}{1 - D_1}. \tag{4.1.2}$$

For the L_2 voltage, v_{L2}, considering that $v_{C1} = V_{C1}$ is constant, we have:

$$v_{L2}(t) = L_2 \frac{di_{L2}}{dt} = V_2 \text{ during } \Delta t_{2\text{on}} = D_2 T \text{ (S}_3\text{=on) and} \tag{4.1.3.a}$$

$$v_{L2}(t) = V_2 - V_{C1} \text{ during } \Delta t_{2\text{on}} = (1 - D_2 T) \text{ (S}_3\text{=off).} \tag{4.1.3.b}$$

Thus, the ratio between V_2 and V_{C1} is:

$$V_{C1} = \frac{V_2}{1 - D_2}. \tag{4.1.4}$$

For L_3, the same procedure can be done. By analyzing the v_{L3}, we obtain:

$$v_{L3}(t) = V_2 + V_{C1} = L_3 \frac{di_{L3}}{dt} \text{ during } \Delta t_{2\text{on}} = D_2 T \text{ (S}_3\text{=on) and} \tag{4.1.5.a}$$

$$v_{L3}(t) = V_2 - V_3 = L_3 \frac{di_{L3}}{dt} \text{ during } \Delta t_{2\text{off}} = (1 - D_2) T \text{ (S}_3\text{=off).} \tag{4.1.5.b}$$

then considering that the increase of i_{L3} from (4.1.5.a) during $\Delta t_{2\text{on}}$ is equal to the decrease in i_{L3} during $\Delta t_{2\text{off}}$ from (4.1.5.b):

$$(V_2 + V_{C1}) + (1 - D_2)(V_2 - V_3) = 0 \tag{4.1.6}$$

thus, using (4.1.4), the ratio between V_2 and V_3 can be obtained:

$$V_3 = \frac{V_2}{(1 - D_2)^2} \tag{4.1.7}$$

which gives a high-gain conversion ratio.

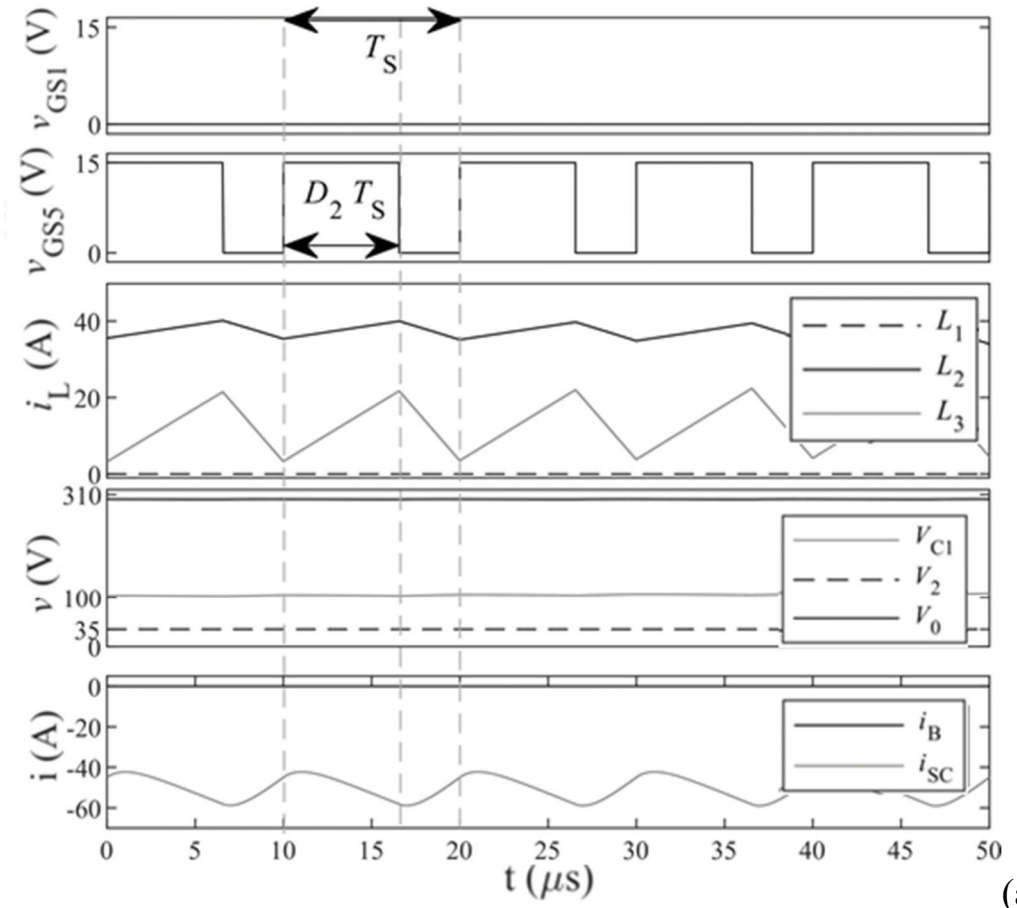

(a)

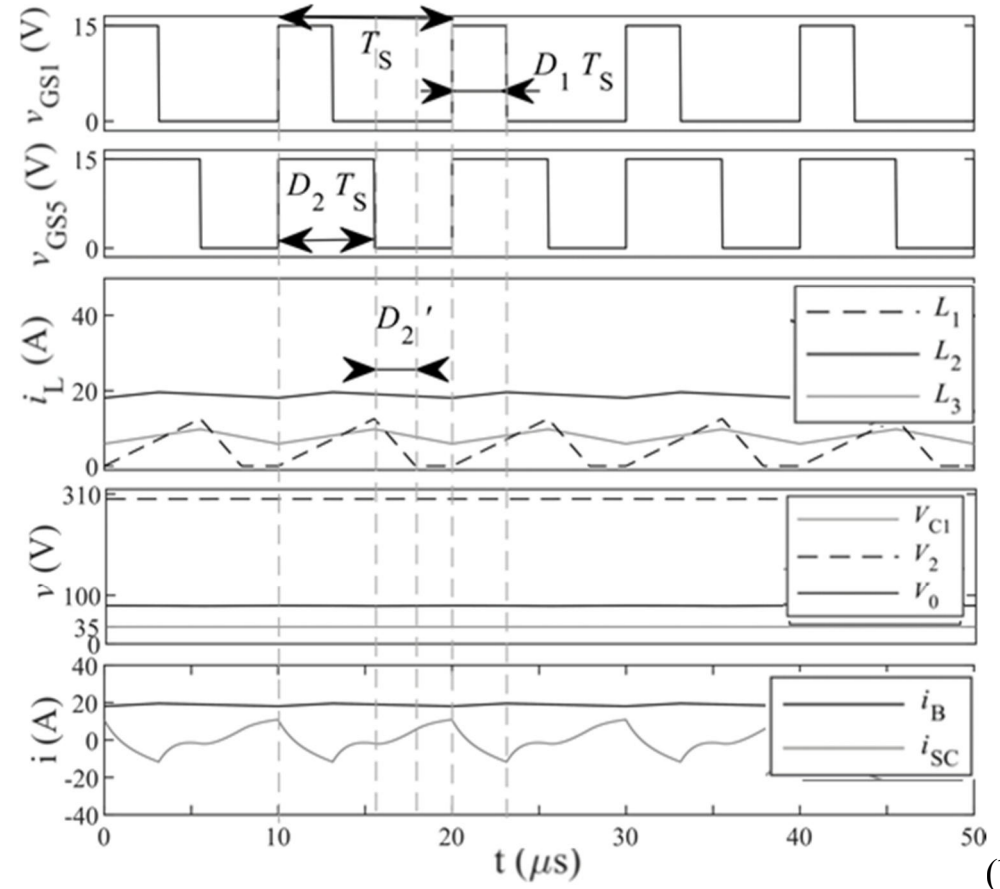

(b)

Figure 4.1.2–Step-up mode: (a) Port 1 delivers power to port 3, (b) port 2 delivers power to port 3, $v_{GS3}=v_{GS5}$

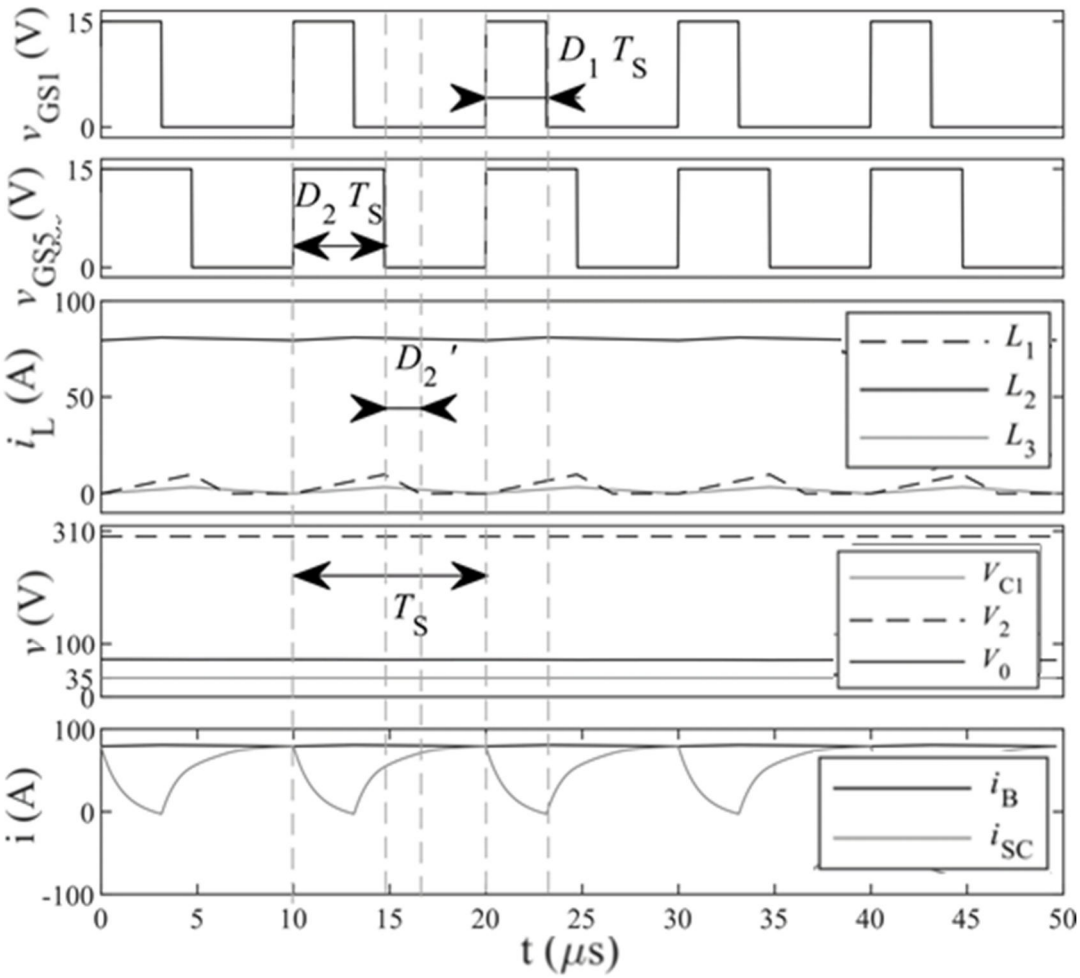

Figure 4.1.3–Step-up mode: port 1 delivers power to port 2, v_{GS3}=v_{GS5}

S_1 controls the port 1 current, i_1, and the ratio between i_{L2} and i_{L3} is controlled by D_2 based on the C_1 voltage:

$$i_{C1}(t) = C_1 \frac{dv_{C1}}{dt} = -i_{L3} \text{ during } \Delta t_{2\text{on}} = D_2 T \quad (S_3\text{=on}) \tag{4.1.8.a}$$

and

$$i_{C1}(t) = i_{L2} \text{ during } \Delta t_{2\text{off}} = (1 - D_2)T \quad (S_3\text{=off}). \tag{4.1.8.b}$$

Considering that inductors behave as current sources, with averaged values equal to I_{L1}, I_{L2} and I_{L3}:

$$I_{L2} = \frac{D_2 I_{L3}}{1 - D_2}, \tag{4.1.9.a}$$

$$I_1 = I_{L1} \tag{4.1.9.b}$$

$$\langle i_{s2} \rangle = I_{L1}(1 - D_1), \tag{4.1.9.c}$$

where $\langle i_{s2} \rangle$ is the average current within a cycle in S_2. In addition, the average of i_2, I_2, using Figure 4.1.2 and (4.1.9) is:

$$I_2 = (1 - D_1)I_{L1} - I_{L2}\,(2 - D_2). \tag{4.1.10}$$

Therefore, to transfer energy directly from port 1 to port 3, $(1 - D_1)I_{L1} - I_{L2}\,(2 - D_2) = 0$, must be satisfied. D_1 controls the battery current as it will be shown in the next subsection and by controlling D_2, I_2 can be zero. This is the a) mode.

In addition, port 1 can only deliver power to port 2 using D_1. For that, $D_2 = 0$, thus S_3, S_4, S_5 and S_6 are off. This is the b) mode. Finally, in the c) mode, port 2 delivers energy to the port 3 using D_2 while $D_1 = 0$. Figure 4.1.2 and Figure 4.1.3 show the three modes. If the current in L_3 reaches zero during the off time, the converter operates in Discontinuous Conduction Mode (DCM). In order to keep using the same analysis, the off-time which was previously $\Delta t_{2\text{off}} = (1 - D_2)T$, in DCM is replaced by $\Delta t_{2\text{off}} = D_2{}'T$. This is the subinterval where the inductor's current, i_{L3} goes to zero as shown in Figure 4.1.2 (b) and Figure 4.1.3, resulting:

$$V_3 = \frac{V_2}{D_2{}'^{\,2}}, \tag{4.1.11}$$

if $D_2{}'$ is known, the analysis is still valid. The value of $D_2{}'$ can be obtained using the same techniques as in a buck converter using DCM as it depends on the load.

The step-down mode. In the step-down mode, S_1, S_3 and S_5 are off. The duty cycle D_1 controls S_2 and the duty cycle D_2 controls S_4 and S_6. Again, the three switches turn on at the same time and S_1 turns off at D_1T and S_4 and S_6 at D_2T respectively. Following the same procedure as in the step-up mode, the main relations can be obtained.

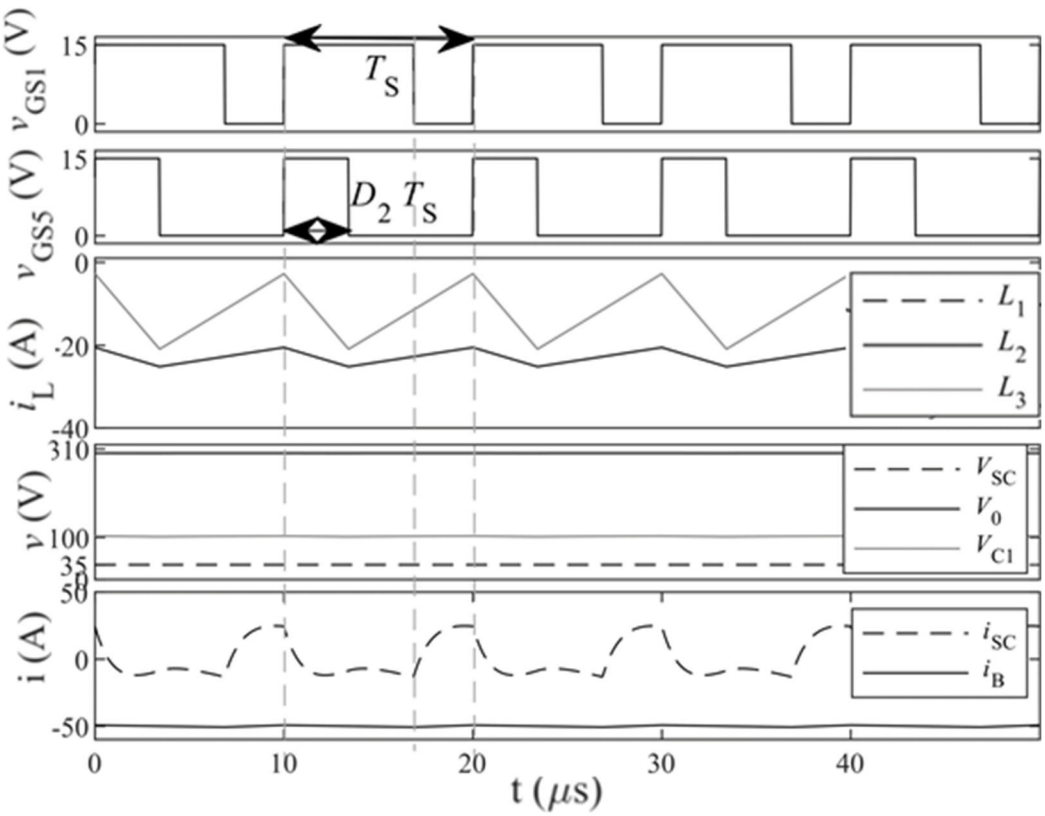

Figure 4.1.4–Step-down mode: Port 2 absorbs power from port 3, v_{GS3}=v_{GS5}

First, the relation between V_1 and V_2 is:

$$V_1 = D_1 V_2, \tag{4.1.12}$$

then, for C_1 and V_2:

$$V_2 = D_2 V_{C1}, \tag{4.1.13}$$

next, applying the same procedure for V_2 and V_3

$$V_2 = (D_2)^2 V_3. \tag{4.1.14}$$

In this mode, I_{L3} can be expressed as:

$$I_{L3} = \frac{D_2 I_{L2}}{1 - D_2}, \tag{4.1.15}$$

and the average current $\langle i_{s2} \rangle$ is

$$\langle i_{s2} \rangle = D_1 I_{L1}, \tag{4.1.16}$$

finally, the resulting I_2 is:

$$I_2 = \langle i_{s2} \rangle - I_{L2} - I_{L3} = D_1 I_{L1} - \frac{I_{L2}}{1 - D_2}. \tag{4.1.17}$$

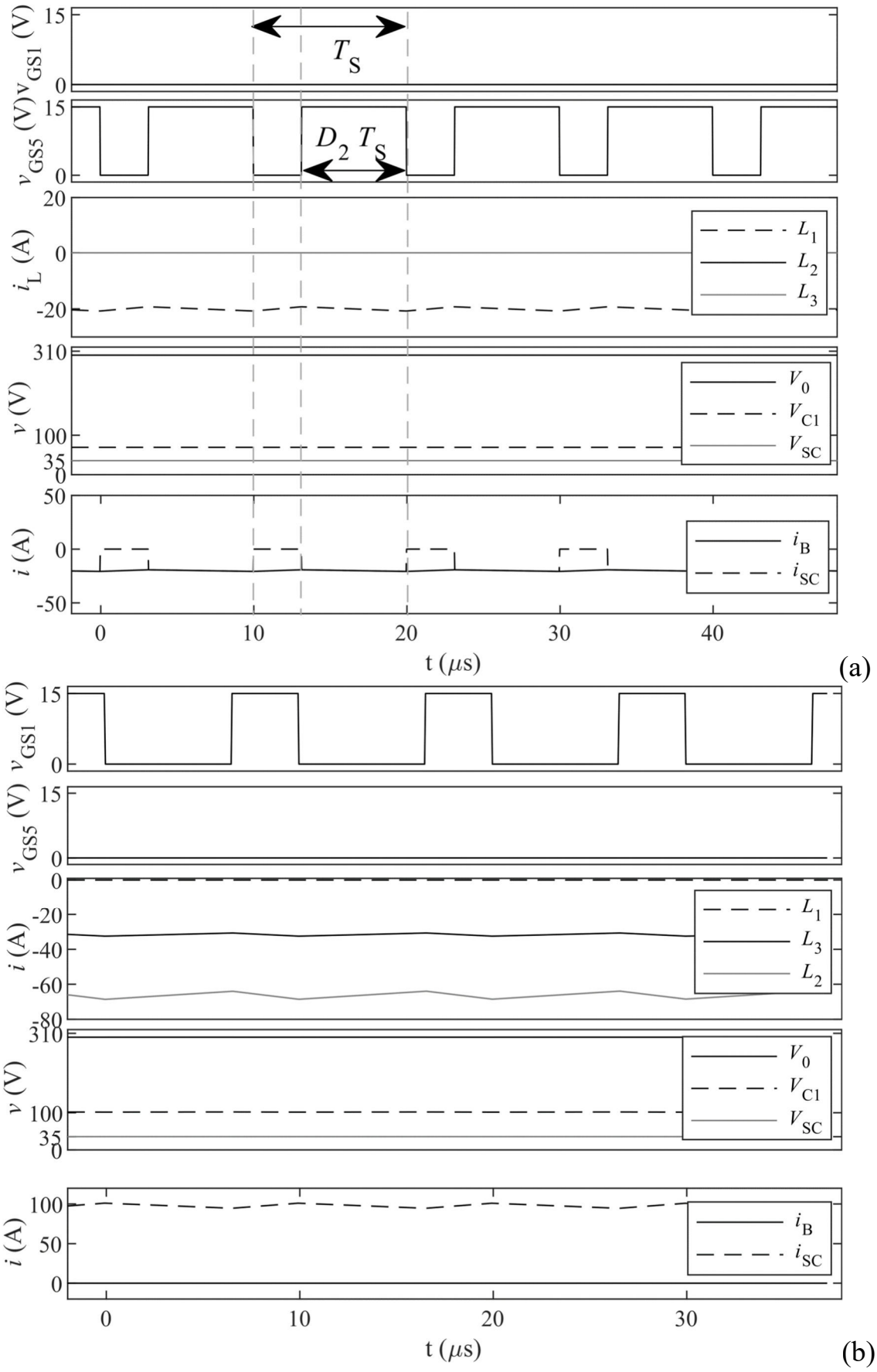

Figure 4.1.5–Step-down mode, (a) port 1 absorbs power from port 3 and (b) port 2 delivers power to port 1, v_{GS3}=v_{GS5}

Therefore, by controlling D_1 and D_2 different operation modes can be obtained. For the d) mode, i_2=0, then:

$$D_1 = \frac{I_{L2}/I_{L1}}{1 - D_2}, \tag{4.1.18}$$

For the e) mode, $I_1 = 0$, so $I_{L1} = 0$, S_1 and S_2 are off and D_1=0:

$$I_2 = -\frac{I_{L2}}{1 - D_2}. \tag{4.1.19}$$

Finally, for the f) mode, D_2=0, so:

$$I_2 = D_1 I_{L1}. \tag{4.1.20}$$

Figure 4.1.4 and Figure 4.1.5 shows the three operation modes in the step-down mode.

4.1.3. Multi-port high-gain converter: small-signal analysis and its controller

The proposed design can be understood as two cascaded converters because V_2 is an input voltage source. Thus, the dynamics of the first part is governed by $d_1(t) = D_1 + \tilde{d}_1(t)$ considering $v_1(t) = V_1 + \tilde{v}_1(t)$ and $v_2(t) = V_2 + \tilde{v}_2(t)$, where V_1 and V_2 are the averaged values and $\tilde{v}_1$ and $\tilde{v}_2$ the perturbations around the average point. The second part is governed by D_2, using only v_2.

The first part of the converter is a half-bridge converter, which works in one direction as a step-up (boost) and in the other as a step-down (buck) converter. In the continuous mode, in which the L_1 current is always greater than zero (in step-up mode), two models can be defined: for the on-time and for the off-time of S1. The models are:

$$\frac{di_{L1}}{dt} = \frac{v_1}{L_1} \text{(on-time)} \quad \text{and} \quad \frac{di_{L1}}{dt} = \frac{v_1 - v_2}{L_1} \text{(off-time)}. \tag{4.1.21}$$

Using the averaging technique during one period T, the averaged model becomes [35, 190]:

$$\frac{d\langle i_{L1}\rangle}{dt} = \frac{v_1 - (1 - d_1).v_2}{L_1}, \tag{4.1.22}$$

where $\langle x \rangle$ means the averaged value of x during T. Then, considering explicitly the small perturbations $\langle x \rangle = X + \tilde{x}$, the model becomes ($\frac{dX}{dt} = 0$, so $\frac{dI_{L1}}{dt} = 0$):

$$\frac{d\widetilde{\iota_{L1}}}{dt} = \frac{V_1 - (1 - D_1).V_2}{L_1} + \frac{\tilde{v}_1 - (1 - D_1).\tilde{v}_2}{L_1} + \frac{V_2.\tilde{d}_1}{L_1}. \tag{4.1.23}$$

Finally, this model can be transformed into Laplace domain to obtain the control to output transfer function where ($\tilde{v}_1 = \tilde{v}_2 = 0$) and the perturbation transfer functions are:

$$\left.\frac{\widetilde{\iota_{L1}}(s)}{\widetilde{d_1}(s)}\right|_{\tilde{v}_1=\tilde{v}_2=0} = \frac{V_2}{sL_1}, \qquad \left.\frac{\widetilde{\iota_{L1}}(s)}{\widetilde{v_2}(s)}\right|_{\tilde{d}_1=\tilde{v}_1=0} = \frac{-(1-D)}{sL_1} \text{ and}$$
$$\left.\frac{\widetilde{\iota_{L1}}(s)}{\widetilde{v_1}(s)}\right|_{\tilde{d}_1=\tilde{v}_2=0} = \frac{1}{sL_1}. \tag{4.1.24}$$

This means that L_1 current, which is the same as the port 1 current can be controlled by a single proportional controller because the converter itself is an integrator. Figure 4.1.6 shows the main controller.

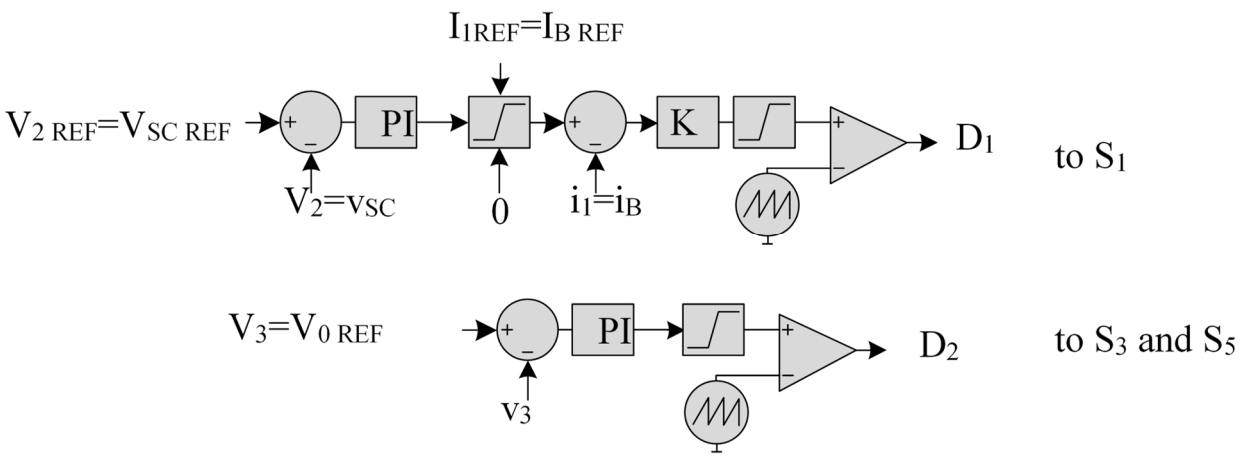

Figure 4.1.6–Main controller basic diagram

For the second part, the same procedure can be done to obtain the averaged model. In this case, the perturbation is only $\tilde{v}_2$ and $\tilde{d}_2$, considering that v_3 is the controllable output:

$$\frac{d}{dt}\underbrace{\begin{pmatrix}\widetilde{i_{L2}}\\ \widetilde{i_{L3}}\\ \widetilde{v_{C1}}\\ \widetilde{v_{CO}}\end{pmatrix}}_{x}=\begin{pmatrix}\frac{-r_{L2}}{L_2} & 0 & \frac{-(1-D_2)}{L_2} & 0\\ 0 & \frac{-r_{L3}}{L_3} & \frac{D_2}{L_3} & \frac{D_2-1}{L_3}\\ \frac{(1-D_2)}{C_1} & \frac{-D_2}{C_1} & 0 & 0\\ 0 & \frac{(1-D_2)}{C_0} & 0 & \frac{-1}{RC_0}\end{pmatrix}x$$
$$+\begin{pmatrix}\frac{V_{C1}}{L_2} & \frac{1}{L_2}\\ \frac{V_{C1}+V_O}{L_3} & \frac{1}{L_3}\\ -\frac{I_{L3}+I_{L2}}{C_1} & 0\\ -\frac{I_{L3}}{C_O} & 0\end{pmatrix}\begin{pmatrix}\tilde{d}_2\\ \tilde{v}_2\end{pmatrix}. \tag{4.1.25}$$

In order to calculate the transfer function, the Laplace transform must be applied to (4.1.25) and from there, different control-to-output and input-to-output transfer functions can be obtained:

$$\left.\frac{\widetilde{v_3}(s)}{\widetilde{d_2}(s)}\right|_{\widetilde{v_2}=0}\widetilde{d_2}(s)=(0\ 0\ 0\ 1)\left(s\bar{\bar{I}}-A\right)^{-1}.B\begin{pmatrix}\widetilde{d_2})\\ 0\end{pmatrix} \tag{4.1.26.a}$$

$$\left.\frac{\widetilde{i_2}(s)}{\widetilde{d_2}(s)}\right|_{\widetilde{v_2}=0}\widetilde{d_2}(s)=(1\ 1\ 0\ 0)\left(s\bar{\bar{I}}-A\right)^{-1}.B\begin{pmatrix}\widetilde{d_2}\\ 0\end{pmatrix} \tag{4.1.26.b}$$

$$\left.\frac{\delta v_0(s)}{\delta v_{SC}(s)}\right|_{\widetilde{d_2}=0}\widetilde{v_2}(s)=(0\ 0\ 0\ 1)\left(s\bar{\bar{I}}-A\right)^{-1}.B\begin{pmatrix}0\\ \widetilde{v_2}\end{pmatrix}, \tag{4.1.26.c}$$

where $\bar{\bar{I}}$ is the identity matrix. To understand the dynamics of the system, the poles of the system can be extracted as the roots of the characteristic polynomial, which is the determinant of matrix $\left(s\bar{\bar{I}}-A\right)^{-1}$:

$$det(sI-A)^{-1}=\frac{s^4}{\omega_1^2\omega_2^2}+\frac{s^3}{Q_1\omega_1\ \omega_2^2}+s^2\left(\frac{1}{\omega_1^2}+\frac{1}{\omega_2^2}+\frac{1}{\omega_{12}^2}+\frac{\sigma_0\sigma_2+\sigma_2\sigma_3+\sigma_3\sigma_0}{\omega_1^2\omega_2^2}\right) \tag{4.1.27.a}$$

where:

$$\omega_1=\frac{1-D_2}{(L_3C_0)^{\frac{1}{2}}},\ \omega_2=\frac{1-D_2}{(L_2C_1)^{\frac{1}{2}}},\ \omega_{12}=\frac{(1-D_2)^2}{D_2(L_2C_0)^{\frac{1}{2}}} \tag{4.1.27.b}$$

$$\text{and } \sigma_0 = \frac{1}{RC_0}, \sigma_2 = \frac{r_{L2}}{L_2}, \sigma_3 = \frac{r_{L3}}{L_3}. \tag{4.1.27.c}$$

$$Q_1 = \frac{\omega_1}{\sigma_0 + \sigma_2 + \sigma_3}. \tag{4.1.27.d}$$

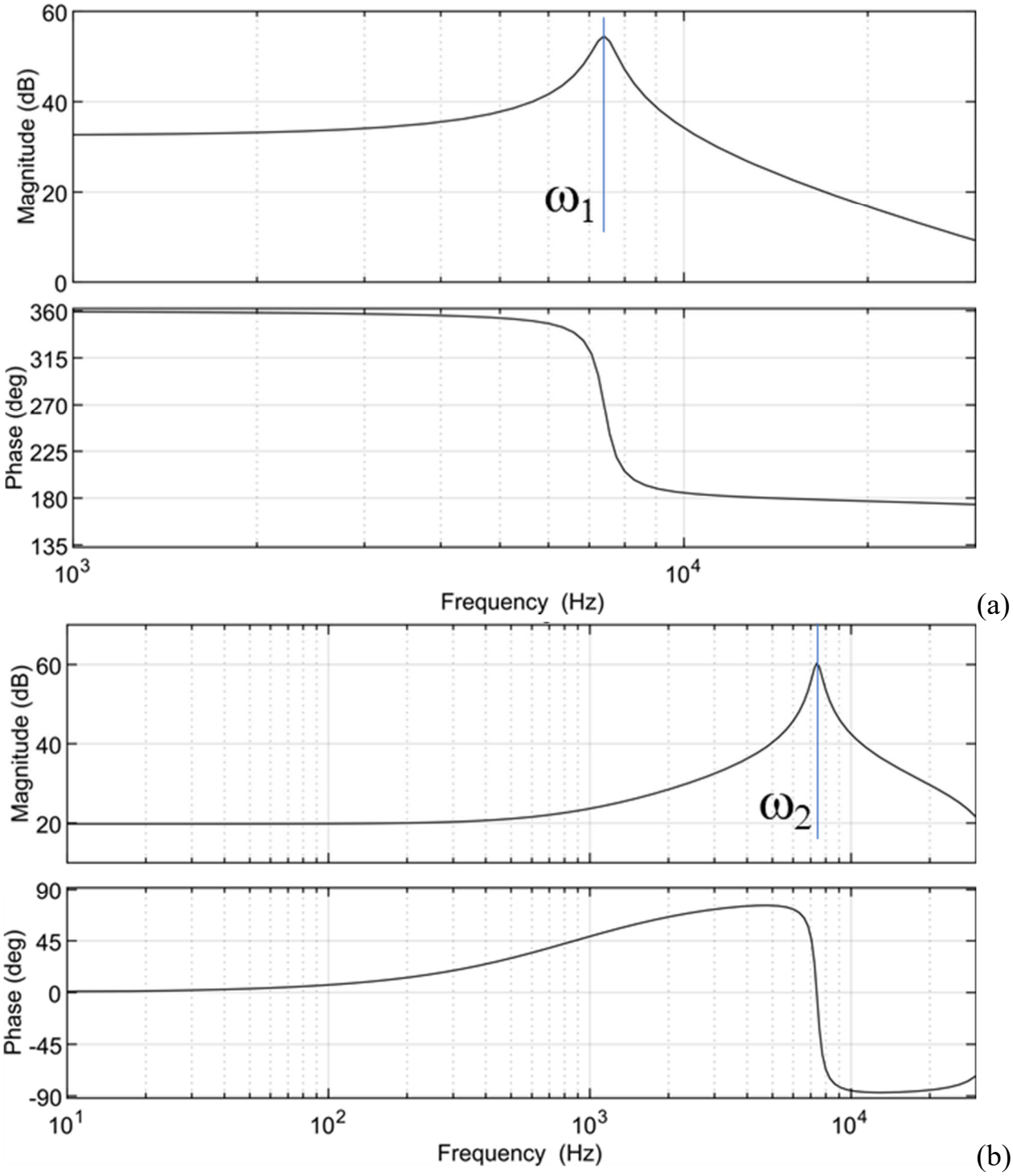

Figure 4.1.7–Frequency response for (a) the output voltage and (b) input current as a function of the duty cycle D_2

Figure 4.1.7(a) shows the frequency response of the converter based on the model and components listed in Table 4.1.1. ω_1 and ω_2 are the resonant frequencies of the circuit, and ω_{12} is the interaction between these two resonant frequencies. This is the reason why the peak in the amplitude is not exactly at ω_1 and ω_2. Notice that ω_1 has a damping related to the output resistor but ω_2 has not, so the dumping depends on the quality of the reactive elements (σ_2 and σ_3). In the figure, they are considered as a Q factor equals to 50 at the resonant frequency. Simulations and real experiments will show the real transfer function. Anyway, it is important to notice that these two resonant frequencies will severely affect the bandwidth of the converter.

In order to stabilize the close loop, a proportional gain must mitigate the peak amplitude in ω_1 and ω_2 of the open loop transfer function. The easiest method to design a controller is to ensure that at ω_1 and ω_1 the gain is below 0dB, so the proportional gain is defined as inverse of the maximum gain. Then, a simple integrator can be added at lower frequencies in order to achieve zero DC error, at frequencies at least 5 times lower than ω_1. Figure 4.1.6 shows the diagram of the controller including the controller for the second part and Figure 4.1.7 shows the open loop transfer function. More advanced controllers or control techniques can be found in [190,191,192].

The control diagram presented in Figure 4.1.6 tries to keep V_3 constant, with also the current reference of port 1 and the limits in the voltage of port 2. So, there are two references. In that diagram, the first three operation modes are being used in that diagram. This scheme is for the step-up mode.

In the step-down mode, the converter imposes the maximum current in the port 1 as a current source and the limits in the port 1 and 2 in terms of voltage as Figure 4.1.8(a) shows. Thus, the second three modes are presented there. In addition, other control strategies can be used, for example, if the port 2 is a supercapacitor (SC) and must be charged while at port 3, the output port, the voltage must be kept constant, the references are on V_2 and V_3 with limiting the port 1 current. This is mode e) and it is shown in Figure 4.1.8(b).

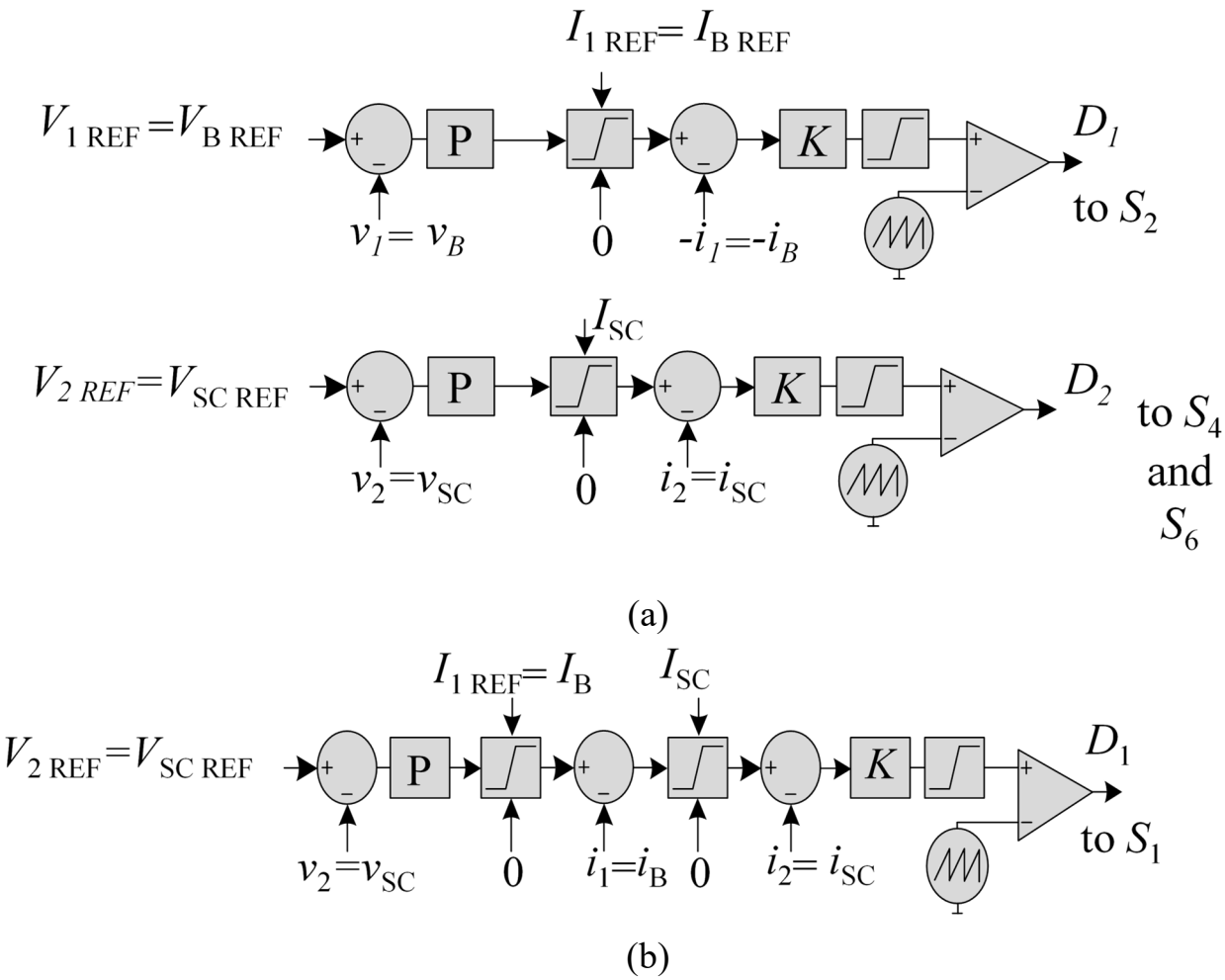

Figure 4.1.8–Control diagram for different strategies: (a) to charge the battery at constant voltage keeping SC and battery within the voltage limits, (b) to charge the SC with the battery keeping the output voltage constant and limiting the battery current

4.1.4. Comparison analysis

This section summarizes all the converter's characteristics and details and compares it with other topologies. Table 4.1.1 presents the comparison which is focused on the part count and their output voltage. In order to make a fair comparison, only non-isolated converters are analyzed, the ones discussed at the beginning of the section, finally, only DC blocking capacitors will be considering for the part count.

The converter presented in [179] is the simplest one as it only needs one inductor to accommodate both input sources, but this requires incorporating two bypass diodes

which affects the total efficiency of the converter. The conversion gain is equivalent to two conventional cascaded converters; hence no high gain can be achieved. Yet, the controller is not so complex.

A reconfigurable converter is presented in [180], allowing to directly connect the battery/supercapacitor cells and operate in multiple modes. This converter has the highest part count and due the fact that 2 relays are used the lifetime of the system will be reduced, although they can be replaced by placing back-to-back MOSFETs this would then compromise the efficiency of the converter. Finally, the conversion gain is presented as a traditional single DC/DC converter.

The resonant multi-input converter presented in [186] can achieve better efficiency due it is resonant design and the ability to achieve zero current switching; however, this converter has the drawbacks of limited power delivery and slow dynamic response. In [187], the analyzed converter has a better conversion ratio but due the increased number of passive elements efficiency is not as high as the other converters. Moreover, the converter is not fully bidirectional. The multi-input-port converter of [188] has the lowest part count and exhibits better efficiency than the previous converters as there are no diodes or MOSFETs involved. However, the conversion gain ratio is equivalent to twice a traditional boost converter and half a traditional buck converter. Moreover, the converter is intended to use similar energy sources at the input.

The proposed converter has the highest conversion gain, and the part count is moderate enough with no diodes or other elements that can reduce the efficiency of the system. Moreover, by placing the SCs at the input of the high-gain converter's section it is possible to take advantage of them in terms of power density usage. However, it is only intended for low to medium power HESSs.

Table 4.1.1 Comparison between non-isolated multi-port converters

Converter	Output voltage	Part count				Drawbacks
		S	*D*	*L*	*C**	
[179]	$V_0 = \frac{V_1 d_1 + V_2 d_2}{(1 - d_3)}$	4	2	1	0	Low efficiency
[180]	$V_0 = \frac{V}{(1 - d_{boost})}$	14 + 2·n_{Bcells} + 2·$n_{SCcells}$	6	2	0	The high number of components
[186]	$V_O = \alpha E_{in}$	4	8	5	0	Limited power delivery and slow dynamic response
[187]	$\frac{V_O}{V_{1,2}} = \frac{1 - d + d^2}{(1 - d)^2}$	4	8	2	0	Increased losses due to the number of passive elements
[188]	$V_0 = \frac{2V_{in}}{(1 - d_{boost})}$	4	0	2	1	No high-gain conversion ratio
Proposed	$V_o = \frac{V_{SC}}{(1 - D_2)^2}$	6	0	3	1	Applicable in medium and low power HESSs

*Only DC blocking capacitors are considered.

4.1.5. Simulations and experimental results

The purpose of this subsection is to validate the analysis from the subsection 4.1.2 and 4.1.3. For that reason, several simulations and experimental results were conducted. A prototype of 300W using a STM32 Micro-Controller Unit (MCU) in charge of both D_1 and D_2 control signals of the converter, with two input ports: port 1 connected to a battery at 4.2V and port 2 connected at 12.5V for a supercapacitor bank (SC) and port 3 as an output port at 24V is shown in Figure 4.1.9. The SC stack with active balancing is shown in Figure 4.1.9 and the DC grid is made of a power supply when working in the step-down mode and a set of resistors at the output when working in the step-up mode. The details of the converter are presented in Table 4.1.2.

Table 4.1.2 Details of the converter

Component	Value	Details
L_1, L_2	4.7uH Wurth 2815	1.31mOhm
S_1, S_2	2x BSC022N04LS6	2.2mOhm 40V
L_3	15uH Wurth 2815	1.31mOhm
S_3, S_4	2x BSC098N10NS5	9.8mOhm 100V
C_1	3x 0.68uF 200V	X7R
S_5, S_6	2x BSC160N15NS5	16mOhm 150V
SC stack	5x 700F 2.85V	-

The first simulations and experimental results are the waveforms. The simulations are already presented in Figure 4.1.3 and Figure 4.1.5. Experimental results are in concordance with the simulations as Figure 4.1.10 shows.

The second simulations and experimental results are the open-loop transfer functions. Figure 4.1.11 shows the transfer function of the model which does not include the exact model of switches, inductors and capacitors. Figure 4.1.11 shows the experimental results of the control-to-output transfer functions. Notice that the theoretical one (from Figure 4.1.7(a)) approaches the experimental one, in the experimental part the phase shift of 180° occurs at higher frequencies due the fact that the capacitance of C_0 is reduced due the electrolytic type of capacitor used and the magnitude does not present the peak at ω_1 as the theoretical part excludes the ESR for the capacitors, but in overall, the behavior remains the same, so, the design methodology is validated.

Once the controller was designed using the guidelines from Section 4.1.3, the converter in closed loop was tested using the control diagram of Figure 4.1.6 and Figure 4.1.8(a). Experimental results are shown in Figure 4.1.12, the step in the load changes the power from 100W to 1W and vice versa for both step-up and step-down modes, for each input ports and output port the voltage and current are presented. The voltage output remains stable, and if the current limit is reached for the battery then the SCs provide the rest of the required power. During these experiments, it was considered that in step-up mode, the converter feeds the DC grid, and no other voltage source was present. Thus, the converter was working as a voltage source.

Figure 4.1.12 (a) was obtained by connecting at the output a set of resistors as a load, hence there is a voltage drop due to the dynamic transient of the converter. In Figure

4.1.12 (b), a power supply was used as DC grid in the output port and the battery and SC port were used to connect a set of resistors. The controller was working in the step-up mode.

The next set of experimental tests is useful to analyze the efficiency of the converter at multiple power operation points in both modes of operation, charging and discharging, Figure 4.1.13 shows the results. The prototype was used only to validate the operation of the proposed converter and it was not fully optimized, efficiency can be further increased by properly selecting the switches and passive elements.

To analyze the conversion gain ratio a fourth set of experimental tests were done by varying D_2 in open loop mode and fixing i_B=0 in both step-up and step-down modes. Figure 4.1.14 shows the results. Higher gain ratios can be achieved by selecting transistors with greater breakdown voltage capabilities. With the proposed converter's prototype, a gain ratio of 5 is easily achieved for D_2.

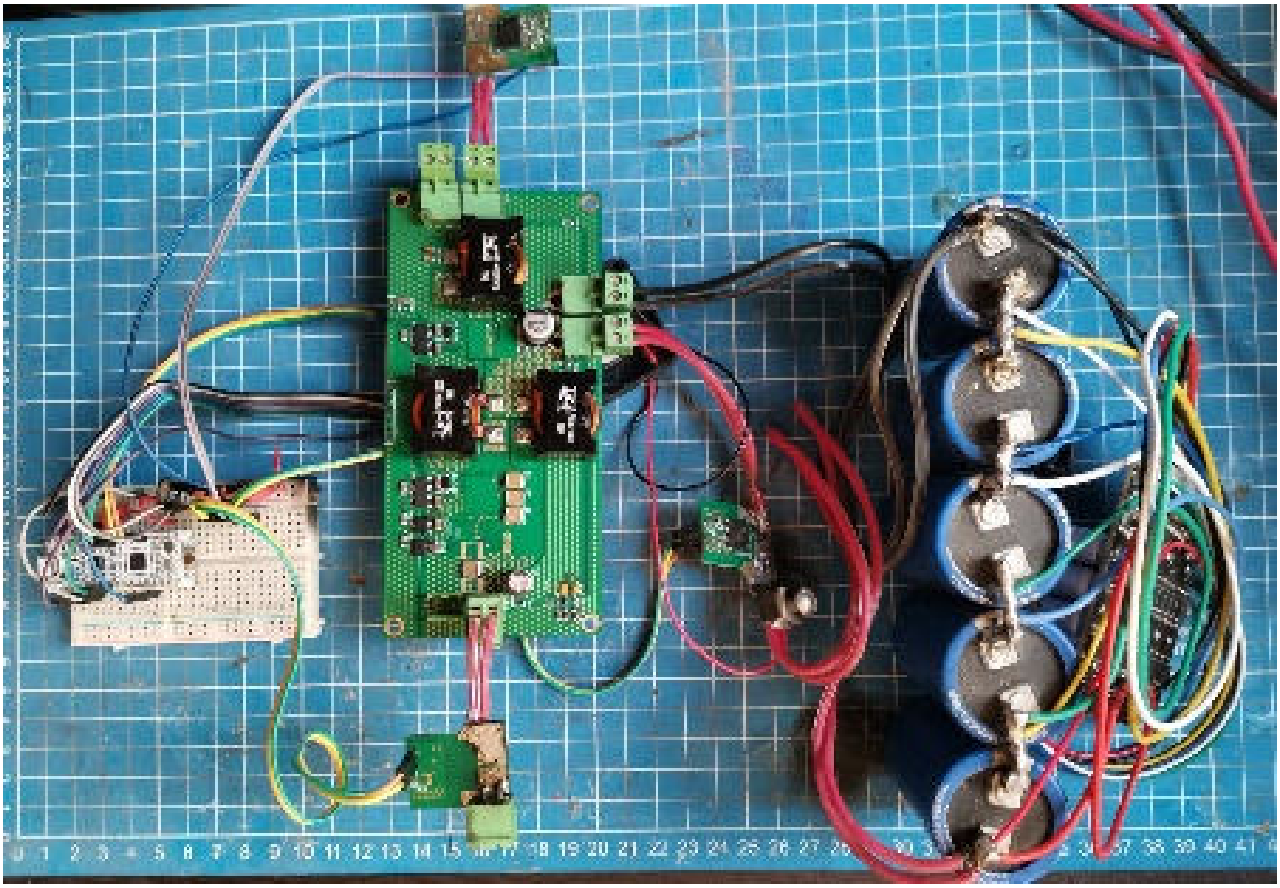

Figure 4.1.9–Prototype photograph

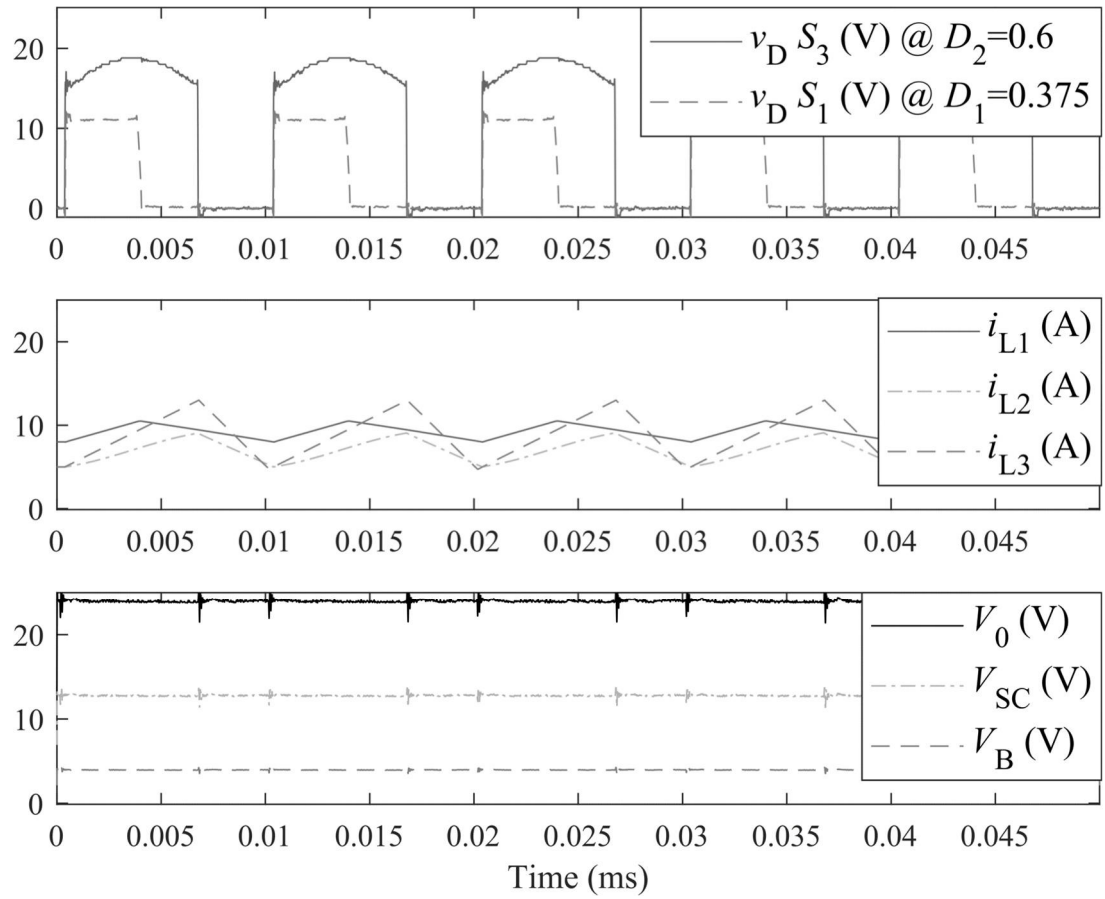

Figure 4.1.10–Waveforms

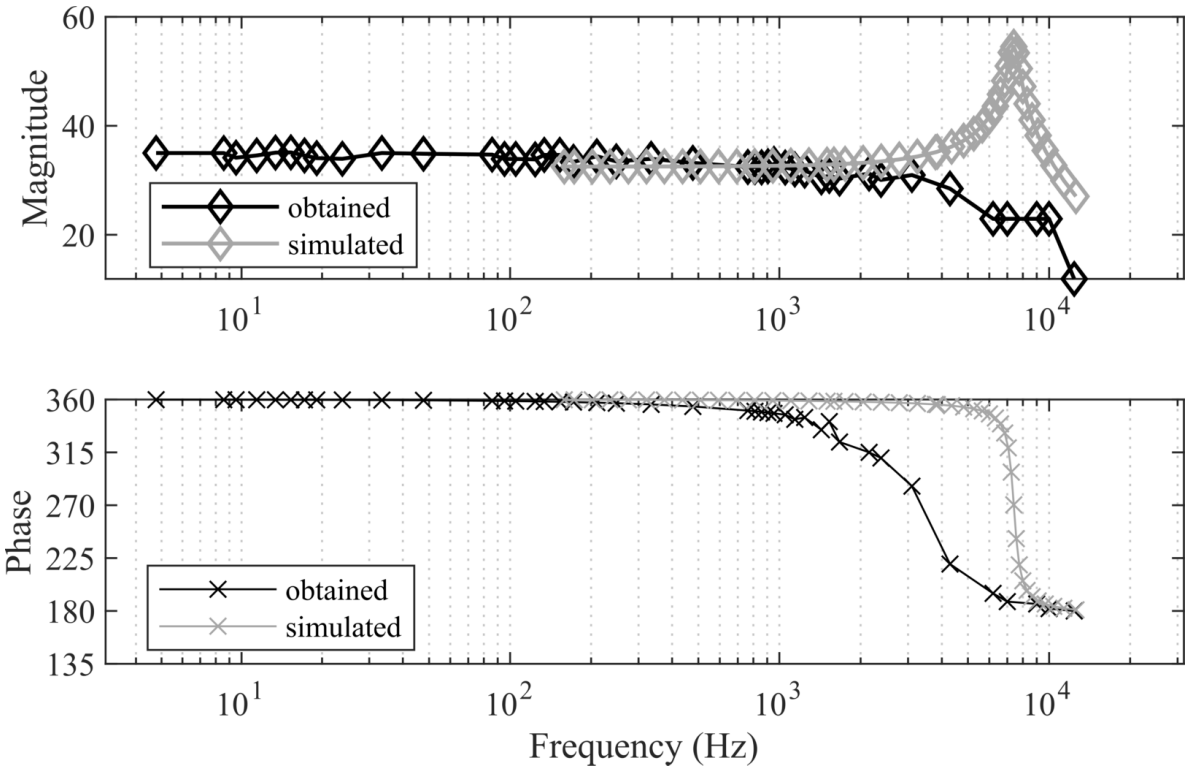

Figure 4.1.11–Open-loop transfer function from V_2 to V_3

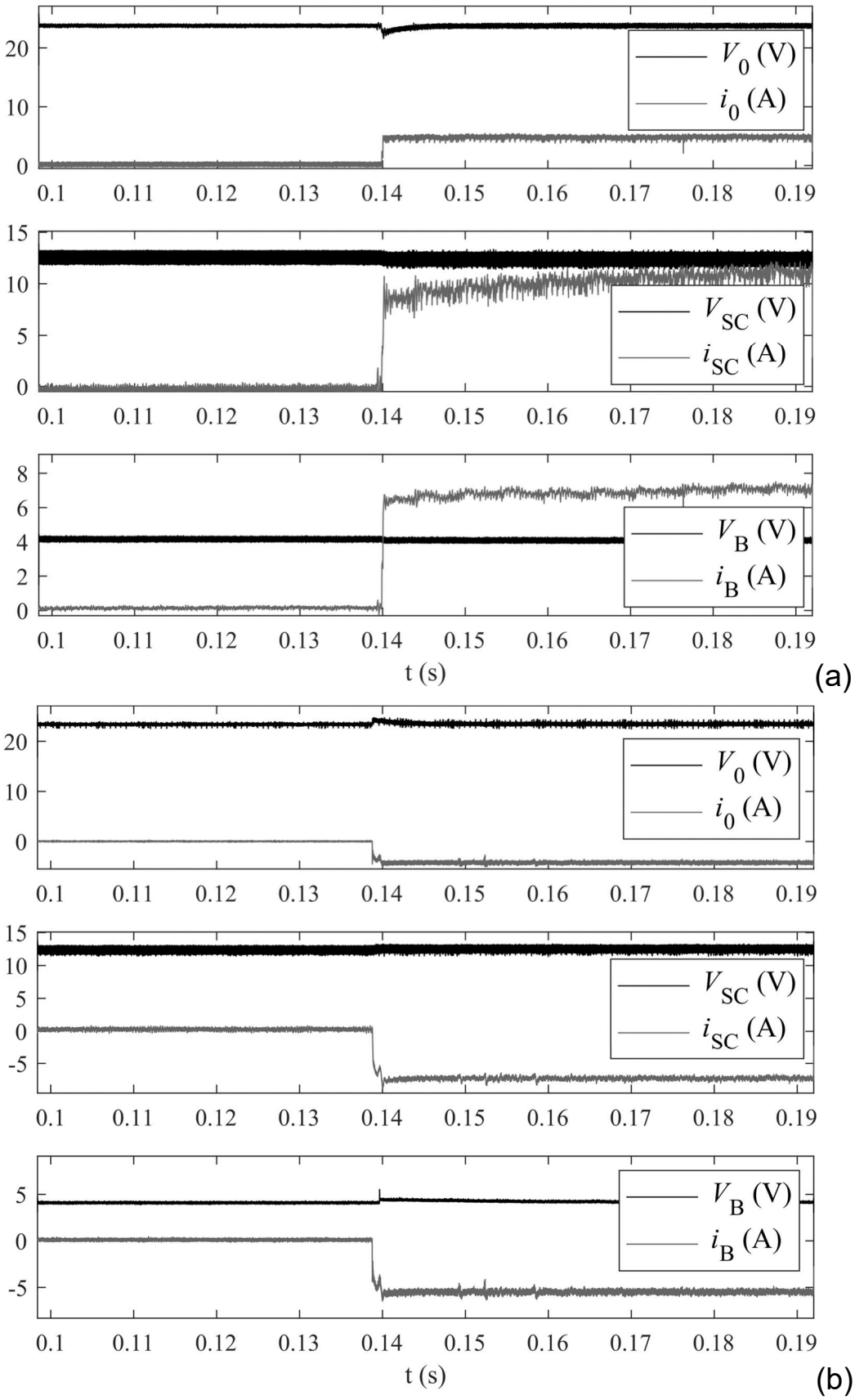

Figure 4.1.12–Step-load response (a) boost mode, (b) buck mode

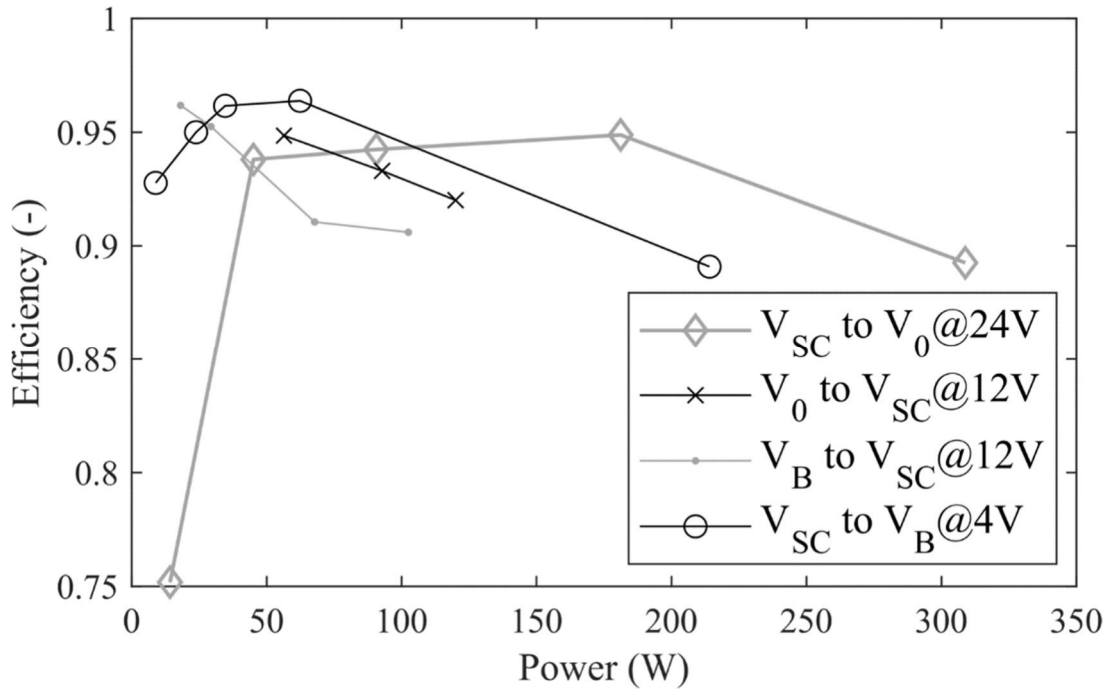

Figure 4.1.13–Efficiency at both buck and boost mode

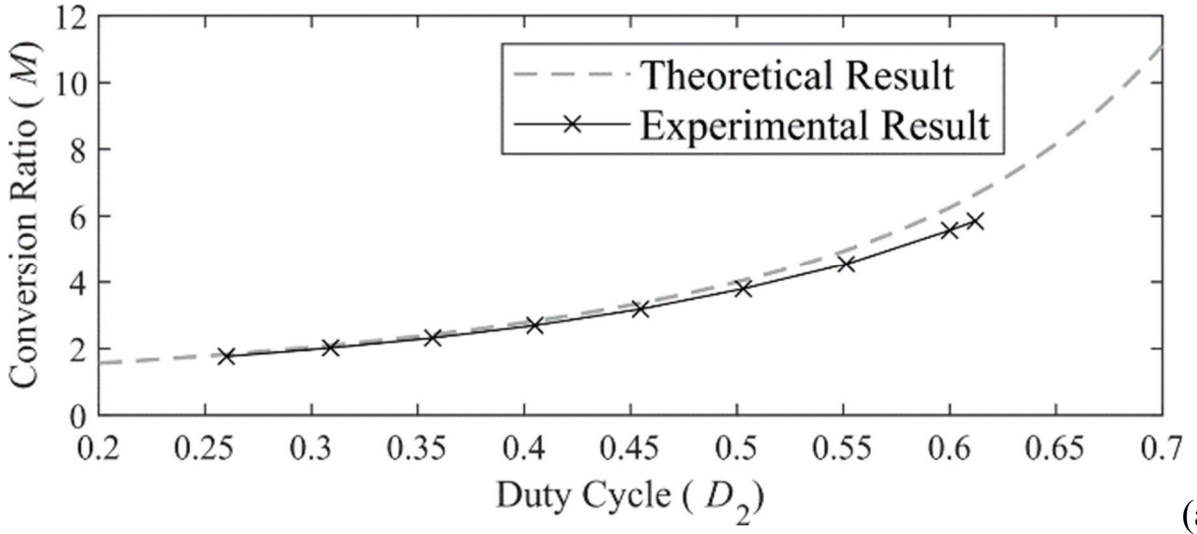

(a)

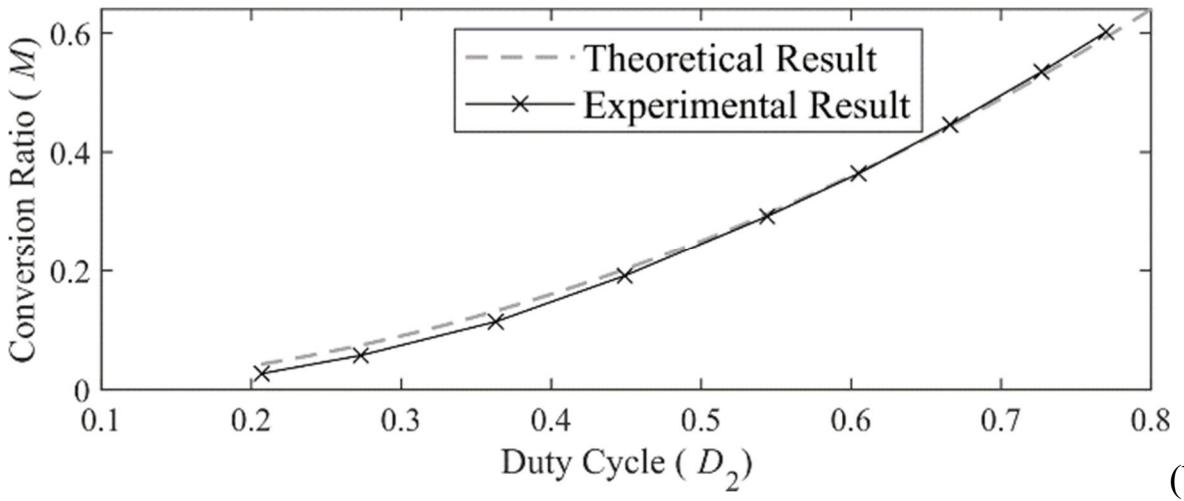

(b)

Figure 4.1.14–Conversion gain ratio (a) boost mode, (b) buck mode

4.1.6. Summary

This section presents an alternative circuit to the multi active bridge topology in applications that non-isolated ports are allowed, for example, where the critical ports are already isolated. The proposal is a multi-port high-gain DC/DC converter in which the first input port is oriented to a battery at low voltage, the second port is oriented to another battery or a SC stack at higher voltage, while the 3rd port is at much higher voltage and it can be connected to the grid by an inverter. Thus, it fits well in applications that connect the grid (rectified at ~340V) with low-voltage devices such as low power scooters and bikes. The converter allows to independently control each energy source by adjusting only two control signals, hence no complex controller is needed to operate the converter.

The converter operating principles, the modeling, the controller design and a comparison with other converters are addressed thoroughly. Furthermore, the proposed converter is validated with a small-scale prototype by evaluating the step response, efficiency and the conversion ratio in the different modes of operation as well as the open-loop transfer function for control purposes. Therefore, the proposed converter is a suitable solution for small to medium DC power systems. In case of connection to the grid, the inverter should provide the isolation if it is needed. The details of the section were published in [189].

4.2. Isolated Series Resonant DC/DC converters – Discontinuous mode

The dissertation has extensively discussed the isolated multiple port DC/DC converter based on a MAB in Chapter 2. In addition, in Section 4.1, a non-isolated alternative was also presented. This section is focused on an alternative two-port bidirectional converter which is the origin of a multi-port resonant converter which will be discussed in the last section of this chapter. In order to understand the main novelties

of that converter, the two-port bidirectional series resonant converter will be discussed in this section and in the following.

As was mentioned in Chapter 2, MAB converters are an extension of the dual active bridge [193] converter with more ports. Another interesting approach is to use resonant converters, which are also similar to DAB converters. However, in that case, the energy flow is exclusively around the resonant frequency of the converter. The details of the proposed technique were published in [32,33, 35, 36, 111,211].

This section introduces the series resonant converter working in the step-down and the step-up mode. The latter is the main novelty of this section, which allows using the series resonant converter in bidirectional applications. Based on this mode, the last section will transform the DC/DC converter to a three-port DC/AC converter, which is the last proposal to implement a compact EV charger.

4.2.1. Series resonant converter for bidirectional applications

Traditionally, the series-resonant DC/DC converter (SRC) has been used with a voltage conversion gain that achieves its maximum at the resonant frequency. The converter's output voltage is controlled by shifting the switching frequency above or below the resonance [30, 194, 195]. There are two main operational modes for resonant converters, continuous and discontinuous. Both modes are used in several unidirectional and bidirectional resonant topologies [196][197][198]. In the continuous mode [199], where current flows continuously in the resonant branch, there are many methods for adjusting the output values [200] [201] [202] [203]. These control strategies use impedance variation with frequency to adjust the output values. The discontinuous mode is based on the concept of energy packets. The source port delivers energy packets to the output port. The procedure for adjusting the output values consists of controlling the time between each energy packet [204, 205].

Figure 4.2.1 shows the basic diagram of a series resonant converter. It consists of a bridge (or half-bridge) to create a HF signal, a resonant network and a rectifier. The

rectifier can be a half-bridge, a full-bridge or another type. Particularly, Figure 4.2.2(b) shows a new rectifier introduced by the author with low losses [110]. The voltage conversion gain (*M*) for any type of bidirectional DC/DC converter, according to the ports defined in Figure 4.2.1, is defined as $M_{T12} = V_{2DC}/V_{1DC}$ ($M_{T21} = V_{1DC}/V_{2DC}$) when the power flow is from (to) V_{1DC} to (from) V_{2DC}. In order to increase the output voltage and to provide galvanic isolation, many converters include a transformer, and thus M_{T12} and M_{T21} depend on the transformer turns ratio (*n*). In these cases, a normalized voltage conversion gain can be defined as $M_{12} = V_{2DC}/(V_{1DC} \cdot n)$ and $M_{12} = n \cdot V_{1DC}/V_{1DC}$, where the influence of the transformer turns ratio is excluded. Therefore, the voltage conversion gain of a system including a transformer is expressed in eq. (4.2.1).

$$M_{T12} = M_{12} \cdot n \tag{4.2.1.a}$$

$$M_{T21} = M_{21}/n. \tag{4.2.1.b}$$

In an SRC both M_{12} and M_{21} are less than one [35]. Therefore, in order to increase the output voltage, a transformer is needed so M_{T12} can be greater than one. Figure 4.1 shows the circuit diagram, including a transformer. It consists of an LC series filter (L_R and C_R) with a transformer attached to an inverter at one side and to a rectifier at the other side. The transformer is considered ideal, its leakage inductance is included in L_R, and the magnetizing inductance is negligible because its value is much greater than L_R. The LC filter is used to produce the soft-switching technique to reduce switching losses and increase efficiency.

In some applications, an M (M_{12} and/or M_{21}) greater than one is required, but this is not possible with the common control technique. In this section, a novel control method is developed, which consists of the accumulation of energy packets to raise the output voltage, making it possible to have an M greater than one. This novel technique allows the SRC to be attached to several energy storage devices, such as batteries and supercapacitors [206][207]. In general, an energy storage device has a minimum and a maximum working voltage, and it is commonly attached to a constant DC line through a DC/DC converter in a power train [208][209]. In Figure 4.2.1, V_{1DC} is attached to the energy storage device and V_{2DC} is attached to a load at constant voltage. Considering the minimum and maximum voltage values of the energy storage device, the M_{12} values that

make V_{2DC} constant are expressed in (4.2.2.a) and (4.2.2.b). In the opposite direction, the boundary of the M_{21} values are expressed in (4.2.2.c) and (4.2.2.d) with V_{2DC} constant.

$$V_{2DC} = M_{12MAX} \cdot n \cdot V_{1DCmin} \quad (4.2.2.a)$$

$$V_{2DC} = M_{12min} \cdot n \cdot V_{1DCMAX} \quad (4.2.2.b)$$

$$V_{1DCmin} = M_{21min} \cdot V_{2DC}/n \quad (4.2.2.c)$$

$$V_{1DCMAX} = M_{21MAX} \cdot V_{2DC}/n. \quad (4.2.2.d)$$

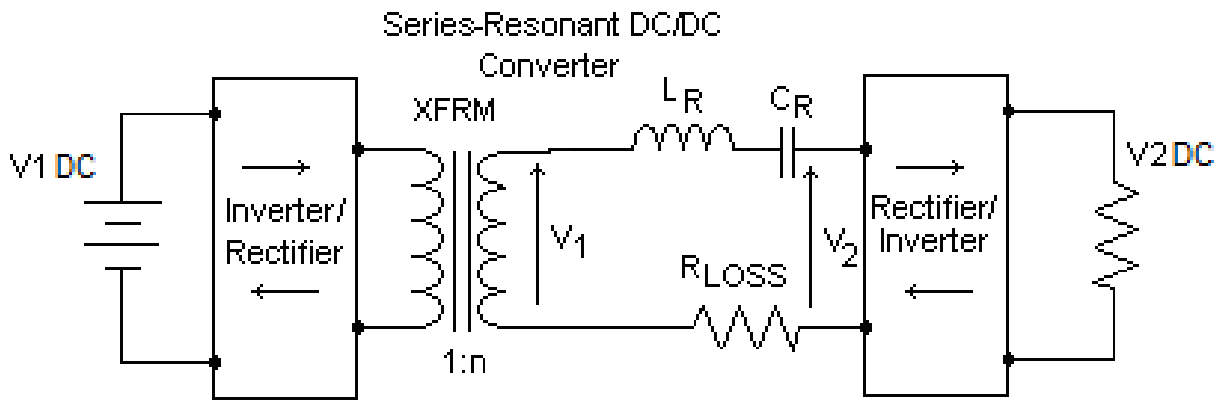

Figure 4.2.1–Series-resonant DC/DC converter with transformer

It can be seen that when V_{1DC} has the minimum voltage, M_{12} should be the maximum (4.2.2.a) and M_{21} the minimum (4.2.2.c). Multiplying (4.2.2.a) with (4.2.2.c) and (4.2.2.b) with (4.2.2.d), a pair of relations is obtained in (4.2.3). These equations show the necessity of having an M (in both directions) greater than one. Presuming that the converter in Figure 4.2.1 is a common SRC (where $M \leq 1$) and the ideal case, where M_{12MAX} and M_{21MAX} are equal to one, then the minimum values ($M_{12\,min}$ and $M_{21\,min}$) should also be one to satisfy (4.2.3). However, this is not possible because $V_{1Dc\,min} < V_{1DCMAX}$, so $M_{21\,min} < M_{12MAX}$. Therefore, this operation mode for the converter is not suitable for this type of applications. M should be able to vary from values below to values above one in order to satisfy :

$$1 = M_{12MAX} \cdot M_{21min} \quad (4.2.3.a)$$

$$1 = M_{21MAX} \cdot M_{12min}. \quad (4.2.3.b)$$

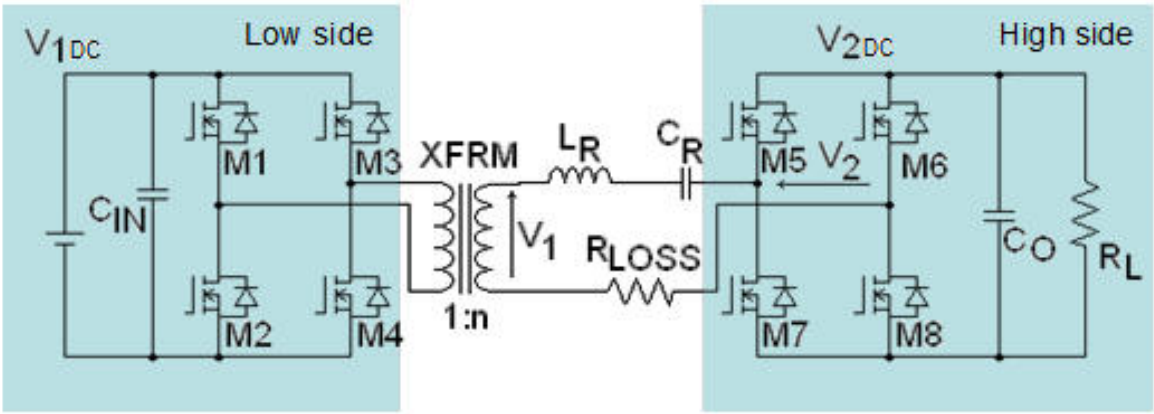

(a)

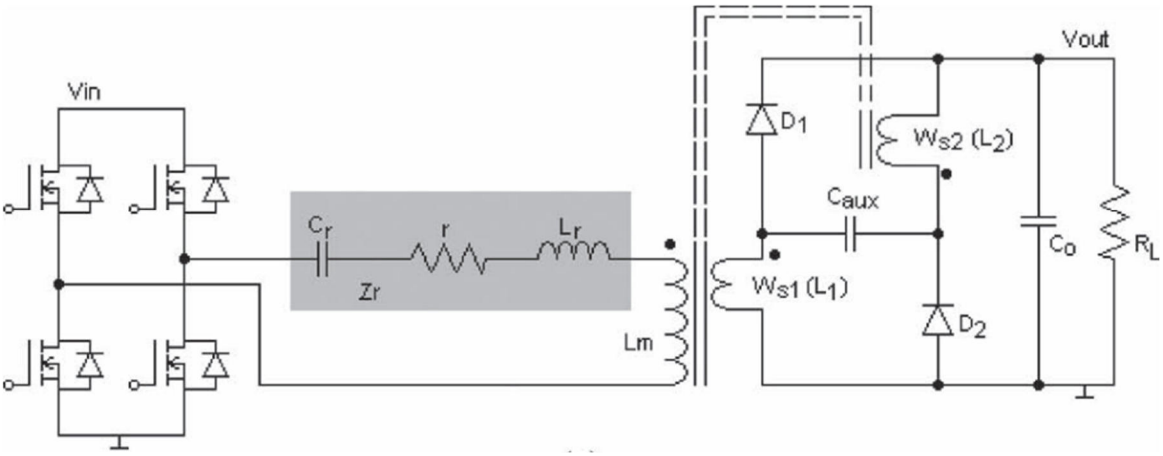

(b)

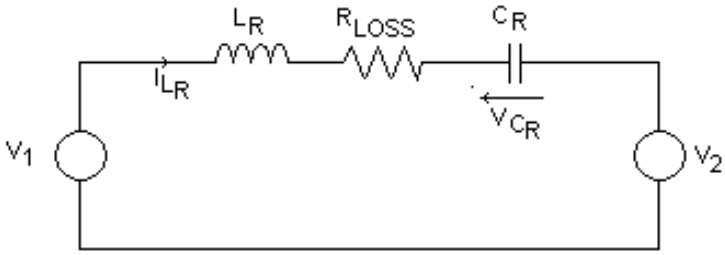

(c)

Figure 4.2.2–Bidirectional DC/DC series resonant circuit (a) double full bridge schematic, with new proposed rectifier (b) simplified circuit

4.2.2. Discontinuous mode – discrete states

A series-resonant DC/DC (SRC) converter is formed of an inverter, a resonant circuit and a rectifier. The inverter can be used as a rectifier and the rectifier can be used as an inverter to change the energy flow direction. Figure 4.2.2(a) shows a possible

scheme using for the inverter/rectifier a MOSFET full-bridge but other topologies can also be implemented [110] [209]. The inverters/rectifiers stage are "seen" from the resonant circuit as a constant voltage sources, V_1 and V_2, during certain time states. Therefore, a simplified circuit is proposed in Figure 4.2.2(b) in order to analyze each state. This circuit is symmetrical, so the analysis is the same in both directions. Thus, the results obtained in one of the two power flow directions are also valid in the opposite direction. Here, V_{1DC} and V_{2DC} will be chosen for the input and output ports, respectively, so V_i is defined as $V_{1DC} \cdot n$ and V_o as V_{2DC}. The normalized voltage conversion ratio due to these redefinitions is $M = V_o/V_i$. According to this, the voltage sources can assume the values expressed in (4.2.4) depending on the current state. In addition, Table 4.2.1 presents the definitions of the most relevant variables of the following analysis.

$$[V_1, V_2] = \begin{cases} [+V_{1BUS}, +V_{2BUS}] & for\ T_1 - state \\ [-V_{1BUS}, -V_{2BUS}] & for\ T_2 - state \\ [V_{1BUS}, 0]\ or\ [0, V_{2BUS}] & for\ A - state \\ [-V_{1BUS}, V_{2BUS}]\ or\ [V_{1BUS}, -V_{2BUS}] & for\ C - state \end{cases} . \tag{4.2.4}$$

Table 4.2.1 More relevant variables

Symbol	Description
V_{1DC}, (V_{2DC})	Low (high) side port
M_{T12}, (M_{T21})	Total voltage conversion ratio from V_{1DC} (V_{2DC}) to V_{2DC} (V_{1DC})
Vo, Vi	Output and input port for the symmetric circuit
M	Voltage conversion ratio for symmetric circuit (V_o/V_i)
V_1 (V_2)	Voltage source sees due to V_i (V_o) through the inv.(rect.) from the resonant circuit.
L_R, C_R, R_{LOSS}	Components of the series resonant branch
i_L, $i_{L(n)}$	Resonant current, n indicates the current state.
$v_C(t)$, $v_{Ci(n)}$	C_R voltage, C_R initial condition for n state
T_0 , ω_0	Natural resonant period: $2 \cdot \pi \cdot \sqrt{L_R C_R}$ and resonant frequency in rad/s.
t_{off}	Off-time
Z_0	Characteristic impedance $\sqrt{L_R / C_R}$
λ	Loss factor
x, x_C, x_0, $x_{1/2}$	Normalized variable, x limit between case 1 and 2, x for t_{off}/T_0=1/2, x for t_{off}/T_0=1/2
r_L; r_{LOSS}	Normalized load R_L/Z_0 and loss resistance R_{LOSS}/Z_0

As mentioned previously, the converter transfers energy in packets. In order to send these packets from one port to the other, the circuit uses transfer states called T_1 and T_2, which last for a fixed time interval. In these states, the source port is the port that has the inverter attached to it, and the destination port is the one that has the rectifier attached to it. During the T_1-state, the resonant current (i_L) flows in the positive direction, while in the T_2-state, it flows in the negative direction (Figure 4.2.3(a)). The A-state is the accumulation state, where the inverter works in the same way as in the transfer states, but the rectifier has its input short-circuited and no energy is transferred to the output port, so the resonant branch only sees V_1. The capacitor, C_R, increases its voltage and in the next transfer state it delivers this accumulated energy to the output, raising V_2 and, consequently, V_o. Therefore, it is possible to achieve an M greater than one. There are three active states: T_1, T_2 and A-state. There are also two passive states: the off-state and the clamping state (C-state). In the active states, the current in the resonant branch and the voltage in the capacitor can be obtained by solving (4.2.5) with the initial condition in (4.2.6), where $v_{C(n)}(t)$ is the capacitor voltage of the n state, and n can be T_1, T_2, A or the C-state. Inductor's current and capacitor's voltage are described by:

$$V_1 - V_2 = L_R \cdot \frac{di_L(t)}{dt} + \frac{1}{C_R} \cdot \int_0^t i_L(\tau) \cdot d\tau + v_{Ci} + R_{LOSS} \cdot i_L(t) \tag{4.2.5}$$

with

$$i_L(t = 0) = 0 \tag{4.2.6.a}$$

$$v_{C(n)}(t = 0) = v_{Ci(n)} = v_{C(n-1)}(t = T_0/2). \tag{4.2.6.b}$$

The solutions are:

$$v_C(t) \approx \left(v_{Ci(n)} - V_1 + V_2\right) \cdot cos(\omega_0 \cdot t) \cdot exp(-t/\tau) + V_1 - V_2 \tag{4.2.7.a}$$

$$i_L(t) \approx -\frac{\left(v_{Ci(n)} - V_1 + V_2\right)}{Z_0} \cdot sin(\omega_0 \cdot t) \cdot exp(-t/\tau) \tag{4.2.7.b}$$

where

$$\tau = \frac{2L}{R_{LOSS}} \quad \wedge \quad \omega_0 = \frac{1}{\sqrt{LC}} \quad \wedge \quad \omega_0 \cdot \tau >> 1. \tag{4.2.7.c}$$

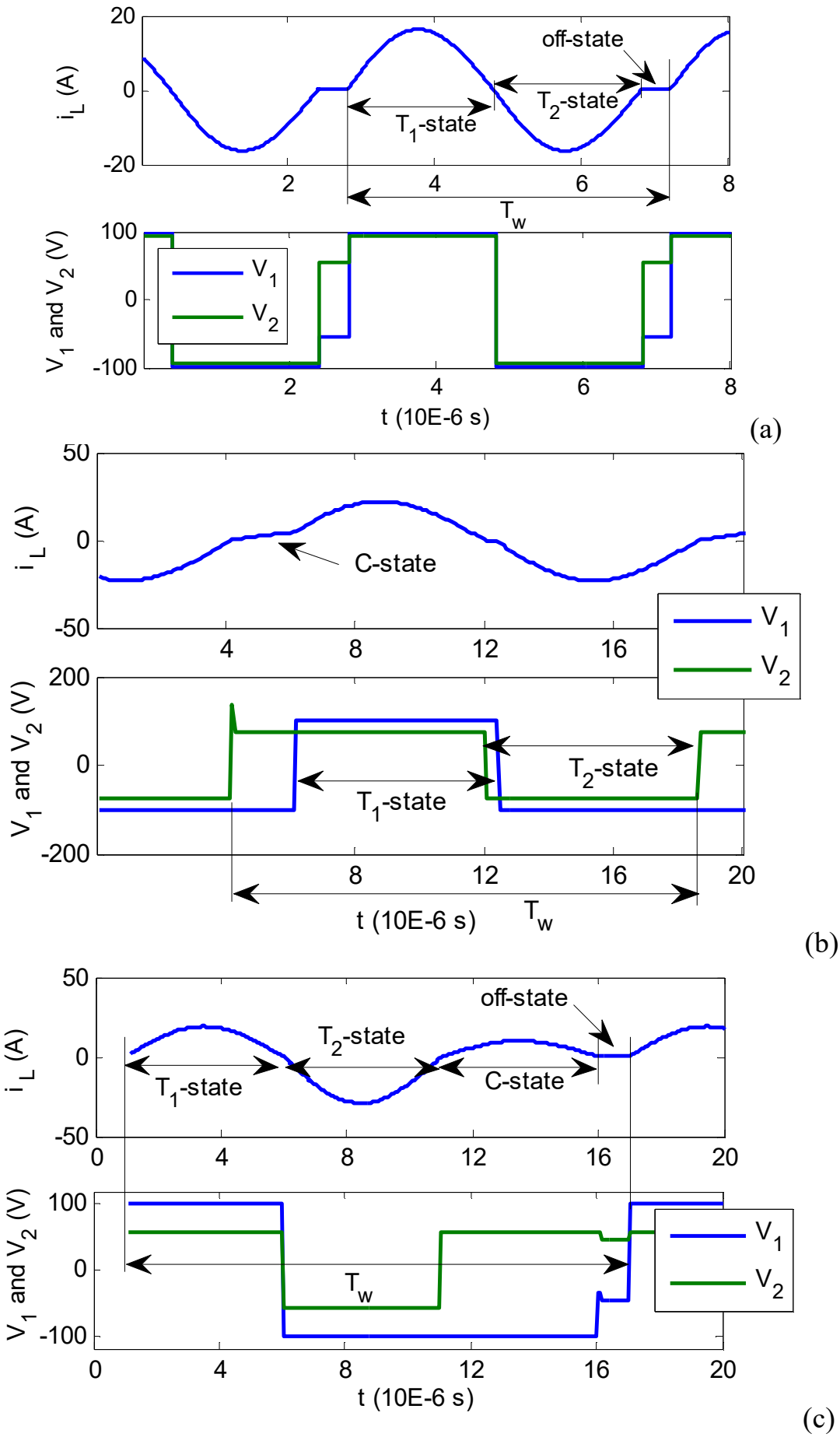

Figure 4.2.3–Waveforms for the reduction mode for different cases (a) case 1, (b) case 2, (c) case 3

The C-state occurs when the capacitor has a voltage greater than $V_i + V_o$. It produces a current that discharges the capacitor, delivering energy to V_1 and V_2, and thus both the inverter and rectifier act as rectifiers. In the off-state, no current flows through the series branch. The full-bridge commutates when the current is zero, at the end of each state. Hence, the converter operates in a soft switching mode by reducing the power losses [210]. The converter can work with an *M* that is less than (step-down mode) or greater than one (step-up mode). Each mode is based on a pattern of the states mentioned above. The following sections analyze both modes in detail. Subsequently, a design methodology is proposed and a prototype is developed to show the results.

This model is the basis to understand the behavior of a SRC working in step-up mode, a more realistic model considers the value of the magnetizing inductance. This inductance can produce an anomalous step-up conversion when the load is light, when the $R_L >> Z_0$. The details of the analysis, following the same approach, is in subsection 4.2.5 but considering the magnetizing inductance as well. All of the details can be found in [32, 211].

4.2.3. Step-down mode

This mode consists of two transfer states and an off-time. Figure 4.2.3 shows a simulation in PSIM software for the three possible cases:

• Case 1: The off-time consists only on the off-state, so no current flows through the resonant branch (Figure 4.2.3(a)).

• Case 2: The off-time consists only on the C-state. Current flows though the resonant branch, hence the initial zero current condition is not valid (Figure 4.2.3(b)).

• Case 3: The off-time consist on a C-state first and then an off-state, so at the end the resonant current is zero (Figure 4.2.3(c)).

The voltage conversion ratio is calculated for each case as a function of the off-time, t_{off}. The method calculates the mean value of the output current, which corresponds

to the resonant current during the transfer states and the C-state. Once the mean output current is calculated, the output voltage is easily obtained by Ohm's law.

Case 1. In this case, the mean value of the output current is:

$$I_0 = \frac{1}{T_w} \cdot \left[\underbrace{\int_0^{\frac{T_0}{2}} i_L(t) \cdot dt}_{T_1} + \underbrace{\int_0^{\frac{T_0}{2}} -i_L(t) \cdot dt}_{T_2} + \underbrace{\int_0^{toff} 0 \cdot dt}_{off-state} \right] = \frac{V_0}{R_L}, \tag{4.2.8}$$

where I_0 is the mean value of the output current. R_L is the load resistance and T_W is the working period. The amplitude of i_L depends on the capacitor's initial value of each state. The method for obtaining these initial values consists of finding the final value of each state, which is equal to the initial value of the next one. In this case, the converter has three states, but in the off-state the voltage in the capacitor remains constant. Therefore, there are only two initial conditions to find. The system of equations is:

$$\begin{aligned} v_{Ci(2)} &= -\left(v_{Ci(1)} - V_{SC} + V_{2BUS}\right) \cdot e^{-\lambda} + V_{SC} - V_{2BUS} \\ v_{Ci(3)} &= -\left(v_{Ci(2)} + V_{SC} - V_{2BUS}\right) \cdot e^{-\lambda} - V_{SC} + V_{2BUS} \\ v_{Ci(1)} &= v_{Ci(3)}, \end{aligned} \tag{4.2.9}$$

where $\lambda = \pi/(\omega_0 \tau)$. By solving this linear system, the initial values are obtained. Finally, the voltage conversion gain can be calculated using (4.2.7), (4.2.8) and (4.2.9), the result as a function of t_{off} is:

$$M|_{case1} = \frac{1}{1 + \frac{1 - e^{-\lambda}}{1 + e^{-\lambda}} \cdot x} \qquad case\ 1:\ \ x < x_C \tag{4.2.10}$$

where $x = \pi \cdot \left(1 + t_{off}/T_0\right)/(2r_L)$ and $r_L = \frac{R_L}{Z_0}$ is the ratio between the load resistance, R_L, and the characteristic impedance, $Z_0 = \sqrt{L_R/C_R}$. T_0 is the natural period of the resonant branch: $T_0 = 2\pi\sqrt{L_R C_R}$, and t_{off} is the off-time. The voltage conversion gain using this variable is in (4.2.10). The x variable simplifies the design methodology

Case 2. The waveforms of this case are presented Figure 4.2.3(b). It shows that the states overlap. Therefore, the initial zero-current condition is not valid. It can be solved analytically based on the same procedure as in (4.2.5) and (4.2.6). Anyway, this case

occurs only for a small range of the normalized variable x, therefore it can be approximated by a linear function.

Case 3. In this case four states are present: T_1, T_2, C-state and the off-state. Equation (4.2.11) shows M as a function of x. The procedure to obtain M is the same as in case 1 but with four states instead of three.

$$M|_{case3} = \frac{1+e^{-\lambda}}{1-e^{-2\lambda}+x\cdot\frac{1+e^{-3\lambda}}{1+e^{-\lambda}}} \quad case3: x > x_C \ \wedge \ x > x_{1/2}, \tag{4.2.11}$$

The voltage transfer ratio of the converter was calculated by segments. In order to join them, the limit condition of each segment should be defined. As mentioned previously, case 1 does not have C-state. The reason for this is that the voltage in the resonant capacitor, C_R, is below V_i+V_o. Hence, when both inverters are turned off, C_R cannot deliver any current. The limit of this case occurs when the voltage in C_R at the end of state T_2 is equal to $-(V_i+V_o)$. Replacing this condition in the linear equation system (4.2.9), the ratio between V_{1DC} and V_{2BUS} is obtained. Then, using (4.2.10), the upper limit value of x for case 1, x_C, is calculated:

$$x_C = e^{\lambda} + 1. \tag{4.2.12}$$

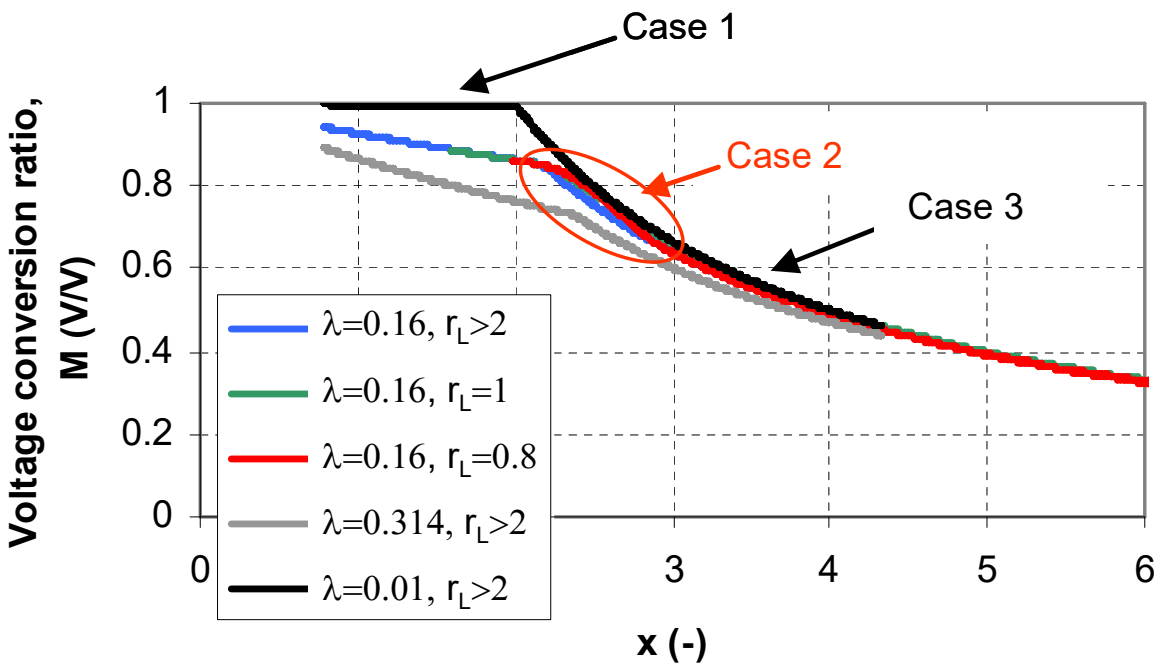

Figure 4.2.4–Voltage conversion ratio, M, as a function of the x-variable and parametrized for different λ

The lower limit for case 1 occurs when the off-time is zero (x_0). For case 2, the lower limit occurs at $x=x_C$ and the upper limit occurs when the off-time reaches $T_0/2$, represented by $x_{1/2}$. Both x_0 and $x_{1/2}$ are presented in (4.2.13). Case 3 begins when $x>x_{1/2}$ and $x>x_C$. M is plotted in Figure 4.2.4 for the whole range of x and for different values of r_L and λ. Case 2 can only be distinguished for r_L =0.8. This happens when $x_C<x<x_{1/2}$, which means $2.17<x<3$ (red line in Figure 4.2.4).

$$x_0 = \frac{\pi}{2} \cdot \frac{(1+0)}{r_L} \quad \wedge \quad x_{1/2} = \frac{\pi}{2} \cdot \frac{(3/2)}{r_L}. \tag{4.2.13}$$

4.2.4. Step-up mode

The difference between this mode and the step-down mode consists on the addition of an A-state. So, the whole working period is formed of one A-state, one transfer state and the off-time that controls the transfer function. Again, the off-time can be formed only by the off-state, only by the C-state or both.

Figure 4.2.5 shows a simulation in PSIM software of the three possible cases. The method for analyzing this mode is equivalent to the one used to study the step-down mode. Equations (4.2.4), (4.2.5), (4.2.6), (4.2.7) and a linear system similar to (4.2.9) are used to calculate the voltage conversion ratio (M) for each case.

Case . 1Figure 4.2.5(a) shows i_L, V_1 and V_2 for this case. The A-state happens when V_2 is zero, so the current flow is only due to voltage V_1. The T_2 state, when V_1 and V_2 are negative, and the off-state, when the current is zero, are also shown. In this case, the only state that delivers energy to the load is T_2. The A-state accumulates energy in C_R and the off-state controls the output voltage. Based on the method explained in the step-down mode, M is presented in (4.2.14) for this case.

$$M|_{case1} = \frac{2}{1 + 4 \cdot x \cdot \left(\frac{1-e^{-\lambda}}{1+e^{-\lambda}}\right)} \quad case1: x < x_C. \tag{4.2.14}$$

The maximum value of M is two, which corresponds to the limit when x tends to zero.

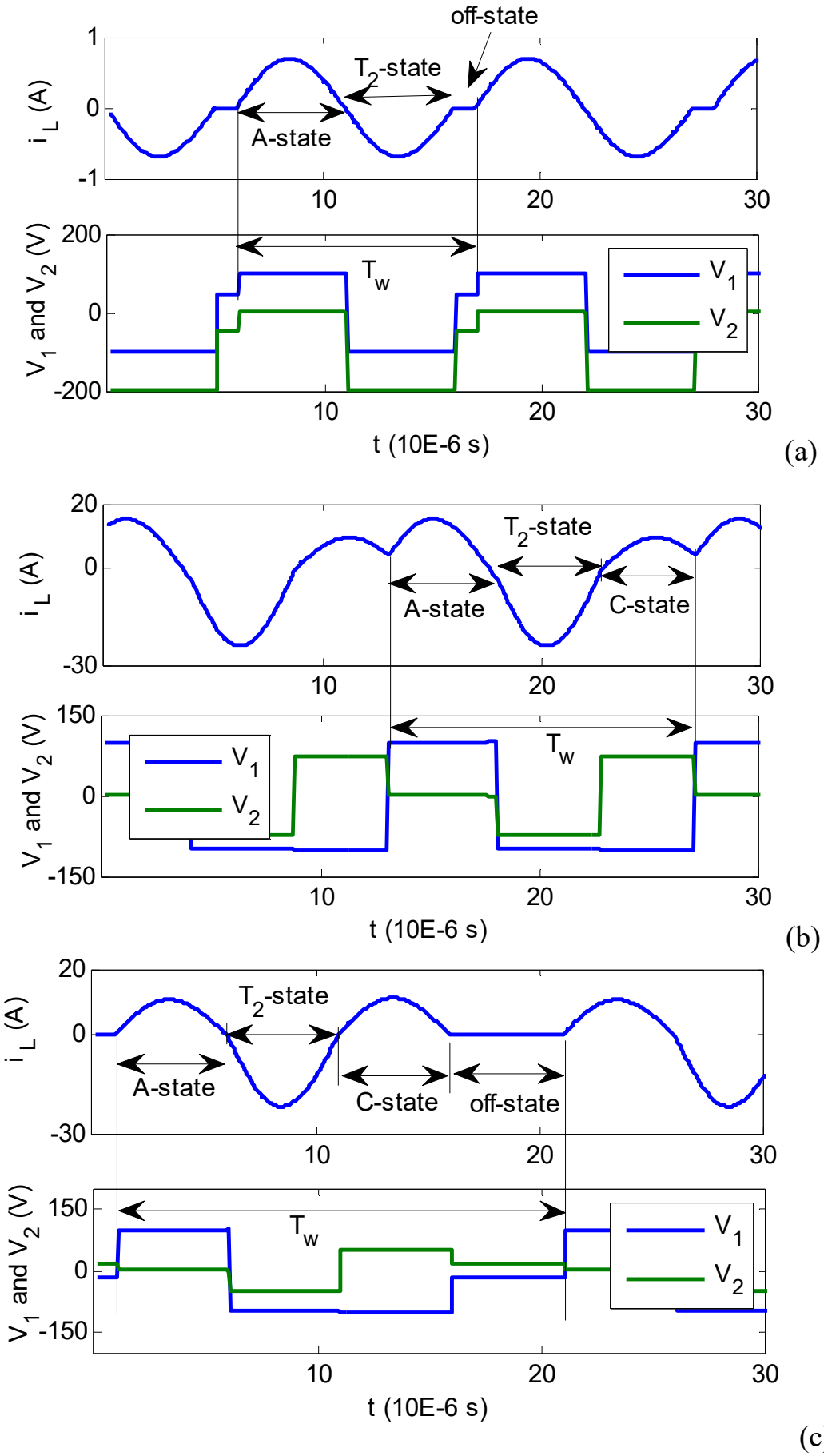

Figure 4.2.5-Waveforms for the step-up mode for different cases (a) case 1, (b) case 2, (c) case 3

Case 2. Similarly, to the one in the step-down mode, it does not achieve zero-current switching. Figure 4.2.5(b) shows the waveforms of this case. i_L does not reach a zero value when the A-state begins because the C-state does not last half of a resonant period, $T_0/2$. It is not possible to calculate the voltage gain using the equations presented before. Equation (4.2.6) is no longer valid and it is preferable to obtain M numerically. In this case, M is not only a function of x, it also depends on the normalized resistance, r_L. Figure 4.2.6 shows M for the three cases. Case 1 is on the left, case 3 is on the right and between them is case 2, where M is parameterized by r_L. For large values of r_L case 2 tends to case 3, because i_L in the clamping state is low. Differences are appreciable for values of r_L less than two.

Case 3. The waveforms for this case are shown in Figure 4.2.5(c). The current and voltage plots clearly show clearly the off-state, A-state, transfer and C-states. All of these states last $T_0/2$, so the equation (4.2.7) is valid, which means that each state starts and ends with zero-current. The integral to find M is in (4.2.15). In this case, T_2 and C-states deliver energy to the load

$$I_o = \frac{1}{T_0 + t_{off}} \left(\underbrace{\int_0^{T_0/2} -i_{L(2)}(t) \cdot dt}_{T_2-state} + \underbrace{\int_0^{T_0/2} i_{L(C)}(t) \cdot dt}_{C-state} \right) = \frac{V_o}{R_L}. \tag{4.2.15}$$

This equation has been solved to obtain M, which is:

$$M|_{case3} = \frac{2}{4 \cdot x \cdot \frac{1 + e^{-3 \cdot \lambda}}{(1 + e^{-\lambda})^3} + 3 \cdot \frac{1 - e^{-\lambda}}{1 + e^{-\lambda}}}. \tag{4.2.16}$$

As in the step-down mode, it is important to know the limits of each case. So again, x_C is obtained by considering that the final C_R voltage equals -(V_i+V_o) in T_2 for case 1. The value of x for this condition is

$$x_C = \frac{\left(e^{+\lambda} + 1\right)}{2}. \tag{4.2.17}$$

This analysis gives the voltage conversion ratio of the converter for the whole range of x. Also, the RMS value of i_L is important in order to calculate the power losses and efficiency. Once M is calculated, the currents and voltages in each component can be

obtained using (4.2.7), and thus efficiency can be calculated which is used in the design process.

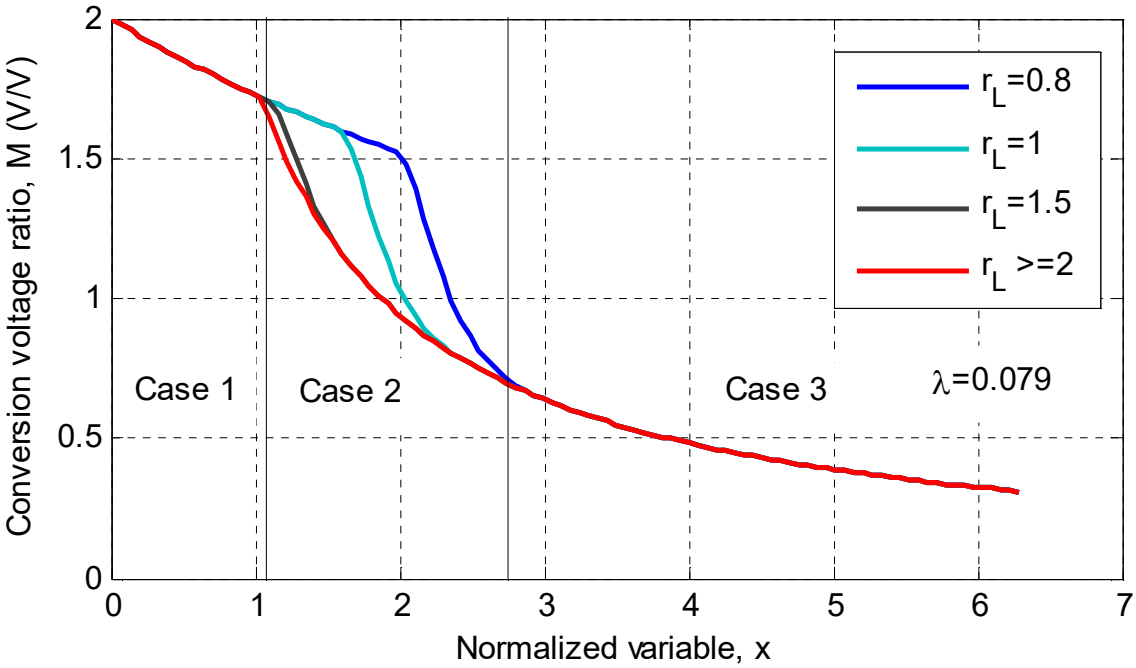

Figure 4.2.6–Transfer voltage gain for different normalized load resistance at λ =0.079

4.2.5. Design guidelines

The first step to design this type of DC/DC converter is to list the specifications:

- Transfer range without transformer (M_{Umin}, M_{UMAX})
- Load range (R_{Lmin}, R_{LMAX})
- Minimum efficiency (η_{min})
- Resonant frecuency (ω)

Once, the specifications are well-defined. The procedure to obtain the component values of the converter consists on few steps. The first is the mode selection: reduction or elevation mode. The second is to obtain the range of *x*. This can be done analytically using (4.2.12-17) and a numerical approach for the case 2 or a linear interpolation. Also, it can be done graphically with Figure 4.2.4 and Figure 4.2.6.

The third step is the selection of the minimum λ that achieves the efficiency. In order to estimate the converter efficiency, it is important to know the RMS current through the resonant branch. The efficiency of the converter can be estimated considering that all the power losses are represented by R_{LOSS}. This estimation is presented in (4.2.18). Thus, every component is lossless and the losses of each component are included in R_{LOSS}.

$$\eta = \frac{1}{1 + \underbrace{\left(\frac{I_{LRMS}}{I_0}\right)^2 \frac{1}{r_L}}_{F(x)} \cdot r_{LOSS}} = \frac{1}{1 + F(x) \cdot \frac{2 \cdot \lambda}{\pi}}, \tag{4.2.18}$$

where I_{LRMS} is the RMS current through the resonant branch, I_0 is the output current, r_{LOSS} is the normalized loss resistance and $F(x)$ shows that this term is a function of the normalized variable. Figure 4.2.7 shows the efficiency of the converter of the elevation mode for different loads and λ.

At this point, λ is selected. The next step is to fix the minimum t_{off}, it should close to zero, as an example $T_0/10$. Then, with the x_{min} extracted by the minimum voltage conversion ratio, r_{Lmin} is calculated. With r_{Lmin} and R_{Lmin} the characteristic impedance is obtained. Then, by using the desired resonant frequency, C_R and L_R are easily calculated. Finally, with λ and the definitions in (4.2.7) R_{LOSS} is calculated. It should be noted that R_{LOSS} includes the losses of the passive and the active components, so the quality factor of the inductor should be better than the obtained by λ.

4.2.6. Simulations and experimental validation

In order to verify this analysis and design methodology, a prototype was developed using the design procedure. This prototype was used to transfer energy from/to a 36V battery bank to/from a 165V DC line. The battery bank consisted of 10 VL45E lithium-ion cells from SAFT batteries. The specifications are shown in Table 4.2.2. As noted in the subsection 4.2.1, the step-up mode had to be used. In order to get an M below 1.5, the transformer turns ratio was fixed at five. The range of M is in Table 4.2.2. Using these data

and Figure 4.2.6, the range of x was obtained: from 1.8 to 2.6 in the discharge mode and from 1.6 to 2.6 in the charge mode. The discharge mode corresponds to the case when the power flows from $V_{1DC} = V_{1BUS}$ to $V_{2DC} = V_{2BUS}$, while in the charge mode the power flows in the opposite direction.

As efficiency needed to be around 90%, by using Figure 4.2.7, λ was calculated to be approximately 0.05. By setting the minimum t_{off} to $T_0/10$ and using the x definition, r_{Lmin} was 1.72. Considering the maximum output power and the output voltage, R_L was calculated. In addition, 7.9Ω was obtained for Z_0. Using this value and the resonant frequency, the inductance L_R and capacitance C_R values were calculated: 16uH and 250nF. R_{LOSS} could be up to 0.25Ω. Note that r_{Lmin} was high enough to allow a higher λ while maintaining almost the same efficiency. As shown in Figure 4.2.7(b), as r_L increases, case 2 is reduced and the minimum for the efficiency curve increases. L_R is the sum of the transformer leakage inductance (4.3uH) and an external inductor L_1 (12uH).

Table 4.2.2 Specifications for DC-DC converter

Parameter	Symbol	Value			Unit
	-	Min	Typ	Max	-
Input Voltage (battery side)	V_{1DC}	27	36	42	V
Output Voltage	V_{2DC}	-	165	200	V
Output Power	P_O	-	-	2000	W
Efficiency	η	-	90	-	%
Resonant Frequency	f_0	-	80	-	kHz
Discharge current	I_{DISC}	-	-	80	A
Charge current	I_{CHARGE}	-	-	10	A
Transformer turns-ratio	n	-	5	-	-
Voltage Conversion Ratio	M_{12}	0.78	-	1.22	-
	M_{21}	0.8	-	1.43	-

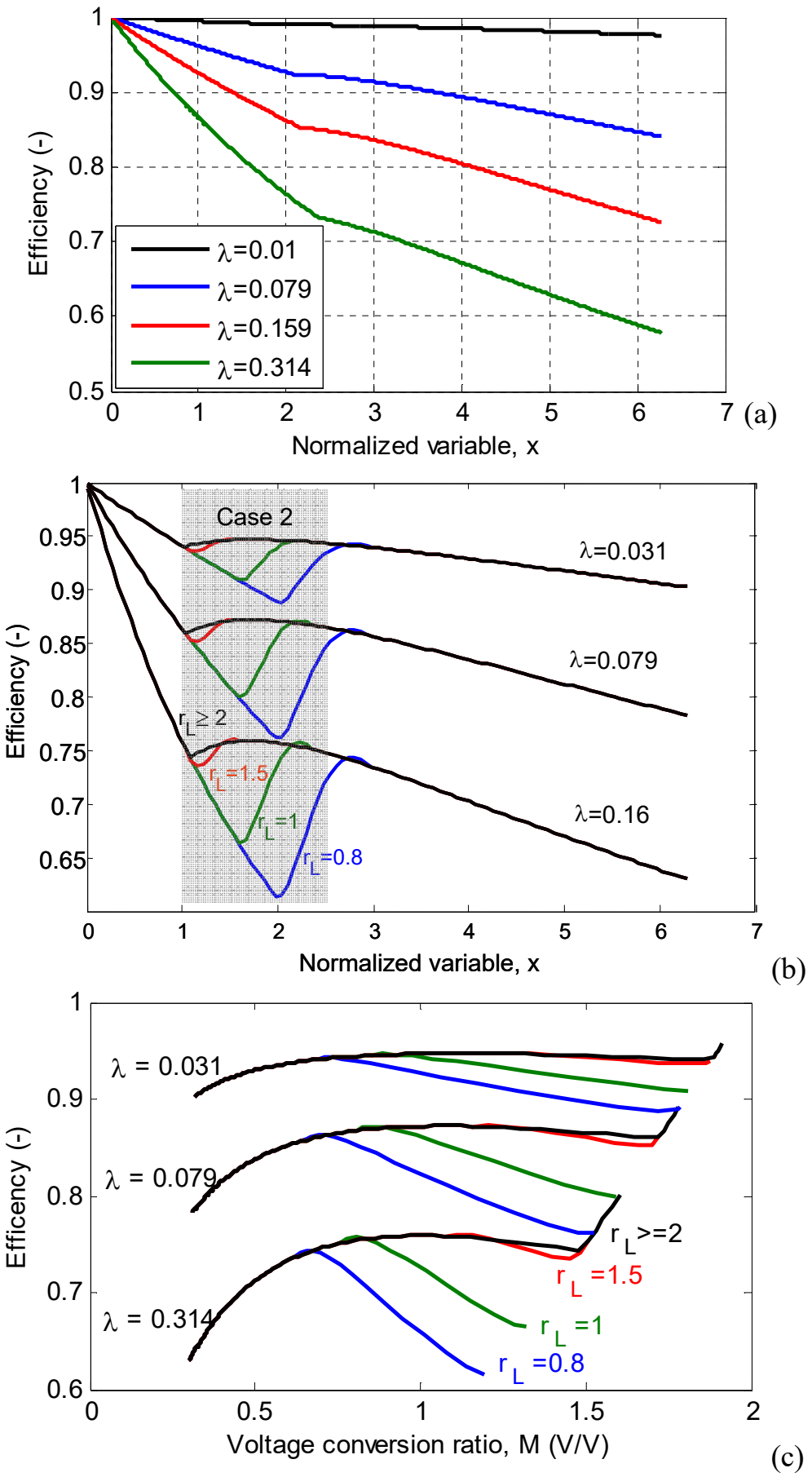

Figure 4.2.7-Efficiency of the converter at different λ and loads for (a) step-down and (b) step-up modes versus *x* and efficiency versus *M* in step-up mode

Figure 4.2.8 shows the prototype. It uses two MOSFET full-bridges, a planar transformer with a turns ratio of five and a capacitor (C_R) of 220 nF with low series resistance. The circuit is similar to the schematic in Figure 4.2.2(a). The high and low side MOSFETs are IXFH88N30P and IXFP4110PbF respectively. IXFH88N30P can withstand a voltage of up to 300V and has an on-resistance of 40mΩ, and IXFP4110PbF can withstand up to 100V and has an on-resistance of 4.5mΩ. In order to reduce the conduction losses, the low side full-bridge has its switches duplicated.

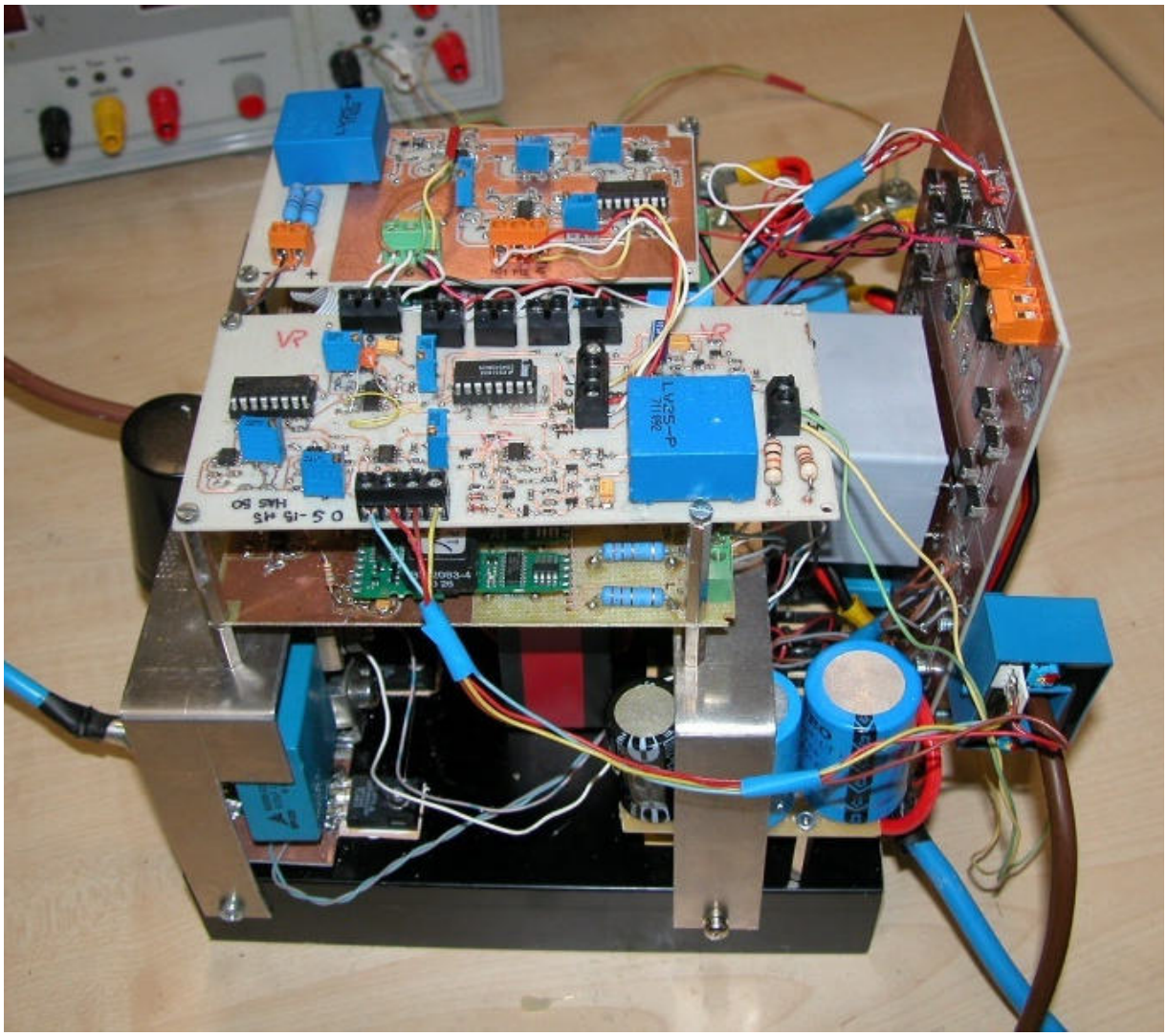

Figure 4.2.8–Prototype

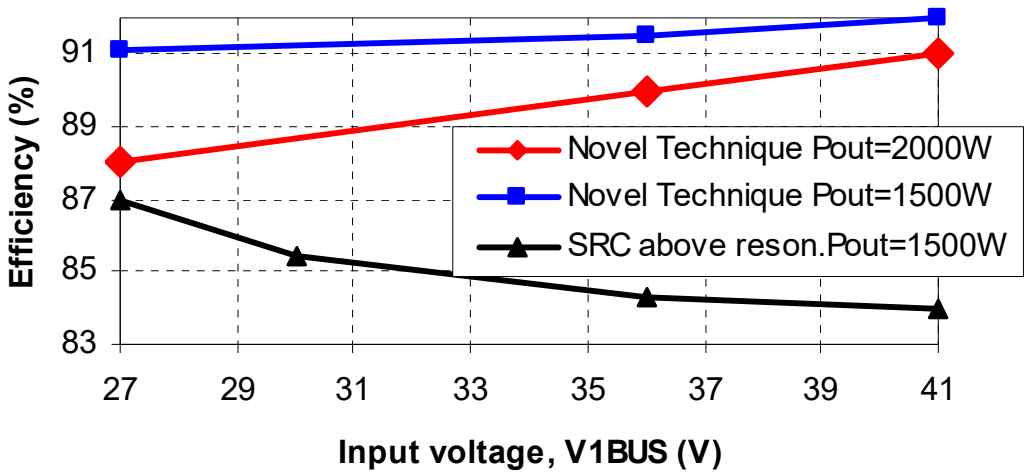

(a)

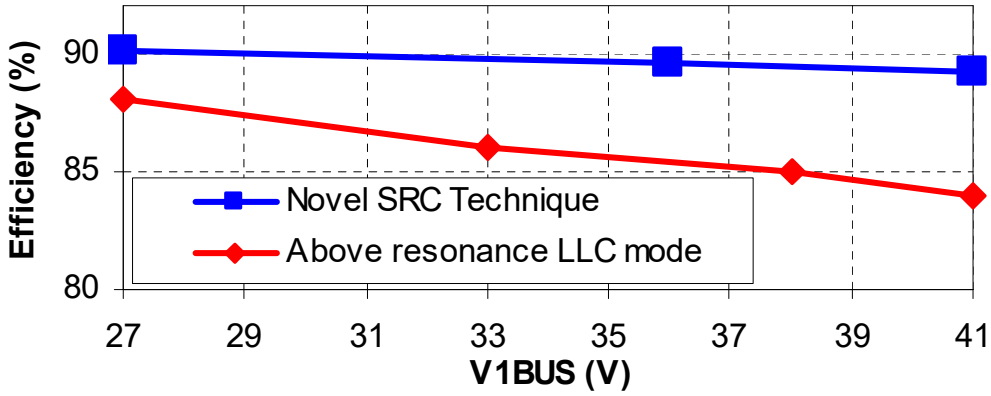

(b)

Figure 4.2.9-Efficiency (a) Discharging process (b) charging process, constant I_{1BUS} current = 10A (V_{1BUS}=V_{1DC})

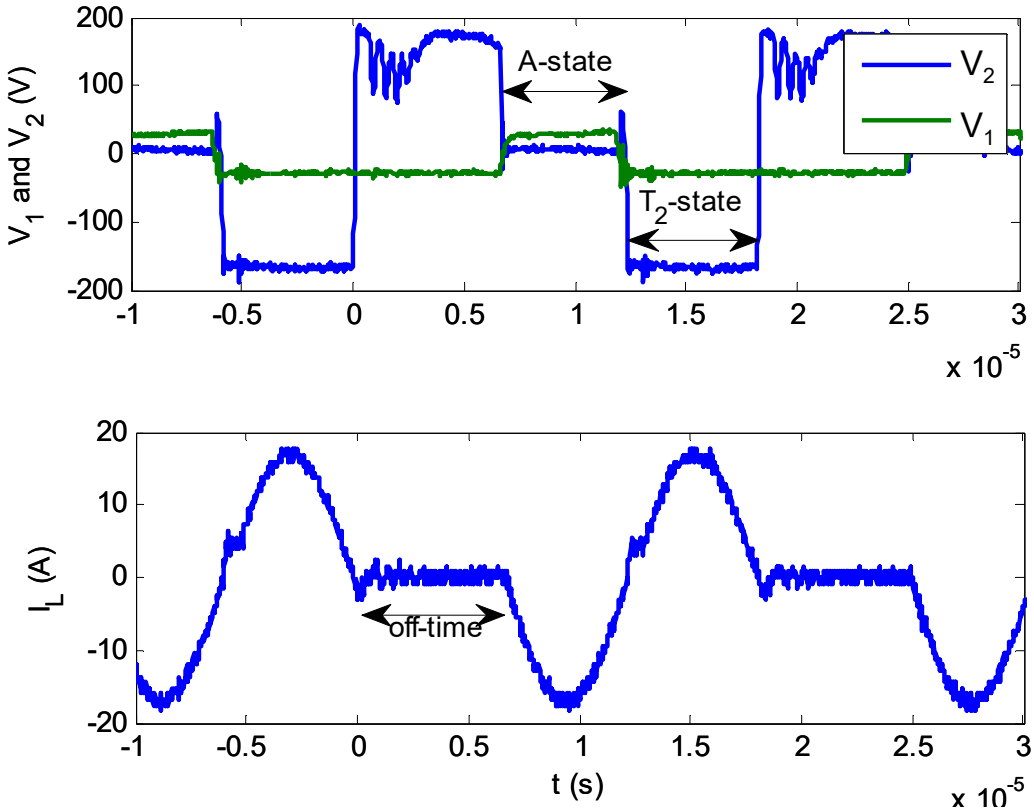

Figure 4.2.10-Resonant branch waveforms

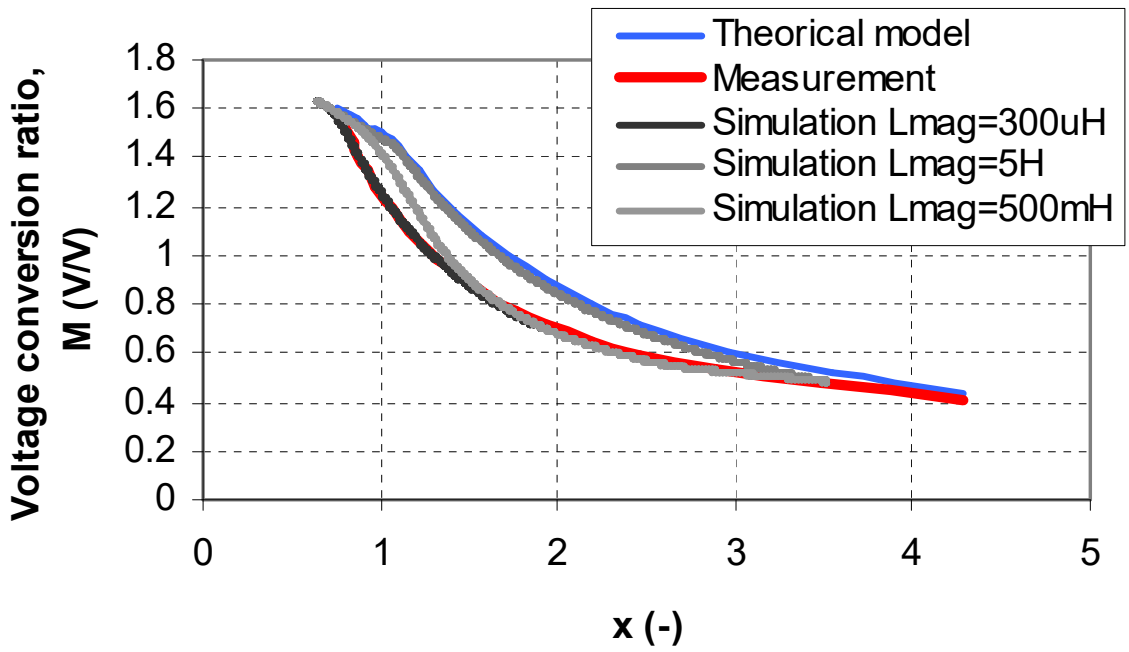

Figure 4.2.11-Measurement and simulation of voltage conversion ratio, M

4.2.7. Comparison of the step-up bidirectional SRC with other topologies

The proposed converter is useful in applications that involve bidirectional power flow. It can be attached to energy storage devices such as batteries or supercapacitors to transfer energy to a regulated DC line, which can be the inverter in an EV charger. Other topologies that have been traditionally used for this purpose are the bidirectional half-bridge [212] or the dual active bridge DC-DC converter (*DAB*) [193] [213] [214]. It is particularly useful to compare the proposed converter with the LLC converter because both have almost the same topology [194][214]. The LLC converter is an asymmetrical circuit, so its behavior is different in each direction. In one direction, it works as an LLC, and in the other direction it works as an SRC. When it works as an SRC, it acts as a step-down converter plus the transformer turns ratio (traditional SRC). In the other direction the transformer reduces the voltage, so having a $M > 1$ is necessary to compensate for the step-down effect of the transformer. High M values are needed, and this reduces the efficiency of the LLC technique. Figure 4.2.9 shows measurements for the LLC technique using the same components of the prototype presented here, but modifying the magnetizing inductance at *200uH* and controlling the converter above resonance. It can

be seen that due to the high M required, $M>2$, efficiency decreases. A symmetric LLC also appears in the literature [215] [216], but because of the high currents in the low side of the transformer (up to 100A), good results are not achieved because the capacitor losses at high currents is notable.

4.2.8. Extension of use of discontinuous mode step-up bidirectional SRC with other sequences of states.

The sequences of states shown in subsection 4.2.3 and subsection 4.2.4 can be modified in order to add more A-states or T-states thus, the voltage conversion gain shown in Figure 4.2.6 can be increase or decrease, for example, in Figure 4.2.12(a) the mode of 1 A-state with 2 T-states is presented and in Figure 4.2.12(b) the mode of 2 A-states and 3 T-states. Notice that using that states combination, the number of states is odd, during the half of the working period, the A and T states generate currents in one direction and in the following half working period they generate currents opposite direction. Thus, the use of the transformer is balanced, reducing the risk of saturation of the magnetic material. Combining modes or sequences of states, the converter works in a multi-mode operation. Using this multi-mode, the converter increases its efficiency by minimizing the t_{off}. The best mode for a certain power and voltage conversion gain can be selected. Efficiency of the difference modes are shown in Figure 4.2.13(a) and the efficiency of the multi-mode converter is in Figure 4.2.13(b). Further details can be found in [32][211].

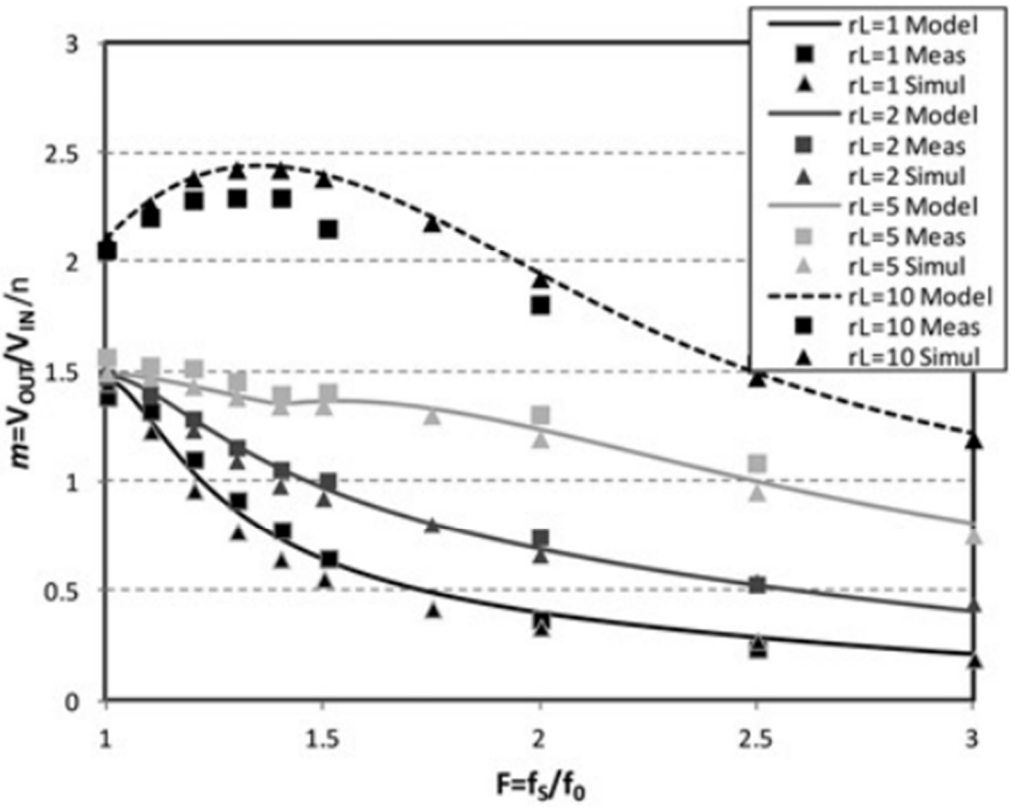

(a)

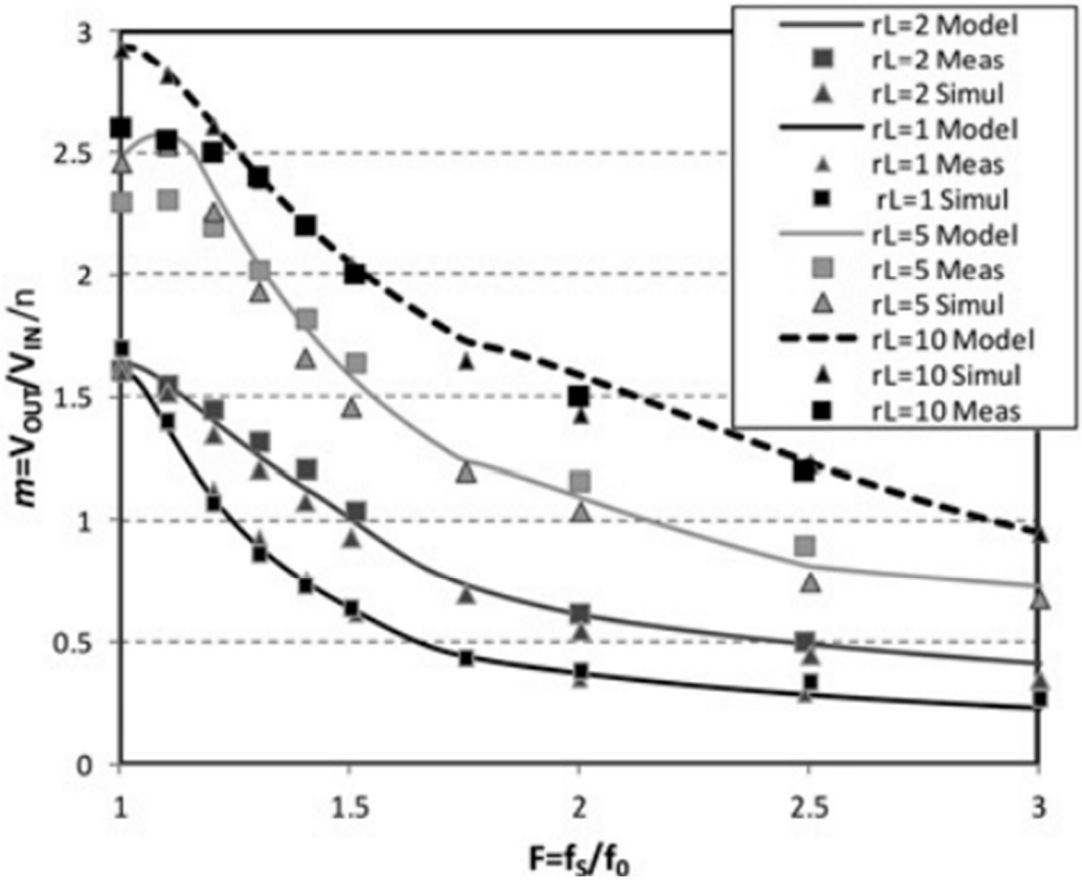

(b)

Figure 4.2.12–Static measurements: voltage conversion ratio as a function of normalized frequency, F, for (a) M1/3 mode, (b) M2/5 mode

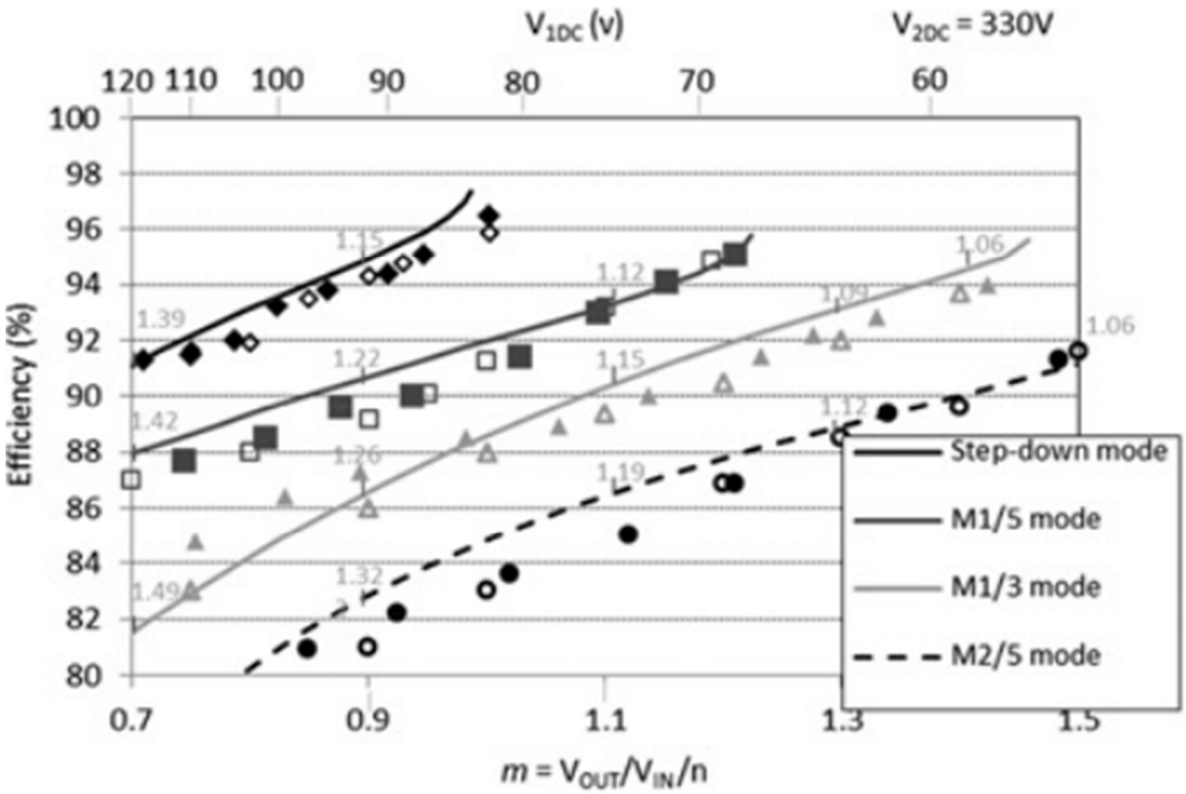

(a)

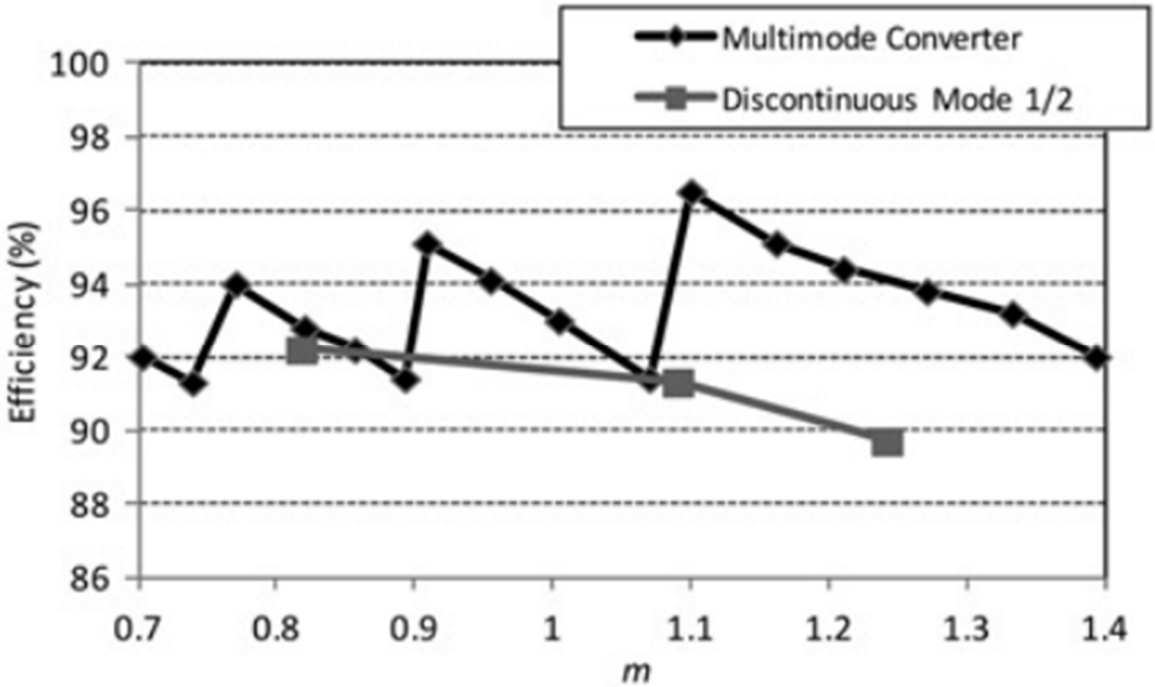

(b)

Figure 4.2.13–(a) Analytical model for efficiency curves, at maximum power (6 kW), compared with measurements in both power directions (the filled markers are measurements that transfer power from low to high voltage and the non-filled markers are measurements that transfer the power in the other direction), F is in grey and (b) Comparison with the M1/2 (normal step-up) mode in the same prototype

4.2.9. Anomalous behavior at light loads

When a bidirectional step-down series resonant converter (SRC) operates with light loads working above or below resonance, an anomalous operation appears. In normal step-down operation (heavy load), it is well known that SRCs have a maximum voltage conversion ratio (*M*) equal to one. This occurs when the switching frequency (f_S) equals the resonant frequency (f_0) and power losses are neglected. This maximum can also be obtained for $f_S<f_0$ when the switches are turned on during a half-resonant period. Thus, zero-current switching can be achieved at both the turn-on and turn-off processes. However, anomalous step-up behavior is found when the converter is attached to light loads. The reason for that is the activation of the diodes in the output bridge, the current through the drain-source capacitance (C_{DS}) of the switches and the transformer magnetizing inductance. A comprehensive analysis of this phenomenon in the time-domain and in the state-plane is presented in [32, 211]. Based on the latter, an expression that estimates *M* and shows the influences of the parameters is obtained and it is shown in Figure 4.2.14. The model is in concordance with simulations and experiments as the figure shows.

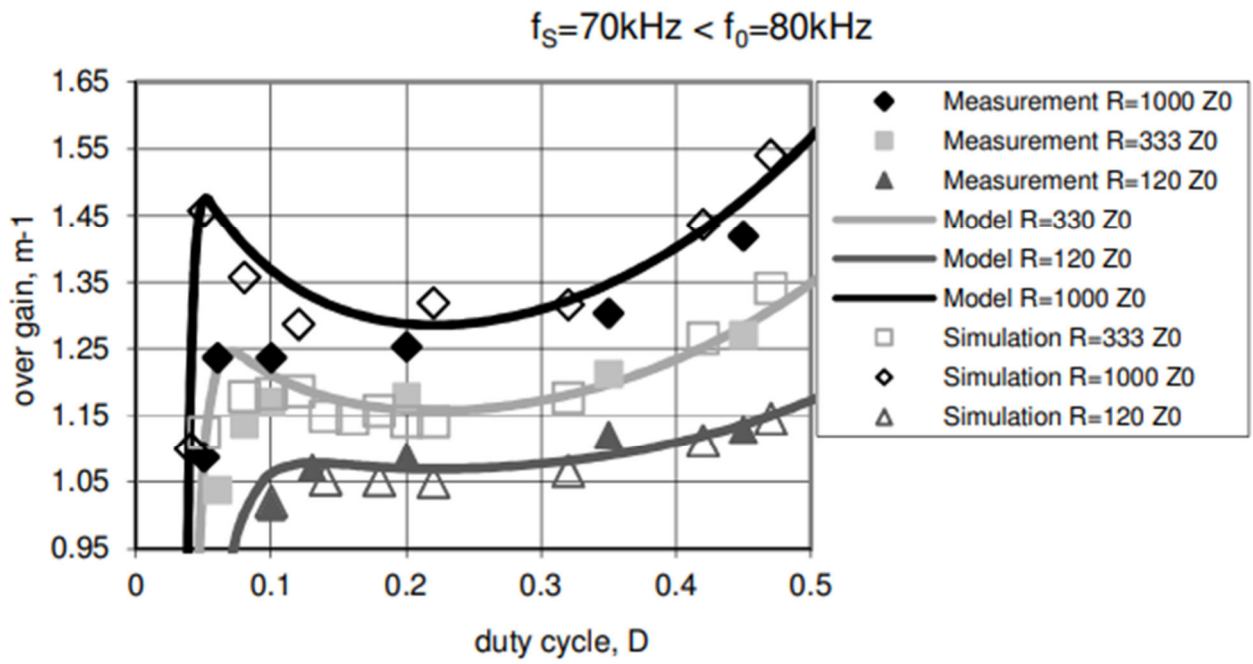

Figure 4.2.14- Voltage conversion gain in the anomalous light load condition in step-down mode

Based on the analysis of the parasitic elements, two alternatives for reducing the over-gain (m-1) are presented. The first one is to modify the magnetizing inductance or to select switches with reduced drain-source capacitances. However, this may not be possible, so the second alternative is to modulate the duty cycle, *D,* at light load. This will reduce the ringing time-interval and increase the off-time, where the magnetizing current discharges the C_{DS}, which results in keeping a soft turn-off process at low currents and reducing the over-gain. For heavy loads, the *D* reduction produces an interruption in the resonant current, and thus a hard-switching turn-off process occurs. This effect is only noticeable for very small *D*s. This was validated through simulation data and experimental results in [32].

4.2.10. Summary

This section is devoted to a two-port isolated DC/DC converter: the series resonant converter (SRC), particularly in the discontinuous mode. Resonant converters are known for their high efficiency. The analysis has divided the converter behavior into different time intervals called states. It was shown that the circuit could be used in a step-down mode as well as in a novel step-up mode; in order to achieve this, an accumulation state was introduced. This state allowed the converter to have a voltage conversion ratio (*M*) of up to two for the $M_{1/2}$ or normal step-up mode. *M* and efficiency were analytically calculated for both operation modes to show the possibilities of the circuit.

A step-by-step design methodology was proposed using these curves. Subsequently, a prototype was designed and implemented in order to verify the methodology. This prototype can deliver power up to 2000W and to a load at 165VDC from a low voltage port that is attached to lithium-ion batteries. The batteries have a voltage of 36V, but due to battery voltage variations, the input port range should accept values from 27 to 41V, so this side must be able to deliver more than 70A. The results show that the proposed methodology is useful for calculating the values of the components.

Experimental results confirm that this circuit can be used in applications related to batteries or supercapacitors, which is an advantage compared to the traditional SRC and LLC. Efficiency analysis showed that the main power losses are produced in the low side inverter/rectifier and also in the transformer. If a better converter is needed, a synchronous rectifier, of different inverter/rectifier topologies can be used such as the rectifier proposed in Figure 4.2.2(b) [110][209].

In addition, by selecting the sequence of states, different M can be chosen from the traditional step-down mode to many step-up modes that can achieve M values higher than 2.5. The section introduces and validates with numerical simulations and experiments two extra step-up modes, $M_{2/5}$ and $M_{1/3}$. These modes are analyzed because they are odd modes (1/3, one accumulation interval in three intervals, 2/5, two accumulation intervals in five intervals) and produce a symmetric inductor and transformer current, which means no DC current, then lower losses are expected in the circuit than in the even modes. One of the contributions of these modes is the ability to select the proper mode in order to increase converter efficiency in comparison with the initially introduced $M_{1/2}$ allowing a multimode operation.

This section also, based on the model, analyses the converter operation with light loads. Based on the model, the section obtains the voltage conversion ratio for the undesired M, explaining why a non-desired step-up behavior appears. The reason to produce this step-up mode is the drain-source capacitance (C_{DS}) of the switches and the transformer magnetizing inductance. The section suggests two methods for mitigating this behavior: a) modifying the magnetizing inductance or to select switches with reduced drain-source capacitances, or b) modulating the duty cycle, D. For light loads, the duty cycle should be reduced. The anomalous effect is modelled and validated through simulation data and experimental results.

To conclude, this section introduces the resonant converter for applications related to storage charging and discharging which are important in EV chargers. In contrast with the techniques detailed in Chapter 2, resonant converters work with frequency control instead of duty cycle control. However, in any case, they provide isolation and even high efficiency due to its soft-switching mechanism. This circuit is only a two-port isolated

DC//DC converter, increasing the number of ports will increase notably the complexity. In order to be a better alternative to the converter described in Chapter 2, the AC port should be incorporated to the circuit as well avoiding an extra inverter. For that reason, the technique described here will be the basis of the section 4.4 to achieve a multiple port system with AC and DC ports. The details of the proposed technique were published in [32, 33, 35, 36, 111, 211].

4.3. Isolated Series Resonant DC/DC converters – Continuous mode

The same circuit can work in continuous mode, where the current in the inductor has no off-state. This section will explain the modeling of a resonant converter working in continuous mode. The details of this section were published in [34, 111].

4.3.1. Steady-state modeling

The power stage schematic circuit of the SRC is presented again in Figure 4.3.1(a). Switches M1 to M8 are controlled by a square wave with 50% duty cycle, operating above the resonant frequency (f_0). The system transfers energy from V_{1DC} to V_{2DC} at the switching frequency, f_S. The gates of M1, 2, 3, 4, 7 and 8 (M5 and M6 remain off) are triggered as shown in Figure 4.3.1(b). For reverse power flow, the gate signals of M2, 4, 5, and 8 correspond to those of M1, 4, 7, and 8, respectively, while M6 and M7 follow the pattern of M2 and M3. A simplified circuit is shown in Figure 4.3.1(c), which will be used to develop the steady-state model and its characteristics. V_1 and V_2 from Figure 4.3.1(c) represent voltage sources that remain constant in a time interval. As shown in Figure 4.3.1(c), the analysis does not consider the transformer turns ratio of the real converter, so the analysis is completely symmetric and can be applied in both directions. The addition

of the transformer increases the voltage conversion ratio of the whole converter in one direction and decreases it in the same proportion in the opposite direction. This analysis considers that $n \cdot V_{1DC}$ is V_{IN}, V_{2DC} is V_{OUT} and R is the load resistor.

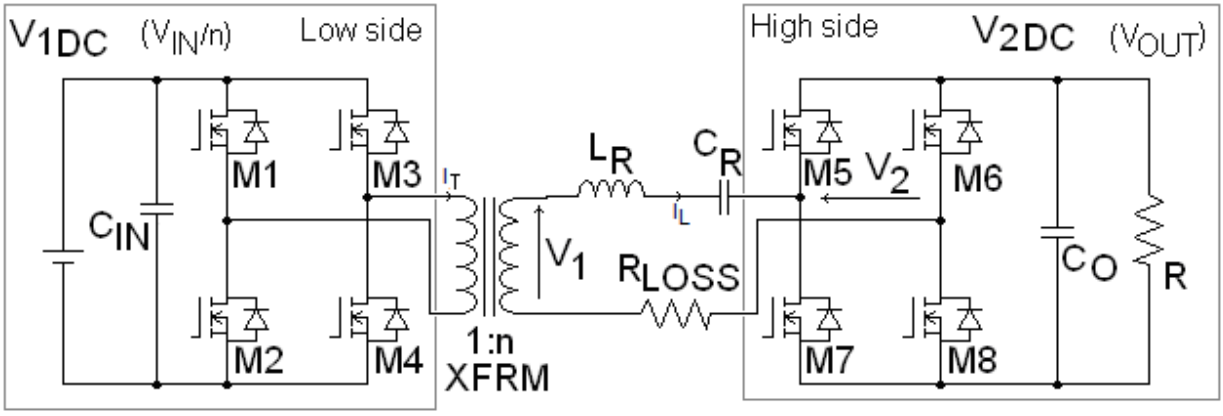

(a)

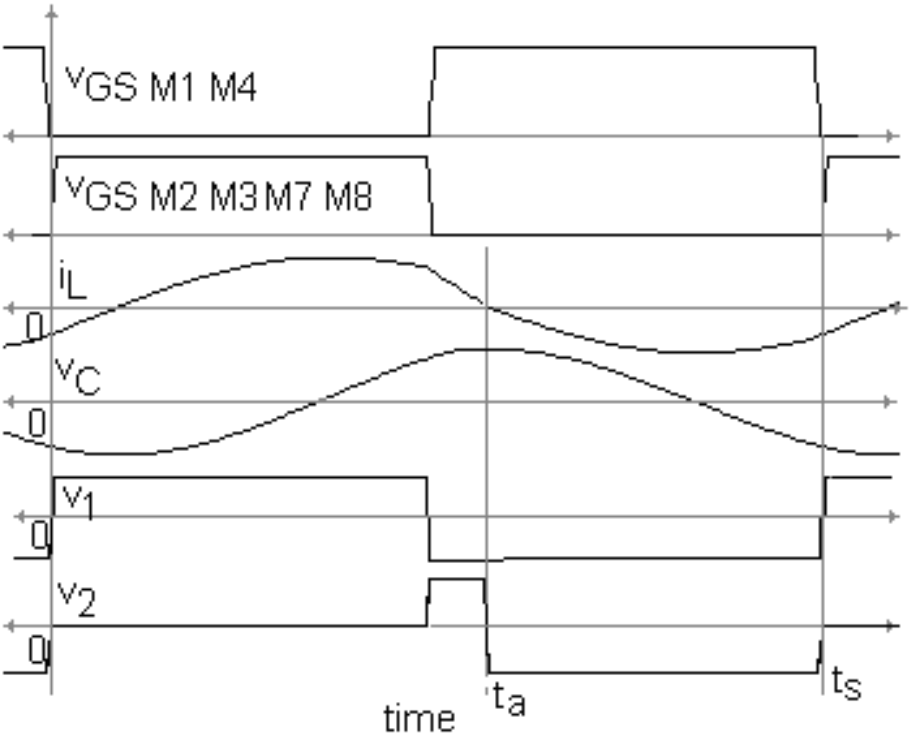

(b)

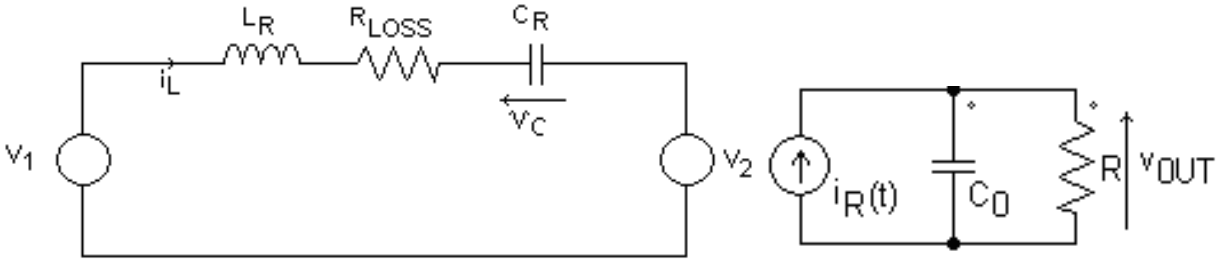

(c)

Figure 4.3.1–DC/DC converter: (a) schematic, (b) waveforms, (c) simplified circuit

The circuit has three time intervals (t_1, t_2 and t_3) due to the commutation of switches M1 to M8, so the three possible values for the (V_1,V_2) pair are listed in (4.3.1). The time intervals are related as shown in (4.3.2). F is the normalized frequency: f_S/f_0.

$$(V_1, V_2) = \begin{cases} V_{IN}, 0 \\ -V_{IN}, V_{OUT} \\ -V_{IN}, -V_{OUT} \end{cases} \quad V_T = V_1 - V_2 \tag{4.3.1}$$

$$t_1 = t_2 + t_3 = \frac{\pi}{\omega_S} = \frac{\pi}{\omega_0 \cdot F}. \tag{4.3.2}$$

The LC branch is governed by:

$$V_T = L_R \cdot C_R \cdot \frac{d^2 v_C}{dt^2} + R_{LOSS} \cdot C_R \frac{dv_C}{dt} + v_C \tag{4.3.3.a}$$

$$i_L = C_R \frac{dv_C}{dt}. \tag{4.3.3.b}$$

The solution is:

$$v_{C(n)} = v_{C1(n)} \cdot cos(\omega_0 \cdot t + \phi_n) \cdot e^{-kt} + V_{T(n)} \tag{4.3.4.a}$$

$$i_{L(n)} \approx -\frac{v_{C1(n)}}{Z_0} \cdot sin(\omega_0 \cdot t + \phi_n) \cdot e^{-kt} \tag{4.3.4.b}$$

where $v_{C(n)}$, $v_{C1(n)}$, φ_n are the capacitor voltage, the capacitor initial voltage and the initial phase for the n-th interval. The attenuator factor is $k=R_{LOSS}/(2L_R)$ and the characteristic impedance $Z_0=(L_R/C_R)^{1/2}$. Eq. (4.3.4) can be normalized based on the state-plane method [217, 218]. This method is commonly used in the analysis of continuous and discontinuous series and parallel resonant converters. The solution based on the normalization is:

$$m_{C(n)}(t) = H_{(n)} \cdot cos(\omega_0 \cdot t + \phi_n) \cdot e^{-kt} + m_{T(n)} \tag{4.3.5.a}$$

$$j_{L(n)} \approx -H_{(n)} \cdot sin(\omega_0 \cdot t + \phi_n) \cdot e^{-kt}. \tag{4.3.5.b}$$

The method normalizes the capacitor voltage with the input voltage V_{1DC}, and the inductor current with the input voltage and the characteristic impedance $Z_0=(L_R/C_R)^{1/2}$. Consequently, the normalized capacitor voltage is $m_C = v_C/V_{IN}$, the normalized inductor current is $j_L = i_L \cdot Z_0/V_{IN}$ and the conversion voltage ratio of each time interval is $m_{T(n)}=V_{T(n)}/V_{1N}$. Therefore, in the m_C-j_L plane, the solution represents an arc of radius $H_{(n)}$

(for R_{LOSS}=0) with the center in (m_C,j_L)=(0, $m_{T(n)}$). The subscript *n* refers to the time interval from 1 to 3. Thus, three arcs form a closed curve in the plane as shown in Figure 4.3.2. A lossless example is shown in order to clarify the concepts. If power losses are considered, the arcs have an initial radius and a smaller final radius. Each arc starts when the previous one finishes due to the capacitor voltage and inductor current continuity constrains. This is the key to obtaining the voltage conversion gain, *M*. This analysis does not consider any transformer ratio so *m*=*M*. The whole curve in Figure 4.3.2. was obtained by simulating the circuit in Figure 4.3.1(a) in PSIM software, and it shows the particular case when F=1.1. In addition, the values of A_1 to A_3 are shown. The arc with A_1 radius represents half of the switching period, $t_S/2$. γ, α, β are the arc angles of the 1st, 2nd and 3rd interval respectively, and ϕ represents the initial angle.

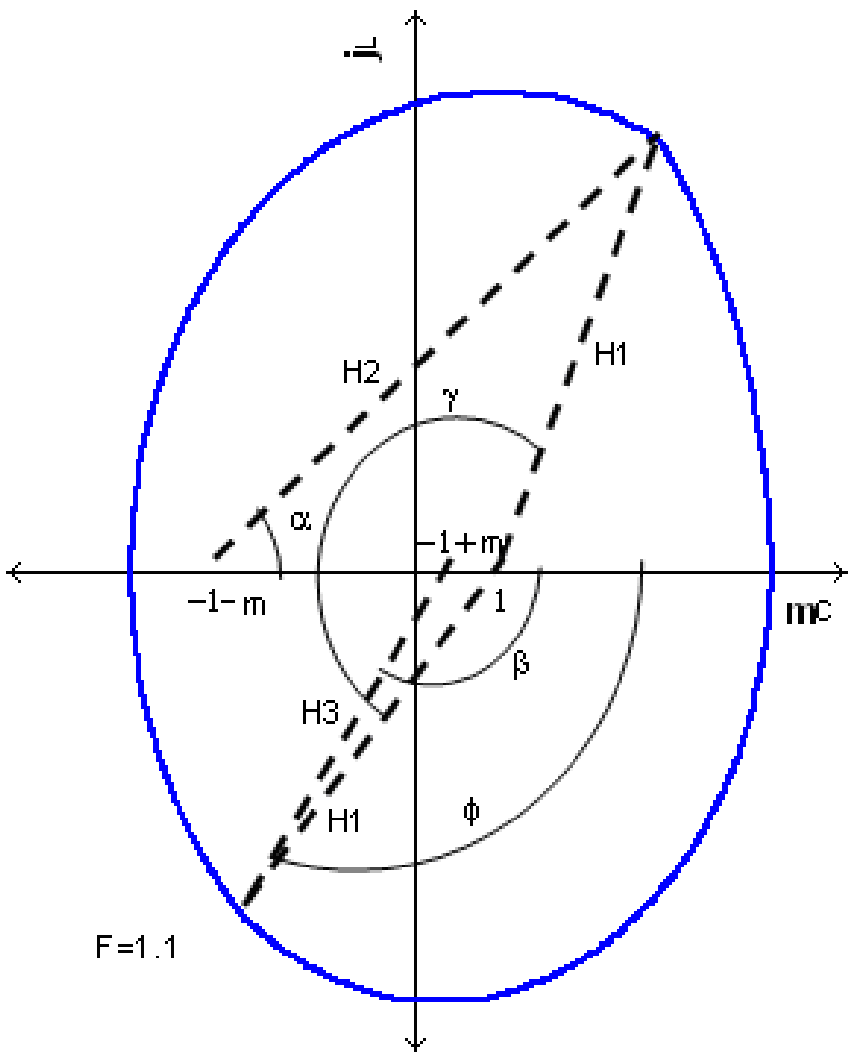

Figure 4.3.2 State-plane representation of the step-up SRC (R_{LOSS}=0)

In the traditional analysis, the state plane provides enough information to obtain a closed-form expression for the voltage conversion gain as a function of R and f_S. Unfortunately, for this converter the solution could not be obtained analytically, so it was obtained numerically. The equations that should be solved to obtain *m*, including the losses, are presented in (4.3.7). The first five equations in (4.3.7) are the initial conditions for the three time-intervals mentioned above. The sixth equation is the relation between the angle (γ) of the accumulation time-interval (the first half of the switching period) and the resonant frequency. Each angle is defined as:

$$\gamma = \omega_0 \cdot t_1 \tag{4.3.6.a}$$

$$\omega_0 = 2 \cdot \pi \cdot f_0 \tag{4.3.6.b}$$

$$\alpha = \omega_0 \cdot t_2 \tag{4.3.6.c}$$

$$\beta = \omega_0 \cdot t_3. \tag{4.3.6.d}$$

The other time-intervals (energy transfer intervals) form the second half of the switching period. The last equation relates the converter output voltage with the state-plane. That equation is based on the electric charge of C_R. The maximum difference in C_R voltage (which in the state-plane is m_{CMAX}-m_{Cmin}) is proportional to the charge transferred to the load. This charge is $I_{OUT}.T_S$. Normalizing this, $m_{CMAX} - m_{C\min} = 2 \cdot \gamma \cdot m / r$ where r is the normalized load resistor (R/Z_0) (4.3.7.g). The first member of the seventh equation in (4.3.7) is obtained from Figure 4.3.2, but includes the power losses.

$$H_1 \cdot exp(\frac{-k\gamma}{\omega_0}) \cdot cos(\varphi + \gamma) + 1 = H_2 \cdot cos(\alpha) - 1 - m \tag{4.3.7.a}$$

$$H_2 \cdot exp(\frac{-k\alpha}{\omega_0}) - 1 - m = H_3 - 1 + m \tag{4.3.7.b}$$

$$H_3 \cdot exp(\frac{-k\beta}{\omega_0}) \cdot cos(\beta) - 1 + m = H_1 \cdot cos(\varphi) + 1 \tag{4.3.7.c}$$

$$H_1 \cdot exp(\frac{-k\gamma}{\omega_0}) \cdot sin(\varphi + \gamma) = H_2 \cdot cos(\alpha) \tag{4.3.7.d}$$

$$H_3 \cdot exp(\frac{-k\beta}{\omega_0}) \cdot sin(\beta) = H_1 \cdot sin(\varphi) \tag{4.3.7.e}$$

$$\frac{f_S}{f_0} = \frac{\gamma}{\pi} = \frac{\alpha + \beta}{\pi} \tag{4.3.7.f}$$

$$H_1 \cdot exp\left[\frac{-k(\pi - \varphi)}{\omega_0}\right] + H_3 - 2 + m = \frac{m \cdot 2 \cdot \gamma}{r} \tag{4.3.7.g}$$

Using (4.3.7), Figure 4.3.3 shows *m* as a function of F for different values of the load resistor (Q factor is defined as Q=1/r = Z_0/R for a lossless circuit). The influence of considering a loss resistance is shown in Figure 4.3.4 for the particular case in which R=Z_0. It can be observed that the maximum value of m is reduced as R_{LOSS} increases (ideally m=2 for lossless case).

This converter—similar to other converters such as the dual active bridge, DAB [213, 219], single active bridge [220], and many resonant converters [221, 222, 223]—has a gain *m* that depends on both the load and the switching frequency. Figure 4.3.5 shows the output characteristics of the converter by considering the lossless case. In the figure, two load lines are plotted; this plot is useful because if the load and the *m* ranges are defined, the frequency variation is known. As an example, if the normalized load variation is from 1 to 2, and *m* is from 0.8 to 1.35, the frequency variation is from f_S=f_0 to f_S=1.5f_0. Figure 4.3.6 shows α and β as function of F for r=1.

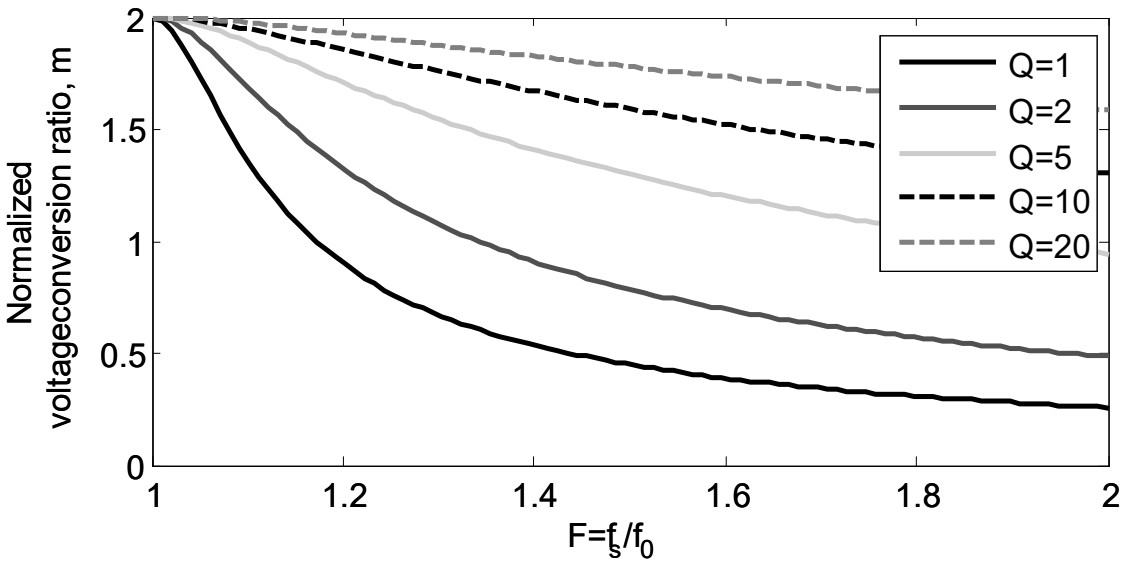

Figure 4.3.3–Normalized voltage conversion ratio, m versus f_s/f_0 for different quality factors (Q)

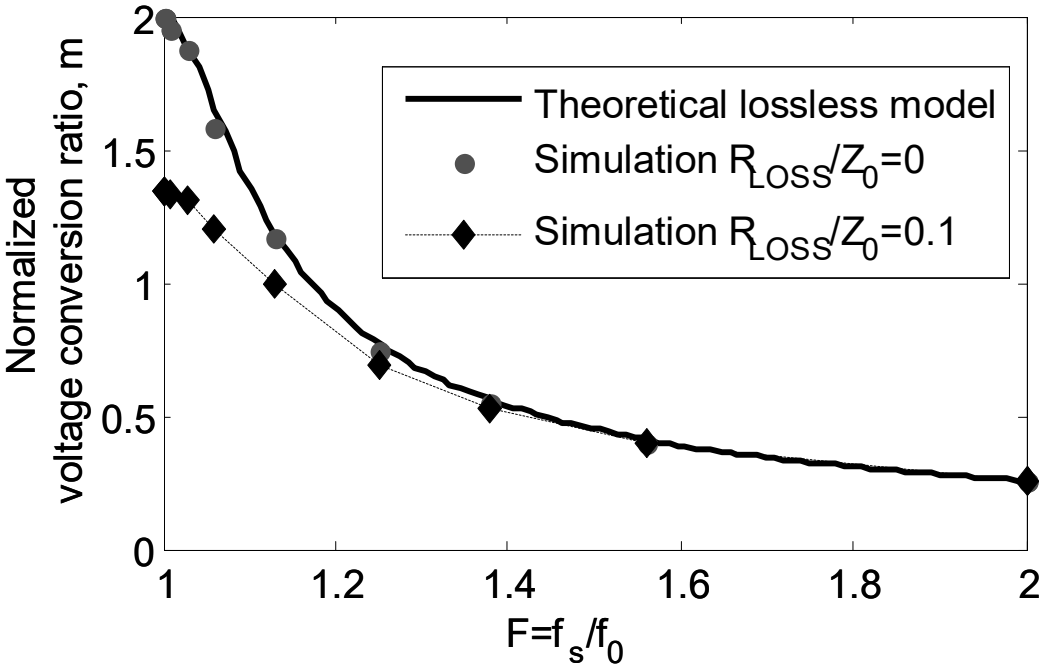

Figure 4.3.4–Normalized voltage conversion ratio, m versus f_s/f_0 including R_{LOSS} for $R=Z_0$

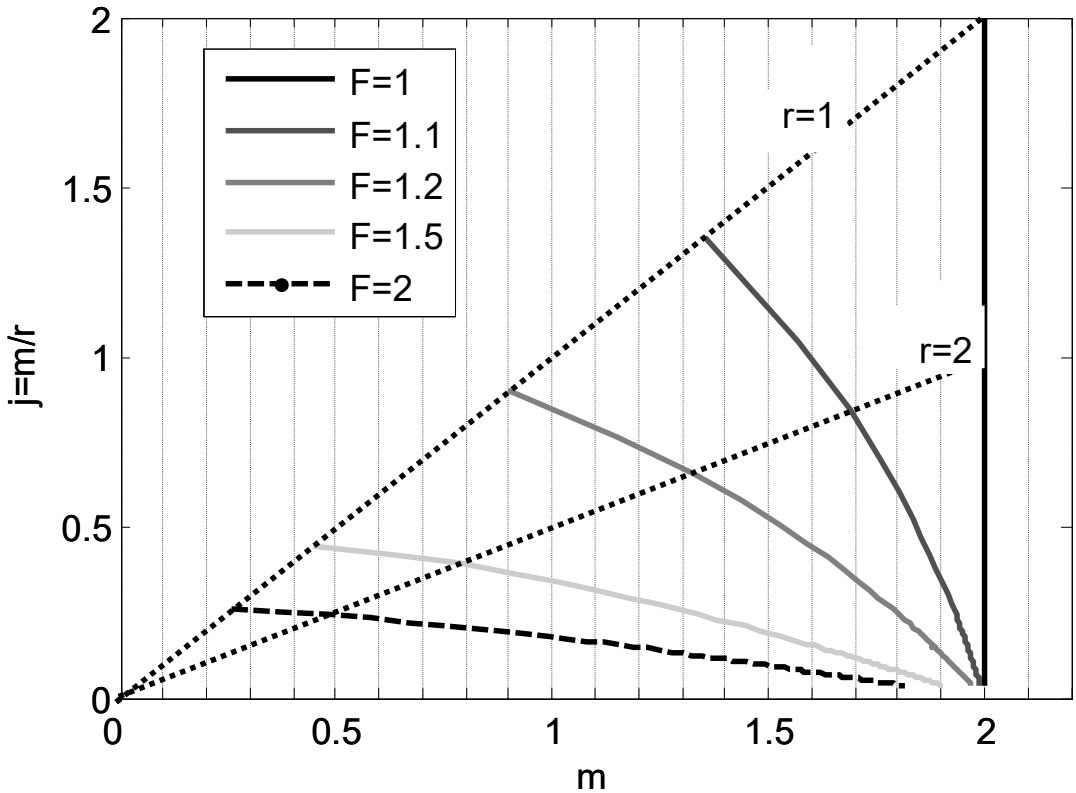

Figure 4.3.5–Output characteristics of a step-up SRC

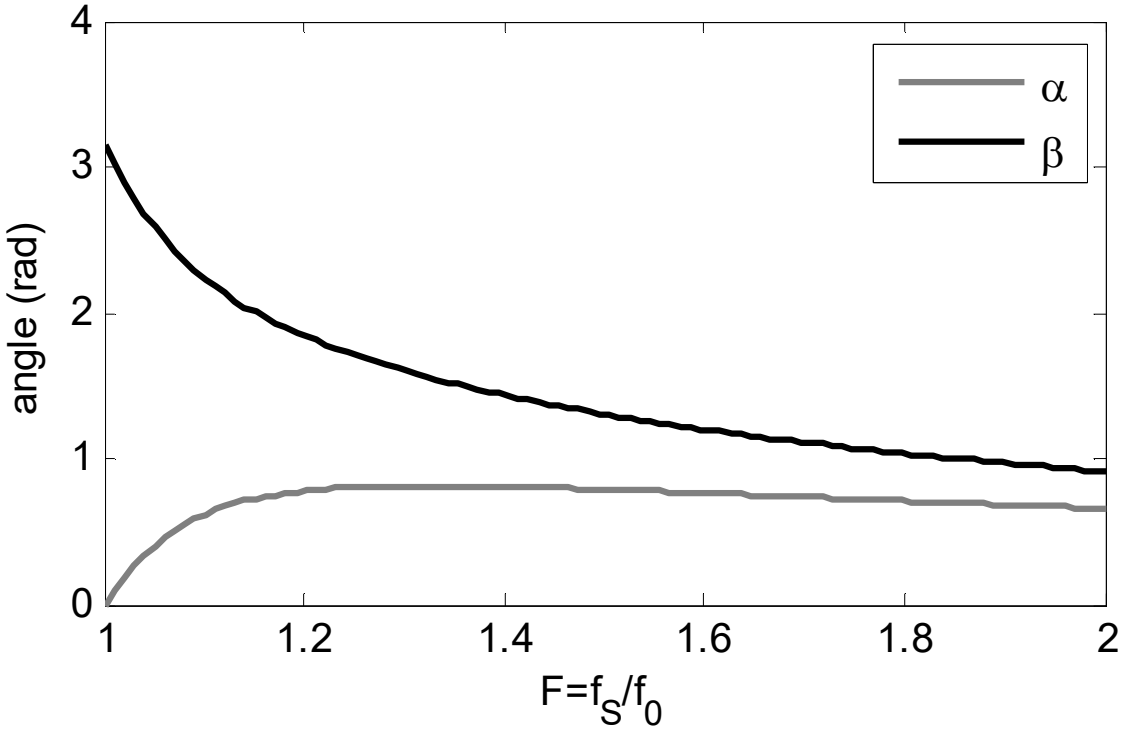

Figure 4.3.6 Angle of the transfer arcs (α and β) versus F, r=1

4.3.2. Small-signal modeling

The steady-state modeling and analysis are useful for selecting components and determining the switching frequency range. However, a small-signal modeling, in which the control transfer function can be obtained, is needed in order to design the controller of the converter. Thus, a proper control that modifies the switching frequency to regulate the output voltage can be designed. There are several methods for analyzing the small-signal variation of resonant DC/DC converters [224-228]. In this section, the averaged state-space method is used. First, the state-space model is solved for each time interval. Then continuity constrains in i_L and v_C are applied in the boundary conditions to join the solutions corresponding to each time interval. The analysis is based on the circuit in Figure 4.3.1(c), where i_R is defined as the rectified current, meaning that i_R is zero for the accumulation time interval and it is $|i_L|$ for the transfer intervals (2nd and 3rd interval). Thus, steady-state equations for the state and output variables are first obtained, and then small-

signal perturbations are applied to those equations in order to get the AC small-signal characteristics of the system. In this section, only the control-to-output transfer function is presented, but any other transfer function can be calculated by this method. A detailed exampled is given in [229].

The state-space models for the three time-intervals are shown in (4.3.8). The state vector is $x(t)=[i_R\ v_C\ v_{OUT}]^T$ for any time interval.

$$\frac{dx}{dt} = \boldsymbol{A_n} \cdot \boldsymbol{x} + \boldsymbol{b_n} \cdot v_{IN} \quad v_{OUT} = \boldsymbol{c} \cdot x, \text{ where n can be 1, 2, 3 and} \tag{4.3.8}$$

$$\mathbf{A_1} = \begin{bmatrix} -\frac{R_{LOSS}}{L_R} & \frac{-1}{L_R} & 0 \\ 1/C_R & 0 & 0 \\ 0 & 0 & \frac{1}{RC_0} \end{bmatrix}, \ \mathbf{b_1} = \begin{bmatrix} \frac{1}{L_R} \\ 0 \\ 0 \end{bmatrix},$$

$$\mathbf{A_2} = \begin{bmatrix} -\frac{R_{LOSS}}{L_R} & \frac{-1}{L_R} & \frac{-1}{L_R} \\ 1/C_R & 0 & 0 \\ \frac{1}{C_0} & 0 & \frac{1}{RC_0} \end{bmatrix}, \ \mathbf{b_3} = \mathbf{b_2} = -\mathbf{b_1},$$

$$\mathbf{A_3} = \begin{bmatrix} -\frac{R_{LOSS}}{L_R} & \frac{-1}{L_R} & \frac{1}{L_R} \\ 1/C_R & 0 & 0 \\ \frac{-1}{C_0} & 0 & \frac{1}{RC_0} \end{bmatrix}, \ \mathbf{c} = \begin{bmatrix} 0 & 0 & 1 \end{bmatrix}.$$

The solution is:

$$\begin{aligned} \boldsymbol{x}(t) &= e^{\boldsymbol{A_1} \cdot t} \cdot \boldsymbol{x}(0) + \boldsymbol{A_1^{-1}} \cdot e^{\boldsymbol{A_1} \cdot t} \cdot \boldsymbol{b_1} \cdot V_{IN} \quad 0 \le t \le \frac{T_S}{2} \\ \boldsymbol{x}(t) &= e^{\boldsymbol{A_2} \cdot t} \cdot \boldsymbol{x}(\frac{t_S}{2}) + \boldsymbol{A_2^{-1}} \cdot e^{\boldsymbol{A_2} \cdot t} \cdot \boldsymbol{b_2} \cdot V_{IN} \quad \frac{T_S}{2} \le t \le t_a \\ \boldsymbol{x}(t) &= e^{\boldsymbol{A_3} \cdot t} \cdot \boldsymbol{x}(t_a) + \boldsymbol{A_3^{-1}} \cdot e^{\boldsymbol{A_3} \cdot t} \cdot \boldsymbol{b_3} \cdot V_{IN} \quad t_a \le t \le T_S. \end{aligned} \tag{4.3.9}$$

The steady-state condition means that $\mathbf{x}(0) = \mathbf{x}(T_S)$. Thus, by using (4.3.8) and (4.3.9), t_a can be obtained, which is directly related with α in the DC analysis. In addition, v_{OUT} can be obtained as: $v_{OUT}(t) = \mathbf{c} \cdot \mathbf{x}(t)$. The averaged method calculates the two basic equations that should be perturbed to perform the AC analysis:

$$T_S \cdot V_{OUT} = \int_0^{t_S} v_{OUT}(t) \cdot dt = \boldsymbol{k_1} \cdot \boldsymbol{x}(0) + k_2 \cdot V_{IN} \tag{4.3.10.a}$$

$$\boldsymbol{x}(T_S) = \boldsymbol{A} \cdot \boldsymbol{x}(0) + \boldsymbol{B} \cdot V_{IN}. \tag{4.3.10.b}$$

Eq. (4.3.10.a) is the average of the output value and (4.3.10.b) is extracted from (4.3.9) in order to represent **x(T$_S$)** as an explicit function of **x(0)** and V_{IN}. k_1 and k_2 can be obtained by solving (4.3.11.a). The variables that depend on f_S should be perturbed, e.g., $T_S = \overline{T}_S + \tilde{t}_S$, $t_a = \overline{T}_a + \tilde{t}_a$, $\boldsymbol{x}(0) = \overline{\boldsymbol{X}}(0) + \tilde{\boldsymbol{x}}(0)$, etc., with $\hat{t}_S = -1/\overline{F}_S^2 \cdot \tilde{f}_S$, etc. The variable with a line in the top lindicates averaged values in one period, T_S, while the variables with the tilde (~) indicate a small perturbation. Thus, two perturbed equations are obtained from (4.3.10):

$$\begin{aligned}&\left(\overline{V}_{OUT} + \tilde{v}_{OUT}\right) \cdot \left(\overline{T}_S + \tilde{t}_S\right)\\ &\qquad = \left(\overline{\boldsymbol{k}}_{\boldsymbol{1}} + \tilde{\boldsymbol{k}}_{\boldsymbol{1}}\right) \cdot \left[\overline{\boldsymbol{X}}(0) + \tilde{\boldsymbol{x}}(0)\right] + \left(\overline{k}_2 + \tilde{k}_2\right) \cdot V_{IN}\end{aligned} \tag{4.3.11.a}$$

$$\tilde{\boldsymbol{x}}(T_S) + \overline{\boldsymbol{X}}(T_S) = \left[\overline{\boldsymbol{A}} + \tilde{\boldsymbol{A}}\right] \cdot \left[\overline{\boldsymbol{X}}(0) + \tilde{\boldsymbol{x}}(0)\right] + \left[\overline{\boldsymbol{B}} + \tilde{\boldsymbol{B}}\right] \cdot V_{IN}. \tag{4.3.11.b}$$

The control-to-output transfer function is obtained from (4.3.11.a) by expressing the equation as an explicit function of $\tilde{f}_S$ and $\tilde{\boldsymbol{x}}(0)$ and by replacing them with their Laplace transforms ($f_S(s)$ and $\mathbf{x}(s)$). Eq. (4.3.11.b) is used to express **x**(s) as a function of $f_S(s)$. The final equations are:

$$v_{OUT}(s) = \boldsymbol{h^T} \cdot \boldsymbol{x}(s) + k_S \cdot f_S(s) \tag{4.3.12.a}$$

$$\boldsymbol{x}(s) = [\boldsymbol{I}e^{sT_S} - \boldsymbol{A}]^{-1} \cdot \boldsymbol{d_S} \cdot f_S(s), \tag{4.3.12.b}$$

where $\boldsymbol{h}$, k_S and $\boldsymbol{d_S}$ are obtained from (4.3.11) and depend on R_{LOSS}, L_R, C_R, R, V_{IN} and C_0. Thus, the control-to-output transfer function is obtained from (4.3.12). A computer program was developed in MATLAB to compare the theoretical model with results from simulations and experimental measurements.

4.3.3. Simulations and experimental results

In order to validate the theoretical analysis presented in subsection 4.3.1 and 4.3.2, the voltage conversion ratio and the control-to-output transfer function were measured in a prototype shown in Figure 4.3.7. This prototype can deliver up to 6kW between two ports: the low side port accepts voltages from 60 to 120V and the high side port has a fixed voltage of 360V. The resonant frequency is 40 kHz. L_R, C_R and C_0 are 72uH, 220nF and 160uF, respectively. Two load resistors are tested: $R_1=20\Omega$ and $R_2=140\Omega$.

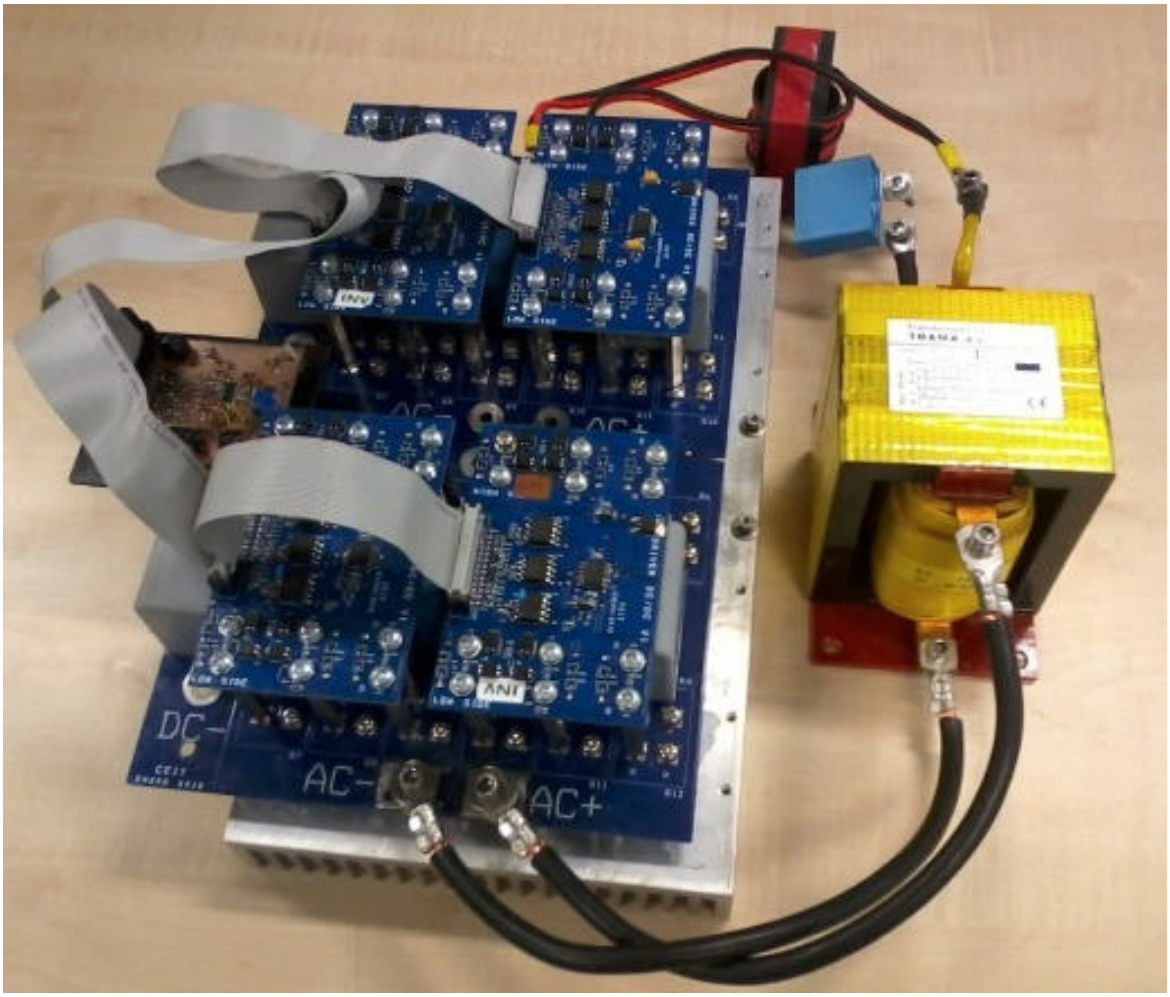

Figure 4.3.7 Prototype

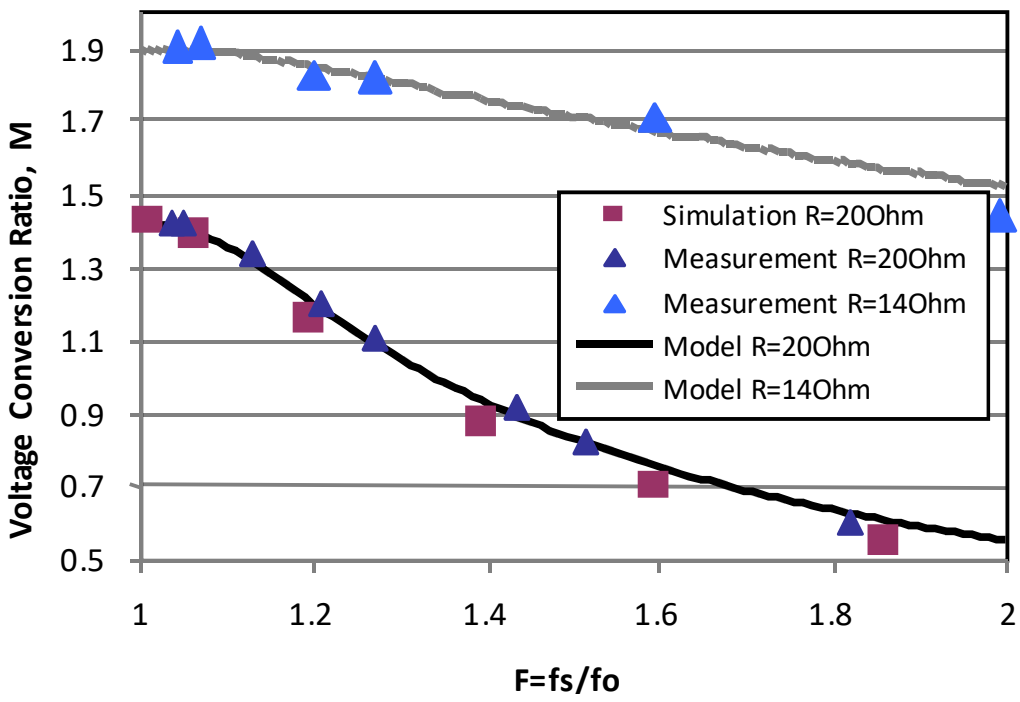

Figure 4.3.8 DC characteristics

Figure 4.3.8 shows the comparison of the voltage conversion ratio between the theoretical model, the data extracted from simulations in PSIM software, and the measurements for the two loads. It can be noted that the results obtained from the theoretical model are in good agreement with the experimental and the simulated data. The waveforms of M1 and M7 are shown in Figure 4.3.9 and Figure 4.3.10 for both R_1 and R_2 resistors. It can be seen that the turn-on process occurs at zero voltage for M1 (and also M2,3 and 4 because the waveforms are the same). This soft turn-on is because the converter works above its resonance frequency. The turn-off process is still hard switching, but for high loads (low R value) the converter works near its resonance so the i_D current at turn-off is reduced compared to a phase-shift dual active bridge (DAB) [230]. The waveforms of M7 show that it does not achieve a soft turns-on but a soft turn-off at zero voltage. M4 and M5 work as diodes and M8 has similar waveforms as M1 to M4 so it achieves a turn-on at zero voltage. In addition, as the converter always works above the resonance frequency the impedance that the input bridge (M1 to M4 for the low to high voltage power flow) "sees" is inductive so current lags the voltage. Thus, the turn-on process is a zero-voltage transition even in transient conditions.

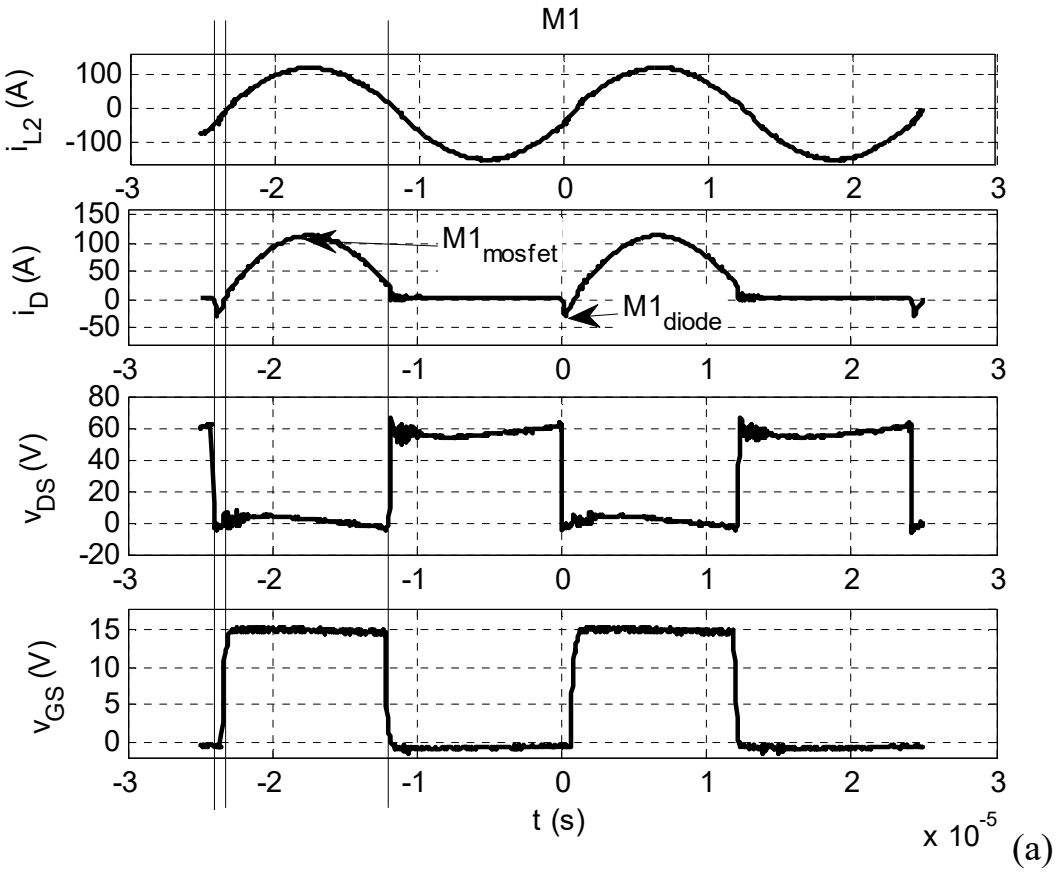

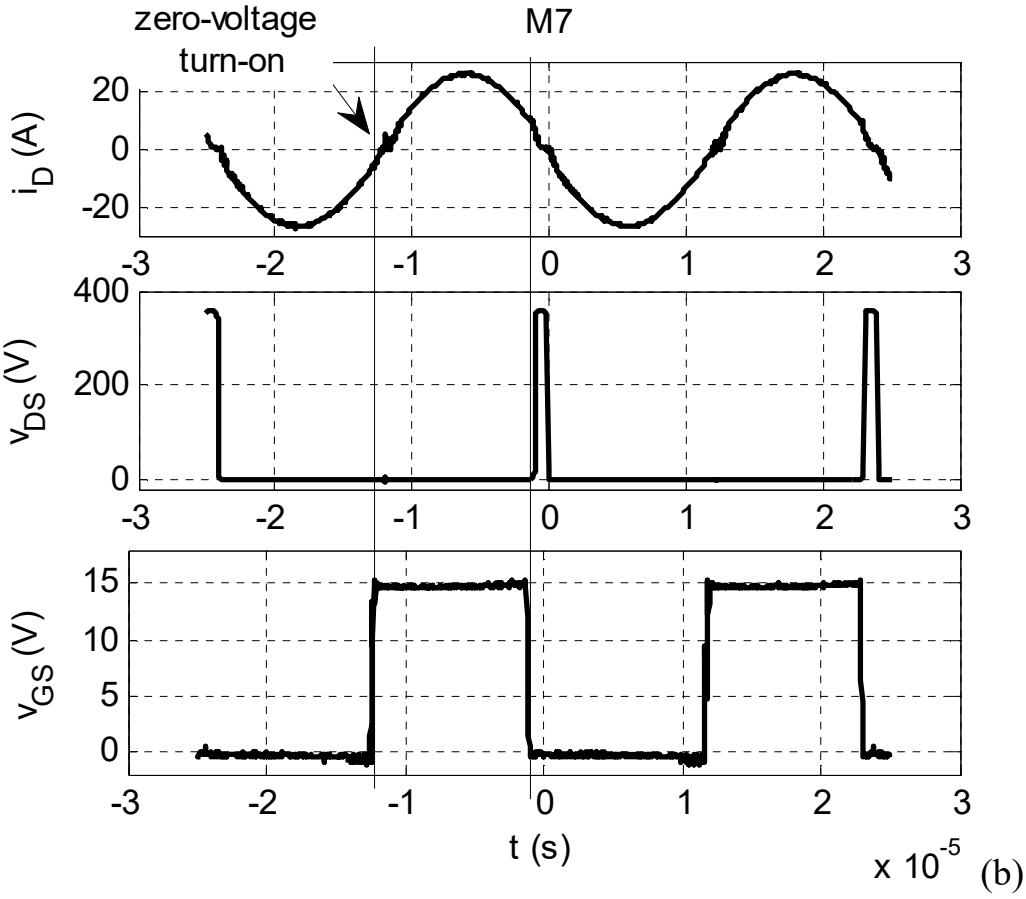

Figure 4.3.9. M1 and M7 switching waveforms for full-load condition.

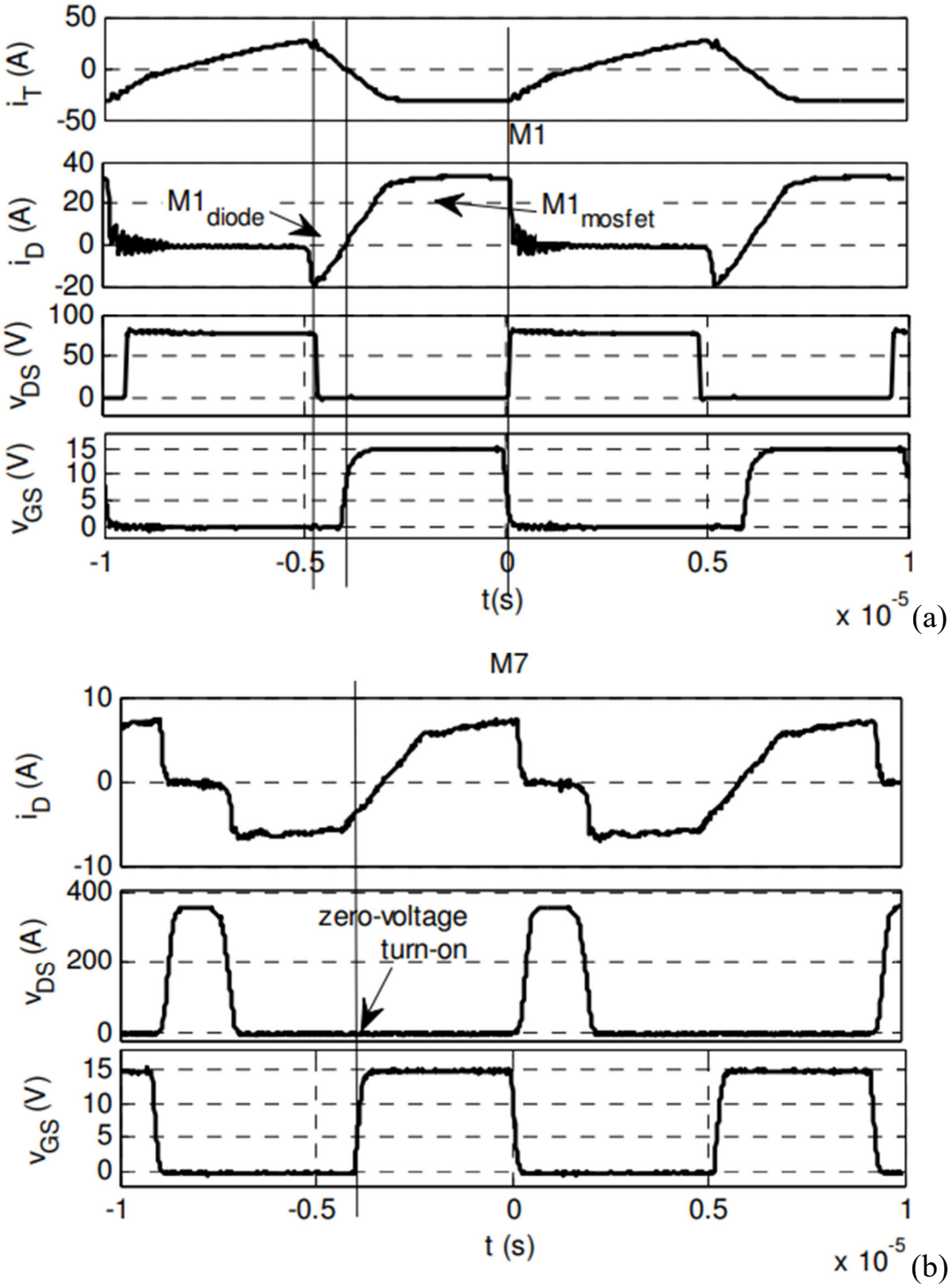

Figure 4.3.10-M1 and M7 switching waveforms for light load condition

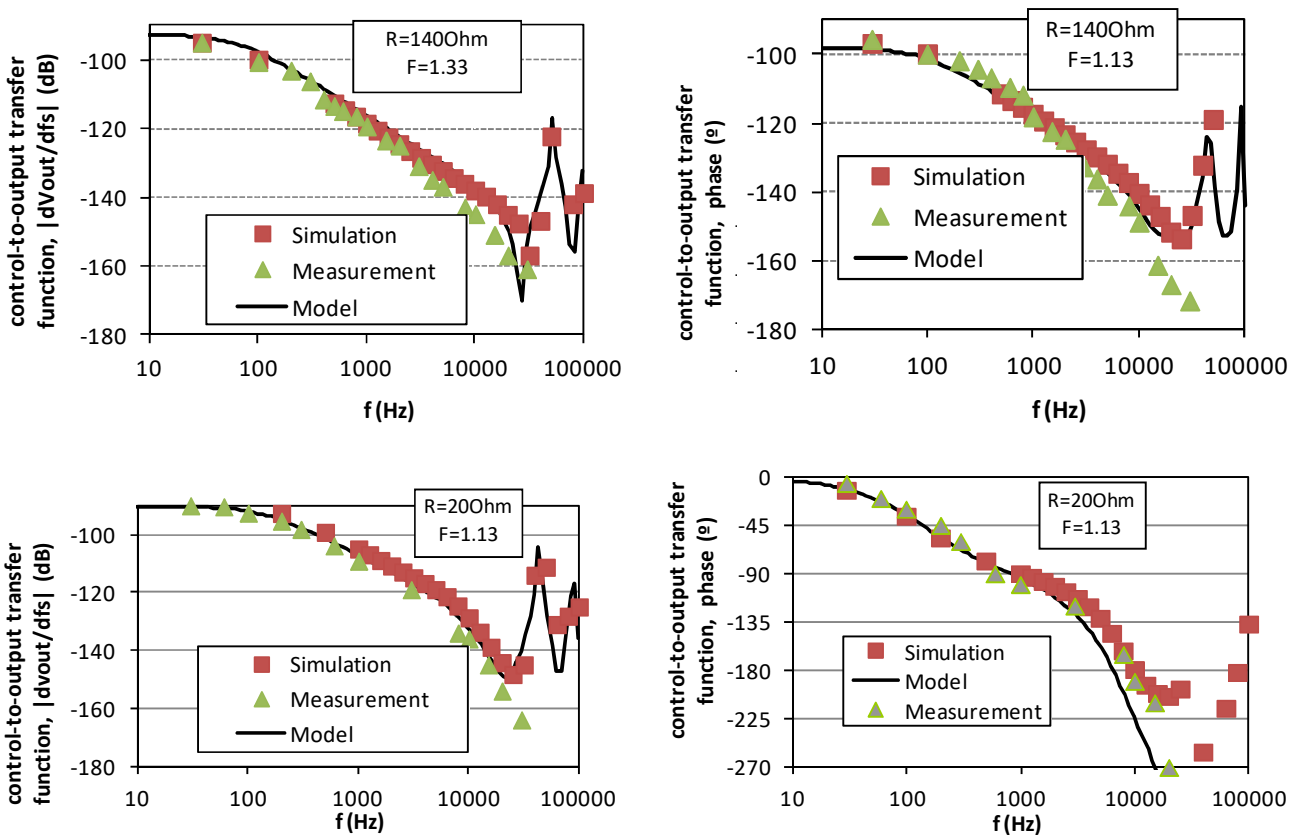

Figure 4.3.11- Control-to-output transfer function for several static points

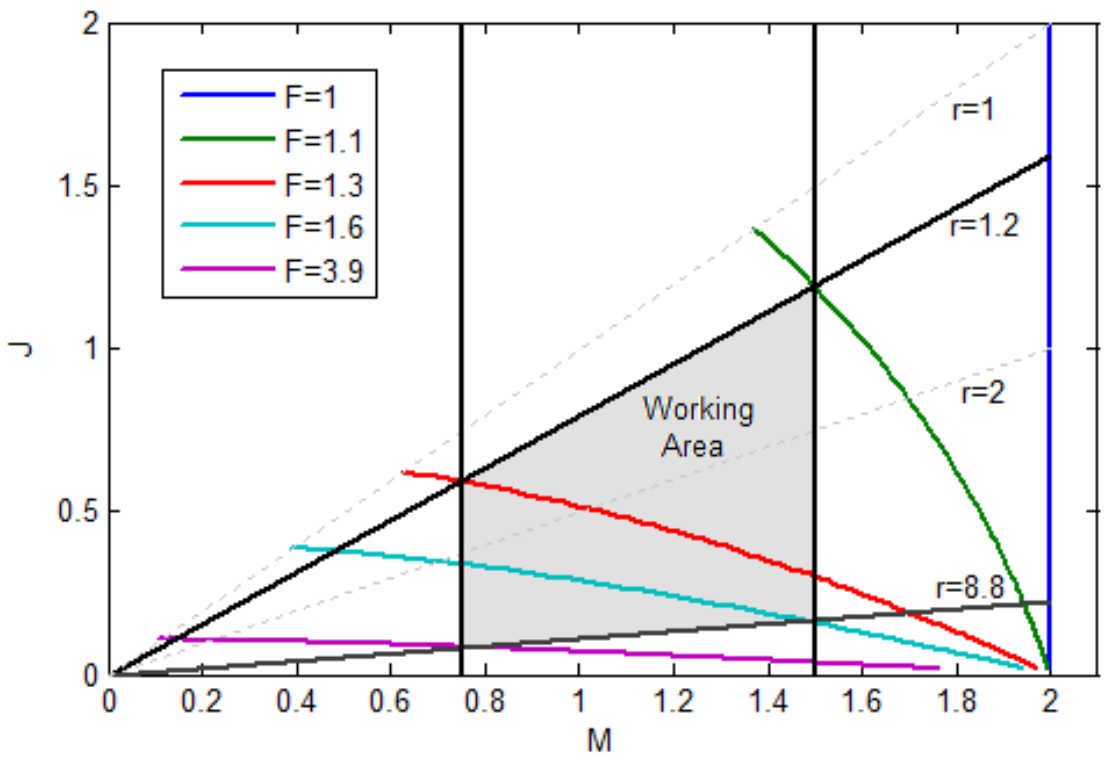

Figure 4.3.12-Control diagram

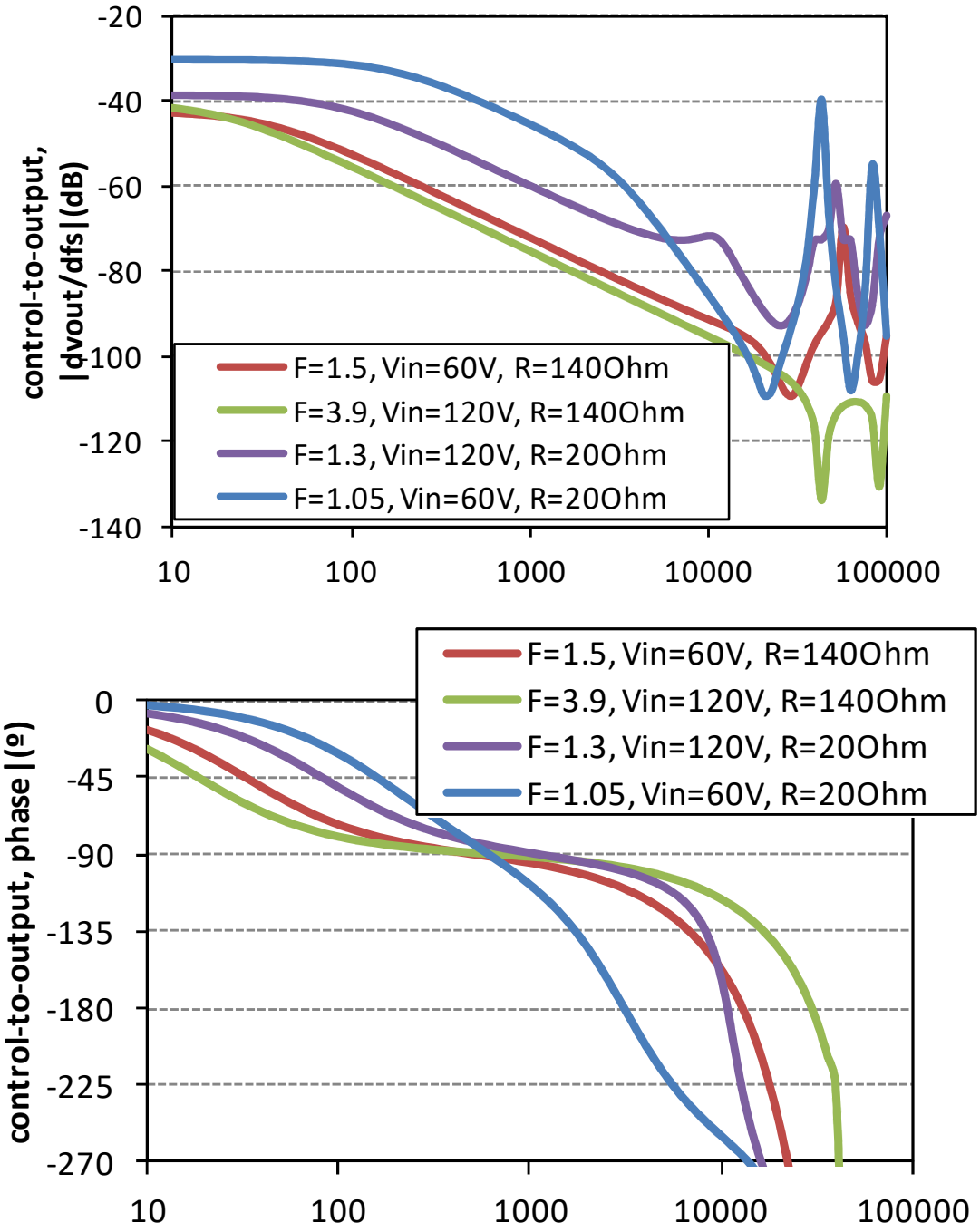

Figure 4.3.13 Control-to-output transfer function modeled for the prototype

Figure 4.3.11 shows the AC behavior of the system. The absolute value of the control-to-output transfer function was measured, simulated and modeled for the two loads at different frequencies. It can be observed that there is good agreement for low frequencies and a tolerable deviation for higher frequencies. The deviation is small enough to design the controller.

The design procedure begins with the plot of the output characteristics for the lightest and the heaviest load resistors and for the two limits of *M*: 0.75 and 1.5 (step-up). Figure 4.3.12 shows this plot, which can be used to determine the normalized frequency switching range (F): in this case from 1.05 to 3.9 (loads from 20 to 140Ω). Then, based on the proposed AC model, the control-to-output transfer function is plotted in Figure 4.3.13 for the following four cases: maximum/minimum load and maximum/minimum input voltage. These transfer functions include the variation in V_{IN}, and thus their values become similar at low frequencies. Based on shown transfer functions, the controller can be obtained [34].

An efficiency comparison between the present converter and a dual active bridge (DAB) converter using phase shift control is presented in Figure 4.3.14. The design was aided by [230]. It can be seen that the DAB converter is very efficiency at high power, but as the output power decreases so does its efficiency. Numerical simulations were carried out using the same model for the MOSFETs in both DAB and SRC converters. However, in the case of the DAB converter, a value of $R_{LOSS}/2$ was used instead of the value R_{LOSS}, which was used for the SRC. This is because the DAB converter does not have the series capacitor C_R, so there is one fewer component in series in the R_{LOSS} branch.

R_{LOSS} was adjusted by taking into account the efficiency of the converter in the lowest input voltage condition (60V). Figure 4.3.14 shows that SRC efficiency remains flatter and degrades less than DAB efficiency at lower power. This is mainly attributed to the shape of the current in the R_{LOSS} branch, and it represents the main advantage of the SRC over the DAB converter controlled by phase shift modulation. For heavy loads, the both converters have similar efficiency. The SRC has lower switching losses because the switching turn-off transitions occur close to zero-current (f_S close to f_0) than DAB. However, the conduction losses for SRC are higher than DAB because of its sinusoidal waveforms with higher current peaks. So, the efficiency is quite similar.

On the other hand, for light loads, the DAB keeps high currents circulating its inductor although the output current is not high while the SRC increases its impedance by increasing the switching frequency. Thus, the conduction losses go down. This is the reason to have a better behavior at light loads. The switching losses remain because the

switching current decreases but the switching frequency increases. The main disadvantage of this SRC is its variable switching frequency, requiring components to perform well across the entire frequency range.

As the circuit is completely symmetric, the efficiency plot is only presented in one direction. For reverse power flow, M5–M8 operate analogously to M1–M4 in the forward direction. M5, M8, M2 and M4 are triggered as M2, M3, M7 and M8 in Figure 4.3.1(b) and M6 and M7 are triggered as M1 and M4. The waveforms of Figure 4.3.9 are similar but changing M1 for M6 and M7 for M4.

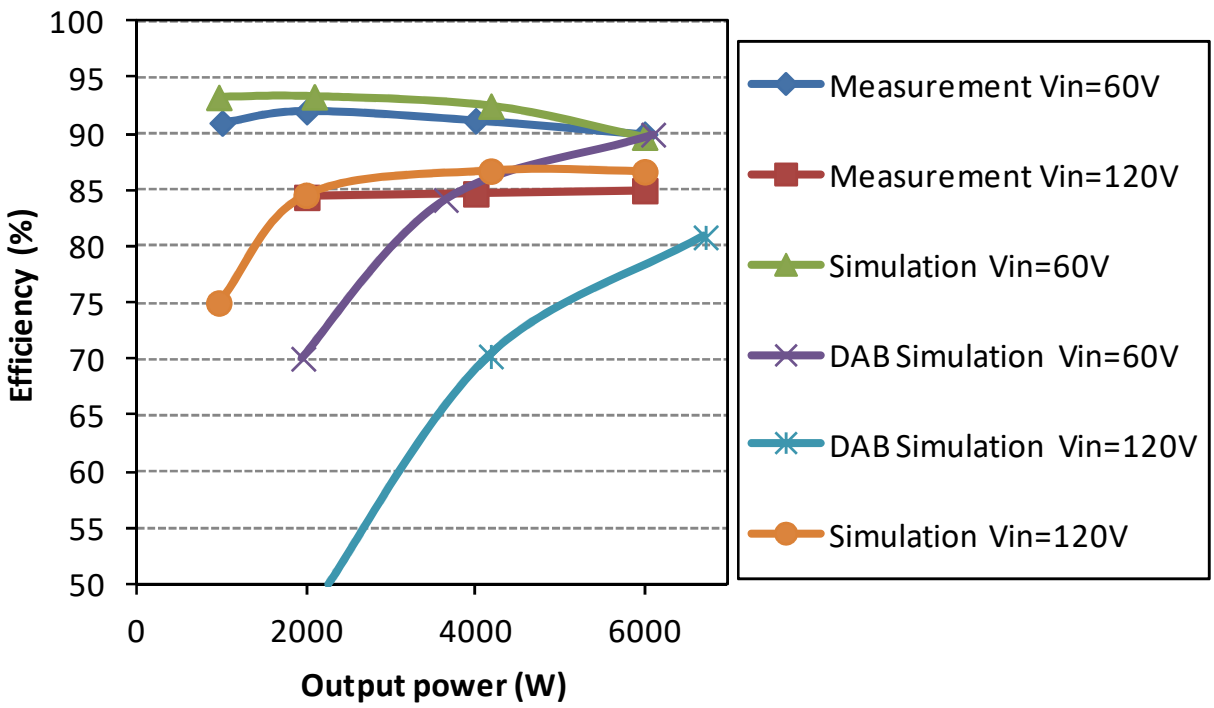

Figure 4.3.14– Efficiency

4.3.4. Summary

This section shows a comprehensive analysis for series resonant converters (SRCs) working in continuous mode. This includes the modeling of the converter in both the steady-state and small-signal AC behaviors. It shows that the new proposed step-up technique based on accumulation states makes possible to use the classical SRC as a step-up converter in continuous mode. This is particularly useful for bidirectional power flow applications where one port is attached to an energy accumulator device, such as a battery

or supercapacitor bank, and the other port is attached to a fixed DC line, such as an inverter. The section validates the modeling in numerical simulations and under real conditions through a prototype of a bidirectional DC/DC converter that can transfer power up to 6kW. Both simulations and experimental measurements are in concordance with the proposed mathematical model.

Finally, the converter efficiency is plotted for several transfer power values and compared to the simulated results of a dual active bridge converter controlled by phase-shift modulation, which is the main competitor. It shows that the series resonant converter presents similar efficiency for high power transfer and it presents greater efficiency for light loads, which represents the main advantage of this converter [34, 111].

Related to the EV charger application, this converter can be used due to its high efficiency, bidirectional power flow, and isolation. However, multiple port feature is also required and at least and AC port, for that, the next section will introduce the changes that are needed to enhance the converter. The details of this section were published in [34].

This section extends the modeling of step-up series resonant converters to continuous-current operation. Both sections (Section 4.2 and 4.3) are the basis of the operation of a multiple port system with AC and DC ports which will be described in section 4.4.

4.4. Isolated resonant multi-port inverter

In this section, the knowledge of bidirectional series resonant converters discussed in Sections 2 and 3 of this chapter, the multiple port discussion in Chapter 2 and the inverter techniques in Chapter 3 will be combined in a resonant three-port DC//DC/AC. This converter has an isolated DC port (denoted by //) and two non-isolated ports: one DC and one AC. If more non-isolated ports are needed, the converter in Section 4.1 can be connected to any DC port. For more isolated ports, the techniques from Chapter 2 may be applied. Figure 4.4.1 shows the general connection block, notice that the non-isolated

multi-port DC/DC converter is now optional if more sources need to be connected. This section details how to achieve the partial isolation and the AC/DC transformation using the resonant techniques introduced in sections 4.2 and 4.3 from this chapter. The details of this section were published in [31].

4.4.1. Resonant solution for obtaining a multiple port converter with AC and DC ports

This section shows a comprehensive analysis including the modeling of the converter in both the steady-state and small-signal AC behaviors. It demonstrates that the proposed technique enables the use of a classical series resonant converter as a step-up converter for both AC and DC sources. When the converters are connected to variable DC sources such as batteries, supercapacitors and PV panels, step-up converters are needed (see Section 4.2, Chapter 4). Solution using a combination of DC/DC converters and inverters were reviewed in Chapter 2. Here, Figure 4.4.1 shows a multi-port DC//DC/AC converter with one isolated port using a high frequency transformer. A similar approach is shown in [231] for a high-voltage high-frequency isolated bidirectional AC/DC, that uses a multilevel technique. That is a very promising circuit for high voltages but the circuit is too complex to use in applications at 400V AC levels.

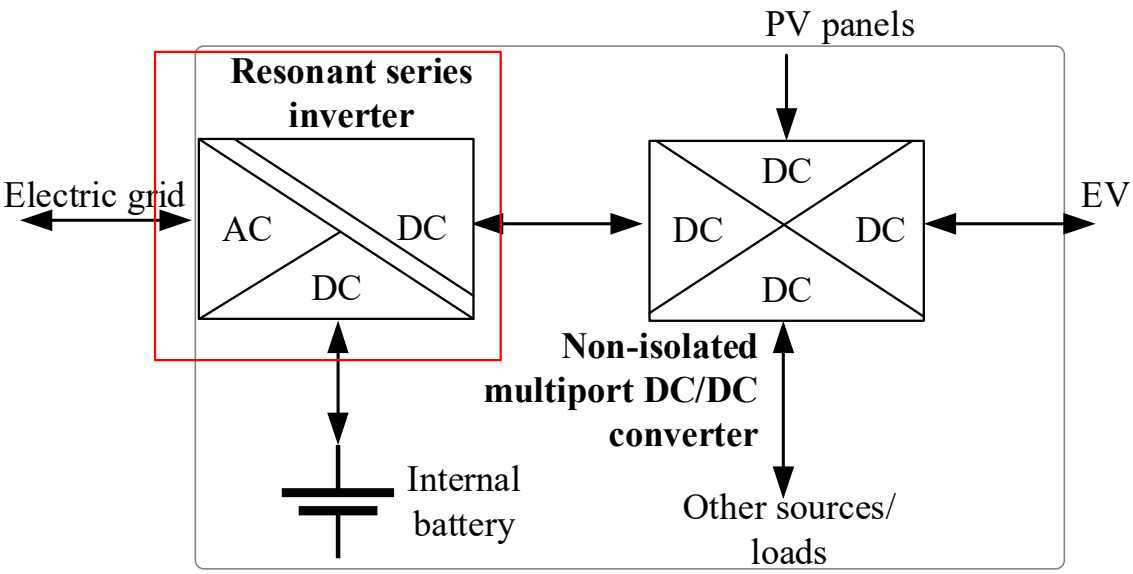

Figure 4.4.1– Electric charger partial isolated resonant DC/AC

The main contribution of this section is the introduction of a series-resonant DC/AC converter with isolation, by using the concepts of sections 4.2 and 4.3. It generates a regulated, constant DC link, which serves as the basis for producing the AC power signals. Therefore, it performs isolation, the DC/DC and DC/AC conversion in one circuit. This eliminates the need for a 50Hz output transformer. This novel converter will be compared with two alternative topologies in [111] and in ZSI [232]. This section is organized as follows. Subsection 4.4.2 presents the main circuit modeling and analyzes its behavior in discharging and charging modes. It also gives some design guidelines and presents the basic control diagram. Subsection 4.4.3 proposes the converter control method, subsection 4.4.4 presents the voltage conversion ratio, subsection 4.4.5 discusses the soft-switching technique, subsection 4.4.6 validates the model using numerical simulations and subsection 4.4.7 confirms it experimentally. Finally, subsection 4.4.8 presents the conclusions of the technique.

4.4.2. Multiple port converter with AC and DC ports – basic analysis

The basic schematic circuit is shown in Figure 4.4.2(a). It consists of two full bridges interconnected with a series resonant branch (L_r-C_r) as in sections 4.2 and 4.3. Switches M1-M4 form the first bridge. Its DC port is connected to the energy storage (DC port 1, DC1), which can be a supercapacitor stack or a battery. The bridge's DC and AC port voltages are V_{DC1} and v_1, respectively. The bridge can act as an active bridge (delivering energy) or as a rectifier (absorbing energy). Thus, v_1 can adopt $+V_{DC1}$, $-V_{DC1}$ and 0.

The second bridge is connected to C_0 at its DC port, DC2. C_0 has a constant voltage, V_{DC2} and delivers energy to the load. The DC and AC port voltages are $V_{DC2}= V_{C0}$ and v_2, respectively. In the traditional DC/DC series resonant converters, the voltage conversion ratio is always smaller than or equal to one and v_2 can only adopt $+V_{DC2}$, $-V_{DC2}$ [30].

However, by creating a new state where v_2 is 0, the resonant branch is in short circuit and can store energy in its reactive elements, as it was detailed in Section 4.2 and 4.3. Thus, the voltage conversion ratio can reach a value greater than one [33-36].

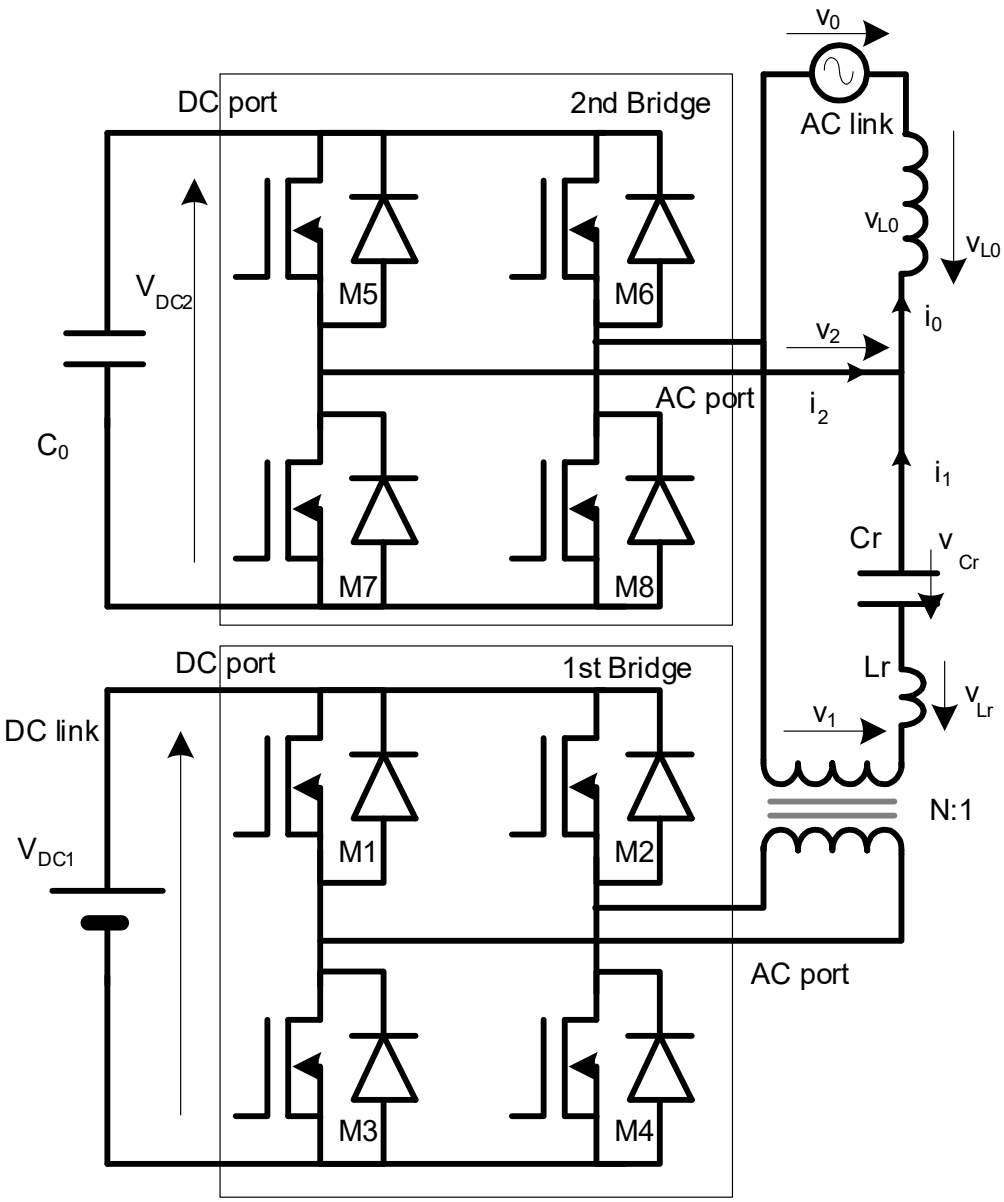

(a)

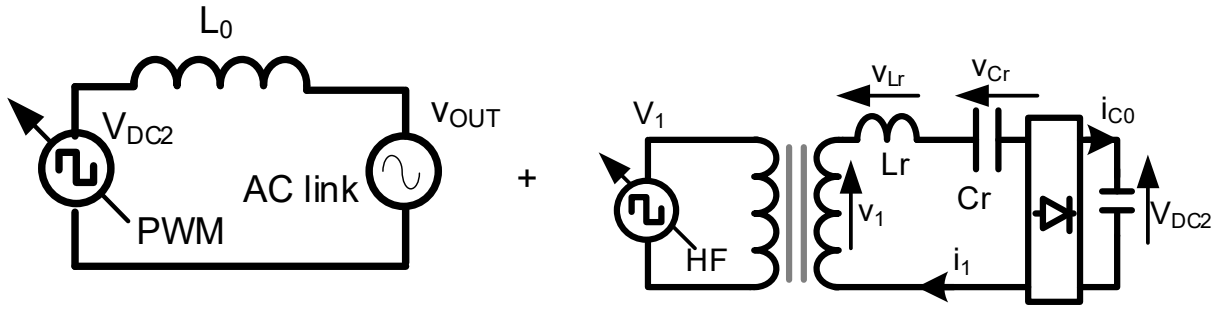

(b)

Figure 4.4.2. Proposed bidirectional DC/AC converter: (a) circuit, (b) simplified circuit for low and high frequency.

The resonant circuit consists of a high frequency (HF) transformer, which provides isolation between the bridges, a resonant inductor (L_r), and a capacitor (C_r). This resonant circuit allows for energy transferring around the resonant frequency, $\omega_r=(L_rC_r)^{-0.5}$ and blocks the low frequency (LF) power signals such as the AC grid signals (~50Hz). In addition, the series resonant branch allows switches M1-M8 to turn on and off with a soft switching operation so the converter can work partially with reduced switching losses. Finally, the output filter L_0 delivers the LF AC signals and blocks the HF signals. Therefore, the distortion at the AC port of the converter is based on this filter and the modulation technique; a better filter can be introduced if it is needed [119, 233].

While the proposed circuit is single-phase, the same technique can be extended to three-phase converters. The circuit performs the DC/DC and DC/AC conversion by using a DC/DC topology, that works in both power flows: from the DC1 port (or DC2 port) to the AC port and vice versa. The circuit can be interpreted as two circuits that act simultaneously, as shown in Figure 4.4.2(b). On the left side, there is a pulse generator that has V_{DC2} amplitude and is controlled by the PWM signal to generate the low frequency AC (50 or 60 Hz) waveform, as in a traditional unipolar PWM voltage source inverter (VSI). On the right side, it shows the high frequency (~80 kHz) circuit that charges C_0 (at DC2). The high frequency signals are produced in the first bridge and received by the second bridge (in the discharge mode, where the energy is delivered from the storage device at DC to the AC link). The AC link (or port) only interacts with the low frequency circuit while a high-frequency power signal is charging the C_0 capacitor. A time-domain analysis is given in the next subsection.

Time-domain analysis – discharging mode. The circuit will be analyzed in the discharging mode, where the energy from V_{DC1} is transferred to v_0 (AC port). However, as the circuit is completely symmetric, the charging mode is the same. The analysis of the circuit and waveforms is based on Figure 4.4.3 and Figure 4.4.4 and it considers that $V_{DC2}>V_{DC1}$, therefore the voltage conversion ratio, defined as $M=V_{DC2}/V_{DC1}$ is bigger than one (considering the transformer turns ratio equal to 1). The circuit works in three

different behaviors (or group of intervals): the discharging C_0 and charging C_0 intervals and the waiting time. The second bridge can be considered as a traditional unipolar inverter in which during the off-time high-frequency (HF) pulses are injected to keep C_0 at a constant value. The quantity of the pulses depends on the duration of off time, which is the time available for charging C_0 at DC2. As the off time increases (or duty cycle, D, of the PWM signal that controls v_0, decreases), more pulses are injected. This means that for high output voltages, (D is close to 1), there is a long-time interval where the circuit is delivering energy to the load and there are few pulses to charge C_0. In contrast, for low output voltages there are many pulses that charge C_0 and a short interval for discharging it. The duration of the pulses is fixed to the half of the resonant period ($T_{HF}/2$), and, in general, the off time is not a multiple of $T_{HF}/2$, so a waiting time interval appears when there is not enough time to inject a complete pulse.

During the discharging C_0 time intervals, the first bridge is off and the energy is extracted from C_0 and delivered to the AC link by modulating the second bridge with a modified pulse width modulation (PWM) signal. It is called modified because high frequency (HF) pulses are added to the original unipolar PWM signals. The energy is delivered to the AC port during the during the PWM signal's on-time, where those HF pulses do not appear.

During the charging C_0 group (within PWM signal's off-time), the first bridge is active, producing a HF square signal in the transformer's primary winding (v_1) and transferring it to the secondary winding (v_2). This voltage produces a current signal at the resonance frequency of the LC series branch (L_r and C_r) and charges the C_0 capacitor. This current is not flowing to the AC port because of the high L_0 impedance. In addition, the second bridge is also active to increase the voltage conversion ratio of the resonant converter. Figure 4.4.4 shows the waveforms of the charging group. Finally, during the waiting time (also within PWM signal's off-time), the second bridges presents a zero at its output (v_2) and waits for the condition to be active.

Particularly, in this analysis, the output AC voltage and current are considered positive and the converter is delivering energy to the load. The first bridge is active (M1-M4), and it is transferring energy from the input port (DC1) to the second bridge (DC2)

and then to the AC link. The gate signals of M1 and M4 are equal to M2 and M3, respectively. The gate signals from M5 and M8 are active (while PWM signal is on) during the positive semi-cycle of the output AC signal (and M6 and M7 are active during the negative semi-cycle). Moreover, a superposed HF signal is injected during the time when the main PWM signals are off. This means that M5-M8 are triggered by the HF signals.

Table 4.4.1 Initial and final values for each interval in the discharge mode

Time interval	v_1	v_2	i_{Lr0}	$v_{Cr0(n)}$	i_1 dir	End. cond.
1st	$+V_{DC1}$	0	0	$v_{Cf(5)}$	$i_1>0$	PWM
2nd	$-V_{DC1}$	$-V_{DC2}$	0	$v_{Crf(1)}$	$i_1<0$	PWM
3rd	$+V_{DC1}$	$+V_{DC2}$	0	$v_{Crf(2)}$	$i_1>0$	PWM
Waiting	$+V_{DC1}$	0	0	$v_{Crf(3)}$	$i_1<0$	PWM
Discharge	Off*	$+V_{DC2}$	$f(T_W)$	$v_{Crf(W)}$	$i_1=0$*	PWM
4th	$sign(i_1)V_{DC1}$	$+V_{DC2}$	$f(T_W)$	$v_{Crf(W)}$	$i_1<0$	$i_1=0$
5th	$sign(i_1)V_{DC1}$	$+V_{DC2}$	$f(T_W)$	$v_{Crf(4)}$	$i_1=f(M)$	$i_1=0$

* after 4th and 5th interval.

Time High-frequency pulses: time intervals for charging C0 and the waiting time. The charging C_0 group consists of several high frequency energy pulses that charge C_0. These pulses are delivered by the first bridge and received by the second bridge. This subsection analyzes the static behavior of the circuit, so it considers a fixed DC output value at the AC port. The AC power signal is the result of a sinusoidal reference, so a similar analysis can be done for any output voltage. Figure 4.4.4 shows 3 time intervals in the charging group, a waiting time and a discharging group. However, as the discharging group, which governs the output signal, becomes smaller, more charging time intervals can be added in order to keep C_0 charged. The same procedure can be used for analyzing any quantity of HF pulses. The objective of the analysis is to find the design equations of the converter.

In the 1st time interval, (Δt_1), the first bridge sets $+V_{DC1}$, in its AC port (v_1), and v_2 is 0; this is called the accumulation time interval (A+). The current through M1 and M4 starts at zero current (so soft switching process). i_1 increases with a sinusoidal waveform and i_2 is reduced following $i_0=i_1+i_2$. In this analysis, i_0 is considered to be constant in each interval which ends at the half of the resonant period ($T_{HF}/2$) when the first bridge changes v_1 from V_i to $-V_i$. The equations that govern this interval are:

$$\Delta V = L_r \cdot \frac{di_1}{dt} + v_{Cr}, \quad i_{Cr} = i_1 = C_r \cdot \frac{dv_{Cr}}{dt}, \tag{4.4.1.a}$$

whose solutions are:

$$v_{Cr}(t) = \Delta V - (\Delta V - v_{Cr0})\, cos(\omega_r t) + i_{Lr0} \cdot Z_r \cdot sin(\omega_r t) \tag{4.4.2.a}$$

$$i_1(t) = (\Delta V - v_{Cr0}) \cdot sin(\omega_r t)/Z_r + i_{Lr0} \cdot cos(\omega_r t) \tag{4.4.2.b}$$

$$with \quad 0 < t < \Delta t_1,$$

where $Z_r=(L_r/C_r)^{0.5}$, $\omega_r=(L_r.C_r)^{-0.5}$, $T_{HF} = 2\pi/\omega_r$ is the period of the high frequency signal and ΔV is v_1-v_2. i_{Lr0} and v_{Cr0} are the initial current and voltage of L_r and C_r respectively and i_{Lr0} is 0 at the beginning of the switching period (T_S). These values are equal to the inductor current and capacitor voltage at the end of the previous time interval. Table 4.4.1 shows, for each time interval, the initial conditions of the inductor (i_{Lr0}) and capacitor (v_{Cr0}), v_1 and v_2 and how the interval ends. The "0" and "f" sub-indexes represent the initial and final conditions of a certain interval. Normally, the final condition of the previous interval is the initial condition of the present one. However, this is not correct when the intervals are superposed, such as the 4th and the discharge time intervals. Figure 4.4.3(a) shows the simplified circuit from (1). The final value of any time interval (the initial value of the next one) in the charging group that starts with zero current and lasts $T_{HF}/2$ is:

$$v_{Cr0(n+1)} = v_{Crf(n)} = \Delta V_n + \left[\Delta V_n - v_{Cr0(n)}\right]. \tag{4.4.3}$$

Therefore, for the accumulation time interval, the final value (and the initial value of the next one) is:

$$v_{Cr0(2)} = 2V_{DC1} - v_{Cr0(1)}. \tag{4.4.4}$$

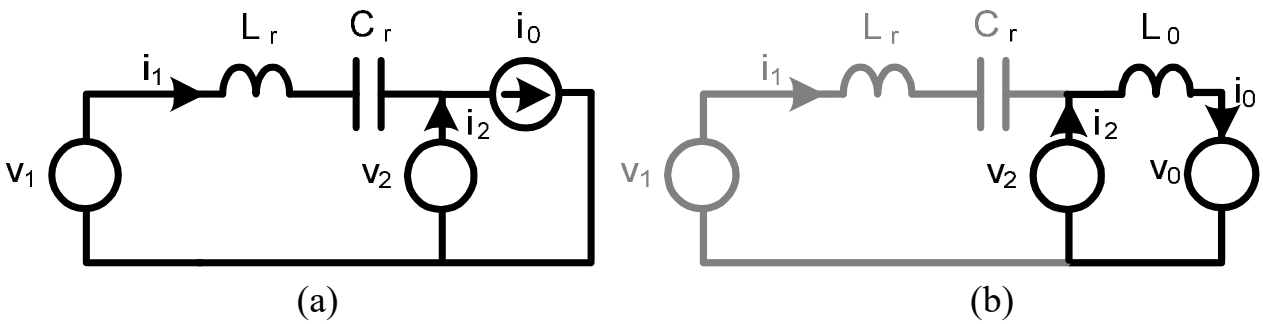

Figure 4.4.3. Simplified circuits for each time interval: (a) when the bridges transfer currents, (b) when the energy is delivered to v_0.

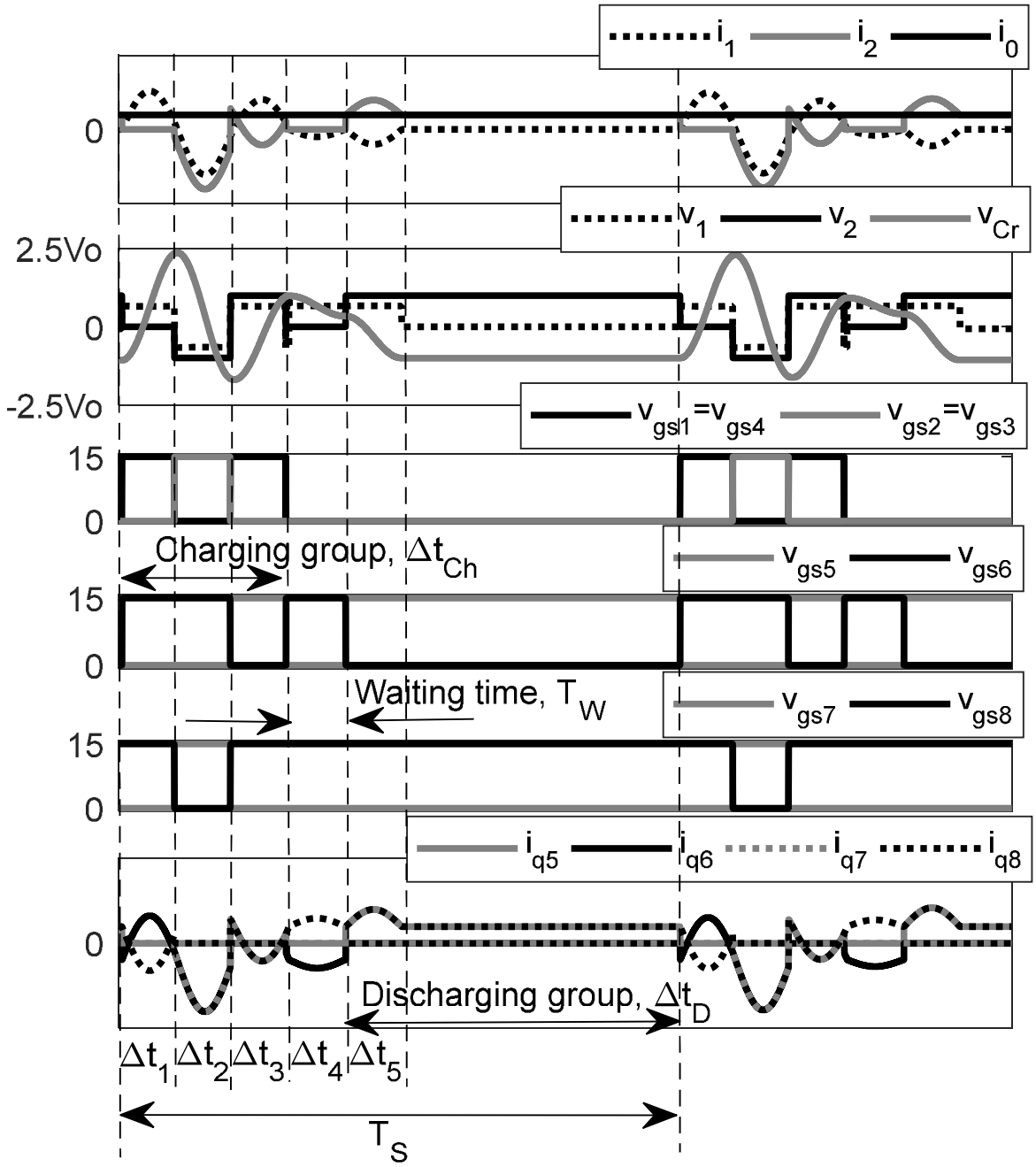

Figure 4.4.4– Waveforms in discharge mode

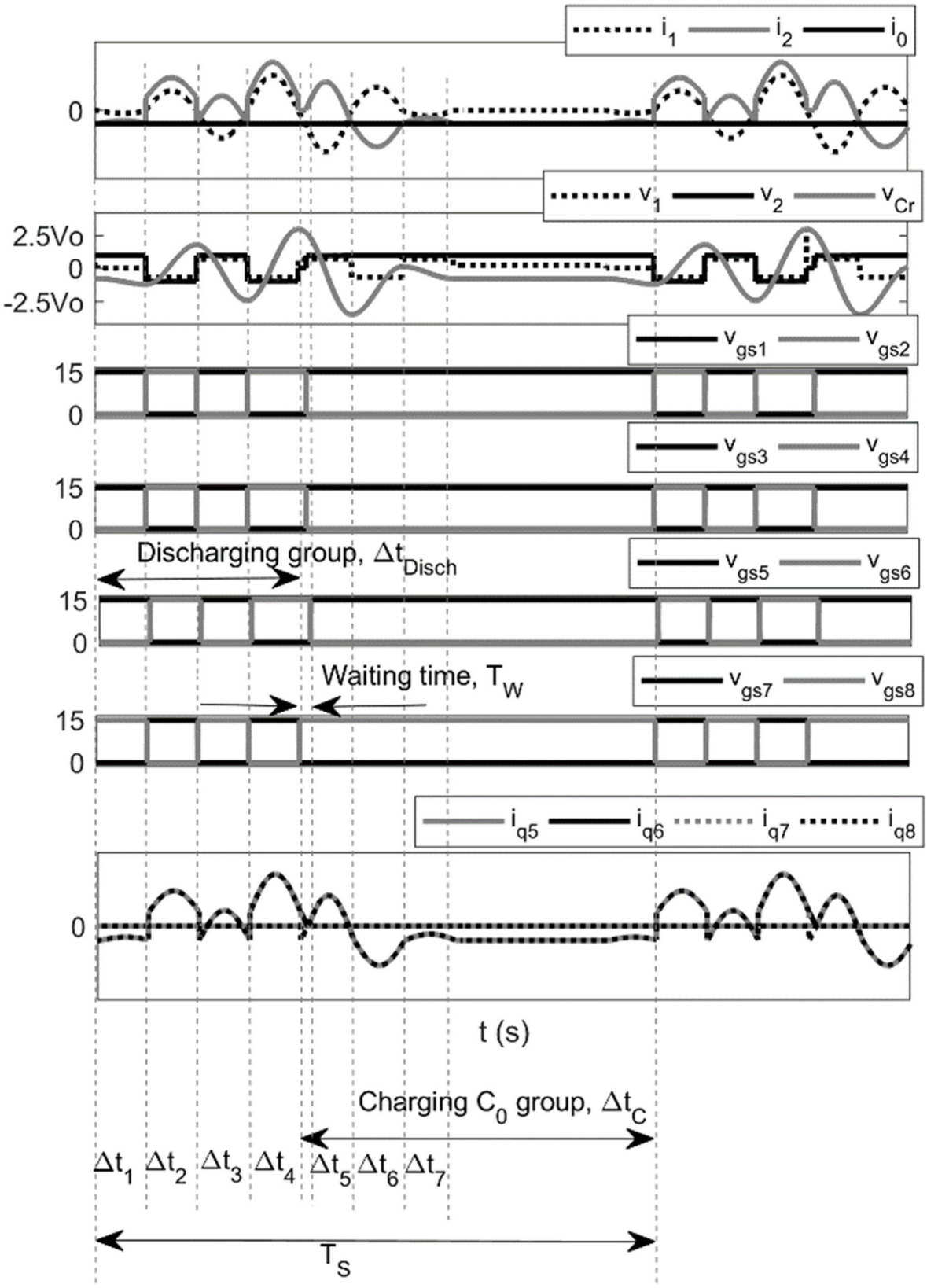

Figure 4.4.5–Waveforms in the charge mode

During the 2nd time interval (Δt_2), v_1 is $-V_{DC1}$, v_2 is $-V_{C0}=V_{DC2}$ and the energy stored in the previous interval is transferred to the second bridge and charges C_0. This is a negative transfer interval (T-) because the voltage in v_1 and v_2 are negative. It lasts $T_{HF}/2$ after that v_1 changes to $+V_{DC1}$. The equation that governs this interval is (4.4.1) and the simplified circuit is in Figure 4.4.3(a). The initial value of the next time interval is:

$$v_{Cr0(3)} = -4V_{DC1} + 2V_{DC2} + v_{Cr0(1)}. \tag{4.4.5}$$

The 3rd time interval is a positive transfer time interval (T+), because v_1 is V_{DC1}, v_2 is V_{DC2} and it lasts $T_{HF}/2$. Again, this interval follows (4.4.1), so the initial value of the next interval is:

$$v_{Cr0(4)} = 6V_{DC1} - 4V_{DC2} - v_{Cr0(1)}. \tag{4.4.6}$$

The 3rd time interval is the last one in the charging group, the next one is the waiting time interval (T_W), which can last from 0 to $T_{HF}/2$. It is variable, depending on the PWM signal's duty cycle. During the waiting time, the first bridge (M1-M4) is off, and $v_2=0$. Therefore, depending on the C_r voltage, i_1 can flow and deliver some charge to v_0 or to V_{DC1}. For the design purposes we will consider only the limits: $T_W=0$ and $T_W=T_{HF}/2$. If $T_W=0$, the discharging group of intervals starts immediately. Otherwise, if $T_W = T_{HF}/2$, i_1 is negative and turns on the diodes of the first bridge so v_1 is V_{DC1} and v_2 is 0. The initial value of the next interval is:

$$v_{Cr0(5)} = -4V_{DC1} + 4V_{DC2} + v_{Cr0(1)}, \quad \text{if } T_W = T_{HF}/2. \tag{4.4.7}$$

After this time interval, the discharging C_0 group starts.

Time intervals for the discharging C_0. During these time intervals, it is possible to split the circuit into two: one that delivers energy to the load, Figure 4.4.3(b), during Δt_D (PWM signal's on-time), and the other that discharges L_r-C_r, Figure 4.4.3(a).

If there is not waiting time, the 4th and 5th time interval appear in the discharging group to discharge C_r. This happens because of $v_{Cr0(4)}+v_2>v_1$ with $v_1=V_{DC1}$ and $v_2=V_{DC2}$ and $v_{Cr0(4)}$ is positive. So, the 4th interval appears and the next value of the capacitor is:

$$v_{Cr0(5)} = -4V_{DC1} + 2V_{DC2} + v_{Cr0(1)} \tag{4.4.8}$$

And in the 5th interval, $v_1=-V_{DC1}$ and $v_2=V_{DC2}$, so

$$v_{Crf(5)} = 2V_{DC1} - v_{Cr0(1)} = v_{Cr0(1)} \tag{4.4.9}$$

After these two intervals, the v_{Cr0} does not satisfy the condition $v_{Crf(5)}+v_2>v_1$ anymore, so the resonant branch is off and $v_{Crf(5)}$ is the initial value for the next T_S with $i_{Lr0}=0$. Using (4.4.9), the initial capacitor voltage can be found: $v_{Cr0(1)}=V_{DC1} - 2V_{DC2} = V_{DC1}(1-2M)$, defining M as the voltage conversion ratio, $M=V_{DC2}/V_{DC1}$. Therefore, the condition $v_{Cr0(4)}+v_2>v_1$, and $v_{Cr0(5)}+v_2<-v_1$, can be re-written, by using (4.4.7) and (4.4.8) as: $M<2$. In the proposed converter $0.75<M<1.5$, so it is valid in the whole operation range.

In case that there is a waiting time interval, Again the fifth time interval appears, but there are two possible conditions: $v_{Cr0(5)}+V_{DC2}>V_{DC1}$ or $v_{Cr0(5)}+V_{DC2}<-V_{DC1}$. By following the same procedure, it can be found that:

$$\begin{aligned} v_{Cr0(1)} &= 3V_{DC1} - 3V_{DC2},\ \textit{if } M>1 \text{ and} \\ v_{Cr0(1)} &= V_{DC1} - 3V_{DC2},\ \textit{if } M<1, \end{aligned} \tag{4.4.10}$$

in any case fifth time intervals appears.

In order to calculate the resonant capacitor, it is important to balance the charge that C_0 delivers to the load with the charge that C_0 receives from the resonant branch. Therefore, the mean value of i_2 should be 0. The charge from the resonant branch can be calculated as charge of each time interval with the sign of v_2 in this interval:

$$q_{ChC0} = \int_0^{T_S} sign(v_2(t)) \cdot i_1(t)\, dt \tag{4.4.11.a}$$

$$\begin{aligned} q_{ChC0} = &\underbrace{\int_0^{T_{HF}/2} 0.\, i_1(t)\, dt}_{A+} - \underbrace{\int_{\frac{T_{HF}}{2}}^{T_{HF}} i_1(t)\, dt}_{T-} + \underbrace{\int_{T_{HF}}^{\frac{3T_{HF}}{2}} i_1(t)\, dt}_{T+} \\ &+ \underbrace{\int_{\frac{3T_{HF}}{2}}^{2T_{HF}} i_1(t)\, dt + \int_{2T_{HF}}^{\frac{5T_{HF}}{2}} i_1(t)\, dt.}_{discharge\ \ Cr} \end{aligned} \tag{4.4.11.b}$$

The five time-intervals of the analysis are shown in (4.4.11) (if the charging group has more charging time intervals, they should be added to the equation). The first time-interval (A+) does not contribute to the charge of C_0 because $v_2=0$. Then the two next

intervals (T-,T+) always contribute and finally the last two exist for discharging C_r. Eq. (4.4.11) shows the case when $T_W=0$, if $T_W \neq 0$, the 4th term of the second member will be zero because during T_W, $v_2=0$. The charge integral can be easily calculated by considering the voltage difference in a time interval and the capacitance C_r. For example, the charge of T- is $q_{T-} = -C_r\left(v_{Crf(2)} - v_{Cr0(2)}\right) = -C_r\left(v_{Cr0(3)} - v_{Cr0(2)}\right)$. The results of (4.4.11), by using (4.4.2)-(4.4.10) in the three cases are:

$$q_{ChC0}|_{TW=0} = C_r 8V_{DC1} \tag{4.4.12.a}$$

$$q_{ChC0}|_{TW=\frac{T_{HF}}{2},M>1} = 8C_r V_{DC1} \tag{4.4.12.b}$$

$$q_{ChC0}|_{TW=T_{HF}/2,M<1} = 16C_r V_{DC1}. \tag{4.4.12.c}$$

q_{ChC0} must be equal to the charge delivered to the load. So,

$$q_{ChC0} = q_{DChC0} = \sum_{n=1}^{m_f/2=\frac{T_0/2}{T_S}} \int_{(n-1)T_S}^{(n-1+D_n)T_S} i_0(t)dt \approx \int_0^{T_0} d(t)\cdot i_0(t)dt \tag{4.4.13}$$

where T_0 is the period of the low frequency signal (50Hz), D_n is the duty cycle in the n cycle, $d(t)$ is the "continuous" duty cycle, which can be defined as $d(t)=v_0/V_{DC2}$. The AC port equation is:

$$V_{DC2} - v_0 = L_0 \cdot \frac{di_0}{dt} \tag{4.4.16}$$

and the solution is:

$$i_0(t) = \frac{(V_{DC2}-v_0)}{L_0}\cdot t \quad with \quad 0 < t < \Delta t_D = DT_S. \tag{4.4.17}$$

Following (4.4.17), i_0 is not constant. It increases during the discharge group (for positive half cycle) and decreases during the charging group. However, in order to simplify the analysis, it is considered to be constant in each interval of the charging group and its value decreases from one interval to the next one following:

$$i_{0(n+1)} = i_{0(n)} - \frac{\left(V_{DC2} - v_{2(n)}\right)}{L_0}\cdot\frac{T_{HF}}{2T_S}, \tag{4.4.18}$$

where $i_{0(n)}$ is the output current for the current time-interval. For the first time-interval, $i_{0(1)}$ coincides with $i_0(DT_S)$ at the end of the discharging group.

Time-domain analysis: charging mode. In the charging mode, the circuit works like in the previous mode, but in this case, the second bridge delivers the HF pulses and they are received by the first bridge and the energy is transferred from C_0 to V_{DC1}. Again, the same three groups appear: the time intervals for discharging C_0 (and charging the input source), the time intervals for charging C_0 (receiving energy from the AC link) and waiting time interval. It is important to keep the average of v_2 during the PWM off-time equals to 0, in order to not disturb the output current waveform. Therefore, an equal time of positive and negative pulses are needed, which means an even number of pulses in the charging mode. For example, if the PWM signal allows to have 3 pulses, only two pulses can be transferred and the last one will be a waiting time. In the discharging case, it was the opposite, due to the accumulation time interval, which fixes v_2=0, the minimum number of pulses were 3, so odd number and multiples of 3 could be selected.

Figure 4.4.5 shows the waveforms and the three groups of intervals for the case where the output voltage is positive (positive half cycle) and the converter is absorbing energy, meaning $i_0<0$. As the analysis of the waveforms is similar to the discharging mode, it is omitted. In this particular case, there are four time intervals in the charging V_{DC1} (or discharging C_0) group ($\Delta t_1, \Delta t_2, \Delta t_3, \Delta t_4$), one in the charging C_0 group (Δt_D), which overlaps with $\Delta t_5, \Delta t_6$ and Δt_7 and there is a small waiting time. For the charging mode with negative output voltage, the gate signals for M5 and M8 are replaced by the gate signals for M7 and M6, and vice versa. As the analysis of the waveforms is similar to the discharging mode, it is omitted.

Design guidelines. The time-domain analysis shows the method to calculate C_r for a constant output. However, the output is a sinusoidal waveform, and the time for delivering energy pulses varies as a function of the off-time of the PWM output signal. So, the estimation of q_{ChC0} depends on the quantity of accumulation, transfer and discharge pulses during $T_0/2$. As an example, it will be considered that the HF signal can produce as much as $m_{HF}=10$ time intervals of $T_{HF}/2$, so it means that the resonant frequency is five times the switching frequency. It will be from 0 to 10 high frequency pulses during T_S. If the off-time of the PWM is smaller than $3T_{HF}/2$ then, no pulses will be injected because, it is needed to have at least one accumulation time (A+) to produce

M>1 and in order to keep the average value of v_2 during the off time equal to zero, an even number of transfer intervals are needed. Therefore, thee pulses are the minimum. If there is time to add a 4th pulse, again, it will unbalance v_2, so a waiting time of $T_{HF}/2$ is added. For five pulses, the operation is one (A+), and four transfer intervals (T-,T+,T-,T+). For six pulses, it is possible to add 2 accumulation time intervals, so the pattern will be: A+,T-,T+,A-,T+,T-. A- means that v_1=-V_{DC1}, and $v_2=0$. The other patterns are shown in Table 4.4.2. Figure 4.4.6 shows how many pulses are injected as a function of the duty cycle signal (reference signal). The x-axis is the n-th switching period starting from zero at the beginning of the sine curve. HF pulse injection appears when D is lower than 0.7 ($m_{HF}=10$), because the converter needs at least 3 pulses to transfer energy to C_0. If m_{HF} is higher than 10 then it is possible to have pulse injection with a higher D. Figure 4.4.6(b) shows the case for a modulation index, m_A, of 0.7 where there is always HF pulses.

Following the same procedure that was explained to obtain (4.4.13), q_{ChC0} can be obtained but considering that each T_S has its own pattern of pulses. The value of each pattern was obtained by following the same procedure as (4.4.11), and the results are shown in Table 4.4.2.

In order to calculate C_0, it is needed to estimate which is the C_0 (v_{DC2}) voltage variation during one T_S. If the converter is working with switching periods that do not include the injection of pulses, as shown Figure 4.4.6(a), a high capacitance is needed in order to have a small decrease in voltage in DC2. So, in this case, the voltage variation (Δv_{DC2}) can be calculate by:

$$q_{DChC0_without_pulses} = C_0 \Delta v_{DC2} = \frac{1}{V_{DC2}} \int_{n_1 T_S}^{n_2 T_S} p_0(t) dt \tag{4.4.19}$$

where n_1T_S and n_2T_S is the time interval where these is not injection of HF pulses. By using (4.4.19), a high capacitance is expected. Low ESR Electrolytic capacitors should be used or a combination with electrolytic and polypropylene capacitors.

If the converter is working always with pulse injection (for $m_{HF}=10$, means that $m_A<0.7$), then:

$$q_{DChC0_with_pulses}\Big|_{MAX} = C_0 \Delta v_{DC2} = \frac{\hat{I}_0 \hat{V}_0 T_S}{V_{DC2}} \tag{4.4.20}$$

where ^ means peak value. It is considered that maximum charge that the capacitor should delivered to the load is the peak power multiplied by the switching period (energy) and divided by the average voltage of the capacitor. These equations are used to select C_0. In this case C_0 is much lower than in (4.4.19), so polypropylene capacitors are preferred.

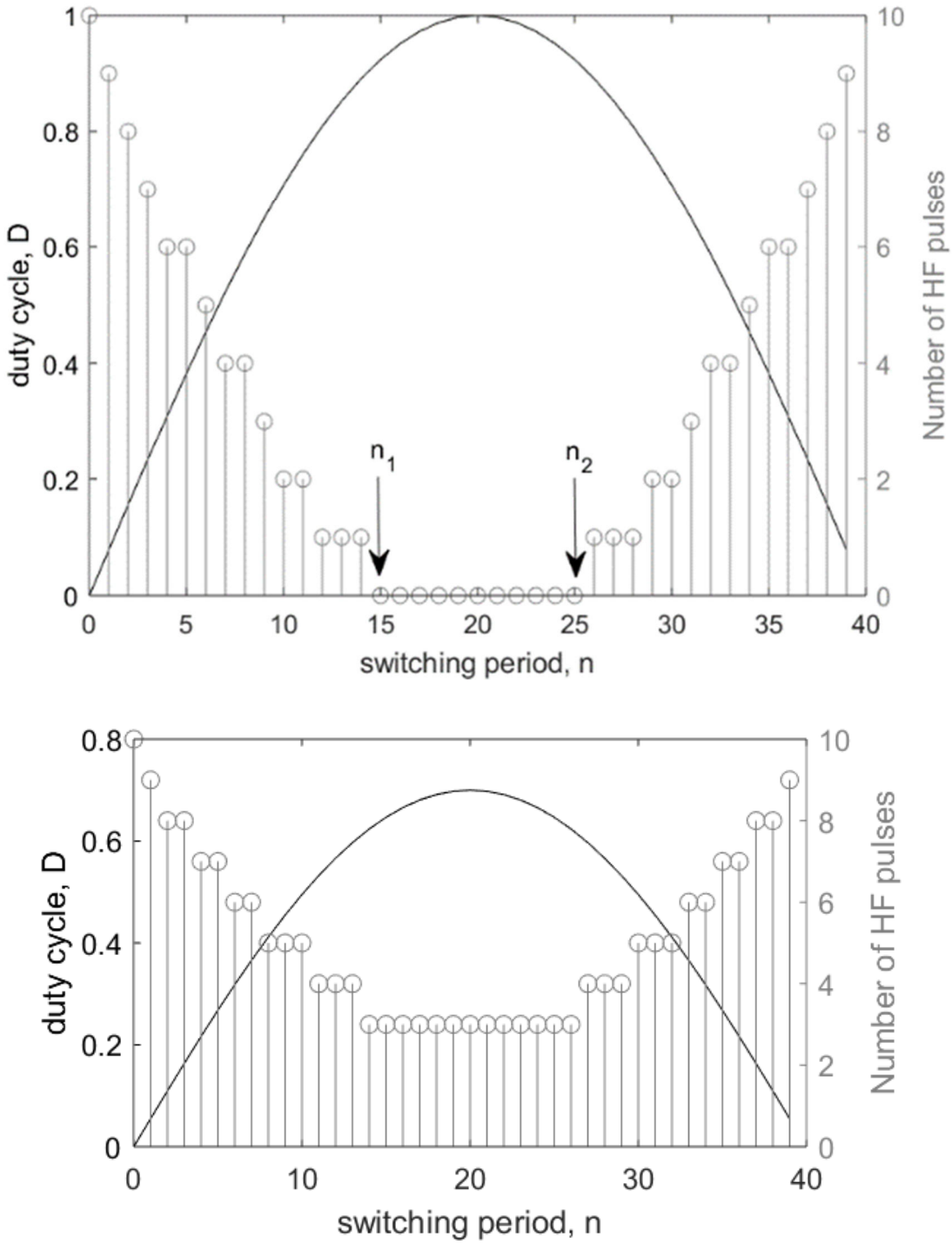

Figure 4.4.6– Output voltage as a function of the input reference for two cases

.

Table 4.4.2 Patterns for different HF pulses, for $M_{HF}=2T_S/T_{HF}=10$

Duty cycle	N of pulses	Charge delivered to C_0 q_{ChC0}	Pattern
0	10	20ViCr	A+, T-, T+, A-, T+, T-, A+, T-,T+, W
$0 < D \leq 0.1$	9	20ViCr	A+, T-, T+, A-, T+, T-, A+, T-,T+
$0.1 < D \leq 0.2$	8	20ViCr	A+, T-, T+, A-, T+, T-, T+,T-
$0.2 < D \leq 0.3$	7	16ViCr	A+, T-, T+, A-, T+, T-, W
$0.3 < D \leq 0.4$	6	12ViCr	A+, T-, T+, A-, T+, T-
$0.4 < D \leq 0.5$	5	8ViCr	A+, T-, T+, T-, T+
$0.5 < D \leq 0.6$	4	8ViCr	A+, T-, T+, W
$0.6 < D \leq 0.7$	3	8ViCr	A+, T-, T+
$0.7 < D \leq 1$	0-2	0	0

In order to calculate C_r, it is needed to balance the electric charge that charges C_0 with the one that feeds the load, during the half of the output signal period ($T_0/2$). The total electric charge, q_{TCHC0}, that charges C_0 is the sum of the contribution of each T_S during $T_0/2$. Therefore, it is needed to sum the charge of different T_S with different patterns. Table 4.4.2 shows the q_{ChC0} for each pattern, so the total charge can be calculated as:

$$q_{TChC0} = \sum_{n=1}^{N_P} q_{ChC0(n)} = \frac{\hat{I}_0 \hat{V}_0 T_0}{2V_{DC2}} \tag{4.4.21}$$

For example, if we considered $M=1.5$ and $m_A=0.7$ with a sinusoidal output waveform, which is the limit to have at least 3 pulses in T_S (for $m_{HF}=10$), the charge is:

$$q_{TChC0} = 422 V_{DC1} C_r|_{M=1.5, m_A=0.7} = \frac{\hat{I}_0 \hat{V}_0 T_0}{2V_{DC2}} \tag{4.4.22}$$

then, C_r can be calculated. If $M<1.5$, the $q_{TChC0}>q_{DChC0}$ so the control loop will stop the charging process. The same happens for a smaller m_A.

4.4.3. Control diagram

The control diagram is shown in Figure 4.4.7. The AC port of the converter is controlled by a sinusoidal reference $m_A(t)=(m_A.sin\omega t+\phi)$, where m_A is the modulation index. This signal is previously synchronized with the grid through a digital PLL circuit as was discussed in Chapter 3. After that the m_A is multiply by the constant v_{DC2}, which is the C_0 voltage in the steady state. In addition, v_{DC2} go through a limiter and a low pass filter to reduce the noise in the signal. Then, the reference signal, is multiplied by 0.7 so the final modulation index is defined as: $m'_A = \hat{V}_0/v_{DC2}$. This goes to the duty factory which creates the PWM signals for the second bridge (M5-M8). The 0.7 factor is included in order to reduce the maximum of the reference signal to 0.7, and thus, the maximum of the duty cycle is 0.7. This way, the converter has at least 3 HF pulses in each T_S.

$v_{DC2}=v_{C0}$ also dictates the operation mode by the mode selector block. It selects the charge mode, if the v_{C0} is higher than a limit, or the discharge mode, if v_{C0} is lower than the limit. In the charge mode, the storage device in DC1 is being charged by the extra electric charge of C_0 and in the discharge mode, energy is extracted from the storage device to charge C_0.

The HF pulse generators create the HF pulses by using a HF oscillator (160 kHz), the mode selector output signal and the reference in order to know how many pulses can be injected in the current T_S. Finally, the HF pulses generator for M5-M8 output signals are summed to the PWM signals and the results are injected to the gates of M5-M8. The other HF pulse generator creates the signals for M1 and M4.

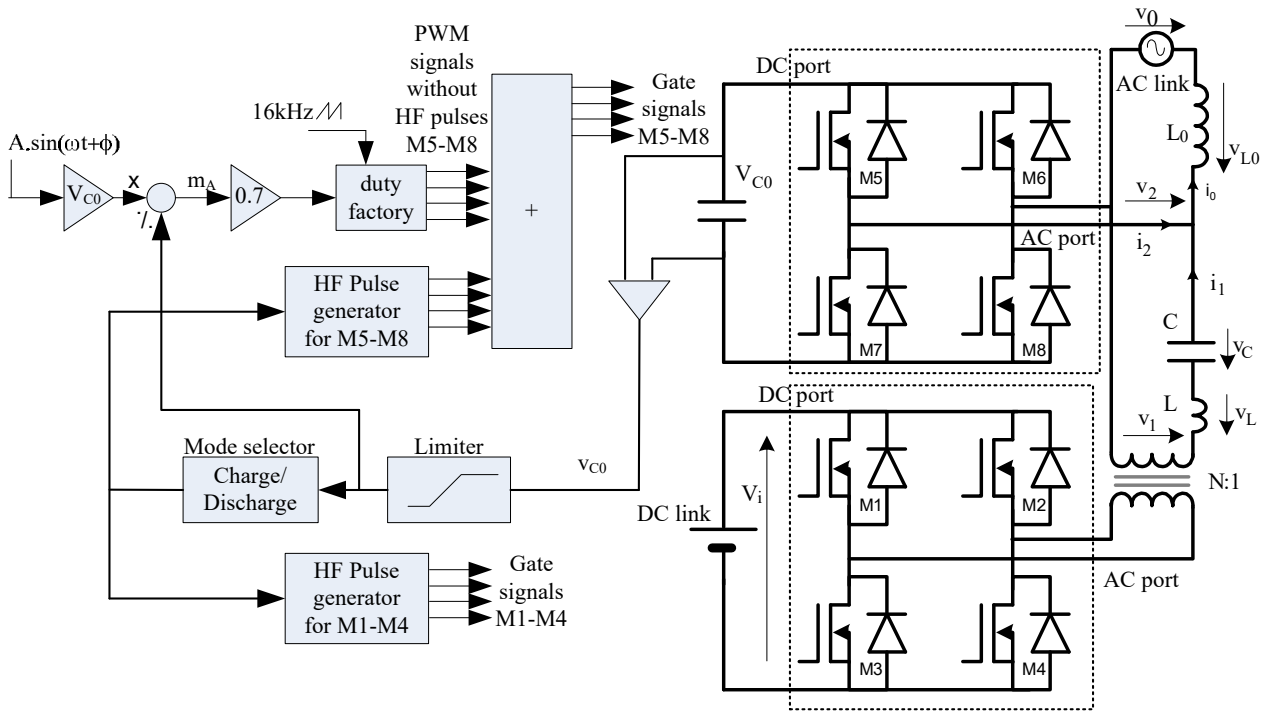

Figure 4.4.7–Control diagram

4.4.4. Voltage Conversion Ratio

The output voltage is a function of C_0 (V_{DC2}) voltage and the PWM signal created by the input reference. The duty cycle of the PWM signal that triggers the second bridge is proportional to the $m_A(t)$. This means that 0.7 of the input reference is equal to 70% of the duty cycle in a PWM signal that triggers M5 and M8. When the input reference is negative, the PWM is the same as when it is positive, but it triggers M6 and M7 because the unipolar PWM is used.

The output voltage can be approximated based on the average values of v_2 during one T_S. If the input reference is positive, then for the discharging C_0 time (Δt_D):

$$v_2 = V_{DC2} = V_{C0} \tag{4.4.23}$$

and for the charging C_0 time (Δt_{Ch}):

$$\langle v_{2Ch} \rangle = 0 \tag{4.4.24}$$

where $\langle v_{2Ch} \rangle$ is the average value of v_2 during Δt_{Ch}. And also, during the waiting time $v_2=0$. Therefore $<v_2>$, which is the average value of v_2 during a whole period T_S, is:

$$\langle v_2 \rangle = V_{DC2} \cdot D = V_{DC2} \cdot \frac{t_D}{T_S} \tag{4.4.25}$$

If it is needed to have pulses in every period. the maximum voltage conversion ratio was fixed to 70% of $V_{DC2}=V_{C0}$ if $m_{HF}=10$ (a minimum of 3 pulses). In case of fluctuations in C_0 voltage, $V_{DC2}=V_{C0}$ is replaced by the time dependent value, v_{DC2}, and in addition, the duty cycle can be considered as a continuous signal proportional to $m_A'(t)=m_A'sin(\omega t+\phi)$ for low frequencies. Thus, the expression is:

$$v_2(t)|_{atlowfrequencies} \approx v_{C0} \cdot d(t) \approx v_{C0} \cdot m'_A \cdot sin(\omega t + \varphi) \tag{4.4.26}$$
$$\approx 0.7 \cdot V_{C0} \cdot m_A \cdot sin(\omega t + \varphi)$$

The voltage conversion ratio between V_{DC2} and V_{DC1} is $M=V_{DC2}/V_{DC1}$. It can be calculated by considering the transfer of electric charge in each time interval (Section 4.4.2). As the converter needs V_{DC2} to be higher than v_0 while the input voltage, V_{DC1}, is delivering energy and being discharged, M should be greater than one in the discharge mode without considering the transformer turns-ratio, which means that $m_{DCh}=M_{DCh}/n_T>1$. Otherwise, if $m_{DCh}<1$ and n_T is used to keep the voltage difference, when the converter works in the opposite direction, V_{DC1} will not reach a voltage higher than V_{DC2}/n_T. Therefore, a step-up conversion is mandatory [33-36]. That is why in the discharging mode, when the first bridge is charging V_{DC2}, the second bridge is forced to $v_2=0$ in some intervals, which are called the accumulation time intervals, and during the next interval this energy is released and m_{DIS} reaches a value greater than one. The same behavior happens in the charging mode, $M_{Ch}=V_{DC1}/V_{DC2}$ and m_{Ch} is $M_{Ch}.n_T$. In this mode, $m_{HF\ CH}$ should be again higher than one to charge V_{DC1} in the whole voltage range.

4.4.5. Soft-switching process

This converter achieves soft-switching in many of its commutations. In the discharge mode, it has turn-on and –off at zero current for M1-M4 switches. The

commutations of the second bridge are not soft and they are similar to any unipolar PWM inverter. However, as the converter has more commutations because of the HF pulses, more switching losses are expected than the traditional unipolar PWM inverter. The waveforms of the current in M5-M8 are in Figure 4.4.4, notice that the turn-on and turn-off currents are not the resonant current (i_1) but i_0. i_1 is zero in the commutations but i_0 is depends on the load. A simple model for estimating the switching losses is:

$$E_{SW} \approx \sum_{n=1}^{N=T_0/T_S} \frac{1}{2} V_{C0} \cdot n_{SW} \cdot I_0 |sin(n\omega_0 n T_S)| \cdot \Delta t_{sw} \tag{4.4.27}$$

This express that the energy losses due to the switching, E_{SW}, in a period is equal to sum of the switching losses in each T_S. The losses in each T_S is a function of the quantity of HF pulses plus the PWM pulses. Δt_{sw} is the duration of the switching process, $I_0 sin(n\omega_0 n T_S)$ is the value of i_0 in each T_S, which is considered constant during T_S to simplified the calculus. n_{SW} is the number of switching process, for example to change v_2 from V_{DC2} to 0 only one leg of the bridge is switched, therefore only one switching process, however if v_2 changes from $-V_{DC2}$ to V_{DC2} there are two switching processes (the two legs of the bridge commutate). In order to compare the different techniques, Figure 4.4.8 shows E_{SW} normalized with the losses of a bipolar inverter for the unidirectional modulation in a VSI and the proposed converter at different phase angle between the output voltage and current. Particularly, the losses are minimized when the converter is transferring active power and the losses are reduced as m_A is increased. There is a tradeoff between increasing the m_A and decreasing C_0. For high values of m_A, C_0 should be big in order to deliver the current while there is not HF pulses that charges it. Increasing the frequency of the pulses allows increasing m_A but also increasing the power losses, so there is another trade-off between the HF frequency and the switching power losses.

During the charging mode, Figure 4.4.3 shows that in M5-M8, the commutation is a hard-switching process, because of the output current (i_0). Therefore, although the resonant current starts and ends at zero in each switching pulse, the continuous i_0 produces the same switching losses as in the discharge mode.

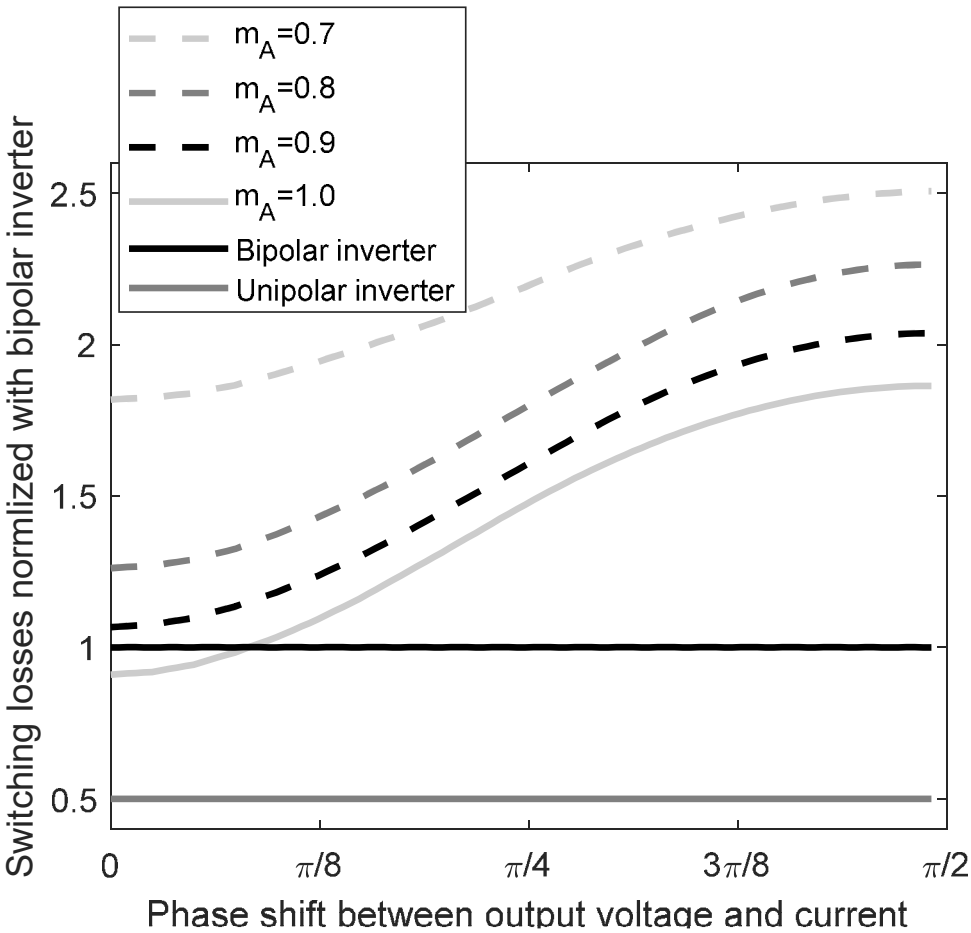

Figure 4.4.8–Power losses and distortion comparison for MHF=10

4.4.6. Numerical simulations

In order to validate the proposed multi-port converter, simulations and experimental tests were performed. Figure 4.4.10 shows the waveforms obtained by simulating a converter consuming and delivering power from an AC energy source with the components listed in Table 4.4.3 and based on the diagram in Figure 4.4.2(a).

The converter was simulated with PSIM software in three different tests: delivering energy to the grid, absorbing energy from the grid, and a discharge-charge cycle test of a supercapacitor in port DC1. Figure 4.4.9(a) shows the whole discharging process and Figure 4.4.9(b) shows the details in order to see the output waveforms. Figure 4.4.10(a) presents a complete charging process and Figure 4.4.10(b) the details of the output waveforms. The input source (supercapacitors in this case) were discharged and then

charged at a constant power of 7.5kW. The capacitance of the input source was 1.6F and the voltage was between 225 V-125 V, which means 90 SC in series.

Table 4.4.3 Converter's main components

Components	Symbol	Value
Resonant inductor	Lr	26.uH
Resonant capacitor	Cr	150nF
Transformer ratio	n_T	1:2
Transformer magnetizing inductance	L_m	20mH
DC Link capacitor	C_0	400uF
Output inductance	L_0	20mH
Main switching frequency	f_S	16kHZ
High resonant frequency	f_{HF}	80kHz
MOSFETS Bridge 1	M1-M4	IXFN80N50
MOSFETS Bridge 2	M5-M8	IXFN60N80P

Figure 4.4.10 shows that the converter can transfer constant power in the whole input voltage range in both directions. It shows the output current and a filtered output voltage before the output inductance ($v_{2\ filtered}$), from which the phase shift between the converter and the grid that controls the power flow direction can be observed. When the converter is delivering energy, v_2 leads v_{grid} (Figure 4.4.9 (b)), and when it is absorbing energy, v_2 lags v_{grid} (Figure 4.4.10(b)). In addition, the distortion on the current is around 3%. Figure 4.4.11 shows a diagram of total harmonic distortion (THD) as a function of the output power for several input voltages in both power directions. The converter has a THD lower than 5% at maximum power in the whole voltage range when it is absorbing power. However, when delivering power, the distortion is, on one hand, higher at high power because of the voltage perturbation at v_{DC2}. Distortion increases at lower power because i_0 is reduced but the switching process remains equal. Therefore, for low power the distortion is higher. In order to reduce distortion, the designer can improve the output filter or increase the switching frequency. For comparison, the distortion of a traditional

unipolar and bipolar PWM inverters with the same output filter is also plotted in Figure 4.4.11.

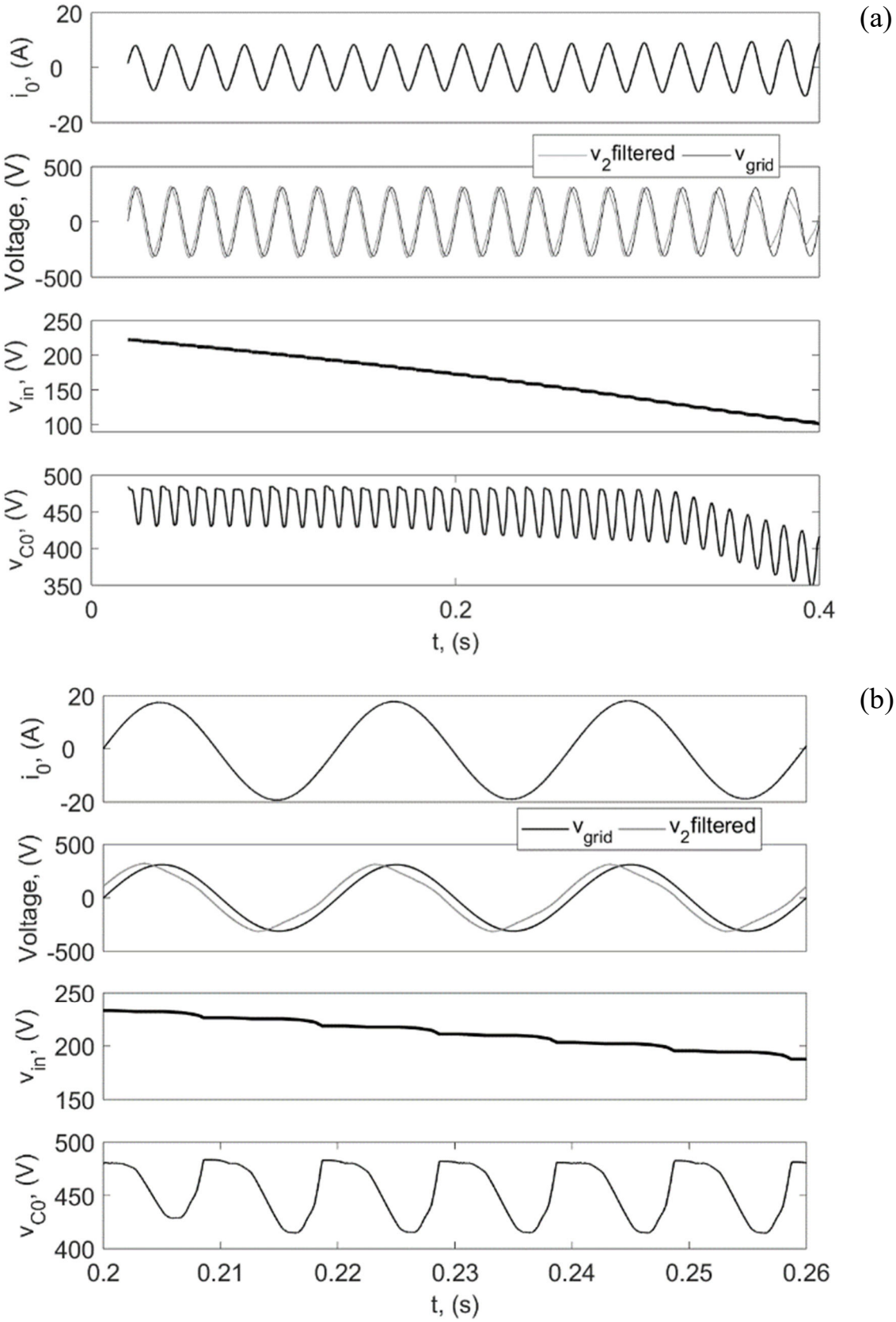

Figure 4.4.9–Charging and discharging input source at constant power: (a) discharging process, (b) detail of the discharging process

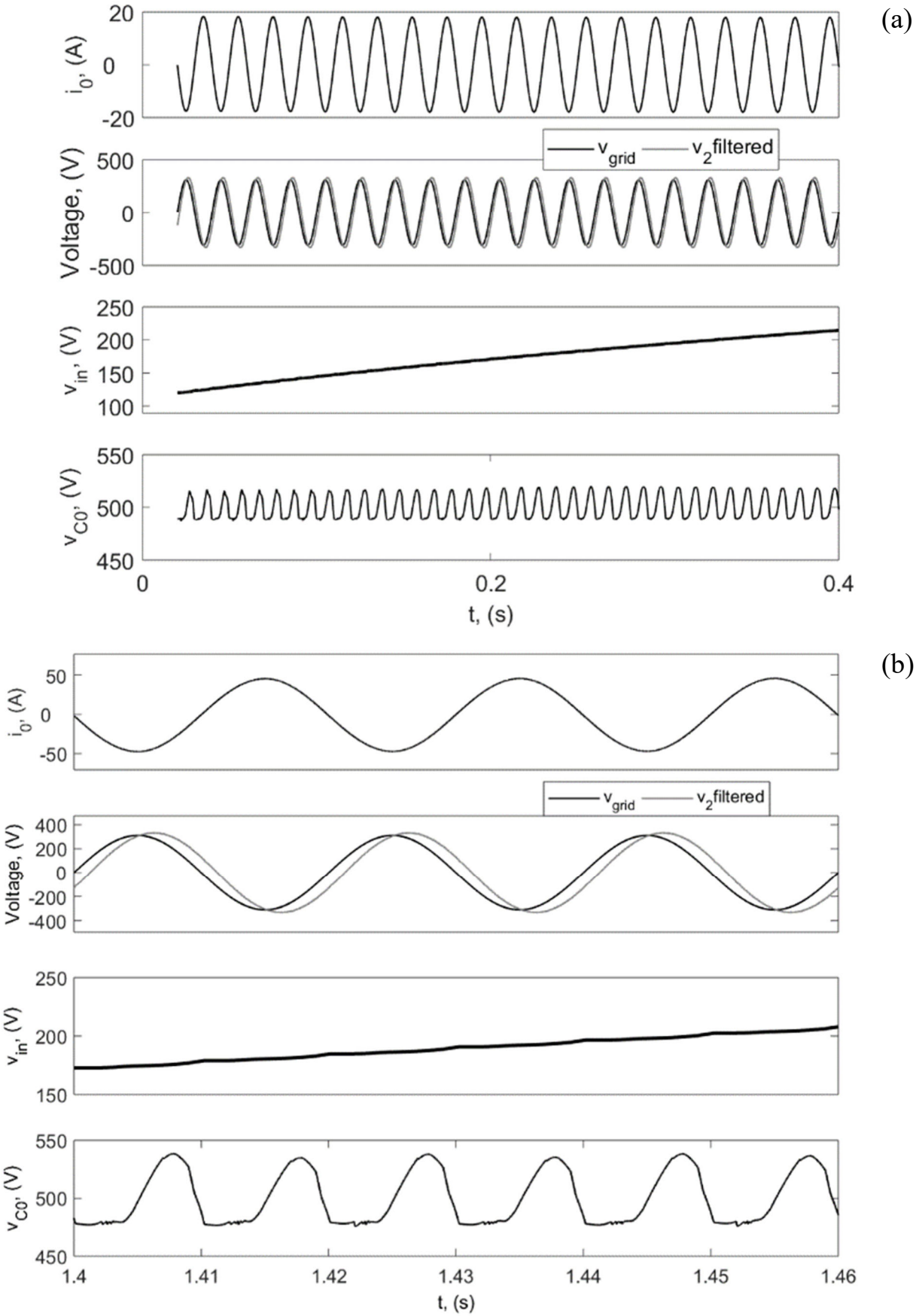

Figure 4.4.10–(a) Charging input source at constant power, (b) detail of the charging process

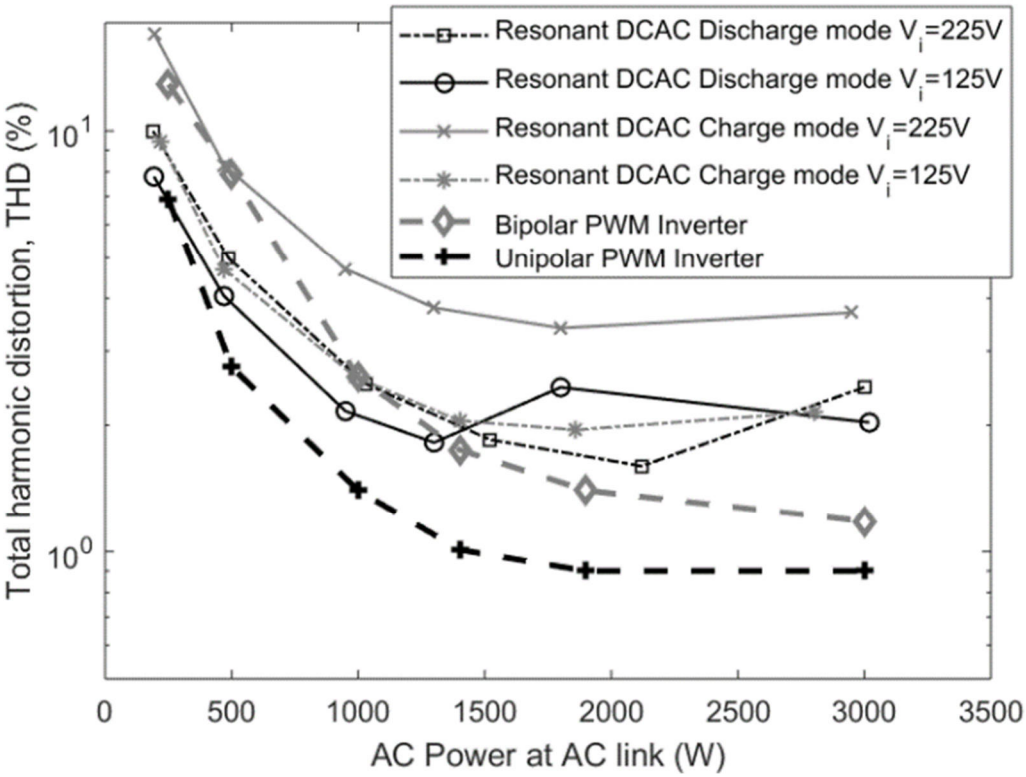

Figure 4.4.11–Total harmonic distortion (THD) as a function of the power at the AC link for several input voltages V_i=V_{DC1}

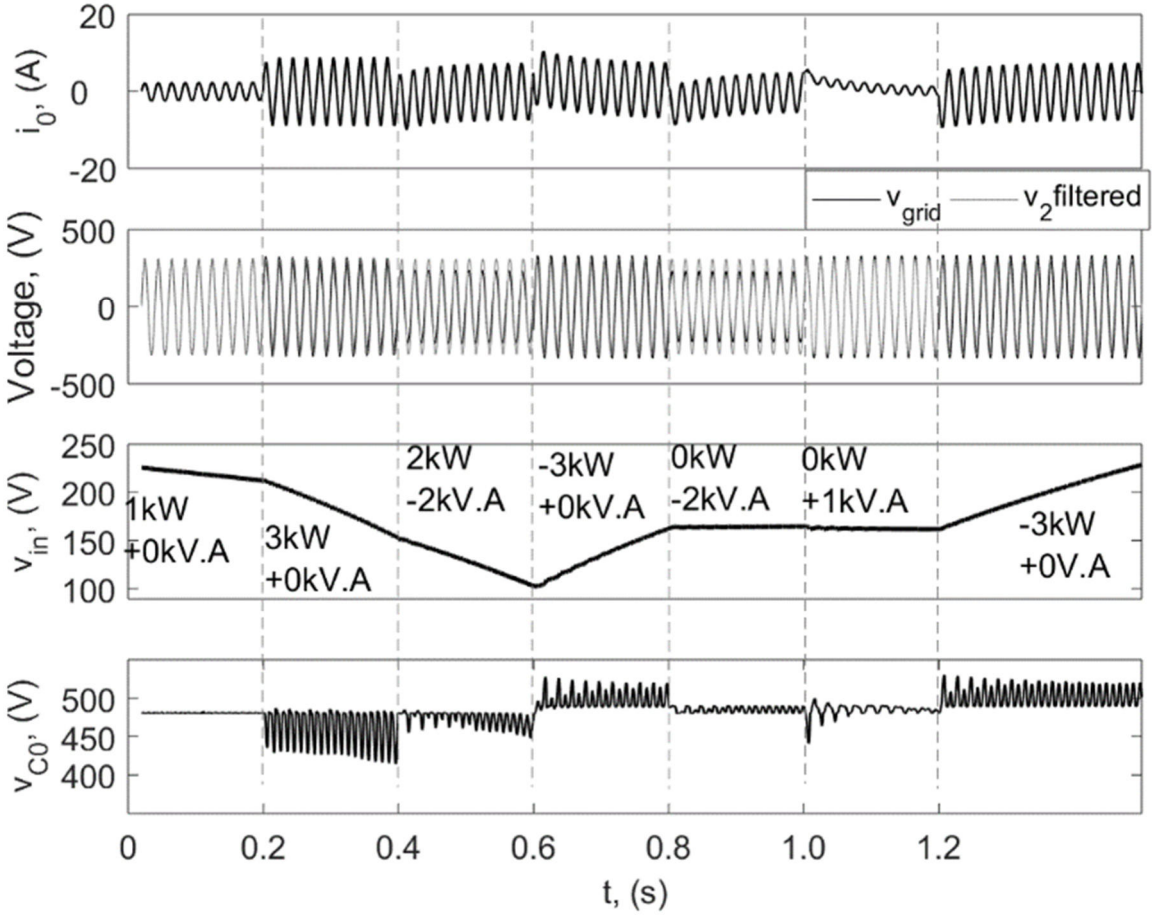

Figure 4.4.12–Delivering and absorbing active and reactive power to/from the grid

Figure 4.4.12 shows a discharge-charge cycle, which delivers active and reactive energy. The dynamic response analysis of the system is not within the scope of this section, but it can be based on [228].

4.4.7. Experimental results

A prototype was developed for transferring up to 3000W to the grid from an input source (V_i=V_{DC1}) in the range from 225 V to 115 V in order to emulate the voltage range of a 90 SC stack. Figure 4.4.13 shows the prototype, which has two bridges, C_0, the resonant branch, the output filter, the measuring stage and the DSP controller.

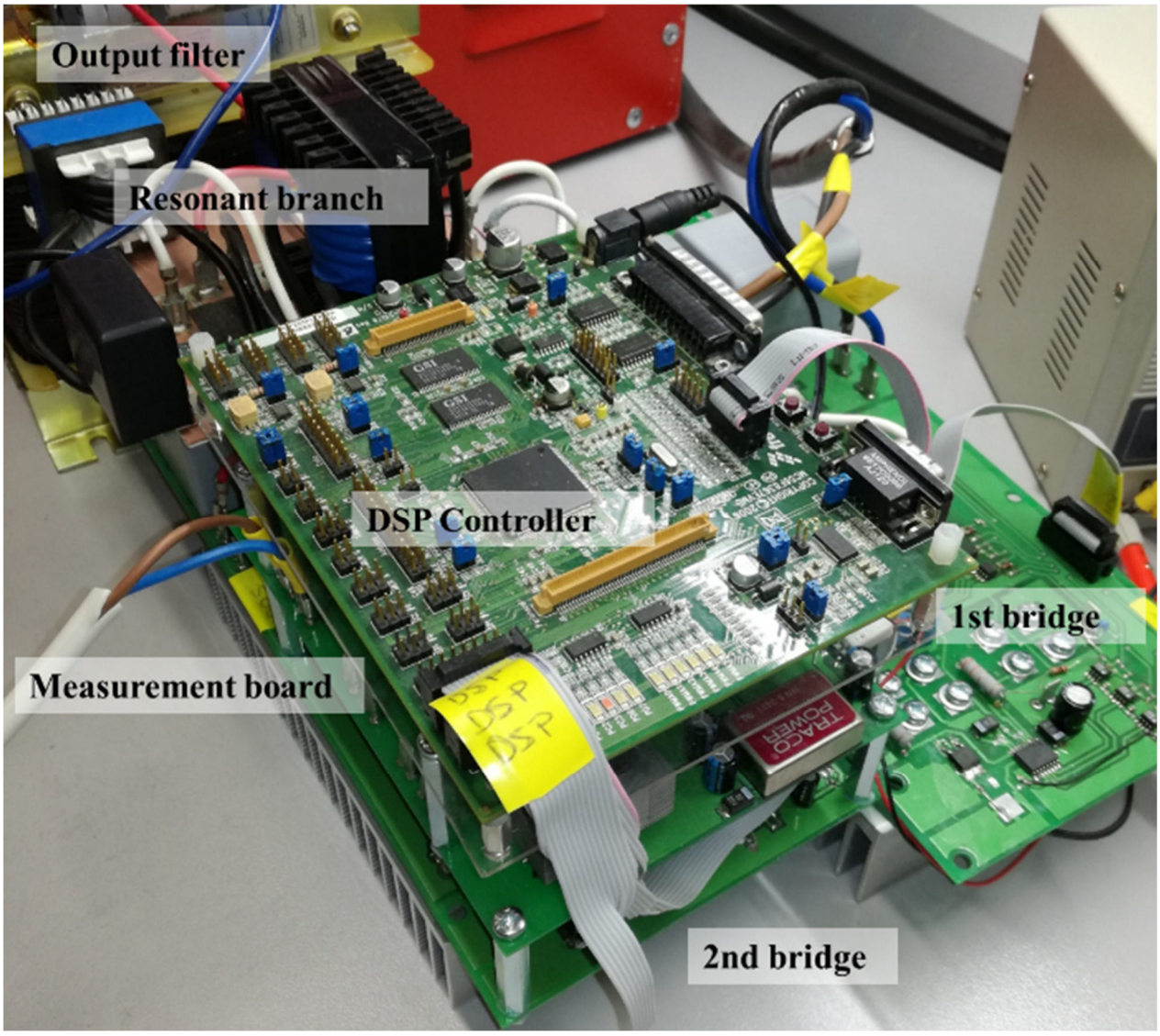

Figure 4.4.13–Prototype

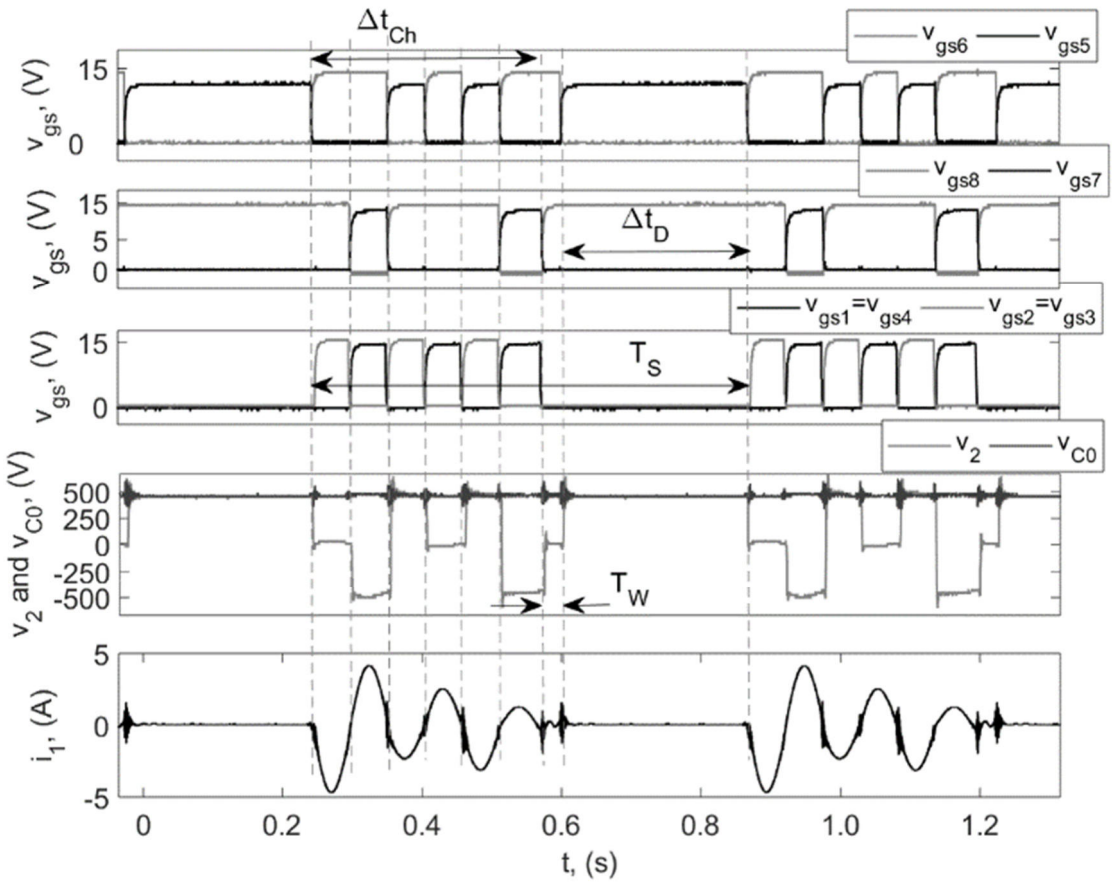

(a)

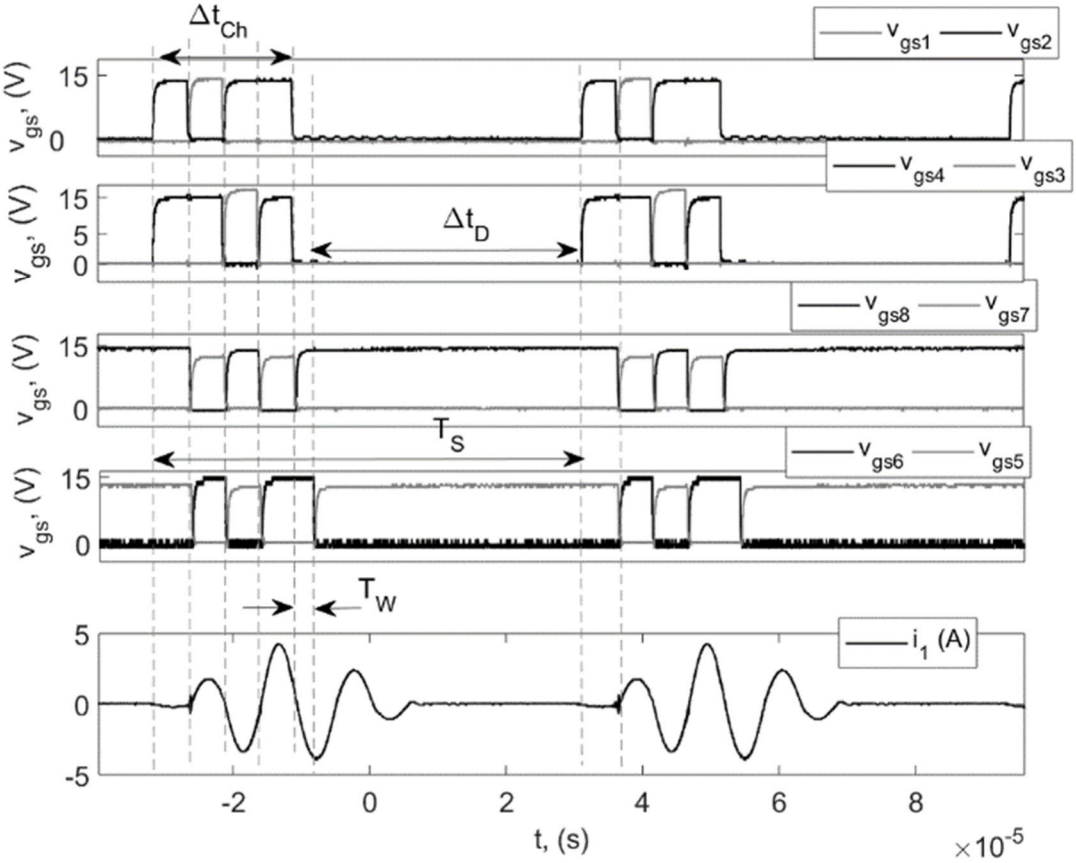

(b)

Figure 4.4.14–Experimental results, main waveforms of (a) discharging mode, (b) charging mode

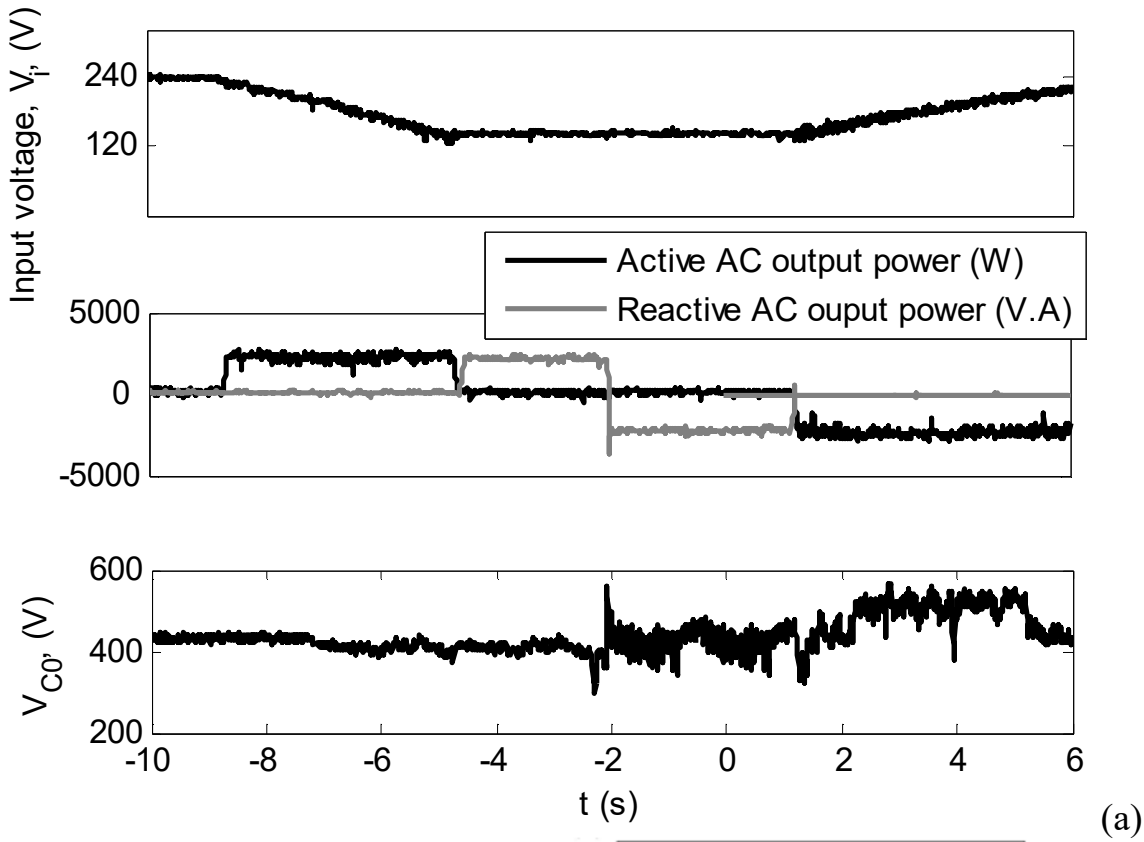

(a)

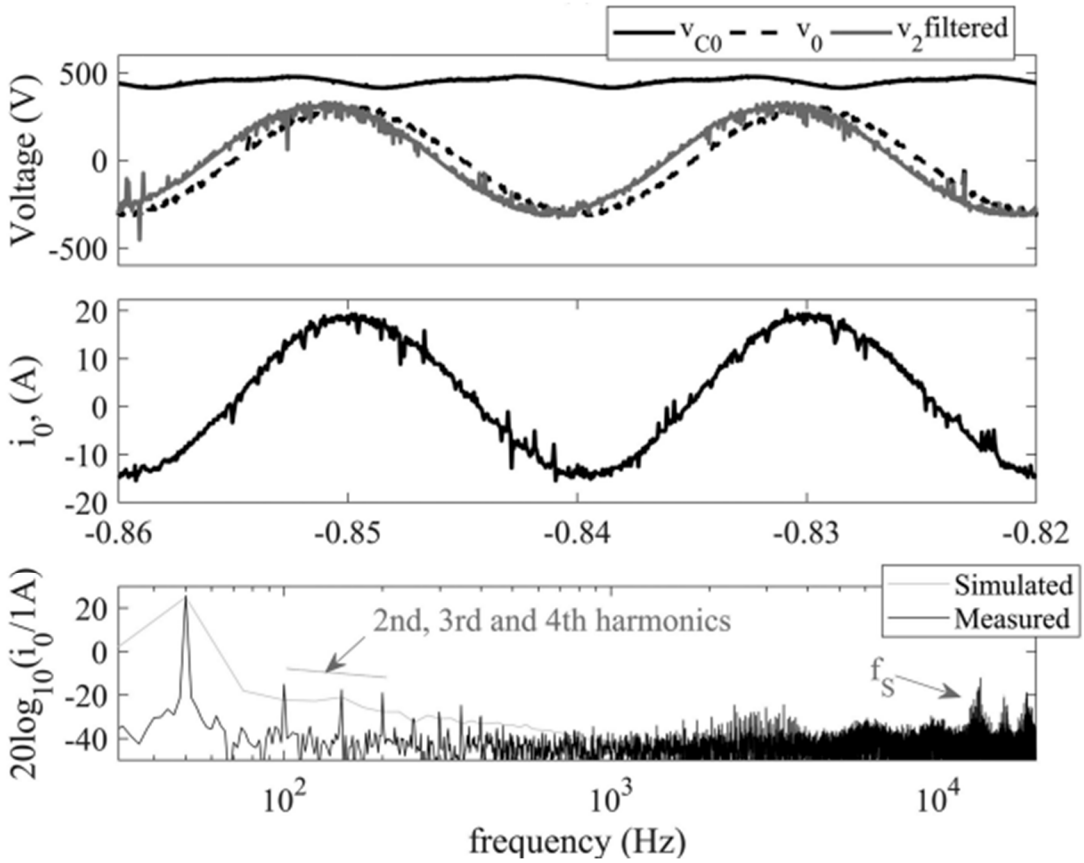

(b)

Figure 4.4.15–Transferring active and reactive power to/from the grid: (a) complete cycle, detail for (b) 3kW active

The prototype was built to validate the modulation technique and it is not optimized in volume and weight. The parameters are listed in Table 4.4.3. Figure 4.4.14(a) and (b) show the waveforms for charging and discharging modes for one T_S. The charging C_0 and discharging C_0 groups can be seen. Notice that the resonant current is flowing during the off-time, the resonant current starts at zero value at the beginning of $T_{HF}/2$ and ends at zero at the end of the interval. Therefore, the soft-switching behavior can be appreciated. This is the current that charges C_0 when v_{DC1} is delivering energy in Figure 4.4.14(a). In addition, the accumulation and transfer time intervals are shown in the figure. Figure 4.4.14(b) shows the same signals but when the converter is extracting energy from the C_0 and delivering to V_{DC1}. Again, the different time intervals can be appreciated.

Figure 4.4.15(a) shows a complete charge and discharge process from an input source in the range of 225 V to 115 V. The grid is absorbing and delivering the power. The converter can work from the maximum voltage to almost 50% of the maximum voltage, which is the recommended voltage for supercapacitors. If a wider voltage range is needed, a bigger C_0 should be added. In addition, some disturbances in $V_{DC2}=V_{C0}$ can be seen due to the converter trying to keep V_{DC2} in a proper range by changing the modes (charging and discharging mode) every switching cycle.

Figure 4.4.15(b) shows the output signals when the prototype is delivering active power. In spite of the noisy v_2 signal, the output current has low distortion. In Figure 4.4.15(b), the spectrum of this signals is plotted, it can be seen that the main harmonics are the 2nd, the 3rd and the 4th, and the experimental measurements match with the simulations.

Figure 4.4.16 shows the measured efficiency of the converter as a function of the output power in both modes: charging and discharging the energy storage device at two voltage levels. The efficiency of the proposed converter is compared with two traditional inverters: unipolar PWM and bipolar PWM inverters (obtained by simulations). The same power level, switching frequency and switches were used. These topologies are very efficient but they work as a step-down converter. Therefore, they do not increase the voltage to charge the energy storage device, so they need a step-up DC/DC converter in cascade and they do not provide isolation. The proposed converter is also compared to a

cascade between the bipolar PWM converter, a bidirectional series resonant converter [111] with a impedance-source inverter (ZSI) [232] (again by simulation and by using the same switches and switching frequency and power level). The results show that the proposed converter has a lower efficiency than the cascade of a bipolar PWM and a series resonant DC/DC converter. However, the reduction of switches makes the converter attractive. The efficiency can be increased by adding switches in parallel, because as the converter has reduced switching losses, the conduction power losses are the main component of the losses.

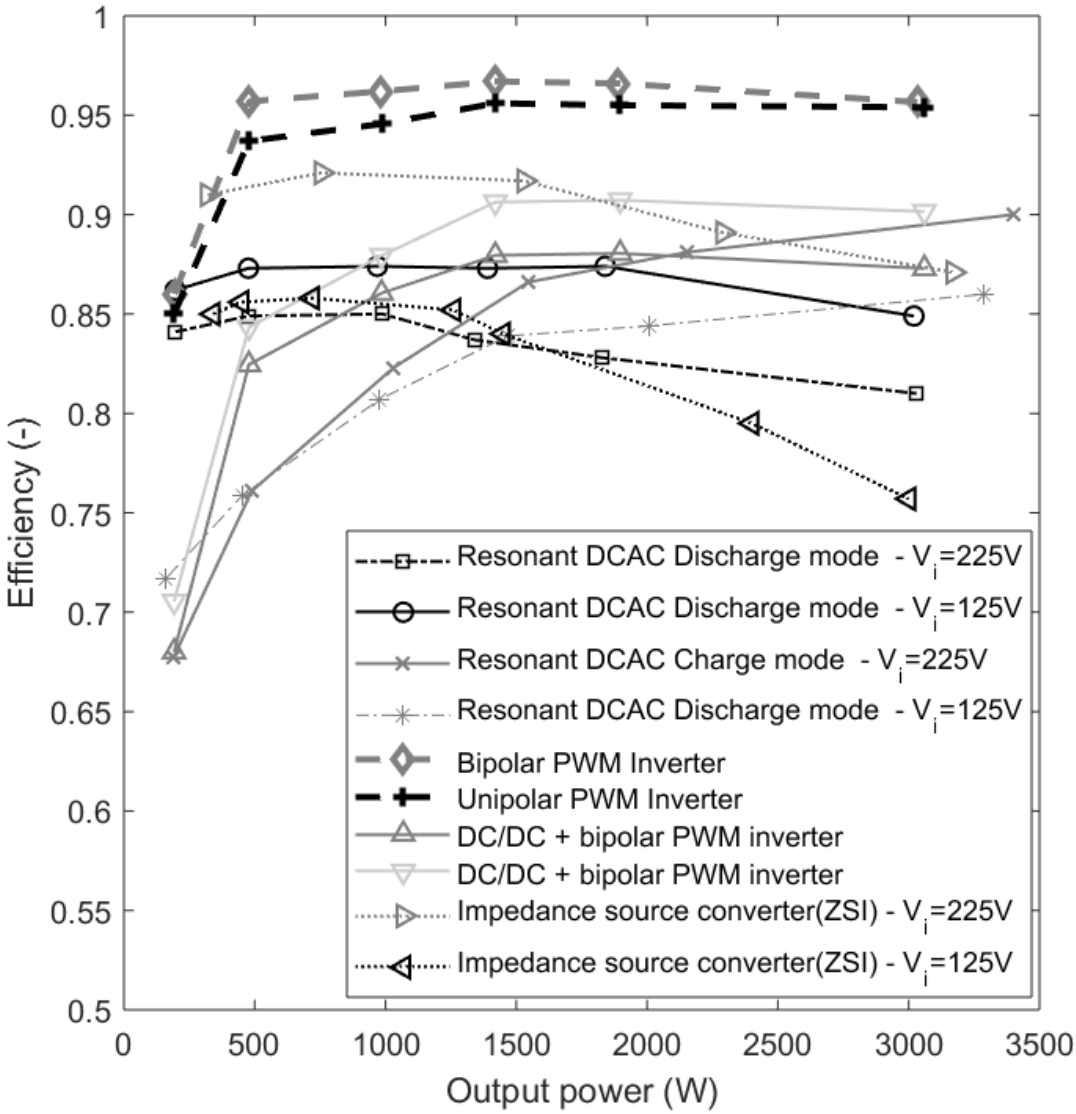

Figure 4.4.16–Efficiency

4.4.8. Summary

This section presents a novel bidirectional series resonant DC//DC/AC converter for energy storage applications. This converter delivers an AC signal with the traditional series resonant DC/DC dual active bridge topology. However, in the proposed operation mode, a high frequency signal charges a DC link capacitor located at port DC2 while the output filter delivers the AC low-frequency power signal. By using this technique, it is not necessary to use a step-up DC/DC converter in cascade with an inverter, as the converter can perform both the DC/DC and the DC/AC conversions. Furthermore, as the topology includes a HF transformer, a grid-frequency isolation transformer is not needed in the AC side. This reduces the cost of the whole energy storage system. Therefore, the proposed circuit can replace the three power stages of a traditional ESS: the converters and the isolation transformer. This is the main novelty of the converter: a three-port system with one isolated DC port, non-isolated DC port and an AC port.

However, the main drawback is that distortion is slightly increased in comparison with unipolar and bipolar PWM inverters and the efficiency is decreased. The distortion can be controlled based on the switching and resonant frequencies and the output filter. The efficiency can also be increased by adding MOSFETs in parallel, because the power losses are mainly conduction losses due to the soft switching technique. The section gives some guidelines to the design procedure based on the model and shows a prototype that validates the design.

The proposed topology was also compared with other topologies such as ZSI and cascading a DC/DC and a DC/AC, the results shows that efficiency is slightly lower but the proposed technique reduces many components of the system. Thus, it can be applied for low and medium power systems. The details of this section were published in [31].

To conclude, this new circuit allows the possibility to have in a single circuit as a combination of a DC isolated port, a non-isolated DC port and a non-isolated AC port: AC/DC//DC. This resonant partial isolated converter opens new possibilities for compact solutions which will reduce price in EV chargers. The solution proposed here is a single-

phase inverter, therefore, as future works, three-phase AC port must be included. In addition, in case that more ports are needed non-isolated converters can be attached as shown in Section 4.1, or eventually a multiple-winding transformer can be added as in the multiple active bridge converter in Chapter 2. The current challenge in this compact solution is the reduced efficiency, thus, main efforts must be done on increasing the converter efficiency.

CONCLUSIONS

The research work explains in detail the current state of the art of the elements in an EV charger, and proposes several contributions to increase its features in terms of new functions, smaller size and higher efficiency. The work focuses on the development of new control techniques and new circuit topologies that allow multiple port systems such as EV chargers to work efficiently in terms of low power losses with ease of extending to large number of ports and implementation in real hardware based on industrial microprocessors. The dissertation has three main parts: multiple port converters, advanced modeling and control for inverters and partially isolated converters. The main contributions of each part are summarized below.

Multiple port converters: Based on Multiple Active Bridge (MAB) converter topology, a new modeling inspired on grid-tied inverters was developed in order to create a new control method which allows MAB converters to have a variable range of DC voltage in each port. The results are new possibilities for using that circuit to connect directly to batteries, supercapacitors, PV panels and other DC sources. The results show that a high-efficient multiple port converter can be used in many applications such as EV chargers, smart houses, multi-source/multi-load systems, hybrid energy storage systems and many others.

It is worth mentioning that, in comparison to other solutions for multi-port systems, such as a set of two-port converters, this research work opens new possibilities for the use of multiple active bridge converter. The impact of this work is on the cost and size of the multi-port system in terms of reducing the number of components and efficiency increase. In comparison with other control methods using the same topology, it was clarified in the research work that the modulations and control technique was oriented to variable DC ports and, in that condition, the proposal has a better efficiency.

Particularly, the results show a validation of a new mathematical model for describing the multiple active bridge based on dq-frame working at high-frequencies, at the switching frequency of the converter. Using that model, a decoupling control method

that allows the use of any number of ports in a multiple active bridge converter and allows transferring energy from any port to any other port without sending power to any third port was proposed. The method also allows controlling the reactive power in the converter for the first time. With this new degree of freedom, soft-switching techniques can be implemented to reduce the power losses. In addition, the control method compensates the effect of the voltage change in the DC ports which results in a higher converter's efficiency in comparison with other control methods (single phase shift method) in the condition of non-equal voltage at the DC ports. As an additional novelty, a specific modulation called "dual duty" was proposed and implemented in order to reduce conduction losses and increase efficiency for power delivery. The aim of this modulation technique is to minimize the root mean square current through the transformer's windings.

Advanced modeling and control for inverters. Emphasis was put on improving the active and reactive power sharing in the grid using inverters. In the future, EV chargers should be able to absorb energy from the grid (charging the EV battery) but also provide services to the grid by delivering energy (vehicle-to-grid, V2G mode). For that, inverters can be used in multi-master mode, connected to the grid and control the voltage in their nodes but also accept power from other nodes in a power-sharing fashion. This thesis introduces new elements for improving transients and reducing power oscillations when inverters are connected to the grid as masters or grid-forming inverters. Concretely, the results are a reduction in power oscillations during connection transients by means of power filters, virtual impedance and the introduction of a phase limiter. The phase limiter is a new method to control and limit the output power of inverters during transients. Moreover, the controller of the inverter should tolerate changes in the grid, thus, an adaptive controller was proposed which controls the output current of the inverter and compensated the possible harmonics.

Partially isolated multi-port converters. The previous solution guarantees that all ports have galvanic isolation which increases the safety of the system. However, it might not be required that all of the ports have this feature but only some of them. Then, two main alternatives can be used: non-isolated converters with isolated inverter, which can give a partial isolated solution for EV chargers, however, isolated inverters are bulky.

This dissertation introduces a better solution based on resonant inverters. This resonant multi-port converter is a more compact alternative, but has a limited number of isolated ports. The proposed solution is based on resonant power flow and an overmodulation which allow an AC grid-frequency power flow and a resonant power flow through high frequency transformers to provide isolation.

The proposed resonant partial isolated converter is promising due to the compactness of the solution. However, this circuit is still in an early stage due to its limited efficiency. This makes the MAB converter combined with the inverter a more viable industrial solution. The main drawback of the resonant converter is its efficiency transferring energy from AC to isolated DC due to the hard-switching technique in the AC/DC conversion process. Advanced semiconductors and soft-switching techniques can be applied to improve the converter's efficiency and make it more competitive.

Future works are also divided in different aspects. In MAB converters: the use of reactive power control to achieve soft-switching and increase efficiency in its current form. In addition, other impedance structures can be explored such as multi-port resonant converters and the use of bidirectional switches in order to transform some of the DC ports of a MAB converter to AC ports to be able to connect to the grid.

In inverters, further tests in distributions grids should be done in order to achieve cooperation between them to assist the grid. This thesis shows the basis but the interaction between inverters and the grid can still be explored.

Finally, in terms of partially isolated converters, the proposed solution is ambitions but suffers from low efficiency. Efforts should be done to achieve soft-switching in that configuration and to explore a three-phase version.

In general, all of the topics can be implements in the power electronic industry in the close future because they do not require any special element, thus, the proposed benefits can be included in future products.

PUBLICATIONS OF THE AUTHOR ON THE SUBJECT OF THE DISSERTATION

A1. AlSadat M. Using low bandwidth communication through power lines to enhance reactive power sharing for inverters-based microgrids / M. AlSadat, F.M. Ibanez, I. Elghanam, V. Terzija // International Journal of Electrical Power & Energy Systems – 2024 – Vol. 159 – P. 110043

A2. Ibanez, F.M. Control method based on real–imaginary decomposition at the switching frequency for multiple active bridge converters / F.M. Ibanez, A. Shubnaya, F. Martin // IET Power Electron – 2024 – Vol. 17 – P. 1287–1300..

A3. A. Shubnaya. Minimizing conduction losses in multiple active bridge converters across wide voltage ranges using advanced dual-duty modulation / A. Shubnaya, M. Koksharov, F. Martin, A. Galarza, F.M. Ibanez // IET Power Electron. – 2024 – Vol 17 – P. 2698–2713.

A4. Ibanez F.M. Improving the power sharing transients in droop-controlled inverters with the introduction of an angle difference limiter / F.M. Ibanez, M. AlSadat, Y. Vlasov, V. Peric, P. Vorobev // International Journal of Electrical Power & Energy Systems – 2023 – Vol. 153 – P. 109371.

A5. P.K. Barik. A novel negative feedback phase locked loop-based reference current generation technique for shunt active power filter / Barik PK, Shankar G, Sahoo P.K., Elavarasan RM, Kumar S, Ibanez F.M., Houran M. A., Srivastava A. K., Terzija V. // International Journal of Electrical Power & Energy Systems – 2023 – Vol. 153 – P. 109389.

A6. Davalos Hernandez F. A Dual-Input High-Gain Bidirectional DC/DC Converter for Hybrid Energy Storage Systems in DC Grid Applications / F. Davalos Hernandez, R. Samanbakhsh, P. Mohammadi, F.M. Ibanez // IEEE Access – 2021 –Vol. 9 – P. 164006-164016.

A7. Ibanez F.M. Bidirectional Series Resonant DC/AC Converter for Energy Storage Systems / F.M. Ibanez // IEEE Transactions on Power Electronics – 2019 –Vol.

34(4) – P. 3429-3444.

A8. Florez-Tapia AM. Small signal modeling and transient analysis of a Trans quasi-Z-source inverter / AM Florez-Tapia, FM Ibanez, J Vadillo, I Elosegui, J.M. Echeverria // Electric Power Systems Research – 2017 – Vol. 144 – P. 52-62.

A9. Ibanez F.M. State-Plane Analysis of Anomalous Step-Up Behavior in Series-Resonant Converters / F.M. Ibanez, J.M. Echeverria, J. Vadillo, L. Fontan // IEEE Journal of Emerging and Selected Topics in Power Electronics – 2016 – Vol 4. No 3 – P. 1026-1035.

A10. Ibanez, F.M. Multimode step-up bidirectional series resonant DC/DC converter using continuous current mode / F.M. Ibanez, J.M. Echeverria, D. Astigarraga, L. Fontan // IET Power Electronics – 2016 – Vol. 9 – P. 710-718.

A11. Ibanez F.M. A Step-Up Bidirectional Series Resonant DC/DC Converter Using a Continuous Current Mode / F.M. Ibanez, J.M. Echeverria, J. Vadillo, L. Fontan // IEEE Trans. on Power Electronics – 2015 –Vol. 30(3) – P. 1393-1402.

A12. Ibanez F. M. High-Current Rectifier Topology Applied to a 4-kW Bidirectional DC–DC Converter / F. Ibanez, J. M. Echeverria, J. Vadillo L. Fontan // IEEE Transactions on Industry Applications – 2014 – Vol. 50(1) – P. 68-77.

A13. Ibanez, F.M. Frequency response analysis for bidirectional series-resonant DC/DC converter in discontinuous mode / F. M. Ibanez, J.M. Echeverria, J. Vadillo, L. Fontan // IET Power Electronics – 2014 – Vol. 7 – P. 2374-2386.

A14. F. M. Ibanez. Novel technique for bidirectional series-resonant DC/DC converter in discontinuous mode / F.M. Ibanez, J.M. Echeverria, L. Fontan // IET Power Electronics – 2013 – Vol. 6. – P. 1019-1028.

A15. Veretennikov I. Proportional Multiresonant Controller with Automatic Gains Adjustment for Grid-Connected Inverters / I. Veretennikov, Y. Vlasov, F.M. Ibanez, V. Terzija, A.A. Nazeri // Proc. IEEE Belgrade PowerTech –2023 –P. 1-6. DOI: 10.1109/PowerTech55446.2023.10202847

A16. AlSadat M. Improving Transients for Droop-Controlled Inverters / M. AlSadat, Y. Vlasov, P. Vorobev, V. Terzjia, F. Ibanez, V.S. Perić // Proc. IEEE Appl.

Power Electron. Conf. Expo. (APEC) – 2023 –P. 1-6. DOI: 10.1109/APEC43580.2023.10131238.

A17. Shubnaya A. Compensating measurement delays in decoupling blocks of dq control technique for multiple active bridge converter / A. Shubnaya, F.M. Ibanez, P. Rodriguez Cortes // Proc. 48th Annu. Conf. IEEE Ind. Electron. Soc. (IECON) –2022 – P. 1-6. DOI: 10.1109/IECON49645.2022.9968549.

A18. Ibanez F.M. Limiting transients for grid-forming inverters using a phase limiter / F.M. Ibanez, M. AlSadat, Y. Vlasov, P. Vorobev, V. Terzija, P. Pant, V. Peric // Proc. of 11th International Conference on Renewable Energy Research and Application (ICRERA) – IEEE – 2022 –P. 1–6. DOI: 10.1109/ICRERA55966.2022.9922712.

A19. Nazeri A.A. Paralleled Modified Droop-Based Voltage Source Inverter for 100% Inverter-Based Microgrids / A.A. Nazeri, P. Zacharias, F.M. Ibanez, I. Idrisov // Proc. IEEE Ind. Applic. Soc. Annu. Meeting (IAS) – 2021 –P. 1-6. DOI: 10.1109/IAS48185.2021.9677365.

A20. AlSadat M. Reactive Power Sharing Utilizing Low Bandwidth Communication Through Power Lines / M. AlSadat, F.M. Ibanez // Proc. IEEE Power Energy Soc. Gen. Meet. (PESGM) – 2021 –P. 1-5. DOI: 10.1109/PESGM46819.2021.9638164.

A21. Nazeri A.A. Design of Proportional-Resonant Controller with Zero Steady-State Error for a Single-Phase Grid-Connected Voltage Source Inverter with an LCL Output Filter / A.A. Nazeri, P. Zacharias, F.M. Ibanez, S. Somkun // Proc. IEEE Milan PowerTech –2019 –P. 1-6. DOI: 10.1109/PTC.2019.8810649.

A22. Majidi M. A guideline for modeling voltage and frequency controls in ac microgrids: The influence of line impedance on transient time / M. Majidi, A.A. Nazeri, F.M. Ibanez, D. Pozo // Proc. IEEE Milan PowerTech – 2019 –P. 1-6. DOI: 10.1109/PTC.2019.8810772.

A23. Mohammadi P. High Frequency Transformer Design for Specific Static Magnetising and Leakage Inductances Using Combination of Multi-Layer Perceptron Neural Networks and FEM Simulations / P. Mohammadi, R. Samanbakhsh, P. Koohi, F. Ibanez // Proc. of IEEE 10th International Symposium on Power Electronics for

Distributed Generation Systems (PEDG), IEEE – 2019 – P. 1–6. DOI: 10.1109/PEDG.2019.8807556.

A24. Mohammadi P. A Novel Non-Coupled Non-Isolated Double-Input Bidirectional High-Gain Converter for Hybrid Energy Storage System / P. Mohammadi, R. Samanbakhsh, F.D. Hernandez, P. Koohi, F.M. Ibanez // Proc. IEEE 10th Int. Symp. Power Electron. Distrib. Gener. Syst. (PEDG) – 2019 –P. 1-6. DOI: 10.1109/PEDG.2019.8807556.

A25. Ibanez F.M. Anomalous step-up behavior in discontinuous series resonant converters / F.M. Ibanez, J. Vadillo, J.M. Echeverria, L. Fontan // Proc. IEEE Workshop Control Model. Power Electron. (COMPEL) –2014 –P. 1-6. DOI: 10.1109/COMPEL.2014.6877129

A26. Ibanez F. M. 100kW bidirectional DC/DC converter for a supercapacitor stack / F. M. Ibanez, J. Vadillo, J. M. Echeverria L. Fontán // IEEE PES ISGT Europe – 2013 –P. 1-5. DOI: 10.1109/ISGTEurope.2013.6695246.

A27. Ibanez F. M. 25kW DC/DC Converter applied to a supercapacitor stack / /F. M. Ibanez, J. M. Echeverria, J. Vadillo and L. Fontán // Proc. 2012 Electrical Systems for Aircraft, Railway and Ship Propulsion – 2012 – P. 1-6. DOI: 10.1109/ESARS.2012.6387429.

A28. Патент No 2831526 Российская Федерация, СПК H02J 7/00 (2024.08). ЗАРЯДНОЕ УСТРОЙСТВО ДЛЯ ЭЛЕКТРОМОБИЛЕЙ С НЕСКОЛЬКИМИ ИСТОЧНИКАМИ ЭНЕРГИИ: No 2024122493: заявлено 06.08.2022: опубликовано: 09.12.2024 / Ибаниес Федерико Мартин, Власов Ярослав, Сергеевич, Веретенников Илья Олегович, Идрисов Ильдар Наилевич, Афонин Михаил, Михайлович.; заявитель и патентообладатель Сколковский институт науки и технологий. – 14 с.

BIBLIOGRAPHY

1. Lu. J. Multimode Operation for On-Line Uninterruptible Power Supply System / J. Lu., M. Savaghebi, S. Golestan, J. C. Vasquez, J. M. Guerrero, A. Marzabal // IEEE J. Emerg. Sel. Top. Power Electr. – 2019 – Vol. 7(2) – P. 1181–1196.

2. Wu F. TAB Series-Resonant DC-DC Converter and Multi-Phase-Shift Based Global Optimization Modulation/ F. Wu, K. Wang, J. Su // Appl. Sci. (Basel) – 2022 – Vol. 12(13) – P. 67-83.

3. Oluwasogo E.S. Self-Current Sharing in Dual-Transformer-Based Triple-Port Active Bridge DC–DC Converter With Reduced Device Count / E. S. Oluwasogo, H. Cha // IEEE Trans. Power Electron. – 2021 – Vol. 36(5) – P. 5290–5301

4. Zhang X. Research on Power Decoupling and Parameter Mismatch of Three-Port Isolated Resonant DC-DC Converter Applied Switch Controlled Capacitor / X. Zhang, H. Liu, P. Wheeler, F. Wu // IEEE Trans. Ind. Electron. – 2023 – Vol. 70(8) – P. 8098–8107.

5. Pereira T. Self-Tuning Multiport Resonant DC/DC Converter Based on Actively-Controlled Inductors for Hybrid Storage System Integration / T. Pereira, Y. Wei, Y. Pascal, H. A. Mantooth, M. Liserre // IEEE, Transl. Power Electron – 2022 – Vol. 38(4) – P. 4787-4804.

6. Cao L. An Immittance-Network-Based Multiport ZVS Bidirectional Converter With Power Decoupling Capability / L. Cao, J. Lin, X. Jiang, C. S. Wong, K. Loo // IEEE Trans. Power Electron – 2022 – Vol. 37(10) – P.12729–12740.

7. Zhao C. An isolated three-port bidirectional dc-dc converter with decoupled power flow management / C. Zhao, S. D. Round, J. W. Kolar // IEEE Trans. Power Electron. – 2008 – Vol. 23(5) – P. 2443–2453.

8. Koohi P. A survey on multi-active bridge dc-dc converters: Power flow decoupling techniques, applications, and challenges / P. Koohi, A. J. Watson, J. C. Clare, T. B. Soeiro, P. W. Wheeler // Energies – 2023 – Vol. 16(16) – P. 5927.

9. Mohammadi P. High Frequency Transformer Design for Specific Static Magnetising and Leakage Inductances Using Combination of Multi-Layer Perceptron Neural Networks and FEM Simulations / P. Mohammadi, R. Samanbakhsh, P. Koohi, F. Ibanez // Proc. of IEEE 10th International Symposium on Power Electronics for Distributed Generation Systems (PEDG), IEEE – 2019 – P. 1–6. DOI: 10.1109/PEDG.2019.8807556.

10. Shao S. Modeling and Advanced Control of Dual-Active-Bridge DC–DC Converters: A Review / S. Shao, L. Chen, Z. Shan, F. Gao, H. Chen, D. Sha, T. Dragičević // IEEE Trans. Power Electron – 2022 – Vol. 37(2) – P. 1524–1547.

11. Ibanez F. M. An Impedance Based Modeling Towards the Aging Prediction of Lithium-Ion Battery for EV Applications / Ibanez, T. Ahmed, I. Idrisov, J. S. Gutierrez // Proc. of 8th International Conference on Renewable Energy Research and Applications (ICRERA) – IEEE, 2019 – P. 1–6. DOI: 10.1109/ICRERA47325.2019.8996931.

12. Ibanez F. M. Design Balancing Systems for Supercapacitors Based on Their Stochastic Model / F. M. Ibanez, I. Idrisov, F. Martin, A. Rujas // IEEE Trans. Energ. Convers. – 2020 – Vol. 35(2) – P. 733–745

13. Zhao C. A novel three-phase three-port UPS employing a single high-frequency isolation transformer / C. Zhao, J.W. Kolar // Proc. of IEEE 35th Annual Power Electronics Specialists Conference (APEC'04) – IEEE – 2004 – P. 4061–4067. DOI: 10.1109/PESC.2004.1354917

14. Wang L. Asymmetrical duty cycle control and decoupled power flow design of a three-port bidirectional DC-DC converter for fuel cell vehicle application / L. Wang, Z. Wang, H. Li // IEEE Trans. Power Electron. – 2012 – Vol. 27(2) – P. 891–904.

15. Duarte J.L. Three-port bidirectional converter for hybrid fuel cell systems. / J. L. Duarte, M. Hendrix, M. G. Simoes // IEEE Trans. Power Electron. – 2007 – Vol. 22 No 2 – P. 480–487.

16. Neubert M. Performance analysis of a triple-active bridge converter for interconnection of future dc-grids / M. Neubert, A. Gorodnichev, J. Gottschlich, R.W. De Doncker // Proc. of IEEE Energy Conversion Congress and Exposition (ECCE'16) – IEEE – 2016 – P. 1–8. DOI: 10.1109/ECCE.2016.7855317.

17. Falcones S. A DC–DC multiport-converter-ba.sed solid-state transformer integrating distributed generation and storage / Falcones, S., Ayyanar, R., Mao, X. // IEEE Trans. Power Electron – 2013 – Vol. 28(5) – P. 2192–2203.

18. Costa L.F. Optimum design of a multiple-active-bridge DC–DC converter for smart transformer / L.F. Costa, G. Buticchi, M. Liserre // IEEE Trans. Power Electron. – Vol. 33(12) – P. 10112–10121.

19. Karanayil B. Power flow management of isolated multiport converter for more electric aircraft / B. Karanayil, M. Ciobotaru, V.G. Agelidis // IEEE Trans. Power Electron – 2017 – Vol. 32(7) – P. 5850–5861.

20. N.D. Dao. High-efficiency SiC-based isolated three-port DC/DC converters for hybrid charging stations / Dao, N.D., Lee, D., Phan, Q.D. // IEEE Trans. Power Electron. – 2020 – Vol 35(10) – P. 10455–10465.

21. Rashidi, M. Design and development of a high-frequency multiport solid-state transformer with decoupled control scheme / M. Rashidi, N.N. Altin, S.S. Ozdemir, A. Bani-Ahmed, A. Nasiri // IEEE Trans. Ind. Appl. – 2019 – Vol.55(6) – P. 7515–7526.

22. Hebala O.M. Generalized active power flow controller for multiactive bridge DC–DC converters with minimum-current-point-tracking algorithm / O.M. Hebala, A.A. Aboushady, K.H. Ahmed, I. Abdelsalam // IEEE Trans. Ind. Electron. – 2022 – Vol. 69(4) – P. 3764–3775.

23. Vermulst B.J. Scalable multi-port active-bridge converters: Modelling and optimised control / B.J. Vermulst, J.L Duarte, E.A. Lomonova, K.G. Wijnands // IET Power Electron – 2017 –Vol. 10 – P. 80–91.

24. Yazdania A. Voltage-Sourced Converters in Power Systems: Modeling, Control, and Applications / A. Yazdani, R. Iravani. – Hoboken : Wiley-IEEE Press, 2010. – 552 p.

25. Bin W. Current-Source Converter and Cycloconverter Topologies for Industrial Medium-Voltage Drives / W. Bin, J. Pontt, J. Rodriguez, S. Bernet, S. Kouro // IEEE Transactions on Ind. Electronics – 2008 – Vol. 55(7) – P. 2786–2797.

26. Gupta K. K. Multilevel Inverter Topologies With Reduced Device Count: A Review / K. K. Gupta, A. Ranjan, P. Bhatnagar, L. K. Sahu, S. Jain // IEEE Transactions on Power Electron – 2016 – Vol. 31(1) – P. 135-151.

27. Liu Q. Review and Comparison of Grid-Tied Inverter Controllers in Microgrids / Q. Liu, T. Caldognetto and S. Buso // IEEE Transactions on Power Electronics – 2020 – Vol. 35(7) – P. 7624-7639.

28. Kumar Barik P. A novel negative feedback phase locked loop-based reference current generation technique for shunt active power filter / P. Kumar Barik, G. Shankar, P. Kumar Sahoo, R. Madurai Elavarasan, Sachin Kumar, F. M. Ibanez, M. Abou Houran, Ankit Kumar Srivastava, Vladimir Terzija // International Journal of Electrical Power & Energy Systems – 2023 – Vol. 153 – P. 109389.

29. Meng X. A Generalized Droop Control for Grid-Supporting Inverter Based on Comparison Between Traditional Droop Control and Virtual Synchronous Generator Control / X. Meng, J. Liu, Z. Liu // IEEE Trans Power Electron. – 2019 – Vol. 34(6) – P. 5416–5438.

30. Kazimierczuk M. K. Resonant Power Converters / M.K. Kazimierczuk, D. Czarkowski. – New York: Wiley-Interscience, 1995 – 456 p.

31. Ibanez F.M. Bidirectional Series Resonant DC/AC Converter for Energy Storage Systems / F.M. Ibanez // IEEE Transactions on Power Electronics – 2019 –Vol. 34(4) – P. 3429-3444.

32. Ibanez F.M., State-Plane Analysis of Anomalous Step-Up Behavior in Series-Resonant Converters / F.M. Ibanez, J.M. Echeverria, J. Vadillo, L. Fontan // IEEE Journal of Emerging and Selected Topics in Power Electronics – 2016 – Vol 4.(3) – P. 1026-1035.

33. Ibanez, F.M. Multimode step-up bidirectional series resonant DC/DC converter using continuous current mode / F.M. Ibanez, J.M. Echeverria, D. Astigarraga, L. Fontan // IET Power Electronics – 2016 – Vol. 9 – P. 710-718.

34. Ibanez F.M. A Step-Up Bidirectional Series Resonant DC/DC Converter Using a Continuous Current Mode / F.M. Ibanez, J.M. Echeverria, J. Vadillo, L. Fontan // IEEE Trans. on Power Electronics – 2015 – Vol. 30(3) – P. 1393-1402.

35. Ibanez F.M. Frequency response analysis for bidirectional series-resonant DC/DC converter in discontinuous mode / F. M. Ibanez, J.M. Echeverria, J. Vadillo, L. Fontan // IET Power Electronics – 2014 – Vol. 7 – P. 2374-2386.

36. Ibanez F. M. Novel technique for bidirectional series-resonant DC/DC converter in discontinuous mode / F.M. Ibanez, J.M. Echeverria, L. Fontan // IET Power Electronics – 2013 – Vol. 6 – P. 1019-1028.

37. Ibanez F.M. Limiting transients for grid-forming inverters using a phase limiter / F.M. Ibanez, M. AlSadat, Y. Vlasov, P. Vorobev, V. Terzija, P. Pant, V. Peric // Proc. of 11th International Conference on Renewable Energy Research and Application (ICRERA) – IEEE – 2022 – P. 1–6. DOI: 10.1109/ICRERA55966.2022.9922712.

38. Heider F. Vehicle to grid: Realization of power management for the optimal integration of plug-in electric vehicles into the grid / F. Heider, M. Büttner, J. Link, and C. Wittwer // Proc. Int. Battery, Hybrid Fuel Cell Electr. Vehicle Symp. (EVS) – Stavanger – 2009 – P. 1–8. ID EVS-24-1860016.

39. Deb S. Review of impact of electric vehicle charging station on the power grid / S. Deb, K. Kalita, and P. Mahanta // Proc. Int. Conf. Technol. Advancements Power Energy (TAP Energy) – 2017 – P. 1–6. DOI: 10.1109/TAPENERGY.2017.8397302.

40. Deb S. Impact of electric vehicle charging station load on distribution network / S. Deb, K. Tammi, K. Kalita, and P. Mahanta // Energies – 2018 – Vol. 11(1) – P. 178.

41. Gamboa G. Control strategy of a multi-port, grid connected, direct-DC PV charging station for plug-in electric vehicles. / G. Gamboa, C. Hamilton, R. Kerley, S. Elmes, A. Arias, J. Shen, and I. Batarseh // Proc. Energy Convers. Congr. Expo. (ECCE) – 2010 – P. 1173–1177. DOI: 10.1109/ECCE.2010.5618051

42. Deb S. Review of recent trends in charging infrastructure planning for electric vehicles / S. Deb, K. Tammi, K. Kalita, and P. Mahanta // WIREs Energy Environ – 2018 – Vol. 7(6) – P. 306.

43. Khalid M. R. A Comprehensive Review on Structural Topologies, Power Levels, Energy Storage Systems, and Standards for Electric Vehicle Charging Stations and Their Impacts on Grid / M. R. Khalid, I. A. Khan, S. Hameed, M. S. J. Asghar and J. Ro // IEEE Access – 2021 – Vol. 9 – P. 128069-128094.

44. Onar O. C. and A. Khaligh, Grid interactions and stability analysis of distribution power network with high penetration of plug-in hybrid electric vehicles / O. C. Onar, A. Khaligh // Proc. 25th Annu. IEEE Appl. Power Electron. Conf. Expo. (APEC) – 2010 – P. 1755-1762. DOI: 10.1109/APEC.2010.5433583.

45. Das T. Small-signal stability analysis of power system integrated with PHEVs / T. Das, D. C. Aliprantis // Proc. IEEE Energy Conf. – 2008 – P. 1–4. DOI: 10.1109/ENERGYCON.2008.4793956

46. Yan J. Battery fast charging strategy based on model predictive control / J. Yan, G. Xu, H. Qian, Y. Xu // Proc. IEEE 72nd Veh. Technol. Conf.-Fall – 2010 – P. 1–5. DOI: 10.1109/VETECF.2010.5594472

47. Wang B. Aggregated electric vehicle load modeling in large-scale electric power systems / B. Wang, D. Zhao, P. Dehghanian, Y. Tian, and T. Hong // IEEE Trans. Ind. Appl. – 2020 – Vol. 56(5) – P. 5796-5810.

48. Chukwu U. C. The impact of load patterns on power loss: A case of V2G in the distribution network / U. C. Chukwu // Proc. Clemson Univ. Power Syst. Conf. (PSC) – 2020 – P. 1–4. DOI: 10.1109/PSC50246.2020.9131268.

49. Chukwu U. C. The impact of V2G on power factors / U. C. Chukwu // Proc. Clemson Univ. Power Syst. Conf. (PSC) – 2020 – P. 1–4. DOI: 10.1109/PSC50246.2020.9131269.

50. McCarthy D. The HV system impacts of large scale electric vehicle deployments in a metropolitan area / D. McCarthy, P. Wolfs // Proc. 20th Australas. Univ. Power Eng. Conf. – 2010 – P. 1–6. DOI: 10.1109/AUPEC.2010.5699970.

51. Kaur K. Demand-response management using a fleet of electric vehicles: An opportunistic-SDN-based edge-cloud framework for smart grids / K. Kaur, S. Garg, G. Kaddoum, S. H. Ahmed, F. Gagnon, and M. Atiquzzaman // IEEE Network. – 2019 –Vol. 33(5) – P. 46-53.

52. Johnston D. Impact of electric vehicles on power distribution networks // G. A. Putrus, P. Suwanapingkarl, D. Johnston, E. C. Bentley, M. Narayana // Proc. IEEE Vehicle Power Propuls. Conf. – 2009 – P. 827–831. DOI: 10.1109/VPPC.2009.5289690.

53. Mahalik M. Impacts of plug-in hybrid electric vehicles on the electric power system in Illinois / M. Mahalik, L. Poch, A. Botterud, A. Vyas // Proc. IEEE Conf. Innov. Technol. Efficient Reliable Electr. Supply – 2010 – P. 341–348. DOI: 10.1109/ITCEES.2010.5627698

54. Yano H. A novel charging-time control method for numerous EVs based on a period weighted prescheduling for power supply and demand balancing / H. Yano, K. Kudo, T. Ikegami, H. Iguchi, K. Kataoka, K. Ogimoto // Proc. IEEE PES Innov. Smart Grid Technol. (ISGT) – 2012 – P. 1–6. DOI: 10.1109/ISGT.2012.6175612

55. Canevese S. EV flexibility supply via participation in balancing services: Possible profitability for Italian end users // S. Canevese, D. Cirio, M. Gallanti, A. Gatti // Proc. AEIT Int. Annu. Conf. (AEIT) – 2019 – P. 1–6. DOI: 10.23919/AEIT.2019.8893419.

56. Bayram I. S. Unsplittable load balancing in a network of charging stations under QoS guarantees / I. S. Bayram, G. Michailidis, M. Devetsikiotis // IEEE Trans. Smart Grid – 2015 – Vol. 6(3) – P. 1292-1302.

57. Rodrigues N. A regulated electric vehicle charging scheme in coordination with utility pricing and transformer loading / N. Rodrigues, J. Sharma, S. Vyas, and A. Datta // Proc. IEEE Transp. Electric. Conf. (ITEC-India) – 2019 – P. 1–5. DOI: 10.1109/ITEC-India.2019.8865560.

58. Rizvi S. A. A. Electric vehicles and their impacts on integration into power grid: A review / S. A. A. Rizvi, A. Xin, A. Masood, S. Iqbal, M. U. Jan, and H. Rehman // Proc. 2nd IEEE Conf. Energy Internet Energy Syst. Integr. (EI) – 2018 – P. 1–6. DOI: 10.1109/EI2.2018.8582491.

59. Ramadan H. Assessment of plug-in electric vehicles charging impacts on residential low voltage distribution grid in Hungary / H. Ramadan, A. Ali, and C. Farkas // Proc. 6th Int. Istanbul Smart Grids Cities Congr. Fair (ICSG) – 2018 – P. 105-109.

60. Blumsack S. Long-term electric system investments to support plug-in hybrid electric vehicles / S. Blumsack, C. Samaras, and P. Hines // Proc. IEEE Power Energy Soc. Gen. Meeting-Convers. Del. Electr. Energy 21st Century – 2008 – P. 1-6. DOI: 10.1109/PES.2008.4596843.

61. Farmer C. Modeling the impact of increasing PHEV loads on the distribution infrastructure / C. Farmer, P. Hines, J. Dowds, and S. Blumsack // Proc. 43rd Hawaii Int. Conf. Syst. Sci. (HICSS) – 2010 – P. 1-10. DOI: 10.1109/HICSS.2010.299.

62. Hutchinson S. Power supply for an electric vehicle charging system for a large parking deck / S. Hutchinson, M. Baran, S. Lukic // Proc. IEEE Ind. Appl. Soc. Annu. Meeting (IAS) – 2009 – P. 1-6. DOI: 10.1109/IAS.2009.5324888.

63. Papadopoulos P. Impact of residential charging of electric vehicles on distribution networks, a probabilistic approach / P. Papadopoulos, S. Skarvelis-Kazakos, I. Grau, B. Awad, L.M. Cipcigan, N. Jenkins // Proc. Univ. Power Eng. Conf. (UPEC) – 2010 – P. 1-5. DOI: 10.1109/UPEC.2010.5633307.

64. Fernández L. P. Assessment of the impact of plug-in electric vehicles on distribution networks / L. P. Fernández, T. G. S. Román, R. Cossent, C. M. Domingo, P. Frías // IEEE Trans. Power Syst. – 2011 – Vol. 26(1) – P. 206-213.

65. Zdraveski V. Analyzing the impact of battery electric vehicles on distribution networks using nondeterministic model / V. Zdraveski, P. Krstevski, J. Vuletic, J. Angelov, A.K. Mateska, M. Todorovski // Proc. IEEE 18th Int. Conf. Smart Technol. (EUROCON) – 2019 – P. 1-7. DOI: 10.1109/EUROCON.2019.8861837.

66. Veldman E. Unlocking the hidden potential of electricity distribution grids / E. Veldman, M. Gibescu, A. Postma // Proc. 20th Int. Conf. Exhib. Electr. Distrib. (CIRED) – 2009 – P. 1-4. DOI: 10.1049/cp.2009.0747.

67. Schlee J. The effects of plug-in electric vehicles on a small distribution grid / J. Schlee, A. Mousseau, J. Eggebraaten, B. Johnson, H. Hess, B. Johnson // Proc. 41st North Amer. Power Symp. – 2009 – P. 1-6. DOI: 10.1109/NAPS.2009.5484036.

68. Evans P.B. Impacts of plug-in vehicles and distributed storage on electric power delivery networks / P.B. Evans, S. Kuloor, B. Kroposki // Proc. IEEE Vehicle Power Propuls. Conf. – 2009 – P. 838-846. DOI: 10.1109/VPPC.2009.5289691.

69. Yazdani A. A DC distribution system for power system integration of plug-in hybrid electric vehicles / A. Yazdani, M. Tabari // Proc. IEEE Power Energy Soc. Gen. Meeting – 2013 – P. 1-5. DOI: 10.1109/PESMG.2013.6672772.

70. Orr J. A. Current harmonics, voltage distortion, and powers associated with battery chargers Part I: Comparisons among different types of chargers / J. A. Orr, A. E. Emanuel, D. G. Pileggi // IEEE Trans. Power App. Syst. – 1982 –Vol. PAS-101(8) – P. 2703-2710.

71. Megha A. Analysis of harmonic contamination in electrical grid due to electric vehicle charging / A. Megha, N. Mahendran, R. Elizabeth // Proc. 3rd Int. Conf. Smart Syst. Inventive Technol. (ICSSIT) – 2020 – P. 608-614. DOI: 10.1109/ICSSIT48917.2020.9214165.

72. Kütt L. Electric vehicle charger load current harmonics variations due to supply voltage level differences –Case examples / L. Kütt, E. Saarijärvi, M. Lehtonen, H. Mõlder, J. Niitsoo // Proc. Int. Symp. Power Electron. Electr. Drives Automat. Motion – 2014 – P. 917-922. DOI: 10.1109/SPEEDAM.2014.6872009.

73. Irshad U. B. A Battery Energy Storage Sizing Method for Parking Lot Equipped With EV Chargers / U. B. Irshad, M. S. H. Nizami, S. Rafique, M. J. Hossain, S. C. Mukhopadhyay // IEEE Systems Journal – 2021 – Vol. 15(3) – P. 4459-4469.

74. Sbordone D. EV fast charging stations and energy storage technologies: A real implementation in the smart micro grid paradigm / D. Sbordone, I. Bertini, B. Di Pietra, M. C. Falvo, A. Genovese, L. Martirano // Electric Power Systems Research – 2015 – Vol. 120 – P. 96-108.

75. Castello C.C. Control strategies for electric vehicle (EV) charging using renewables and local storage / C.C. Castello, T.J. LaClair, L.C. Maxey // Proc. IEEE Transp. Electrific. Conf. Expo. (ITEC) – 2014 – P. 1-7. DOI: 10.1109/ITEC.2014.6861835.

76. Yan Q. Optimized Operational Cost Reduction for an EV Charging Station Integrated With Battery Energy Storage and PV Generation / Q. Yan, B. Zhang, M. Kezunovic // IEEE Transactions on Smart Grid – 2019 –Vol. 10(2) – P. 2096-2106.

77. Jia-You Lee. A new UPS topology employing a PFC boost rectifier cascaded high-frequency tri-port converter / Jia-You Lee, Yu-Ming Chang, Fang-Yu Liu // IEEE Transactions on Industrial Electronics – 1999 – Vol. 46(4) – P. 803-813.

78. Ahmed Adam. Analysis, Design, and Performance of Isolated Three-Port UPS Converter for High-Power Applications / Ahmed Adam, A.H. Hou, S. Chen, J. // Proc. IEEE Int. Conf. Environ. Electr. Eng. IEEE Ind. Commer. Power Syst. Eur. (EEEIC/I&CPS Europe) – 2019. DOI: 10.1109/EEEIC.2019.8783501.

79. M. Alsolami. A Gallium-Nitride-Device-Based Switched Capacitor Multiport Multilevel Converter for UPS Applications / Alsolami, M., Potty, K. A., & Wang, J. // IEEE Transactions on Power Electronics – 2017 – Vol.32(9) – P.6853–6862.

80. Li K. Design and Implementation of Four-Port Megawatt-Level High-Frequency-Bus Based Power Electronic Transformer / K. Li et al. //IEEE Transactions on Power Electronics – 2021 – Vol. 36 (6) – P. 6429-6442.

81. S. Granata. Power Electronics Converters for the Internet of Energy: A Review / Granata S, Di Benedetto M, Terlizzi C, Leuzzi R, Bifaretti S, Zanchetta P. // Energies – 2022 – Vol. 15(7) – P. 2604.

82. Yang, Y. Benefit analysis of using multi-port and multi-function power electronic transformer connecting hybrid AC/DC power grids / Y. Yang, W. Pei, W. Deng, S. Zhang // The Journal of Engineering – 2019 – P.1076-1080.

83. Jiang W. Multi-port Power Electric Interface for Renewable Energy Sources / W. Jiang, B. Fahimi // Proc. 24th Annu. IEEE Appl. Power Electron. Conf. Expo. (APEC) – 2009 – P. 347-352. DOI: 10.1109/APEC.2009.4802680.

84. Babaei E. An overview of different topologies of multi-port dc/dc converters for dc renewable energy source applications / E. Babaei, O. Abbasi, S. Sakhavati // Proc. 13th Int. Conf. Electr. Eng./Electron. Comput. Telecommun. Inf. Technol. (ECTI-CON) – 2016 – P. 1-6. DOI: 10.1109/ECTICon.2016.7561420.

85. J. Zeng. An Isolated Multiport DC–DC Converter for Simultaneous Power Management of Multiple Different Renewable Energy Sources / Zeng, J., Qiao, W., Qu, L., & Jiao, Y. //IEEE Journal of Emerging and Selected Topics in Power Electronics – 2014 – Vol. 2(1) – P. 70–78.

86. Swaminathan N. An Overview of High-Conversion High-Voltage DC–DC Converters for Electrified Aviation Power Distribution System / N. Swaminathan Y. Cao // IEEE Transactions on Transportation Electrification – 2020 – Vol. 6(4) – P. 1740-1754.

87. Buticchi G. Multi-port DC/DC converter for the electrical power distribution system of the more electric aircraft / Giampaolo Buticchi, Levy Ferreira Costa, Marco Liserre // Mathematics and Computers in Simulation – 2019 – Vol. 158 – P. 387-402.

88. Ibanez F. M. Extending the Autonomy of a Battery for Electric Motorcycles // F. M. Ibanez, A. M. Beizama Florez, S. Gutiérrez J. M. Echeverrría / IEEE Transactions on Vehicular Technology – 2019 – Vol. 68(4) – P. 3294-3305.

89. Ali M. H. Power Management Strategies for Vanadium Redox Flow Battery and Supercapacitors in Hybrid Energy Storage Systems / M. H. Ali, D. Slaifstein, F. M. Ibanez, C. Zugschwert M. Pugach // 2022 IEEE PES Innovative Smart Grid Technologies Conference Europe (ISGT-Europe) – 2022 – P. 1-5. DOI: 10.1109/ISGT-Europe54678.2022.9960352.

90. Murat Mustafa Savrun. Modeling and control of a new multi-port converter for hybrid energy system integration / Murat Mustafa Savrun, Alihan Atay // Journal of Energy Storage – 2024 – Vol. 96 – P. 112700.

91. Bandyopadhyay S. Control of Multiactive Bridge Converters Using Linear Active Disturbance Rejection / S. Bandyopadhyay, Z. Qin, P. Bauer // IEEE Trans. Ind. Electron. – 2021 – Vol. 61(11) – P. 10688–10698.

92. Cai Y. A Modular Modulation Decoupling Algorithm for Multiple Active Bridge Based Multiport EV Charger / Y. Cai, J. Li, C. Gu, J. Yang, S. Guenter, G. Buticchi, et al. // IEEE J. Emerg. Sel. Top. Power Electron. – 2024 – Vol. 12(4) – P. 3637–3649.

93. Ibanez, F.M. Control method based on real–imaginary decomposition at the switching frequency for multiple active bridge converters / F.M. Ibanez, A. Shubnaya, F. Martin // IET Power Electron – 2024 – Vol. 17 – P. 1287–1300.

94. Shubnaya A. Compensating measurement delays in decoupling blocks of dq control technique for multiple active bridge converter / A. Shubnaya, F.M. Ibanez, P. Rodriguez Cortes // Proc. 48th Annu. Conf. IEEE Ind. Electron. Soc. (IECON) –2022 – P. 1-6. DOI: 10.1109/IECON49645.2022.9968549.

95. Патент No 2831526 Российская Федерация, СПК H02J 7/00 (2024.08). ЗАРЯДНОЕ УСТРОЙСТВО ДЛЯ ЭЛЕКТРОМОБИЛЕЙ С НЕСКОЛЬКИМИ

ИСТОЧНИКАМИ ЭНЕРГИИ: No 2024122493: заявлено 06.08.2022: опубликовано: 09.12.2024 / Ибаниес Федерико Мартин, Власов Ярослав, Сергеевич, Веретенников Илья Олегович, Идрисов Ильдар Наилевич, Афонин Михаил, Михайлович.; заявитель и патентообладатель Сколковский институт науки и технологий. – 14 с.

96. Shubnaya A. Minimizing conduction losses in multiple active bridge converters across wide voltage ranges using advanced dual-duty modulation / A. Shubnaya, M. Koksharov, F. Martin, A. Galarza, F.M. Ibanez // IET Power Electron. – 2024 – Vol 17 – P. 2698–2713.

97. Chandwani A. Three-loop multi-variable control of triple active bridge converter with power flow optimization / A. Chandwani, A. Mallik // Proc. IEEE Appl. Power Electron. Conf. Expo. (APEC) – 2022 – P. 2008-2013. DOI: 10.1109/APEC43599.2022.9773613.

98. Dey S. Switching network loss minimization through multivariable modulation in a multiactive bridge converter / S. Dey, A. Mallik // IEEE Transactions on Industrial Electronics – 2023 – Vol. 70, (11) – P. 10833–10847.

99. Xiao X. Efficiency optimization scheme for isolated triple active bridge DC-DC converter based on minimized reactive power / X. Xiao, K. Wu, H. Wang, X. Zhang // Proc. IEEE Int. Power Electron. Appl. Conf. Expo. (PEAC) – 2022 – P. 1398-1403. DOI: 10.1109/PEAC56338.2022.9959216.

100. Minami K. Machine learning aided optimized modulation in triple active bridge converter / K. Minami, S. Okutani, M. Ohura, P.Y. Huang, Y. Kado // Proc. 48th Annu. Conf. IEEE Ind. Electron. Soc. (IECON) – 2022 – P. 1-6. DOI: 10.1109/IECON49645.2022.9968921.

101. Li J. Efficiency optimization scheme for isolated triple active bridge dc–dc converter with full softswitching and minimized rms current / J. Li, Q. Luo, T. Luo, D., Mou, M. Liserre // IEEE Transactions on Power Electronics – 2022 – Vol. 37(8) – P. 9114–9128.

102. Ibrahim A.A. Conduction loss reduction of isolated bidirectional dc-dc triple active bridge / A.A. Ibrahim, T. Caldognetto, P. Mattavelli // Proc. IEEE 4th Int. Conf. DC Microgrids (ICDCM) – 2021 – P. 1-8. DOI: 10.1109/ICDCM50975.2021.9505009.

103. Zeb K. A comprehensive review on inverter topologies and control strategies for grid connected photovoltaic system / Kamran Zeb, Waqar Uddin, Muhammad Adil Khan, Zunaib Ali, Muhammad Umair Ali, Nicholas Christofides, H.J. Kim // Renewable and Sustainable Energy Reviews – 2018 – Vol. 94 – P. 1120-1141.

104. Veretennikov I. Proportional Multiresonant Controller with Automatic Gains Adjustment for Grid-Connected Inverters / I. Veretennikov, Y. Vlasov, F.M. Ibanez, V. Terzija, A.A. Nazeri // Proc. IEEE Belgrade PowerTech – 2023 – P. 1-6. DOI: 10.1109/PowerTech55446.2023.10202847.

105. Nazeri A.A. Design of Proportional-Resonant Controller with Zero Steady-State Error for a Single-Phase Grid-Connected Voltage Source Inverter with an LCL Output Filter / A.A. Nazeri, P. Zacharias, F.M. Ibanez, S. Somkun // Proc. IEEE Milan PowerTech – 2019 – P. 1-6. DOI: 10.1109/PTC.2019.8810649.

106. Chowdhury, V.R. Robust Control Scheme for a Three Phase Grid-Tied Inverter With LCL Filter During Sensor Failures / V. R. Chowdhury, J. W. Kimball // IEEE Trans. Ind. Electron – 2020 – Vol. 68 – P. 8253–8264.

107. Skogestad S. Multivariable Feedback Control: Analysis and Design / S. Skogestad, I. Postlethwaite. – Hoboken : John Wiley & Sons, 2005 – 592 p.

108. Somkun S. Unified unbalanced synchronous reference frame current control for single-phase grid-connected voltage source converters / S. Somkun, V. Chunkag // IEEE Trans. Ind. Electron. – 2016 – Vol. 63(9) – P. 1398-1409.

109. Konstantinos G. Extending the Symmetrical Optimum criterion to the design of PID type-p control loops / Konstantinos G. Papadopoulos, Nikolaos I. Margaris // Journal of Process Control – 2012 – Vol. 22(1) – P. 11-25.

110. Ibanez F. M. High-Current Rectifier Topology Applied to a 4-kW Bidirectional DC–DC Converter / F. Ibanez, J. M. Echeverria, J. Vadillo L. Fontan // IEEE Transactions on Industry Applications – 2014 – Vol. 50(1) – P. 68-77.

111. Ibanez F. M. 100kW bidirectional DC/DC converter for a supercapacitor stack / F. M. Ibanez, J. Vadillo, J. M. Echeverria L. Fontán // IEEE PES ISGT Europe – 2013 – P. 1-5. DOI: 10.1109/ISGTEurope.2013.6695246.

112. Dannehl J. Limitations of voltage-oriented PI current control of grid-connected PWM rectifiers with LCL filter / J. Dannehl, C. Wessels, F. W. Fuch, // IEEE Trans. Ind. Electron. – 2009 – Vol. 56(2) – P. 380-388.

113. Preitl S. Controller Design Methods for Driving Systems Based on Extensions of Symmetrical Optimum Method with DC and BLDC Motor Applications / Stefan Preitl, Alexandra-Iulia Stînean, Radu-Emil Precup, Zsuzsa Preitl, Emil M. Petriu, Claudia-Adina Dragoş, Mircea-Bogdan Rădac // IFAC Proceedings – 2012 – Vol. 45(3) – P. 264-269.

114. Ali A. Single-Phase Grid-Connected Voltage Source Converter for LCL Filter with Grid-Current Feedback / A. Ali, P. Shanmugham, S. Somkun // Proc. IEEE Electrical Eng. Cong. – 2017 – P. 1-6. DOI: 10.1109/EEC.2017.8242987.

115. Wang J. Delay-dependent stability of single-loop controlled grid-Connected inverters with LCL filters / J. Wang, J. D. Yan, L. Jiang, J. Zou // IEEE Trans. on Power Electron. – 2016 – Vol. 31(1) – P. 743-757.

116. Ufnalski B. Robust tuning of multiresonant current controllers for grid-tied converters and erroneous use of the naslin polynomial method / B. Ufnalski, M. Michalczuk, A. Galecki // IEEE Access – 2022 – Vol. 10 – P. 88211–88225.

117. Zmood D. N. Stationary frame current regulation of PWM inverters with zero steady-state error / D. N. Zmood D. G. Holmes // IEEE Trans. on Power Electron. – 2003 – Vol. 18(3) – P. 814-822.

118. Ibanez F.M. Improving the power sharing transients in droop-controlled inverters with the introduction of an angle difference limiter / F.M. Ibanez, M. AlSadat, Y. Vlasov, V. Peric, P. Vorobev // International Journal of Electrical Power & Energy Systems – 2023 – Vol. 153 – P. 109371.

119. Dannehl J. Filter-based active damping of voltage source converters with LCL filter / J. Dannehl, M. Liserre, F. W. Fuchs // IEEE Trans. Ind. Electron. – 2011 – Vol. 58(8) – P. 3623–3633.

120. Dash P.K. An extended complex Kalman filter for frequency measurement of distorted signals / P.K. Dash, R. K. Jena, G. Panda, A. Routray // IEEE Trans. Instrum. Meas – 2000 – Vol. 49(4) – P. 746–53.

121. McGrath B.P. Power converter line synchronization using a discrete Fourier transform (DFT) based on a variable sample rate / B. P. McGrath, D.G. Holmes, J.J.H. Galloway // IEEE Trans. Power Electron – 2005 – Vol. 20 (4) – P. 877–84.

122. Simon G. An efficient non linear least square multisine fitting algorithm / G. Simon, R. Pintelon, L. Sujbert, J. Schoukens // IEEE Trans. Instrum. Meas. – 2002 – Vol. 51(4) – P. 750–5.

123. Mojiri M. Estimation of power system frequency using adaptive notch filters / M. Mojiri, M. Karimi-Ghartemani, A. Bakshai // IEEE Trans Instrum Meas – 2007 – Vol. 56(6) – P. 2470–7.

124. Lai L. Real-time frequency and harmonic evaluation using artificial neural networks / L. Lai, W. Chan // IEEE Trans. Power Deliv. – 1999 – Vol. 14(1) – P. 52–9.

125. Wang Y.F. Analysis and digital implementation of cascaded delayed-signal-cancellation PLL / Y. F. Wang, Y. W. Li // IEEE Trans. Power Electron. – 2011 – Vol. 26(4) – P. 1067–80.

126. Chen L. PLL-based battery charge circuit topology / L. Chen // IEEE Trans. Ind. Electron. – 2004 – Vol. 51(6) – P. 1344–6.

127. Rodríguez P. A stationary reference frame grid synchronization system for three-phase grid-connected power converters under adverse grid conditions / P. Rodríguez, A. Luna, R. S. Muñoz-Aguilar, I. Etxeberria-Otadui, R. Teodorescu, F. Blaabjerg // IEEE Trans. Power. Electron. – 2012 – Vol. 27(1) – P. 99–112.

128. Jaalam, N. A comprehensive review of synchronization methods for grid-connected converters of renewable energy source / N. Jaalam, N. A. Rahim, A. H. A. Bakar, C. Tan, A. M. A. Haidar // Renewable and Sustainable Energy Reviews – 2016 – Vol. 59 P. 1471–1481.

129. Nazeri A.A. Paralleled Modified Droop-Based Voltage Source Inverter for 100% Inverter-Based Microgrids / A.A. Nazeri, P. Zacharias, F.M. Ibanez, I. Idrisov // Proc. IEEE Ind. Applic. Soc. Annu. Meeting (IAS) – 2021 – P. 1-6. DOI: 10.1109/IAS48185.2021.9677365.

130. Majidi M. A guideline for modeling voltage and frequency controls in ac microgrids: The influence of line impedance on transient time / M. Majidi, A.A. Nazeri,

F.M. Ibanez, D. Pozo // Proc. IEEE Milan PowerTech – 2019 – P. 1-6. DOI: 10.1109/PTC.2019.8810772.

131. Guerrero J. M. Hierarchical control of droop-controlled ac and dc microgrids— a general approach toward standardization / J. M. Guerrero, J. C. Vasquez, J. Matas, L. G. De Vicuna, M. Castilla // IEEE Transactions on Industrial Electronics – 2010 –Vol. 58(1) – P. 158–172.

132. Savaghebi M. Autonomous voltage unbalance compensation in an islanded droopcontrolled microgrid / M. Savaghebi, A. Jalilian, J. C. Vasquez, J. M. Guerrero // IEEE Transactions on Industrial Electronics – 2012 – Vol. 60 (4) – P. 1390–1402.

133. Pogaku N. Modeling, analysis and testing of autonomous operation of an inverter-based microgrid / N. Pogaku, M. Prodanovic, T. C. Green // IEEE Transactions on power electronics – 2007 – Vol. 22(2) – P. 613–625.

134. Vasquez J. C. Modeling, analysis, and design of stationary-reference frame droop-controlled parallel three-phase voltage source inverters / J. C. Vasquez, J. M. Guerrero, M. Savaghebi, J. Eloy-Garcia, R. Teodorescu // IEEE Transactions on Industrial Electronics – 2013 – Vol. 60(4) – P. 1271–1280.

135. Guerrero J. M. Advanced control architectures for intelligent microgrids-part i: Decentralized and hierarchical control / J. M. Guerrero, M. Chandorkar, T.-L. Lee, P. C. Loh // IEEE Transactions on Industrial Electronics – 2013 – Vol. 60(4) – P. 1254–1262.

136. AlSadat M. Improving Transients for Droop-Controlled Inverters / M. AlSadat, Y. Vlasov, P. Vorobev, V. Terzjia, F. Ibanez, V.S. Perić // Proc. IEEE Appl. Power Electron. Conf. Expo. (APEC) – 2023 – P. 1-6. DOI: 10.1109/APEC43580.2023.10131238.

137. Guerrero J. M. Decentralized control for parallel operation of distributed generation inverters using resistive output impedance / J. M. Guerrero, J. Matas, L. G. de Vicuna, M. Castilla, J. Miret // IEEE Transactions on industrial electronics – 2007 – Vol. 54(2) – P. 994–1004, 2007.

138. Lasseter R. H. Grid-Forming Inverters: A Critical Asset for the Power Grid/ R. H. Lasseter, Z. Chen D. Pattabiraman // IEEE Journal of Emerging and Selected Topics in Power Electronics – 2020 – Vol. 8(2) – P. 925-935.

139. Rathnayake D. B. Grid Forming Inverter Modeling, Control, and Applications / D. B. Rathnayake et al. // IEEE Access – 2021 – Vol. 9 – P. 114781-114807.

140. Zhong Q. Universal Droop Control of Inverters With Different Types of Output Impedance / Q. Zhong Y. Zeng // IEEE Access – 2016 – Vol. 4 – P. 702-712.

141. Meng X. A Generalized Droop Control for Grid-Supporting Inverter Based on Comparison Between Traditional Droop Control and Virtual Synchronous Generator Control / X. Meng, J. Liu Z. Liu // IEEE Transactions on Power Electronics – 2019 – Vol. 34(6) – P. 5416-5438.

142. Denis G. The Migrate project: the challenges of operating a transmission grid with only inverter-based generation. A grid-forming control improvement with transient current-limiting control / G. Denis, T. Prevost, M-S. Debry et al. // IET Renewable Power Generation – 2018 –Vol. 12(5) – P. 523-529.

143. Khodadoost Arani A.A. Improving power sharing between parallel voltage source inverters using enhanced droop controller / A.A. Khodadoost Arani, A.H. Nazeri Ardekani, G.B. Gharehpetian // Proc. Smart Grid Conf. (SGC) – 2014 – P. 1-5. DOI: 10.1109/SGC.2014.7090903.

144. Pattabiraman D. Transient Stability Modeling of Droop-Controlled Grid-Forming Inverters with Fault Current Limiting / D. Pattabiraman, R.H. Lasseter, T.M. Jahns // Proc. IEEE Power Energy Soc. Gen. Meet. (PESGM) – 2020 – P. 1-5. DOI: 10.1109/PESGM41954.2020.9281569.

145. Macana C.A. Adaptive synchronous reference frame virtual impedance controller for accurate power sharing in islanded ac-microgrids: A faster alternative to the conventional droop control / C.A. Macana, H.R. Pota // Proc. IEEE Energy Convers. Congr. Expo. (ECCE) – 2017 – P. 3728-3735. DOI: 10.1109/ECCE.2017.8096659.

146. AlSadat M. Reactive Power Sharing Utilizing Low Bandwidth Communication Through Power Lines / M. AlSadat, F.M. Ibanez // Proc. IEEE Power

Energy Soc. Gen. Meet. (PESGM) – 2021 – P. 1-5. DOI: 10.1109/PESGM46819.2021.9638164.

147. Rodríguez P. Flexible Grid Connection and Islanding of SPC-Based PV Power Converters / P. Rodríguez, C. Citro, J.I. Candela, J. Rocabert, A. Luna // IEEE Trans. Ind. Appl. –2018. – Vol. 54(3) – P. 2690-2702.

148. Azevedo G.M.S. A control of microgrid power converter with smooth transient response during the change of connection mode / G.M.S. Azevedo, M.C. Cavalcanti, F.A.S. Neves, L.R. Limongi, F. Bradaschia // Proc. Brazilian Power Electron. Conf. – 2013 – P. 1008-1015. DOI: 10.1109/COBEP.2013.6785238.

149. Farrokhabadi M. Evaluation of droop-based controls in an islanded microgrid with electronically interfaced distributed energy resources / M. Farrokhabadi, C.A. Cañizares, K. Bhattacharya // Proc. IEEE Eindhoven PowerTech – 2015 – P. 1-6. DOI: 10.1109/PTC.2015.7232431.

150. Harasis S. Improved Transient Power Sharing of Droop Controlled Islanded Microgrids / S. Harasis, Y. Sozer // Proc. IEEE Appl. Power Electron. Conf. Expo. (APEC) – 2020 – P. 2346-2351. DOI: 10.1109/APEC39645.2020.9124245.

151. Tamrakar U. Virtual Inertia: Current Trends and Future Directions / U. Tamrakar, D. Shrestha et al. // Applied Sciences – 2017. –Vol. 7(7) – P. 654.

152. Fang J. On the Inertia of Future More electronics Power Systems / J. Fang, H. Li, Y. Tang, F. Blaabjerg // IEEE J. Emerg. Sel. Top. Power Electron. –2019. –Vol. 7(4) – P. 2130-2146.

153. Zhang H. Distributed adaptive virtual impedance control for accurate reactive power sharing based on consensus control in microgrids / H. Zhang, S. Kim, Q. Sun, J. Zhou // IEEE Trans. Smart Grid – 2017 – Vol. 8(4) – P. 1749-1761.

154. Guerrero J.M. Advanced control architectures for intelligent microgrids—part i: Decentralized and hierarchical control / J.M. Guerrero, M. Chandorkar, T. Lee, P.C. Loh // IEEE Trans. Ind. Electron. –2013 – Vol. 60(4) – P. 1254-1262.

155. Hao W. Droop control method of inverter based on variable virtual impedance / W. Hao, C. Zheng, Q. Wang, T. Rui // Proc. 14th IEEE Conf. Ind. Electron. Appl. (ICIEA) – 2019 – P. 1167-1172. DOI: 10.1109/ICIEA.2019.8834228.

156. Lin X. Droop control based on improved virtual impedance in a stand-alone microgrid / X. Lin, R. Zamora, C. Baguley // Proc. IEEE PES GTD Grand Int. Conf. Expo. Asia (GTD Asia) – 2019 – P. 883-888. DOI: 10.1109/GTDAsia.2019.8715894.

157. Marwali M.N. Control of distributed generation systems –part ii: Load sharing control / M.N. Marwali, J.-W. Jung, A. Keyhani // IEEE Trans. Power Electron. – 2004 – Vol. 19(6) – P. 1551–1561.

158. J He J. Analysis, design, and implementation of virtual impedance for power electronics interfaced distributed generation / J. He, Y.W. Li // IEEE Trans. Ind. Appl. – 2011 – Vol. 47(6) – P. 2525–2538.

159. Borup U. Sharing of nonlinear load in parallel connected three-phase converters / U. Borup, F. Blaabjerg, P.N. Enjeti // IEEE Trans. Ind. Appl. – 2001 – Vol. 37(6) – P. 1817–1823.

160. Y. Gupta, K. Chatterjee, S. Doolla, A simple control scheme for improving reactive power sharing in islanded microgrid, IEEE Transactions on Power Systems – 2020 – Vol. 35(4) – P. 3158–3169.

161. Islam S. Distributed secondary controller to ensure proportional sharing of reactive power in ac microgrid / S. Islam, A. Iqbal, S. De, F.I. Bakhsh // Energy Rep. – 2022 – Vol. 8. – P. 6779–6793.

162. Han H. An improved droop control strategy for reactive power sharing in islanded microgrid / H. Han, Y. Liu, Y. Sun, M. Su, J.M. Guerrero // IEEE Trans. Power Electron. – 2015 – Vol. 30(6) – P. 3133–3141.

163. Lyu Z. Adaptive virtual impedance droop control based on consensus control of reactive current / Z. Lyu, Q. Wei, Y. Zhang, J. Zhao, E. Manla // Energies – 2018 – Vol. 11(7) – P. 1801.

164. Babayomi O. Distributed consensus-based reactive power sharing in microgrids: A predictive virtual capacitance control technique / O. Babayomi, Y. Li, Z. Zhang // Int. J. Electr. Power Energy Syst. – 2022 – Vol. 141 – P. 108-139.

165. Micallef A. Performance comparison for virtual impedance techniques used in droop controlled islanded microgrids / A. Micallef, M. Apap, C. Spiteri-Staines, J.M.

Guerrero // Proc. Int. Symp. Power Electron. (SPEEDAM) – 2016 – P. 695-700. DOI: 10.1109/SPEEDAM.2016.7526021.

166. Gothner F. Virtual impedance design for power quality and harmonic sharing improvement in microgrids / F. Gothner, O. Midtgård, R. Torres-Olguin, J. Roldan-Perez // Proc. 20th Workshop Control Model. Power Electron. (COMPEL) – 2019 – P. 1-7. DOI: 10.1109/COMPEL.2019.8769674.

167. Hou S. Distributed control strategy for voltage and frequency restoration and accurate reactive power sharing for islanded microgrid / S. Hou, J. Chen, G. Chen // Energy Rep. –2023 – Vol. 9. – P. 742-751.

168. Yu D. A new modulation-demodulation approach to dc power-line data transmission for srg-integrated microgrid / D. Yu, Y. Hua, S. Yu, P. Zhang, H.H.C. Iu, T. Fernando // IEEE Trans. Power Electron. –2020. – Vol. 35(11) – P. 12370-12382.

169. Liu H. Power talk: A novel power line communication in dc microgrid / H. Liu, Y. Yang, P.C. Loh, F. Blaabjerg, M. Angjelichinoski, C. Stefanovic, P. Popovski // Proc. IEEE 8th Int. Power Electron. Motion Control Conf. (IPEMC-ECCE Asia) – 2016 – P. 2870-2874. DOI: 10.1109/IPEMC.2016.7512825.

170. Choi H.-J. Enhanced power line communication strategy for dc microgrids using switching frequency modulation of power converters / H.-J. Choi, J.-H. Jung // IEEE Trans. Power Electron. – 2017 – Vol. 32(6) – P. 4140-4144.

171. Rathor B. Smart modern ac microgrid monitoring system using power line communication / B. Rathor, G. Jain, R. Jain, P. Sonwane // Proc. 5th IEEE Int. Conf. Recent Adv. Innov. Eng. (ICRAIE) – 2020 – P. 1-5. DOI: 10.1109/ICRAIE51050.2020.9358335.

172. Miller D. The use of power line communication in standalone microgrids / D. Miller, G. Mirzaeva, C.D. Townsend, G.C. Goodwin // IEEE Trans. Ind. Appl. – 2021 – Vol. 57(3) – P. 3029-3037.

173. Mao W. A research on power line communication based on parallel resonant coupling technology in pv module monitoring / W. Mao, X. Zhang, R. Cao, F. Wang, T. Zhao, L. Xu // IEEE Trans. Ind. Electron. –2018. – Vol. 65(3) – P. 2653-2662.

174. AlSadat M. Using low bandwidth communication through power lines to enhance reactive power sharing for inverters-based microgrids / M. AlSadat, F.M. Ibanez, I. Elghanam, V. Terzija // Int. J. Electr. Power Energy Syst. – 2024 – Vol. 159 – P. 110043.

175. Han Y. Review of active and reactive power sharing strategies in hierarchical controlled microgrids / Y. Han, H. Li, P. Shen, E.A.A. Coelho, J.M. Guerrero // IEEE Trans. Power Electron. –2017 –Vol. 32(3) – P. 2427-2451.

176. Albarracin R. Photovoltaic reactive power limits / R. Albarracin, M. Alonso // Proc. 12th Int. Conf. Environ. Electr. Eng. – 2013 – P. 13-18. DOI: 10.1109/EEEIC.2013.6549630.

177. Wang B. A review of impedance matching techniques in power line communications / B. Wang, Z. Cao // Electronics. – 2019 –Vol. 8(9) – P. 1022.

178. Ullah N.R. Wind farms as reactive power ancillary service providers-technical and economic issues / N.R. Ullah, K. Bhattacharya, T. Thiringer // IEEE Trans. Energy Convers. –2009. – Vol. 24(3) – P. 661-672.

179. Kumar L. A multiple source DC/DC converter topology / L. Kumar, S. Jain // Int. J. Electr. Power Energy Syst. – 2013 – Vol. 51 –P. 278-291.

180. Momayyezan M. Integrated reconfigurable configuration for battery/ultracapacitor hybrid energy storage systems / M. Momayyezan, D.B.W. Abeywardana, B. Hredzak, V.G. Agelidis // IEEE Trans. Energy Convers. – 2016 – Vol. 31(4) – P. 1583-1590.

181. Liu D. A ZVS bi-directional DC-DC converter for multiple energy storage elements / D. Liu, H. Li // IEEE Trans. Power Electron. – 2006 – Vol. 21(5) – P. 1513-1517.

182. Ling Z. A new three-port bidirectional DC/DC converter for hybrid energy storage / Z. Ling, H. Wang, K. Yan, Z. Sun // 2015 IEEE 2nd Int. Future Energy Electron. Conf. (IFEEC) – 2015 – P. 1-5. DOI: 10.1109/IFEEC.2015.7361598.

183. Khosrogorji S. A short review on multi-input DC/DC converters topologies / S. Khosrogorji, H. Torkaman, F. Karimi // 2015 6th Int. Power Electron. Drive Syst. Technol. Conf. (PEDSTC) – 2015 – P. 650-654, DOI: 10.1109/PEDSTC.2015.7093351.

184. Ding Z. A novel soft-switching multiport bidirectional dc-dc converter for hybrid energy storage system / Z. Ding, C. Yang, Z. Zhang, C. Wang, S. Xie // IEEE Trans. Power Electron. – 2014 – Vol. 29(4) – P. 1595-1609.

185. Mohammadi P. A Novel Non-Coupled Non-Isolated Double-Input Bidirectional High-Gain Converter for Hybrid Energy Storage System / P. Mohammadi, R. Samanbakhsh, F.D. Hernandez, P. Koohi, F.M. Ibanez // Proc. IEEE 10th Int. Symp. Power Electron. Distrib. Gener. Syst. (PEDG) – 2019 – P. 1-6. DOI: 10.1109/PEDG.2019.8807556.

186. Jabbari M. Resonant Multi-input/Multi-output/Bidirectional ZCS Step-Down DC-DC Converter with Systematic Synthesis for Point-To-Point Power Routing / M. Jabbari, M.S. Dorcheh // IEEE Trans. Power Electron. – 2018 – Vol. 33(7) – P. 6024-6032.

187. Kardan F. A New Three Input DC/DC Converter for Hybrid PV/FC/Battery Applications / F. Kardan, R. Alizadeh, M.R. Banaei // IEEE J. Emerg. Sel. Top. Power Electron. – 2017 – Vol. 5(4) – P. 1771-1778.

188. Zhu B. A multi-input-port bidirectional DC/DC converter for DC microgrid energy storage system applications / B. Zhu, H. Hu, H. Wang, Y. Li // Energies – 2020 – Vol. 13(11) – P. 1-20.

189. Davalos Hernandez F. A Dual-Input High-Gain Bidirectional DC/DC Converter for Hybrid Energy Storage Systems in DC Grid Applications / F. Davalos Hernandez, R. Samanbakhsh, P. Mohammadi, F.M. Ibanez // IEEE Access – 2021 – Vol. 9 – P. 164006-164016.

190. Basso C.P. Switch-Mode Power Supply: SPICE Simulations and Practical Designs / C.P. Basso. – New York : McGraw-Hill Professional, 2008 – 608 p.

191. Bacha S. Power Electronic Converters Modeling and Control with Case Studies / S. Bacha, I. Munteanu, A.I. Bratcu – London : Springer, 2014 – 400 p.

192. Rashid M.H. Power Electronics Handbook / M.H. Rashid – Burlington : Academic Press, 2007 – 1200 p.

193. De Doncker R.W. A three-phase soft-switched high-power density dc/dc converter for high power applications / R.W. De Doncker, D.M. Divan, M.H. Kheraluwala // IEEE Trans. Ind. Electron. – 1991 – Vol. 27(1) – P. 63-73.

194. Lazar J.F. Steady-State Analysis of the LLC Series Resonant Converter / J.F. Lazar, R. Martinelli // Proc. IEEE Appl. Power Electron. Conf. (APEC) – 2001 – Vol. 2 – P. 728-735.

195. Ibanez F. M. 25kW DC/DC Converter applied to a supercapacitor stack / /F. M. Ibanez, J. M. Echeverria, J. Vadillo and L. Fontán // Proc. 2012 Electrical Systems for Aircraft, Railway and Ship Propulsion – 2012 – P. 1-6. DOI: 10.1109/ESARS.2012.6387429.

196. Lee B. Comparative analysis of charging modes of series resonant converter for a energy storage capacitor / B. Lee, C. Hanju // Proc. IEEE Appl. Power Electron. Conf. (APEC) – 2012 – P. 2200-2205. DOI: 10.1109/APEC.2012.6166096.

197. Wolfs P. An analysis of a resonant half bridge dual converter operating in continuous and discontinuous modes / P. Wolfs, L. Quan // Proc. IEEE Power Electron. Spec. Conf. (PESC) – 2002 – P. 1313-1318. DOI: 10.1109/PSEC.2002.1023056.

198. Belaguli V. Series-parallel resonant converter operating in discontinuous current mode / V. Belaguli, A.K.S. Bhat // IEEE Trans. Circuits Syst. I – 2000 – Vol. 47 No.4 – P. 433-442.

199. Li X. Analysis and Design of High-Frequency Isolated Dual-Bridge Series Resonant DC/DC Converter / X. Li, A.K.S. Bhat // IEEE Trans. Power Electron. – 2010 – Vol. 25 No.4 – P. 850-862.

200. Du Y. A Novel Wide Voltage Range Bi-directional Series Resonant Converter with Clamped Capacitor Voltage / Y. Du, X. Bian, S. Lukic, B.S. Jacobson, A.Q. Huang // Proc. IEEE Ind. Electron. Conf. (IECON) – 2009 – P. 82-87. DOI: 10.1109/IECON.2009.5415115.

201. Youssef M.Z. A review and performance evaluation of control techniques in resonant converters / M.Z. Youssef // Proc. IEEE Ind. Electron. Conf. (IECON) – 2004 – P. 215-221. DOI: 10.1109/IECON.2004.1433343.

202. Youssef M.Z. Series-Parallel Resonant Converter in Self-Sustained Oscillation Mode / M.Z. Youssef, P.K. Jain // IEEE Trans. Ind. Electron. – 2007 – Vol. 54(3) – P. 1329-1341.

203. Corradini L. Minimum Current Operation of Bidirectional Dual-Bridge Series Resonant DC/DC Converters / L. Corradini, D. Seltzer, D. Bloomquist, R. Zane, D. Maksimovic, B. Jacobson // IEEE Trans. Power Electron. – 2012 – Vol. 27(7) – P. 3266-3276.

204. Ho W.C. Design and analysis of discontinuous mode series resonant converter / W.C. Ho, M.H. Pong // Proc. IEEE Int. Conf. Ind. Technol. – 1994 – P. 486-489. DOI: 10.1109/ICIT.1994.383999.

205. Chuang Y.C. Battery Float Charge Technique Using Parallel-Loaded Resonant Converter for Discontinuous Conduction Operation / Y.C. Chuang, Y.L. Ke, H.S. Chuang, S.Y. Chang // Proc. IEEE Ind. Commer. Power Syst. Tech. Conf. – 2012 – P. 1-8. DOI: 10.1109/ICPS.2012.6249671.

206. Chu A. Comparison of commercial supercapacitors and high-power lithium-ion batteries / A. Chu, P. Braatz // J. Power Sources – 2002 – Vol. 102(1) – P. 236-246.

207. Zhang Y. Study of Supercapacitor in the Application of Power Electronics / Y. Zhang, L. Wei, X. Shen, H. Liang // WSEAS Trans. Circuits Syst. – 2009 – Vol. 8(6) – P. 508-517.

208. Jarushi A.M. Battery and supercapacitor combination for a series hybrid electric vehicle / A.M. Jarushi, N. Schofield // Proc. IET Int. Conf. Power Electron. Mach. Drives (PEMD) – 2010 – P. 1-6. DOI: 10.1049/cp.2010.0333.

209. Garcia F.S. Control Strategy for Battery-Ultracapacitor Hybrid Energy Storage System / F.S. Garcia, A.A. Ferreira, J.A. Pomilio // Proc. IEEE Appl. Power Electron. Conf. (APEC) – 2009 – P. 826-832. DOI: 10.1109/APEC.2009.4802783.

210. Choi W.Y. Zero-current soft-switching bidirectional DC-DC converter for high efficiency DC uninterruptible power supply / W.Y. Choi, J.H. Ju, S.J. Park, K.H. Kim, Y.C. Lim // Proc. IEEE Int. Telecommun. Energy Conf. (INTELEC) – 2009 – P. 1-3. DOI: 10.1109/INTLEC.2009.5351905.

211. Ibanez F.M. Anomalous step-up behavior in discontinuous series resonant converters / F.M. Ibanez, J. Vadillo, J.M. Echeverria, L. Fontan // Proc. IEEE Workshop Control Model. Power Electron. (COMPEL) – 2014 – P. 1-6. DOI: 10.1109/COMPEL.2014.6877129.

212. Ibanez F.M. 30kW DC-DC Converter with Regenerative Mode for Electric Cars / F.M. Ibanez, J. Vadillo, M. Martinez-Iturralde, J.M. Echeverria // J. Power Electron. – 2012 – Vol. 12(2) – P. 233-241.

213. Jain A.K. PWM Control of Dual Active Bridge: Comprehensive Analysis and Experimental Verification / A.K. Jain, R. Ayyanar // IEEE Trans. Power Electron. – 2011 – Vol. 26(4) – P. 1215-1227.

214. Pledl G. Theory of operation, design procedure and simulation of a bidirectional LLC resonant converter for vehicular applications / G. Pledl, M. Tauer, D. Buecherl // Proc. IEEE Veh. Power Propuls. Conf. (VPPC) – 2010 – P. 1-5. DOI: 10.1109/VPPC.2010.5729177.

215. Jung J.H. Design Methodology of Bidirectional CLLC Resonant Converter for High-Frequency Isolation of DC Distribution Systems / J.H. Jung, H.S. Kim, M.H. Ryu, J.W. Baek // IEEE Trans. Power Electron. – 2013 – Vol. 28 No.4 – P. 1741-1755.

216. Jung J.H. An efficient isolated bi-directional half bridge resonant DC/DC converter / J.H. Jung, H.S. Kim, M.H. Ryu, J.W. Baek // Proc. IEEE Int. Conf. Sustain. Energy Technol. (ICSET) – 2012 – P. 48-53. DOI: 10.1109/ICSET.2012.6357446.

217. Lee C.Q. Analysis and Design of Series Resonant Converter by State-Plane Diagram / C.Q. Lee, K. Siri // IEEE Trans. Aerosp. Electron. Syst. – 1986 – Vol. 22(6) – P. 757-763.

218. Siri K. Frequency response for the conventional parallel resonant converter based on the state-plane diagram / K. Siri, I. Batarseh, C.Q. Lee // IEEE Trans. Circuits Syst. I – 1993 – Vol. 40(1) – P. 33-42

219. Kheraluwala M.N. Performance characterization of a high-power dual active bridge DC-to-DC converter / M.N. Kheraluwala, R.W. Gascoigne, D.M. Divan, E.D. Baumann // IEEE Trans. Ind. Appl. – 1992 – Vol. 28(6) – P. 1294-1301.

220. Demetriades G.D. Characterisation of the Soft-switched Single-Active Bridge Topology / G.D. Demetriades, H.P. Nee // Proc. IEEE Power Electron. Spec. Conf. (PESC) – 2005 – P. 1947-1951. DOI: 10.1109/PESC.2005.1581909

221. Kazimierczuk M.K. A new phase-controlled parallel resonant converter / M.K. Kazimierczuk, D. Czarkowski, N. Thirunarayan // IEEE Trans. Ind. Electron. – 1993 – Vol. 40(6) – P. 542-552.

222. Chia C.L. A Novel Robust Control Method for the Series-Parallel Resonant Converter / C.L. Chia, E.K.K. Sng // IEEE Trans. Power Electron. – 2009 – Vol. 24(8) – P. 1896-1904.

223. Beiranvand R. A Design Procedure for Optimizing the LLC Resonant Converter / R. Beiranvand, B. Rashidian, M.R. Zolghadri, S.M.H. Alavi // IEEE Trans. Power Electron. – 2012 – Vol. 27(8) – P. 3749-3763.

224. Batarseh I. Generalized approach to the small signal modelling of DC-to-DC resonant converters / I. Batarseh, K. Siri // IEEE Trans. Aerosp. Electron. Syst. – 1993 – Vol. 29(3) – P. 894-909.

225. Sanders S.R. Generalized averaging method for power conversion circuits / S.R. Sanders, J.M. Noworolski, X.Z. Liu, G.C. Verghese // IEEE Trans. Power Electron. – 1991 – Vol. 6(2) – P. 251-259.

226. Ninomiya T. A unified analysis of resonant converters / T. Ninomiya, M. Nakahara, T. Higashi, K. Harada // IEEE Trans. Power Electron. – 1991 – Vol. 6 No.2 – P. 260-270.

227. Witulski A.F. Small signal equivalent circuit modeling of resonant converters / A.F. Witulski, A.F. Hernandez, R.W. Erickson // IEEE Trans. Power Electron. – 1991 – Vol. 6(1) – P. 11-27.

228. Vorperian V. Approximate small-signal analysis of the series and the parallel resonant converters / V. Vorperian // IEEE Trans. Power Electron. – 1989 – Vol. 4(1) – P. 15-24.

229. Vorperian V. Analysis of resonant converters / V. Vorperian // Ph.D. Dissertation, California Inst. Technol. – 1984.

230. dos Santos W.M. Design and conception of a DAB converter using the gyrators theory / W.M. dos Santos, M.S. Ortmann, R. Schweitzer, S.A. Mussa, D.C. Martins // Proc. Brazilian Power Electron. Conf. (COBEP) – 2013 – P. 1-6. DOI: 10.1109/COBEP.2013.6785218.

231. Han B.M. New Bidirectional Intelligent Semiconductor Transformer for Smart Grid Application / B.M. Han, N.S. Choi, J.Y. Lee // IEEE Trans. Power Electron. – 2014. – Vol. 29(8) – P. 4058-4066.

232. Florez-Tapia AM. Small signal modeling and transient analysis of a Trans quasi-Z-source inverter / AM Florez-Tapia, FM Ibanez, J Vadillo, I Elosegui, J.M. Echeverria // Electric Power Systems Research – 2017 – Vol. 144 – P. 52-62

233. Wu T.F. An Improved Resonant Frequency Based Systematic LCL Filter Design Method for Grid-Connected Inverter / T.F. Wu, M. Misra, L.C. Lin, C.W. Hsu // IEEE Trans. Ind. Electron. – 2017 – Vol. 64(8) – P. 6412-6421.

LIST OF FIGURES

Figure 1–Electric charger: (a) using 2-port converters and (b) using a MAB converter (c) partial isolation solution based on non-isolated converter (d) partial isolated resonant DC/AC. 12
Figure 2–Example of a MAB converter: QAB (quad-active bridge) power stage diagram, which can be easily extended to a larger number of ports. 14
Figure 1.3.1–UPS using a tri-port converter [77] 31
Figure 1.3.2–Power Electronic Transformer using multiple port converters [80]..... 32
Figure 1.3.3–Multiple port converter applied to electric grids in planes [86] 33
Figure 2.2.1–Example of a MAB converter: QAB (quad-active bridge) power stage ... 38
Figure 2.2.2–Example of MAB: (a) AC simplified diagram and (b) transformer model39
Figure 2.2.3–Single bridge diagram: (a) waveforms, (b) control logic diagram 40
Figure 2.2.4-Control diagram: (a) (coupling) power stage, (b) decoupling control stage, (c) equivalent current loop diagram and (d) DC power control loop..... 45
Figure 2.2.5–dq-transformation for AC currents 47
Figure 2.2.6–Frequency response plot of (a) the open-loop current loop, $i_{d1}^R/(I_{dREF1}^R - i_{d1}^R)$ and (b) closed-loop transfer function, i_{d1}^R/I_{dREF1}^R. The ideal model is the model which was considered in the design guide with exact decoupling..... 52
Figure 2.2.7–Simulations using DC power control diagram (a) power response after a step in the references and (b) dq-frame currents 53
Figure 2.2.8–Simulation waveforms at different power and voltages: (a) AC voltages, (b) AC currents and (c) DC currents 54
Figure 2.2.9–Prototype 56
Figure 2.2.10–Power step test: (a) Power at three DC powers when the reference changes to several points: P_{DC1},P_{DC2}=[-400W,0W], [200W,200W], [0W,400W], (b) waveforms within the intervals, (c) AC harmonic active and reactive power distribution 57
Figure 2.3.1–TAB: block diagram 61

Figure 2.3.2–Control diagram: (a) (coupling) power stage, (b) decoupling control stage with delays, (c) equivalent current loop diagram and (d) DC power control loop 62
Figure 2.3.3–Control Transfer functions for the conventional dq-frame control with measurement delays: (a) open loop transfer functions, (b) $I_{d\,m}/I_{q\,ref}$ closed loop transfer functions 66
Figure 2.3.4–Decoupling block with compensated reference current 67
Figure 2.3.5–Transfer functions for the dq-frame control, decoupled with the compensated reference currents: (a) Open loop transfer function (b) Closed loop transfer function, (c) $I_{d\,m}/I_{q\,ref}$ closed loop transfer function..... 68
Figure 2.3.6–dq-frame currents simulation results for decoupling with the compensated reference currents: (a) using simple compensator with phase lead compensator, (b) using advanced compensator 69
Figure 2.3.7- Transfer functions for the dq-frame control, decoupled with the advanced compensated reference currents: (a) Closed-loop transfer function, (b) $I_{d\,m}/I_{q\,ref}$ closed loop transfer function 70
Figure 2.3.8–Simulation results: (a) DC powers for port 1-2, (b) transformer currents, (c) transformer voltages..... 72
Figure 2.4.1–(a) proposed dual-duty modulation, (b) control logic diagram for dual-duty modulation including lookup tables 77
Figure 2.4.2–Complete block diagram of the proposed solution. 82
Figure 2.4.3–Conducting and switching losses estimation compared to MCP [22] and PSO [101] (a) at fixed DC voltages ($V_{DC1,2,3}$={900V, 650V 650V} and varying DC powers and (b) at fixed DC powers and varying DC voltage at port 1, while others are at 650V 88
Figure 2.4.4–Simulation waveforms for our approach and PSO [101] for V_{DC1} = 900 V, P_{DC1} = 0 W, P_{DC2} = 5 kW..... 89
Figure 2.4.5–Simulations using DC power control diagram. Power response after a step in the references..... 90
Figure 2.4.6–Efficiency for tests under different DC voltages, compared to MCP and PSO approaches..... 92

Figure 2.4.7–Prototype waveforms for our approach and PSO [101] for V_{DC1} = 220 V, V_{DC1} = V_{DC2} = 150 V, P_{DC1} = P_{DC2} = 300 W, Time base: 10us/div, Port 1 in blue, Port 2 in red, Port 3 in green 94
Figure 2.4.8–Power steps in different directions 94
Figure 3.2.1–Complete block diagram of the proposed solution 98
Figure 3.2.2–Modulation signal and PWM [24] 99
Figure 3.2.3–Phasor representation in the complex plane [24] 102
Figure 3.2.4–$\alpha\beta$-frame and dq-frame coordinate systems [24] 106
Figure 3.3.1–Model of inverter connected to the grid in the $\alpha\beta$-frame coordinate systems [24] 109
Figure 3.3.2–Current-control loop in $\alpha\beta$-frame coordinate systems of a grid-connected inverter [24] 110
Figure 3.3.3–The overall diagram of a single-phase grid-connected bidirectional VSI with an LCL filter employing PR controller 114
Figure 3.3.4–Frequency response of (a) different controllers, (b) the practical PR controller with a varying ωc parameter 116
Figure 3.3.5–Comparison between ideal and practical PR controller with harmonic compensations 118
Figure 3.3.6 The frequency response of the system with β=10 121
Figure 3.3.7–The simulated transient response of the VSI (Rectifier/Inverter operation) with a step change in ($i_{d,ref}$) and ($i_{q,ref}$) with line current i_g (t) error 122
Figure 3.3.8–Harmonic order of the grid side current i_g (t) 122
Figure 3.3.9–Single-phase grid-tied inverter with PR controller in real time simulator 123
Figure 3.3.10–Transient response of the VSI in the PR controller with a step change in line current in real time simulator 124
Figure 3.3.11–Closed loop plot of the system with the grid current feedback in the PR controller ($\beta=10$) in the real-time simulator 125
Figure 3.3.12–The experimental prototype of the system with real loads in the real-time simulator 125

Figure 3.4.1–Basic diagram of the three-phase inverter with proportional resonant converter 127
Figure 3.4.2–Frequency response of PMR current-controlled converter (I_{LS}/error in Figure 4.1) with the impact of the grid impedance for high (6 Ω) and low (0.3 Ω) impedance: (a) using high resonant gains, (b) using reduced gains for a worse case .. 128
Figure 3.4.3–Proposed real-time attenuation algorithm..... 129
Figure 3.4.4–Evolution in time of a single harmonic gains (k_{Ih}) for h=7 following the proposed algorithm [104]. In red, G_{PMR} output of the 7th harmonic, in blue, filtered signal with 100Hz bandwidth and in yellow for 400Hz bandwidth 130
Figure 3.4.5–Simulation of a three-phase grid-connected inverted with the adaptive gain controller..... 131
Figure 3.4.6–Harmonics of the injected current: (a) using only fundamental PR controller, (b) adding harmonic compensator 134
Figure 3.4.7–Simulation with (a) static-gains control, (b) the proposed auto-adjusted technique..... 135
Figure 3.4.8–Experimental setup: (a) front view, three-phase inverter, (b) side view. Rectifier as a non-linear load..... 136
Figure 3.4.9–Injected current, phase A, using: (a) static-gains control, (b) auto-adjusted control 136
Figure 3.5.1– Overview of grid synchronization methods [128]..... 139
Figure 3.5.2–Diagram of a synchronous reference phase-locked loop [118]..... 141
Figure 3.5.3–Example of a PLL open-loop gain..... 144
Figure 3.5.4–Example of a PLL closed-loop gain 144
Figure 3.5.5–Example of a PLL. Time-domain response under a distorted grid. The PLL is able to keep the tracking 145
Figure 3.5.6. Diagram of a synchronous reference phase-locked loop [118]..... 146
Figure 3.5.7–PLL with line impedance effect, the blue line is the PLL without considering the line effect, the red one, considers the line effects, a RHP pole appear, and the system is almost unstable (phase margin almost zero)..... 148

Figure 3.5.8–Time-domain simulation of the PLL tracking with the line impedance effect injecting reactive power 148
Figure 3.5.9–Time-domain simulation of the PLL tracking with the line impedance effect injecting active power 149
Figure 3.5.10–Schematic diagram of a proposed negative feedback PLL, NFPLL [28] 149
Figure 3.5.11–Time-domain simulation of the NFPLL tracking compared with the previous one, the synchronous frame PLL in the same conditions..... 151
Figure 3.5.12–Schematic diagram of an inverter with a current controller in dq-frame [24]..... 152
Figure 3.5.13–Simplified current control loops [24] (iinv d = id and iinv q = iq).... 154
Figure 3.5.14–Complete current control loops [24] (iinv d = id and iinv q = iq, vg d = vs d and vg q = vs q) 154
Figure 3.5.15–Simplified current control loop including phase errors from PLL..... 155
Figure 3.6.1–Full diagram of a three-phase grid-connected inverter with current and voltage control loops and droop control power sharing method..... 158
Figure 3.6.2–Open- and closed-loop transfer functions for the inner current control obtained from Section 3.3 and 3.4..... 159
Figure 3.6.3–Direct form II transpose (DFIIt) structure for digital implementation of a PR controller..... 160
Figure 3.6.4–Voltage-source inverter connected to the grid through a line impedance in a grid-forming mode: (a) Power flow through the line impedance, (b) vector diagram of the power flow 162
Figure 3.6.5–Diagram of the simulations of the inverter grid 165
Figure 3.6.6. Simulation tests of three inverters delivering power the different loads and being connected and disconnected to the system to observe the power sharing, and the harmonic compensation in non-linear loads..... 165
Figure 3.6.7–Frequency in each inverter..... 166
Figure 3.6.8–Power sharing..... 166
Figure 3.6.9–Experiment of two inverters connected in parallel for power sharing 169

Figure 3.6.10–Current and voltage waveforms from real inverters controlled under real-time simulators 169
Figure 3.6.11–Frequency response of each inverter from real-time simulator..... 170
Figure 3.7.1–(a) Typical grid-forming inverter, (b) simplified output circuit..... 175
Figure 3.7.2–(a) Inverter's output power as a function of Z_v and (b) $\theta(t)$- $\varphi(t)$ as a function of Z_v at different output powers 178
Figure 3.7.3–Modified droop control method..... 179
Figure 3.7.4–Simplified grid for inverter connection: (a) grid with a generator and a load, (b) equivalent circuit of the grid, (c) small-signal model of an inverter in droop control connected to the grid 181
Figure 3.7.5–Phase difference transient in the moment of connection..... 186
Figure 3.7.6–Root-locus as a function of (a) filter cut-off frequency (ω_C) (simplified model) eq. (22), (b) filter cut-off frequency (ω_C) (advanced model)..... 188
Figure 3.7.7–Root-locus as a function of (a) total (including virtual) reactance (X_T) at fixed resistance of 0.02, (b) virtual resistance (R_C)..... 189
Figure 3.7.8–Simulation diagram for testing 195
Figure 3.7.9–Simulations: inverter 1 connected at 0s change from fixed frequency to droop mode in 0.1s, inverter 2 connected at 0.3s, utility grid connected at 0.7s..... 197
Figure 3.7.10–Experimental Setup for validation (a) set-up (b) main diagram..... 198
Figure 3.7.11–Inverters connection with (a) filter cut-off frequency of 5 rad/s, (b) filter cut-off frequency of 10 rad/s and (c) filter cut-off frequency of 100 rad/s..... 199
Figure 3.7.12. Settling time with respect to power filter cut-off frequency 200
Figure 3.7.13–Inverters connection with (a) no angle limitation (b) angle limitation of 25 ^{o}, (c) angle limitation of 10°..... 201
Figure 3.7.14–Virtual resistance adjustment during inverter connection providing soft start operation 202
Figure 3.7.15–Inverters connection with (a) R_V = 0.1 Ω, X_V = 2 Ω, (b) R_V = 0.3 Ω, X_V = 2 Ω. at angle limitation of 10° 203
Figure 3.7.16–Two-inverter based microgrid connected to the main grid..... 205
Figure 3.8.1–Power through a power line: (a) circuit diagram, (b) phasor diagram 211

Figure 3.8.2–Inverter with an adaptive virtual impedance controller 213
Figure 3.8.3–Power line – Low Bandwidth Communication (PL-LBC) Scheme 216
Figure 3.8.4–Simulink model 221
Figure 3.8.5–Open-loop transfer function $(q_2 - q_1)/error(s)$, for several communication delays. Approximate model in continuous line, markers are the simulations points in the Simulink model 222
Figure 3.8.6–(a) Active and (b) Reactive powers under normal operation (No signal loss) 223
Figure 3.8.7–(a) Active and (b) Reactive powers with 50% signal loss 225
Figure 3.8.8–(a) Active and (b) Reactive powers with 80% signal loss 226
Figure 3.8.9–Experimental Test Setup 227
Figure 3.8.10–Experimental demonstration of proposed power line communication technique 229
Figure 3.8.11–Experimental demonstration of proposed power line communication technique, blue: injected communication signal by inverter 1, orange: detected signal by inverter 2 229
Figure 3.8.12. (a) Active power output of both inverters, (b) Reactive power of both inverters, no reactive power control. 230
Figure 3.8.13–(a) Frequency of both inverters, (b) Voltage magnitude of both inverters, without reactive power control. 231
Figure 3.8.14–(a) Active power output of both inverters, (b) Reactive power of both inverters, with reactive power control 232
Figure 3.8.15. (a) Frequency of both inverters, (b) Voltage magnitude of both inverters, with reactive power control. 232
Figure 4.1–Electric charger using partial isolation solution based on non-isolated converter 234
Figure 4.1.1–Proposed converter (a) topology, (b) interval D_2T and (b) interval $(1-D_2)T$ 236
Figure 4.1.2–Step-up mode: (a) Port 1 delivers power to port 3, (b) port 2 delivers power to port 3, $v_{GS3}=v_{GS5}$ 239

Figure 4.1.3–Step-up mode: port 1 delivers power to port 2, v_{GS3}=v_{GS5} 240
Figure 4.1.4–Step-down mode: Port 2 absorbs power from port 3, v_{GS3}=v_{GS5} 242
Figure 4.1.5–Step-down mode, (a) port 1 absorbs power from port 3 and (b) port 2 delivers power to port 1, v_{GS3}=v_{GS5} 243
Figure 4.1.6–Main controller basic diagram 245
Figure 4.1.7–Frequency response for (a) the output voltage and (b) input current as a function of the duty cycle D_2 247
Figure 4.1.8–Control diagram for different strategies: (a) to charge the battery at constant voltage keeping SC and battery within the voltage limits, (b) to charge the SC with the battery keeping the output voltage constant and limiting the battery current. 249
Figure 4.1.9–Prototype photograph 253
Figure 4.1.10–Waveforms 254
Figure 4.1.11–Open-loop transfer function from V_2 to V_3 254
Figure 4.1.12–Step-load response (a) boost mode, (b) buck mode 255
Figure 4.1.13–Efficiency at both buck and boost mode 256
Figure 4.1.14–Conversion gain ratio (a) boost mode, (b) buck mode 256
Figure 4.2.1–Series-resonant DC/DC converter with transformer 260
Figure 4.2.2–Bidirectional DC/DC series resonant circuit (a) double full bridge schematic, with new proposed rectifier (b) simplified circuit 261
Figure 4.2.3–Waveforms for the reduction mode for different cases (a) case 1, (b) case 2, (c) case 3 264
Figure 4.2.4–Voltage conversion ratio, *M*, as a function of the *x*-variable and parametrized for different λ 267
Figure 4.2.5–Waveforms for the step-up mode for different cases (a) case 1, (b) case 2, (c) case 3 269
Figure 4.2.6–Transfer voltage gain for different normalized load resistance at λ =0.079 271
Figure 4.2.7–Efficiency of the converter at different λ and loads for (a) step-down and (b) step-up modes versus *x* and efficiency versus *M* in step-up mode 274
Figure 4.2.8–Prototype 275

Figure 4.2.9–Efficiency (a) Discharging process (b) charging process, constant I_{1BUS} current = 10A (V_{1BUS}=V_{1DC}) 276
Figure 4.2.10–Resonant branch waveforms 276
Figure 4.2.11–Measurement and simulation of voltage conversion ratio, M 277
Figure 4.2.12–Static measurements: voltage conversion ratio as a function of normalized frequency, F, for (a) M1/3 mode, (b) M2/5 mode 279
Figure 4.2.13–(a) Analytical model for efficiency curves, at maximum power (6 kW), compared with measurements in both power directions (the filled markers are measurements that transfer power from low to high voltage and the non-filled markers are measurements that transfer the power in the other direction), F is in grey and (b) Comparison with the M1/2 (normal step-up) mode in the same prototype 280
Figure 4.2.14- Voltage conversion gain in the anomalous light load condition in step-down mode 281
Figure 4.3.1–DC/DC converter: (a) schematic, (b) waveforms, (c) simplified 285
Figure 4.3.2–State-plane representation of the step-up SRC (R_{LOSS}=0) 287
Figure 4.3.3–Normalized voltage conversion ratio, m versus f_s/f_0 for different quality factors (Q) 289
Figure 4.3.4–Normalized voltage conversion ratio, m versus f_s/f_0 including R_{LOSS} for R=Z_0 290
Figure 4.3.5–Output characteristics of a step-up SRC 290
Figure 4.3.6–Angle of the transfer arcs (α and β) versus F, r=1 291
Figure 4.3.7–Prototype 294
Figure 4.3.8–DC characteristics 295
Figure 4.3.9. M1 and M7 switching waveforms for full-load condition. 296
Figure 4.3.10–M1 and M7 switching waveforms for light load condition 297
Figure 4.3.11– Control-to-output transfer function for several static points 298
Figure 4.3.12–Control diagram 298
Figure 4.3.13–Control-to-output transfer function modeled for the prototype 299
Figure 4.3.14– Efficiency 301
Figure 4.4.1– Electric charger partial isolated resonant DC/AC 304

Figure 4.4.2. Proposed bidirectional DC/AC converter: (a) circuit, (b) simplified circuit for low and high frequency. 306
Figure 4.4.3. Simplified circuits for each time interval: (a) when the bridges transfer currents, (b) when the energy is delivered to v_0. 310
Figure 4.4.4– Waveforms in discharge mode 310
Figure 4.4.5–Waveforms in the charge mode 311
Figure 4.4.6– Output voltage as a function of the input reference for two cases 317
Figure 4.4.7–Control diagram 320
Figure 4.4.8–Power losses and distortion comparison for MHF=10 323
Figure 4.4.9–Charging and discharging input source at constant power: (a) discharging process, (b) detail of the discharging process 325
Figure 4.4.10–(a) Charging input source at constant power, (b) detail of the charging process 326
Figure 4.4.11–Total harmonic distortion (THD) as a function of the power at the AC link for several input voltages V_i=V_{DC1} 327
Figure 4.4.12–Delivering and absorbing active and reactive power to/from the grid 327
Figure 4.4.13–Prototype 328
Figure 4.4.14–Experimental results, main waveforms of (a) discharging mode, (b) charging mode 329
Figure 4.4.15–Transferring active and reactive power to/from the grid: (a) complete cycle, detail for (b) 3kW active 330
Figure 4.4.16–Efficiency 332

LIST OF ACRONYMS AND ABREVIATIONS

Acronym	Description
A	
AC	Alternating Current
ADC	Analog-to-Digital Converter
AI	Artificial Intelligence
ANF	Adaptive Notch Filter
C	
CAN-BUS	Controller Area Network Bus
CCM	Continuous Conduction Mode
CL Tf	Closed-Loop Transfer Function
CP	Cut-off Frequency (ω_C)
D	
DAB	Dual Active Bridge (Converter)
DC	Direct Current
DCM	Discontinuous Conduction Mode
DG	Distributed Generator
DGs	Distributed Generators
DFT	Discrete Fourier Transform
DPS	Double-Phase-Shift (Modulation)
DQ	Direct-Quadrature (Frame)
DSC	Delayed Signal Cancellation
DSOGI-FLL	Dual Second-Order Generalized Integrator Frequency-Locked Loop
DSP	Digital Signal Processor
E	
EPS	Extended-Phase-Shift (Modulation)

ESR	Equivalent Series Resistance
EV	Electric Vehicle
F	
FHA	First Harmonic Approximation
FLL	Frequency-Locked Loop
FM	Frequency Modulation
FSK	Frequency Shift Keying
G	
G2V	Grid-to-Vehicle
H	
HC	Harmonic Compensator
HESS	Hybrid Energy Storage System
HF	High Frequency
I	
IEC	International Electrotechnical Commission
IEEE	Institute of Electrical and Electronics Engineers
IGBT	Insulated-Gate Bipolar Transistor
K	
kHz	Kilohertz (frequency)
L	
LC	Inductor-Capacitor (Filter)
LCL	Inductor-Capacitor-Inductor (Filter)
LF	Low Frequency
LLC	Inductor-Inductor-Capacitor (resonant converter)
LPF	Low-Pass Filter
L-r	Inductor-resistor (Filter)
LV	Low Voltage (grid)
M	
MAB	Multiple Active Bridge (Converter)

MCP	Minimum Current Point (optimization technique)
MCU	Microcontroller Unit
MOSFET	Metal-Oxide-Semiconductor Field-Effect Transistor
N	
NFPLL	Negative Feedback Phase-Locked Loop
NLS	Nonlinear Least Square
NPC	Neutral Point Clamped (topology)
O	
OL Tf	Open-Loop Transfer Function
P	
PCC	Point of Common Coupling
PFC	Power Factor Correction
PET	Power Electronic Transformer
PI	Proportional-Integral (Controller)
PLL	Phase-Locked Loop
PL-LBC	Power Line Low-Bandwidth Communication
PM	Phase Margin
PMR	Proportional Multi-Resonant (Controller)
PR	Proportional-Resonant (Controller)
PSK	Phase Shift Keying
PSO	Particle Swarm Optimization
PV	Photovoltaic (panels)
PWM	Pulse Width Modulation
Q	
QAB	Quad-Active Bridge (converter)
QAM	Quadrature Amplitude Modulation
R	
RES	Renewable Energy Sources
RHP	Right-Half Plane (en análisis de estabilidad)

RMS	Root Mean Square (current/voltage)
RS485	Recommended Standard 485 (communication protocol)
S	
SC	Supercapacitor
SiC	Silicon Carbide
SISO	Single-Input Single-Output
SPS	Single-Phase-Shift (modulation)
SRC	Series Resonant Converter
SVM	Space Vector Modulation
T	
TAB	Triple Active Bridge (converter)
THD	Total Harmonic Distortion
TPS	Triple-Phase-Shift (Modulation)
U	
UPS	Uninterruptible Power Supply
V	
V2G	Vehicle-to-Grid
VAC	AC Voltage
VDC	DC Voltage
VSC-HVDC	Voltage-Source Converter High-Voltage Direct Current
VSI	Voltage Source Inverter
X	
X/R	Reactance-to-Resistance ratio
Z	
ZCD	Zero-Crossing Detection
ZOH	Zero-Order Hold
ZSI	Impedance Source Inverter
ZVS	Zero-Voltage Switching
αβ	

αβ	Alpha-Beta (Frame, Clarke Transformation)

ACKNOWLEDGEMENTS

First and foremost, I would like to express my gratitude to my supervisor, Prof. Abakumov, for his support throughout my years at Skoltech.

I sincerely appreciate the time and effort invested by my dissertation committee members in reviewing my work. In addition, my gratitude to Dr. Grigory Kopelevich for his time and patience discussing formalities of the dissertation.

My heartfelt thanks go to my colleagues at Skolkovo Institute of Science and Technology—Mr. Yaroslav Vlasov, Mr. Ildar Idrisov, Dr. Mikhail Pugach, and Mr. Mikhail Afonin—for their camaraderie, stimulating discussions, and technical assistance. I am equally grateful to my international collaborators and friends—Dr. Fernando Martín, Dr. Vedran Perić, Dr. Vladimir Teržija, Dr. Ainhoa Galarza, Dr. José Martín Echeverría, and Dr. Luis Fontán—for their intellectual contributions to many fruitful discussions.

Special recognition goes to my students—Anna Shubnaya, Ilya Verennikov, Dr. Fernando Dávalos, Mahmoud AlSadat, Ahmad Ali Nazeri, and many others—with whom I worked side by side in the laboratory. I am particularly indebted to Dr. Francisco Piero Diodati, who served as my research mentor for several years.

This research would not have been possible without the support of the Center for Energy Science and Technology, the Skoltech internal grant "Energy Hub," and the Megagrant AMPaC.

To my family—my loving wife for her unconditional support and sacrifices, my mother for teaching me how to realize objectives, my father for inspiring me to pursue this path, and my brothers for their encouragement from afar—I owe my deepest personal gratitude.

To my friends, thank you for keeping me grounded and reminding me of life beyond research. Finally, I acknowledge the countless researchers whose pioneering work laid the foundation for this study. Any errors or omissions in this dissertation remain my sole responsibility.